# Regional $CO_2$ Flux Estimates for South Africa through Inverse Modelling




Alecia Nickless

Department of Statistical Sciences

University of Cape Town

A thesis submitted for the degree of

*Doctor of Philosophy*

February 2018

## Plagiarism Declaration

This thesis has been submitted to the Turnitin module and I confirm that my supervisor has seen my report and any concerns revealed by such have been resolved with my supervisor.

I hereby declare that all the work presented in this thesis, titled "*Regional $CO_2$ flux estimates for South Africa through inverse modelling*", is my own, except where otherwise stated in the text. This thesis has not been submitted in whole or in part for a degree at any other university.

SIGNATURE: Signed by candidate DATE: 16/02/2018

STUDENT NAME: Alecia Nickless STUDENT NUMBER: KRTALEC02

This thesis is dedicated

To my parents,
Walter Henry Kirton and Theone Valecia Kirton,
who have always supported me, and who sacrificed so much so that I could have all the opportunities in the world.

To my husband,
David Reginald Nickless,
who supported me, fed me, and tolerated me during these long PhD years.

To Prof. Peter Rayner,
without whom I could not have completed this PhD. Peter has been a constant source of encouragement, and has been a guiding light even during the darkest times. I would not have made it to the end of this journey without your kindness and motivation. Thank you.

# Acknowledgements

This PhD was made possible by many small - some much larger - commitments from people who did not have to say yes, but did anyway.

I would like to thank Karen Small of the Strategic Development Information and Geographic Information System Department of the City of Cape Town for providing the Western Cape census shape files, and Sarah Ward and Ed Filby of the City of Cape Town for providing access to emission data collected by the City of Cape Town.

I would like to thank and acknowledge Dr. Thomas Lauvaux for the helpful discussion on the implementation and post processing of the LPDM, and for useful discussion on the boundary contribution in the inversion; and Marek Uliasz for providing access to the code for his LPDM model.

I would like to thank and acknowledge Dr. Tilo Ziehn for useful discussion on the post-processing of the LPDM particle counts.

I would like to thank Dr. Francois Engelbrecht of the CSIR for providing the CCAM outputs required to run the LPDM model.

I would like to thank Laurie Butgereit for participating in the fun side-project where we managed to get the Picarro's at Robben Island and Hangklip to send tweets on the current $CO_2$ concentrations.

I would like to acknowledge and thank Ernst-Günther Brunke, Dr. Casper Labuschagne and Danie van der Spuy of the South African Weather Service for their assistance in maintaining the instruments at Robben Island and Hangklip, and Dr. Casper Labuschagne for his guidance on processing the instantaneous $CO_2$ concentration data; Dr. Martin Steinbacher for

providing guidance and schematics on the calibration system used on the Picarro instruments; Robin Poggenpoel and Jacobus Smith of Transnet for allowing us access to the lighthouses; Peter Saaise of Transnet, the Robben Island lighthouse keeper, (and his daughter) for assisting when the instrument was not responding; Keith Moir, Rooi Els, for providing wind data near Hangklip. I would like to give additional thanks to Ernst Brunke for his constant encouragement and enthusiasm for this project.

Use was made of the University of Cape Town ICTS-HPC cluster. Please see `http://hpc.uct.ac.za/` for details. I would like to thank Andrew Lewis of the University of Cape Town HPC facility for providing useful advice on improving the efficiency of the Python runs.

This research was funded by competitive parliamentary grant funding from the Council of Scientific and Industrial Research awarded to the Global Change Competency Area towards the development of the Variable-Resolution Earth System Model (VRESM; Grants EEGC030 and EECM066) and for investigating the implementation of a Bayesian atmospheric inversion framework for South Africa (Grant JECOS81). Additional funding was obtained from the South African National Research Foundation for the Picarro instrumentation.

I would like to thank and acknowledge my supervisors: Prof. Peter Rayner, Prof. Bob Scholes, Dr. Birgit Erni, and Prof. Les Underhill.

I would like to acknowledge and thank Prof. Bob Scholes for teaching me about $CO_2$ fluxes, letting me near very expensive equipment, and starting me off on this Inverse Modelling adventure. Working in the field of carbon science has opened the world to me. It allowed me to meet incredible scientists from all over the world. I got to visit places in Africa I never would have otherwise, and in the time I was working at the CSIR, I was lucky enough to visit five different continents. Not least of all, I got to spend a gloriously large amount of my time in the Kruger National Park.

I would like to thank the University of Melbourne for allowing me the opportunity to visit Prof. Peter Rayner, who subsequently signed on as my co-supervisor. This opportunity allowed me the chance to establish the necessary skills in coding required for the implementation of the inversion, and to rapidly become acquainted with the area of Bayesian inverse modelling. The collaboration and support received from Prof. Peter Rayner during the time that has followed have been invaluable and instrumental to the successful completion of this PhD project.

On a personal note, I would like to thank: My family and friends for their support and encouragement, and for their forgiveness of my absence from many special occasions; My church family at Aldersgate Methodist Church for their constant encouragement and the Almighty for providing me with the strength and perseverance to endure, even when things were hard, with no end in sight; To Ly-Mee Yu for pushing me to get to the end; To J.R.R Tolkien for The Lord of the Rings, my PhD road map and trusted source of wisdom; To Elvis Presley, Roy Orbison and Tomaso Albinoni for providing the soundtrack to this PhD; To Jonathan Brandis for inspiring me to take up a life of science, even if it was for all the wrong reasons; And, of course, to my cat, Claw, for keeping me company through it all.

# Abstract

Bayesian inverse modelling provides a top-down technique of verifying emissions and uptake of carbon dioxide ($CO_2$) from both natural and anthropogenic sources. It relies on accurate measurements of $CO_2$ concentrations at appropriately placed sites and "best-guess" initial estimates of the biogenic and anthropogenic emissions, together with uncertainty estimates. The Bayesian framework improves current estimates of $CO_2$ fluxes based on independent measurements of $CO_2$ concentrations while being constrained by the initial estimates of these fluxes.

Monitoring, reporting and verification (MRV) is critical for establishing whether emission reducing activities to mitigate the effects of climate change are being effective, and the Bayesian inverse modelling approach of correcting $CO_2$ flux estimates provides one of the tools regulators and researchers can use to refine these emission estimates. South Africa is known to be the largest emitter of $CO_2$ on the African continent. The first major objective of this research project was to carry out such an optimal network design for South Africa. This study used fossil fuel emission estimates from a satellite product based on observations of night-time lights and locations of power stations (Fossil Fuel Data Assimilations System (FFDAS)), and biogenic productivity estimates from a carbon assessment carried out for South Africa to provide the initial $CO_2$ flux estimates and their uncertainties. Sensitivity analyses considered changes to the covariance matrix and spatial scale of the inversion, as well as different optimisation algorithms, to assess the impact of these specifications on the optimal network solution. This question was addressed in Chapters 2 and 3.

The second major objective of this project was to use the Bayesian inverse modelling approach to obtain estimates of $CO_2$ fluxes over Cape Town and surrounding area. I collected measurements of atmospheric $CO_2$ concentrations from March 2012 until July 2013 at Robben Island

and Hangklip lighthouses. CABLE (Community Atmosphere Biosphere Land Exchange), a land-atmosphere exchange model, provided the biogenic estimates of $CO_2$ fluxes and their uncertainties. Fossil fuel estimates and uncertainties were obtained by means of an inventory analysis for Cape Town. As an inventory analysis was not available for Cape Town, this exercise formed an additional objective of the project, presented in Chapter 4. A spatially and temporally explicit, high resolution surface of fossil fuel emission estimates was derived from road vehicle, aviation and shipping vessel count data, population census data, and industrial fuel use statistics, making use of well-established emission factors.

The city-scale inversion for Cape Town solved for weekly fluxes of $CO_2$ emissions on a 1 km $\times$ 1 km grid, keeping fossil fuel and biogenic emissions as separate sources. I present these results for the Cape Town inversion under the proposed best available configuration of the Bayesian inversion framework in Chapter 5. Due to the large number of $CO_2$ sources at this spatial and temporal resolution, the reference inversion solved for weekly fluxes in blocks of four weeks at a time. As the uncertainties around the biogenic flux estimates were large, the inversion corrected the prior fluxes predominantly through changes to the biogenic fluxes. I demonstrated the benefit of using a control vector with separate terms for fossil fuel and biogenic flux components.

Sensitivity analyses, solving for average weekly fluxes within a monthly inversion, as well as solving for separate weekly fluxes (i.e. solving in one week blocks) were considered. Sensitivity analyses were performed which focused on how changes to the prior information and prior uncertainty estimates and the error correlations of the fluxes would impact on the Bayesian inversion solution. The sensitivity tests are presented in Chapter 6. These sensitivity analyses indicated that refining the estimates of biogenic fluxes and reducing their uncertainties, as well as taking advantage of spatial correlation between areas of homogeneous biota would lead to the greatest improvement in the accuracy and precision of the posterior fluxes from the Cape Town metropolitan area.

## Inclusion of Publications in Thesis

I confirm that I have been granted permission by the University of Cape Town's Doctoral Degrees Board to include the following publications in my PhD thesis, and where co-authorships are involved, my co-authors have agreed that I may include the publications:

**Chapter 2**: Nickless, A., Ziehn, T., Rayner, P. J., Scholes, R. J., and Engelbrecht, F.: Greenhouse gas network design using backward Lagrangian particle dispersion modelling – Part 2: Sensitivity analyses and South African test case, **Atmos. Chem. Phys.**, 15, 2051-2069, doi: 10.5194/acp-15-2051-2015, 2015.

**Chapter 3**: Nickless, A., Rayner, P. J., Erni, B., and Scholes, R. J.: Comparison of the genetic algorithm and incremental optimisation routines for a Bayesian inverse modelling based network design, **Inverse Probl.**, in review.

**Chapter 4:** Nickless, A., Scholes, R.J., Filby, E.: Spatial and temporal disaggregation of anthropogenic $CO_2$ emissions from the City of Cape Town. **S. Afr. J. Sci.**, 111(11/12), Art. #2014-0387, doi: 10.17159/sajs.2015/20140387, 2015.

**Chapter 5**: Nickless, A., Rayner, P. J., Engelbrecht, F., Brunke, E.-G., Erni, B., and Scholes, R. J.: Estimates of $CO_2$ fluxes over the City of Cape Town, South Africa, through Bayesian inverse modelling, **Atmos. Chem. Phys. Discuss.**, https://doi.org/10.5194/acp-2017-604, in review, 2017.

**Chapter 6:** Nickless, A., Rayner, P. J., Engelbrecht, F., Erni, B., and Scholes, R. J.: An atmospheric inversion over the City of Cape Town: sensitivity analyses, **Atmos. Chem. Phys.**, in preparation.

SIGNATURE: _____ DATE: 16/02/2018

STUDENT NAME: Alecia Nickless STUDENT NUMBER: KRTALE002

SEEC - Statistics in Ecology, Environment and Conservation

## Author contribution statement – Chapter 2

### Manuscript

Nickless, A., Ziehn, T., Rayner, P. J., Scholes, R. J., and Engelbrecht, F.: Greenhouse gas network design using backward Lagrangian particle dispersion modelling – Part 2: Sensitivity analyses and South African test case, Atmos. Chem. Phys., 15, 2051-2069, doi: 10.5194/acp-15-2051-2015, 2015.

### Author contributions

I (Alecia Nickless) designed the study, set up and ran the Lagrangian particle dispersion model (LPDM) for South Africa, and performed all the inversions in python, including coding the matrix multiplication to run on two different computing systems. I adopted the algorithm by Seibert and Frank (2004) to incorporate the particle counts from the Lagrangian particle dispersion model to derive sensitivities of the modelled concentrations to the surface fluxes for the South African case, as well as exporting the appropriate particle counts for boundary influence. This was verified by Dr. Tilo Ziehn and Prof. Peter Rayner. I wrote the manuscript in full, created all figures and tables, and had comments from all authors on the structure and presentation of the results.

Dr. Francois Engelbrecht provided the output from the CCAM regional climate model. Prof. Bob Scholes provided estimates of the terrestrial carbon fluxes. Prof. Peter Rayer provided overall supervision of the inversion work, contributed to the design of the study, verified the inversion code, assisted in verifying the results of the Lagrangian particle dispersion model, reviewed the inversion theoretical framework presented in the paper, and contributed to the manuscript revisions.

Date: 8 January 2018

Dr. Tilo Ziehn

Prof. Peter J. Rayner

Dr. Francois Engelbrecht

Prof. Robert J. Scholes

SEEC - Statistics in Ecology, Environment and Conservation

## Author contribution statement – Chapter 3

### Manuscript

Nickless, A., Rayner, P. J., Erni, B., and Scholes, R. J.: Comparison of the genetic algorithm and incremental optimisation routines for a Bayesian inverse modelling based network design, Inverse Probl., in review.

### Author contributions

I (Alecia Nickless) designed the study, set up and ran the Lagrangian particle dispersion model (LPDM) for South Africa, and performed all the inversions in python, including coding the matrix multiplication to run on two different computing systems, and adapted the code for the different scenarios considered. I wrote the manuscript in full, created all figures and tables, and had comments from all authors on the structure and presentation of the results.

Prof. Bob Scholes provided estimates of the terrestrial carbon fluxes and advised on presentation of the results. Dr. Birgit Erni provided statistical supervision of the measures of dissimilarity presented in the manuscript. Prof. Peter Rayer provided overall supervision of the inversion work, contributed to the design of the study, reviewed the inversion theoretical framework presented in the paper, and contributed to the manuscript revisions.

Date: 3 January 2018

Prof. Peter J. Rayner

Dr. Birgit Erni

Prof. Robert J. Scholes

SEEC – Statistics in Ecology, Environment and Conservation

## Author contribution statement – Chapter 4

### Manuscript

Nickless, A., Scholes, R.J., Filby, E.: Spatial and temporal disaggregation of anthropogenic $CO_2$ emissions from the City of Cape Town. S. Afr. J. Sci., 111(11/12), Art. #2014-0387, doi: 10.17159/sajs.2015/20140387, 2015.

### Author contributions

I (Alecia Nickless) designed the study, downloaded all publicly available activity data, researched the emission conversion equations, and converted the activity data into emissions of $CO_2$. I derived all the error propagation equations, and created all figures and tables.

Prof. Bob Scholes provided overall supervision of the project and provided advice on the presentation of results. Ed Filby provided fuel usage data for the industrial point sources, and commented on the final manuscript.

Date: 8 January 2018

Prof. Robert J. Scholes

Ed Filby

SEEC - Statistics in Ecology, Environment and Conservation

## Author contribution statement – Chapter 5

### Manuscript

Nickless, A., Rayner, P. J., Engelbrecht, F., Brunke, E.-G., Erni, B., and Scholes, R. J.: Estimates of $CO_2$ fluxes over the City of Cape Town, South Africa, through Bayesian inverse modelling, Atmos. Chem. Phys. Discuss., https://doi.org/10.5194/acp-2017-604, in review, 2017.

### Author contributions

I (Alecia Nickless) designed the study, adapted the python code to perform the inversion at the city scale for Cape Town and to run on the UCT HPC computing facility, installed the instrumentation and performed regular maintenance, and obtained all measurements at the Robben Island and Hangklip sites. I processed the measurements from Cape Point to be used as background concentrations in the inversion. I processed all the instantaneous measurements of $CO_2$ to obtain hourly measures. I adapted and ran the Lagrangian particle dispersion model for the city scale Cape Town inversion. I reprojected and rescaled the estimates of net ecosystem exchange and net primary productivity from the CABLE model, and converted the inventory $CO_2$ estimates from Chapter 4 to be used as prior estimates of the fossil fuel fluxes. I wrote the full manuscript, and created all figures and tables.

Prof. Peter Rayner provided overall supervision of the project, particularly on the Bayesian inversion theoretical framework. Dr. Francois Engelbrecht provided the output from the CCAM regional climate model. Ernst-Günther Brunke provided assistance in the installation and maintenance of the equipment, and provided the Cape Point $CO_2$ measurements. Dr. Birgit Erni provided supervision on statistical aspects of the manuscript, and Prof. Bob Scholes contributed to the conception of the inversion over City of Cape Town project and provided supervision on the interpretation of the biogenic flux estimates.

Date: 3 January 2018

Prof. Peter J. Rayner

Dr. Francois Engelbrecht

Ernst-Günther Brunke

Dr. Birgit Erni

Prof. Robert J. Scholes

SEEC - Statistics in Ecology, Environment and Conservation

## Author contribution statement – Chapter 6

### Manuscript

Nickless, A., Rayner, P. J., Engelbrecht, F., Erni, B., and Scholes, R. J.: An atmospheric inversion over the City of Cape Town: sensitivity analyses, Atmos. Chem. Phys., in preparation.

### Author contributions

I (Alecia Nickless) designed the study, adapted the inversion code for all scenarios and performed all inversions, downloaded and reprojected the ODIAC fossil fuel product, reprojected the terrestrial carbon assessment products for net ecosystem exchange and net primary productivity, preformed all sensitivity analyses, and created all plots and tables in the manuscript.

Prof. Peter Rayner provided overall supervision of the project, particularly on the Bayesian inversion theoretical framework. Dr. Francois Engelbrecht provided the output from the CCAM regional climate model. Ernest Brunke provided assistance in the installation and maintenance of the equipment, and provided the Cape Point $CO_2$ measurements. Dr. Birgit Erni provided supervision on statistical aspects of the manuscript, and Prof. Bob Scholes contributed to the conception of the inversion over City of Cape Town project and provided supervision on the interpretation of the biogenic flux estimates.

Date: 3 January 2018

Prof. Peter J. Rayner

Dr. Francois Engelbrecht

Dr. Birgit Erni

Prof. Robert J. Scholes

# Contents

# List of Figures

# Project Summary

Bayesian inverse modelling provides a top-down technique of verifying emissions and uptake of carbon dioxide ($CO_2$) from both natural and anthropogenic sources. It relies on accurate measurements of $CO_2$ concentrations at suitably located sites which can collect information about these sources at different spatial and temporal scales. The concentration measurements on their own are not sufficient to solve for the emission sources as there are many more sources of $CO_2$ than there are measurements of the concentrations. Therefore well-informed initial estimates of the biogenic and anthropogenic emissions are required, together with uncertainty estimates, which are used to regularise the problem. The Bayesian framework allows the estimates of the fluxes of $CO_2$ to depend on the independent measurements of $CO_2$ concentrations while being constrained by the initial estimates of these sources. In effect, the Bayesian inverse solution provides corrected estimates of the initial information so that the modelled concentrations better align with the observed concentrations. This approach has been used to estimate global, continental, regional and more recently city-scale fluxes of $CO_2$.

Monitoring, reporting and verification (MRV) is critical for establishing whether emission-reducing activities to mitigate the effects of climate change are being effective, and the Bayesian inverse modelling approach of correcting $CO_2$ flux estimates provides one of the tools regulators and researchers can use to refine these source estimates. South Africa is known to be the largest emitter of $CO_2$ on the African continent. Earlier attempts at obtaining regional estimates of $CO_2$ have identified the Southern Hemisphere, particularly sub-Saharan Africa, as a region requiring additional measurements of $CO_2$ to better constrain estimates. Currently the large uncertainty in the $CO_2$ fluxes leads to global inversions that produce hugely varying estimates for South America and southern Africa if assumptions are only slightly altered (such as the size and shape of the regions) as there are insufficient measurements to provide correction to the initial estimates for these regions. As the available measurements in these regions is sparse, the uncertainty of the resulting estimates remains large.

To remedy this situation, and ultimately provide better estimates of $CO_2$ sources and sinks at least in South Africa, additional measurement capacity has been secured. Therefore, the first major objective of this PhD study was to optimise the placement of these five new instruments for the purpose of observing the total national $CO_2$ flux of South Africa. To maximise the information gain from observations made with the

newly acquired measurement equipment, site selection for these devices needs to be carefully considered. One way of doing this is to make use of the posterior covariance matrix produced by a Bayesian inversion. No information is required about the concentration measurements. Estimates are required of the prior flux uncertainty and error in the modelled concentrations, and the sensitivity matrix which relates the surface fluxes to the concentrations observed at each of the hypothetical measurement sites. In my optimal network design, historical output from a regional climate model CCAM (Conformal Cubic Atmospheric Model) (based on good quality climate reanalysis data) coupled to a Lagrangian particle dispersion model (LPDM) was used to produce a sensitivity matrix which could be used to assess how much uncertainty in the initial flux estimates would be resolved if a site was placed in any of the hypothetical locations within the domain of interest. An optimisation algorithm was then used to determine the placement of sites that would result in the greatest reduction in uncertainty.

As prior estimates, I used fossil fuel flux estimates from a satellite product based on observations of night-time lights and locations of power stations, and biogenic flux estimates from an assessment of terrestrial carbon stocks carried out for South Africa. I considered several sensitivity analyses to determine how changes to the covariance matrix, the spatial scale for the fluxes solved for by the inversion, the heights for the surface layer, as well as to the optimisation algorithm, impacted on the optimal network solution.

Having used a Bayesian framework to solve for uncertainties at the national level, I next set out to implement a similar framework to constrain flux estimates with atmospheric observations for a small region in South Africa. The second major objective of this project was to use the Bayesian inverse modelling approach to obtain estimates of $CO_2$ fluxes over the City of Cape Town and surrounding area. A city-scale inversion was selected to ensure that measurements were feasible within the confines of a PhD project. I collected measurements of atmospheric $CO_2$ concentrations, by means of Picarro Cavity Ring-down Spectroscopy (CRDS) analysers, from March 2012 until July 2013 at Robben Island and Hangklip lighthouses. CCAM, this time run at a much higher resolution of 1 km $\times$ 1 km over the Cape Town, provided the climate inputs. CCAM was coupled to CABLE (Community Atmosphere Biosphere Land Exchange), a land-atmosphere exchange model, which provided the biogenic estimates of $CO_2$ fluxes and their uncertainties. Fossil fuel estimates and uncertainties were obtained by means of an inventory analysis for the City of Cape Town. As an inventory analysis was not available for Cape Town, this exercise formed an additional

objective of the project. A spatially and temporally explicit, high resolution surface of fossil fuel emission estimates was derived from road vehicle, aviation and shipping vessel count data, population census data, and industrial fuel use statistics, making use of well-established emission factors.

Both the national and city-scale Bayesian inversion frameworks can be considered mesoscale inversions, and solve for gridded fluxes in a defined limited domain. The grid sizes differed according to the resolution of the regional climate model run for each of these applications. The spatial resolution of the regional climate model has a large impact on the transport model's ability to accurately model a concentration at a measurement site. Higher resolutions lead to reduced aggregation errors, but finer scaled atmospheric transport is more uncertain as more processes need to be reproduced by the model. The way that concentrations at the boundary influence the modelled concentrations also differs between the national and city scales. Therefore, the inversion frameworks differ between these two scales. The city-scale inversion for Cape Town solved for weekly fluxes of $CO_2$ emissions on a 1 km $\times$ 1 km grid, keeping fossil fuel and biogenic emissions as separate sources. I present these results for the reference Cape Town inversion. Due to the large number of $CO_2$ sources at this spatial and temporal resolution, the reference inversion solved for weekly fluxes in blocks of four weeks at a time. As the uncertainties around the biogenic flux estimates was large, the inversion corrected the prior fluxes predominantly through changes to the biogenic fluxes. I demonstrated the benefit of using a control vector with separate terms for fossil fuel and biogenic flux components.

I performed sixteen different sensitivity analyses on the Cape Town inversion. Sensitivity analyses, solving for an average weekly flux for the month, as well as solving for separate weekly fluxes (i.e. solving in one week blocks) were considered. Sensitivity analyses were performed which focused on how changes to the prior information and prior uncertainty estimates and the correlations between fluxes would impact on the Bayesian inversion solution. These sensitivity analyses indicated that refining the estimates of biogenic fluxes and reducing their uncertainties, as well as taking advantage of spatial error correlation between areas of homogeneous biota would lead to the greatest improvement in the accuracy and precision of the posterior fluxes over the City of Cape Town.

Countries such as the United Kingdom are using high quality measurements of $CO_2$ and other trace gases, including satellite-based measurements and measurements of isotopologues, to verify UK greenhouse gas emissions reported to the IPCC (Intergovernmental Panel on Climate Change). This project provides a starting point for

such a network to be developed for South Africa, which could provide verification of national emissions, and also target high intensity regions. This project highlights that to proceed further, either at the national scale or at the city scale, it is important to work towards more reliable estimates of natural fluxes. This means that additional measurements, such as those from eddy-covariance measurements, and from carbon stock inventories need to continually be developed and improved for South Africa. This project only considered in situ measurements, but a verification network would need to make use of a wider selection of platforms, such as satellite-based and aerial-based $CO_2$ measurements.

# Research Objectives

The goals of this PhD are to:

1. Assess the best locations in South Africa to locate high precision $CO_2$ monitoring sites to obtain the most reliable estimates of national total $CO_2$ fluxes, and assess the sensitivity of this solution to the Bayesian framework, such as changes to the spatial resolution.

2. Construct an inventory of anthropogenic $CO_2$ emission for the City of Cape Town, together with uncertainty limits.

3. Obtain estimates of the City of Cape Town $CO_2$ fluxes by means of Bayesian inverse modelling technique using $CO_2$ concentrations measured at sites located at Robben Island and Hangklip lighthouses.

4. Assess the sensitivity of the Cape Town inversion solution to different specifications of the prior information and prior flux uncertainty estimates.

# Chapter 1

# Introduction

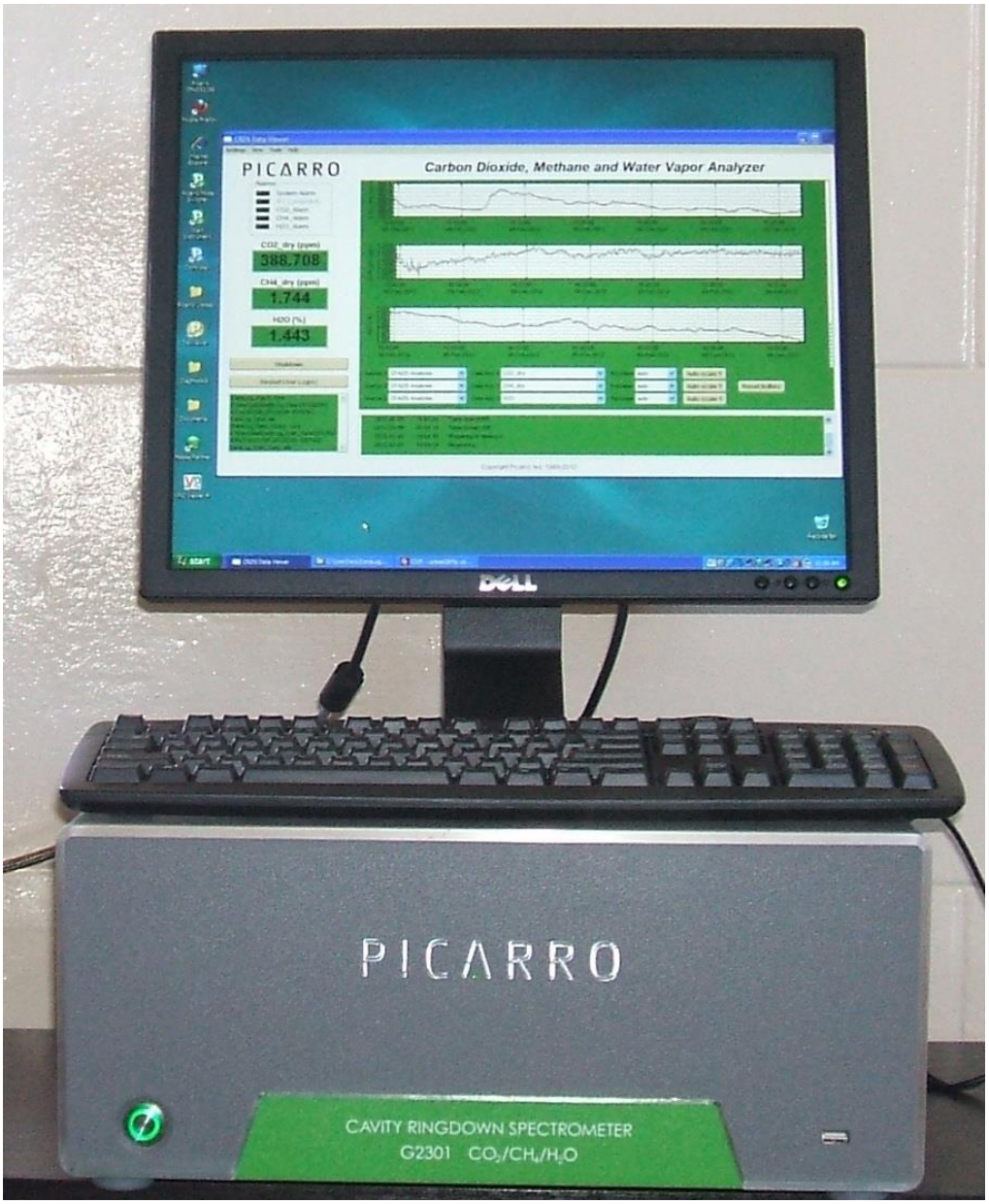


**Photo: Alecia Nickless**

# Chapter 1

# Literature Review

## 1.1 Introduction

This PhD study is concerned with understanding the movement of carbon dioxide ($CO_2$) within a region and the observation of this movement. This literature review attempts to summarise some of the underlying processes which govern the global movement of $CO_2$. It then goes on to describe the seminal works which have attempted to model $CO_2$ sources and sinks at different scales, and describes the inputs and considerations required to perform a Bayesian inversion.

Interest in understanding the global carbon cycle has intensified over the last two decades as $CO_2$ has been recognised as the greatest contributor to the anthropogenic greenhouse gas effect (Houghton, 2007; Denman et al., 2007), and features as the second most important of the greenhouse gases after water vapour (Denman et al., 2007). Other potent greenhouse gasses included methane ($CH_4$), nitrous oxide ($N_2O$), and sulphur hexafluoride ($SF_6$) (Myhre et al., 2013). Greenhouse gases induce climate change by affecting the radiative balance of the earth by affecting the absorption, scattering and emission of radiation within the atmosphere and at the Earth's surface (Kaminski et al., 1999a; Enting, 2002; Denman et al., 2007; Myhre et al., 2013). In the last decade, the radiative forcing of $CO_2$ has increased by 13 to 14%, which is solely as a result of increasing $CO_2$ concentrations in the atmosphere (Denman et al., 2007; Myhre et al., 2013), and in 2012 we reached doubling of the radiative forcing by $CO_2$ compared with pre-industrial times when global concentrations exceeded 393 ppm (Myhre et al., 2017). Fossil fuel emission estimates (Andres et al., 1999a) and $CO_2$ fluxes due to land use change (Houghton, 2007) have been estimated and compared to the increase in atmospheric $CO_2$ concentration over the past 200 years. These comparisons have concluded that approximately half of human induced emissions have been taken up by the atmosphere, and therefore the remaining half has been

Table 1.1: Contemporary carbon budgets (in Pg C year$^{-1}$± standard deviation) as calculated for the IPCC 2007 (Denman et al., 2007) and Le Quéré et al. (2015).

| | **1980's** | **1990's** | **2000's** | **2004-2013** |
|---|---|---|---|---|
| Atmospheric uptake | 3.3 ± 0.1 | 3.2 ± 0.1 | 4.1 ± 0.1 | 4.3 ± 0.1 |
| Anthropogenic emissions | | | | |
| (fossil fuel burning + cement) | 5.4 ± 0.3 | 6.4 ± 0.4 | 7.8 ± 0.4 | 8.9 ± 0.4 |
| Net ocean-atmosphere flux | -1.9 ± 0.5 | -2.2 ± 0.5 | -2.4 ± 0.5 | -2.6 ± 0.5 |
| Net land-atmosphere flux | -0.3 ± 0.9 | -1.0 ± 0.6 | -0.9 ± 0.6 | -2.0 ± 0.8* |
| *Partitioned as:* | | | | |
| *Land use change flux* | 1.4 ± 0.5 | 1.6 ± 0.5 | 1.0 ± 0.5 | 0.9 ± 0.5 |
| *Residual terrestrial uptake* | -1.6 ± 0.8 | -2.7 ± 0.8 | -2.4 ± 0.8 | -2.9 ± 0.8 |

sequestered by the marine and terrestrial biosphere (Bousquet et al., 2000; Ciais et al., 2000). This uptake of $CO_2$ is mitigating the effects of climate change by reducing the rate of increase of $CO_2$ into the atmosphere.

It is important to understand how much of the $CO_2$ uptake is attributed to each of the marine and terrestrial biospheres, and the processes governing this uptake and how these change over time, in order to be able to reliably predict future levels of $CO_2$ in the atmosphere. One way to partition the uptake of $CO_2$ to each of the biospheres is through the acquisition of high precision atmospheric observations of $CO_2$ and oxygen ($O_2$) (in the form of $O_2$:$N_2$ ratios) (Rayner et al., 1999; Schimel et al., 2001). The previous IPCC assessment and a recent assessment by Le Quéré et al. (2015) gave estimates of -1.9 ± 0.5 Pg carbon per year (Pg C yr$^{-1}$) for the 1980's; -2.2 ± 0.5 Pg C yr$^{-1}$ for the 1990's, -2.2 ± 0.5 Pg C yr$^{-1}$ for the early 2000's; and -2.6 ± 0.5 Pg C yr$^{-1}$. A land-to-atmosphere flux of -0.3 ± 0.9 Pg C yr$^{-1}$ was calculated for the 1980's; -1.0 ± 0.6 Pg C yr$^{-1}$ for the 1990's; -0.9 ± 0.6 Pg C yr$^{-1}$ for the early 2000's; and -2.0 ± 0.8 Pg C yr$^{-1}$ for the period 2004 to 2013 (Table 1.1). In the section to follow I describe several atmospheric global inversion studies which have attempted to further partition $CO_2$ sources and sinks.

Around the globe there exists high precision $CO_2$ observation networks. Although the laboratories which administer these sites may use different measurement techniques, common calibration standards, which trace back to specific labs and times, ensure that sites are measuring on the same scale (Masarie et al., 2014; Palmer et al., 2018). Atmospheric inverse modelling uses these observations of high precision $CO_2$ concentrations and atmospheric transport models to infer the mean spatial distribution of $CO_2$ fluxes, which reveals whether a region is a net sink or source of $CO_2$, along with its magnitude. Atmospheric inversions result in a solution of surface fluxes that

produces the best match between modelled and observed concentrations (Ciais et al., 2000). This method of obtaining surface fluxes is hampered by the unbalanced distribution of monitoring stations, with gross undersampling particularly in the tropics and southern land regions (Fan et al., 1998; Ciais et al., 2000; Gurney et al., 2003; Peylin et al., 2013; Shirai et al., 2017). Many of the original atmospheric monitoring sites were located to provide information about background conditions characteristic of large spatial scales and long term trends, such as those in the GLOBALVIEW product, and therefore most of these stations have been positioned in remote oceanic locations. More recently stations have been positioned with the intention of capturing the continental signal (Bousquet et al., 2000; Suntharalingam et al., 2003; Shirai et al., 2017).

The majority of inversions have concluded that there exists a terrestrial carbon sink somewhere in the Northern Hemisphere. This conclusion is based on evidence drawn from the analysis of land inventory data, atmospheric $CO_2$ data, atmospheric $O_2$ data, isotopic analyses, studies of land-use change, and ecosystem process models (Schimel et al., 2001). Fossil fuel emissions are much higher in the Northern Hemisphere and therefore a decrease in $CO_2$ concentration by 4 to 5 ppm is expected between north and south. The observed difference is smaller, which implies an uptake of $CO_2$ in the north (Fan et al., 1998). This issue was discussed in several of the early inversion studies.

The location and magnitude of this "missing" sink (now referred to as the residual land sink (Denman et al., 2007)) has remained controversial. Table 1.1 shows the huge range in estimates from atmospheric inversions and bottom up studies which have been considered within the IPPC AR4 report (Denman et al., 2007). Less certainty can be placed on broad longitudinal partitions since the difference in $CO_2$ concentrations is smaller than that for latitudinal partitions (Schimel et al., 2001). In addition, the lack of data over the continental areas, even in North America which has the highest concentration of monitoring stations, poorly constrains the flux estimates (Peylin et al., 2002; Butler et al., 2010; Masarie et al., 2014), and the continental sites have shown a much higher spatial and interannual variability in fluxes, compared to the oceanic sites (Bousquet et al., 2000). A large amount of variation occurs in estimates of terrestrial fluxes, and these are usually associated with wide confidence intervals. For example, Ciais et al. (2000) estimated a sink of -0.5 $\pm$ 0.6 Pg C $yr^{-1}$ over North America, and sink of -0.3 $\pm$ 0.8 Pg C $yr^{-1}$ over Europe for the period from 1985 to 1995, whereas Fan et al. (1998), for the period from 1988 to 1992, gave

an estimate -1.7 ± 0.5 Pg C $yr^{-1}$ over North America and -0.1 ± 0.9 Pg C $yr^{-1}$ over Eurasia – North Africa.

Observations of atmospheric concentrations of $CO_2$ alone cannot be used to obtain flux estimates from atmospheric inversions. Due to the small amount of data relative to the number of sources to be estimated, the problem is highly underdetermined. For a given set of concentrations and for a given atmospheric transport model, multiple flux fields exist which would minimise the difference between observed and modelled concentrations. Therefore, further constraints need to be placed on the model parameters in order to ensure an optimal solution with acceptable uncertainties.

The Bayesian inversion approach is the most popular method for minimising the difference between observed and modelled $CO_2$ concentrations, and is used by the majority of the atmospheric inversion community (Kaminski et al., 1999b; Rayner et al., 1999; Bousquet et al., 2000; Ciais et al., 2000; Schimel et al., 2001; Gurney et al., 2003; Peters et al., 2007; Rayner et al., 2008; Göckede et al., 2010; Peylin et al., 2013; Shirai et al., 2017). A Bayesian synthesis requires that *a priori* flux estimates and uncertainties for the source regions be specified. The best solution is then one which simultaneously minimises the difference between the *a priori* fluxes and the modelled fluxes, and the difference between the observed $CO_2$ concentrations and modelled concentrations. Prior estimates are required for fluxes from the biosphere and for anthropogenic fluxes. Prior estimates of the ocean fluxes are based on air-sea partial pressure $CO_2$ ($pCO_2$) measurements (Rayner et al., 1999). Estimates from land surface biosphere models can be used to obtain prior estimates for the terrestrial fluxes (Kaminski et al., 1999b). For global inversions, background fluxes are also specified, such as a fossil fuel flux, which is very tightly constrained due to the confidence in the fossil fuel emission estimates (Gurney et al., 2003).

Obtaining reliable estimates of fluxes from the terrestrial biosphere is challenging. Estimates for the tropics have large uncertainties (Gurney et al., 2002), due to the lack of $CO_2$ monitoring sites, and due to the poor availability of data necessary for constraining the inversion solution, such as data on land-use change, deforestation and regrowth, and information on the processes contributing to the carbon cycle in these regions (Houghton, 2007; Bayer et al., 2017), increasing the *a priori* uncertainty on parameters, and thereby increasing the dependency of the solution on the few available observations (Shirai et al., 2017). Because of the large *a priori* uncertainty for these regions, atmospheric inversion posterior fluxes can be very different from prior estimates with only a small penalty. This makes the estimates vulnerable to small perturbations in the observed data.

Prior estimates of regional biogenic fluxes are usually obtained through process-based modelling using terrestrial biosphere models (Prentice et al., 2000; Dargaville et al., 2002). These models provide detailed information on how the terrestrial carbon cycle operates, giving details on photosynthesis, respiration, decomposition, water relations and other processes which respond to environmental drivers such as light, moisture, temperature, $CO_2$ concentrations, and nutrients (Houghton, 2009). The drawback of these models is that they needed to be parameterised, usually by data collected at eddy covariance towers, and there are usually only a limited number of sites available, representing only a small area relative to the regional scale required. Therefore upscaling can result in large uncertainty in the estimates of fluxes at large spatial scales (Dargaville et al., 2002; Houghton, 2009). Instead of using these models independently, they can be used in conjunction with atmospheric inverse modelling to produce *a priori* estimates and uncertainties of flux estimates (Dargaville et al., 2002; Peylin et al., 2005). Alternatively, the results of inversions can be used to validate estimates from these models. If the inverse model initialised with estimates from the process-based model results in little adjustment to the *a priori* estimates, then the inversion has validated the model, and if large adjustments are required, the direction of the adjustment can assist in improving the process-based model (Dargaville et al., 2002).

Estimating terrestrial biogenic fluxes requires modelling of several processes in an inter-related way. Correctly modelling plant photosynthesis and respiration requires knowledge of the state of the landscape within in the region of interest. Regrowth on abandoned farmland and previously logged forests has been suggested as a major contributor to the Northern Hemisphere sink (Fan et al., 1998; Schimel et al., 2001). This type of response is brought about by recovery to disturbance, human-induced land-use change or change due to land-management practices. Other processes leading to terrestrial uptake of $CO_2$ include woody encroachment due to fire suppression or grazing practices; afforestation and reforestation, which have resulted in human-induced regional sinks in China; and improved agricultural practices on carbon-depleted soils, e.g. by introducing tillage, have created a temporary sink of carbon on agricultural land in the USA (Denman et al., 2007; Houghton, 2007). Terrestrial carbon losses occur to processes such as deforestation, which accounts for a large proportion of the atmospheric carbon budget  up to a third of anthropogenic emissions (Denman et al., 2007; Houghton, 2007; De Sy et al., 2015). Estimating fluxes due to these processes requires detailed record keeping of forest inventories and land-use change statistics,

which is lacking in the tropical regions, and particularly in South America and Africa (Houghton, 2009; De Sy et al., 2015).

There are also the vegetation responses to climatic variables, such as temperature, sunlight and soil moisture. The carbon flux response to these drivers is complex and dependent on factors such as soil characteristics and nutrient availability (Levis et al., 2000; Denman et al., 2007; Houghton, 2007). Models which predict future carbon budgets must account not only for current responses to climate, but also future climate and atmospheric composition projections as there are strong feedbacks between the carbon cycle and climate (Levis et al., 2000; Denman et al., 2007; Schut et al., 2015). These processes are also affected by human-induced changes such as elevated $CO_2$ and nitrogen fertilization. There is some doubt as to how $CO_2$ fertilization will affect productivity. Some studies have shown that elevated levels of $CO_2$ increase productivity for at least some vegetation types (Long et al., 2006; Degener, 2015), whereas others have shown that in the long term, the biosphere's response to increased $CO_2$ is overwhelmed by positive feedbacks due to the temperature dependence of soil organic matter decomposition, and therefore this increase will stabilise and productivity revert back to previous levels before the $CO_2$ fertilization due to other limiting resources, such as nutrients (Houghton, 2007; O'ishi et al., 2009; Schut et al., 2015). Some of the climate change scenarios in the IPCC predict that $CO_2$ fertilization will result in the stimulation of $CO_2$ uptake, but the rates of uptake are not all consistent with observations (Long et al., 2006; Denman et al., 2007; Smith et al., 2016).

The response of tropical forests to rising temperatures is likely to be a less efficient sink of $CO_2$ (Mitchard, 2018), owing to increases in leaf temperature and evaporative demand, and reduced canopy conductance (Doughty and Goulden, 2008), but this is highly uncertain (Le Quéré et al., 2009; Wood et al., 2012). Research on the ability of tropical vegetation to take up $CO_2$ has been conducted at different spatial and temporal scales, and the results often lead to contradictory conclusions. Large-scale observational studies confound multiple factors, such as the effect of climate, soils, and vegetation on the uptake of $CO_2$, while small-scale studies fail to address the interconnectedness of above- and below-ground processes and are challenging to upscale (Wood et al., 2012). Therefore, inversions play an important role in assessing estimates from competing models (Molina et al., 2015).

Agriculture's direct role in greenhouse gas emissions is predominantly through the emission of potent greenhouse gases such as $CH_4$ and $N_2O$, but indirectly agriculture results in emissions of $CO_2$ through the induced deforestation and land use change

required to transform a region into agricultural land (Numata et al., 2011; Bayer et al., 2017). Uncertainties in emissions from land use change are partly due to missing information on historical land-cover change. Bookkeeping models make use of land use and land cover change, and estimates of carbon densities, to calculate changes in carbon pools. A recent study by Houghton and Nassikas (2017) attributes the highest emission of $CO_2$ due to land use and land cover change to the tropics, with an estimate of 102 $\pm$ 5.8 Pg C for the period 1850 to 2015 out of a global emission of 145 $\pm$ 16 Pg C.

Another process strongly associated with land use change is biomass burning. Emissions from fires can contribute greatly to the variation observed in terrestrial $CO_2$ fluxes (Patra et al., 2005; Shi and Matsunaga, 2017). These emissions are normally accounted for by means of inventories derived from satellite data (Shi and Matsunaga, 2017) and added to bookkeeping models for the purposes of determining the global carbon budget, rather than modelled explicitly in dynamic global vegetation models (DGVMs) (Le Quéré et al., 2018).

Biogenic fluxes from the ocean are the net result of several inter-related processes. The main processes responsible for carbon uptake in the oceans are the ocean's carbon chemistry, the air-sea exchange, the mixing between surface and deep waters, and ocean biology (Lauderdale et al., 2016). In the long term, the concentration of atmospheric $CO_2$ is controlled by $pCO_2$ in the oceans (solubility pump). Over geological time periods, minerals dissolved in the ocean have caused it to become slightly alkaline, and since $CO_2$ is a slightly acid gas, it is highly soluble in sea water (Denman et al., 2007; Houghton, 2007). At a much slower rate, advection causes mixing of the surface waters and deep waters (Houghton, 2007). Ocean carbon occurs in three forms: dissolved inorganic carbon (DIC), dissolved organic carbon (DOC), and particulate organic carbon (POC – living and dead organisms). Carbon dioxide is fixed into POC in the ocean through photosynthesis in the surface layers and then sinking of organic matter into the deeper layers (the organic pump). This is limited by the availability of light and nutrients (Denman et al., 2007). $CO_2$ is released when plankton produce $CaCO_3$ shell material ($CaCO_3$ counter pump). A certain amount of these $CaCO_3$ particles sink to the deeper ocean and accumulate in sediments. This POC sink is small, but plays a vital role in keeping DIC concentrations low in the surface layers and high in the deeper layers (Denman et al., 2007). Perturbations in any of these processes will cause significant changes in atmospheric $CO_2$ concentrations (Denman et al., 2007; Houghton, 2007).

The global carbon budget is clearly complex, and we still have a long way to go before we can accurately model $CO_2$ fluxes such that all processes are accounted for, as well as and the feedbacks between these processes. With rising levels of $CO_2$ in the atmosphere and increasing global mean temperatures, whether the oceanic and terrestrial sinks will continue to keep the airborne fraction of total $CO_2$ emissions at an average of 40 to 50% is unclear. It is important to be able to assimilate data from different platforms that allow us to sense check our models and determine if $CO_2$ levels and the processes that affect $CO_2$ are responding and progressing in time in the way we expect, or if we need to update our expectations. For example, if a large proportion of the current terrestrial sink is due to forest regrowth, then this sink will diminish through time (Doughty and Goulden, 2008; Mitchard, 2018). Previous climate change scenarios have assumed that the current terrestrial sink will not only be maintained, but increase in proportion to growing $CO_2$ levels. This is not in agreement with observations. Miller et al. (2005) observed a north-south difference in $CO_2$ concentrations of 1 ppm higher in 2003 than it was in 1992, and this difference could not be explained by an increase in fossil fuel emissions, and therefore there is evidence from observations the Northern Hemisphere sink may be shrinking (Houghton, 2007). In terms of ocean fluxes, the ocean is becoming more acidic as more and more $CO_2$ is dissolved, thereby reducing the effectiveness of the solubility pump. The ocean is getting warmer, which also reduces the solubility of $CO_2$. Upwelling is driven by changes in density, and warming of the surface waters could result in stability of the water column. The latitudinal gradient in surface ocean temperature will also be reduced, reducing ocean mixing. This will affect nutrient availability for the biological pump (Houghton, 2007). Therefore three of the most important oceanic processes for maintaining the ocean as a sink of $CO_2$ are impacted by rising atmospheric $CO_2$ levels and rising temperatures, and if models do not account for the feedbacks, the size of the future sink will be overestimated. The most recent IPCC report has stated with high confidence that the feedback between climate change and land and ocean processes will lead to an offset in the increase in $CO_2$ sinks, which will lead to more emitted $CO_2$ left in the atmosphere (IPCC, 2014). Monitoring of carbon fluxes through atmospheric inversions based on observed $CO_2$ data can be used in validation processes of models predicting carbon fluxes in order to ascertain which models are supported by the data, and also to signal if regional sinks are being reduced or sources becoming larger.

In an attempt to mitigate human-induced climate change, it is essential to be able to examine the progress that has been made towards emission reductions using

objective methods reliant on observation. Governments and international governing bodies have recognised the importance of reducing emissions from fossil fuel burning and land use change, and have legislated policy which outline emission targets or have signed international treaties, such as the Paris Climate Agreement (Horowitz, 2016), that outline commitments to reduced emissions (Houghton, 2007). This requires monitoring of $CO_2$ fluxes at global and regional scales, in order to determine if these goals are being achieved. The 2006 United Nations Framework Convention on Climate Change stipulated the objective of stabilization of greenhouse gas concentrations in the atmosphere at a level that would prevent dangerous anthropogenic interference with the climate system, which was signed by 189 nations (Houghton, 2007). Therefore, continued improvement of our understanding of the carbon cycle and its role in climate change is essential. Monitoring of emissions at global and regional scales, as well as monitoring of areas of intense activity, such as cities, is necessary in order to track progress towards climate change goals, and atmospheric inversions are valuable data assimilation tool for this purpose.

This literature review focuses on the literature related to $CO_2$ inversions, but this methodology has also been employed for other gaseous species, such as carbon monoxide (CO) and $N_2O$ (Müller and Stavrakou, 2005; Ganesan et al., 2015), $SF_6$ (Ganesan et al., 2014), and particularly for $CH_4$ (Miller et al., 2013; Ganesan et al., 2015; Houweling et al., 2017; Rigby et al., 2017). Methods for these species need to account for species-specific chemistry, such as oxidation of methane through the hydroxyl radical (OH) in the troposphere (Rigby et al., 2017). Methods for methane were initially adopted from $CO_2$ inversion methodology, and have been adapted to account for this chemistry (Houweling et al., 2017).

The purpose of this review is to

i. present results from previous atmospheric inversions, particularly the estimates obtained for southern Africa and the tropics,

ii. present the techniques used by the inversion community to obtain flux estimates,

iii. describe recent applications of city-scale atmospheric inversions,

iv. discuss the potential to model fluxes at a regional level over southern Africa

## 1.2 Past Atmospheric Inversions

### 1.2.1 Global Scale Inversions

Although this PhD study is not focused on global inversions, I provide a brief summary of the seminal papers that paved the way for mesoscale inversions. Global scale inversions were the first applications of this type of methodology to obtain estimates of $CO_2$ sources and sinks at the continental level. Fan et al. (1998) carried out an atmospheric inversion in order to confirm the presence of a Northern Hemisphere sink, and to determine the partition of this sink between North America and Eurasia. They used annually averaged $CO_2$ values calculated from data collected at 63 sampling stations in the 1996 version of the GLOBALVIEW database (GLOBALVIEW-$CO_2$; Cooperative Atmospheric Data Integration Project Carbon Dioxide. NOAA ESRL, Boulder, Colorado (available at: `http://www.esrl.noaa.gov/gmd/ccgg/globalview/`)) over the period from 1988 to 1992. Using their particular approach to the inversion, they calculated that they would need at least 10 stations per region to obtain estimates with sufficient accuracy. Due to the location of the sites, which is not optimal for partitioning the fluxes from continental regions, three terrestrial regions were selected: North America, Eurasia and North Africa, and the Tropics and Southern Hemisphere; and three ocean regions: North Atlantic, North Pacific, and Tropics and Southern Hemisphere. Both the terrestrial and oceanic regions in the Southern Hemisphere were poorly constrained by the available observation data, resulting in the combination of all land masses in the Southern Hemisphere into one region. To assess the sensitivity of the inversion results to the atmospheric transport model and to the pattern of average annual atmospheric $CO_2$ imposed, two different transport models (The Global Chemical Transport Model (GCTM) and the SKYHI model, and two different models for net sea-air $CO_2$ flux (OBM and T97) were used, resulting in four different inversions. To provide *a priori* estimates of the terrestrial fluxes, the Carnegie-Ames-Stanford Approach (CASA) was used. They predicted a mean sink of -1.7 $\pm$0.5 Pg C $yr^{-1}$ for North America, a neutral flux for Eurasia (-0.1 $\pm$0.7 Pg C $yr^{-1}$), and a neutral flux for the Tropics and Southern Hemisphere, with a large standard deviation (0.2 $\pm$0.9 Pg C $yr^{-1}$). They concluded that more sampling was required on continental areas to constrain estimates for Eurasia, South America, Africa and Australia, more sampling was required in the Southern Hemisphere oceans, and that the uncertainty of atmospheric transport models needed to be reduced.

Rayner et al. (1999) performed a similar inversion for the period from 1980 to 1995, but in this case a monthly time step was used, and atmospheric observations

from only 25 stations were used from the NOAA-CMDL network, as well as further constraint from isotopic $\delta^{13}$C observations, which can be used to infer global totals of fluxes from land and ocean. The transport model used in this case was the Goddard Institute of Space Sciences (GISS) Chemical Transport Model. The ocean was split into 12 regions and the land into 14 regions. The purpose of this approach was to match large scale ocean circulation features and different biomes or regions with characteristic atmospheric transport. Prior ocean fluxes were based on $\Delta pCO_2$ measurements summarised in (Tans et al., 1990), and fossil fuel flux estimates were based on national statistics on fossil fuel burning and cement production, and spatially distributed according to population density. The magnitude and seasonality of the monthly terrestrial prior fluxes were based on the biome which dominated the region, but the monthly fluxes were allocated such that the annual mean for each region was equal to zero, with the uncertainty set at 1.2 Pg C yr$^{-1}$. A large uncertainty was specified to allow the fluxes to respond freely to the concentration data. They calculated the annual mean flux of the northern extratropics to be -1.9 Pg C yr$^{-1}$, 0.4 Pg C yr$^{-1}$ for the tropics and -1.2 Pg C yr$^{-1}$ for the southern extratropics (error estimates for these means not given). They particularly considered the interannual variability and found it to be large on most time scales.

Bousquet et al. (1999) performed an atmospheric inversion for the period from 1985 to 1995 on data collected at 70 sites in the GLOBALVIEW-$CO_2$ database as well as isotopic $\delta^{13}$C observations. Monthly data on 11 terrestrial regions and eight oceanic regions were used. They used the TM2 atmospheric transport model. Each of the terrestrial regions was split into a gross primary production source (GPP), an ecosystem respiration source (RES), and a net uptake source. The annual gross net biotic fluxes were taken from Friedlingstein et al. (1995), and the sum of the GPP and RES sources for each region specified to equal the net uptake source, which was initialised as zero uptake with large variances for each region. The *a priori* oceanic fluxes were based on monthly maps of $\Delta pCO_2$ from Takahashi et al. (1997). They concluded that 80% of the biospheric sink was located at the mid to high latitudes of the Northern Hemisphere (-2.1 Pg C yr$^{-1}$), against 15% in the Tropics and only 5% in the Southern Hemisphere, with an estimate of 0.2 $\pm$0.6 Pg C yr$^{-1}$.

Ciais et al. (2000), the same lab which carried out the previous inversion, reported results for the same period – 1985 to 1995 – where they used monthly averaged data of atmospheric observations from 77 sites from the GLOBALVIEW-$CO_2$ database. The continents were split into 11 regions, and then consolidated into seven regions for the final presentation of the regional fluxes, and the ocean into eight regions. They

again used the TM2 atmospheric transport model, and specified GPP, RES and net uptake sources for each region, but this time they used the SIB-2 global biosphere model to obtain *a priori* estimates of the GPP and RES fluxes. They determined in this inversion that the North American sink was -0.5 ± 0.6 Pg C $yr^{-1}$, -0.3 ± 0.8 Pg C $yr^{-1}$ for Europe, and that the sum for South America and Africa was a slight source of +0.3 ± 0.8 Pg C $yr^{-1}$. As in the previous inversions, lack of data in the tropics and in the southern Hemisphere limited the degree to which regions could be partitioned.

Schimel et al. (2001) performed a review of atmospheric inversions carried out over the 1980-1996 period, and obtained flux estimates for the split between Eurasia and North America which did not show the imbalance as observed in earlier studies. They determined the North American net land-atmosphere carbon flux to have a mean estimate of -0.8 Pg C $yr^{-1}$ (ranging between -2.1 and +0.1), for Eurasia to be -1.7 Pg C $yr^{-1}$ (-2.5 to -0.2), and the combined flux of Tropical and southern temperate regions to be -0.4 Pg C $yr^{-1}$ (-1.2 to +0.8). They noted in the review of these estimates, that the large deforestation flux expected for the tropical regions was not observed, indicating that a sink of up to -2.0 Pg C $yr^{-1}$ may exist in the tropics. They observed that the net terrestrial sink appeared to increase from the 1980's to the 1990's.

Gurney et al. (2002, 2003) presented results from a control inversion where 16 atmospheric transport models were used. They used annual means of observations from 76 sites for the period from 1992-1996 from the GLOBALVIEW-$CO_2$ database. Eleven terrestrial and eleven oceanic regions were specified, and the seasonal biospheric exchange for the *a priori* estimates were derived from the CASA model and from Takahashi et al. (1999) for the oceanic exchange. The mean estimate for the combined south land regions was -0.2 ± 1.1 Pg C $yr^{-1}$, and for the north land regions was -2.3 ± 1.1 Pg C $yr^{-1}$. They found that the partition in Northern Hemisphere sink was more evenly distributed, as determined by Schimel et al. (2001).

A follow-up study by the same group of researchers (Baker et al., 2006) performed the same type of control inversion on 13 different transport models, using the same 22 regions as in the previous study, using data from 78 sites, but now for the period 1988 to 2003 and this time using seasonally averaged means. They were particularly interested in the combined uncertainty from interannual variability and different transport models. As in the previous study, the inversions were initialised with estimates from the CASA model and from Takahashi et al. (1999). They reported the mean result for the 1992-1996 period, and found the results were relatively similar to the previous

inversions. They also reported the estimated fluxes for southern Africa from the two studies. The previous study obtained a mean -0.29 while the more recent study found a mean of -0.51 Pg C $yr^{-1}$ (over the full period from 1992 to 1996). The estimated posterior error on these estimates was 0.48, of which the atmospheric transport model error was 0.31 Pg C $yr^{-1}$, estimated as the standard deviation between the model estimates from the 13 inversion solutions, each using a different transport model. They determined that the greater part of the global interannual variability in $CO_2$ uptake could be attributed to tropical land regions. They also discussed the increased lank sink due to the Mount Pinatubo eruption. They suggested that the anomalous land uptake in the early 1990's was more likely in Europe than North America, as suggested by Bousquet et al. (2000), as the spike in the North American uptake occurred in 1994, too long after the eruption.

Peylin et al. (2013) reviewed eleven distinct sets of global inversion results based on updated methodology. The inversions compared included those referred to in Patra et al. (2005), Rödenbeck (2005), Gurney et al. (2008a), Rayner et al. (2008), Piao et al. (2009), Chevallier et al. (2010), Peters et al. (2007, 2010), Maki et al. (2010), and Niwa et al. (2012). Many of these inversions are updated over time with current observations and results made available through the Global Carbon Atlas (`http://www.globalcarbonatlas.org/en/content/atmospheric-inversions`). These inversions differed in the inversion method, the observation data, the transport model, and the choice of prior information. The period in common between these inversions was 2001-2004. Peylin et al. (2013) found that these inversions produced consistent estimates at the global and latitudinal scales, indicating large uptake in the north (-3.4 Pg C $yr^{-1}$ ($\pm$ 0.5 Pg C $yr^{-1}$)), a source in the tropics with more variation in the estimates (1.6 Pg C $yr^{-1}$ ($\pm$ 0.9 Pg C $yr^{-1}$)), and a sink in the south (-1.4 Pg C $yr^{-1}$ ($\pm$ 0.5 Pg C $yr^{-1}$)), which is mainly attributed to uptake by the oceans. The balance between the tropic source and southern sink is what was most variable between inversions. This is consistent with what we would expect due to the sparsity of observations. They also concluded that the interannual variability in $CO_2$ fluxes was larger for the land than for the ocean, with a standard deviation of 1.06 versus 0.33 Pg C $yr^{-1}$, with tropical land fluxes explaining the majority of the land flux variation.

In summary, the mean estimates of regional fluxes obtained from previous global inversions show a great deal of variation with wide uncertainty limits. Recent inversions have placed uncertainty limits on the tropical terrestrial fluxes that are almost twice as wide as those for northern temperate regions (0.9 Pg C $yr^{-1}$ versus 0.5 Pg C

$yr^{-1}$). All of these previous global inversion studies are consistent in their conclusions that more observations, particularly in the tropics and on continental land regions, would benefit the estimates. The regional flux for southern Africa has in general not been determined, but rather grouped together in a larger southern Hemisphere region. Estimates for this region are then dependent on atmospheric concentration values from sites which are very far removed from each other, measuring very different land areas.

#### 1.2.1.1 Sensitivity Analysis

A number of sensitivity analyses have come out of the Transcom 3 experiment (Gurney et al., 2002, 2003; Law et al., 2003; Baker et al., 2006), which was an intercomparison project set up with the goal of determining the sensitivity of atmospheric inversions to the various specifications. One of the primary goals of this intercomparison exercise was to determine the amount of uncertainty attributable to the atmospheric transport model. Sixteen different atmospheric transport models were compared in the first phase (Gurney et al., 2002, 2003). The inversion consisted of 26 basis functions which corresponded to four background fluxes and 22 regional fluxes. The background fluxes consisted of two fossil fuel emission fields, an annually balanced, seasonal terrestrial biosphere exchange and air-sea gas exchange. These background fluxes are given very small prior uncertainties so that their prior estimates are essentially fixed. In this phase of the comparison, the observational sites, *a priori* estimates and spatial distribution of the sites remained constant. They concluded that model transport was a large contributor to the inversion uncertainty. They examined how the individual model inversion responded to the background fluxes and found that models which exhibited large $CO_2$ concentration maxima near and downwind of large background fluxes estimated large uptake in those regions in order to best match the $CO_2$ observations, whereas models with small $CO_2$ concentration maxima estimated less uptake near the background fluxes but compensated further downwind over ocean regions with weaker sources or smaller sinks. They found that model differences were large for the annual response to seasonal biospheric $CO_2$ exchange. Almost all the models simulated elevated $CO_2$ concentrations at the surface in the northern middle latitudes due to the covariance between seasonal exchange and seasonal transport (the seasonal rectifier effect), but with differences of up to 3 ppm between models. Peylin et al. (2002) also performed a sensitivity analysis using three different transport models: TM2, TM3, and GCTM. They found that the seasonal rectification gradient was very

different between models. They concluded that better quantification of this effect was necessary in order to obtain robust estimates of regional fluxes.

Baker et al. (2006) performed a follow up sensitivity analysis to the work of Gurney et al. (2003) where inversions using monthly data, as opposed to annually averaged data, were performed using different transport models, particularly to determine the effect of atmospheric transport uncertainty on interannual variability of regional flux estimates. They determined that by using a 13 model inversion, compared to a single model inversion, the significance of the interannual variability signal in the fluxes was higher, suggesting that the real signal in fluxes was observed better through a multi-model inversion.

Law et al. (2003) performed a sensitivity analysis on the use of different data selection criteria. One of the criteria used in many inversions is that a site record needs to be at least 70% complete for it to be included in the inversion. They tested the sensitivity of the inversion to different levels of this criterion. They also compared the case where all sites were included from the GLOBALVIEW-$CO_2$ database versus the case where only sites from the NOAA-CMDL database. In addition, they tested the sensitivity of the inversion to different years of data. They found that for most of the sensitivity tests, that the mean flux estimates were within the uncertainty range determined for the control inversion. In selecting sites, they found that those sites which were badly mismatched in the inversion were either non-representative of the region they were allocated to, or the amount of missing data was large, and therefore relied heavily on interpolation. Therefore the criterion of selecting sites with at least 70% intact data is a good criterion to follow. They also concluded that for their mean annual inversion, the choice of which years of data to include had a relatively small impact. This could be due to the deliberate design of the inversion to estimate long term mean fluxes, since equilibrium response functions are used. Suntharalingam et al. (2003) reported results on a sensitivity analysis on different configurations of the global observation network, following the same inversion methodology as Fan et al. (1998), but using the GISS II Chemical Transport Model. They determined that the inclusion or omission of a few important stations in and around the northern continents could result in shifts in regional estimates of up to 1.5 Pg C $yr^{-1}$. They also looked at two different cases of including site observation uncertainty. In the first case they assumed that measurement errors were independent and normally distributed with constant variance. In the second case, the assumed heterogeneous variance of data uncertainty, and therefore solved for a weighted least squares estimator instead of the ordinary least squares estimator as used by Fan et al. (1998). Using this

method, they found that the estimate of the North American sink was reduced, but less sensitive to the observational network. This was due to the diminished role of several continental stations with high uncertainty, particularly the Key Biscayne site, which when excluded resulted in the between model total estimate difference of 0.08 Pg C $yr^{-1}$ instead of -0.43 Pg C $yr^{-1}$.

The sensitivity analysis of Peylin et al. (2002) also looked at the effect of time discretisation (annual versus monthly) and spatial resolution of the fluxes. They presented the results of 27 Bayesian inversions, where the number of flux regions varied (7, 12 or 17 regions), the time discretisation (monthly observations to obtain monthly fluxes, monthly observations to obtain annual fluxes, or annually averaged observations to obtain annual fluxes), and three different transport models. They determined that the time discretisation was a significant contributor to the uncertainty in regional flux estimates. In the case where monthly data was used to estimate annual fluxes, it was determined that the magnitude or phase of the *a priori* seasonal cycles of fluxes can cause very large differences at the measurement sites in certain months. Matching the modelled concentrations to the observed concentrations during these months could drive the solution in a very different direction compared to the annual mean measurement solution. Therefore using monthly data to solve for annual fluxes may be more appropriate for fitting the seasonal cycles, but might do worse in estimating the annual mean flux. On the other hand, the results from the case using monthly data to obtain monthly fluxes compared well with the case using annually averaged data. This finding is supported by the comparison in Baker et al. (2006) between the inversions using annually averaged and monthly averaged data.

In terms of the spatial resolution of the regions used in an inversion, they determined that for the tropics, almost all of the variability was attributed to differences between the number of regions solved for by the inversion. They concluded, that an optimal number of regions exists which minimises the sum of the random estimation error and the systematic aggregation error. As explained in Kaminski and Heimann (2001), if only a few large regions are used, this avoids the problem of underdetermination of sources due to too few observations. But this assumes perfect correlation between the grid cells within these large regions. Having only a few regions reduces the estimation error. But the bias due to small scale processes may add up using this approach, leading to aggregation error, which decreases as the number of regions increases. This source of error has not been well examined in the literature, yet the number and size of regions vary from study to study.

During the atmospheric transport model intercomparison, Gurney et al. (2003) also ran a sensitivity test on the specification of *a priori* information. The changes they made included increasing the prior flux uncertainties until essentially reaching levels where the inversion was not constrained by the prior flux estimates; using zero land flux prior estimates; setting the background biospheric exchange to zero (which tests the sensitivity of the flux estimates to the rectifier); setting the uncertainty of the background biospheric flux to 100% to determine the size of the rectifier; and setting the background ocean exchange to zero. They found that for regions with strong data constraints, the fluxes were insensitive to changes in the prior estimates, whereas regions which had few observations were sensitive to both prior information and the errors in the transport model. Removal of the background biospheric fluxes had large impacts in some of the northern regions due to the strong rectifier effect. By allowing the model to estimate the rectifier effect from the data, results for the northern regions were obtained between the control inversion and the no rectification case. Removing the background ocean flux resulted in larger changes in the land fluxes compared to the oceanic fluxes, most likely due to the larger prior uncertainties of the land fluxes. Law et al. (2003) and Peylin et al. (2002) suggest specifying data uncertainties such that the $\chi^2$-criterion, which is twice the cost function at its minimum divided by the number of observations, is close to one. A value greater than one indicates that the residuals (from the measurements or from the *a priori* fluxes) are larger than the uncertainties initially assumed. Values lower than one indicate that the prior uncertainties could have been decreased to ensure a better correlation between the model and the data.

A more recent inter-comparison of eleven inversion studies was carried out by Peylin et al. (2013). This sensitivity analysis did not focus on varying one characteristic of the inversion set-up, but compared these eleven studies which differed in the atmospheric observations used, the transport model used, the spatial and temporal flux resolution of the inversion, the prior fluxes specified, and the observational errors and prior flux error assigned. When this inter-comparison was carried out, there were over 50 sites measuring $CO_2$ continuously and over 100 sites making weekly flask measurements. Most of these sites were part of the GLOBALVIEW-$CO_2$ network. Prior estimates for biogenic emissions for the inversion studies were generally obtained from terrestrial or oceanic biogeochemical models. Anthropogenic $CO_2$ emissions were obtained from Andres et al. (2011 and 2012), where the uncertainty of these estimates is within 5 to 10% of the mean estimate at the global scale. But the uncertainty is much higher when the emissions are disaggregated spatially and temporally, and is

expected to be highly spatially heterogeneous. Although this uncertainty could impact on the estimates of emissions over land masses, in global inversions assessed for this sensitivity analysis anthropogenic emissions were generally prescribed and their uncertainties ignored. These studies either solved for monthly or weekly fluxes. The spatial resolution varied between studies, but results were resampled onto a $1^\circ \times 1^\circ$ grid to facilitate comparisons between studies.

The average global land and ocean sinks were estimated to be -1.32 $\pm$ 0.39 Pg C $yr^{-1}$ and -1.79 $\pm$ 0.30 Pg C $yr^{-1}$ across the eleven inversion studies. The mean flux estimates at different latitude bands show a large sink in the north of -3.4 $\pm$ 0.50 Pg C $yr^{-1}$, a source of the tropics of 1.6 $\pm$ 0.90 Pg C $yr^{-1}$, and a smaller southern sink of -1.4 $\pm$ 0.50 Pg C $yr^{-1}$. The spread of estimates at the scale of latitudinal bands is much higher compared with the global estimates. For example, one inversion estimates the total uptake in the north to be -2.7 Pg C $yr^{-1}$ whereas another estimates it to be -4.3 Pg C $yr^{-1}$. The assessment of the inversion results at the latitudinal band scale leads to a separation of the inversions into two groups. The inversions in the first group provide estimates close to -1.2 $\pm$ 0.10 Pg C $yr^{-1}$ in the south, and a release of 0.8 to 1.0 Pg C $yr^{-1}$ in the tropics. The second group have this release in the tropics as much higher, with compensating larger uptake in the south and north. There are at least two possible differences between the approaches used by these two groups. The first group used observations at the sampled times, rather than the monthly means used in second group, which would allow group 1 to better represent baseline-selected data. A second difference is that the first group solves for the fluxes at the same spatial resolution as used by the transport model or solves for small ecosystem-based regions over land, whereas the second group solves for larger regions. All the inversions agreed on a large ocean uptake in the south of close to -1.3 Pg C $yr^{-1}$, but over land the estimates deviate between -0.6 to 0.5 Pg C $yr^{-1}$.

The amplitude of the seasonal cycle for northern land regions ranged between 3.0 to 3.5 Pg C $yr^{-1}$, with the spread in estimates largest during the growing season, with the onset differing between groups of inversions. There was less agreement between inversions in both the phase and magnitude of the ocean seasonal cycle. In the Southern Ocean, there was general agreement between inversions, with uptake estimated to take place in austral winter. The inversions generally agreed on the inter-annual variations of the land and ocean fluxes, as well as on the land/ocean partitioning. This held more strongly for the Northern Hemisphere than for the Southern Hemisphere, where observations were sparser.

In summary, there are a large number of possible ways errors could be introduced into an inversion, therefore careful consideration needs to go into each component of an inversion. Running an inversion with multiple atmospheric transport models is preferable to using only one model. During site selection, sites with minimum missing data, and sites that are representative of the regions selected, should be chosen. The time discretisation of the data should depend on the purpose of the inversion. Long term trends in regional fluxes estimated from global inversions may be better estimated with annually averaged data, whereas monthly averaged data should be used if the seasonal cycle is of interest. The spatial resolution of the inversion should optimise the sum of the estimation error caused by having too many regions, and the aggregation error caused by aggregating over spatially heterogeneous regions. Prior information should not be included arbitrarily, but given careful consideration as these specifications influence the flux estimates of an inversion.

### 1.2.2 Regional Scale Inversions

The atmospheric inversions discussed above were all conducted at a global level. Due to the aggregation error induced by the low spatial resolution, these approaches have been too coarse to capture vegetation and climate variability at small sub-grid scales, and therefore these previous global atmospheric inversions cannot be used directly to provide information on the mechanisms that drive the underlying carbon processes (Gourdji et al., 2010). In order to validate flux estimates from process based models, and to be able to monitor and design better carbon management policies, estimates at a much more detailed spatial and temporal resolution are required (Peylin et al., 2005; Gourdji et al., 2010). More recently, studies have been conducted using inverse methodology to resolve flux estimates at much finer spatial and temporal resolution, termed regional or mesoscale inversions (Peylin et al., 2005; Lauvaux et al., 2008; Göckede et al., 2010; Gourdji et al., 2010). The advantage of using a high spatial resolution is that aggregation error (i.e. error in modelling the concentrations due to assuming atmospheric transport occurs over homogeneous regions) is reduced, but correctly representing small-scale variability in areas with complex terrain or structures, and with multiple sources of $CO_2$, in an atmospheric transport model is more difficult and the uncertainty is relatively unknown (Gourdji et al., 2010). The error in modelling concentrations can be reduced by collecting additional high resolution data for the target region, and restricting the rest of the world, by reducing the resolution outside of the target region (Peylin et al., 2005), but retaining the global domain, or alternatively by specifying boundary layer fluxes as additional unknowns

and operating at a mesoscale domain (Lauvaux et al., 2008; Gourdji et al., 2010). When conducting a mesoscale inversion, it can be desirable to work in the global domain because of the high sensitivity of the concentrations measured at observing sites to fluxes beyond the boundaries of the specific region (Peylin et al., 2005). This avoids the need to know or model the concentrations at the boundaries of the limited domain. To account for the influence of boundary conditions on variations observed at observation sites in a limited domain inversion, the boundary concentrations can be included in the model as additional unknowns, even if the boundaries are set to be crude representations of reality. Initial estimates of these concentrations can be obtained from forward models, and by including them as unknowns in the inversion it allows for the investigation of the sensitivity of the modelled concentrations to these conditions (Lauvaux et al., 2008). The influence of the boundary and initial conditions can be further reduced by ensuring that the domain of the inversion is much larger than the area of interest (Gerbig et al., 2003).

Peylin et al. (2005) carried out their inversion for the region of Western Europe. They operated their inversion at a daily timescale, but noted that by doing this the diurnal cycle of the fluxes was not resolved. This ignores the complexity in atmospheric transport such that the skill of the transport model may not be equal when simulating the day time and night time transport. There is also the diurnal rectifier effect, similar to the seasonal rectifier effect of the global large scale inversions, which is not accounted for. To explain further, the seasonal rectifier effect can be seen in the annual mean $CO_2$ concentration at the surface and is as a result of the temporal covariations between terrestrial $CO_2$ fluxes and atmospheric transport, which can be as large or larger than net industrial, terrestrial or ocean fluxes (Stephens et al., 1999; Chan et al., 2008). During the summer, the planetary boundary layer (PBL) is relatively deep and vertical mixing is vigorous. Due to the net $CO_2$ uptake from photosynthesis, there is a deficit in $CO_2$ concentrations at the surface, but the size of this deficit is mitigated by the deep PBL. In contrast, during the winter months, the PBL is much shallower and vertical mixing is diminished, and therefore $CO_2$ resulting from a positive net terrestrial flux becomes trapped near the surface (Stephens et al., 1999). Therefore, even if the net annual $CO_2$ flux is zero, this covariation typically results in a north-south gradient, with higher annual mean $CO_2$ concentrations near the northern polar regions than the tropics and Southern Hemisphere. This has important consequences for modelling sources and sinks of $CO_2$ (Chan et al., 2008). Similarly, a diurnal rectifier effect occurs because photosynthesis takes place during the day when the PBL is deeper with more vertical mixing, compared with the night

when photosynthesis is absent and the PBL is deeper with less vertical mixing. Therefore mean daytime $CO_2$ concentrations at the surface are lower than those during the night due to both $CO_2$ uptake at the surface and the deeper PBL. This gives rise to nonzero average changes in concentrations even if the net daily flux is zero.

Peylin et al. (2005) used the LMDZ global transport model, which can be zoomed over a particular region of the globe, and used a retro-transport approach, as an alternative to the adjoint method, to obtain the response functions for the inversion. In studies with a short time scale, a spin up period to calculate the background flux cannot be afforded, therefore, for each grid cell, initial estimates of concentrations would normally be required. By means of SVD of the Jabobian matrix, the matrix of sensitivities to the initial conditions can be reduced to the rank of the number of observations, reducing in this instance the number of required initial estimates from $5\times105$ to 180. They concluded that the LMDZ model could satisfactorily represent the phase of the major synoptic events in the concentration record over the short monthly period. For short periods of less than 20 days it was necessary to provide accurate initial concentrations. They determined that the choice of the correlation length and covariance structure strongly affects the patterns of both uncertainty reduction and flux increment.

Lauvaux et al. (2008), Gourdji et al. (2010) and Göckede et al. (2010) carried out inversions at a mesoscale level, rather than retaining the global domain. Lauvaux et al. (2008) used a coupled non-hydrostatic atmospheric mesoscale model MesoNH to the Lagrangian particle dispersion model LPDM (Uliasz, 1993) to simulate atmospheric dynamics at a high resolution. They used hourly tower continuous measurements, as well as three minute data from flights which were conducted over the four day time period of interest. Since the inversion was operating at a mesoscale, boundary fluxes needed to be specified to account for the influence of long range transport, particularly on tall towers. The found that for the four day period, the inversion produced estimates for more than 50% of the target region that had errors reduced from their prior levels by at least 30% due to constraint from the available observations. Due to the influence of long range transport, particularly on the tall towers, maintenance of the global scale to constrain estimates of the boundary fluxes may be critical.

Gourdji et al. (2010) used a geostatistical approach to the inversion, and did not stipulate any prior flux values or auxiliary information in order to determine the extent to which observations would constrain the flux estimates. The inversion was carried out on synthetic data from towers located in North America in order to determine the importance of resolving the diurnal effect of the concentrations and

fluxes. The geostatistical approach to the inversion is still Bayesian, but only requires a deterministic model of the trend that estimates the relationship of the $CO_2$ flux to key covariates, and a prior covariance matrix that describes the expected variability in flux departures from the trend as a function of separation distance in space and time between individual gridscale fluxes. The trend function can be a simple mean unknown flux across the domain, or it could be a more complex function of based on auxiliary variables related to $CO_2$ flux processes. In their inversion they used the Stochasitic Time-Inverted Lagrangian Transport Model (STILT) and operated at a 1° by 1° spatial resolution. They operated on several different temporal resolutions ranging from three hourly to four days in order to investigate temporal aggregation error. They determined that estimating fluxes at a temporal resolution that can adjust for diurnal variability was critical for both recovering covariance parameters directly from atmospheric data, and for inferring accurate ecoregion-scale fluxes.

Göckede et al. (2010) used the standard Bayesian inversion approach, but used remotely sensed data to accurately describe the model domain, and a terrestrial biosphere $CO_2$ flux model (BioFlux), which was trained on eddy covariance data, to obtain prior flux estimates. They decoupled the number of prior estimates from the spatial resolution of the inversion by separating the model domain into surface types based on remotely sensed data for land cover type, ecoregion and disturbance history. This makes possible a highly detailed description of the surface domain of the target region that reduces potential representation errors. Instead of optimising the flux rates, the individual base rates were solved for GPP, autotrophic respiration (RA) and heterotrophic respiration (RH). Fossil fuel fluxes were also included from emission inventories from Gurney et al. (2008b). In this study the mesoscale atmospheric model WRF (Weather Research and Forecast) was coupled with the STILT transport model. This study performed a sensitivity analysis using different time scales and different spatial scales, with the base scenario operating at an hourly time step and at a spatial resolution of less than one kilometre, with 120 different surface type classifications. Their temporal resolution sensitivity test indicated that smoothing the data into four-hourly bins resulted in the best optimisation. This could be due to the relatively short towers which were included, which are more prone to transport errors in the near field, and due to heterogeneity in the source/sink strength in the footprint, which is higher compared to tall towers. They determine a very low sensitivity of the inversion to spatial resolutions less than 16 km. The limited impact of the horizontal resolution was attributed to the low number of observation towers (only two used) relative to the high number of surface type classifications. A detailed

surface type classification may only be useful when there are enough measurement sites to resolve the fluxes of these different regions. They determined that specifying multiple disturbance regimes was negligible and that using only one disturbance regime was sufficient. Stand age had a larger impact. Specifying only two ecoregions (humid and semi-arid) as opposed to ten, still captured the major differences in plant functional types, but fit the observed concentrations better compared to the case where no ecoregions were specified.

Inversions carried out at the smaller scales have the potential to provide detailed flux estimates over spatial and temporal scales, which can be related to process driving the carbon cycle. To improve estimates from these inversions, transport models need to have improved transport of tracers at night. The propagation of error due to transport is an important component of the overall estimation error. Although many of these recent studies have used mesoscale domains, and not retained the global domain, this may prove to be necessary due to the sensitivity of tall towers to long range transport. The treatment of spatial and temporal covariances between flux uncertainties and temporal observation error correlations has also been highlighted as an important component in the mesoscale inversion. These specifications are discussed further in the next section.

## 1.3 The Bayesian Atmospheric Inversion

The Bayesian inversion method presented here is the most commonly used formulation in the literature. This method has been implemented by Bousquet et al. (1999), Kaminski et al. (1999b), Rayner et al. (1999), Gurney et al. (2002), Peylin et al. (2002), Gurney et al. (2003), Law et al. (2003), Baker et al. (2006), Ciais et al. (2010), and Peylin et al. (2013). This methodology is described in detail in Enting (2002) and Tarantola (2005).

A Bayesian atmospheric inversion is the technique whereby the size of fluxes from a prespecified set of source regions is inferred from a number of time series $CO_2$ concentration observational datasets at different spatial locations within the domain of interest on and an atmospheric transport model. The solution of $CO_2$ fluxes is obtained through Bayesian optimisation procedure. The main inputs required are the concentration observational datasets, the atmospheric transport model which is used to derive a sensitivity matrix, prior estimates of the fluxes and the covariance matrix describing the uncertainty in the prior fluxes, and the covariance matrix describing the errors in modelling the observational data.

Let $\boldsymbol{c}$ be a vector of observed concentrations, $\boldsymbol{s}$ be a vector of sources (any part of the domain which can emit or take up $CO_2$) and $\boldsymbol{s}_0$ be a vector of prior estimates of the sources. The vector $\boldsymbol{c}_{mod}$ represents the modelled concentrations from the true sources $\boldsymbol{s}$. The vector $\boldsymbol{s}$ can be referred to as the control vector, and can be comprised of surface fluxes and boundary concentrations.

If the relationship between $\boldsymbol{s}$ and $\boldsymbol{c}$ can assumed to be linear then $\boldsymbol{s} = \mathbf{G}\boldsymbol{c}$. When the theoretical model on which this estimate is based is also linear then $\boldsymbol{c} \approx \boldsymbol{c}_{mod} = \mathbf{H}\boldsymbol{s}$, where $\mathbf{H}$ is the sensitivity matrix which relates the concentrations to fluxes from the various sources, which is derived from an atmospheric transport model. Due to the linearity of transport, this use of a linear estimator is valid. For a good estimator, $\mathbf{G}$ is an approximate inverse of $\mathbf{H}$ such that $\mathbf{GH} \approx \mathbf{I}$ and $\mathbf{HG} \approx \mathbf{I}$, where $\mathbf{I}$ represents the identity matrix.

Tarantola (2005) and Enting (2002) show that if it can be assumed that the probability of the concentrations given the sources, $\mathrm{p}(\boldsymbol{c} \mid \boldsymbol{s})$, and the probability of the sources, $\mathrm{p}(\boldsymbol{s})$, are multivariate normal with covariance matrices $\mathbf{C}_{\boldsymbol{c}}$ and $\mathbf{C}_{\boldsymbol{s}_0}$, respectively, and respective means $\boldsymbol{c}_{mod} = \mathbf{H}\boldsymbol{s}$ and $\boldsymbol{s}_0$, then the estimated sources can be obtained by minimising the cost function

$$J(\boldsymbol{s}) = \frac{1}{2}\left((\boldsymbol{c}_{mod} - \boldsymbol{c})^T \mathbf{C}_{\boldsymbol{c}}^{-1}(\boldsymbol{c}_{mod} - \boldsymbol{c}) + (\boldsymbol{s} - \boldsymbol{s}_0)^T \mathbf{C}_{\boldsymbol{s}_0}^{-1}(\boldsymbol{s} - \boldsymbol{s}_0)\right) \tag{1.1}$$

which can be shown to give the estimate

$$\boldsymbol{s} = \boldsymbol{s}_0 + \mathbf{C}_{\boldsymbol{s}_0}\mathbf{H}^T\left(\mathbf{H}\mathbf{C}_{\boldsymbol{s}_0}\mathbf{H}^T + \mathbf{C}_{\boldsymbol{c}}\right)^{-1}(\boldsymbol{c} - \mathbf{H}\boldsymbol{s}_0) \tag{1.2}$$

with corresponding covariance matrix

$$\begin{aligned} \mathbf{C}_{\boldsymbol{s}} &= \left(\mathbf{H}^T\mathbf{C}_{\boldsymbol{c}}^{-1}\mathbf{H} + \mathbf{C}_{\boldsymbol{s}_0}^{-1}\right)^{-1} && (1.3)\\ &= \mathbf{C}_{\boldsymbol{s}_0} - \mathbf{C}_{\boldsymbol{s}_0}\mathbf{H}^T\left(\mathbf{H}\mathbf{C}_{\boldsymbol{s}_0}\mathbf{H}^T + \mathbf{C}_{\boldsymbol{c}}\right)^{-1}\mathbf{H}\mathbf{C}_{\boldsymbol{s}_0} && (1.4)\end{aligned}$$

The Bayesian approach results in biased estimates of sources towards the prior estimates. It is this property which compensates for the ill-conditioned (not enough data to result in a unique solution) nature of estimating sources from atmospheric concentrations, and is referred to as regularising the problem (Kaminski et al., 1999b; Enting, 2002).

In a synthesis inversion, the sources are discretised in terms of process as an unknown scale factor, $\boldsymbol{s}_{\boldsymbol{\mu}}$, multiplied by a specified source distribution, referred to as

the basis function (Enting, 2002). The surface flux field is decomposed into prescribed spatiotemporal patterns, and then the transport function is run separately with each source component and the contributions of each of the monitoring sites and times are recorded. These contributions are referred to as Green's function and are a discretised impulse response function that quantifies the response of the modelled concentration at the observational sites and time periods to unit changes in the magnitude of the each source component. Green's function (**H**) is the Jacobian matrix representing the first derivative of the modelled concentration at the observational site and dates with respect to the coefficients of the source components. Performing these runs can limit the number of source components due to the length of time it takes to run the transport model (Kaminski et al., 1999a). Kaminski et al. (1999a) proposed an alternative method, which resulted in reduced number of transport model runs. This method used the adjoint of the three dimensional transport model to calculate the Jacobian matrix, and used the Tangent Linear and Adjoint Model Compiler (TAMC) to do the calculation. This results in a large reduction in running time.

The approach adopted in this study follows the methodology first outlined in Lauvaux et al. (2008). In order to generate the influence functions for the inversion procedure, a Lagrangian particle dispersion model (LPDM) is used. The model implemented for this study is the LPDM model developed by Marek Uliasz (1993). An LPDM simulates the release of a large number of particles from arbitrary emissions sources by tracking the motion of the particles (Uliasz, 1993, 1994). The model can be run backward in time, in receptor-orientated mode, to calculate the influence functions for a given receptor based on the particle counts produced. In this mode, the particles are released from the measurement locations and travel to the surface and the boundaries (Lauvaux et al., 2008).

The following sections describe some of the considerations and approaches which have been used to obtain each of the inversion components, particularly in mesoscale inversions.

### 1.3.1 Atmospheric Observations

There are global networks of atmospheric monitoring stations, where $CO_2$ is measured either continuously in situ, or via flask sampling where discrete samples are collected and then analysed at a central laboratory (Ciais et al., 2010). The continuous measurements need to be made precisely and accurately, and therefore an international protocol needs to be adhered to for the instrumentation, plumbing and calibration.

These measurements represent a continuation and expansion of the monitoring network first established by Bolin and Keeling (1963), with the first two stations at the South Pole and at Mauna Loa. These measurements have been compiled into various global databases, such as GLOBALVIEW-$CO_2$ and ObsPack (Masarie et al., 2014), with the many of the observation sites being run by or in collaboration with the National Oceanic and Atmospheric Administration – Earth System Research Laboratory (NOAA-ESRL) network (Ciais et al., 2010). Calibration gases are available from NOAA and the World Meteorological Organisation (WMO), and can be cross-referenced at CSIRO, Australia. This is important due to slightly different levels of fractionation of $^{13}C$ and $^{18}O$ in atmospheric $CO_2$ between the northern and southern hemispheres. By using these calibration standards, observations can be linked to a lab and time period and allows for the integration of a single site into multiple observation networks (Palmer et al., 2018).

For the purposes of the inversion, the observation data are interpolated to a common time interval and gaps in the data are filled by extrapolation from the marine boundary-layer measurements (Gurney et al., 2003). Only sites with less than 30% extrapolated data are generally included in an inversion (Bousquet et al., 2000; Gurney et al., 2003; Law et al., 2003). Historically, most observation sites were located on the marine boundary layer since they were originally installed to measure large scale sources and sinks at oceanic sites, and therefore the amount of local noise needed to be minimised (Bousquet et al., 2000; Ciais et al., 2010). Over recent years an attempt has been made to reduce the undersampling over continental regions through programs such as the North America Carbon Program and CARBOEUROPE (Ciais et al., 2010). There are now 439 sites listed on the NOAA site which form part of the ObsPack data product (`https://www.esrl.noaa.gov/gmd/ccgg/obspack/labinfo.html`) (Masarie et al., 2014). The tropics and Southern Hemisphere continental areas are still hugely undersampled (Peylin et al., 2013).

The measurements are usually processed further before being used to estimate fluxes. In annual inversions, the data at each site for each year is averaged, and the residuals of the observations from the mean are then used to calculate the uncertainty measure for the data. An alternative method to estimating the data error, used by Peylin et al. (2002) who used both monthly and annually average data, assumes a seasonal cycle in the data, which is repeated each year. The data from each station is then fit to a smooth time series consisting of an annual mean value and a global trend, which was identical at all sites, and a mean seasonal cycle. The standard deviation of all the residuals between the raw flask data and the smooth time series were used

as the monthly data errors, and the error for the annually averaged data was derived from these monthly errors.

### 1.3.2 Atmospheric Transport Model

The atmospheric transport model is a critical component of a tracer inversion. Atmospheric transport modelling is required to solve for the influence of a changing source area on atmospheric measurements. A transfer function links the site level observations to the surrounding terrain (Göckede et al., 2010). The response function **H**, which is linear in the case of transport of a passive constituent, is represented by a numerical model that solves the conservation equations of geophysical fluid mechanics (mass, momentum, energy) on a three dimensional grid covering the atmosphere from the surface up to typically the mid-stratosphere (approximately 20 to 30 km above ground) (Ciais et al., 2010). Most three dimensional atmospheric transport models are based on global circulation models (GCMs) which calculate the physical and dynamical state of the atmosphere (Enting, 2002). Processes which are solved for in these models include large-scale advection and large-scale horizontal diffusion, and sub-grid transport processes are parameterised such as moist convection, vertical diffusion and boundary layer mixing by turbulence (Ciais et al., 2010). The complexity of transport models has increased with computing power. Versions from the 1980's typically operated at a resolution of 10° by 10° by 19 vertical layers, whereas current atmospheric models are operating at a resolution of 1 to 2° with 20 to 50 layers in the vertical.

A diverse set of atmospheric transport models are available, and since atmospheric transport modelling is so complex, these different models have resulted in a significant spread in the flux estimates (Ciais et al., 2010). In global inversions, one of the components which differs between models, and has a large impact on the estimates, is the rectifier effect (Bousquet et al., 1999; Peylin et al., 2002) which produces a large positive south to north latitudinal $CO_2$ gradient. This effect is large in certain models and almost absent in others, and is a significant contributor to the estimation error attributable to transport.

As already mentioned earlier, Green's function is one way of generating the matrix **H**. These functions represent the first derivative of the modelled concentration at the observational sites, and is dated with respect to the coefficients of the source components. Transport equations describe the rate of change of the modelled concentration

$\boldsymbol{c}_{mod}(\mathbf{r}, t)$:

$$\frac{d}{dt}\boldsymbol{c}_{mod}(\mathbf{r}, t) = \boldsymbol{s}(\mathbf{r}, t) + T[\boldsymbol{c}_{mod}(\mathbf{r}, t)] \tag{1.5}$$

and integration of the transport equations provides Green's functions (Enting, 2000). Computationally, to generate Green's functions, if there are $n$ source components, then $n$ transport model runs are needed to obtain the $n$ differential quotients constituting the columns of the Jacobian matrix (Kaminski et al., 1999a).

To avoid this computational cost, the adjoint of the transport model can be used to speed up the calculation of the concentration gradients at the observational locations (Kaminski et al., 1999a). This involves the creation of computer code that directly determines the sensitivity of the observations to the sources. In Kaminski et al. (1999a) the adjoint using the Tangent Linear and Adjoint Model Compiler (TAMC, Giering, 1997, available at `http://www.autodiff.com/tamc/`). However, for many atmospheric transport models a formal adjoint does not exist. A way to avoid the adjoint approach is to use ensembles of randomly perturbed emission fields so that the information in uncertainty covariance matrix of the fluxes is represented in fewer dimensions, for example by using a ensemble Kalman filter. An approximation to the covariance matrix is represented by a finite ensemble of state vectors made up of a mean state and the deviations from this mean state. These vectors can be created as unconditional realisations of uncertainty covariance matrix, for instance through a Cholesky decomposition (Peters et al., 2005). The advantage of the ensemble data assimilation approach is that although it returns an approximation of the uncertainty covariance matrix, it does not need an adjoint model or other linearisation of the observation operator (Peters et al., 2005).

For a mesoscale scale model, which usually is performed over a gridded domain, the sensitivity matrix can be generated by means of a Lagrangian particle dispersion model (LPDM), which is self-adjoint. An LPDM simulates the release of a large number of particles from arbitrary emissions sources by tracking the motion of the particles (Uliasz, 1993, 1994). The model can be run backward in time, in receptor-orientated mode, to calculate the influence functions for a given receptor. In this mode, the particles are released from the measurement locations and travel to the surface and the boundaries (Lauvaux et al., 2008). The influence functions, represented as a source-receptor matrix, describes the sensitivity of a receptor element y to a source element x, where a receptor element could be the average concentration of a given grid cell at a particular point in time, or it could be the measurement at a sampling station, and a source element could be a point, area or a volume source (Seibert and Frank, 2004).

An LPDM is driven by mean horizontal winds (u,v), potential temperature, and turbulent kinetic energy (TKE). These variables are produced by the a regional climate model. Based on these inputs LPDM diagnoses turbulent vertical velocity and dissipation of turbulent energy. Whenever a particle touches the surface, its position and release time are saved. At each timestep, which depends on the TKE (one to 20s), the fraction of particles within some volume, gives the influence of that volume on the receptor. If the volume includes the surface, then this will give the influence of the surface sources (Lauvaux et al., 2008). A matrix of influence functions is produced and this is the same matrix as the Jacobian matrix (**H**) referred to in the inverse modelling procedure. It describes the sensitivity of each observation to each unknown source. The size of this matrix depends on the dimension of the vector of surface fluxes plus the unknown boundary concentrations (Lauvaux et al., 2008).

During the inversion process, all of the parameters of the atmospheric transport are considered to be fixed. Therefore it is assumed that the parameters of the atmospheric transport model are perfectly known. Rather, the error attributed to the atmospheric transport model needs to be included in the observation error covariance matrix, which represents the error in the modelled concentrations (Tarantola, 2005). One way of determining the sensitivity of the inversion to the atmospheric transport model is to run multiple inversions with different atmospheric models, as performed for many of the global inversion studies discussed in the previous section. To assess the modelled concentration error attributed to the transport model a number of approaches are available. The error can be assessed directly through measurements, for example measuring the mixing heights by means of radiosonde's and comparing these to the heights derived from a regional climate model. By propagating this uncertainty into the modelled concentration estimates of the model error attributable to this component of the transport model can be obtained. Gerbig et al. (2008) found that mixing heights estimated by the ECMWF meteorological data for the period May to June 2005 had errors up to 40 % during the day, and up to 100 % during the night, translating to errors in the modelled concentrations of on average 3 ppm. This method is limited by the availability of measurements. Lauvaux et al. (2009) used simulation methods to assess the atmospheric transport error in the attribution of the boundary condition to the observed concentration. The authors perturbed synoptic conditions that were generated by the short range ensemble prediction system PEARP, but maintained the physical and thermodynamic consistency of the coupled higher resolution Eulerian model Méso-NH. The variance in the modelled concentrations from the ensemble of transport models was estimated over the domain, together

with associated spatial and temporal correlations. These could then be used to generate the modelled observation errors and correlations. The computational costs of running the atmospheric transport model and calculating the variances and covariances between the modelled concentrations limits the number of perturbations that can be assessed. Lauvaux et al. (2009) used ten perturbations, but ideally 50 to 100 would have been required to estimate the error correlations.

### 1.3.3 *A Priori* Estimates

An important consideration in any atmospheric inversion is the number and spatial extent of the source regions. The advantage of selecting many source regions over too few regions is that aggregation error is reduced (Rayner et al., 1999), but it is important to take into account the limits of the atmospheric transport model to resolve small-scale detailed transport correctly (Peylin et al., 2002). The aggregation error is due to the degradation of the spatial resolution of the source regions to a resolution that the inversion can accommodate. When there is heterogeneity in the surface fluxes and inhomogeneous transport, averaging the surface fluxes to a coarser resolution leads to errors occurring in the modelled concentrations due to the measurement not representing the larger pixels over which the transport is modelled (Kaminski et al., 2001; Ciais et al., 2010). Kaminski et al. (2001) provides a process for determine the aggregation error in an inversion. On the other hand, the inversion is limited in how many source regions it can realistically solve for by the degrees of freedom for the signal (DFS) (Michalak et al., 2005; Chevallier et al., 2007). The DFS describes the number of independent pieces of information that the observations provide, given the prior fluxes and the prior flux uncertainty covariance matrix. Therefore the DFS are affected not only by the number of source regions, but also by the flux uncertainty correlations. Land regions should be chosen to represent either biomes, or characteristic atmospheric transport influences, whereas oceanic regions should be chosen to represent large-scale ocean circulation features (Rayner et al., 1999). The specification of these regions has been shown to be a large contributor to the uncertainty in the posterior fluxes (Peylin et al., 2002). Misspecification of the prior fluxes from these regions contributes to the model-data mismatch by introducing systematic errors into the modelled concentrations whenever fluxes from these regions are observed at the measurement site (Michalak et al., 2005).

Although the fossil fuel emissions due to man-made activities is known globally to within 5%, there are large uncertainties as to how these emissions are distributed in space and time over industrial regions (Ciais et al., 2010). Andres et al. (2011)

provide a global, monthly emission record for fossil fuel consumption, and in addition, data from car traffic, electricity, heating, and other residential use, as well as census data, provide information on local emissions of $CO_2$. For a local scale inversion, it is necessary to have these data at high spatial and temporal resolutions, and the prior information needs to be provided at the same spatial extent and grid as used for the transport model. Spatially disaggregated fossil fuel emission products are available. Göckede et al. (2010) prescribed fossil emissions to each 10 km $\times$ 10 km grid cell from the inventory made available through the Vulcan project (Gurney et al., 2008b). The concentration enhancement from the fossil fuel emissions were derived and subtracted from the observations. The resulting concentrations were used to solve the inversion. EDGAR is a global product on a $0.1^\circ \times 0.1^\circ$ grid, which provides the total anthropogenic emissions of $CO_2$ as estimated from proxy data such as population counts and information on the road transport network (Janssens-Maenhout et al., 2012). There are also products available that make use of satellite products on night-time lights. The fossil fuel data assimilation system (FFDAS) uses a modified Kaya identity to express emissions as a product of areal population density, per capita economic activity, energy intensity of the economy, and carbon intensity of energy, and this model is further constrained with various observations, including reported national emissions and data on the distribution of night lights and population (Asefi-Najafabady et al., 2014; Rayner et al., 2010). There also exists the more recent ODIAC (Open-source Data Inventory for Anthropogenic $CO_2$) product which makes use of global energy consumption statistics and distributed the emissions from these activities based on known point source emitters, such as power plants, and on a global night light distribution satellite product (Oda and Maksyutov, 2011). Emissions from point sources, such as those from power plants, are estimated separately from the diffuse emissions, for example those due to transport .

Depending on the domain of the atmospheric inversion, grid cells over the ocean are subject to air-sea $CO_2$ fluxes, which are driven by the partial pressure difference between $CO_2$ dissolved in the surface waters and $CO_2$ in the atmosphere above these waters, which is then multiplied by the exchange coefficient describing the mass transfer across this interface. Takahashi et al. (2009) make available a global map of $CO_2$ air-sea flux patterns based on ocean surveys, with additional data available from `http://cdiac.ornl.gov/oceans/`. The degree of confidence in the global uptake of $CO_2$ by the world's oceans is approximately 30%, but the degree of confidence at the scale of ocean gyres, especially in the Southern Ocean where there is relatively fewer sampling incidents, is much lower (Ciais et al., 2010).

The terrestrial vegetation $CO_2$ flux is the net result of uptake of $CO_2$ through photosynthesis, and release of $CO_2$ through respiration of plants and soils, including the decomposition of organic material. The direct measurement of these fluxes can be achieved through the eddy-covariance technique, which determines fluxes from the covariance between fluctuations in anomalous vertical wind and $CO_2$ mixing ratio (see e.g. Aubinet et al. (2000)). But these measurements are limited during unsteady atmospheric conditions and over complex terrain, as well as being difficult to upscale from the landscape level (Chevallier et al., 2006; Ciais et al., 2010) and there being a limited number of these measurement sites. Therefore land-atmosphere modelling schemes are used to estimate these biospheric fluxes. But the uncertainty in these estimates can be as much as 100% of the estimated flux, and therefore the terrestrial biospheric flux represents the greatest uncertainty in surface fluxes (Ciais et al., 2010). As an example, biogenic fluxes used by the Laboratoire des Science du Climat et de l'Environnement (LSCE) (Chevallier et al., 2006, 2010), are derived from the Organizing Carbon and Hydrology In Dynamic EcosystEms model (ORCHIDEE). The CSIRO Atmosphere Biosphere Land Exchange Model (CABLE) land-atmosphere scheme is a similar model, but developed in Australia and parameterised for the semi-arid type landscapes found there. This model calculates carbon, water and heat exchanges between the land surface and atmosphere as described in Kowalczyk et al. (2006). Biogenic fluxes can also be obtained from nationally reported biogenic $CO_2$ emission inventories. A difficulty with biogenic emission inventories which following the United Nations Framework Convention on Climate Change (UNFCCC) reporting requirements is that not all activities are reported, such as lateral transport of carbon that lead to $CO_2$ emissions elsewhere, and these emissions are usually only reported for managed land (Ogle et al., 2015). Therefore to obtained a full carbon balance, these inventories needed to be supplemented with additional information, such as decomposition of waste, agricultural waste burning, $CO_2$ uptake by crops, and respiration by livestock and humans (Ogle et al., 2015).

An additional, certainly large source of $CO_2$ emissions, which are usually not adequately accounted for in most inversions exercises, are disturbances such as combustion by fires, land clearing, pest breakouts, and land use change (Ciais et al., 2010). These events are not accounted for by the land-surface schemes, so would need to be accounted for separately. In a mesoscale inversion, if there is good monitoring data, these events can be explicitly accounted for, by adding estimates of the fluxes due to these disturbances into the prior flux field. The overall flux is then the result of the overlay of these three flux fields, resulting in the net flux in $CO_2$.

In the context of global inversions, in addition to selecting the regions, it is common practice to specify background fluxes as additional sources. The specification of these fluxes differs between studies. In Gurney et al. (2003), four background fluxes were considered, which consisted of two fossil fuel emission fields, an annually balanced, seasonal terrestrial biosphere exchange and an air-sea gas exchange. These fluxes were specified with very small prior uncertainties so that their magnitude could stay fixed. The regional fluxes estimated were then deviations from these mean background fluxes. To initialise the fossil fuel flux, the $1^\circ \times 1^\circ$ mean fossil source estimates of Andres et al. (1996) and Brenkert (1998) were used for the years 1990 and 1995 respectively. The monthly global oceanic exchange derived from $\Delta p\mathrm{CO}_2$ measurements of Takahashi et al. (1999) were used to derive prior estimates for the oceanic exchange, and the CASA model was used to derive $1^\circ$ by $1^\circ$ seasonal biospheric exchange. Prior estimates of the fluxes in the 22 regional basis functions were determined from independent estimates of terrestrial and oceanic exchange. The prior uncertainties for the land fluxes were based on the growing season net flux as provided by CASA, since it was unlikely that an annual net flux would exceed this value. The prior flux uncertainties for the oceanic fluxes were guided by aggregate estimates from Takahashi et al. (1999) and were proportional to the area of the region.

For mesoscale inversions, the concentrations at the boundary of the domain need to be provided as additional unknowns, and therefore prior estimates of the concentrations and their uncertainties are required, or they need to be stipulated, in which case the inversion solves for differential concentration. The observational data which can be used as prior information for the boundaries can be obtained from CarbonTracker (Peters et al., 2007) which is a global scale data assimilation system, trained and validated on measurements from 81 global monitoring sites (Göckede et al., 2010). This is discussed in more detail in section 1.3.5.

Ciais et al. (2000) specified a global fossil fuel flux, but then specified regional sources for the remaining fluxes. The oceanic fluxes were initialised using the estimates from Takahashi et al. (1997). They specified a deforestation flux which was only calculated for tropical land regions, derived from Houghton et al. (1987). For each land region a neutral annually balanced biospheric flux (estimated from GPP and ecosystem respiration from SIB-2), and an anthropic net biospheric flux, which was estimated from Friedlingstein et al. (1995) who modelled processes of such as $\mathrm{CO}_2$ fertilisation, climate variability, and nitrogen fertilisation. The regional flux for the land region was then the sum of the deforestation, neutrally balanced biospheric

flux, and the anthropic net biospheric flux. They specified large prior estimates on all of the prior fluxes to allow the inverse procedure to optimise without constraints.

Kaminski et al. (1999b) used a similar procedure, but each region now included a fossil fuel flux as well, as opposed to having a global background fossil fuel flux. They specified, for each region, that the flux was the sum of a seasonal terrestrial biosphere in annual equilibrium, a correction for land use change, the ocean, and fossil fuel burning. The terrestrial biospheric fluxes were derived from the Simple Diagnostic Biosphere Model (SDBM). The correction for land use change was derived from land use statistics of Houghton et al. (1987) and Heimann and Keeling (1989). The oceanic component of the seasonal net exchange fluxes were derived from a simple plankton model, and were not constrained to balance. Fossil fuel burning corrections were derived from Andres et al. (1999b). Compared to the previous study, Kaminski et al. (1999b) used a much more rigorous method of determining prior uncertainties. For regions with land fractions of greater than 1% the terrestrial flux, the flux was considered to be the sum of NPP (net primary productivity), soil respiration, and land use change. For each month the uncertainty was determined by assuming independent uncertainties of 50% for NPP and soil respiration, and 100% for land use change. For oceanic regions, every grid cell with an ocean fraction of more than 1% and with nonzero annual mean fluxes, the minimum uncertainty was assigned (which exceeded 100% of the respective flux). Therefore every grid cell would have a land or ocean component, or both. Proportional uncertainty was assigned to those grid cells which had both.

Lauvaux et al. (2012) performed an inversion to solve for $CO_2$ fluxes over Iowa and the surrounding states, an area dominated by agriculture. Two alternative priors with different spatial configurations were used to prescribe the prior terrestrial biospheric fluxes. Lauvaux et al. (2012) used NEE estimates from SiBcrop vegetation model (Lokupitiya et al., 2009) at a 10 km resolution. The second prior was taken from the CarbonTracker inverse system, which uses atmospheric mixing ratios from the NOAA global network of surface stations to optimize surface fluxes over large ecoregions. The prior fluxes used in the CarbonTracker inverse system are derived from the CASA biogeochemical model, which lacks a description of applied phenology that is specific to crops. Prior boundary concentrations were obtained from CarbonTracker, but were corrected according to aircraft profile measurements of $CO_2$ concentrations. The authors found that while the inversion produced posterior flux estimates that were similar even if a different prior product was used, features of the prior flux fields were maintained in the posterior estimates. The authors found that

the inversion framework was susceptible to large biases resulting for the choice of background conditions.

Göckede et al. (2010) used a terrestrial biosphere $CO_2$ flux model (BioFlux), which assimilated remotely sensed data, surface meteorology, and data from eddy-covariance flux sites to produce estimates of gross primary productivity, autotrophic and heterotrophic respiration, and used these three fluxes to generate NEE estimates. These fluxes were modelled at a spatial resolution of 1 km and a temporal resolution of 1 hour, but instead of solving for individual gridded fluxes, Göckede et al. (2010) solved for posterior flux base rates for surface types, thereby reducing the number of parameters solved for by the inversion. Fossil fuel emissions were obtained from the Vulcan project (Gurney et al., 2008b). These fossil fuel emissions were allocated as fixed fluxes in the inversion framework. Rivier et al. (2010) also prescribed fixed fossil fuel fluxes, these derived from the EDGAR product (Janssens-Maenhout et al., 2012), and used terrestrial biospheric fluxes from the TURC model as prior estimates. TURC is driven by daily climate fields and 10-day Normalised Difference Vegetation Index from satellite products.

Therefore several different approaches are possible for the characterisation of fluxes in the inversion model. Although studies have looked at the contribution of regional selection to the overall estimation error, little information is available for the error introduced by using different flux characterisations. Each set up of fluxes dictates the required prior information, and therefore it is very likely that the atmospheric inversions, even over the same period and using the same atmospheric observations, would result in different regional flux estimates if different flux characterisations, and consequently different prior information, were used.

Additional prior constraints can be included, such as specifying the global atmospheric $CO_2$ growth rate and a global $CO_2$ concentration background value (Gurney et al., 2003), or constraining the global annual net land and ocean uptake (e.g. based on information from a report such as the IPCC) (Bousquet et al., 1999), or specifying the annual uptake implied by the difference of fossil fuel input rate and atmospheric increase rate (Peylin et al., 2002), or partitioning the global uptake by land and ocean using measurements of $O_2/N_2$ and $\delta^{13}C$ (Rayner et al., 1999; Peylin et al., 2002; Rayner et al., 2008).

### 1.3.4 Covariance Matrices

Both the estimation of the posterior fluxes and the posterior uncertainty covariance matrix require the two covariance matrices, $\mathbf{C}_{\boldsymbol{c}}$ and $\mathbf{C}_{\boldsymbol{s}_0}$, of the modelled concentra-

tion errors and prior flux uncertainties respectively. Although these two covariance matrices are critical to the results of an inversion, this is where the greatest discrepancies exist in the literature. The manner in which these matrices are generated varies from study to study, and can be considered as the "greatest single weakness" in many atmospheric inversion studies (Rayner et al., 1999; Michalak et al., 2005).

Related to specifying the uncertainties of the prior estimates is the check of consistency for the atmospheric inversion. As a first check, the measurement residuals (difference between optimised concentrations and the observed concentrations) should be examined. The standard deviation should be similar to the expected measurement error, and the residuals should be approximately normally distributed. A second check is to calculate the global $\chi^2$ statistic. This is defined as twice the cost function of the Bayesian procedure at its minimum, divided by the number of observations (Peylin et al., 2002; Tarantola, 2005). This value should be close to one. Values more than one indicate that the residuals are larger than the uncertainties originally assumed, and this implies some error in the model specification, such as estimating prior uncertainties that are too small, or the transport errors are leading to unrealistic values. Values of $\chi^2$ that are lower than one indicate that the initial data errors could have been decreased to ensure a better fit between model and data (Peylin et al., 2002). This check is necessary but not sufficient as it does not give any indication of the correct ratio of observation uncertainty to prior flux uncertainty. More than one combination of covariance parameters will result in the desired $\chi^2$ statistic (Michalak et al., 2005).

Many of the earlier inversion studies assumed $\mathbf{C_c}$ and $\mathbf{C_{s_0}}$ were diagonal matrices, which reduces computational costs, but some errors are known to be either spatially or temporally correlated (Michalak et al., 2005). In addition to increasing computational costs, these error correlations may be difficult to estimate. The global $\chi^2$ statistic can be used to balance the error correlations with the uncertainties. If the uncertainties can be estimated with at least some degree of certainty, the correlations can be scaled to ensure that the $\chi^2$ statistic is close to one. As the number of regions solved for in an inversion increases, the inverse problem becomes highly under-constrained and hence the reduction of uncertainty for each region remains small. Therefore, as one moves from a global inversion framework to a mesoscale framework the hard constraint of fixed patterns within large regions can be replaced by a softer constraint of correlated fluxes defined at the resolution of the transport model (Peylin et al., 2005). As the density of observations increases, spatial error correlations between observations sites can no longer be ignored (Lauvaux et al., 2009), and temporal error correlations have

also been shown to be significant (Lauvaux et al., 2009), but the estimation of the temporal correlation length is challenging.

#### 1.3.4.1 Observation Error Covariance Matrix

The observation error covariance matrix includes both measurement error and the errors in modelling the observations. Sources of errors include random and systematic measurement errors, which are usually negligible at an accredited measurement station; transport model errors; and aggregation errors (Ciais et al., 2010). Aggregation errors are due to the degradation of the spatial resolution from the original resolution of the transport model to a lower resolution that the inversion can accommodate. When there is heterogeneity in the surface fluxes and inhomogeneous transport, averaging the surface fluxes to a coarser resolution leads to errors occurring in the modelled concentrations due to the measurement not representing the larger pixels over which the transport is modelled (Kaminski et al., 2001; Ciais et al., 2010). This is particularly applicable in mesoscale inversions, where the high resolution transport simulations are more uncertain. The aggregation errors need to be added to the observation errors, as shown by Kaminski et al. (2001) and (Tarantola, 2005).

For a global inversion, Baker (2000) estimated the observation error covariance matrix, $\mathbf{C_c}$, by comparing the monthly observational means at Mauna Loa to a smoothed line and determining the monthly standard deviations. These values ranged between 0.34 and 0.16 ppm, and so a value of 1 ppm was applied to each region, with the assumption that most places would have a higher standard deviation than Mauna Loa. It was also assumed that the matrix was diagonal, and so no correlation between measurement locations was taking into account. The approach taken in the TransCom 3 project (Gurney et al., 2003), in the case of the observation covariance matrix, was to derive the residual standard deviation of the observed $CO_2$ concentrations around a smoothed timeseries provided by GLOBALVIEW-$CO_2$. In the observation error covariance matrix used by (Chevallier et al., 2010), they considered the error of the measurement, the error of the transport model that simulates the concentration from the fluxes, and the representation error (which is the mismatch between the scale of the measurement and the scale of the transport model). Their approach was time independent so that the variance of the observations was set to half the variance of the high frequency variability of the de-seasonalised and de-trended $CO_2$ time series at each particular station. These errors were as small as 0.1 ppm for marine stations and went up to several parts per million for continental stations, reaching up to 6

ppm, which was more than 1 order of magnitude larger than the measurement errors. Due to temporal correlations in the observations, the continuous measurements were further de-weighted by multiplying the observation error by the square root of the number of local data within the selected local time range, and so error correlations were neglected. Lauvaux et al. (2008) carried out a mesoscale inversion on synthetic data. The approach used here to obtain the error covariance matrix was to compare the modelled values of $CO_2$ to aircraft and tower data that were available for the four day period under assessment. They found the largest difference of approximately 3 ppm, and set the diurnal observation error to be 4 ppm, taking into account uncertainty in LPDM. Schuh et al. (2010), who ran a mesoscale inversion for North America based upon a regional meteorology model (RAMS) and an underlying biosphere (SiB3) model, both running on the same 40 km grid over North America, found that transport and representation errors were likely as high as 5 to 6 ppm. The assumed that observation errors were independent and identically distributed. Wu et al. (2013) solved for the standard deviation terms of the observation error covariance matrix, by fitting the parameters by means of maximum likelihood estimation to available data for a mesoscale inversion study. It was assumed that these terms were homogenous over crop regions. The estimated values were between 2.9 and 3.6 ppm.

As well as the diagonal elements of the error covariance matrix, it is also important to consider the off-diagonal elements. Using the maximum likelihood estimation method, Wu et al. (2013) assigned a temporal correlation length of 1 hour, and calculated spatial correlation lengths of between 20 and 45 km. Lauvaux et al. (2009) assessed the spatial and temporal correlations by analysing a statistical ensemble of mesoscale simulations. The ensemble consisted of ten members and a reference simulation using the operational short range forecast PEARP, perturbed using the Singular Vector technique. Lauvaux et al. (2009) found large temporal correlations of more than 0.5 in the afternoon, which then decreased at night. Horizontal correlation lengths were of order 50 km, with significant spatial correlation up to 150 km. This suggested a minimum separation distance of 50 km between sites in order to ensure benefit of adding new stations to the network. This was then used by Lauvaux et al. (2012) to contribute towards the specification of the observation error covariance matrix. The overall $\mathbf{C_c}$ matrix was derived in a four step process. The error from the transport model, WRF, was evaluated by comparing the simulated concentrations to observations from nine aircraft transects. To avoid inconsistencies in the Lagrangian model simulation, observations were removed by assigning large variances to these

observations, when large differences occurred between the direct $CO_2$ concentrations from WRF-Chem$CO_2$ and the backward concentrations from the LPDM. The aggregation and model errors were computed using the standard deviation of the difference between the direct WRF mixing ratios and the backward LPDM mixing ratios over each week. As a sensitivity analysis the error correlations in the observation error covariance matrix were assigned from the ensemble simulations in Lauvaux et al. (2009).

#### 1.3.4.2 Prior Flux Uncertainty Covariance Matrix

For a global inversion, Baker (2000) estimated the prior flux uncertainty covariance matrix, $\mathbf{C}_{s_0}$, to have a standard deviation of 2.0 Pg C $yr^{-1}$ applied to each of the monthly flux estimates over land, and 1.0 Pg C $yr^{-1}$ to each of the ocean regions. This covariance was also assumed to be diagonal, and so the covariances between months and between sites was assumed to be zero (assuming both spatial and temporal independence). The Transcom 3 project (Gurney et al., 2003) used, for land prior flux covariances, the growing season net flux (GSNF) obtained from the CASA model of net ecosystem production, which was used as a ecologically relevant upper bound. The ocean prior estimates were guided by the aggregate estimates of Takahashi et al. (1999).

In a mesoscale inversion Lauvaux et al. (2008) set the prior flux error at 2 g C $m^{-2}$ $day^{-1}$ for the surface and 4 ppm for the boundaries, and assumed uncorrelated flux errors on the domain (no spatial correlation). To calculate the biogenic component of the prior flux covariance matrix, at the same grid scale as for the transport model, Chevallier et al. (2010) set the standard deviations of the fluxes proportional to the hetrotrophic respiration flux of ORCHIDEE. Chevallier et al. (2010) assumed temporal correlations decayed exponentially with a length of one month, and that spatial correlations followed an e-folding length of 1000 km. Schuh et al. (2010) mesoscale inversion for North America used SiB coupled to Regional Atmospheric Modeling System to produce prior estimates of GPP and ecosystem respiration. The spatially and temporally disaggregated Vulcan fossil fuel flux inventory was prescribed as fixed in the inversion. They calculated exponential uncertainty covariances for GPP and ecosystem respiration separately, and assumed correlation lengths of 500 km. In the inversion that Lauvaux et al. (2012) performed over the Mid Continent Intensive (MCI) domain, the focus of the inversion was on solving biogenic fluxes, and two prior flux estimates were considered. The NEE (net ecosystem exchange) estimates

for the SiBcrop vegetation model (Lokupitiya et al., 2009) were compared to the optimised flux estimates from the CarbonTracker inverse system (Peters et al., 2007). Prior flux uncertainties were determined from the weekly flux model-data mismatch at several locations within the domain. The standard deviations were defined as the maximum difference observed between the weekly averaged modelled and observed NEE for each of the three most common vegetation types of the region (corn, soybean, and grassland). This maximum model-data mismatch was normalised for every week following the seasonal variability of the absolute fluxes to define a weekly standard deviation. By combining the observed seasonal cycle and the maximum model-data mismatch the representation errors were reduced. The final standard deviations were between 30 to 50% of the weekly net fluxes. The standard deviations were further adjusted by computing the reduced $\chi^2$ value. The ecosystem spatial error correlation was defined as the minimum of the vegetation fraction for one given ecosystem in the two pixels (following the SiBcrop ecosystem classification, from Lokupitiya et al. (2009)) as follows:

$$C_{m,n}^{eco1} = min(f_m^{eco1}, f_n^{eco1}) \tag{1.6}$$

with $C_{m,n}^{eco1}$ the correlation coefficient between pixel $m$ and $n$ for the ecosystem type $eco1$, and $f^{eco1}$ the fraction of vegetation for $eco1$ in one given pixel. This ecosystem-based error correlation was combined with a distance based error correlation in the following way:

$$C' = (C_{eco}^{1/2} C_{dist}^{1/2})(C_{eco}^{1/2} C_{dist}^{1/2})^T \tag{1.7}$$

where $C_{eco}$ the ecosystem component, $C_{dist}$ the distance component, and $C'$ the correlation matrix in the control variable space. A correlation length of 300 km was used here, decreased by the combination with ecosystem-based correlations. The ML estimation method of Wu et al. (2013) revealed that the optimal estimates for standard deviations associated with the prior fluxes was smaller compared to those used by Lauvaux et al. (2012). Schuh et al. (2013) compared estimates for the MCI domain discussed earlier from the global CarbonTracker inverse system (Peters et al., 2007), a continental inversion over North America, and the mesoscale inversion setup described in Lauvaux et al. (2012). Similar to the inversion described in Schuh et al. (2010), the continental inversion solved for GPP and ecosystem respiration, with prior estimates from the SiBcrop model and error correlation length of 500 km. The authors concluded that the regional flux estimates from each of the three spatially-distinct frameworks showed good agreement with the inventory data, but the continental and

mesoscale inversions were better able to recover the spatial pattern of fluxes for this region.

Göckede et al. (2010) avoided the need to estimate flux uncertainty correlations by assigning each terrestrial grid to an ecoregion and solving for the fluxes within the region. This assumes 100 % error correlations for grids within the same ecoregion, but no correlation between different ecoregions.

### 1.3.5 Boundary Conditions

To obtain estimates of the $CO_2$ concentrations from the inversion when using a mesoscale model, the boundary concentration contribution to each observation needs to be included. In the mesoscale inversion of Göckede et al. (2010), boundary conditions were taken from the high-resolution North American grid of the 2007B release of CarbonTracker (Peters et al., 2007). These advected concentrations were subtracted, together with the fossil fuel concentration enhancements, from the observations, and the resulting differences used to solve the inversion.

Schuh et al. (2010) calculated the boundary concentrations by combining transport from the Parameterized Chemistry Transport Model (PCTM) and pre-calculated archived hourly SiB3 fluxes at a coarser spatial scale. The model was spun up for 2000-2004. These concentrations were then used to calculate the boundary inflow component of the $CO_2$ concentration at the measurement site by convolving the influence functions from the LPDM model over the boundary $CO_2$ concentration fields derived from PCTM. These concentrations were prescribed as fixed in the inversion. The authors compared the inversion using the PCTM boundary concentrations with one using CarbonTracker concentrations, and with one using a fixed concentration of 378 ppm. They found that the inversions had similar spatial and temporal characteristics but differed mainly in the magnitude of the NEE estimates, with the PCTM inversion resulting in a larger sink by 0.1 to 0.2 Pg C $yr^{-1}$. Differences were attributed to the underlying biosphere models in these two chemical transport models - SiB3 in PCTM versus CASA in CarbonTracker. The fixed boundary concentration resulted in a net annual source estimate, with NEE flux estimates differing both in magnitude and spatial distribution compared with the reference inversion.

Lauvaux et al. (2012) also used background conditions from CarbonTracker, but corrected for biases based on aircraft $CO_2$ measurements. Unlike the previous example, Lauvaux et al. (2012) treated the boundary concentrations as additional unknowns in the inversion, using the aircraft data-model mismatch as the standard deviations for these concentrations in the $\mathbf{C}_{\boldsymbol{s}_0}$ matrix. They considered solving for

hourly boundary concentrations or for 90 hour average concentrations. By changing to an averaging period of a few days, 16 Tg of carbon was transferred from the surface fluxes to the boundary inflow. By changing the averaging period, the contribution from the boundaries could change by several ppm when using hourly concentrations at the boundaries or averages over several days. The assumption of longer time resolution at the boundaries can be justified as errors in boundary concentration occur at the time scale of synoptic changes rather than the scale of the local dynamics. In the continental scale inversion carried out by Schuh et al. (2013), boundary inflow was CarbonTracker with bias correction based on interpolated global $CO_2$ from NOAAs GlobalView product, whereas the mesoscale inversion used boundary inflow from CarbonTracker with bias corrections from NOAA aircraft flight measurements near the boundary as for Lauvaux et al. (2012).

Peylin et al. (2005) used a two-step inversion approach to deal with the boundary information. They performed an initial global inversion similar to Gurney et al. (2002), using monthly concentration data from 64 sites. In this step the $CO_2$ fluxes for large regions are obtained. These estimates are used as prior estimates in a higher resolution inversion carried out for Europe, for which diurnally averaged concentrations from six sites within this domain are used to solved for diurnally averaged fluxes. This inversion is still a global inversion, but the regions within Europe are set at a much higher spatial resolution, and the fluxes for regions outside the domain are kept as the same spatial and temporal resolution as the initial monthly inversion. Therefore boundary concentrations are not required in this inversion framework. Rivier et al. (2010) used a similar approach for the mesoscale inversions carried out in their study, where regional transport models were nested within global transport models. In this case the regional model REMO (REgional MOdel) was prescribed with $CO_2$ concentrations at the boundary as interpolated from the TM3 global inversion.

## 1.4 City-Scale Inversions

### 1.4.1 Context

Recent literature on applications of $CO_2$ inverse modelling has focused on city-scale examples (Brioude et al., 2013; Kort et al., 2013; Lauvaux et al., 2013; Bréon et al., 2015; Boon et al., 2016; Lauvaux et al., 2016; Staufer et al., 2016; Wu et al., 2016). Cities are under pressure to reduce their carbon dioxide emissions. In the last 10 years (2006 to 2015), the average annual growth rate of carbon dioxide ($CO_2$) in the atmosphere has been 2.11 ppm per year (Dlugokencky and Tans, 2016), a sharper rise

in $CO_2$ emissions than the preceding decades (IPCC, 2014) (Figure 1.1). Of current anthropogenic greenhouse gas emissions, $CO_2$ contributes 76% (IPCC 2014). While cities cover a mere 2% of the global land surface area, they are responsible for 70% of anthropogenic greenhouse gas emissions (UN-Habitat 2011), and between 71 and 76% of $CO_2$ emissions from global final energy use (Seto et al., 2014). Annual urban $CO_2$ emissions are more than double the net terrestrial or ocean carbon sinks (Le Quéré et al., 2015).

Formal climate action plans are developed by governments and city managers, whereby the roadmap for implementing greener policies is provided, such as encouraging and developing public transport which makes use of low emission technologies, mass and rapid transport systems, and building retrofits (Sugar and Kennedy, 2013; Erickson and Tempest, 2014). Many cities are taking it on themselves to respond to the climate crisis, reacting to limited international and national policy progress, which is viewed to be moving too slowly to address the required need for mitigation against climate change (Hutyra et al., 2014). To determine if the plans implemented are having the anticipated effect of lowering $CO_2$ emissions, monitoring is required. Emissions need to be known at baseline, and monitored through time. Monitoring, reporting and verification (MRV) is a concept which is fundamental to most market and policy-based mechanisms in climate economy (Bellassen and Stephan, 2015). In order for emission reduction strategies to be properly implemented and assessed, an MRV approach should be adopted so that emission reduction claims can be validated in a consistent and reliable manner. Currently, the primary source of this information for cities is by means of emissions inventories. This relies on the collection of activity data to provide an inventory of emissions from different sectors or specific point sources. These inventories are not perfect representations of $CO_2$ emissions, heavily dependent on accurate reporting, emission factors, and on assumptions regarding temporal or spatial disaggregation of emissions (Andres et al., 2012). As the resolution of the inventory analysis increases, so too do the errors associated with these emission estimates (Andres et al., 2014; Hogue et al., 2016). Hogue et al. (2016) have demonstrated for the United States that the largest contribution to uncertainty in the Carbon Dioxide Information Analysis Center (CDIAC) gridded inventory comes from how well the distribution of the proxy (e.g. the population density) represents the distribution of emissions. Pixels which contained large point sources had large associated uncertainties, as were those with large gradients in population density near the boundary of the pixel. In the case of the large point sources, Hogue et al. (2016) showed that errors were due to both the inaccurate locations for these source

and reported magnitude of the emissions from these sources. Gately and Hutyra (2017) developed a high resolution bottom-up Anthropogenic Carbon Emissions System (ACES) for fossil fuel emissions, and they found differences by over 100% when compared to inventories based on proxies, such as population density, at spatial scales of 1°. In urban areas, differences ranged between 50 to 250%.

As the importance of these inventories increases with the need to quantify emissions and assess emission targets, it has become necessary to verify the accuracy of these estimates (NRC, 2010). Adequate MRV implementation requires transparency, quality and comparability of information, with narrow uncertainty estimates (Wu et al., 2016). Currently, uncertainties associated with urban emissions far exceed emission reduction goals, and therefore verification remains challenging. The large amount of uncertainty is due to factors such as incomplete data, inconsistency in reporting between different institutions or facilities, fugitive emissions from point sources such as those caused by gas leaks, and methodology which is rarely checked against scientific standards and procedures (Hutyra et al., 2014). A way of verifying inventory data for a city, and reducing uncertainty of inventory estimates, is by means of the Bayesian atmospheric inversion technique. It is worth noting that MRV may be referred in alternative terminology to avoid the use of regulatory terms, but the premise remains the same.

Originally implemented to determine global, large scale sources and sinks of $CO_2$ (e.g. Chevallier et al. (2010), regional or mesoscale scale atmospheric inversions are becoming more common (Lauvaux et al., 2008, 2009, 2012; Schuh et al., 2013), and more recently city-scale inversion studies are being conducted in Europe and North America Strong et al. (2011); Duren and Miller (2012); McKain et al. (2012); Brioude et al. (2013); Kort et al. (2013); Lauvaux et al. (2013); Bréon et al. (2015); Turnbull et al. (2015). Some of these results are presented in Table 1.2.

South Africa is the single largest emitter of $CO_2$ on the continent of Africa, and the 13th largest emitter in the world (Boden et al., 2011). South African cities are home to 63% of the present population (Statistics South Africa, 2011), and by 2030 this is predicted to be 71%. The City of Cape Town saw its population increase from 2,563,095 in 1996 to 3,740,026 in 2011, an overall increase of 46% (City of Cape Town, 2011). Although cities are by far the largest contributors of anthropogenic emissions, they are also seen as having the greatest potential to provide solutions for emissions reduction and climate change mitigation (Seto et al., 2014; Wu et al., 2016). By mitigating their own $CO_2$ impact, cities play a pivotal role in decreasing their own climate vulnerability, and in so doing obtain other co-benefits, such as reduction in

Table 1.2: City emission estimates obtained from previous studies using observed mixing ratios of atmospheric $CO_2$.

| **City** | **Publication** | **Emission Estimate of City kt $CO_2$ day$^{-1}$** | **Period** | **Original Emission Estimate** |
|---|---|---|---|---|
| **Los Angeles County** | Brioude et al. (2013) | 396.57 ± 25.06* | 2010 | 4590 ± 290 kg $CO_2$ $s^{-1}$ during the day |
| **Los Angeles County** | Brioude et al. (2013) | 359.42 ± 12.96* | 2002 | 4160 ± 150 kg $CO_2$ $s^{-1}$ during the day |
| **South Coast Air Basin** | Brioude et al. (2013) | 667.87 ± 36.29* | 2002 | 7730 ± 420 kg $CO_2$ $s^{-1}$ during the day |
| **Davos** | Lauvaux et al. (2013) | 0.37 ± 0.14 | 23-Dec-11 to 2-Mar-12 | Expressed as daily percentages of average annual emission |
| **Indianapolis** | Lauvaux et al. (2016) | 95.13 ± 3.98 | Sep-12 to 2-Mar-12 | 5.5 ± MtC from Sep-12 to Apr-13 |
| **Paris** | Bréon et al. (2015) | 102.47 ± 5.75 | 2010 2-Mar-12 | 37.4 ± 2.1 Mt $CO_2$ $yr^{-1}$ |
| **Paris** | Staufer et al. (2016) | 112.05 ± 5.75 | 2010 2-Mar-12 | 40.9 ± 2.1 Mt $CO_2$ $yr^{-1}$ |

shorter lived pollutants. These additional co-benefits include improved air-quality, energy access, public health, city liveability, and development of the economy and job creation through advances in green technology (Seto et al., 2014). Policies aimed at reducing $CO_2$ emissions have been shown to have co-benefits in the reduction of other pollutants such as $PM_{2.5}$ (Yang et al., 2016), $SO_2$, $NO_x$, and volatile organic compounds (VOC) van Vuuren et al. (2006), which leads to benefits for human health and the environment.

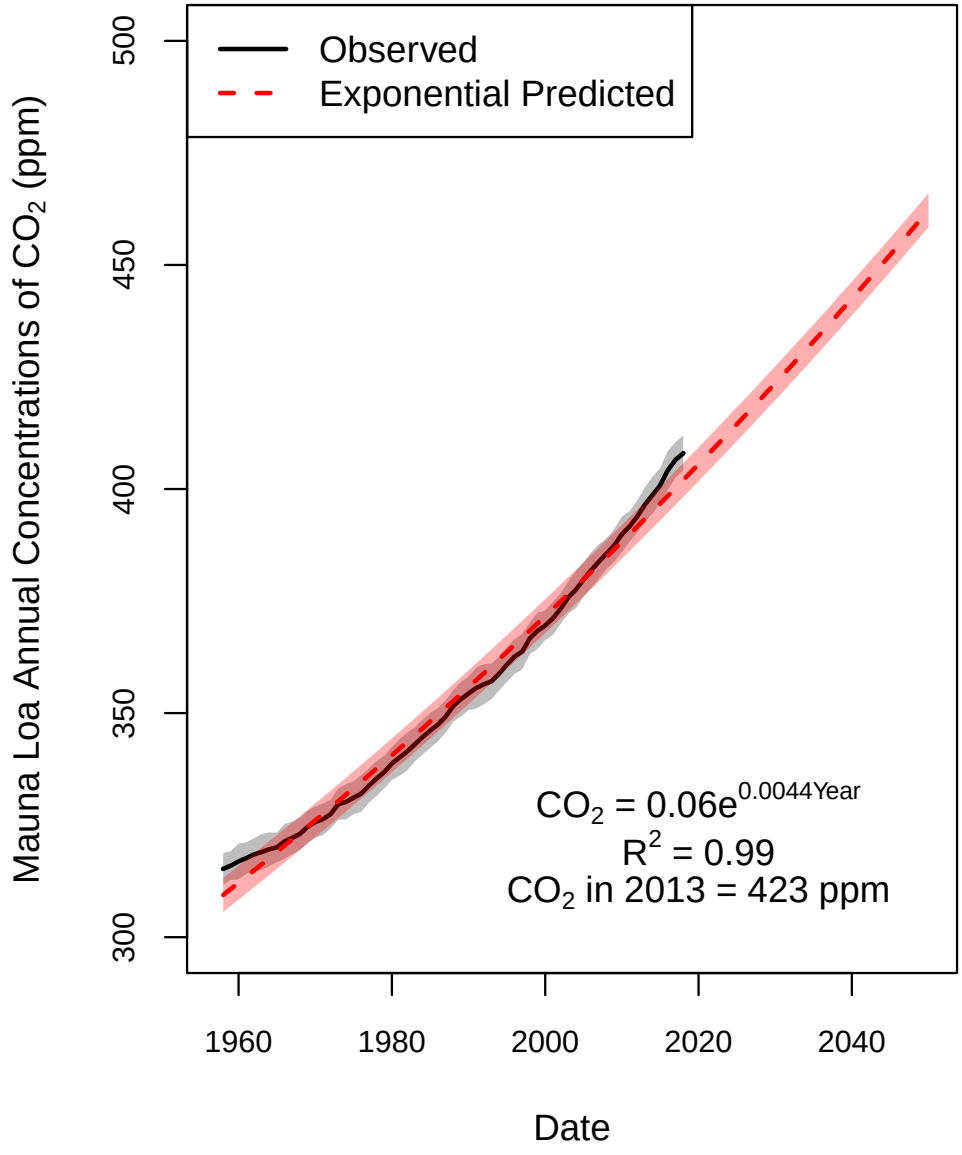


Figure 1.1: Observed annual $CO_2$ concentrations at the Mauna Lao Observatory with 95% confidence limits. The predicted $CO_2$ concentrations from an exponential curve are plotted in red. Current growth of $CO_2$ exceeds that predicted by an exponential curve (Dlugokencky and Tans, 2016).

### 1.4.2 Observations

The instrumentation used at sites specific for city measurements are the same as those used for background sites (usually a version of the Picarro Cavity Ring-Down Spectroscopy (CRDS) Analyser (such as the G1302 or G2301) or a gas chromatograph analyser such as the Agilent HP6890), as the need for accuracy and precision in the measurements is paramount in city-scale inversions. The accuracy of these measurements is usually close to 0.4 ppm or lower, and the precision is usually better at 0.2 ppm or lower (Bréon et al., 2015; Lauvaux et al., 2016). Usually existing tower infrastructure is used where possible, and therefore the height of the measurements is limited to what is available (Bréon et al., 2015; Lauvaux et al., 2016). This means that in a given network, there can be a large amount of variability in the sampling height of the stations. Stations closer to the ground are more influenced by local sources, and therefore these are usually inappropriate as background sites. Stations which measure enhancements from the city region are required to not be overly influenced by nearby sources, and should therefore be placed so that they observe well mixed plumes. Stations also need to be at the correct height (not too low to be overly influenced by local sources, and not too high so that they are not sampling the surface layer). For example, Bréon et al. (2015) found that the Paris tower, where the measurements occurred at a height of 300 m above the city and located in the middle of their area of interest, was not appropriate for the inversion solution under the gradient method approach. No urban transport modelling scheme was incorporated into their atmospheric transport model, and this may have contributed to the transport modelling errors at the centre of the city. The height of the measurements on the Paris tower was likely too high to be representative of the surface layer, and was probably sampling near the PBL. Turnbull et al. (2015), as part of the INFLUX experiment, used measurements that were obtained from 12 towers located within and around the urban area. The height of most towers was near 100 m, with the maximum height at 136 m above ground. Using a similar gradient approach, they found that urban enhancements count be satisfactorily detected during winter months, but during summer months with contributions from biospheric fluxes this could lead to underestimates for the background site, and therefore a more sophisticated approach using an atmospheric transport model was required. Miles et al. (2017), also for the INFLUX experiment, compared the $CO_2$ measurements of the 12 sites to those concentrations simulated using a mesoscale atmospheric transport model and an emission inventory for Indianapolis, and found that these were highly

correlated, but with simulated modelled enhancements on average at 53% of those from the observations.

Atmospheric modelling within the city is complex and prone to error. If the site is very close to certain sources, the site will show large enhancements when the plume of the source is directly over the measurement site. Small errors in the atmospheric transport model could result in the incorrect allocation of when the measurement site is observing enhancements from these nearby sources, leading to large errors in the modelled concentrations during these periods. Particularly for the gradient approach, there is a preference to have measurement sites located on the fringes of the city domain, where the sites can obtain measurements of well mixed air from all of the sources indicated by the sensitivity matrix, and where atmospheric transport modelling is less complex. Appropriate observations for this approach are only available when the wind is blowing above a threshold and in the right direction. In the case of Bréon et al. (2015), a threshold of 2 $ms^{-1}$ was used, resulting in the use of 70% of the potential measurements. For the year long inversion for Paris carried out by Staufer et al. (2016), the wind speed threshold was increased to 3 $ms^{-1}$ and the wind direction was limited to $\pm 15^{\circ}$ of the transect between the two towers. This used only 65% of the observations in the original inversion, and resulted in a loss of 92% of the hourly observations. Nevertheless, this strict limitation on the use of the observations still resulted in uncertainty reductions of between 9 and 50% for the monthly emissions.

### 1.4.3 Transport Modelling and Associated Errors

A popular regional climate model used to simulate meteorological data in several regional and city-scale atmospheric inversions is the Weather Research and Forecasting (WRF) mesoscale research model (Lauvaux et al., 2012; Lauvaux et al., 2013; Brioude et al., 2013; Lauvaux et al., 2016). These regional climate models are driven by reanalysis products, such as the National Centers for Environmental Prediction (NCEP) Eta/NAM analysis product, for initial and boundary meteorological and surface conditions. In Lauvaux et al. (2013) and Lauvaux et al. (2016) the WRF model was run in four-dimensional data assimilation (FDDA) mode, nudged by meteorological observations from the region. This allowed for more accurate representation of the dynamics of the climate system at finer scales compared to previous uses of the WRF model. Both the Paris and London atmospheric inversions used the CHIMERE mesoscale atmospheric chemistry-transport model driven by European Centre for Medium Range Weather Forecasts (ECMWF) analysed meteorology at 3 hour temporal resolution

and 15 km spatial resolution was used (Bréon et al., 2015; Boon et al., 2016; Staufer et al., 2016; Wu et al., 2016). Neither of these regional climate models used an urban scheme, but compared to studies which had used these schemes, there were no significant differences found in the simulated $CO_2$ mole fractions (Bréon et al., 2015).

In order to obtain source-receptor relationships for the sensitivity matrix, Lauvaux et al. (2012); Lauvaux et al. (2016) used the Lagrangian Particle Dispersion Model (LPDM) described by Uliasz (1994), and Brioude et al. (2013) used the FLEXPART Lagrangian particle dispersion model, used in the same way as described for regional scale models. In the case of the Paris atmospheric inversions, the sensitivity matrix is obtained directly from the CHIMERE transport model (Bréon et al., 2015).

Atmospheric inversion models have their own sources of uncertainty, which include atmospheric transport modelling errors (particularly at night when the PBL is very shallow); incorrect characterisation of prior errors (which includes errors from the inventory analysis); atmospheric measurement errors; representation errors (which occur due to a point measurement representing the average of a grid box volume), and aggregation errors (which occur as emissions are coerced into homogenous grid cells across different data sources). In the case of cities, atmospheric transport modelling is further complicated by small-scale turbulence, highly heterogeneous surface characteristics, and urban heat island effects (Hutyra et al., 2014; Bréon et al., 2015). Working at high resolutions required for a city inversion means that modelling needs to take place at the plume level, which contains a great deal of variability and is difficult to reproduce for atmospheric transport models. At night and in the morning the atmosphere is relatively stable, and so $CO_2$ accumulates in the surface layer. The modelled $CO_2$ values are sensitive to local fluxes and vertical mixing which is challenging to model. To avoid these errors, the night-time and morning observations are often excluded, and the inversion is based only on the afternoon observations (Bréon et al., 2015; Boon et al., 2016; Lauvaux et al., 2016; Staufer et al., 2016). Low wind speeds can also be associated with large observation errors. Reasons for this could be due to larger representativity errors of subgrid patterns, or larger errors in the modelling of vertical mixing. The gradient method of solving for the differences between two sites is an attempt to avoid large modelling errors in the inversion, as the gradient can more accurately be modelled relative to the absolute concentration values when there are large unaccounted sources outside of the domain (Bréon et al., 2015). For the Paris inversion exercises, this meant that the stations used for the reference inversion were limited to those which had matching up- or downwind counterparts, and so data from three stations of the available five stations were used. The height

of the tower also determines the extent of observation errors, and is a critical specification for city-scale inversions. Even in well mixed conditions, a 40 m tower may still be influenced by vertical gradients in the surface layer, and therefore if a tower is located near emission sources the modelled concentrations can contain large errors (Lauvaux et al., 2016). Bréon et al. (2015) showed that a tower at 300 m could suffer from large modelling errors due to the transport model being unable to resolve the sources contributing to measurement at the site. At this height there may well have been sampling from the PBL, and therefore contributions from sources from outside of the domain which were not accounted for, which contributed to the model-data mismatch. Ideally stations should be situated and have a sampling height such that they can measure well mixed conditions of sources within the domain (Miles et al., 2017). Deng et al. (2017) showed that urban atmospheric transport modelling using WRF with four dimensional data assimilation capability could be substantially improved if PBL wind observations were used to drive the WRF model.

These sources of error in the modelled concentrations are accounted for in the observation error covariance matrix. (Lauvaux et al., 2016) performed a three step approach to determine these errors. First the errors were scaled by the normalised distance of a $\chi^2$ distribution over each 5-day period, providing an average variance over the period. The variance for every hour was then adjusted for the wind speed and direction, and lastly the variances were re-adjusted by computing the normalised distance of a $\chi^2$ distribution. The normalised distance, $\lambda$, was calculated as:

$$\lambda = \frac{1}{n}[(\boldsymbol{c} - \mathbf{H}\boldsymbol{s}_0)^T(\mathbf{H}\mathbf{C}_{\boldsymbol{s}_0}\mathbf{H}^T + \mathbf{C}_{\boldsymbol{c}})^{-1}(\boldsymbol{c} - \mathbf{H}\boldsymbol{s}_0)] \tag{1.8}$$

Correlations between observations at different locations are generally ignored if the towers are far apart from one another. Lauvaux et al. (2016) had a relatively dense network of stations, with distances of close to 40 km between stations, and therefore spatial correlation was assumed to be non-negligible. An exponential decaying model for distance was applied, using a correlation of 10 km. The correlation coefficients for the off-diagonal elements of $\mathbf{C}_{\boldsymbol{c}}$ were calculated as:

$$C_c(i,j) = exp(-\frac{h_{i,j}^2}{L_{obs}^2}) \tag{1.9}$$

where $h_{i,j}$ is the distance between stations and $L_{obs}$ is the correlation length. No temporal correlation was included since it was felt that further investigation was needed to quantify the impact of hourly observation correlations on block estimates of the emissions.

Bréon et al. (2015) included neither spatial nor temporal correlations in the observation error covariance matrix. They estimated the observation errors to be 3 ppm, based on two statistical diagnostics described by Desroziers et al. (2005) to infer typical observation error variances. They considered the agreement between the sum of the uncertainty from the prior estimate of the control parameters and the sum of the observation error with the Root Mean Square (RMS) of the prior misfits to the assimilated data. They also considered the agreement between the observation error with the mean of the product of prior and posterior misfits to the assimilated data.

Previous studies on estimating $CO_2$ emission for cities have found that errors in atmospheric transport modelling is a significant contributor to the overall uncertainty of emission estimates (Lauvaux et al., 2013; Bréon et al., 2015; Lauvaux et al., 2016), and therefore more work is required to refine these models so that they can perform more reliably during these periods of high uncertainty before they can be used to infer emission estimates at all times of the day. Generally the approach has been to discard night-time and morning observations, to ensure that the inverse solution is only obtained during periods when atmospheric transport modelling is the most reliable (Lauvaux et al., 2013; Bréon et al., 2015; Lauvaux et al., 2016; Staufer et al., 2016). If a large amount of observation error needs to be assigned to the remaining observations, then the ability of the model to correct prior flux estimates is reduced. To ensure the fluxes were only inverted during periods when transport modelling was reliable, Staufer et al. (2016) only selected observations during a very narrow wind direction range, and when wind speeds were above 3 $ms^{-1}$. This resulted in better correlation of the inverted fluxes with heating degrees, which is known to account for approximately 43% of the total emissions of Paris. The annual emissions also agreed better with the independent high resolution inventory (AirParif 2010 inventory) for Paris.

### 1.4.4 Background Contributions

Measurement sites will measure contributions from both inside and outside of the city, and this needs to be separated by the inversion. The inflow and outflow of $CO_2$ at the boundaries needs to be accounted for in any limited domain inversion application. For city-scale inversions, this has either been achieved by using a measurement tower as representative of the background conditions (Lauvaux et al., 2013, 2016) or by using the gradient approach (Bréon et al., 2015; Staufer et al., 2016; Wu et al., 2016). Using a background measurement site ensures that the background values are accurate, but may not represent the spatial variability that would be available through modelled

$CO_2$ concentrations (Lauvaux et al., 2016). Modelled concentrations at the boundary are prone to large errors (Lauvaux et al., 2012). Bréon et al. (2015) made use of the boundary conditions modelled by the Monitoring Atmospheric Composition and Climate (MACC) inversion (Chevallier et al., 2010). These were temporally and spatially very smooth and had little impact on the spatial gradients of the emissions. They found that certain sites were significantly underestimated by the atmospheric modelling due to unaccounted sources. Staufer et al. (2016) modelled the boundary conditions by using the CHIMERE model to simulate signatures of anthropogenic emissions outside of the domain from the EDGAR database. Boundary concentrations can either be taken as totally constrained, or they can be solved for in the inversion, using the measurements only as prior estimates of the concentrations. Recent examples have used the former approach (Lauvaux et al., 2013, 2016; Bréon et al., 2015; Staufer et al., 2016).

In the gradient approach, measurement sites are selected such that one site is representative of inflow concentrations and the other represents both the inflow and additional enhancements from the areas of interest. This is useful when no individual site can be selected as a background site due to non-background influences from outside of the domain of interest, and also when there are large unaccounted sources outside of the domain which impact on the measurement sites in the observation network. The differences in the concentrations are used as the observations in the analysis. This approach can lead to smaller model-measurement errors (Bréon et al., 2015), provided that atmospheric transport model errors do not lead to selection of periods when the difference between sites is not representative of the enhancements from the area of interest. For this reason, Staufer et al. (2016) removed one set of gradients which sampled only a very narrow residential area of Paris, and was determined to be unrepresentative of the city at large. The selection of measurements usually relies entirely on modelled wind direction. This implies the assumption that air will move from the inflow site straight to the outflow site, and not proceed along any complex path that may result in contributions from surface sites outside of the area of interest. Since only a subset of the observations are used during the inversion procedure, a large amount of information from the measurement sites may be discarded.

### 1.4.5 Prior Estimates

In city-scale inversions, emissions are generally separated out into biogenic and anthropogenic emissions, with the intention of estimating the total for each pixel. At-

mospheric top down approaches to determining $CO_2$ emissions have the simultaneous advantage and disadvantage of capturing information from all sources and sinks, some of which may have been excluded from the inventory analysis of the domain. All emissions are observed as an aggregated total, therefore all emission sources are accounted for, but it is challenging to separate out these $CO_2$ emissions into different components of the total $CO_2$ budget without additional measurements, such as $\Delta^{14}C$ and $\delta^{13}C$ isotope measurements (Newman et al., 2016). At the moment background conditions are not sufficiently characterised in order to use isotope tracers to differentiate between fossil fuel and biogenic sources, as these measurements are far rarer than atmospheric measurements of $CO_2$ mole fractions (Turnbull et al., 2015). Even then it would not be possible to assign anthropogenic $CO_2$ emissions to each sector. Therefore it is necessary to conduct an atmospheric inversion study in conjunction with detailed $CO_2$ inventory analysis if no such inventory exists, where all the main contributors to the anthropogenic $CO_2$ budget are considered. This inventory needs to be as detailed as possible and should be resolved both spatially and temporally. This analysis underpins the assumptions of human behaviour driving the anthropogenic emissions. It is important to verify these assumptions regarding human activity in order to assess if mitigation interventions are having the desired impact (Strong et al., 2011). Better understanding of the underlying processes at the urban scale and improved quantification will contribute information towards policy of urban practitioners, and improve understanding of urban dynamics and inform future scenarios (Hutyra et al., 2014).

An example of this is the detailed street level inventory analysis undertaken in the Hestia project for U.S. cities Indianapolis, Los Angeles, Phoenix and Salt Lake City (Gurney et al., 2012). A wide range of data sources were used to quantify emissions, including traffic monitoring, property tax data, power plant emissions monitoring and air quality reporting from industrial point sources. The Hestia inventory used for Indianapolis by Lauvaux et al. (2016) was available for 2011, but was scaled to 2012 and 2013 levels by using fuel statistics published for those years, and therefore the relative emissions between sub-county spatial structures remained the same, but the magnitude of the emissions changed. Spatial and temporal proxies were included in the data product to resolve the emissions at a high spatial resolution and at an hourly time step. Preceding Hestia was the Vulcan inventory which covers contiguous U.S. (Gurney et al., 2009). These detailed inventories have made possible atmospheric inversion exercises or other top down methods for obtaining urban $CO_2$ flux estimates

for these cities (Strong et al., 2011; Brioude et al., 2013; Lauvaux et al., 2016). Lauvaux et al. (2016) also performed a sensitivity analysis by replacing the Hestia product with the Open-source Data Inventory for Anthropogenic $CO_2$ (ODIAC), which had a different spatial distribution of emissions based on power plant location and remotely sensed nightlight data. The errors associated with these emissions were larger, but overall estimates of the city domain were similar between the inverse solutions of the two inventory products. The spatial distribution of the emissions on the other hand was largely influenced by the spatial distribution provided for the prior emissions. Running sensitivity analyses on the atmospheric inversion under different inventory configurations allows for an assessment of how sensitive the inversion solution is to the prior configuration of the emissions.

For the Paris inversions (Bréon et al., 2015; Staufer et al., 2016), the AirParif 2008 inventory of greenhouse gas emissions was used. This inventory is resolved at 1 km spatial resolution and an hourly time resolution, although the atmospheric transport model was only available for a 2 km spatial resolution. It includes almost 80 different sources which are either linear, such as vehicle transport emissions, point sources such as industrial emitters or power stations, or diffuse, such as emissions from the residential and commercial sectors. The inventory provides emissions for five typical months, and therefore does not aim to provide information about specific events. The inventory reported emissions in the city centre to be in the order of 100's g $CO_2$ $m^{-2}$ $day^{-1}$ and in the 10's g $CO_2$ $m^{-2}$ $day^{-1}$ in the suburban areas. The inventory has an embedded diurnal cycle in the emissions from each section, but this is most pronounced for the transport emissions. Point sources had the flattest emissions profile, with only a few of these sources in the Paris domain. The residential emissions were scaled by season to account mainly for differences in emissions due to heating requirements.

A detailed inventory analysis was not available for any of the South Africa cities, and therefore a detailed spatially and temporally disaggregated inventory analysis of direct $CO_2$ emissions was undertaken for the City of Cape Town specifically for the use of this atmospheric inversion exercise (Chapter 4, Nickless et al. (2015a)).

In order to be able to verify emissions from underlying processes, higher resolution inverse modelling systems are needed to better understand and quantify emissions from different sectors. Lauvaux et al. (2016) considered sector specific anthropogenic emissions but ignored biogenic emissions. This was possible due to the selection of the dormant period when biogenic emissions would have been at a minimum, estimated at only 5% of total emissions during that period. When considering longer

periods which includes the growing season, or for cities in regions which may not have a dormant vegetation period, this assumption will not be valid, particularly for a medium-sized city, where natural processes can be a significant contributor to the carbon budget. Such would be the case for South African cities, such as Cape Town and Johannesburg, where large national parks and other natural areas are located near or within city limits and within city vegetation growth is non-negligible. Additionally, Cape Town is surrounded by large agricultural sector consisting on winelands and fruit orchards. Ironically, there are features of cities which allow for better plant growth. For example, the urban heat island effect leads to a longer growing season for plants, and reduced wind within cities leads to less plant stress resulting in better plant growth (Buyantuyev and Wu, 2012). In addition, nitrogen deposition within cities leads to increased nutrient availability, and particularly in arid regions, cities cause augmented water availability for plants (Hutyra et al., 2014). If allowed growing space, plants can make a significant contribution to the carbon budget of a city.

Biogenic emissions in cities should not be ignored (Turnbull et al., 2015), and within atmospheric inversion studies are usually accounted for by means of a land surface exchange model (Bréon et al., 2015; Staufer et al., 2016). Bréon et al. (2015) and Staufer et al. (2016) made use of the C-TESSEL land atmosphere scheme which is used in the ECMWF forecasting system. Biogenic fluxes were taken as the NEE component, and a diurnal cycle for each month was derived. The NEE values had a similar magnitude compared to the anthropogenic emissions, but with strong anticorrelation in the diurnal cycle. During the winter months, the anthropogenic emissions dominated, but in summer and spring the uptake would be larger in magnitude than the anthropogenic emissions. Bréon et al. (2015) used the period from October to December when winter anthropogenic emissions would dominate, but Staufer et al. (2016) considered a full year, which required careful consideration of the prior estimates of NEE and its uncertainties. Monthly NEE was optimised within larger grid cells compared to the anthropogenic emissions. As for the anthropogenic emissions, scaling parameters were solved for, so that the magnitude of the NEE fluxes could be adjusted but not the relative relationship.

The spatial and temporal scales of the sources in the domain determine how the prior flux information needs to be disaggregated. These scales need to be carefully considered, as this will inform the error estimates of the fluxes, and correlations between these fluxes, as discussed in the next section. In Lauvaux et al. (2016) five day fluxes at 1 km spatial resolution were solved, and the period was deliberately selected when biogenic emissions would be at a minimum, so that the interpretation of the

solved fluxes could relate to anthropogenic emissions. For anthropogenic emissions, Bréon et al. (2015) solved for the scaling parameters of six hourly fluxes at a spatial resolution of 2 km. Biogenic emissions were homogenised over larger grids and only the average over the month was solved for in the inversion. As only the afternoon measurements were used, innovation was mainly with respect to the daytime flux estimates.

Brioude et al. (2013) avoided the use of prior $CO_2$ flux estimates by using the flux ratio inversion method, based on the linear relationship between the concentrations of $CO_2$ and CO in the atmosphere. The observations were obtained from aircraft flights during May to June 2010 over the Los Angeles Basin area. Inventory data was still required for CO and NOx emissions, which were obtained from National Emission Inventory (NEI) 2005 inventory.

### 1.4.6 Prior Estimate Uncertainties

It is challenging to define the uncertainties for a highly complex emission product such as Hestia at high resolution. A simplified approach of applying a percentage of the net emission as the uncertainty has been adopted (Lauvaux et al., 2016). In this example, standard deviation errors for fossil fuel fluxes were set at 60% of the net emissions in a 1 km  1 km pixel, except in the case of power station emissions, as these were better constrained. Over the aggregated domain, this resulted in a prior uncertainty of 25% of the total flux. For the spatial error correlations between pixels, a distance-based correlation matrix was first created and then combined with land cover types for each land cover type assuming no correlation between urban and non-urban pixels. Correlation lengths between 4 and 12 km were tested. As five day emissions were inverted, temporal correlations were assumed to be negligible. The spatial correlation length was found to be a strongly influential parameter, with the ability to alter the total emissions and to change the spatial distribution of these sources. The correlation length is difficult to estimate, and remains an important source of error in any inversion setup.

In the case of the Paris inversions six hourly fluxes were solved for each day, and a 50% uncertainty allocation was applied to the prior fossil fuel estimate for each period and 75% to NEE fluxes (Bréon et al., 2015; Staufer et al., 2016). A relatively arbitrary correlation of 0.4 between anthropogenic emissions from adjacent periods, and 0.2 between non-adjacent periods, of the same day was allocated, with exponentially decaying correlation between different days. As scaling parameters were solved for, and not the individual fluxes, no spatial error correlation was considered.

In the case of the biogenic emissions, an uncertainty level of 70% was applied to the NEE prior estimates. No spatial or temporal error correlation was specified between biogenic flux pixels or between NEE and anthropogenic fluxes.

### 1.4.7 Results from Previous Studies

The results of recent city-scale inversions demonstrate that top-down and bottom-up approaches are not independent, but rather atmospheric inversion is a means of verifying or refining inventories. A summary of emission estimates from recent city-scale inversions, where the estimates at the city level have been converted into kt $CO_2$ per day, are presented in Table 1.2. Lauvaux et al. (2016) used atmospheric inversion to investigate the contribution from different anthropogenic sectors in the city of Indianapolis. They found that traffic emissions were the largest contributor, at 45% of the total emissions. From their inversion results, they obtained a similar percentage at 44% of enhancements due to traffic emissions. They were able to reduce the mismatch between prior and observed concentrations from -0.52 ppm to -0.11 pmm, with the error in the five day emissions reducing from 25% to 9% of the emissions. Overall, emissions were increased so that over the eight month period, the total emissions increased from 16.7 Mt $CO_2$ to 20.2 Mt $CO_2$. Because only daytime concentrations were used, the innovation was mainly contained within the daytime emissions.

They performed different sensitivity tests to determine which specifications had the largest impact on the inversion solution. Replacing the fossil fuel emission product with one that had lower overall emissions and larger associated errors compared with the reference, resulted in slightly lower total emissions, but larger error reduction. They also investigated different strategies for assigning the background concentration. In the reference approach one tower was used, which was representative of background conditions 60% of the time, but they also considered the use of two towers, where the background reference would depend on the wind direction as well as using the minimum concentration from the main background site. Of these three approaches, using the minimum was the least representative and led to larger estimates of the emissions. The specification which had the largest impact on the final inversion results was the assignment of correlation length to the prior error statistics, where they tested values between 4 and 12 km. The correlation length impacted on both the spatial distribution of emissions and the total emission estimate. Correlation lengths which were short resulted in posterior emissions that were less constrained by the observations. The assumption regarding correlation is highly uncertain, but

determines the number of towers required to obtain optimal constraint of the emissions estimates over the domain.

Bréon et al. (2015) and Staufer et al. (2016) performed atmospheric inversion for the city of Paris. Their network contained towers on the fringes of the city and also the Eiffel tower, located in the middle of their domain. They found that they could not reproduce the measurements at the Eiffel tower at 300 m above the surface, and therefore this tower was excluded from the reference inversion. They proposed that the atmospheric transport model at a spatial resolution of 2 km was not of sufficient resolution to accurately attribute the many nearby sources to the station. When modelling the concentrations at the sites, they found that several sites to the north of the city were significantly underestimated. For this reason, the gradient method was seen as superior to the approach of modelling the absolute concentrations, despite the reduction in available observations. The results of the inversion showed improvement in the agreement of the posterior modelled concentrations with the observations compared with the prior modelled values. The uncertainty in the emissions was reduced even for those days when there were no usable observations, due to the temporal correlation structure specified between the six hourly anthropogenic fluxes. Due to the use of the afternoon observations only, the innovation was mainly limited to the afternoon fluxes. Despite the large reduction in available data, significant uncertainty reductions were achieved.

As the inversion focused on periods when the data was most informative about city emissions, due to the gradient method approach, uncertainty reductions were greater for the anthropogenic emissions than for the biogenic emissions. Vegetation located within the city can still lead to significant negative biogenic fluxes, which can lead to underestimates of the anthropogenic emissions if not included in the inversion setup. Separate estimates were produced for the anthropogenic and biogenic emissions. This was justified by explaining that the assigned anthropogenic and biogenic flux errors had different spatial and temporal patterns which could be exploited by the inversion system to attribute the concentration signal to specific sectors. This is highly dependent on the prior specifications, which will contain errors. Therefore, the ability of the system to theoretically disentangle biogenic and anthropogenic fluxes is only as good as these prespecifed error structures. The temporal correlation length was found to have a large impact on the results, with significant differences in the estimates between an inversion setup using a seven day correlation versus a 30 day correlation.

Bréon et al. (2015) and Staufer et al. (2016) did not account for human respiration in the inversion. At an estimate of 1 kg $CO_2$ $day^{-1}$ per person and 11.7 million people within the city of Paris, this leads to an approximate source of 4.2 Mt $CO_2$ per year, which is approximately 8% of the AirParif 2008 fossil fuel inventory. If human respiration is not accounted for in the inversion, it will be prescribed to the anthropogenic emissions by the inversion due to a similar spatial distribution. Lauvaux et al. (2013) accounted for human respiration, which was set at 3% of the total emissions. Since the emissions were considered for the city as a whole, this value was straight forward to accommodate. Lauvaux et al. (2016) did not account for human respiration in the Indianapolis inversion. The estimated human respiration rate for a large city like Indianapolis was 2.5% total $CO_2$ fossil fuel emissions. Therefore in a city with many fossil fuel sources, the contribution of human respiration is much smaller.

Bréon et al. (2015) and Staufer et al. (2016) found that the match between the observed and modelled concentration values improved significantly after the inversion. Using the configuration of Bréon et al. (2015), Staufer et al. (2016) determined the annual emissions for Paris to be 37.4 $\pm$2.1 Mt $CO_2$ $yr^{-1}$. With the controls specified by Bréon et al. (2015), Staufer et al. (2016) found that when comparing the monthly emission rates between NE and SW gradients, different solutions were obtained. With stricter controls on the use of observations, this agreement was improved. The annual estimate of emissions for 2010 was determined to be 40.9 Mt $CO_2$ $yr^{-1}$. This estimate is closer to the annual estimate of the AirParif 2010 inventory of 41.8 Mt $CO_2$. Sensitivity analyses were performed specifying a flat prior for the month, instead of the 6 hourly estimates provided in the original configuration. Large differences were observed in the annual estimates, but in all cases the inverted estimates were closer to the reference inversion than the prior estimates. They noted that the sign of the correction to the prior flux depended more on value of the flat prior than on the uncertainty of the prior. An alternative inventory for Paris was used in place of the AirParif 2008 inventory. This resulted in annual budget of 39.0 Mt $CO_2$. There were significant differences between the monthly inverted fluxes compared the monthly solutions for the AirParif 2008 inventory. The sensitivity of the monthly estimates was generally smaller compared to the differences between the prior and posterior estimates.

To improve the posterior estimates, ideally more sites, and therefore more available gradients, are required so that better coverage of the city can been provided by the observations. Wu et al. (2016) performed an optimal network design for the city of Paris, and determined with 10 stations, the uncertainty in the total monthly city

emission estimates could be reduced by 42%, and by increasing this to 70 stations, it would become feasible to reduce uncertainty in the emissions at a sectoral level. Many challenges, particularly related to atmospheric transport modelling, still remain before atmospheric inversion can be relied on as an MRV approach for anthropogenic emissions from cities. This study attempts to perform the first city-scale inversion in the Southern Hermisphere, for a city located at the tip of the African continent, with the Atlantic Ocean as a boundary to the west and south of the city. The LPDM model will be implemented, as for previous studies by Lauvaux et al. (2012, 2013, 2016), but will be driven by the CCAM GCM in regional model, which has been validated over southern Africa.

## 1.5 Alternative Methods of Solving for Emissions

In order to circumvent one or more of the requirements or limitations of a typical Bayesian inverse modelling framework, alternative methods have been implemented. In this section I briefly introduce some of these approaches.

As discussed in the previous sections, one of the challenges of a Bayesian inversion is to specify observation error covariance matrix, $\mathbf{C}_{\boldsymbol{c}}$, and the prior flux uncertainty covariance matrix, $\mathbf{C}_{\boldsymbol{s}_0}$, and is often based on expert opinion. The specification of these matrices is critical as they determine the relative weight of the prior information versus the observations in estimating the fluxes and are key in determining the posterior covariance matrix of the fluxes, and therefore the uncertainty associated with the posterior fluxes. As an alternative to the expert-opinion based prior information, Michalak et al. (2005) proposed using a Maximum Likelihood (ML) approach to estimate the covariance parameters, using the atmospheric data. They derived the ML estimates of these parameters, given the prior flux estimates, $\boldsymbol{s}_0$, the observations, $\boldsymbol{c}$, and the sensitivity matrix, $\mathbf{H}$. They derived the probability density function of the covariance parameters, $\boldsymbol{\theta}$, according to Bayes' rule and assuming no prior information about these parameters. This results in the likelihood of $\boldsymbol{\theta}$ being proportional to the likelihood of the observations. Michalak et al. (2005) shows that the ML estimates for $\boldsymbol{\theta}$ can then be obtained by minimising the negative logarithm of the Gaussian probability density function of $p(\boldsymbol{c}|\mathbf{H}, \boldsymbol{s}_0, \boldsymbol{\theta})$, which is equal to:

$$J(\boldsymbol{\theta}) = \frac{1}{2} ln|\mathbf{H}\mathbf{C}_{\boldsymbol{s}_0}\mathbf{H}^T + \mathbf{C}_{\boldsymbol{c}}| + \frac{1}{2}(\boldsymbol{c} - \mathbf{H}\boldsymbol{s}_0)^T(\mathbf{H}\mathbf{C}_{\boldsymbol{s}_0}\mathbf{H}^T + \mathbf{C}_{\boldsymbol{c}})^{-1}(\boldsymbol{c} - \mathbf{H}\boldsymbol{s}_0). \quad (1.10)$$

The minimisation solution can be obtained with respect to $\boldsymbol{\theta}$ by implementing the Gauss-Newton method. This method was applied to a global inversion solving for $CO_2$ fluxes using observations from the NOAA Climate Monitoring and Diagnostics Laboratory (CMDL) cooperative air sampling network sites. The covariance parameters predicted using the ML approach ensured that the residuals had the variance specified in the covariance matrix, i.e. a $\chi^2$ statistic equal to one. The estimates of the covariance parameters were consistent with the physical understanding of the relative variance of observations from the different stations in the network and the fluxes of the specified regions. In addition, this method provides uncertainty bounds on the covariance parameters. As the number of covariance parameters are increased, the higher their uncertainty. This is due to there being fewer observations to constrain the covariance parameters.

A method which avoids the specification of prior flux estimates is the geostatistical approach. This method has been implemented by Michalak et al. (2004) and Gourdji et al. (2010) as a way of solving for high resolution gridded fluxes rather than solving for fluxes of large prescribed regions. In this approach the prior information is defined only on the basis of the spatial or temporal correlation between fluxes. The approach is still Bayesian, but in order to obtain the flux estimates and the posterior covariance matrix, a deterministic model is required that describes the relationship between the $CO_2$ fluxes and key covariates, and a prior covariance matrix that describes the variability in the departures of the $CO_2$ fluxes from this relationship as a function of the separation distance in space and time. The Bayesian cost function which needs to be minimised for the geostatistical approach is:

$$J(\boldsymbol{s}) = \frac{1}{2}\left((\boldsymbol{c}_{mod} - \boldsymbol{c})^T \mathbf{C}_{\boldsymbol{c}}^{-1}(\boldsymbol{c}_{mod} - \boldsymbol{c}) + (\boldsymbol{s} - \mathbf{X}\boldsymbol{\beta})^T \mathbf{C}_{\boldsymbol{s}_0}^{-1}(\boldsymbol{s} - \mathbf{X}\boldsymbol{\beta})\right) \tag{1.11}$$

where $\mathbf{X}$ is a known matrix of covariates, and $\boldsymbol{\beta}$ is a vector of unknown drift parameters. The matrix $\mathbf{X}$ can contain information about whether a flux is an ocean or terrestrial flux, or in which biome the terrestrial flux is located. The prior covariance matrix $\mathbf{C}_{\boldsymbol{s}_0}$ provides the spatial and temporal correlation structure, and therefore has non-zero diagonal elements. The model chosen for $\boldsymbol{X\beta}$ should be as simple as possible to ensure that the number of elements in the vector $\boldsymbol{\beta}$ is small. Although a simpler model may lead to estimates with higher uncertainties, specifying a more complex model incorrectly will lead to biased estimates. The prior covariance matrix $\mathbf{C}_{\boldsymbol{s}_0}$ will be associated with a variogram which defines the expected variance of the deviation

away from the mean behaviour as a function of separation distance. Michalak et al. (2004) used an exponential covariance function which had the associated variogram

$$\gamma(h|\sigma^2, l) = \sigma^2(1 - exp(-\frac{h}{l})) \tag{1.12}$$

where $h$ is the separation distance between two points, $l$ is the integral scale, and $\sigma^2$ is a variance, which implies that as the distance between two fluxes tends to infinity, the unknown function's deviations from its mean behaviour at these points approaches $\sigma^2$. Gourdji et al. (2010) used a similar exponential covariance function. Michalak et al. (2004) showed that to solve for the unknown parameters in this framework, a linear system of equations needs to be solved for as defined by:

$$\begin{bmatrix} \mathbf{H}\mathbf{C}_{\boldsymbol{s}_0}\mathbf{H}^T + \mathbf{C}_{\boldsymbol{c}} & \mathbf{H}\mathbf{X} \\ \mathbf{H}\mathbf{X}^T & \mathbf{0} \end{bmatrix} \begin{bmatrix} \boldsymbol{\Lambda}^T \\ \mathbf{M} \end{bmatrix} = \begin{bmatrix} \mathbf{H}\mathbf{C}_{\boldsymbol{s}_0} \\ \mathbf{X}^T \end{bmatrix}$$

where

$$\mathbf{M} = (\mathbf{X}^T\mathbf{H}^T(\mathbf{H}\mathbf{C}_{\boldsymbol{s}_0}\mathbf{H}^T + \mathbf{C}_{\boldsymbol{c}})^{-1}\mathbf{H}\mathbf{X})^{-1}(\mathbf{C}_{\boldsymbol{s}_0}\mathbf{H}^T(\mathbf{H}\mathbf{C}_{\boldsymbol{s}_0}\mathbf{H}^T + \mathbf{C}_{\boldsymbol{c}})^{-1}\mathbf{H}\mathbf{X} - \mathbf{X})^T \tag{1.13}$$

and

$$\hat{\boldsymbol{s}} = \boldsymbol{\Lambda}\boldsymbol{c}. \tag{1.14}$$

If the number of elements in $\boldsymbol{\beta}$ are small, then the size of the matrix which needs to be inverted should be almost the same size as the matrix inversion in a classical Bayesian approach. Both Michalak et al. (2004) and Gourdji et al. (2010) applied this approach to synthetic data, Michalak et al. (2004) at the global scale and Gourdji et al. (2010) for a mesoscale domain, and found that the approach was able to return posterior fluxes that were in good agreement with this those used to simulate the data. This method allows for inference of the statistical parameters of the surface fluxes and observation error variance. The integral scales and variances inferred from the observations were similar to those calculated from the surface fluxes used to simulate the data, which would be unknown in a real-data application.

An approach that avoids expensive pre-calculations of the sensitivity matrix $\mathbf{H}$ and inversions of large covariance matrices is an ensemble Kalman Filter (EnKF) approach. The example I give here is the implementation described in Peters et al. (2005), which is the method used for the CarbonTracker inversions (Peters et al., 2007). In an EnKF approach, the same Bayesian framework as described in section 1.3 is assumed, and prior information on fluxes and their uncertainty covariances

are required. The EnKF represents the information in $\mathbf{C}_{\boldsymbol{s}}$ in fewer dimensions, with dimensions equal to $N$, the number of ensemble members. Each ensemble member, $\boldsymbol{s_i}$, is drawn from the assumed Gaussian distribution of $\boldsymbol{s}$ such that

$$\boldsymbol{s_i} = \bar{\boldsymbol{s}} + \boldsymbol{s'_i} \tag{1.15}$$

where $\bar{\boldsymbol{s}}$ can be set equal to the prior estimate of $\boldsymbol{s}$, and the deviations $\boldsymbol{s'_i}$ are set such that

$$\mathbf{S} = \frac{1}{\sqrt{N-1}}(\boldsymbol{s'_1}, \boldsymbol{s'_2}, ..., \boldsymbol{s'}_N)^T = \frac{1}{\sqrt{N-1}}(\boldsymbol{s_1} - \bar{\boldsymbol{s}}, \boldsymbol{s_2} - \bar{\boldsymbol{s}}, ..., \boldsymbol{s}_N - \bar{\boldsymbol{s}})^T \tag{1.16}$$

where $\mathbf{S}$ is the square root of the covariance matrix $\mathbf{C}_{\boldsymbol{s}}$ such that $\mathbf{C}_{\boldsymbol{s}} = \mathbf{S}\mathbf{S}^T$. In an EnKF with a finite number of members, $\mathbf{C}_{\boldsymbol{s}}$ is approximated. The variance of a individual element of $\boldsymbol{s}$ can be obtained from the spread of the corresponding elements in the ensemble. By means of methods such as Cholesky decomposition, the vectors $\boldsymbol{s'_i}$ can be created as unconditional realisations of $\mathbf{C}_{\boldsymbol{s}}$.

Peters et al. (2005) implemented an ensemble square root filter (EnSRF) which allows observations to be processed one at a time, which is possible without loss of accuracy if the observations are assumed to be independent. To calculate the Kalman gain matrix $\mathbf{K}$, where

$$\mathbf{K} = \mathbf{C}_{\boldsymbol{s}_0}\mathbf{H}^T(\mathbf{H}\mathbf{C}_{\boldsymbol{s}_0}\mathbf{H}^T + \mathbf{C}_{\boldsymbol{c}})^{-1} \tag{1.17}$$

the following approximations can be used:

$$\mathbf{H}\mathbf{C}_{\boldsymbol{s}_0}\mathbf{H}^T \approx \frac{1}{N-1}(\mathcal{H}(\boldsymbol{s'_1}), \mathcal{H}(\boldsymbol{s'_1}), ..., \mathcal{H}(\boldsymbol{s'}_N)) \cdot (\boldsymbol{s'_1}), ..., \mathcal{H}(\boldsymbol{s'}_N))^T \tag{1.18}$$

$$\mathbf{C}_{\boldsymbol{s}_0}\mathbf{H}^T \approx \frac{1}{N-1}(\boldsymbol{s'_1}, \boldsymbol{s'_2}, ..., \boldsymbol{s'}_N)(\boldsymbol{s'_1}), ..., \mathcal{H}(\boldsymbol{s'}_N))^T \tag{1.19}$$

where $\mathcal{H}$ denotes the transport operator. When we consider one observation at a time, $\mathbf{H}\mathbf{C}_{\boldsymbol{s}_0}\mathbf{H}^T$ is a scalar which is calculated from the dot product of two vectors, and $\mathbf{C}_{\boldsymbol{s}_0}\mathbf{H}^T$ is a vector that has the same length as $\boldsymbol{s}$. Dealing with one observation at time in this way removes the restriction of linear transport. Through the above two equations, the Kalman gain matrix is used to update the mean state vector using the Bayesian solution to the posterior fluxes which is defined in section 1.3. The deviations from the mean are updated independently using:

$$\boldsymbol{s'_i} = \boldsymbol{s'_{0i}} - \tilde{\mathbf{k}}\mathcal{H}(\boldsymbol{s'_{0i}}) \tag{1.20}$$

where the vector $\tilde{\mathbf{k}}$ is related to the Kalman gain matrix $\mathbf{K}$ by a scalar $\alpha$ as:

$$\tilde{\mathbf{k}} = \mathbf{K} \cdot \alpha \tag{1.21}$$

$$\alpha = (1 + \sqrt{\frac{\mathbf{C_c}}{\mathbf{HC_{s_0}H}^T + \mathbf{C_c}}})^{-1} \tag{1.22}$$

and because only one observation is considered at a time, the scalar $\alpha$ is calculated by evaluating scalars $\mathbf{C_c}$ and $\mathbf{HC_{s_0}H}^T + \mathbf{C_c}$. By independently updating the state vector and the deviations, this prevents the underestimation of $\mathbf{C_s}$.

The analysed mean and ensemble state from one observation will serve as the prior information for the subsequent observation. But in order to calculate the next Kalman gain matrix, the ensemble of sampled $CO_2$ concentrations $\mathcal{H}(\boldsymbol{s'_{0i}})$ needs to be updated to reflect the new information in the state vector. To avoid having to rerun the atmospheric transport model for each observation, the ensemble of sampled $CO_2$ concentrations is updated in a similar way to the state vector, using the ensemble averaged information in the Kalman gain matrix:

$$\mathcal{H}(\boldsymbol{s})_\mathbf{m} = \mathcal{H}(\boldsymbol{s}_0)_\mathbf{m} + \mathbf{H_m K}((\mathbf{c}) - \mathcal{H}(\boldsymbol{s}_0)) \tag{1.23}$$

where $\mathcal{H}(\boldsymbol{s})_\mathbf{m}$ is a modelled $CO_2$ concentration corresponding to an observation, denoted $\mathbf{m}$, that has yet to be assimilated. The deviations are updated using:

$$\mathcal{H}(\boldsymbol{s'_i})_\mathbf{m} = \mathcal{H}(\boldsymbol{s'_{0i}})_\mathbf{m} - \mathbf{H_m}\tilde{\mathbf{k}}\mathcal{H}(\boldsymbol{s'_{0i}}) \tag{1.24}$$

where the operator $\mathcal{H}_m$ is replaced with $\mathbf{H_m}$ in the right hand side term. To calculate these equations it is necessary to note that only $\mathbf{H_m K}$ needs to be calculated, which is made easier by realising that this term contains $\mathbf{H_m C_{s_0} H}^T$ which is a scalar that can be calculated using equation 1.18, where the first term contains an ensemble of modelled $CO_2$ concentration yet to be assimilated and the last term contains the modelled $CO_2$ concentration currently being assimilated. Once the ensemble of modelled $CO_2$ concentrations is updated, the algorithm continues onto the next observation. The transport operator can either be run as the full operator, or it can be derived from the ensemble, and in that way the full linear matrix $\mathbf{H}$ in never needed. In addition, the large covariance matrix $\mathbf{C_{s_0}}$ does not need to be inverted.

A non-Bayesian approach, such as a multiple box approach (Strong et al., 2011), can be used instead. This approach relies on a mass balance equation for $CO_2$ assuming diffusion is negligible:

$$\frac{\delta C_i}{\delta t} = \frac{Q_{a,i}}{h} + \frac{Q_{b,i}}{h} - u_i(\frac{\delta C}{\delta x})_i + \frac{H}{h}\frac{\delta h}{\delta t}(C_h - C_i) \tag{1.25}$$

where C is the $CO_2$ concentration at the measurement site (in kg $m^{-3}$), $A$ is a box horizontal area, $h$ is the box height, $Q_a$ is the anthropogenic $CO_2$ flux (in kg $m^{-2}s^{-1}$), $Q_b$ is the net biological $CO_2$ flux, with positive fluxes indicating emissions into the box (Strong et al., 2011). The terms $u$ and $v$ are the horizontal components of the wind in the model's x and y direction respectively. The term $H$ is the Heaviside step function. It is equal to 1 when $\frac{\delta h}{\delta t} \geq 0$ and 0 otherwise. The model boxes are arranged horizontally on the grid. Dividing by A and assuming that $h$ depends only on time, the solution for box $i$ becomes:

$$\frac{\delta CAh}{\delta t} = (Q_a + Q_b)A - u\frac{\delta(CAh)}{\delta x} - v\frac{CAh}{\delta y} + HC_h\frac{\delta h}{\delta t}A \tag{1.26}$$

This implies that the $CO_2$ flux is equal to the anthropogenic and biogenic fluxes plus the entrainment minus the advection. To solve for the flux, the above equation was integrated using the Crank-Nicolson method, which meant that the terms on the right hand side were approximated by the average of their finite difference values at time $j$ and $j$+1. This approach allows for the assessment of the roles that meteorology, anthropogenic and biological processes have in the diurnal $CO_2$ cycle (Strong et al., 2011) .

Finally, to finish of the section on alternative methods, an approach used by Lauvaux et al. (2013) to estimate emissions from the city of Davos is briefly described. In this application the city was limited to just three pixels in the mesoscale domain. Due to the absence of other anthropogenic emissions and the dormancy of the vegetation during the period of the atmospheric inversion, the emissions were solved for the whole city, and not spatially resolved. Under these circumstances, the $CO_2$ emissions could be solved using the following relationship:

$$\frac{[CO_2]_X}{CO_2}_{prior} = \alpha\frac{F_X}{F_{prior}} \tag{1.27}$$

Using this method, it is assumed that the atmospheric transport is perfectly modelled, and does not require uncertainties for prior fluxes or for the observation errors. A linear regression technique can be used to solve for the mixing ratio mismatch.

## 1.6 Requirements for a Regional Atmospheric Inversion over South Africa

In order to run a mesoscale inversion for the region of southern Africa, the necessary observational data and *a priori* information are required. Whittlestone et al. (2009)

reported on a study conducted on the Cape Point Global Atmosphere Watch (GAW) tower data, which aimed to characterise trace gas measurements. They determined that for species with fairly uniform source such as radon or CO (carbon monoxide), their regional selection criteria worked well, but for $CO_2$ the respiration and photosynthesis cycle from very close vegetation overwhelmed the signal. The model used for atmospheric transport was the Conformational Cubic Atmospheric Model (CCAM), originally described by McGregor (1987). This is a GCM which can be configured to operate in variable resolution mode as a regional climate model (Engelbrecht et al., 2009). The CSIRO Atmosphere Biosphere Land Exchange Model (CABLE) is coupled to CCAM. This model calculates carbon, water and heat exchanges between the land surface and atmosphere as described in Kowalczyk et al. (2006). CCAM was able to model the origin of radon and CO with sufficient accuracy, but the sources used to resolve $CO_2$ were not sufficient. To improve on the analysis conducted here it would be necessary to configure CCAM to trace the transport of simulated species from smaller regions, and to output more detailed information about $CO_2$ fluxes from the region, but the authors concluded that it could be possible to use inversion modelling of carefully selected data to obtain estimates of fluxes at a regional level. Additional work which has been conducted on CCAM over the southern African region has been based on climate modelling (Engelbrecht et al. 2009) and weather prediction (Landman et al., 2010).

In South Africa, the Cape Point Global Atmospheric Watch station has been measuring surface atmospheric $CO_2$ since 1977. It is the only recognised continuous atmospheric monitoring tower in Africa (Ciais et al., 2010). Two additional stations were installed near Cape Town to complement the record obtained from Cape Point, for the purpose of obtaining estimates of $CO_2$ fluxes at a high spatial resolution from a South African city, Cape Town. This was achieved through a city-scale inversion, which used the atmospheric measurements of a local network and treated the boundaries of the regional domain as separate source terms (Chapter 5, Nickless et al. (2018a)).

Remotely sensed data products promise a future avenue for atmospheric observations of $CO_2$ at high spatial resolutions. Remotely sensed products on $CO_2$ are available from AIRS, SCIAMACHY, GOSAT, and OCO-2 which are currently in orbit. AIRS and SCIAMACHY measure spectral intervals that contain $CO_2$ absorption bands, but were not designed originally to measure $CO_2$ (Houweling et al., 2004). GOSAT, launched in January 2009, is the first instrument in orbit that is designed to measure the $CO_2$ mixing ratio at sufficient accuracy and sensitivity down to the

Earth's surface to allow world-wide estimation of regional sources and sinks of $CO_2$ (Houweling et al., 2010). Algorithms for obtaining estimates of $CO_2$ concentrations in different layers of the atmosphere are being developed and validated against observed data (Saitoh et al., 2016), and GOSAT's estimates of column-averaged $CO_2$ concentrations ($XCO_2$) have already been used for atmospheric inversions (Wang et al., 2018). A second mission, GOSAT-2, is to be launched on the 29th October 2018 (`http://www.gosat-2.nies.go.jp/`). NASA's OCO-2 (Orbiting Carbon Observatory  the first mission which was to be launched in 2007 failed), launched February 2014 (`http://oco.jpl.nasa.gov`), and a subsequent mission, OCO-3, is already in the pipeline. OCO-2 provides measures of $XCO_2$ (Miller et al., 2018). TanSat also provides remotely sensed $XCO_2$ measurements. This mission is supported by the Ministry of Science and Technology of China, the Chinese Academy of Sciences, and the China Meteorological Administration and was launched in December 2016 (Yang et al., 2018). Algorithms have been developed to extract the $XCO_2$ measurements (Yang et al., 2018). A-SCOPE (Advanced Space Carbon and Climate Observation of Planet Earth) mission (`http://www.esa.int`) and CarbonSat (`http://www.iup.uni-bremen.de/carbonsat/`) were ESA proposed missions, but were unfortunately not successful in their bids. CarbonSat is to replaced with the Sentinel-7 programme. The added complexity in using satellite-derived $CO_2$ information is the potential for correlated uncertainties and bias, which estimated $CO_2$ fluxes would be sensitive to under the high quantity of remotely sensed data (Houweling et al., 2010). There are concerns about how transport models, which have been validated mostly on surface measurements, can simulate the vertical column weighted average $CO_2$ mixing ratio that is provided by satellites (Houweling et al., 2010).

Currently, the best solution to the lack of data $CO_2$ data over the southern Africa region would be the addition of a tall tower monitoring site. But the location of this site would need to be carefully considered in order to retrieve the maximum benefit from the data in obtaining regional flux estimates of important tracers, particularly $CO_2$. This assessment of where best to locate the tower would need to involve an analysis of atmospheric transport using a model such as CCAM. In this study an optimal network design was performed in order to find the best placement of new stations in South Africa in order to reduce the current uncertainty in $CO_2$ from the region (Chapters 2 and 3, Nickless et al. (2015b, 2018b), ).

Additional data sources which would assist in constraining the flux estimates include a fossil fuel emission field, land-use maps, detailed vegetation cover maps, and

the inputs required to populate a terrestrial biosphere model such as CABLE. The fossil fuel emission field can be derived from the fossil fuel emission database provided by the Carbon Dioxide Information Analysis Center (Boden et al., 2010). South Africa has recently invested in a National Atmospheric Emissions Inventory database system. This system is in the process of being assembled (`https://saaqis.environment.gov.za/`). For this to be helpful for atmospheric inversion work, it should ideally make available emissions estimates in a temporally and spatially disaggregated way, and include appropriate uncertainty estimates. The SANBI Vegetation Map of South Africa, Lesotho and Swaziland (Mucina and Rutherford, 2006) provides detailed information on vegetation cover, and land use maps can be derived from the National Land Cover (NLC) 2000 data. CABLE is a complex model which calculates the temporal evolution of $CO_2$, radiation, heat, water and momentum fluxes at the surface, resulting in several equations for each of these fluxes which need to be parameterised. The equations are explained in detail in Kowalczyk et al. (2006). Data from the Skukuza eddy covariance tower is an example of one data source which could be used to derive many of the required parameter values.

In summary, regional or mesoscale inversions of $CO_2$ fluxes over southern Africa are possible under the current data limitations, but would be improved if further measurements of $CO_2$ were available. A model of atmospheric transport is already available and has been trained and validated for southern Africa. A procedure for classifying data from the Cape Point GAW tower has already been initiated, and this work can be continued to determine the best method for sampling data from continental $CO_2$ sources. The remaining data required for prior estimates is readily available at a regional level, but at the resolution required for a city-scale inversion, additional information is required, such as the inventory of anthropogenic emissions that needed to be created for the city of Cape Town (Nickless et al., 2015a).

## 1.7 Conclusions

Atmospheric inversions are a valuable tool for determining regional fluxes for $CO_2$, but careful treatment of each component of the procedure is required to obtain reliable estimates. Previous inversions have not produced consistent estimates of regional fluxes, mainly due to the use of different atmospheric models and different treatment of the data. A major encumbrance to global inversions has been the lack of data in the tropics and Southern Hemisphere. Due to the low number of observation stations, these regions have often been grouped together, despite great spatial heterogeneity

within these regions. A finding from these previous inversions is the existence of a Southern Hemisphere or tropical sink which is balancing the expected deforestation emission of $CO_2$, resulting in near neutral flux estimates.

Atmospheric inversions have in the vast majority of cases been based on the Bayesian synthesis approach of (Tarantola, 2005) and (Enting, 2002). This requires not only the observational data, but also prior estimates of fluxes and uncertainties. This regularises the problem, and makes possible an optimal solution with acceptable uncertainty limits despite the ill-conditioned nature of the problem. The solution of the inversion has been shown to be sensitive to the atmospheric transport model, the number and location of regions, the temporal averaging of the data, and selection of observational towers. This indicates that in general it is better to run inversions under multiple specifications in order to determine the error attributable to each component, allowing better assessment of the estimation error. Sensitivity analyses are a valuable tool for inversion exercises to assess the reliability of the estimates obtained. In this study sensitivity analyses are preformed for both the optimal network design (Chapters 2 and 3, Nickless et al. (2015b, 2018b)) and the city-scale inversion (Chapters 5 and 6, Nickless et al. (2018a,c)).

Mesoscale inversions, as well as city-scale inversions, have been more recently reported in the literature. Here, fluxes are solved for at high spatial and temporal resolutions over a specified target region. This relies on atmospheric transport models operating at their spatial maximum resolution, such as the CCAM model, capable of resolving local transport sufficiently accurately in order to resolve a gridded surface of fluxes. For mesoscale and city-scale inversions it is better to operate at a time scale which allows the diurnal variability to be determined in order to obtain accurate flux estimates. Regional inverse estimates are consistent for mesoscale inversions, but disagree at the sub-regional scales, while regional estimates obtained from global inversions tend to disagree, even when aggregating over broad latitudinal bands (Schuh et al., 2013).

Mesoscale inversions are possible over southern Africa, as demonstrated by Whittlestone et al. (2009), made possible by the Cape Point GAW station, but careful classification of the data measured at the station will first need to take place in order to select data representing the continent. This work will first need to take place before a mesoscale inversion is possible. The addition of a within-continent tower would greatly improve the ability of atmospheric inversions to resolve regional fluxes over southern Africa. Satellite missions, such as OCO-2 and GOSAT are able to provide a

great deal of high resolution $CO_2$ data, and these data are being calibrated and validated against data from surface stations, which has known accuracy and precision, and being incorporated into inversion studies. Sources for auxiliary data required to run the mesoscale inversion are readily available.

# Bibliography

Andres, R. J., Marland, G., Fung, I. and Matthews, E.: A 1°× 1° distribution of carbon dioxide emissions from fossil fuel consumption and cement manufacture, 19501990. Global Biogeochem. Cy., 10, 419–429, doi: 10.1029/96GB01523, 1996.

Andres, R. J., Fielding D. J., Marland G., Boden T. A., Kumar N., Kearney A. T.: Carbon dioxide emissions from fossil-fuel use, 17511950, Tellus B, 51, 759-765, doi: 10.1034/j.1600-0889.1999.t01-3-00002.x, 1999a.

Andres, R. J., Marland, G., Boden, T., and Bischoff, S.: Carbon dioxide emissions from fossil fuel consumption and cement manufacture 1751 to 1991 and an estimate for their isotopic composition and latitudinal distribution, in: Wigley, T.M.L and Schimel, D. (Eds.), The Carbon Cycle, Cambridge University, New York, 1999b.

Andres, R. J., Gregg, J. S., Losey, L., Marland, G., and Boden, T. A.: Monthly, global emissions of carbon dioxide from fossil fuel consumption, Tellus B, 63, 309–327, doi:10.1111/j.1600- 0889.2011.00530.x, 2011.

Andres, R. J., Boden, T. A., Bréon, F. -M., Ciais, P., Davis, S., Erickson, D., Gregg, J. S., Jacobson, A., Marland, G., Miller, J., Oda, T., Olivier, J. G. J., Raupach, M. R., Rayner, P., and Treanton, K.: A synthesis of carbon dioxide emissions from fossil-fuel combustion, Biogeosciences, 9, 1845–1871, doi: 10.5194/bg-9-1845-2012, 2012.

Andres, R. J., Boden, T. A., and Higdon, D.: A new evaluation of the uncertainty associated with CDIAC estimates of fossil fuel carbon dioxide emission, Tellus B, 66, 23616, doi: 10.3402/tellusb.v66.23616, 2014.

Asefi-Najafabady, S., Rayner, P. J., Gurney. K. R., McRobert, A., Song, ., Coltin K., Huang, J., Elvidge, C., and Baugh, K.: A multiyear, global gridded fossil fuel $CO_2$ emission data product: Evaluation and analysis of results, J. Geophys. Res., 119, doi: 10.1002/2013JD021296, 2014

Aubinet, M., Grelle, A., Ibrom, A., Rannik, Ü., Moncrieff, J., Foken, T., Kowalski, A. S., Martin, P. H., Berbigier, P., Bernhofer, C., Clement, R., Elbers, J., Granier, A., Grnwald, T., Morgenstern, K., Pilegaard, K., Rebmann, C., Snijders, W., Valentini, R., Vesala, T.: Estimates of the annual net carbon and water exchange of Europeran forests: the EUROFLUX methodology, Adv. Ecol. Res., 30, 113–75, 2000.

Baker, D. F.: An inversion method for determining time-dependent surface $CO_2$ fluxes, in: P. Kasibhatla, P., Heimann, M., Rayner, P., Mahowald, N., Prinn, R. G., and Hartley, D. E. (Eds.), Inversion methods in global biogeochemical cycles, Geophysical Monograph 114, American Geophysical Union, 279–293, Washington, D.C., 2000.

Baker, D. F., Law, R. M., Gurney, K. R., Rayner, P., Peylin, P., Denning, A. S., Bourquet, P., Bruhwiler, L., Chen, Y., Ciais, P., Fung, I.Y., Heimann, M., John, J., Maki, T., Maksyutov, S., Masarie, K., Prather, M., Pak, B., Taguchi, S., Zhu, Z.: TransCom 3 inversion intercomparison: Impact of transport model errors on the interannual variability of regional $CO_2$ fluxes, 1988–2003, Global Biogeochem. Cy., 20, GB1002, doi: 10.1029/2004GB002439, 2006.

Bayer, A. D., Lindeskog, M., Pugh, T. A. M., Anthoni, P. M., Fuchs, R., and Arneth, A.: Uncertainties in the land-use flux resulting from land-use change reconstructions and gross land transitions, Earth Syst. Dynam., 8, 91-111, doi: 10.5194/esd-8-91-2017, 2017.

Bellassen, V. and Stephan, N.: Accounting for Carbon: Monitoring, Reporting and Verifying Emissions in the Climate Economy, Cambridge University Press, Cambridge, UK, 2015.

Boden, T. A., Marland, G., and Andres, R. J.: Global, Regional, and National Fossil-Fuel $CO_2$ Emissions, Carbon Dioxide Information Analysis Center, Oak Ridge National Laboratory, U.S. Department of Energy, Oak Ridge, Tenn., U.S.A., doi: 10.3334/CDIAC/00001_V2010, 2010.

Boden, T. A., Marland, G., and Andres, R. J.: Global, Regional, and National Fossil-Fuel $CO_2$ Emissions, Carbon Dioxide Information Analysis Center, Oak Ridge National Laboratory, U.S. Department of Energy, Oak Ridge, Tenn., U.S.A., doi: 10.3334/CDIAC/00001_V2011, 2011.

Bolin, B. and Keeling, C.D.: Large-scale atmospheric mixing as deduced from the seasonal and meridional variations in carbon dioxide, J. Geophys. Res., 68 (13), 3899-3920, doi: 10.1029/JZ068i013p03899, 1963.

Boon, A., Broquet, G., Clifford, D. J., Chevallier, F., Butterfield, D. M., Pison, I., Ramonet, M., Paris, J. -D., and Ciais, P.: Analysis of the potential of near-ground measurements of $CO_2$ and $CH_4$ in London, UK, for the monitoring of city-scale emissions using an atmospheric transport model, Atmos. Chem. Phys., 16, 6735–6756, doi:10.5194/acp-16-6735-2016, 2016.

Bousquet, P., Ciais, P., Peylin, P., Ramonet, M., and Monfray, P.: Inverse modeling of annual atmospheric $CO_2$ sources and sinks: 1. Method and control inversion, J. Geophys. Res., 104, 26161-26178, doi: 10.1029/1999JD900342, 1999.

Bousquet, P., Peylin, P., Ciais, P., Le Quéré, C., Friedlingstein, P., and Tans, P.P.: Regional changes in carbon dioxide fluxes of land and oceans since 1980, Science, 290, 1342-1346, doi: 10.1126/science.290.5495.1342, 2000.

Brenkert, A.L.: Carbon dioxide emission estimates from fossil-fuel burning, hydraulic cement production, and gas flaring for 1995 on a one degree grid cell basis, Carbon Dioxide Information Analysis Center (CDIAC), Oak Ridge National Laboratory (ORNL), doi: 10.3334/CDIAC/ffe.ndp058.2003, 1998. (http://cdiac.esd.ornl.gov/ndps/ndp058a.html).

Bousquet, P., Ciais, P., Peylin, P., Ramonet, M., and Monfray, P.: Inverse modeling of annual atmospheric $CO_2$ sources and sinks: 1. Method and control inversion, J. Geophys. Res., 104, 26161–26178, doi: 10.1029/1999JD900342, 1999.

Bréon, F. M., Broquet, G., Puygrenier, V., Chevallier, F., Xueref-Remy, I., Ramonet, M., Dieudonné, E., Lopez, M., Schmidt, M., Perrussel, O., and Ciais, P.: An attempt at estimating Paris area $CO_2$ emissions from atmospheric concentration measurements, Atmos. Chem. Phys., 15, 1707–1724, doi: 10.5194/acp-15-1707-2015, 2015.

Brioude, J., Angevine, W. M., Ahmadov, R., Kim, S. -W., Evan, S., McKeen, S. A., Hsie, E. -Y., Frost, G. J., Neuman, J. A., Pollack, I. B., Peischl, J., Ryerson, T. B., Holloway, J., Brown, S. S., Nowak, J. B., Roberts, J. M., Wofsy, S. C., Santoni, G. W., Oda, T., and Trainer, M.: Top-down estimate of surface flux in the

Los Angeles Basin using a mesoscale inverse modeling technique: assessing anthropogenic emissions of CO, NOxand $CO_2$ and their impacts, Atmos. Chem. Phys., 13, 3661–3677, doi: 10.5194/acp-13-3661-2013, 2013.

Buyantuyev, A. and Wu, J.: Urbanization diversifies land surface phenology in arid environments: interactions among vegetation, climatic variation, and land use pattern in the Phoenix metropolitan region, USA, Landscape Urban Plan., 105, 149–159, doi:10.1016/j.landurbplan.2011.12.013, 2012.

Butler, M. P., Davis, K. J., Denning, A. S., and Kawa, S. R.: Using continental observations in global atmospheric inversions of $CO_2$: North American carbon sources and sinks. Tellus B, 62 (5), 550–572, doi: 10.1111/j.1600-0889.2010.00501.x, 2010.

Chan, D., Ishizawa, M., Higuchi, K., Maksyutov, S., and Chen, J.: Seasonal $CO_2$ rectifier effect and large-scale extratropical atmospheric transport, J. Geophys. Res., 113, D17309, doi:10.1029/2007JD009443, 2008.

Chevallier, F., Viovy, N., Reichstein, M., and Ciais, P.: On the assignment of prior errors in Bayesian inversions of $CO_2$ surface fluxes. Geophys. Res. Lett., 33, LL13802, doi: 10.1029/2006GL026496, 2006.

Chevallier, F., F.-M. Bréon, P. J. Rayner (2007), The contribution of the Orbiting Carbon Observatory to the estimation of $CO_2$ sources and sinks: Theoretical study in a variational data assimilation framework, J. Geophys. Res., 112, D09307, doi:10.1029/2006JD007375, 2007.

Chevallier, F., Ciais, P., Conway, T. J., Aalto, T., Anderson, B. E., Bousquet, P., Brunke, E. G., Ciattaglia, L., Esaki, Y., Fröhlich, M., Gomez, A., Gomez-Pelaez, A. J., Haszpra, L., Krummel, P. B., Langenfelds, R. L., Leuenberger, M., Machida, T., Maignan, F., Matsueda, H., Morgui, J. A., Mukai, H., Nakazawa, T., Peylin, P., Ramonet, M., Rivier, L., Sawa, Y., Schmidt, M., Steele, L. P., Vay, S. A., Vermeulen, A. T., Wofsy, S., and Worthy, D.: $CO_2$ surface fluxes at grid point scale estimated from a global 21 year reanalysis of atmospheric measurements, J. Geophys. Res., 115, D21307, doi: 10.1029/2010JD013887, 2010.

Ciais, P., Peylin, P., Bousquet, P.: Regional biospheric carbon fluxes as inferred from atmospheric $CO_2$ measurements, Ecol. Appl., 10(6), 1574–1589, doi: 10.2307/2641225, 2000.

Ciais, P., Rayner, P., Chevallier, F., Bousquet, P., Logan, M., Peylin, P., and Ramonet, M.: Atmospheric inversions for estimating $CO_2$ fluxes: methods and perspectives, Climatic Change, 103, 69–92, 2010.

City of Cape Town: State of energy and energy futures report. Cape Town: City of Cape Town, urlhttp://www.capetown.gov.za/en/EnvironmentalResourceManagement/publications/Documents/State_of_Energy_+_Energy_Futures_Report_2011_revised_2012-01.pdf, 2011.

Dargaville, R., McGuire, A. D., and Rayner, P.: Estimates of large-scale fluxes in high latitudes from terrestrial biosphere models and an inversion of atmospheric $CO_2$ measurements, Clim. Chang., 55, 273–285, doi: 10.1023/A:1020295321582, 2002.

De Sy. V., Herold, M., Achard, F., Beuchle, R., Clevers, J. G. P. W., Lindquist, E., and Verchot, L.: Land use patterns and related carbon losses following deforestation in South America, Environ. Res. Lett., 10, 124004, doi:10.1088/1748-9326/10/12/124004, 2015.

Degener, J.F., 2015. Atmospheric $CO_2$ fertilization effects on biomass yields of 10 crops in northern Germany, Front. Environ. Sci., 3, 48, doi: 10.3389/fenvs.2015.00048, 2015.

Deng, A., Lauvaux, T., Davis, K. J., Gaudet, B. J., Miles, N., Richardson, S. J., Wu, K., Sarmiento, D. P., Hardesty, R.M., Bonin, T. A., Brewer, W. A., and Gurney, K. A.: Toward reduced transport errors in a high resolution urban $CO_2$ inversion system. Elem. Sci. Anth., 5, 20, doi: https://doi.org/10.1525/elementa.133, 2017.

Denman, K. L., Brasseur, G., Chidthaisong, A., Ciais, P., Cox, P. M., Dickinson, R. E., Hauglustaine, D., Heinze, C., Holland, E., Jacob, D., Lohmann, U., Ramachandran, S., da Silva Dias, P. L., Wofsy, S. C., and Zhang, X.: Couplings between changes in the climate system and biogeochemistry, in: Climate Change 2007: The Physical Science Basis. Contribution of Working Group I to the Fourth Assessment Report of the Intergovernmental Panel on Climate Change, edited by: Solomon, S., Qin, D., Manning, M., Chen, Z., Marquis, M., Averyt, K. B., Tignor, M., and Miller, H. L., Cambridge University Press, Cambridge, UK and New York, NY, USA, 499–587, 2007.

Desroziers, G., Berre, L., Chapnik, B., and Poli, P.: Diagnosis of observation, background and analysis-error statistics in observation space, Q. J. Roy. Meteor. Soc., 131, 3385-3396, doi:10.1256/Qj.05.108, 2005.

Dlugokencky, E. and Tans, P.: Trends in atmospheric carbon dioxide, National Oceanic & Atmospheric Administration, Earth System Research Laboratory (NOAA/ESRL), available at: http://www.esrl.noaa.gov/gmd/ccgg/trends/global.html, last access: 29 September 2016.

Doughty, C. E. and Goulden, M. L.: Measuring the carbon emissions of megacities, J. Geophys. Res., 113, G00B07, doi: 10.1029/2007JG000632, 2008.

Duren, R. M. and Miller, C. E.: Are tropical forests near a high temperature threshold?, J. Ge, 2, 560–562, doi: 10.1038/nclimate1629, 2012.

Engelbrecht, F. A., McGregor, J. L. and Engelbrecht, C. J.: Dynamics of the conformal-cubic atmospheric model projected climate-change signal over southern Africa, Int. J. Climatol., 29, 1013-1033., doi: 10/1002/joc.1742.29., 2009.

Engelbrecht, F. A., Landman, W. A., Engelbrecht, C. J., Landman, S., Bopane, M. M., Roux, B., McGregor, J. L., and Thatcher, M.: Multi-scale climate modelling over Southern Africa using variable-resolution global model, Water Research Commission 40-Year Celebration Conference, Kempton Park, 31 August - 1 September 2011, doi: 10.4314/wsa.v37i5.2, 2011.

Enting, I. G.: Green's function methods of tracer inversion, in: Kasibhatla, P., Heimann, M., Rayner, P., Mahowald, N., Prinn, R.G., and Hartley, D.E. (Eds.), Inversion methods in global biogeochemical cycles, Geophysical Monograph 114, American Geophysical Union, 19–31, Washington, D.C., 2000.

Enting, I. G.: Inverse Problems in Atmospheric Constituent Transport, Cambridge Univ. Press, New York, 2002.

Erickson, P. and Tempest, K.: Advancing climate ambition: Cities as partners in global climate action, Produced by Stockholm Environment Institute (SEI) in support of the UN Secretary-General's Special Envoy for Cities and Climate Change and C40, 2014.

Fan, S., Gloor, M., Mahlman, J., Pacala, S., Sarmiento, J., Takahashi, T., Tans, P.: A large terrestrial carbon sink in North America implied by atmospheric and oceanic carbon dioxide data and models, Science, 282, 442-446, doi: 10.1126/science.282.5388.442, 1998.

Friedlingstein, P., Fing, I., Holland, E., John, J., Brasseur, G., Erickson, D., and Schimel, D.: On the contribution of $CO_2$ fertilization to the missing biospheric sink, Global Biogeochem. Cy., 9, 541-556, 1995.

Ganesan, A. L., Rigby, M., Zammit-Mangion, A., Manning, A. J., Prinn, R. G., Fraser, P. J., Harth, C. M., Kim, K.-R., Krummel, P. B., Li, S., Mühle, J., O'Doherty, S. J., Park, S., Salameh, P. K., Steele, L. P., and Weiss, R. F.: Characterization of uncertainties in atmospheric trace gas inversions using hierarchical Bayesian methods, Atmos. Chem. Phys., 14, 3855-3864, doi: 10.5194/acp-14-3855-2014, 2014.

Ganesan, A. L., Manning, A. J., Grant, A., Young, D., Oram, D. E., Sturges, W. T., Moncrieff, J. B., and O'Doherty, S.: Quantifying methane and nitrous oxide emissions from the UK and Ireland using a national-scale monitoring network, Atmos. Chem. Phys., 15, 6393-6406, doi: 10.5194/acp-15-6393-2015, 2015.

Gately, C. K. and Hutyra, L. R.: Large uncertainties in urban-scale carbon emissions, J. Geophys. Res., 122(11), 242–11, doi: 10.1002/2017JD027359, 2017.

Gerbig, C., Lin, J. C., Wofsy, S. C., Daube, B. C., Andrews, A. E., Stephens, B. B., Bakwin, P. S., and Grainger, C. A.: Toward constraining regional-scale fluxes of $CO_2$ with atmospheric observations over a continent: 1. Observed spatial variability from airborne platforms, J. Geophys. Res., 108(D24), 4756, doi:10.1029/2002JD003018, 2003.

Gerbig, C., Korner, S., and Lin, J. C.: Vertical mixing in atmospheric tracer transport models: error characterization and propagation, Atmos. Chem. Phys., 8, 591–602, doi: 10.5194/acp-8-591-2008, 2008.

Göckede, M., Michalak, A.M., Vickers, D., Turner, D.P., and Law, B.E.: Atmospheric inverse modeling to constrain regional scale $CO_2$ budgets at high spatial and temporal resolution, J. Geophys. Res., 115, D15113, doi:10.1029/2009JD012257, 2010.

Gourdji, S.M., Hirsch, A.I., Mueller, K.L., Yadav, V., Andrews, A.E., and Michalak, A.M.: Regional-scale geostatistical inverse modeling of North American $CO_2$ fluxes: a synthetic data study, Atmos. Chem. Phys., 10, 6151-6167, doi:10.5194/acp-10-6151-2010, 2010.

Gurney. K. R., Law, R. M., Denning, A. S., Rayner, P. J., Baker, D., Bousquet, P., Bruhwiler, L., Chen, Y., Ciais, P., Fan, S., Fung, I. Y., Gloor, M., Heimann, M., Higuchi, K., John, J., Maki, T., Maksyutov, S., Masarie, K., Peylin, P., Prather, M., Pak, B. C., Randerson, J., Sarmiento, J., Taguchi, S., Takahashi, T., and Yuen, C.: Towards robust regional estimates of $CO_2$ sources and sinks using atmospheric transport models, Nature, 405, 626–630, 2002.

Gurney, K. R., Law, R. M., Denning, A. S., Rayner, P. J., Baker, D., Bousquet, P., Bruhwiler, L., Chen, Y., Ciais, P., Fan, S., Fung, I. Y., Gloor, M., Heimann, M., Higuchi, K., John, J., Kowalczyk, E., Maki, T., Maksyutov, S., Peylin, P., Prather, M., Pak, B. C., Sarmiento, J., Taguchi, S., Takahashi, T., and Yuen, C.: TransCom 3 $CO_2$ inversion intercomparison: 1. Annual mean control results and sensitivity to transport and prior flux information, Tellus B, 55, 555–579, 2003.

Gurney, K. R., Baker, D., Rayner, P., and Denning, S., Interannual variations in continental-scale net carbon exchange and sensitivity to observing networks estimated from atmospheric $CO_2$ inversions for the period 1980 to 2005, Global Biogeochem. Cy., 22, GB3025, doi:10.1029/2007GB003082, 2008.

Gurney, K. R., et al., The VULCAN inventory, Version 1.0, edited, Purdue University, 2008.

Gurney, K. R., Mendoza, D. L., Zhou, Y. Y., Fischer, M. L., Miller, C. C., Geethakumar, S., Du Can, S. D.: High resolution fossil fuel combustion $CO_2$ emission fluxes for the United States. Environ. Sci. Technol., 43 (14), 5535–5541, doi: 10.1021/es900806c, 2009.

Gurney, K. R., Razlivanov, I., Song, Y., Zhou, Y., Benes, B., and Abdul–Massih, M.: Quantification of fossil fuel $CO_2$ emissions on the building/street scale for a large U.S. city, Environ. Sci. Technol., 46, 12194–12202, doi: 10.1021/es3011282, 2012.

Heimann, M., and Keeling, C.D.: A three-dimensional model of atmospheric CO transport based on observed winds, 2, model description and simulated tracer experiments, in: Peterson, D.H. (Ed.), Aspects of Climate Variability in the Pacific and the Western Americas, Geophysical Monograph Series 55, 237-275, AGU, Washington, D. C., 1989.

Hogue, S., Marland, E., Andres, R. J., Marland, G., and Woodard, D.: Uncertainty in gridded $CO_2$ emissions estimates, Earth's Future, 4, 225–239, doi: 10.1002/2015EF000343, 2016.

Horowitz, C.: Paris Agreement. International Legal Materials, 55(4), 740–755. doi: 10.1017/S0020782900004253, 2016.

Houghton, R. A., Boone, R. D., Fruci, J. R., Hobbie, J. E., Melillo, J. M., Palm, C. A., Peterson, B. J., Shaver, G. R., Woodwell, G. M., Moore, B., Skole, D. E., and Myers, N.: The flux of carbon from terrestrial ecosystem to the atmosphere in 1980 due to changes in land use: geographic distribution of the global flux, Tellus B, 39, 122-139, 10.1111/j.1600-0889.1987.tb00277.x, 1987.

Houghton, R. A.: Balancing the global carbon budget. Annu. Rev. Earth Planet. Sci., 35, 313-347, doi: 10.1146/annurev.earth.35.031306.140057, 2007.

Houghton, R. A., Gloor, M., Lloyd, J., and Potter, C.: The regional carbon budget, in: Keller. M., Bustamante, M., Gash, J., and Silva Dias, P. (Eds.), Amazonia and Global Change, Geophysical Monograph Series 186, American Geophysical Union, Washington, DC, doi: 10.1029/2008GM000728, 2009.

Houghton, R. A. and Nassikas, A. A.: Global and regional fluxes of carbon from land use and land cover change 18502015, Global Biogeochem. Cy., 31, 456–472, doi:10.1002/2016GB005546, 2017.

Houweling, S., Breon, F.-M., Aben, I., Rdenbeck, C., Gloor, M., and Ciais, P.: Inverse modeling of $CO_2$ sources and sinks using satellite data: a synthetic inter-comparison of measurement techniques and their performance as a function of space and time, Atmos. Chem. Phys., 4, 523-538, doi:10.5194/acp-4-523-2004, 2004.

Houweling, S., Aben, I., Breon, F.-M., Chevallier, F., Deutscher, N., Engelen, R., Gerbig, C., Griffith, D., Hungershoefer, K., Macatangay, R., Marshall, J., Notholt, J., Peters, W., and Serrar, S.: The importance of transport model uncertainties

for the estimation of $CO_2$ sources and sinks using satellite measurements, Atmos. Chem. Phys., 10, 9981-9992, doi:10.5194/acp-10-9981-2010, 2010.

Houweling, S., Bergamaschi, P., Chevallier, F., Heimann, M., Kaminski, T., Krol, M., Michalak, A. M., and Patra, P.: Global inverse modeling of $CH_4$ sources and sinks: an overview of methods, Atmos. Chem. Phys., 17, 235-256, doi: 10.5194/acp-17-235-2017, 2017.

Hutyra, L., Duren, R., Gurney, K. R., Grimm, N., Kort, E. A., Larson, E., Shrestha, G.: Urbanization and the carbon cycle: Current capabilities and research outlook from the natural sciences perspective. Earth's Future, 2: 473–495. doi: 10.1002/2014EF000255, 2014.

IPCC: Climate Change 2007: Synthesis Report. Contribution of Working Groups I, II and III to the Fourth Assessment Report of the Intergovernmental Panel on Climate Change [Core Writing Team, Pachauri, R.K and Reisinger, A. (Eds.)]. IPCC, Geneva, Switzerland, 104 pp, 2007.

IPCC: Climate Change 2014: Synthesis Report. Contribution of Working Groups I, II and III to the Fifth Assessment Report of the Intergovernmental Panel on Climate Change [Core Writing Team, Pachauri, R.K. and Meyer, L.A. (Eds.)]. IPCC, Geneva, Switzerland, 151 pp, 2014.

Janssens-Maenhout, G., Pagliari, V., Guizzardi, D., and Muntean, M.: Global emission inventories in the Emission Database for Global Atmospheric Research (EDGAR) Manual (I). Gridding: EDGAR emissions distribution on global gridmaps. Joint Research Centre, Luxembourg: European Union, 33 pp, doi: 10.2788/81454, 2012.

Kaminski, T., Heimann, M. and Giering, R.: A coarse grid three-dimensional global inverse model of the atmospheric transport: 1. Adjoint model and Jacobian matrix, J. Geophys. Res., 104(D15), 18535–18553, doi: 10.1029/1999JD900147, 1999a.

Kaminski, T., Heimann, M., and Giering, R.: A coarse grid three dimensional global inverse model of the atmospheric transport, 2. Inversion of the transport of $CO_2$ in the 1980s, J. Geophys. Res., 104, 18555–18581, 1999b.

Kaminski, T. and Heimann, M.: Inverse modeling of atmospheric carbon dioxide fluxes, Science, 294, 259, doi: 10.1126/science.294.5541.259a, 2001a.

Kaminski, T., Rayner, P .J., Heimann, M., and Enting, I. G.: On aggregation errors in atmospheric transport inversions, J. Geophys. Res., 106, 4705–4715, 2001b.

Kort, E. A., Angevine, W. M., Duren, R., and Miller, C. E.: Surface observations for monitoring urban fossil fuel $CO_2$ emissions: minimum site location requirements for the Los Angeles megacity, J. Geophys. Res., 118, 1–8, doi: 10.1002/jgrd.50135, 2013.

Kowalczyk, E. A., Wang, Y. P. and Law, R. M.: CSIRO Atmosphere Biosphere Land Exchange model for use in climate models and as an offline model, CSIRO Marine and Atmospheric Research technical paper xxV ISBN 1 921232 39 0, 2006.

Landman, W. A., Engelbrecht, F., Park, R., Bopane, M., Lötter, D.: Atmospheric modelling and prediction at time scales from days to seasons. CSIR Science real and relevant conference 2010, Pretoria, 2010.

Lauderdale, J. M., Dutkiewicz, S. ,Williams, R. G. and Follows, M. J.: Quantifying the drivers of ocean-atmosphere $CO_2$ fluxes, Global Biogeochem. Cycles, 30, 983–999, doi: 10.1002/2016GB005400, 2016.

Lauvaux, T., Uliasz, M., Sarrat, C., Chevallier, F., Bousquet, P., Lac, C., Davis, K. J., Ciais, P., Denning, A. S., and Rayner, P. J.: Mesoscale inversion: first results from the CERES campaign with synthetic data, Atmos. Chem. Phys., 8, 3459–3471, doi: 10.5194/acp-8-3459-2008, 2008.

Lauvaux, T., Pannekoucke, O., Sarrat, C., Chevallier, F., Ciais, P., Noilhan, J., and Rayner, P. J.: Structure of the transport uncertainty in mesoscale inversions of $CO_2$ sources and sinks using ensemble model simulations, Biogeosciences, 6, 1089–1102, doi: 10.5194/bg-6-1089-2009, 2009.

Lauvaux, T., Schuh, A. E., Uliasz, M., Richardson, S., Miles, N., Andrews, A. E., Sweeney, C., Diaz, L. I., Martins, D., Shepson, P. B., and Davis, K. J.: Constraining the $CO_2$ budget of the corn belt: exploring uncertainties from the assumptions in a mesoscale inverse system, Atmos. Chem. Phys., 12, 337–354, doi: 10.5194/acp-12-337-2012, 2012.

Lauvaux, T., Miles, N. L., Richardson, S. J., Deng, A., Stauffer, D. R., Davis, K. J., Jacobson, G., Rella, C., Calonder, G. -P., and DeCola, P. L.: Urban emissions

of $CO_2$ from Davos, Switzerland: the first real-time monitoring system using atmospheric inversion technique, J. Appl. Meteorol. Climatol., 52, 2654–2668, doi: 10.1175/JAMC-D-13-038.1, 2013.

Lauvaux, T., Miles, N. L., Deng, A. Richardson, S. J., Cambaliza, M. O., Davis, K. J., Gaudet, B., Gurney, K. R., Huang, J., O'Keefe, D., Song, Y., Karion, A., Oda, T., Patarasuk, R., Razlivanov, I., Sarmiento, D., Shepson, P., Sweeney, C., Turnbull, J., and Wu, K.: High-resolution atmospheric inversion of urban $CO_2$ emissions during the dormant season of the Indianapolis Flux Experiment (INFLUX), J. Geophys. Res. Atmos., 121, 5213–5236, doi: 10.1002/2015JD024473, 2016.

Law, R. M., Chen, Y., Gurney, K. R., and Transcom 3 Modellers: TransCom 3 $CO_2$ inversion intercomparison: 2. Sensitivity of annual mean results to data choices, Tellus B, 55, 580–595, doi: 10.1034/j.1600-0889.2003.00053.x, 2003.

Levis, S., Foley, J. A., and Pollard, D.: Large-scale vegetation feedbacks on a doubled $CO_2$ climate, J. Clim., 13, 1313–1325, doi: 10.1175/1520-0442(2000)013¡1313:LSVFOA¿2.0.CO;2.

LeQuere, C., Raupach, M., Canadell, J., Marland, G., Bopp, L., Cias, P., Conway, T., Doney, S., Feely, R., Foster, P., Friedlingstein, P., Gurney, K., Hougton, R., House, J., Hungtingford, C., Levy, P., Lomas, M., Majkut, J., Metzl, N., Ometto, J., Peters, G., Prentice, I. C., Randerson, J., Running, S., Sarmiento, J., Schuter, U., Sitch, S., Takahashi, T., Viovy, N., Werf, G. v. d., and Woodward, F.: Trends in the sources and sinks of carbon dioxide, Nature Geosci., 2, 1831–1836, doi: 10.1038/ngeo1689, 2009.

Le Quéré, C., Moriarty, R., Andrew, R. M., Canadell, J. G., Sitch, S., Korsbakken, J. I., Friedlingstein, P., Peters, G. P., Andres, R. J., Boden, T. A., Houghton, R. A., House, J. I., Keeling, R. F., Tans, P., Arneth, A., Bakker, D. C. E., Barbero, L., Bopp, L., Chang, J., Chevallier, F., Chini, L. P., Ciais, P., Fader, M., Feely, R. A., Gkritzalis, T., Harris, I., Hauck, J., Ilyina, T., Jain, A. K., Kato, E., Kitidis, V., Klein Goldewijk, K., Koven, C., Landsch"utzer, P., Lauvset, S. K., Lef'evre, N., Lenton, A., Lima, I. D., Metzl, N., Millero, F., Munro, D. R., Murata, A., Nabel, J. E. M. S., Nakaoka, S., Nojiri, Y., O'Brien, K., Olsen, A., Ono, T., Pérez, F. F., Pfeil, B., Pierrot, D., Poulter, B., Rehder, G., Rödenbeck, C., Saito, S., Schuster, U., Schwinger, J., Séférian, R., Steinhoff, T., Stocker, B. D., Sutton, A. J., Takahashi, T., Tilbrook, B., van der Laan-Luijkx, I. T., van der Werf, G. R.,

van Heuven, S., Vandemark, D., Viovy, N., Wiltshire, A., Zaehle, S., and Zeng, N.: Global Carbon Budget 2015, Earth Syst. Sci. Data, 7, 349–396, doi: 10.5194/essd-7-349-2015, 2015.

Le Quéré, C., Andrew, R. M., Friedlingstein, P., Sitch, S., Pongratz, J., Manning, A. C., Korsbakken, J. I., Peters, G. P., Canadell, J. G., Jackson, R. B., Boden, T. A., Tans, P. P., Andrews, O. D., Arora, V. K., Bakker, D. C. E., Barbero, L., Becker, M., Betts, R. A., Bopp, L., Chevallier, F., Chini, L. P., Ciais, P., Cosca, C. E., Cross, J., Currie, K., Gasser, T., Harris, I., Hauck, J., Haverd, V., Houghton, R. A., Hunt, C. W., Hurtt, G., Ilyina, T., Jain, A. K., Kato, E., Kautz, M., Keeling, R. F., Klein Goldewijk, K., K"ortzinger, A., Landsch"utzer, P., Lef'evre, N., Lenton, A., Lienert, S., Lima, I., Lombardozzi, D., Metzl, N., Millero, F., Monteiro, P. M. S., Munro, D. R., Nabel, J. E. M. S., Nakaoka, S.-I., Nojiri, Y., Padin, X. A., Peregon, A., Pfeil, B., Pierrot, D., Poulter, B., Rehder, G., Reimer, J., Rödenbeck, C., Schwinger, J., Séférian, R., Skjelvan, I., Stocker, B. D., Tian, H., Tilbrook, B., Tubiello, F. N., van der Laan-Luijkx, I. T., van der Werf, G. R., van Heuven, S., Viovy, N., Vuichard, N., Walker, A. P., Watson, A. J., Wiltshire, A. J., Zaehle, S., and Zhu, D.: Global Carbon Budget 2017, Earth Syst. Sci. Data, 10, 405–448, doi: 10.5194/essd-10-405-2018, 2018.

Lokupitiya, E., Denning, S., Paustian, K., Baker, I., Schaefer, K., Verma, S., Meyers, T., Bernacchi, C. J., Suyker, A., and Fischer, M.: Incorporation of crop phenology in Simple Biosphere Model (SiBcrop) to improve land-atmosphere carbon exchanges from croplands, Biogeosciences, 6, 969–986, doi:10.5194/bg-6-969-2009, 2009.

Long, S. P., Ainsworth, E. A., Leakey, A. D. B., Nösberger, J., and Ort, D. R.: Food for thought: lower-than-expected crop yield stimulation with rising $CO_2$ concentrations, Science, 312, 1918–1921, doi: 10.1126/science.1114722, 2006.

Masarie, K. A., Peters, W., Jacobson, A. R., and Tans, P. P.: ObsPack: a framework for the preparation, delivery, and attribution of atmospheric greenhouse gas measurements, Earth Syst. Sci. Data, 6, 375-384, doi: 10.5194/essd-6-375-2014, 2014.

Maki, T., Ikegami, M., Fujita, T., Hirahara, T., Yamada, K., Mori, K., Takeuchi, A., Tsutsumi, Y., Suda, K., and Conway, T. J., New technique to analyse global distributions of $CO_2$ concentrations and fluxes from non-processed observational data, Tellus B, 62, 797809, doi: 10.1111/j.1600-0889.2010.00488.x, 2010.

McGrath, J. M., and Lobell, D. B.: Regional disparities in the $CO_2$ fertilization effect and implications for crop yields, Environ. Res. Lett., 8, 014054, doi: 10.1088/1748-9326/8/1/014054, 2013.

McGregor, J.L.: Accuracy and initialization of a two-time-level split semi-Lagrangian model, Collection of papers presented at WMO/IUGG NWP symposium, Tokyo, 4-8, August 1987, 233-246, 1987.

McGregor, J. L. and Dix, M. R.: The CSIRO conformal-cubic atmospheric GCM, in: IUTAM Symposium on Advances in Mathematical Modelling of Atmosphere and Ocean Dynamics, Limerick, Ireland, 2–7 July 2000, edited by: Hodnett, P. F., Kluwer, Dordrecht, 197–202, 2001.

McKain, K., Wofsy, S. C., Nehrkorn, T., Eluszkiewicz, J., Ehleringer, J. R., and Stephens, B. B.: Assessment of ground-based atmospheric observations for verification of greenhouse gas emissions from an urban region, Proc. Natl. Acad. Sci. U. S. A., 109(22), 8423–8428, doi: 10.1073/pnas.1116645109, 2012.

Michalak, A. M., Bruhwiler, L., and Tans, P. P.: A geostatistical approach to surface flux estimation of atmospheric trace gases, J. Geophys. Res., 109, D14109, doi: 10.1029/2003JD004422, 2004.

Michalak, A. M., Hirsch, A., Bruhwiler, L., Gurney, K. R., Peters, W., and Tans, P. P.: Maximum likelihood estimation of covariance parameters for Bayesian atmospheric trace gas surface flux inversions, J. Geophys. Res., 110, D24107, doi: 10.1029/2005JD005970, 2005.

Miles, N. L., Richardson, S. J., Lauvaux, T., Davis, K. J., Balashov, N. V., Deng, A., Turnbull, J. C., Sweeney, C., Gurney, K. R., Patarasuk, R., Razlivanov, I., Cambaliza, M. O. L., Shepson, P. B.: Quantification of urban atmospheric boundary layer greenhouse gas dry mole fraction enhancements in the dormant season: Results from the Indianapolis Flux Experiment (INFLUX), Elem Sci Anth, 5, 27, doi: https://doi.org/10.1525/elementa.127, 2017.

Miller, J. B., Tans, P. P., White, J. W. C., Masarie, K. A., Conway, T. J., Vaughn, B. H., Suits, N. S., and Randerson, J. T.: A decreasing trend in northern hemisphere carbon uptake since 1992, Seventh Int. Conf. Carbon Dioxide, Broomfield, CO, 2005.

Miller, S. M., Wofsy, S. C., Michalak, A. M., Kort, E. A., Andrews, A. E., Biraud, S. C., Dlugokencky, E. J., Eluszkiewicz, J., Fischer, M. L., Janssens-Maenhout, G., Miller, B. R., Miller, J. B., Montzka, S. A., Nehrkorn, T., and Sweeney, C.: Anthropogenic emissions of methane in the United States, PNAS, 110, 2001820022, doi: 10.1073/pnas.1314392110, 2013.

Miller, S. M., Michalak, A. M., Yadav, V., and Tadí(c), J. M.: Characterizing biospheric carbon balance using CO2 observations from the OCO-2 satellite, Atmos. Chem. Phys., 18, 6785-6799, doi: 10.5194/acp-18-6785-2018, 2018.

Mucina, L. and Rutherford, M.C. (Eds).: The vegetation of South Africa, Lesotho and Swaziland. Strelitzia 19. Pretoria, South African Biodiversity Institute, 2006.

Mitchard, E. T. A.: The tropical forest carbon cycle and climate change, Nature, 559, 527–534, doi: 10.1038/s41586-018-0300-2, 2018.

Molina, L., Broquet, G., Imbach, P., Chevallier, F., Poulter, B., Bonal, D., Burban, B., Ramonet, M., Gatti, L. V., Wofsy, S. C., Munger, J. W., Dlugokencky, E., and Ciais, P.: On the ability of a global atmospheric inversion to constrain variations of $CO_2$ fluxes over Amazonia, Atmos. Chem. Phys., 15, 8423-8438, doi: 10.5194/acp-15-8423-2015, 2015.

Müller, J.-F. and Stavrakou, T.: Inversion of CO and NOx emissions using the adjoint of the IMAGES model, Atmos. Chem. Phys., 5, 1157-1186, doi: 10.5194/acp-5-1157-2005, 2005.

Myhre, G., Shindell, D., Bron, F.-M., Collins, W., Fuglestvedt, J., Huang, J., Koch, D., Lamarque, J.-F., Lee, D., Mendoza, B., Nakajima, T., Robock, A., Stephens, G., Takemura, T., and Zhang, H.: Anthropogenic and natural radiative forcing, in: Climate Change 2013: The Physical Science Basis. Contribution of Working Group I to the Fifth Assessment Report of the Intergovernmental Panel on Climate Change, edited by: Stocker, T. F., Qin, D., Plattner, G.-K., Tignor, M., Allen, S. K., Boschung, J., Nauels, A., Xia, Y., Bex, V., and Midgley, P. M., Cambridge University Press, Cambridge, United Kingdom and New York, NY, USA, 659740, 2013.

Myhre, G., Myhre, C. L., Forster, P. M., and Shine, K. P.: Halfway to doubling of $CO_2$ radiative forcing, Nat. Geosci., 10, 710–711, doi: 10.1038/ngeo3036, 2017.

Newman, S., Xu, X., Gurney, K. R., Hsu, Y. K., Li, K. F., Jiang, X., Keeling, R., Feng, S., O'Keefe, D., Patarasuk, R., Wong, K. W., Rao, P., Fischer, M. L., and Yung, Y. L.: Toward consistency between trends in bottom-up $CO_2$ emissions and top-down atmospheric measurements in the Los Angeles megacity, Atmos. Chem. Phys., 16, 3843–3863, doi: 10.5194/acp-16-3843-2016, 2016.

Nickless, A., Scholes, R. J. and Filby, E.: Spatial and temporal disaggregation of anthropogenic $CO_2$ emissions from the City of Cape Town, S. Afr. J. Sci., 111(11/12), Art. #2014 − 0387, 8 pages, doi: 10.17159/sajs.2015/20140387, 2015a.

Nickless, A., Ziehn, T., Rayner, P. J., Scholes, R .J., and Engelbrecht, F.: Greenhouse gas network design using backward Lagrangian particle dispersion modelling – Part 2: Sensitivity analyses and South African test case, Atmos. Chem. Phys., 15, 2051–2069, doi: 10.5194/acp-15-2051-2015, 2015b.

Nickless, A., Rayner, P. J., Engelbrecht, F., Brunke, E.-G., Erni, B., and Scholes, R. J.: Estimates of $CO_2$ fluxes over the city of Cape Town, South Africa, through Bayesian inverse modelling, Atmos. Chem. Phys., 18, 4765-4801, doi: 10.5194/acp-18-4765-2018, 2018a.

Nickless, A., Rayner, P. J., Erni, B., and Scholes, R. J.: Comparison of the genetic algorithm and incremental optimisation routines for a Bayesian inverse modelling based network design, Inverse Problems, 34, 055006, doi: 10.1088/1361-6420/aab46c, 2018b.

Nickless, A., Rayner, P. J., Scholes, R. J., Engelbrecht, F., and Erni, B.: An atmospheric inversion over the city of Cape Town: sensitivity analyses, Atmos. Chem. Phys. Discuss., doi: 10.5194/acp-2018-535, in review, 2018c.

Niwa, Y., Machida, T., Sawa, Y., Matsueda, H., Schuck, T. J., Brenninkmeijer, C. A. M., Imasu, R., and Satoh, M.: Imposing strong constraints on tropical terrestrial $CO_2$ fluxes using passenger aircraft based measurements, J. Geophys. Res., 117, D11303, doi: 10.1029/2012JD017474, 2012.

NRC (Committee on Methods for Estimating Greenhouse Gas Emissions): Verifying greenhouse gas emissions: methods to support international climate agreements (9780309152112), The National Academies Press, Washington, D.C., 2010.

Numata, I., Cochrane, M. A., Souza, C. M., and Sales, M. H.: Carbon emissions from deforestation and forest fragmentation in the Brazilian Amazon, Environ. Res. Lett., 6, 044003, doi: 10.1088/1748-9326/6/4/044003, 2011.

O'ishi, R., Abe-Ouchi, A., Prentice, C., and Sitch, S.: Vegetation dynamics and plant $CO_2$ responses as positive feedbacks in a greenhouse world, Geophys. Res. Lett., 36, L11706, doi: 10.1029/2009GL038217, 2009.

Oda, T. and Maksyutov, S.: A very high-resolution (1 km×1 km) global fossil fuel $CO_2$ emission inventory derived using a point source database and satellite observations of nighttime lights, Atmos. Chem. Phys., 11, 543-556, doi:10.5194/acp-11-543-2011, 2011.

Ogle, S. M., Davis, K. J., Lauvaux, T., Schuh, A., Cooley, D., West, T. O., Heath, L. S., Miles, N. L., Richardson, S. J., Breidt, F. J., Smith, J. E., McCarty, J. L., Gurney, K. R., Tans, P., and Denning, A. S.: An approach for verifying biogenic greenhouse gas emissions inventories with atmospheric $CO_2$ concentration data, Environ. Res. Lett., 10, 034012, doi: 10.1088/1748-9326/10/3/034012, 2015.

Palmer, P. I., O'Doherty, S., Allen, G., Bower, K., Bsch, H., Chipperfield, M. P., Connors, S., Dhomse, S., Feng, L., Finch, D. P., Gallagher, M. W., Gloor, E., Gonzi, S., Harris, N. R. P., Helfter, C., Humpage, N., Kerridge, B., Knappett, D., Jones, R. L., Le Breton, M., Lunt, M. F., Manning, A. J., Matthiesen, S., Muller, J. B. A., Mullinger, N., Nemitz, E., O'Shea, S., Parker, R. J., Percival, C. J., Pitt, J., Riddick, S. N., Rigby, M., Sembhi, H., Siddans, R., Skelton, R. L., Smith, P., Sonderfeld, H., Stanley, K., Stavert, A. R., Wenger, A., White, E., Wilson, C., and Young, D.: A measurement-based verification framework for UK greenhouse gas emissions: an overview of the Greenhouse gAs Uk and Global Emissions (GAUGE) project, Atmos. Chem. Phys., 18, 11753-11777, doi: 10.5194/acp-18-11753-2018, 2018.

Patra, P. K., Ishizawa, M., Maksyutov, S., Nakazawa, T., and Inoue, G.: Role of biomass burning and climateanomalies for land-atmosphere carbon fluxes based on inverse modeling of atmospheric $CO_2$, Global Biogeochem. Cycles, 19, GB3005, doi:10.1029/2004GB002258, 2005.

Peters, W., Miller, J. B., Whitaker, J., Denning, A. S., Hirsch, A., Krol, M. C., Zupanski, D., Bruhwiler, L., and Tans, P. P.: An ensemble data assimilation system

to estimate $CO_2$ surface fluxes from atmospheric trace gas observations, J. Geophys. Res., 110, D24304, doi: 10.1029/2005JD006157, 2005.

Peters, W., Jacobson, A. R., Sweeney, C., Andrews, A. E., Conway, T. J., Masarie, K., Miller, J. B., Bruhwiler, L. M., Pètron, G., Hirsch, A. I., Worthy, D. E. J., van der Werf, G. R., Randerson, J. T., Wennberg, P. O., Krol, M. C., and Tans, P. P.: An atmospheric perspective on North American carbon dioxide exchange: CarbonTracker, PNAS, 104(48), 18925–18930, doi: 10.1073/pnas.0708986104, 2007.

Peters, W., Krol, M. C., van der Werf, G. R., Houweling, S., Jones, C. D., Hughes, J., Schaefer, K., Masarie, K. A., Jacobson, A. R., Miller, J. B., Cho, C.H., Ramonet, M., Schmidt, M., Ciattaglia, L., Apadula, F., Heltai, D., Meinhardt, F., Di Sarra, A. G., Piacentino, S., Sferlazzo, D., Aalto, T., Hatakka, J., Ström, J., Haszpra, L., Meijer, H. A. J., Van der Laan, S., Neubert, R. E. M., Jordan, A., Rodó, X., Morgui, J.-A., Vermeulen, A. T., Popa, E., Rozanski, K., Zimnoch, M., Manning, A. C., Leuenberger, M., Uglietti, C., Dolman, A. J., Ciais, P., Heimann, M., and Tans, P. P.: Seven years of recent European net terrestrial carbon dioxide exchange constrained by atmospheric observations, Glob. Change Biol., 16, 1317-1337, doi: 10.1111/j.1365- 2486.2009.02078.x, 2010.

Peylin, P., Baker, D., Sarmiento, J., Ciais, P., and Bousquet, P.: Influence of transport uncertainty on annual mean and seasonal inversions of atmospheric $CO_2$ data, J. Geophys. Res., 107, 4385, doi: 10.1029/2001JD000857, 2002.

Peylin, P., Rayner, P. J., Bousquet, P., Carouge, C., Hourdin, F., Heinrich, P., Ciais, P., and AEROCARB contributors: Daily $CO_2$ flux estimates over Europe from continuous atmospheric measurements: 1, inverse methodology, Atmos. Chem. Phys., 5, 3173–3186, doi:10.5194/acp-5-3173-2005, 2005.

Peylin, P., Law, R. M., Gurney, K. R., Chevallier, F., Jacobson, A. R., Maki, T., Niwa, Y., Patra, P. K., Peters, W., Rayner, P. J., Rödenbeck, C., van der Laan-Luijkx, I. T., and Zhang, X.: Global atmospheric carbon budget: results from an ensemble of atmospheric $CO_2$ inversions, Biogeosciences, 10, 6699-6720, doi:10.5194/bg-10-6699-2013, 2013.

Piao, S. L., Fang, J. Y., Ciais, P. Peylin, P., Huang, Y., Sitch, S., and Wang, T.: The carbon balance of terrestrial ecosystems in China, Nature, 458, 1009-1014, doi: 10.1038/nature07944, 2009.

Prentice, C., Heimann, M., and Sitch, S.: The carbon balance of the terrestrial biosphere: ecosystem models and atmospheric observations, Ecol. Appl., 6, 1553–1573, doi: 10.2307/2641224, 2000.

Rayner, P. J., Enting, I. G., Francey, R. J., and Langenfelds, R. L.: Reconstructing the recent carbon cycle from atmospheric $CO_2$, $\delta^{13}C$ and $O_2/N_2$ observations, Tellus B, 51, 213–232, 1999.

Rayner, P. J., Law, R. M, Allison, C. E., Francey, R. J., Trudinger, C. M., and Pickett-Heaps, C.: Interannual variability of the global carbon cycle (1992-2005) inferred by inversion of atmospheric $CO_2$ and $\delta^{13}C$ measurements, Global Biogeochem. Cy., 22, GB3008, doi: 10.1029/2007GB003068, 2008.

Rayner, P. J., Raupach, M. R., Paget, M., Peylin, P., and Koffi, E.: A new global gridded data set of $CO_2$ emissions from fossil fuel combustion: mehodology and evaluation, J. Geophys. Res., 115, D19306, doi: 10.1029/2009JD013439, 2010.

Rigby, M., Montzka, S. A., Prinn, R. G., White, J. W. C., Young, D., O'Doherty, S., Lunt, M. F., Ganesan, A. L., Manning, A. J., Simmonds, P. G., Salameh, P. K., Harth, C. M., Mühle, Weiss, R. F., Fraser, P. J., Steele, P., Krummel, P. B., McCulloch, A., and Park, S.: Role of atmospheric oxidation in recent methane growth, PNAS, 114, 5373–5377, doi: 10.1073/pnas.1616426114, 2017.

Rivier, L., Peylin, P., Chias, P., Gloor, M., Rödenbeck, C., Geels, C., Karstens, U., Bousquet, P., Brandt, J., Heimann, M., and Aerocarb experimentalists: European $CO_2$ fluxes from atmospheric inversions using regional and global transport models, Clim. Change, 103, 93–115, doi: 10.1007/s10584-010-9908-4, 2010.

Rödenbeck, C.: Estimating $CO_2$ sources and sinks from atmospheric mixing ratio measurements using a global inversion of atmospheric transport, Technical Report 6, Max Planck Institute for Biogeochemistry, Jena, http://www.bgc-jena.mpg.de/uploads/Publications/TechnicalReports/tech_report6.pdf, 2005.

Saitoh, N., Kimoto, S., Sugimura, R., Imasu, R., Kawakami, S., Shiomi, K., Kuze, A., Machida, T., Sawa, Y., and Matsueda, H.: Algorithm update of the GOSAT/TANSO-FTS thermal infrared $CO_2$ product (version 1) and validation of the UTLS CO2 data using CONTRAIL measurements, Atmos. Meas. Tech., 9, 2119-2134, doi: 10.5194/amt-9-2119-2016, 2016.

Shirai, T., Ishizawa, M., Zhuravlev, R., Ganshin, A., Belikov, D., Saito, M., Oda, T., Valsala, V., Gomez-Pelaez, A. J., Langenfelds, R., and Maksyutov, S.: A decadal inversion of $CO_2$ using the Global EulerianLagrangian Coupled Atmospheric model (GELCA): sensitivity to the ground-based observation network, Tellus B, 69:1, 1291158, doi: 10.1080/16000889.2017.1291158, 2017.

Schimel, D. S., House, J. I., Hibbard, K. A., Bousquet, P., Ciais, P., Peylin, P., Braswell, B. H., Apps, M. J., Baker, D., Bondeau, A., Canadell, J., Churkina, G., Cramer, W., Denning, A. S., Field, C. B., Friedlingstein, P., Goodale, C., Heimann, M., Houghton, R. A., Melillo, J. M., Moore III, B., Murdiyarso, D., Noble, I., Pacala, S. W., Prentice, I. C., Raupach, M. R., Rayner, P. J., Scholes, R. J., Steffen, W. L. and Wirth, C.: Recent patterns and mechanisms of carbon exchange by terrestrial ecosystems, Nature, 414, 169-172, doi: 10.1038/35102500, 2001.

Schuh, A. E., Denning, A. S., Corbin, K. D., Baker, I. T., Uliasz, M., Parazoo, N., Andrews, A. E., and Worthy, D. E. J.: A regional high-resolution carbon flux inversion of North America for 2004, Biogeosciences, 7, 1625-1644, doi: 10.5194/bg-7-1625-2010, 2010.

Schuh, A. E., Lauvaux, T., West, T. O., Denning, A. S., Davis, K., J., Miles, N., Richardson, S., Uliasz, M., Lokupitiya, E., Cooley, D., Andrews, A., and Ogle, S.: Evaluating atmospheric $CO_2$ inversions at multiple scales over a highly inventoried agricultural landscape, Glob. Change Biol., 19, 1424–1439, doi: 10.1111/gcb.12141, 2013.

Schut, A. G. T., Ivits, E., Conijn, J. G., ten Brink, B., and Fensholt, R.: Trends in global vegetation activity and climatic drivers indicate a decoupled response to climate change, PLoS ONE, 10(10), e0138013, doi: 10.1371/journal.pone.0138013, 2015.

Seibert, P. and Frank, A.: Source-receptor matrix calculation with a Lagrangian particle dispersion model in backward mode, Atmos. Chem. Phys., 4, 51–63, doi: 10.5194/acp-4-51-2004, 2004.

Seto, K. C., Dhakal, S., Bigio, A., Blanco, H., Delgado, G. C., Dewar, D., Huang, L., Inaba, A., Kansal, A., Lwasa, S., McMahon, J. E., Müller, D. B., Murakami, J., Nagendra, H., and Ramaswami, A.: Human settlements, infrastructure and spatial planning, in: Climate Change 2014: Mitigation of Climate Change. Contribution of

Working Group III to the Fifth Assessment Report of the Intergovernmental Panel on Climate Change, edited by: Edenhofer, O., Pichs-Madruga, R., Sokona, Y., Farahani, E., Kadner, S., Seyboth, K., Adler, A., Baum, I., Brunner, S., Eickemeier, P., Kriemann, B., Savolainen, J., Schlömer, S., von Stechow, C., Zwickel, T., and Minx, J. C., Cambridge, United Kingdom and New York, NY, USA, 2014.

Shi, Y. and Matsunaga, T.: Temporal comparison of global inventories of CO2 emissions from biomass burning during 20022011 derived from remotely sensed data, Environ. Sci. Pollut. Res., 24, 16905–16916, doi: 10.1007/s11356-017-9141-z, 2017.

Smith, W. K., Reed, S., Cleveland, C., Ballantyne, A. P., Anderegg, W. R. L., Wieder, W. R., Liu, Y. Y., Running, S. W.: Large divergence of satellite and Earth system model estimates of global terrestrial $CO_2$ fertilization, Nat. Clim. Change, 6, 306–310, doi: 10.1038/nclimate2879, 2016.

Statistics South Africa: Census 2011 statistical release, P0301.4., Pretoria: Statistics South Africa, 2011.

Staufer, J., Broquet, G., Bréon, F. -M., Puygrenier, V., Chevallier, F., Xueref-Rémy, I., Dieudonné, E., Lopez, M., Schmidt, M., Ramonet, M., Perrussel, O., Lac, C., Wu, L., and Ciais, P.: The first 1-year-long estimate of the Paris region fossil fuel $CO_2$ emissions based on atmospheric inversion, Atmos. Chem. Phys., 16, 14703–14726, doi: 10.5194/acp-16-14703-2016, 2016.

Stephens, B. B., Wofsy, S. C., Keeling, R. F., Tans, P. P., and Potosnak, M.J.: The $CO_2$ budget and rectification airborne study: Strategies for measuring rectifiers and regional fluxes, Inverse Methods in Global Biogeochemical Cycles, P. Kasibhatla et al., eds., Geophysical Monograph Series, volume 114, American Geophysical Union, 1999

Strong, C., Stwertka, C., Bowling, D. R., Stephens, B. B. and Ehleringer, J. R.: Urban carbon dioxide cycles within the Salt Lake Valley: A multiple-box model validated by observations, J. Geophys. Res., 116, D15307, doi: 10.1029/2011JD015693, 2011.

Sugar, L. and Kennedy, C.: A low carbon infrastructure plan for Toronto, Canada, Can. J. Civ. Eng., 40, 86–96, doi: 10.1139/cjce-2011-0523, 2013.

Suntharalingam, P., Spivakovsky, C. M., Logan, J. A., and McElroy, M. B.: Estimating the distribution of terrestrial $CO_2$ sources and sinks from atmospheric

measurements: sensitivity to configuration of the observation network, J. Geophys. Res., 108 (D15), 4452, doi: 10.1029/2002JD002207, 2003.

Takahashi, T., Feely, R. A., Weiss, R. F., Wanninkhof, R. H., Chipman, D. W., Sutherland, S. C., and Takahashi, T. T.: Global air-sea flux of $CO_2$: an estimate based on measurements of sea-air $pCO_2$ difference. Proc. Natl. Acad. Sci., 94(16), 8292–8299, 1997.

Takahashi, T., Wanninkhof, R. H., Feely, R. A., Weiss, R. F., Chipman, D. W. and coauthors.: Net seaair $CO_2$ flux over the global oceans: An improved estimate based on the seaair $pCO_2$ difference, Proceedings of the 2nd International Symposium $CO_2$ in Oceans, Tsukuba, Japan, January 1999, 1999.

Takahashi, T., Sutherland, S. C., Wanninkhof, R., Sweeney, C., Feely, R. A., Chipman, D. W., Hales, B., Friederich, G., Chavez, F., Watson, A., Bakker, D. C. E., Schuster, U., Metzl, N., Yoshikawa-Inoue, H., Ishii, M., Midorikawa, T., Nojiri, Y., Sabine, C., Olafsson J., Arnarson, T. S., Tilbrook, B., Johannessen, T., Olsen, A., Bellerby, R., Körtzinger, A., Steinhoff, T., Hoppema, M., de Baar, H. J. W., Wong, C. S., Delille, B. and Bates, N. R.: Climatological mean and decadal changes in surface ocean $pCO_2$, and net sea-air $CO_2$ flux over the global oceans. Deep-Sea Res. II, 56, 554-577, 2009.

Tans, P. P., Fung, I. Y. and Takahashi, T.: Observational constraints on the global atmospheric $CO_2$ budget, Science, 247, 1431–1438, 1990.

Tarantola, A.: Inverse Problem Theory and Methods for Model Parameter Estimation, Society for Industrial and Applied Mathematics , Philadelphia, 2005.

Turnbull, J. C., Sweeney, C., Karion, A., Newberger, T., Lehman, S. J., Tans, P. P., Davis, K. J., Lauvaux, T., Miles, N. L., Richardson, S. J., Cambaliza, M. O., Shepson, P. B., Gurney, K., and Patarasuk, P.: Toward quantification and source sector identification of fossil fuel $CO_2$ emissions from an urban area: Results from the INFLUX experiment, J. Geophys. Res. Atmos., 120, 292–312, doi: 10.1002/2014JD022555., 2015.

Uliasz, M.: The atmospheric mesoscale dispersion modeling system, J. Appl. Meteorol., 31, 139–149, 1993.

Uliasz, M.: Lagrangian particle modeling in mesoscale applications, in: Environmental Modelling II, Computational Mechanics Publications, Southampton, UK, 71–102, 1994.

UN–Habitat: Cities and climate change: global report on human settlements 2011, Earthscan, United Nations Human Settlements Programme (UN–Habitat), 2011.

van Vuuren, D. P., Cofala, J., Eerens, H. E., Oostenrijk, R., Heyes, C., Klimont, Z., den Elzen, M. G. J., and Amann, M.: Exploring the ancillary benefits of the Kyoto Protocol for air pollution in Europe, Energy Policy, 34, 444–460, doi: 10.1016/j.enpol.2004.06.012, 2006.

Wang, J. S., Kawa, S. R., Collatz, G. J., Sasakawa, M., Gatti, L. V., Machida, T., Liu, Y., and Manyin, M. E.: A global synthesis inversion analysis of recent variability in CO2 fluxes using GOSAT and in situ observations, Atmos. Chem. Phys., 18, 11097-11124, doi: 10.5194/acp-18-11097-2018, 2018.

Whittlestone, S., Kowalczyk, E., Brunke, E. G., and Labuschagne, C.: Source Regions for $CO_2$ at Cape Point Assessed by Modelling 222Rn and Meteorological Data, Technical Report for the South African Weather Service, Pretoria, South Africa, 2009.

Wood, T. E., Cavaleri, M. A., and Reed, S. C: Tropical forest carbon balance in a warmer world: a critical review spanning microbial- to ecosystem-scale processes, Biol. Rev., 87, 912–927, doi: 10.1111/j.1469-185X.2012.00232.x, 2012.

Wu, L., Bocquet, M., Chevallier, F., Lauvaux, T., and Davis, K.: Hyperparameter estimation for uncertainty quantification in mesoscale carbon dioxide inversions, Tellus B, 65, 20894, doi: 10.3402/tellusb.v65i0.20894, 2013.

Wu, L., Broquet, G., Ciais, P., Bellassen, V., Vogel, F., Chevallier, F., Xueref-Remy, I., and Wang, Y.: What would dense atmospheric observation networks bring to the quantification of city $CO_2$ emissions?, Atmos. Chem. Phys., 16, 7743–7771, doi: 10.5194/acp-16-7743-2016, 2016.

Yang, S., Chen, B., and Ulgiati, S.: Co-benefits of $CO_2$ and $PM_{2.5}$ emission reduction, Energy Procedia, 104, 92–97, doi: 10.1016/j.egypro.2016.12.017, 2016.

Yang, D. X., Liu, Y., Cai, Z. N., Chen, X., Yao, L., and Lu, D. R.: First global carbon dioxide maps produced from TanSat measurements, Adv. Atmos. Sci., 35(6), 621-623, doi: 10.1007/s00376-018-7312-6, 2018.

# Chapter 2

# Greenhouse Gas Network Design Using Backward Lagrangian Particle Dispersion Modelling: Sensitivity Analyses and South African Test Case

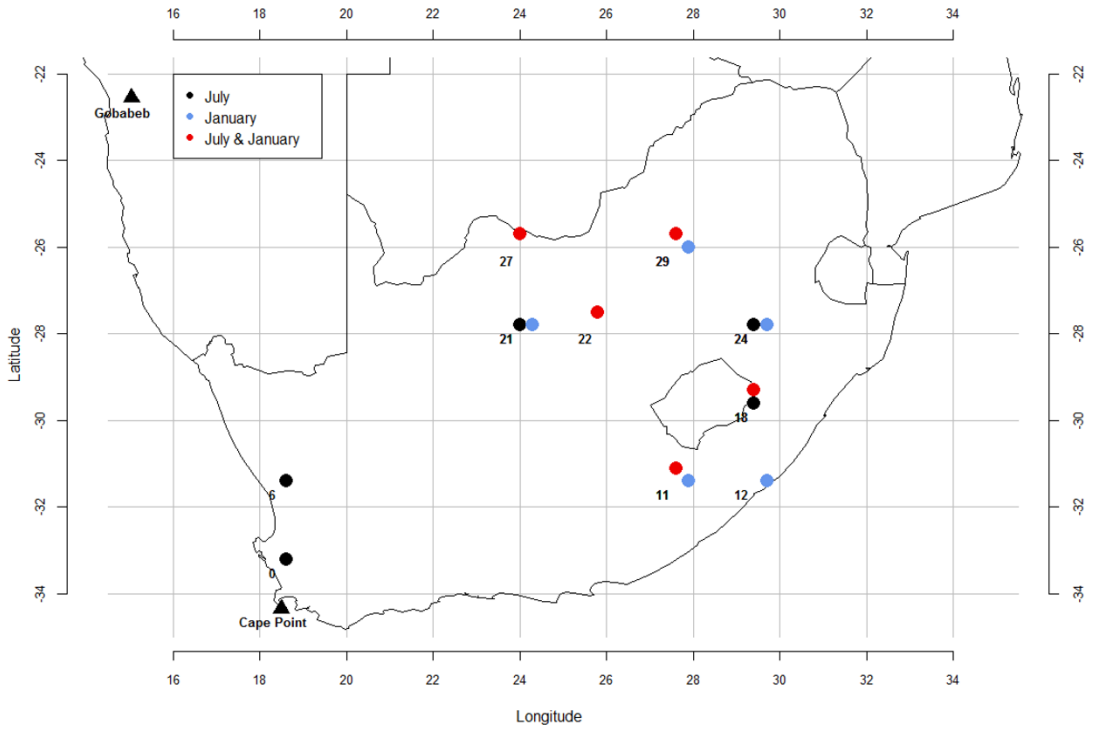

Atmos. Chem. Phys., 15, 2051–2069, 2015
www.atmos-chem-phys.net/15/2051/2015/
doi:10.5194/acp-15-2051-2015


Atmospheric Chemistry and Physics Open Access

# Greenhouse gas network design using backward Lagrangian particle dispersion modelling – Part 2: Sensitivity analyses and South African test case

**A. Nickless[1,2], T. Ziehn[3], P.J. Rayner[4], R.J. Scholes[1], and F. Engelbrecht[5]**

[1]Global Change and Ecosystem Dynamics, CSIR, Pretoria, 0005, South Africa
[2]Department of Statistical Sciences, University of Cape Town, Cape Town, 7701, South Africa
[3]Centre for Australian Weather and Climate Research, CSIRO Marine and Atmospheric Research, Aspendale, VIC 3195, Australia
[4]School of Earth Sciences, University of Melbourne, Melbourne, VIC 3010, Australia
[5]Climate Studies and Modelling and Environmental Health, CSIR, Pretoria, 0005, South Africa

*Correspondence to:* A. Nickless (alecia.nickless@phc.ox.ac.uk)

**Abstract.** This is the second part of a two-part paper considering a measurement network design based on a stochastic Lagrangian particle dispersion model (LPDM) developed by Marek Uliasz, in this case for South Africa. A sensitivity analysis was performed for different specifications of the network design parameters which were applied to this South African test case. The LPDM, which can be used to derive the sensitivity matrix used in an atmospheric inversion, was run for each candidate station for the months of July (representative of the Southern Hemisphere winter) and January (summer). The network optimisation procedure was carried out under a standard set of conditions, similar to those applied to the Australian test case in Part 1, for both months and for the combined 2 months, using the incremental optimisation (IO) routine. The optimal network design setup was subtly changed, one parameter at a time, and the optimisation routine was re-run under each set of modified conditions and compared to the original optimal network design. The assessment of the similarity between network solutions showed that changing the height of the surface grid cells, including an uncertainty estimate for the ocean fluxes, or increasing the night-time observation error uncertainty did not result in any significant changes in the positioning of the stations relative to the standard design. However, changing the prior flux error covariance matrix, or increasing the spatial resolution, did.

Large aggregation errors were calculated for a number of candidate measurement sites using the resolution of the standard network design. Spatial resolution of the prior fluxes should be kept as close to the resolution of the transport model as the computing system can manage, to mitigate the exclusion of sites which could potentially be beneficial to the network. Including a generic correlation structure in the prior flux error covariance matrix led to pronounced changes in the network solution. The genetic algorithm (GA) was able to find a marginally better solution than the IO procedure, increasing uncertainty reduction by 0.3 %, but still included the most influential stations from the standard network design. In addition, the computational cost of the GA compared to IO was much higher. Overall the results suggest that a good improvement in knowledge of South African fluxes is available from a feasible atmospheric network, and that the general features of this network are invariable under several reasonable choices in a network design study.

## 1 Introduction

Mitigating climate change is one of the great challenges of our time. To further this end, it has become essential to accurately estimate the emission and uptake of $CO_2$ around the globe. Greenhouse gases affect the absorption, scattering and emission of radiation within the atmosphere and at the Earth's surface (Enting, 2002; Denman et al., 2007). Of these gases, $CO_2$ contributes the greatest forcing on the climate (Canadell et al., 2007). Monitoring $CO_2$ sources and sinks is necessary for validating important components of climate models and for determining the best course of action to mitigate climate change. The method of inverse mod-

# Chapter 2

# Greenhouse gas network design using backward Lagrangian particle dispersion modelling: Sensitivity analyses and South African test case

# Abstract

This is the second part of a two-part paper considering a measurement network design based on a Lagrangian stochastic particle dispersion model developed by Marek Uliasz, which we referred to as LPDM, in this case for South Africa. A sensitivity analysis was performed for different specifications of the network design parameters which were applied to this South African test case. LPDM, which can be used to derive the sensitivity matrix used in an atmospheric inversion, was run for each candidate station for the months of July (representative of the Southern Hemisphere winter) and January (summer). The network optimisation procedure was carried out under a standard set of conditions, similar to those applied to the Australian test case in part 1, for both months and for the combined two months, using the Incremental Optimisation (IO) routine. The optimal network design setup was subtly changed, one parameter at a time, and the optimisation routine re-run under each set of modified conditions, and compared to the original optimal network design. The assessment of the similarity between network solutions showed that changing the height of the surface grid cells, including an uncertainty estimate for the ocean fluxes, or increasing the night time observation error uncertainty did not result in any significant changes in the positioning of the stations relative to the standard design. However, changing the prior flux error covariance matrix, or increasing the spatial resolution, did.

Large aggregation errors were calculated for a number of candidate measurement sites using the resolution of the standard network design. Spatial resolution of the prior fluxes should be kept as close to the resolution of the transport model as the computing system can manage, to mitigate the exclusion of sites which could potentially be beneficial to the network. Including a generic correlation structure in the prior flux error covariance matrix lead to pronounced changes in the network solution. The genetic algorithm (GA) was able to find a marginally better solution than

the IO procedure, increasing uncertainty reduction by 0.3%, but still included the most influential stations from the standard network design. In addition, the computational cost of the GA compared to IO was much higher. Overall the results suggest that a good improvement in knowledge of South African fluxes is available from a feasible atmospheric network, and that the general features of this network are invariable under several reasonable choices in a network design study.

## 2.1 Introduction

Mitigating climate change is one of the great challenges of our time. To further this end, it has become essential to accurately estimate the emission and uptake of $CO_2$ around the globe. Greenhouse gases affect the absorption, scattering and emission of radiation within the atmosphere and at the Earth's surface (Enting, 2002; Denman et al., 2007). Of these gases, $CO_2$ contributes the greatest forcing on the climate (Canadell et al., 2007). Monitoring $CO_2$ sources and sinks is necessary for validating important components of climate models and for determining the best course of action to mitigate climate change. The method of inverse modelling can be used to estimate the magnitude of sources and sinks of $CO_2$ at different temporal and spatial scales (Enting and Mansbridge, 1989; Rayner et al., 1999; Rödenbeck et al., 2003; Chevallier et al., 2010). This method relies on precision measurements of atmospheric $CO_2$ concentrations to refine the prior estimates of the $CO_2$ fluxes. Using the machinery of atmospheric inversion, an optimal network of new sites to add to the existing infrastructure for measurement of atmospheric $CO_2$ concentrations can be derived from a list of potential sites.

Previous optimal network studies run at the global scale have highlighted southern Africa as a region associated with large uncertainty in its terrestrial $CO_2$ fluxes, requiring further constraint by measurements (Patra and Maksyutov, 2002). Measurements over Africa are much sparser compared to other continents. Only the Cape Point Global Atmospheric Watch (GAW) station has a long term $CO_2$ concentration record, measuring since 1992. This tower was located at Cape Point (34.35° S, 18.49° E) predominantly to record baseline measurements of well-mixed, clean air originating over the Southern Ocean. A study by Whittlestone et al. (2009) demonstrated that it would be difficult to improve estimates of terrestrial $CO_2$ fluxes for southern Africa using the Cape Point station alone. In 2012, an atmospheric observatory was installed near the Gobabeb Training and Research Centre, on the west coast of Namibia (22.55° S, 15.03° E), which continuously measures trace gases, including $CO_2$ (Morgan et al., 2012). To build on this rudimentary network, and to improve estimates of $CO_2$ fluxes at least for South Africa, high precision instruments for measuring atmospheric $CO_2$ concentrations have been purchased, which are to be installed at sites yet to be determined, across South Africa. To maximise the impact of these stations on the estimation of $CO_2$ fluxes across South Africa, an optimal network design can be used to indicate the best placement of new stations with the aim of reducing the uncertainty of the terrestrial $CO_2$ source and sink estimates. A reduction

in the uncertainty of the estimated fluxes is only one of many considerations when determining the location of new measurement sites, but an optimal network design with this goal will provide a guide which can be included in the assessment of these new locations. Part 1 of this paper conducted an optimal network design study for Australia, hereafter referred to as part 1, aimed at augmenting its current observation network, and introduced the methodology employed in this study (Ziehn et al., 2014).

An optimal network design requires the theory of atmospheric inversions to generate the posterior error covariance matrix of the $CO_2$ fluxes which would be estimated from a given network of stations. From this the reduction in uncertainty can be determined. The second requirement is an optimisation routine which will select between a list of potential sites (Rayner et al., 1996; Patra and Maksyutov, 2002; Rayner, 2004). Part 1 of this paper sought to reduce the uncertainty of Australian terrestrial fluxes by 50 %, and began by considering the addition of new stations to the existing base network (Ziehn et al., 2014). Similarly, the Cape Point and Gobabeb stations make up a base network of $CO_2$ monitoring stations for southern Africa. This optimal network design will add five new measurement stations to our base network to best reduce the uncertainty in flux estimates across the country, and under the assumption of continuous, hourly measurements of $CO_2$ concentrations.

The posterior flux error covariance matrix used to derive the uncertainty metric does not require any knowledge of the measured concentrations or of the prior fluxes, only of the prior error covariance matrix of the fluxes, the error covariance matrix of the observations, and the sensitivity matrix, which are all determined separately. Basing the cost function of the optimisation procedure on the result of the posterior error covariance matrix of the fluxes under a given network ensures the uncertainty in the estimated fluxes under the final network solution is reduced. As in part 1 (Ziehn et al., 2014), the Incremental Optimisation (IO) procedure was used for the standard optimal network design in this study. We used a regular grid of potential stations for the South African case study. The reason for doing is that, unlike Australia, South Africa does not have the relatively dense network of meteorological stations suitable for atmospheric monitoring. Therefore, if we were to base the network on the existing sparse network of stations, we could exclude important sites which may provide better constraint. Therefore we have chosen the regular grid, and the sites selected in the optimal network can then be further investigated to determine if there is infrastructure available, such as meteorological stations, communication towers or other research facilities, which could be amenable to atmospheric measurements.

As well as providing this first-time optimal network design focusing on $CO_2$ flux estimation over South Africa, the paper presents a sensitivity analysis of several parameters needed in the optimisation routine. For the standard case we used parametrisations which were most commonly implemented in the literature. We then considered alternatives and determined their impact on the network. This analysis is important because as shown by Rayner et al. (1996), certain changes to the optimisation problem, such as changing the quantity to be optimised, even if very similar in nature to the original, can result in drastically different placement of stations. This would ultimately impact on the implemented network design used in deployment of the new stations. By having alternative network solutions based on parametrisation changes, we can assess how important certain stations are, since these should remain constant from one network solution to the next despite these changes, and it provides insight into which parameters are likely to be important for the estimation of fluxes using the new network of measurement sites.

The inversion procedure requires a sensitivity matrix which calculates the contribution of the different sources to the $CO_2$ concentration at a particular measurement site. We used the Lagrangian stochastic particle dispersion model which we refer to as LPDM, driven by the global circulation model CCAM run in stretched grid regional mode, to determine this matrix. One set of parameters that we considered for the sensitivity analyses related to the specified dimensions of the surface grid box in which the particles provided by LPDM are counted. This is determined by the spatial resolution of the problem. The next set of parameters we considered relates to the two error covariance matrices which are needed for the calculation of the posterior flux error covariance matrix. We changed how these matrices were parametrised and assessed the consequences for the optimal network design. Finally we implemented an alternative optimisation procedure to IO and considered the optimisation of a different metric of uncertainty in the fluxes. As the alternative optimisation procedure, we used the genetic algorithm (GA), as described by Rayner (2004), which uses a very different optimisation philosophy to the IO method.

This paper proceeds by introducing the inversion methodology, followed by an explanation of the different sensitivity tests. The results are then presented for the South African optimal network design under the standard conditions, followed by a comparison of the sensitivity tests. The conclusions provide insight into the most influential locations identified, and discuss courses of action to address the optimal network design parameters highlighted in the study.

## 2.2 Methods and the South African Test Case

### 2.2.1 Surface Flux Inversion

The Bayesian synthesis inversion method, first proposed by Tarantola (1987) and used for the network design in this paper, is the most common method used for solving atmospheric inverse problems in the literature (Rayner et al., 1996; Bousquet et al., 1999; Kaminski et al., 1999; Rayner et al., 1999; Gurney et al., 2002; Peylin et al., 2002; Gurney et al., 2003; Law et al., 2003; Baker et al., 2006; Ciais et al., 2010; Enting, 2002). The regional inversion method we implemented is explained in detail in part 1 (Ziehn et al., 2014). The observed concentration ($c$) at a measurement station at a given time can be expressed as the sum of different contributions from the surface fluxes ($c_s$), from the boundaries ($c_b$) and from the initial condition ($c_i$). For the purposes of the network design, the initial concentration is ignored since it is assumed that this condition is constrained by the observations. Peylin et al. (2005) found for their European regional inversion that the initial condition had an effect on the flux estimates for only a few days. In a smaller domain, this effect will be even shorter, and therefore it is assumed that the initial condition will contribute very little to the total flux uncertainty.

The linear relationship used to model the relationship between $c$ and the contribution from the sources ($c_s$ and $c_b$) is as follows:

$$\boldsymbol{c}_{mod} = \mathbf{H}\boldsymbol{s} \tag{2.1}$$

The vector of the modelled concentrations $\boldsymbol{c}_{mod}$ is a result of the contribution from the sources $\vec{s}$, described by the transport or sensitivity matrix $\mathbf{H}$. The vector $\vec{s}$ can be composed of surface fluxes and boundary concentrations (Lauvaux et al., 2012a). The surface fluxes our inversion setup would solve for are the total $CO_2$ fluxes within a pixel, which we take to be the sum of the biospheric and fossil fuel fluxes. We aim to solve for the total flux since there is not enough information to disentangle these fluxes. In this type of inversion setup, the surface fluxes can be separated into biospheric and fossil fuel fluxes after the inversion run, using additional information regarding either the fossil fuel or biospheric fluxes (Chevallier et al., 2014). The contribution from the boundaries was first assessed to determine if its influence on the observation errors was negligible, in which case the boundary conditions could be excluded from the network design process. We developed an algorithm for assessing the contribution of the boundary concentrations on the observation error covariance matrix in section 2.2.7.

As described in part 1, for the network design approach we are only interested in the posterior covariance matrix of the fluxes, since our aim is to obtain a network that reduces the $CO_2$ flux uncertainties (Ziehn et al., 2014). The posterior flux error covariance matrix, $\mathbf{C}_{\boldsymbol{s}}$, can be calculated as follows (Tarantola, 1987):

$$\mathbf{C}_{\boldsymbol{s}} = \left(\mathbf{H}^T \mathbf{C}_{\boldsymbol{c}}^{-1} \mathbf{H} + \mathbf{C}_{\boldsymbol{s}_0}^{-1}\right)^{-1} \tag{2.2}$$

$$= \mathbf{C}_{\boldsymbol{s}_0} - \mathbf{C}_{\boldsymbol{s}_0} \mathbf{H}^T \left(\mathbf{H} \mathbf{C}_{\boldsymbol{s}_0} \mathbf{H}^T + \mathbf{C}_{\boldsymbol{c}}\right)^{-1} \mathbf{H} \mathbf{C}_{\boldsymbol{s}_0} \tag{2.3}$$

where $\mathbf{C}_{\boldsymbol{c}}$ is the covariance matrix of the observation errors, and $\mathbf{C}_{\boldsymbol{s}_0}$ is the prior error covariance matrix of the surface fluxes. $\mathbf{C}_{\boldsymbol{s}}$ is obtained without the vector of observed concentrations $\vec{c}$ or the vector of prior fluxes $\boldsymbol{s}_0$, which means that it is possible to assess the contribution that a hypothetical station can have on the reduction of the flux uncertainty, without the need to generate synthetic data.

### 2.2.2 Lagrangian Particle Dispersion Model (LPDM)

To determine which sources and how much of each of these sources a measurement site sees at a given moment, the sensitivity matrix $\mathbf{H}$ containing the influence functions is required. For a regional inversion this matrix can be directly obtained by running a Lagrangian particle dispersion model in backward mode. The particles are released from the measurement locations and travel to the surface and the boundaries (Lauvaux et al., 2008; Seibert and Frank, 2004). We used the model developed by Uliasz (1994) which we refer to as LPDM. In this mode the model simulates the release of a large number of particles from arbitrary emissions sources by tracking the motion of the particles backward in time (Uliasz, 1993, 1994). By running the model in this receptor-orientated mode the influence functions for a given receptor are calculated, as described in part 1 (Ziehn et al., 2014).

LPDM is driven by the three-dimensional fields of mean horizontal winds ($u$, $v$, $w$), potential temperature and turbulent kinetic energy (TKE). In the case of the South African network design, these variables are produced by the CSIRO Conformal-Cubic Atmospheric Model (CCAM), a variable-resolution global circulation model run in regional mode. We use the regional mode so that we can resolve the atmospheric transport at a high temporal resolution, which requires that the transport model be run at a high spatial resolution as well (Sarrat et al., 2009). CCAM uses a two time-level semi-implicit semi-Lagrangian method to solve the hydrostatic primitive equations (McGregor and Dix, 2008; McGregor, 2005; McGregor and Dix, 2001).

Total-variation-diminishing vertical advection is applied to solve for the advective process in the vertical. CCAM employs a comprehensive set of physical parametrisations, including the Geophysical Fluid Dynamics Laboratory (GFDL) parametrisation for long-wave and shortwave radiation (Schwarzkopf and Fels, 1991) and the liquid and ice-water scheme of Rotstayn (1997) for interactive cloud distributions. A canopy scheme is included, as described by Kowalczyk et al. (1994), having six layers for soil temperatures, six layers for soil moisture (solving Richard's equation), and three layers for snow. The cumulus convection scheme uses mass flux closure and includes both downdrafts and detrainment (McGregor, 2003).

In the simulations performed here CCAM is applied in stretched-grid mode by utilising the Schmidt (1977) transformation. A multiple-nudging strategy was followed. First, a modestly-stretched grid providing 60 km resolution over southern and tropical Africa was applied following Engelbrecht et al. (2009), with subsequent downscaling to a strongly-stretched grid providing 15 km resolution over southern Africa. Away from the high-resolution region over southern and tropical Africa, CCAM was provided with synoptic-scale forcing of atmospheric circulation, from the 2.5° (about 250 km) resolution National Centers for Environmental Prediction (NCEP) reanalysis data set. This forcing was provided at 6-hourly intervals for the period 1979-2010 using a scale-selective Gaussian filter (Thatcher and McGregor, 2009, 2010). CCAM was set up so that it produced output at an hourly time step and at a 0.15° spatial resolution over South Africa. The domain extended far beyond the South African border, from 10° South to 40° South and from 0° West to 60° East. Meteorological inputs for LPDM were extracted for two months in 2010; January for summer and July for winter. For a four week period during each of these months, LPDM was run for each of the hypothetical measurement sites.

During processing of the particle count data from LPDM, particles that were near the surface were allocated to a surface grid cell and the total count within each of these was obtained to determine the surface influence or sensitivity. These counts depended on the dimensions and position of these surface grid boxes. The particle counts were used to calculate the source–receptor ($s$–$r$) relationship, or influence functions, which form the sensitivity matrix $\mathbf{H}$. Here, we followed Seibert and Frank (2004) to derive the elements of that matrix. As described in part 1 (Ziehn et al., 2014), we modified the approach of Seibert and Frank (2004) to account for the particle counts which were produced by LPDM as opposed to the mass concentrations which were outputted by the transport model in their study. The resulting $s$–$r$ relationship between the

measurement site and source $i$ at time interval $n$, which provide the elements of the matrix $\mathbf{H}$, is:

$$\frac{\partial \bar{\chi}}{\partial \dot{q}_{in}} = \frac{\Delta T \mathrm{g}}{\Delta P} \overline{\left( \frac{N_{in}}{N_{tot}} \right)} \frac{29}{12} \times 10^6, \tag{2.4}$$

where $\bar{\chi}$ is a volume mixing ratio (receptor) expressed in ppm and $\dot{q}_{in}$ is a mass flux density (source), $N_{in}$ the number of particles in the receptor surface grid from source grid $i$ released at time interval $n$, $\Delta T$ is the length of the time interval, $\Delta P$ is the pressure difference in the surface layer, g is the gravity of Earth, and $N_{tot}$ the total number of particles released during a given time interval.

For the network design we are interested in weekly fluxes of carbon separated into day and night time contributions, which means that we have to provide the particle count $N_{in}$ as the sum over one week ($\Delta T$=1 week (day/night)). Therefore, the mass flux density $\dot{q}_{in}$ in Eqn. (2.4) has units of g C/m$^2$/week for the day and similarly for the night.

For the standard network design, the surface layer height is set to 50 m which corresponds to approximately 595 Pa ($\Delta P$). If we assume well mixed conditions, then the $s$–$r$ relationship should be independent of the thickness of the surface layer, as long as the layer is not too deep, as the particle count will be adjusted proportional to the volume of the grid box. Under stable conditions, this may not be the case (Seibert and Frank, 2004). To test if changing the surface grid box height affects the optimal network design, we have included two cases in the sensitivity analysis where the height has been adjusted to 60 m and 75 m. The optimisation routine was run under each of these specifications, holding all other choices as for the standard network design.

As for most inversion studies, a compromise needs to be reached between the dimensions imposed on the source regions and the computational resources available (Kaminski et al., 2001; Lauvaux et al., 2012a). To ensure that the computational time of each of the optimisation runs was feasible, the spatial resolution of the surface flux grid boxes was set so that the domain was divided into 50 by 25 grid boxes (a resolution of approximately $1.2^\circ \times 1.2^\circ$) for the standard optimal network design. As a sensitivity test, the resolution of the surface grid boxes was adjusted so that there were 72 by 36 grid boxes (a resolution of $0.8^\circ \times 0.8^\circ$) in one case, and to 100 by 50 grid boxes (a resolution of approximately $0.6^\circ \times 0.6^\circ$) in a second, much closer to the original resolution of the transport model. This change in resolution of the surface grid boxes impacts on the sensitivity matrix, increasing the number of elements in

the matrix by a factor of two in the medium resolution case and by a factor of four in the high resolution case. It has further consequences for the prior flux covariance matrix, which needs to accommodate this change in source dimensions, increasing its element count by a factor of four for the medium resolution case, and a factor of sixteen in the high resolution case, requiring far more computational resources than the standard case.

### 2.2.3 Observation Error Covariance Matrix

Observation errors result in the values of $\vec{c}_{\text{mod}}$ differing from the observed values in $\vec{c}$. Sources of these errors include random and systematic measurement errors, which are usually negligible at an accredited measurement station, transport model errors, and aggregation errors, which are discussed in more detail at the end of this section (Ciais et al., 2010). Baker (2000) estimated the observation error covariance matrix by comparing the monthly observation means at Mauna Loa to a smoothed line and determining the monthly standard deviations. These values ranged between 0.34 and 0.16 ppm, and so in their case a value of 1 ppm was applied for the standard deviation to each region for monthly averaged concentration values, with the assumption that most places would have a higher standard deviation than Mauna Loa. It was also assumed that the measurement sites would be independent of one another and no temporal correlation from month to month, so the matrix was assumed to be diagonal. Wu et al. (2013) fitted the standard deviation terms of the observation error covariance matrix to available data for a mesoscale inversion study, and estimated values between 2.9 and and 3.6 ppm for hourly concentration measurements.

Since both studies were conducted for regions in the Southern Hemisphere, where intra-station measurement variability is usually lower compared to the Northern Hemisphere, we adopted the same observation errors as for the standard case in part 1 of 2 ppm for the hourly averaged concentrations used in this study. This value falls within the range of values reported in the literature. The dominant source of observation error represented here is from the transport model. In part 1 (Ziehn et al., 2014), a sensitivity analysis was conducted by adjusting the error estimate of the observations based on the location of the station. Since there are far fewer existing stations in South Africa from which we can extract data to assess the potential transport model error, we used the same error for all stations. As part of the sensitivity analysis we assessed the impact of increasing the night time observation error uncertainty to 4 ppm to account for known errors in modelling night time atmospheric transport. In atmospheric inversions night time observations are sometimes

not considered at all, achieved by drastically increasing the night time observation error uncertainties (Lauvaux et al., 2012a).

The high resolution test case discussed above allows the opportunity to assess the aggregation error as well. This is the error due to the degradation of the spatial resolution from the original resolution of the transport model to a lower resolution that the inversion can accommodate. When there is heterogeneity in the surface fluxes and inhomogeneous transport, averaging the surface fluxes to a coarser resolution leads to errors occurring in the modelled concentrations due to the measurement not representing the larger pixels over which the transport is modelled (Kaminski et al., 2001; Ciais et al., 2010). The aggregation errors need to be added to the observation errors, as shown by Kaminski et al. (2001) and Tarantola (2005), and must be adjusted if the resolution of the problem is changed. To determine the aggregation error in a feasible manner for each of the potential measurement sites, the $0.6^\circ \times 0.6^\circ$ test case was substituted as the high resolution case in this calculation, where the grid cells of this case fit exactly into the grid cells of the standard low resolution case. This allowed us to follow the method outlined in Kaminski et al. (2001), who determined that the aggregation error $\mathbf{C}_{\boldsymbol{c,m}}$ can be calculated as:

$$\mathbf{C}_{\boldsymbol{c,m}} = \mathbf{H}\mathbf{P}_{-}\mathbf{C}_{\boldsymbol{s}_0}\mathbf{P}_{-}^{T}\mathbf{H}^{T}, \tag{2.5}$$

where $\mathbf{P}_{-} = \mathbf{I} - \mathbf{P}_{+}$ and $\mathbf{P}_{+}$ is the projection matrix which, if multiplied with the prior flux estimates $\mathbf{s}_0$ of the high resolution case, produces the low resolution prior flux estimates in place of the corresponding high resolution estimates. The solution of $\mathbf{C}_{\boldsymbol{c,m}}$ was obtained for each measurement site, and as a conservative approach, the maximum value of the diagonal was assigned as the aggregation error for that measurement site for the standard resolution case. For the medium and high resolution test cases, since aggregation error would certainly exist, but presumably get smaller as the resolution approached that of the transport model (Wu et al., 2011), the aggregation error was reduced according to the increase in number of grid cells. Therefore it was reduced by half for the medium resolution test case, and to a quarter for the high resolution test case.

### 2.2.4 Prior Flux Uncertainty Covariance Matrix

The elements of the prior flux error covariance matrix need to be constructed from the best available knowledge of sources and sinks at the surface and at the boundaries. Lauvaux et al. (2008) carried out a mesoscale inversion on synthetic data, where their

inversion setup included the contributions from the boundaries as part of the sources they wished to solve for. Their approach for obtaining the boundary elements of the prior flux error covariance matrix was to use modelled values of $CO_2$ and adjust them for biases based on observed aircraft and tower data that was available for the four day period under assessment. For the prior error covariance matrix of the fluxes, the error was set at 2 g C $m^{-2}$ $day^{-1}$ for the surface fluxes and 4 ppm for the boundary contributions, and they assumed uncorrelated flux errors on the domain (no spatial correlation). This was further developed by Wu et al. (2013) who used available data to fit hyperparameters, which were the variance and correlation lengths of the prior flux and observation error covariance matrices.

The approach of Chevallier et al. (2010) to obtain the elements of the prior flux error covariance matrix was to set the standard deviations of the fluxes proportional to the hetrotrophic respiration flux of land-surface model ORCHIDEE. This is the approach adopted in the case of the South African optimal network design, where we were interested in the sensitivity of weekly fluxes, separated by day and night, on hourly concentration values. We used a recent carbon assessment study by Scholes et al. (2013) which produced monthly maps of gross primary productivity (GPP), net primary productivity (NPP), hetrotrophic respiration (Rh), autotrophic respiration (Ra) and net ecosystem productivity (NEP) for South Africa. Of these products, most confidence lay in the NPP product. Since NEP = NPP − Rh and in a balanced system NEP should be a small flux (Lambers et al., 2008), NPP was used rather than Rh. The biosphere flux uncertainties for a particular month were estimated using the following simple relationship:

$$\sigma_{\mathrm{NEP}} = \begin{cases} \min(28\,\mathrm{gC/m^2/week},\ \mathrm{NPP}) & \text{if South Africa} \\ \min(28\,\mathrm{gC/m^2/week}, \mathrm{nearest(NPP)}) & \text{if not South Africa} \end{cases} \tag{2.6}$$

where nearest(NPP) represents the NPP estimated for the nearest South African grid cell. As a realistic estimate, areas outside of South Africa, which had no estimates available for NPP from the carbon assessment product, were assigned the NPP estimate from the closest South Africa grid cell for a particular month. In this way, pixels to the east of the continent in the Mozambican region had similar flux uncertainties prescribed as for the northern savanna pixels within South Africa, and those on the west of the continent in Namibia had uncertainties prescribed as for the semi-desert pixels in Northern Cape Province of South Africa. This type of interpolation was carried out to avoid adding unnecessary aggregation errors at the South

African terrestrial borders, which would occur if a blanket estimate for NPP outside of South Africa was used. A blanket estimate would lead to artificially large changes in the flux uncertainties between neighbouring pixels, exaggerating aggregation errors for stations near these borders, and conversely null changes in uncertainty between non-South African terrestrial pixels. Since Ra and GPP were also available, and NPP = GPP − Ra, day time NPP and night time Ra were obtained by assuming that all the GPP took place during the day, and half of the Ra took place during the day and half at night. This meant that the day time NPP values tended to be larger in magnitude than the night time Ra values, which is what we would expect for the South African systems. Using this assumption, the monthly estimates for NPP were converted into weekly values, separately for day and night, to give the final uncertainty values used to construct the prior flux error covariance matrix. The day time NPP and night time Ra values used as proxies for the NEP uncertainties are plotted for July and January (Fig. 2.1). In South African systems much more biological activity occurs during the summer months compared to the winter months, with the consequence that the uncertainty during the summer months is considerably larger.

Since the domain of the network design includes the fossil fuel sources of South Africa, fossil fuel flux uncertainties needed to be derived as well. Previous regional inversions, where the total flux of a source pixel was solved for, had detailed inventory data available for the fossil fuel emissions, and they assumed these were perfectly known (Schuh et al., 2013). Since this information was not available for South Africa, we had to consider errors in the fossil fuel fluxes. As for part 1 (Ziehn et al., 2014), these uncertainties were derived from the Fossil Fuel Data Assimilation System (FFDAS) (Rayner et al., 2010; Asefi-Najafabady et al., 2014). Ten realisations for the year 2010 were obtained from the FFDAS product at the original resolution of $0.1^\circ \times 0.1^\circ$. The fluxes were aggregated to our network design resolution of $1.2^\circ \times 1.2^\circ$ and then the variance calculated for each grid cell. Since the emissions from fossil fuels are usually localised, such as those at power plant locations, the variability in the fossil fuel emissions between grid cells is quite large. But, as shown by Ziehn et al. (2014), the effect of aggregating the data smooths the fossil fuel emissions over the network design domain, and this leads to a reduction in the variability between the different realisations of the FFDAS. It also leads to the aggregation errors discussed in 2.2.2. Figure 2.2 shows that the uncertainties for the ten realisations based on the original $0.1^\circ \times 0.1^\circ$ resolution have much larger maximums for individual grid cells than the uncertainties calculated for the aggregated fluxes (Fig. 2.2). The effect of using a higher spatial resolution for the surface grids, closer to the resolution of the transport

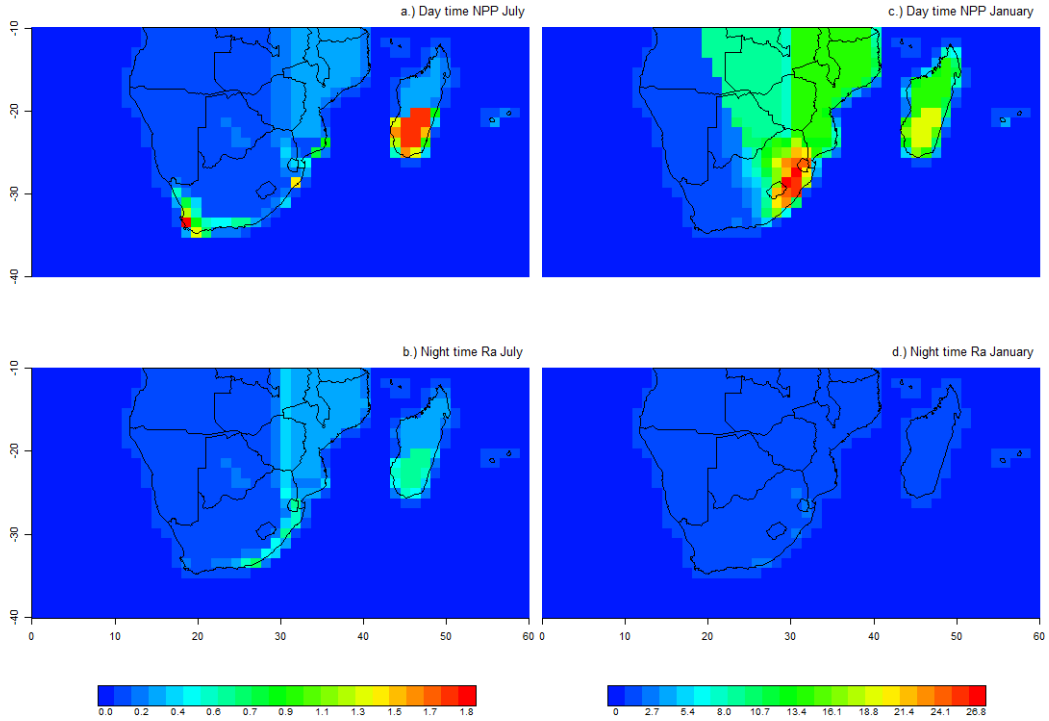


Figure 2.1: The day time net primary productivity (NPP) and night time autotrophic respiration (Ra) data used as standard deviations of net ecosystem productivity (NEP) at the resolution of 1.2° expressed in g C/m$^2$/week for July (left) and January (right). Values for the standard deviation are capped at 28 g C/m$^2$/week. The maximum value (separately for day and night) is assigned to the non-South African land surface, or set at 28 g C/m$^2$/week if the maximum exceeds this value.

model, is considered in the sensitivity analyses as discussed above in section 2.2.2. The fossil fuel uncertainty and NPP surfaces for these higher resolution cases are provided in Fig. 2.3.

For the standard network design, the prior flux error covariance matrix is estimated as a diagonal matrix, where the diagonal elements are the sum of the variances of the biospheric fluxes and the fossil fuel fluxes for that grid cell. The biospheric flux uncertainties were multiplied by the fraction of the grid cell covered by land, separately for day and night. By multiplying with the land fractions we guarantee that the prior uncertainties for coastal grid cells are scaled accordingly and ocean only grid cells are set to zero, since the NEP and fossil fuel products only apply to the land surface. We assumed no correlation in the prior error covariance matrix of the fluxes. This is a necessary assumption since we have no data from which to determine

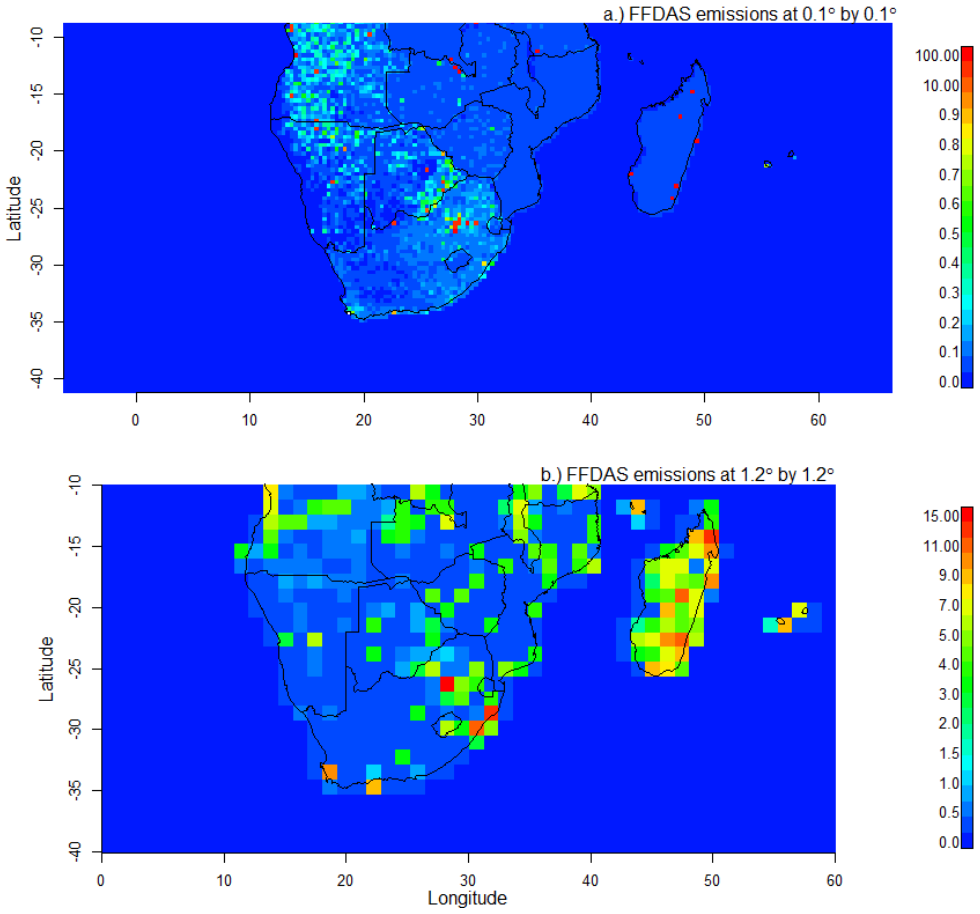


Figure 2.2: The standard deviations of ten realisations (top) of the Fossil Fuel Data Assimilations System (FFDAS) at the original 0.1° resolution in g C/m$^2$/week. The standard deviations of the aggregated fluxes (bottom) (1.2° resolution) showing significant smoothing of the fossil fuel fluxes over the lower resolution.

the best correlation lengths. In reality, grid cells with similar biota and under similar climate will have correlated fluxes. Similarly, fluxes from the same source which occur close in time will also be correlated (Chevallier et al., 2010; Wu et al., 2013). Correlation lengths in space and time are difficult to assess, but have a large impact on the estimated fluxes (Lauvaux et al., 2012b). Independence is assumed, which is a more conservative approach for the optimal network design. Eventual data from the implemented network will then help to resolve the flux correlation estimates during the inversion procedure. To determine what impact assuming positive correlation lengths in the prior flux error covariance matrix could have on the optimal network design, we used the results from Chevallier et al. (2012), and put together a simple correlation structure where it was assumed that temporal correlations for the same

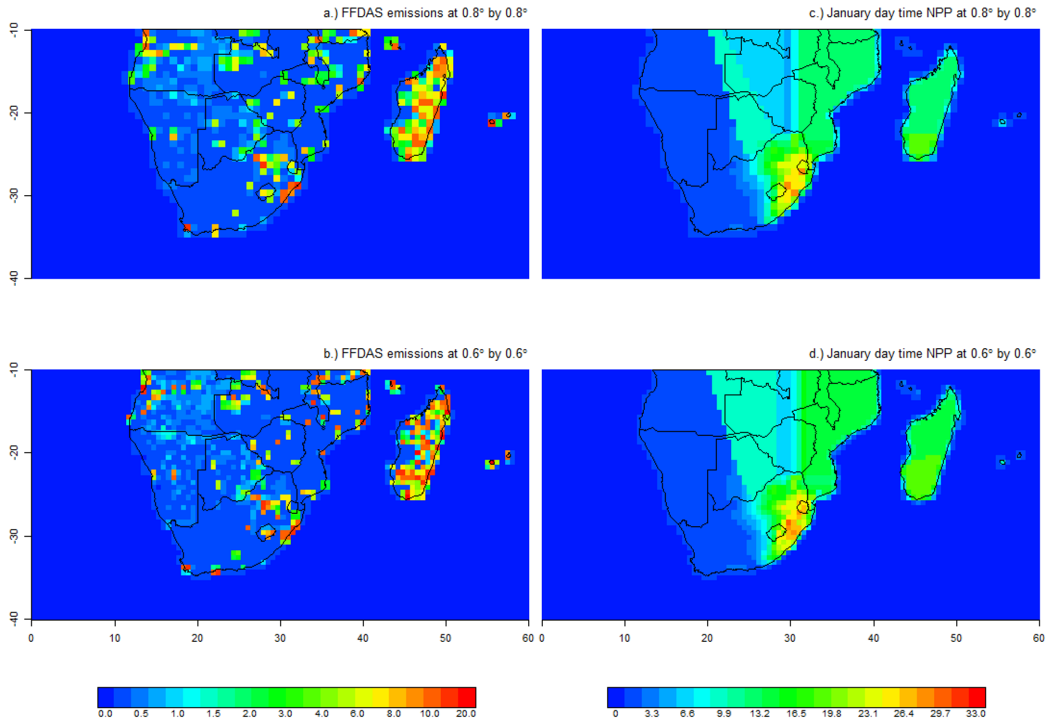


Figure 2.3: The day time net primary productivity (NPP) data used as standard deviations of net ecosystem productivity (NEP) at the resolution of 0.8° expressed in g C/m$^2$/week for January (a), and at the resolution of 0.6° (b). The Fossil Fuel Data Assimilation System standard deviations aggregated over a resolution of 0.8°, also expressed in g C/m$^2$/week (c) and over a resolution of 0.8° (d).

grid cell one week apart had a correlation of 0.5 (independent for day and night), decaying to 0.3 at two weeks apart and 0.1 at three weeks apart. Grid cells adjacent to each other had a correlation of 0.3. The interactions between time and space correlations were determined by the Kronecker product of the spatial and temporal correlation matrices (e.g. two grid cells adjacent to each other but one week apart would have a correlation of $0.3 \times 0.5$). Therefore correlation lengths were relatively short.

In the network design under the standard case, we kept the uncertainties of the ocean-only grid cells set to zero, since our focus is on reducing the flux uncertainty over land. We are not seriously assuming that we know the ocean fluxes perfectly, but for the purposes of this optimal network design, we would prefer if the terrestrial measurements focused on solving for the terrestrial fluxes. Of course, to run a full inversion, knowledge is needed about the ocean fluxes and this would be obtained

through ocean based measurements. The contributions from the ocean can be divided into the 'near-field' and 'far-field'. The far-field contributions are contained within the boundary contributions. The near-field contributions are those within our domain. A sensitivity test was conducted whereby 10% of the maximum land NEP standard deviation was allocated to the ocean grid cells. This uncertainty represents the uncertainty in the ocean productivity models which would be used to obtain prior estimates of ocean fluxes during an inversion, which are similar to the values allocated by Chevallier et al. (2010). A second case was considered where 10% of the nearest land NEP uncertainty was allocated to each ocean grid cell, so that the uncertainties of the ocean grid cells would increase as the uncertainties of nearby land fluxes increased. The purpose of this test case was only to demonstrate the effect implementing a variable ocean uncertainty scheme.

### 2.2.5 Optimisation

Three optimisation routines have been used for optimal network design in the literature, namely IO (Patra and Maksyutov, 2002), GA (Rayner, 2004), and simulated annealing (Rayner et al., 1996). We used the IO routine, as used for part 1 (Ziehn et al., 2014), for the standard network design. This method was previously compared to simulated annealing by Patra and Maksyutov (2002) and found to perform as well or better, with significantly less computational cost.

During the IO procedure we added one station at a time from the candidate list to our base network of two stations and calculated $\mathbf{C}_\mathrm{f}$. We chose the station that resulted in the smallest uncertainty metric and added it to the network, simultaneously removing it from the candidate list. We then repeated the process until we reached our target of five stations. The IO procedure provides us with a stepwise progression of the optimal network.

The overall uncertainty in fluxes can be expressed by two different metrics (Rayner et al., 1996). Either through obtaining the trace of $\mathbf{C}_\mathrm{f}$ ($J_\mathrm{Ct}$) or by summing over all the elements of $\mathbf{C}_\mathrm{f}$ ($J_\mathrm{Ce}$):

$$J_\mathrm{Ct} = \sqrt{\sum_{i=1}^{n} C_{f_{ii}}} \tag{2.7}$$

$$J_\mathrm{Ce} = \sqrt{\sum_{i=1}^{n}\sum_{j=1}^{n} C_{f_{ij}}} \tag{2.8}$$

where $n$ is the number of elements in the diagonal of $\mathbf{C}_\mathrm{f}$. The use of equation 2.7 results in the minimisation of the average variability between surface pixels. Equation 2.8 is the more accepted metric to calculate uncertainty for network designs, and it results in the minimisation of the uncertainty of the total flux over the full domain. As for part 1 (Ziehn et al., 2014) and as used by Rayner et al. (1996), we use $J_\mathrm{Ce}$ as the uncertainty metric for the standard design. In our case, because the domain of the transport model contains terrestrial regions outside of South Africa, we only include the elements of $\mathbf{C}_\mathrm{f}$ which are within South Africa in the calculation of the uncertainty metric.

As a sensitivity test, the $J_\mathrm{Ct}$ uncertainty metric replaced $J_\mathrm{Ce}$. Minimising either of these metrics should result in an optimal network with reduced overall uncertainty in flux estimates across South Africa, but the results could potentially be quite different, particularly if there are large correlations in the posterior flux error covariance matrix.

We evaluated the different networks in terms of their uncertainty reduction:

$$U_R = 1 - \frac{\hat{J}_\mathrm{Ce}}{J_\mathrm{Ce\ base}} \tag{2.9}$$

where $\hat{J}_\mathrm{Ce}$ is the optimised uncertainty metric value and $J_\mathrm{Ce\ base}$ the value of the uncertainty metric calculated from the posterior error covariance matrix of the fluxes if only the base stations are included.

Although IO is expected to be more computationally efficient, optimisation through a GA would also be well suited for this kind of problem, considering that this network design for South Africa is starting with so few existing stations. The GA begins with each of the solutions in the population containing five stations. Therefore all five stations are optimised simultaneously, rather than sequentially. Thus, this method may be more suited to the case where there are multiple deployments, as we have. It is possible under these circumstances that the best solution for a five station network in terms of reducing the overall uncertainty for South Africa, may not include the one station which on its own reduces the uncertainty the most. The GA is highly parallel and so we can take advantage of high performance computing, but the running time of a GA is still higher in comparison to IO.

The approach used to run the GA during the sensitivity analyses is adopted from Rayner (2004). GA procedures are a class of stochastic optimisation procedures for any numerical algorithm which calculates a score based on a function of inputs. In this case the algorithm calculates a score based on the posterior flux error covariance matrix, given a set of stations. A GA does not optimise based on a single solution, but

rather by improving a population of solutions, from which a final solution is selected. New members are added to the population through a process of loss of members which are not sufficiently fit (culling), pairwise combination of previous members (cross-over), and random changes to members (mutation). This represents 'survival of the fittest' and pairwise reproduction and mutation in biological populations.

In this implementation of the GA, elitism is maintained by keeping the best solution from the previous population, without making any changes through cross-over or mutation on this member. The algorithm converges once a given number of iterations is reached, or once a convergence criterion is met. The solution with the best fitness criterion is then selected from this population, where the fitness F is calculated as:

$$F = 1 - \frac{r - 0.5}{N} \tag{2.10}$$

where $r$ is the ordinal ranking of the member and $N$ is the population size, which for our South African case study was taken to be 100 members. A pseudorandom number $x$ is generated and members are then deleted, or culled, if the value of $F$ is less than $x$. The culling process will remove about 50 % of the population members. These need to be regenerated to get the population back to the required size. Members are selected at random from the remaining population, and based on new pseudorandom numbers, members are duplicated if their fitness score is above this random number. Sampling is with replacement, so the members with the highest fitness have a good chance of being duplicated more than once. This continues until all the culled members have been replaced and the population size is back to $N$.

The GA requires a trade-off between the diversity in the solutions, ensuring that the algorithm does not get stuck in local extrema, and strong selection to ensure that the population moves towards the optimum solution. This is achieved by adjusting the mutation rate; high enough to produce diversity in the solutions, but low enough to ensure that members with high fitness persist and so ensure a tendency towards the optimum solution. From previous work (Rayner, 2004) a good mutation rate for network design was found to be 0.01.

The population size and number of iterations affects the computation time of the algorithm. A large population size is favourable because this ensures diversity in the solutions. The more iterations that take place, the more solutions the algorithm can assess and the better the chance of finding the global minimum. High values for both of these parameters results in long computation times. In this study the number of iterations was set at 100 for a single month optimisation, and to 150 for a combined

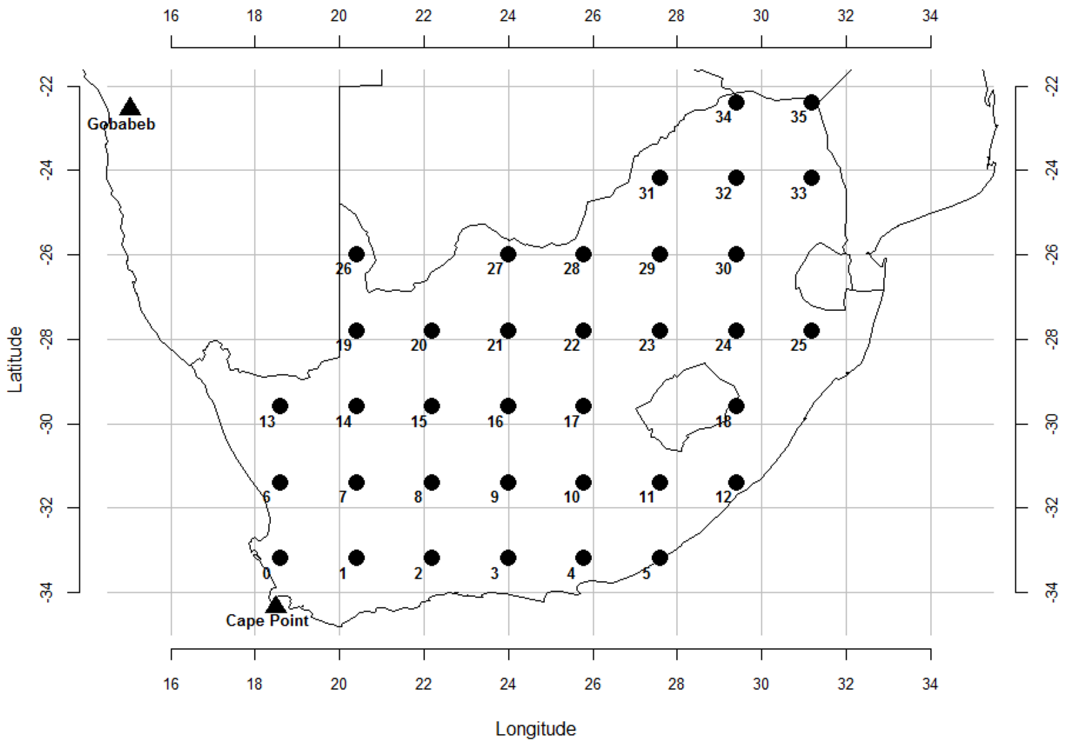


Figure 2.4: The 36 potential locations of the new stations in the optimal network design. The locations were spaced on a regular grid over the surface of South Africa. The existing Cape Point and the Gobabeb GAW stations are marked by the triangles.

month optimisation. These values were determined from GA trials carried out on the data prior to deriving the results for this study.

### 2.2.6 Measurement Sites

Hypothetical stations were selected from a regular grid over South Africa, resulting in 36 equally spaced locations (Fig. 2.4), from which five stations need to be selected. Ultimately, the exact location of the stations will be determined by practical considerations, such as the presence of existing infrastructure, such as communication towers and meteorological stations, available manpower, the relative safety of the instruments, and the accessibility of the sites. The optimal network will be used as a guide as to which locations are ideal. Once the final station sites have been selected, the posterior flux error covariance matrix can be calculated based on these exact tower locations, in order to determine how close to the idealised uncertainty reduction the implemented network will achieve.

### 2.2.7 Influence from Outside the Modelled Domain

Since the surface sources are expressed as fluxes in carbon, the contribution to the concentration at the measurement site is expressed in the amount of carbon seen at the measurement site from a particular source. In the case of the boundary sources (or contributions from outside of the domain) which are given as concentrations, their contributions to the concentration at the measurement site are expressed as a proportion of their concentration, dependent on their influence at the receptor site. Part 1 (Ziehn et al., 2014) showed that the boundary contribution can then be written as:

$$\vec{c}_{\mathrm{b,mod}} = \mathbf{M}_{\mathrm{B}}\vec{c}_{\mathrm{B}} \tag{2.11}$$

where $\mathbf{M}_{\mathrm{B}}$ is the submatrix of $\mathbf{H}$ for the boundary concentrations, $\vec{c}_{\mathrm{B}}$. If the elements of $\mathbf{M}_{\mathrm{B}}$ are large enough it may be necessary to include the boundary concentrations in the network design.

For the network design, four boundaries (north, south, east and west) were used and we calculated the sensitivity of hourly observed concentrations to weekly boundary concentrations. To determine if the influence of the boundary concentrations on the observation errors should be included in the network design, we needed to know whether the uncertainties contributed by the boundary concentrations were significant compared to other contributions. To see this we calculated $\mathbf{M}_{\mathrm{B}}$ for each station. Assuming uncertainties of 1 ppm in the boundary concentrations (reasonable for the Southern Hemisphere) this yielded:

$$\mathbf{C}_{\mathrm{b}} = \mathbf{M}_{\mathrm{B}}\mathbf{C}_{\mathrm{I}}\mathbf{M}_{\mathrm{B}}^{T} \tag{2.12}$$

where $\mathbf{C}_{\mathrm{I}}$ is the prior error covariance matrix of boundary concentrations. The diagonal elements of the error covariance matrix of the boundary concentrations, $\mathbf{C}_{\mathrm{b}}$, provided us with the uncertainty contribution of the boundary concentrations to the observations. If they are much smaller than the observation error uncertainty we can neglect boundary influences in the network design. As the boundary concentrations should be highly correlated, we also considered $\mathbf{C}_{\mathrm{I}}$ to have correlation between boundary concentrations, where correlations of 0.5 were allocated between boundary concentrations during the same week, and values of 0.25 between boundary concentrations separated by a week or more.

### 2.2.8 Comparison of Network Solutions

To compare the utility of the optimal networks from each algorithm run, the uncertainty reduction was assessed for each of these networks. The similarity of the networks in terms of the station locations was assessed using a test statistic from the Chi-squared Complete Spatial Randomness test, measuring the degree of clustering, where the expected value is based on the null hypothesis that the stations are located randomly over the domain. The intention here was not to perform a statistical test based on the Chi-squared distribution, since the network did not constitute a sample nor were there enough stations, but to calculate an indicator that would assess the degree of clustering of the measurements stations for a particular network solution, referred to as the clustering index, which was also used to compare between two networks.

$$\text{Clustering Index} = \sum_{i} \sum_{j} \frac{(O_{ij} - E_{ij})^2}{E_{ij}} \tag{2.13}$$

where $i$ and $j$ are the indicators for the latitude and longitude categories respectively, $O_{ij}$ was the observed number of stations in quadrat $ij$ and $E_{ij}$ the expected number of stations assuming the stations are scattered randomly. The domain was divided into quadrats, in this case 16 equally sized quadrats covering the entire domain.

A dissimilarity index (DI) was calculated as the sum of the distance to the nearest neighbour in the compared network, over all the members in the pair of assessed networks.

$$DI = \sum_{i=1}^{5} \min_{j} \sqrt{\Delta \mathrm{x}_{\mathrm{ij}}^2 + \Delta \mathrm{y}_{\mathrm{ij}}^2} + \sum_{j=1}^{5} \min_{i} \sqrt{\Delta \mathrm{x}_{\mathrm{ij}}^2 + \Delta \mathrm{y}_{\mathrm{ij}}^2} \tag{2.14}$$

where i and j $\in$ [1,2,3,4,5], and $\Delta \mathrm{x}_{\mathrm{ij}}^2$ and $\Delta \mathrm{y}_{\mathrm{ij}}^2$ are the squared differences between the Cartesian coordinates of the ith station in network 1 and the jth station in network 2. In cases where the two networks compared were the same, the index results in a value of zero. The index increases as the networks become more dissimilar in space. This provides a one-number measure of network similarity that can consistently be used for the network comparisons provided each solution consists of the same number of stations. The index provides a measure in kilometres of how different two network solutions are. This allows for an objective assessment of how different the positioning of sites are between two network solutions which may not be obvious to the eye.

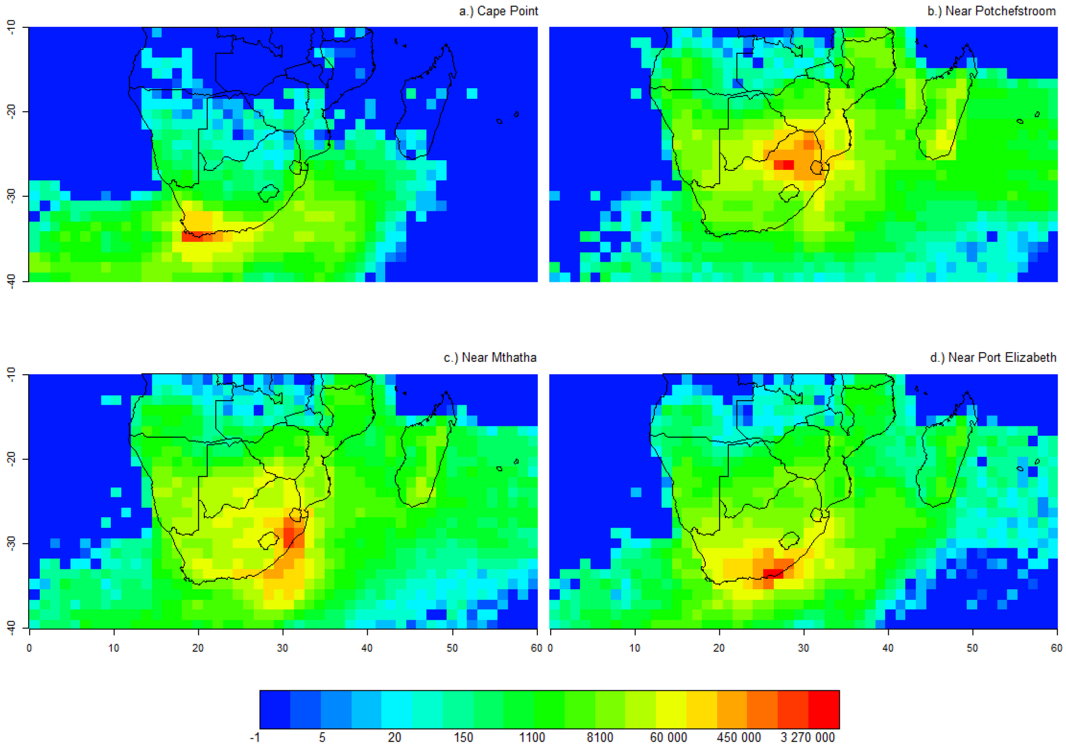


Figure 2.5: The footprint of Cape Point, station 28 (top right), station 18 (bottom left), and station 4 (bottom right) relative to the surface grid cells at a resolution of 1.2° expressed as the count of particles over the month of January for each surface grid cell.

## 2.3 Results and Discussion

### 2.3.1 Influence from the Boundaries

The particle counts generated during the LPDM runs for each station were summed over the month in order to obtain a footprint of each station. To illustrate this, plots of the influence footprint in January (Fig. 2.5) are provided, using a logarithmic scale, for Cape Point and three other candidate stations: 28 (near Potchefstroom), 18 (near Mthatha), and 4 (near Port Elizabeth). For both January and July, the influence footprints show that the three candidate stations have more contributions from terrestrial South African sources than Cape Point has. The plots show that the majority of influence for a site is from the sources in the surrounding pixels.

Using the influence functions now available for each station, the test of the influence from the boundaries on to the observation errors was conducted. Given the large domain over which LPDM was run, it was not surprising that the boundaries

had minimal influence. Overall, the square root of the maximum diagonal element of $\mathbf{C}_b$ for all stations was only 0.012 ppm. The mean of the maximum diagonal elements over all measurement sites was 0.006 ppm with a standard deviation of 0.002 ppm. Even when correlation between the boundary concentrations was included in the covariance matrix of the boundary concentrations, the maximum diagonal element only reached 0.012 ppm, and the maximum diagonal element for a particular station were no more than 40 % higher than for the independent case. We note that the influence of the boundary conditions may be highly correlated i.e. that a given boundary condition may influence many observations in a similar way. However the covariances in $\mathbf{C}_b$ are bounded by its variances. These variances are so much smaller than the values of the error covariance matrix that the impact of the accompanying covariances is guaranteed to be small. We note also that the assumption of boundary conditions changing on the scale of a week is conservative, using more, somewhat independent boundary concentrations would reduce the impact on $\mathbf{C}_b$ yet further.

### 2.3.2 Aggregation Error

Aggregation errors were found to be a significant contributor to the overall observation error covariance matrix. Aggregation errors of as high as 17.10 ppm were found for measurement sites in the north eastern interior, and as low as 0.01 ppm for stations in the south western interior (Fig. 2.6). The average aggregation error across sites was 4.70 ppm with a standard deviation of 5.10 ppm. The sites with the largest aggregation errors were generally those closest to large fossil fuel sources. These large values are due to the significant amount of smoothing of the relatively localised fossil fuel fluxes during the lower resolution case. This results in large heterogeneity between the high resolution fossil fuel fluxes which contribute to the average fossil fuel flux estimate of the low resolution case, which is exactly the circumstances that lead to the generation of aggregation error. Sites near the terrestrial or coastal borders also tended to have large aggregation errors. Site specific aggregation errors were determined, and these errors were added to the diagonal elements of the observation error covariance matrix separately for each site.

When running LPDM to generate the sensitivity matrix, it is imperative to specify a sufficient number of particles per release, as well as to run the model for at least as long as required, with additional time at the beginning of the run. This is to avoid transport errors, and to avoid exaggerating the aggregations errors. Therefore, the aggregation errors were calculated using the last week of the four week sensitivity matrix.

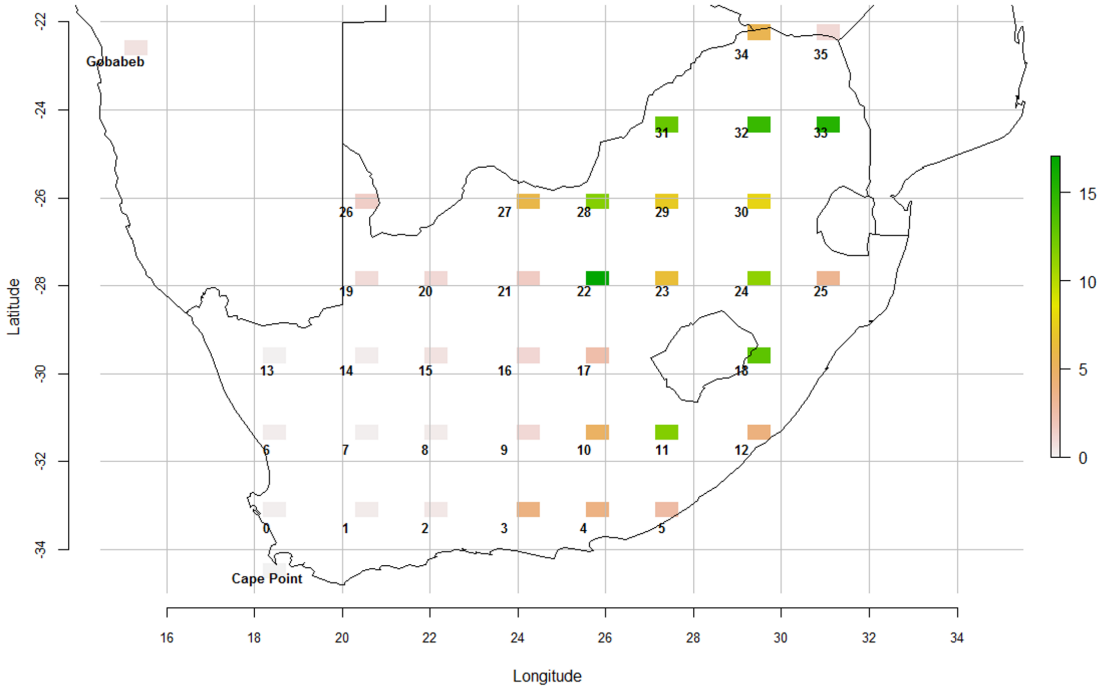


Figure 2.6: Map of the aggregation error values (ppm) associated with each measurement station for the month of January.

The next sections present the results of the optimal network design, first under the basic parametrisations as used in part 1 (Ziehn et al., 2014), and then under the sensitivity tests.

### 2.3.3 Basic Network Design

The network solution for July was able to achieve a reduction in uncertainty in the total South African flux from 6.42 g C/m$^2$/week under the base network to 3.66 g C/m$^2$/week under the optimal network. The results under the standard conditions used in the basic network design for the month of July reveal that the best set of stations to add to the current network would include two stations near the western coast of the country, stations 0 and 6, including one just north of the City of Cape Town (station 0) (Fig. 2.7). These stations are located near the areas of highest NEP uncertainties during the winter months. These areas in the Western Cape fall into the fynbos biome, which is under a winter rainfall regime. Therefore productivity during the winter months is expected to be higher in this area (Fig.2.1 a). In contrast,

Table 2.1: Ranking of the new stations added to the base network for two seasons (winter and summer) represented by July and January, as well as the integrated two months. The cumulative reduction of uncertainty relative to the base uncertainty is provided in brackets.

| Rank | July | January | July + January |
|---|---|---|---|
| 1 | 24 (12.8 %) | 12 (40.0 %) | 18 (53.3 %) |
| 2 | 0 (23.3 %) | 29 (58.0 %) | 29 (77.7 %) |
| 3 | 21 (33.0 %) | 11 (68.0 %) | 11 (80.9 %) |
| 4 | 18 (38.1 %) | 21 (74.5 %) | 22 (82.6 %) |
| 5 | 6 (42.9 %) | 24 (78.3 %) | 27 (84.6 %) |

activity over much of South Africa during the winter months, when water availability is reduced, is expected to be low to almost entirely dormant. Due to the increased uncertainty in NEP in the fynbos regions during this time, as well as the proximity to the City of Cape Town, the optimal network would need a station in this area to reduce the overall uncertainty of South Africa. Two stations are located in the eastern interior of the country (stations 18 and 24), including one on the border of Lesotho, and a station in the central interior of the country (station 21), not far from the Zimbabwean border. These stations are located near to areas with high fossil fuel flux uncertainties. The base network on its own reduced the posterior flux uncertainty by 17.0 %. During the month of July, the best station to add to this network would be station 24, located in the eastern interior of South Africa, just north of Lesotho, which reduced the uncertainty relative to the base network by 12.8 % (Table. 2.1). The second best station to add is station 0, near the south east coast of South Africa. This station reduced the uncertainty by an additional 10.5 %. Since the optimal network included a station near Cape Point during July, it supports the conclusions by Whittlestone et al. (2009) that measurements at Cape Point are not sufficient to estimate fluxes for the Western Cape region. The reduction in uncertainty by the addition of the three remaining stations to the network was an additional 19.3 %. During the winter months, the biospheric fluxes are small, with small uncertainties whereas the fossil fuel flux uncertainties remain high. Due to the penalty imposed by the aggregation error for measurement sites located near fossil fuel sources, the return on uncertainty reduction during the winter months is low, at only 42.9 %.

In January the total flux uncertainty was much higher compared to July, with a total flux uncertainty of 128 g C/m$^2$/week, which was reduced to 27.93 g C/m$^2$/week under the optimal network. The placement of stations changes with respect to July, with the stations all located towards the eastern interior of the country, and no

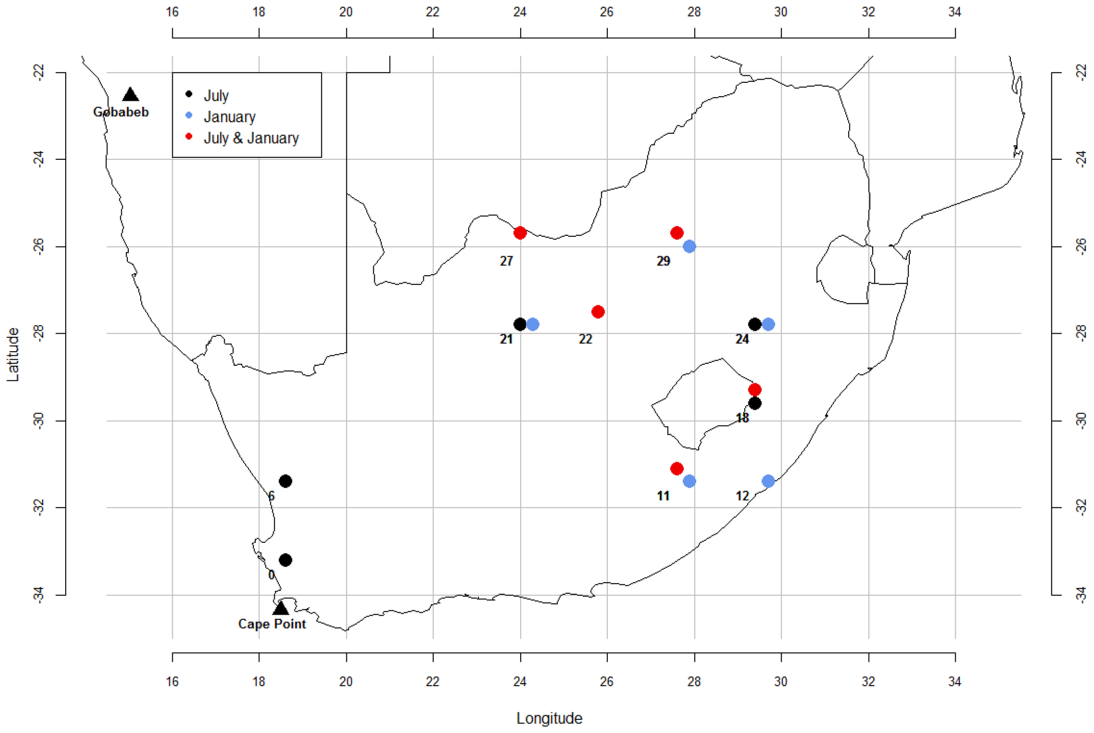


Figure 2.7: Map of the optimal stations to add to the existing network to reduce the overall uncertainty of fluxes in South Africa for July, January, and the combined months of July and January. The standard network design conditions are: 50 m surface grid height, diagonal prior covariance, 2 ppm uncertainty in concentration observations, a 1.2° surface grid resolution, and the sum of the posterior covariance matrix elements used to calculate the uncertainty metric for the IO optimisation procedure.

stations positioned on the western side of South Africa (Fig. 2.7). The stations were located near regions of high summer time NEP uncertainty and in the region where most of the fossil fuel activities in the country are concentrated. In contrast to the winter months, the NEP uncertainty during summer is much higher on the eastern side of the country compared to the mid interior or the west of the country (Fig.2.1 c), resulting in a need to concentrate the new measurement sites in this area. The uncertainty reduction attributable to the base network in January is similar to July, at 16.8 %. The best performing station in the network for January is station 12, located on the eastern coast of South Africa, which further reduces the uncertainty by 40.0 % relative to the base network. The next best performing station was station 29, which reduced the uncertainty by an additional 18.0 %. An additional 10.3 % increase in uncertainty reduction was attained from adding the last three stations

to the network. The total uncertainty reduction achieved in January is much higher compared to July, at 78.3 %. This is due to the ability of the network to view the larger summer biospheric fluxes in areas where the aggregation error penalty is low, or even despite the aggregation error penalty.

The total flux uncertainty under the base network for the combined months of January and July was calculated to be 128.43 g C/m$^2$/week, similar to the month of January. This is reduced to 19.83 g C/m$^2$/week under the optimal network. The network for the combined months has a similar positioning of stations compared to January (Fig. 2.7), locating most of the stations in the eastern interior, as well as a very similar reduction in uncertainty at 84.6 %. The most important station, as ranked by the IO solution, is station 18, which reduces the uncertainty by 53.3 % relative to the base network. This station is located in a region of both high NEP and fossil fuel flux uncertainty (Fig. 2.1 and Fig. 2.2). The second best station to add to the network is station 29, increasing the uncertainty reduction by 24.4 %. This station is located near the area of highest fossil fuel flux uncertainty (Fig. 2.2). The remaining three stations (stations 11, 22 and 27) add only 6.8 % to the uncertainty reduction. The network solution is different to January's, in that the stations are more concentrated around the areas of larger fossil fuel flux uncertainty. This is due to the much lower NEP uncertainty estimates for the winter months across South Africa compared to the summer months, but the fossil fuel flux uncertainties remaining consistent during the year. The optimal network for the combined seasons is therefore dominated by the need to reduce these consistently large uncertainties. The results from the combined months shows that a substantial reduction in the posterior uncertainty for South Africa is possible by introducing only a few additional stations at key locations.

### 2.3.4 Sensitivity Analysis

The results for the sensitivity analyses run for both months, and the combined months of January and July appear in Fig. 2.8. During the winter months, there was consistency between the network solutions from the different sensitivity tests. All of the tests were in agreement that stations 0 and 18 should be included; station 0 near the winter NEP uncertainties, and station 18 near an area of large fossil fuel flux uncertainty. The tests assessing surface grid box height, the doubling of night time observation error uncertainty, and the addition of ocean flux uncertainty, were identical to the standard network design solution. Both the medium resolution and the GA network solutions were very near the standard solution, each obtaining the second smallest DI relative to the standard design of 879. These tests both favoured two

stations which were each one step away from a standard network design station. The solution using the uncertainty metric based on the trace of the posterior flux covariance matrix was similar to these two, but favoured a station near the south coast of South Africa, far from the general concentration of stations, near a localised fossil fuel source. The two test cases most different from the standard solution were the high resolution network solution, and the solution from the case considering correlation between the prior fluxes, obtaining a DI of 1747 and 1343 respectively. They also favoured stations near the south coast, but also located stations in the north eastern interior, near areas of large fossil fuel uncertainty.

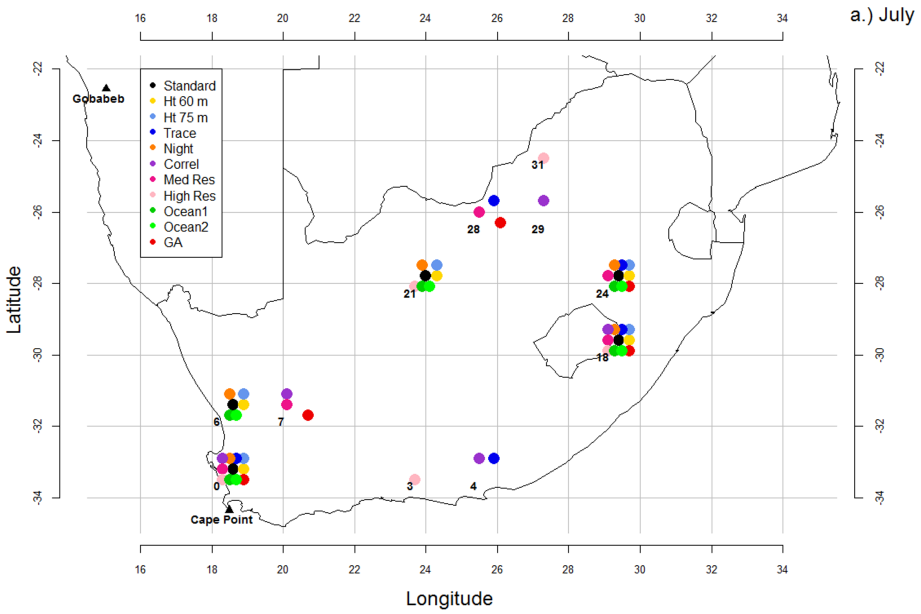
a.) July
Gobabeb
Standard
Ht 60 m
Ht 75 m
Trace
Night
Correl
Med Res
High Res
Ocean1
Ocean2
GA
Cape Point
Latitude
Longitude

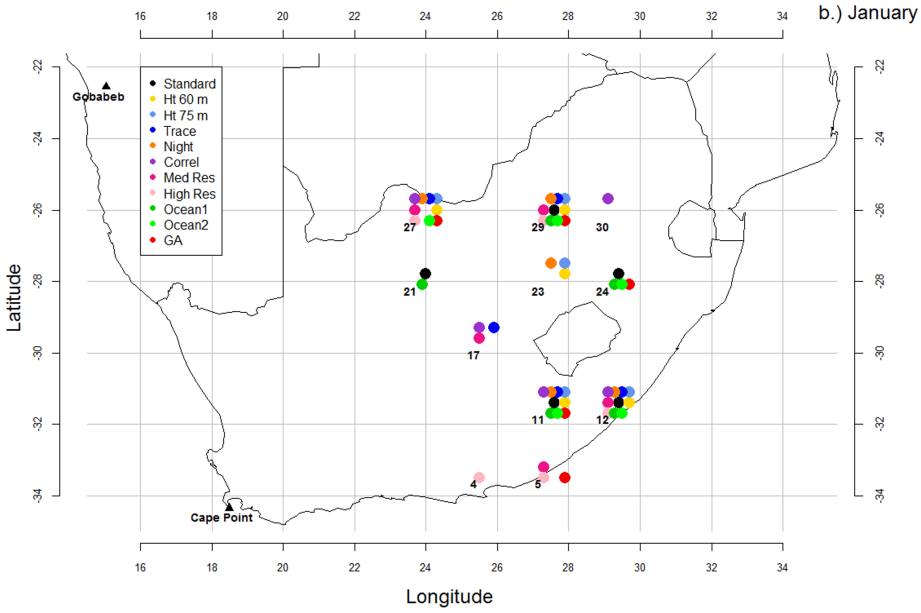
b.) January
Gobabeb
Standard
Ht 60 m
Ht 75 m
Trace
Night
Correl
Med Res
High Res
Ocean1
Ocean2
GA
Cape Point
Latitude
Longitude

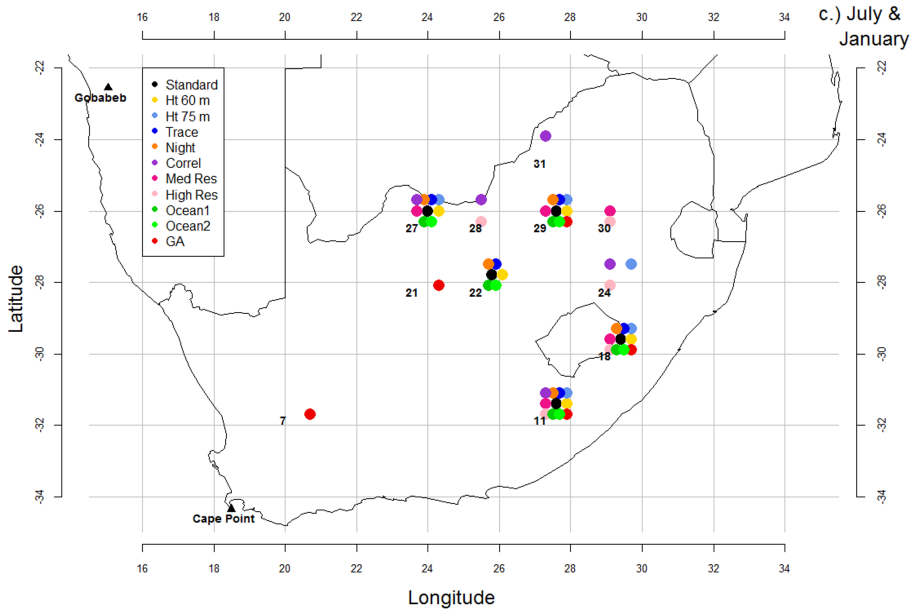


Figure 2.8: Map of the optimal stations to add to the existing network to reduce the overall uncertainty of fluxes in South Africa under the eleven different sensitivity cases for July (top), January (middle), and the combined months of July and January (bottom). The cases include the standard case (Standard), surface grid height set at 60 m (Ht 60 m), surface grid height set at 75 m (Ht 75 m), use of the trace in the uncertainty metric (Trace), doubling of the night time observation error uncertainty (Night), addition of correlation between elements in the prior covariance matrix (Correl), spatial resolution set at 0.8° (Med Res), spatial resolution set at 0.6° (High Res), uncertainty in the ocean sources set at 10 % of the maximum land NPP (Ocean1), uncertainty in the ocean sources set at 10 % of the nearest land NPP (Ocean2), and use of the GA.

The results from the sensitivity tests for January show a great deal more variability between network solutions compared to July, with DI values of greater than zero for almost all network solution comparisons. Similarly to July, the network solutions do appear to converge towards three stations, but not the same stations as July. Under January's conditions, only the homogeneous ocean variance test case resulted in an identical solution to the standard case. There is no single station which all network solutions contained. Stations 29 (north eastern interior) and station 12 (eastern coast) were agreed on by ten out of eleven tests, and stations 27 (northern interior) and 11 (south eastern interior) were agreed on by nine out of eleven tests. These four stations are influenced by areas of large fossil fuel flux uncertainty, and stations 29 and 12 near regions or large summer NEP uncertainty. Sensitivity tests with DI values below 1000 when compared to the standard case include the tests considering surface grid box height, doubling of night time observation error uncertainty, the test considering variable ocean flux uncertainty, the trace uncertainty metric test, and the GA test case. These five test cases show strong agreement. The trace uncertainty metric case favoured a station near the central interior. This station was also included in the solutions of the correlation and medium resolution cases, where these tests obtained DI values of 1225 and 1305 respectively when compared to the standard solution. These tests, as well as the GA and high resolution test cases, included stations near the south coast, near areas of localised fossil fuel uncertainties.

The sensitivity tests from the combined months showed less variability between solutions compared to January (Fig.2.8 c). Station 11 was included in all of the network solutions. Station 18 was agreed upon by ten out of eleven network solutions, and stations 27 and 29 (both in the north eastern interior) were favoured by nine out of eleven solutions. The tests considering 60 m surface height, the trace uncertainty metric, doubling of the night time observation error uncertainty, and inclusion of ocean flux uncertainty have identical solutions to the standard network design. The 75 m surface height and medium resolution tests cases obtained relative low DI values of 468 and 449 respectively when compared to the standard solution (Table 2.2). The high resolution test and test case considering correlation between prior fluxes obtained DI values of 1121 and 1162 respectively. The solutions from these tests focused stations around areas of large fossil fuel flux uncertainty in the north western and eastern interior. The solution from the GA resulted in the largest DI value of 1213 when compared to the standard network, and equal to this or larger when compared to all other network solutions. The station in the GA solution responsible for the disagreement with other solutions is station 7, located in the south western interior,

Table 2.2: Ranking of the new stations added to the base network under ten different sensitivity tests for the combined months of July and January. The tests are presented in the following order: surface grid height set at 60 m; surface grid height set at 75 m; trace of the posterior covariance used in the uncertainty metric; uncertainty of the night time observation errors is doubled; correlation structure is included in the prior covariance of the fluxes; spatial resolution is increased to 0.8°; spatial resolution is increased to 0.6°; ocean sources are assigned 10 % of max NPP variance; ocean sources are assigned 10 % of nearest terrestrial NPP variance; and GA is used for optimisation. The percentage cumulative reduction of uncertainty of the posterior fluxes relative to the base network is provided in brackets.

| Rank | Ht 60 m | Ht 75 m | Trace | Night | Correl | Med Res | High Res | Ocean1 | Ocean2 | GA |
|---|---|---|---|---|---|---|---|---|---|---|
| 1 | 18 (52.3) | 18 (50.9) | 18 (46.8) | 18 (50.9) | 24 (65.4) | 18 (42.9) | 18 (36.3) | 18 (53.1) | 18 (52.3) | 27 |
| 2 | 29 (76.0) | 29 (74.0) | 29 (69.4) | 29 (75.1) | 11 (77.8) | 29 (65.1) | 28 (57.1) | 29 (77.3) | 29 (75.9) | 7 |
| 3 | 11 (79.8) | 11 (78.3) | 11 (73.3) | 11 (78.5) | 28 (83.6) | 11 (70.7) | 11 (62.0) | 11 (80.8) | 11 (80.4) | 29 |
| 4 | 22 (81.5) | 24 (80.1) | 22 (75.1) | 22 (80.6) | 31 (85.3) | 30 (73.6) | 30 (66.4) | 22 (82.5) | 22 (82.1) | 18 |
| 5 | 27 (83.5) | 27 (82.5) | 27 (77.2) | 27 (83.1) | 27 (86.5) | 27 (76.8) | 24 (69.5) | 27 (84.4) | 27 (84.4) | 11 (84.9) |

far from the concentration of stations for most network solutions. The remaining four stations from the GA test are located towards the north western and eastern interior parts of the country. As discussed in the previous section (2.3.3) the three best stations to add to the network according to the IO solution, are stations 18, 29 and 11, with station 18 attaining the greatest uncertainty reduction. All of the network solutions for the combined months of January and July have included station 18, and the three most important stations are all in the solution of the GA.

The statistics for the different sensitivity tests for the combined months (Table 2.3) indicate that the test considering correlation between the prior fluxes obtained the highest uncertainty reduction, followed by the GA test. The GA was able to achieve marginally greater uncertainty reduction by 0.3 % compared to the IO standard solution. Most of the test cases were able to achieve between 80 % and 85 % uncertainty reduction. The test case utilising the trace uncertainty metric achieved a smaller uncertainty reduction, and the two higher resolution tests achieved the smallest uncertainty reduction overall. It should be noted that the uncertainty reduction achieved for the trace sensitivity test was calculated using the $J_{\mathrm{Ct}}$ uncertainty metric, due to the use of this metric for the optimisation procedure. Estimates of the posterior uncertainty for the total flux of South Africa under the base and optimal networks were obtained for each month. Those which differed substantially from the standard network solution were the high and medium resolution test cases, and the correlation test case. Under the assumption of positive correlations between the flux errors, the base network results in a higher total flux uncertainty of 205.82 g C/m$^2$/week for the

Table 2.3: Table of network comparison statistics for the combined months of January and July. The sensitivity tests are presented in the same order as for Table 2.2.

| Sensitivity Test | Uncertainty Reduction | Running Time (hh:mm) | Clustering Index |
|---|---|---|---|
| Standard | 84.6 % | 0:49 | 23.8 |
| Ht 60 m | 83.5 % | 0:49 | 23.8 |
| Ht 75 m | 82.5 % | 0:48 | 23.8 |
| Trace | 77.2 % | 0:48 | 23.8 |
| Night | 83.1 % | 0:48 | 23.8 |
| Correl | 86.5 % | 1:13 | 17.4 |
| Med Res | 76.8 % | 4:23 | 23.8 |
| High Res | 69.5 % | 25:11 | 36.6 |
| Ocean1 | 84.4 % | 5:27 | 23.8 |
| Ocean2 | 84.4 % | 5:12 | 23.8 |
| GA | 84.9 % | 32:01 | 17.4 |

base network which is reduced to 27.79 g C/m$^2$/week under the optimal network, now similar to the result of the standard network solution. Under the base network, the additional covariance terms introduced through the correlation structure are poorly resolved, leading to higher total uncertainties. When there are more stations added to the network this is improved. The high and medium spatial resolution test cases gave total flux uncertainties of 271.55 and 190.14 g C/m$^2$/week respectively under the base network. These were then reduced to 82.82 and 44.19 g C/m$^2$/week respectively under the optimal network. At the spatial resolutions that we've considered in our study, the between pixel variability in the terrestrial fluxes will increase as the spatial resolution is increased, for both the biospheric and fossil fluxes (Turner et al., 2000). For the fossil fuel fluxes, we create the surface of flux uncertainties using the same procedure for each of the different spatial resolution cases. As explained earlier, for each of the ten realisations from the FFDAS product, we regrid the $0.1^\circ \times 0.1^\circ$ fossil fuel emissions onto the surface grid we are using. To obtain the uncertainty estimates the within pixel variance is calculated for the ten realisations. The result of carrying this procedure out at higher spatial resolutions is that the variance values are larger compared to lower resolutions, and the between pixel variability is increased (Asefi-Najafabady et al., 2014). Therefore, the total flux uncertainty derived under a high resolution is expected to be larger than for lower resolutions.

Most network solutions tended towards the same amount of clustering of stations, obtaining a clustering index of 23.8. The GA and test case considering correlation had more dispersed networks, and the high resolution test case had the highest amount of

Table 2.4: Table of dissimilarity indices for the optimal network solutions for the combined months of January and July. The sensitivity tests are presented in the same order as for Table 2.2.

| Sensitivity Test | Standard | Ht 60 m | Ht 75 m | Trace | Night | Correl | Med Res | High Res | Ocean1 | Ocean2 | GA |
|---|---|---|---|---|---|---|---|---|---|---|---|
| Standard | 0 | 0 | 469 | 0 | 0 | 1162 | 449 | 1121 | 0 | 0 | 1213 |
| Ht 60 m | 0 | 0 | 469 | 0 | 0 | 1162 | 449 | 1122 | 0 | 0 | 1213 |
| Ht 75 m | 469 | 469 | 0 | 469 | 469 | 761 | 380 | 720 | 469 | 469 | 1285 |
| Trace | 0 | 0 | 469 | 0 | 0 | 1162 | 449 | 1121 | 0 | 0 | 1213 |
| Night | 0 | 0 | 469 | 0 | 0 | 1162 | 449 | 1121 | 0 | 0 | 1213 |
| Correl | 1162 | 1162 | 761 | 1162 | 1162 | 0 | 1162 | 851 | 1162 | 1162 | 2046 |
| Med Res | 449 | 449 | 380 | 449 | 449 | 1162 | 0 | 741 | 449 | 449 | 1265 |
| High Res | 1121 | 1121 | 720 | 1121 | 1121 | 851 | 741 | 0 | 1121 | 1121 | 1693 |
| Ocean1 | 0 | 0 | 469 | 0 | 0 | 1162 | 449 | 1121 | 0 | 0 | 1213 |
| Ocean2 | 0 | 0 | 469 | 0 | 0 | 1162 | 449 | 1121 | 0 | 0 | 1213 |
| GA | 1213 | 1213 | 1285 | 1213 | 1213 | 2046 | 1265 | 1693 | 1213 | 1213 | 0 |

clustering, with a clustering index of 36.6. We would expect the correlation case to spread stations since a given station will reduce uncertainty everywhere within one correlation length. The GA for the combined months took the longest to run, at over 32 hours, which is 39 times longer than the running time of the standard IO solution. This was followed by the high resolution solution, which took 25.2 hours, and the two ocean flux uncertainty test cases which took over five hours each.

## 2.4 Discussion and Conclusions

Under a reference set of conditions, an optimal network design was obtained for South Africa for two representative months of the year. The resulting designs reduced the uncertainty of carbon fluxes from South Africa compared to the base network by 43 % in July and 78 % in January. These relatively large reductions in uncertainty are due to the lack of coverage by the current network, which only reduces the uncertainty of fluxes from South Africa by 16 % for both July and January. The concentration of stations by all networks tended towards the central interior, near the North West Province of South Africa and in the eastern parts of the country. These represent the areas with the largest uncertainty in biospheric fluxes, as well as fossil fuel emissions, in the country.

Station 11 is located near the uKhahlamba Drakensberg World Heritage Site. Several remote holiday destinations occur in this area, near the town of Mooi River, and road infrastructure is available. Potentially, facilities at or near these holiday destinations could be utilised in order to conduct atmospheric measurements, particularly if there is a communications tower available. Station 18 is located near the peak of Ben

Macdhui. This is near the site of a 1996 atmospheric monitoring campaign, which assessed the ability of transport models to resolve recirculation over and exiting South Africa to the Indian Ocean (Piketh et al., 1999). Station 29 is near the atmospheric monitoring site of the North West University (South Africa), at Welgegund, about 20 km from the Potchefstroom campus. This site was established in collaboration with the University of Helsinki to measure the impact of aerosols and trace gases on the climate and air quality (Tiitta et al., 2014). Therefore, for at least three of the most influential stations, facilities or previous measurement campaigns exist, indicating that it should be possible to establish long term monitoring of $CO_2$ concentrations near these sites.

The sensitivity analysis demonstrated that for most of the network design parameters considered in this study, the stations found to be most important by the standard network design were always identified in the network design solution. Many of the choices required for the optimal network design, such as the height of the surface grid cells, whether to inflate night time observation error uncertainties relative to the day time, and the inclusion of ocean flux uncertainty, have a negligible impact on the final network design. Substituting the trace for the sum of the covariance elements also resulted in similar solutions.

The test cases considering higher spatial resolution tended to result in network solutions different from the standard case, largely due to the increase in spatial heterogeneity in prior flux uncertainties compared to the coarser resolution. The spatial resolution of an inversion study impacts network design in several ways. It is the main determinant of the amount of aggregation error attributed to a measurement site, with aggregation error reducing as the resolution increases. As the spatial resolution is degraded, aggregation errors can become large, leading to the exclusion of sites in the case of an optimal network design, even if they are in view of regions of large flux uncertainty. The spatial resolution of the sources also determines the dimensions of the sensitivity matrix and prior flux covariance matrix, which impacts on the computational resources required to run an inversion or network optimisation. Ideally, the highest manageable resolution should be used, as close as possible to the resolution of the transport model and original spatial products used for obtaining the prior fluxes and their covariances. Alternative approaches, such as the use of multi-scale representation of the source region can be used to mitigate aggregation errors as well (Wu et al., 2011), but these errors should always be considered during an inversion or inversion-based optimal network design exercise.

The GA was able to find marginally better solutions than the IO method, if run with sufficient population size and number of iterations, but in general did include the most influential stations from the IO solution. The increase in uncertainty reduction was found to be marginal, but cost a great deal more in running time before this solution was found. If the resolution of the standard case had been higher, the GA would have taken longer to run, and the current computing system may have had insufficient memory. Moreover, to find a better solution than the IO, the iterations and population size would have had to be set even higher, due to the greater heterogeneity in the prior flux uncertainties in a higher resolution setup, further increasing the computational costs. An additional advantage of the IO method over the GA method is that an evolution of results is generated, which is useful for practical purposes. By identifying the station which on its own best reduces the uncertainty in the posterior fluxes, it gives the decision makers the location of the site which should be prioritised over others in the network.

Even though we accounted for aggregation error, which would have corrected the total flux estimate for the domain, there were still large differences between the total flux uncertainties from the inversion results under different spatial resolutions. This was due to the treatment of the prior uncertainties under the different spatial resolutions. Degrading the spatial resolution results in a loss of information, therefore it is best to run the inversion at as high a resolution as possible. Favouring optimisation techniques like IO, which can more easily accommodate high spatial resolution, over those which could force a reduction in resolution due to high computational demands, such as the GA, may be unavoidable. Techniques like simulated annealing and the GA do not guarantee the global optimum, as demonstrated by Patra and Maksyutov (2002) for simulated annealing and during the initial trials of the GA in this study. Patra and Maksyutov (2002) also showed that as the number of stations in the network increased, the performance of simulated annealing relative to the IO decreased, with IO eventually achieving significantly better uncertainty reductions.

Of the sensitivity tests, including correlation had one of the largest impacts on the final network result, often differing significantly from the standard solution. The correlation structure used in this study was generic, simply assuming that fluxes from nearby grid cells and fluxes at the same location near in time would be correlated, included for the purpose of assessing the impact of correlation in the prior fluxes. For a network to be based on a prior covariance matrix including correlation, there would need to be confidence that this correlation structure and size of correlations between fluxes were accurate. This is generally not the case, and easier to assess when

concentration measurements are available, which is why many network designs have assumed independence between prior fluxes (Rayner, 2004; Patra and Maksyutov, 2002). Including correlations which are too large can lead to an over constrained system (Lauvaux et al., 2012b), which is evidenced in this study where the uncertainty reductions were the largest under the correlation test case.

Overall the results suggest that a good improvement in knowledge of South African fluxes is achievable from a feasible atmospheric network and that the general features of this network are invariable under many reasonable choices in a network design study.

# Bibliography

Asefi-Najafabady, S., Rayner, P. J., Gurney. K. R., McRobert, A., Song, ., Coltin K., Huang, J., Elvidge, C., and Baugh, K.: A multiyear, global gridded fossil fuel $CO_2$ emission data product: Evaluation and analysis of results, J. Geophys. Res., 119, doi: 10.1002/2013JD021296, 2014

Baker, D. F.: An inversion method for determining time-dependent surface CO2 fluxes, in: Kasibhatla, P., Heimann, M., Rayner, P., Mahowald, N., Prinn, R. G., and Hartley, D. E., (Eds.): Inversion methods in global biogeochemical cycles, Geophysical Monograph 114, American Geophysical Union, 279–293 Washington D.C., USA, 2000

Baker, D. F., Law, R. M., Gurney, K. R., Rayner, P., Peylin, P., Denning, A. S., Bourquet, P., Bruhwiler, L., Chen, Y., Ciais, P., Fung, I. Y., Heimann, M., John, J., Maki, T., Maksyutov, S., Masarie, K., Prather, M., Pak, B., Taguchi, S., Zhu, Z.: TransCom 3 inversion intercomparison: impact of transport model errors on the interannual variability of regional $CO_2$ fluxes, 1988–2003, Global Biogeochem. Cy., 20, GB1002, doi: 10.1029/2004GB002439, 2006.

Bousquet, P., Ciais, P., Peylin, P., Ramonet, M., and Monfray, P.: Inverse modeling of annual atmospheric $CO_2$ sources and sinks: 1. Method and control inversion, J. Geophys. Res., 104, 26161–26178, 1999.

Canadell, J. G., Le Quéré, C., Raupach, M. R., Field, C. B., Buitenhuis, E. T., Ciais, P., Conway, T. J., Gillett, N. P., Houghton, R. A., and Marland, G.: Contributions to accelerating atmospheric $CO_2$ growth from economic activity, carbon intensity, and efficiency of natural sinks, P. Natl. Acad. Sci. USA, 104, 18866–18870, doi: 10.1073/pnas.0702737104, 2007.

Chevallier, F., Ciais, P., Conway, T. J., Aalto, T., Anderson, B. E., Bousquet, P., Brunke, E. G., Ciattaglia, L., Esaki, Y., Fröhlich, M., Gomez, A., Gomez-Pelaez, A. J., Haszpra, L., Krummel, P. B., Langenfelds, R. L., Leuenberger, M.,

Machida, T., Maignan, F., Matsueda, H., Morgui, J. A., Mukai, H., Nakazawa, T., Peylin, P., Ramonet, M., Rivier, L., Sawa, Y., Schmidt, M., Steele, L. P., Vay, S. A., Vermeulen, A. T., Wofsy, S., and Worthy, D.: $CO_2$ surface fluxes at grid point scale estimated from a global 21 year reanalysis of atmospheric measurements, J. Geophys. Res., 115, D21307, doi: 10.1029/2010JD013887, 2010.

Chevallier, F., Wang, T., Ciais, P., Maignan, F., Bocquet, M., Arain, M. A., Cescatti, A., Chen, J., Dolman, A. J., Law, B. E., Margolis, H. A., Montagnani, L., and Moors, E. J.: What eddy-covariance measurements tell us about prior land flux errors in $CO_2$-flux inversion schemes, Global Biogeochem. Cy., 26, GB1021, doi: 10.1029/2010GB003974, 2012.

Chevallier, F., Palmer, P. I., Feng, L., Boesch, H., O'Dell, W., and Bousquet, P.: Toward robust and consistent regional $CO_2$ flux estimates from in situ and spaceborne measurements of atmospheric $CO_2$, Geophys. Res. Lett., 41, 1065–1070, doi:10.1002/2013GL058772, 2014.

Ciais, P., Rayner, P., Chevallier, F., Bousquet, P., Logan, M., Peylin, P., and Ramonet, M.: Atmospheric inversions for estimating $CO_2$ fluxes: methods and perspectives, Climatic Change, 103, 69–92, 2010.

Denman, K. L., Brasseur, G., Chidthaisong, A., Ciais, P., Cox, P. M., Dickinson, R. E., Hauglustaine, D., Heinze, C., Holland, E., Jacob, D., Lohmann, U., Ramachandran, S., da Silva Dias, P. L., Wofsy, S. C., and Zhang, X.: Couplings between changes in the climate system and biogeochemistry, in: Climate Change 2007: The Physical Science Basis. Contribution of Working Group I to the Fourth Assessment Report of the Intergovernmental Panel on Climate Change, edited by: Solomon, S., Qin, D., Manning, M., Chen, Z., Marquis, M., Averyt, K. B., Tignor, M., and Miller, H. L., Cambridge University Press, Cambridge, UK and New York, NY, USA, 499–587, 2007.

Engelbrecht, F. A., McGregor, J. L. and Engelbrecht, C. J.: Dynamics of the conformal-cubic atmospheric model projected climate-change signal over southern Africa, Int. J. Climatol., 29, 1013-1033., doi: 10/1002/joc.1742.29., 2009.

Enting, I. G.: Inverse Problems in Atmospheric Constituent Transport, Cambridge Univ. Press, New York, 2002.

Enting, I. G. and Mansbridge, J. V.: Seasonal sources and sinks of atmospheric $CO_2$: direct inversion of filtered data, Tellus B, 41, 111–126, 1989.

Gurney. K. R., Law, R. M., Denning, A. S., Rayner, P. J., Baker, D., Bousquet, P., Bruhwiler, L., Chen, Y., Ciais, P., Fan, S., Fung, I. Y., Gloor, M., Heimann, M., Higuchi, K., John, J., Maki, T., Maksyutov, S., Masarie, K., Peylin, P., Prather, M., Pak, B. C., Randerson, J., Sarmiento, J., Taguchi, S., Takahashi, T., and Yuen, C.: Towards robust regional estimates of $CO_2$ sources and sinks using atmospheric transport models, Nature, 405, 626–630, 2002.

Gurney, K. R., Law, R. M., Denning, A. S., Rayner, P. J., Baker, D., Bousquet, P., Bruhwiler, L., Chen, Y., Ciais, P., Fan, S., Fung, I. Y., Gloor, M., Heimann, M., Higuchi, K., John, J., Kowalczyk, E., Maki, T., Maksyutov, S., Peylin, P., Prather, M., Pak, B. C., Sarmiento, J., Taguchi, S., Takahashi, T., and Yuen, C.: TransCom 3 $CO_2$ inversion intercomparison: 1. Annual mean control results and sensitivity to transport and prior flux information, Tellus B, 55, 555–579, 2003.

Kaminski, T., Heimann, M., and Giering, R.: A coarse grid three dimensional global inverse model of the atmospheric transport, 2. Inversion of the transport of $CO_2$ in the 1980s, J. Geophys. Res., 104, 18555–18581, 1999.

Kaminski, T., Rayner, P .J., Heimann, M., and Enting, I. G.: On aggregation errors in atmospheric transport inversions, J. Geophys. Res., 106, 4705–4715, 2001.

Kowalczyk, E. A., Garratt, J. R. and Krummel, P. B.: Implementation of a soil-canopy scheme into the CSIRO GCM - regional aspects of the model response, CSIRO Div. Atmospheric Research, Melbourne, Australia, Tech Paper No. 32, 59 pp., 1994.

Lambers, H., Chapin, F. S., and Pons, T. L.: Plant Physiology Ecology, Springer Science+Business Media L. L. C., New York, USA, 634 pp., 2008.

Lauvaux, T., Uliasz, M., Sarrat, C., Chevallier, F., Bousquet, P., Lac, C., Davis, K. J., Ciais, P., Denning, A. S., and Rayner, P. J.: Mesoscale inversion: first results from the CERES campaign with synthetic data, Atmos. Chem. Phys., 8, 3459–3471, doi: 10.5194/acp-8-3459-2008, 2008.

Lauvaux, T., Schuh, A. E., Uliasz, M., Richardson, S., Miles, N., Andrews, A. E., Sweeney, C., Diaz, L. I., Martins, D., Shepson, P. B., and Davis, K. J.: Constraining the $CO_2$ budget of the corn belt: exploring uncertainties from the assumptions in a mesoscale inverse system, Atmos. Chem. Phys., 12, 337–354, doi: 10.5194/acp-12-337-2012, 2012a.

Lauvaux, T., Schuh, A. E., Bouquet, M., Wu, L., Richardson, S., Miles, N., and Davis, K. J.: Network design for mesoscale inversions of $CO_2$ sources and sinks, Tellus, 64B, doi:10.3402/tellusb.v64i0.17980, 2012b.

Law, R. M., Chen, Y., Gurney, K. R., and Transcom 3 Modellers: TransCom 3 $CO_2$ inversion intercomparison: 2. Sensitivity of annual mean results to data choices, Tellus B, 55, 580–595, 2003.

McGregor, J. L.: A new convection scheme using a simple closure, in: Current issues in the parameterization of convection, BMRC, Melbourne, Australia, Research Report 93, 33-36, 2003.

McGregor, J. L.: C-CAM: Geometric aspects and dynamical formulation, CSIRO Div. Atmospheric Research, Melbourne, Australia, Tech Paper No. 70, 43 pp., 2005.

McGregor, J. L. and Dix, M. R.: The CSIRO conformal-cubic atmospheric GCM, in: IUTAM Symposium on Advances in Mathematical Modelling of Atmosphere and Ocean Dynamics, Limerick, Ireland, 2–7 July 2000, edited by: Hodnett, P. F., Kluwer, Dordrecht, 197–202, 2001.

McGregor, J. L. and Dix, M. R.: An updated description of the Conformal-Cubic Atmospheric Model, in: High Resolution Numerical Modelling of the Atmosphere and Ocean, edited by: Hamilton, K. and Ohfuchi, W., Springer, New York, USA, 51–76, 2008.

Morgan, E., Lavrič, J., Seely, M., and Heimann, M.: Establishment of an atmospheric observatory for trace gases and atmospheric oxygen in Namibia, Geophys. Res. Abstr., 14, 5122–5122, 2012.

Patra, P. K. and Maksyutov, S.: Incremental approach to the optimal network design for $CO_2$ surface source inversion, Geophys. Res. Lett., 29, 1459, doi:10.1029/2001GL013943, 2001.

Peylin, P., Baker, D., Sarmiento, J., Ciais, P., and Bousquet, P.: Influence of transport uncertainty on annual mean and seasonal inversions of atmospheric $CO_2$ data, J. Geophys. Res., 107, 4385, doi: 10.1029/2001JD000857, 2002.

Peylin, P., Rayner, P. J., Bousquet, P., Carouge, C., Hourdin, F., Heinrich, P., Ciais, P., and AEROCARB contributors: Daily $CO_2$ flux estimates over Europe from continuous atmospheric measurements: 1, inverse methodology, Atmos. Chem. Phys., 5, 3173–3186, doi:10.5194/acp-5-3173-2005, 2005.

Piketh, S. J., Swap, R. J., Anderson, C. A., Freiman, M. T., Zunckel, M., and Held, G.: Ben Macdhui high altitude trace gas and aerosol transport experiment, S. Afr. J. Sci., 95, 35–43, 1999.

Rayner, P. J.: Optimizing $CO_2$ observing networks in the presence of model error: results from TransCom 3, Atmos. Chem. Phys., 4, 413–421, doi: 10.5194/acp-4-413-2004, 2004.

Rayner, P. J., Enting, I. G., and Trudinger, C. M.: Optimizing the $CO_2$ observing network for constraining sources and sinks, Tellus B, 48, 433–444, 1996.

Rayner, P. J., Enting, I. G., Francey, R. J., and Langenfelds, R. L.: Reconstructing the recent carbon cycle from atmospheric $CO_2$, $\delta^{13}C$ and $O_2/N_2$ observations, Tellus B, 51, 213–232, 1999.

Rayner, P. J., Raupach, M. R., Paget, M., Peylin, P., and Koffi, E.: A new global gridded data set of $CO_2$ emissions from fossil fuel combustion: mehodology and evaluation, J. Geophys. Res., 115, D19306, doi: 10.1029/2009JD013439, 2010.

Rödenbeck, C., Houweling, S., Gloor, M., and Heimann, M.: $CO_2$ flux history 1982–2001 inferred from atmospheric data using a global inversion of atmospheric transport, Atmos. Chem. Phys., 3, 1919–1964, doi: 10.5194/acp-3-1919-2003, 2003.

Rotstayn, L. D.: A physically based scheme for the treatment of stratiform clouds and precipitation in large-scale models. I: Description and evaluation of the microphysical processes, Q. J. R. Meteorol. Soc., 123, 1227–1282, 1997.

Sarrat, C., Noilhan, J., Lacarrère, P., Ceschia, E., Ciais, P., Dolmon, A. J., Elbers, E. J., Gerbig, C., Gioli, B., Lauvaux, T., Miglietta, F., Neininger, B., Ramonet, M., Vellinga, O., and Bonnefond, J. M.: Mesoscale modelling of the $CO_2$ interactions between the surface and the atmosphere applied to the April 2007 CERES field experiment, Biogeosciences, 6, 633–646, doi:10.5194/bg-6-633-2009, 2009.

Schmidt, F.: Variable fine mesh in spectral global model, Beitr. Phys. Atmos., 50, 211–217, 1977.

Scholes, R. J., von Maltitz, G. P., Archibald, S. A., Wessels, K., van Zyl, T., Swanepoel, D., and Steenkamp, K.: National Carbon Sink Assessment for South Africa: First Estimate of Terrestrial Stocks and Fluxes, CSIR Technical Report, Pretoria, South Africa, CSIR/NRE/GC/ER/2013/0056/B, 2013.

Schuh, A. E., Lauvaux, T., West, T. O., Denning, A. S., Davis, K., J., Miles, N., Richardson, S., Uliasz, M., Lokupitiya, E., Cooley, D., Andrews, A., and Ogle, S.: Evaluating atmospheric $CO_2$ inversions at multiple scales over a highly inventoried agricultural landscape, Glob. Change Biol., 19, 1424–1439, doi: 10.1111/gcb.12141, 2013.

Schwarzkopf, M. D. and Fels, S. B.: The simplified exchange method revisited: An accurate, rapid method for computation of infrared cooling rates and fluxes, J. Geophys. Res., 96, 9075–9096, 1991.

Seibert, P. and Frank, A.: Source-receptor matrix calculation with a Lagrangian particle dispersion model in backward mode, Atmos. Chem. Phys., 4, 51–63, doi: 10.5194/acp-4-51-2004, 2004.

Tarantola, A.: Inverse Problem Theory and Methods for Model Parameter Estimation, Society for Industrial and Applied Mathematics , Philadelphia, 1987.

Tarantola, A.: Inverse Problem Theory: Methods for Data Fitting and Model Parameter Estimation, Elsevier, Amsterdam, 1987.

Thatcher, M. and McGregor, J. L.: Using a scale-selective filter for dynamical downscaling with the conformal cubic atmospheric model, Mon. Weather Rev., 137, 1742–1752, 2009.

Thatcher, M. and McGregor, J. L.: A technique for dynamically downscaling daily-averaged GCM datasets over Australia using the Conformal Cubic Atmospheric Model, Mon. Weather Rev., 139, 79–95, 2010.

Tiitta, P., Vakkari, V., Croteau, P., Beukes, J. P., van Zyl, P. G., Josipovic, M., Venter, A. D., Jaars, K., Pienaar, J. J., Ng, N. L., Canagaratna, M. R., Jayne, J. T., Kerminen, V. -M., Kokkola, H., Kulmala, M., Laaksonen, A., Worsnop, D. R., and Laakso, L.: Chemical composition, main sources and temporal variability of $PM_1$ aerosols in southern Africa grassland, Atmos. Chem. Phys., 14, 1909–1927, doi: 10.5194/acp-14-1909-2014, 2014.

Turner, D. P., Cohen, W., B., and Kennedy, R. E.: Alternative spatial resolutions and estimation of carbon flux over a managed forest landscape in Western Oregon, Landsc. Ecol., 15, 441–452, 2000.

Uliasz, M.: The atmospheric mesoscale dispersion modeling system, J. Appl. Meteorol., 31, 139–149, 1993.

Uliasz, M.: Lagrangian particle modeling in mesoscale applications, in: Environmental Modelling II, Computational Mechanics Publications, Southampton, UK, 71–102, 1994.

Whittlestone, S., Kowalczyk, E., Brunke, E. G., and Labuschagne, C.: Source Regions for $CO_2$ at Cape Point Assessed by Modelling 222Rn and Meteorological Data, Technical Report for the South African Weather Service, Pretoria, South Africa, 2009.

Wu, L., Bocquet, M., Lauvaux, T., Chevallier, F., Rayner, P. J. and Davis, K.: Optimal representation of source-sink fluxes for mesoscale carbon dioxide inversion with synthetic data, J. Geophys. Res., 116, D21304, doi:10.1029/2011JD016198, 2011.

Wu, L., Bocquet, M., Chevallier, F., Lauvaux, T., and Davis, K.: Hyperparameter estimation for uncertainty quantification in mesoscale carbon dioxide inversions, Tellus B, 65, 20894, doi: 10.3402/tellusb.v65i0.20894, 2013.

Ziehn, T., Nickless, A., Rayner, P. J., Law, R. M., Roff, G., and Fraser, P.: Greenhouse gas network design using backward Lagrangian particle dispersion modelling - Part 1: Methodology and Australian test case, Atmos. Phys. Chem., 14, 9363-9378, 2014.

# Chapter 3

# Comparison of the Genetic Algorithm and Incremental Optimisation Routines for a Bayesian Inverse Modelling Based Network Design

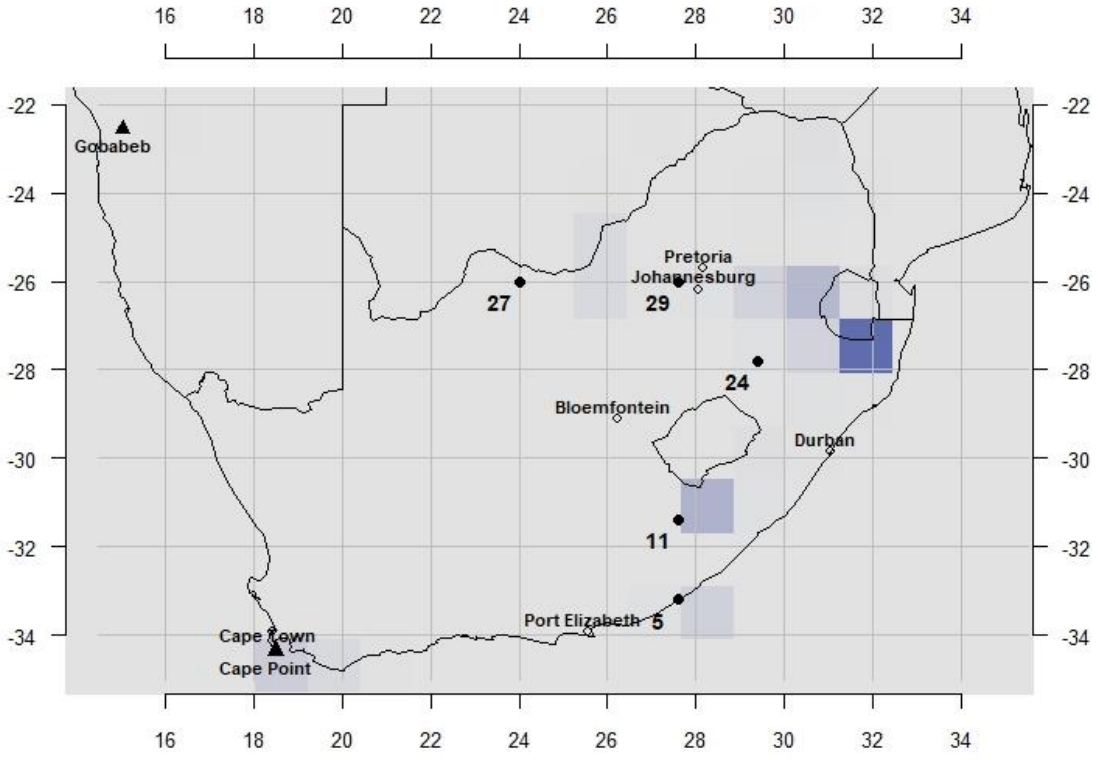

IOP Publishing Inverse Problems

Inverse Problems **34** (2018) 055006 (33pp) https://doi.org/10.1088/1361-6420/aab46c

# Comparison of the genetic algorithm and incremental optimisation routines for a Bayesian inverse modelling based network design

**A Nickless[1,2], P J Rayner[3], B Erni[1,4] and R J Scholes[5]**

[1] Department of Statistical Sciences, University of Cape Town, Cape Town, 7701, South Africa
[2] Department of Primary Care Health Sciences, University of Oxford, Woodstock Road, Oxford OX2 6GG, United Kingdom
[3] School of Earth Sciences, University of Melbourne, Melbourne, VIC 3010, Australia
[4] The Centre for Statistics in Ecology, the Environment and Conservation, University of Cape Town, Cape Town, 7701, South Africa
[5] Global Change Institute, University of the Witwatersrand, Johannesburg, 2050, South Africa

E-mail: alecia.nickless@phc.ox.ac.uk

Received 15 September 2017, revised 26 February 2018
Accepted for publication 6 March 2018
Published 4 April 2018


**Abstract**

The design of an optimal network of atmospheric monitoring stations for the observation of carbon dioxide ($CO_2$) concentrations can be obtained by applying an optimisation algorithm to a cost function based on minimising posterior uncertainty in the $CO_2$ fluxes obtained from a Bayesian inverse modelling solution. Two candidate optimisation methods assessed were the evolutionary algorithm: the genetic algorithm (GA), and the deterministic algorithm: the incremental optimisation (IO) routine.

This paper assessed the ability of the IO routine in comparison to the more computationally demanding GA routine to optimise the placement of a five-member network of $CO_2$ monitoring sites located in South Africa. The comparison considered the reduction in uncertainty of the overall flux estimate, the spatial similarity of solutions, and computational requirements. Although the IO routine failed to find the solution with the global maximum uncertainty reduction, the resulting solution had only fractionally lower uncertainty reduction compared with the GA, and at only a quarter of the computational resources used by the lowest specified GA algorithm. The GA solution set showed more inconsistency if the number of iterations or

# Chapter 3

# Comparison of the genetic algorithm and incremental optimisation routines for a Bayesian inverse modelling based network design

# Abstract

The design of an optimal network of atmospheric monitoring stations for the observation of carbon dioxide ($CO_2$) concentrations can be obtained by applying an optimisation algorithm to a cost function based on minimising posterior uncertainty in the $CO_2$ fluxes obtained from a Bayesian inverse modelling solution. Two candidate optimisation methods assessed were the evolutionary algorithm: the Genetic Algorithm (GA), and the deterministic algorithm: the Incremental Optimisation (IO) routine.

This paper assessed the ability of the IO routine in comparison to the more computationally demanding GA routine to optimise the placement of a five-member network of $CO_2$ monitoring sites located in South Africa. The comparison considered the reduction in uncertainty of the overall flux estimate, the spatial similarity of solutions, and computational requirements. Although the IO routine failed to find the solution with the global maximum uncertainty reduction, the resulting solution had only fractionally lower uncertainty reduction compared with the GA, and at only a quarter of the computational resources used by the lowest specified GA algorithm. The GA solution set showed more inconsistency if the number of iterations or population size was small, and more so for a complex prior flux covariance matrix. If the GA completed with a sub-optimal solution, these solutions were similar in fitness to the best available solution.

Two additional scenarios were considered, with the objective of creating circumstances where the GA may outperform the IO. The first scenario considered an established network, where the optimisation was required to add an additional five stations to an existing five-member network. In the second scenario the optimisation was based only on the uncertainty reduction within a subregion of the domain. The GA was able to find a better solution than the IO under both scenarios, but with only a marginal improvement in the uncertainty reduction. These results suggest that the best use of resources for the network design problem would be spent in

improvement of the prior estimates of the flux uncertainties rather than investing these resources in running a complex evolutionary optimisation algorithm.

The authors recommend that, if time and computational resources allow, that multiple optimisation techniques should be used as a part of a comprehensive suite of sensitivity tests when performing such an optimisation exercise. This will provide a selection of best solutions which could be ranked based on their utility and practicality.

## 3.1 Introduction

In order to understand the role of carbon dioxide ($CO_2$) in climate change, and to monitor mitigation efforts to reduce emissions of $CO_2$, estimates of land-based sources and sinks of $CO_2$ can be obtained through the technique of inverse modelling. This can be achieved with accurate and precise measurement of atmospheric $CO_2$ concentrations at suitably located monitoring sites, a reliable atmospheric transport model, and a Bayesian inverse modelling framework (Jackson, 1979; Jackson and Matsu'ura, 1985; Rodgers, 2000; Enting, 2002; Gurney et al., 2003; Tarantola, 2005; Ciais et al., 2010).

The reason for choosing the Bayesian approach is due to the under-determined nature of the problem - there are far more source regions to solve than there are measurements. Therefore prior information on the surface $CO_2$ fluxes is used to regularise the problem by narrowing the parameter space of the solution. Bottom-up approaches, such as land-atmosphere exchange models and fossil fuel inventory analyses, provide the required prior information on the unknown $CO_2$ fluxes.

Deciding on the placement of measurement sites is not always possible and instead existing measurement infrastructure may be the only source of data. But when new sites are to be installed, it is possible to exploit the experimental design in order to optimise the inversion solution for the unknown parameters (Haber et al., 2008). This paper considers the optimal experimental design for an atmospheric $CO_2$ monitoring network for South Africa. The network optimisation approach we have adopted, based on inverse modelling, was originally based on the work of Hardt and Scherbaum (1994) which optimised the station locations for an inversion problem applied to a seismographic network. This was developed by Rayner et al. (1996), and the approach recently reviewed in Kaminski and Rayner (2017).

Previous studies which have considered this optimisation problem for $CO_2$ atmospheric monitoring networks have implemented three different optimisation methods: simulated annealing (Rayner et al., 1996); incremental optimisation (IO) (Patra and Maksyutov, 2002); and the genetic algorithm (GA) (Rayner, 2004). Simulated annealing and the GA are evolutionary algorithms whereas the IO is a deterministic algorithm. The IO routine has already been compared with simulated annealing (Patra and Maksyutov, 2002) for this application. This paper aims to compare the GA with the IO routine as described by Patra and Maksyutov (2002). Both optimisation routines are plausible candidates for the network design problem, but operate on very different optimisation philosophies. In particular, the performance and resource use

of the GA depends on the specification of the number of iterations and the number of population members. We consider different specifications of these parameters and compare the results with those of the IO method. As the GA performs many more fitness evaluations of the possible solutions compared with the IO, it is fully expected that the GA should therefore perform better than the IO, and we also expect GAs specified with higher number of population members or iterations to find the optimal solution with higher probability than GAs with lower specifications. We wanted to determine what the variation in GA solutions for this problem would look like, and we wanted to determine how close the IO solution would get to the best available GA solution.

The coverage of monitoring sites on land regions of the Northern Hemisphere is far denser compared with the Southern Hemisphere. Previous studies on optimising locations for new monitoring sites for atmospheric $CO_2$ based on uncertainty reduction of surface flux estimates have identified southern Africa as an important region to constrain (Patra and Maksyutov, 2002; Rayner, 2004). To help meet this demand, five new instruments have been acquired by the Council for Scientific and Industrial Research in order to expand the existing network of monitoring stations in South Africa. These instruments need to be placed in optimal locations in order to maximise the investment return on the instruments through reducing the uncertainty of the estimates of $CO_2$ fluxes from subregions in South Africa.

In addition to the original network design problem for South Africa, which required a solution for the placement of five new stations as part of a naive observation network to solve for the aggregated $CO_2$ flux, we also considered two additional hypothetical scenarios. In the first scenario we considered an established network. We used the best solution for the five-member network from the available network solutions of the original problem as the starting point for the base network. We then solved for an additional five stations to add to this network. In the second scenario, we considered optimising the uncertainty reduction over only a portion of the country. We chose a region over the eastern side of South Africa which included the largest fossil fuel emitters of $CO_2$ and the areas of greatest biospheric activity. The purpose of these two additional scenarios was to determine how well the GA performed in relation to the IO when the observation footprints of new towers to be added to the network overlapped with those of the new and existing members of the network, or when the prior covariance matrix of the fluxes was made more complex. We hypothesized that these scenarios would lead to IO solutions that would be inferior to those from an optimally parameterised GA, and that the GA would require a greater number of

evaluations in order to reach a stable solution in comparison with the original network design problem.

We present the Bayesian inverse modelling framework in section 3.2, and describe the optimisation algorithms and how these are used in the context of designing a measurement network aimed at reducing the uncertainty in the total flux of $CO_2$ from South Africa. In section 3.3 we present the network solutions obtained by the IO and repeated implementations of the GA algorithm at different specifications for the number of iterations and population members, followed by network solutions of the two additional scenarios. We discuss these results in section 3.4.

## 3.2 Methodology

### 3.2.1 Inverse Modelling Framework

The Bayesian inverse modelling approach to solve for surface fluxes was first implemented by Enting and Mansbridge (1991) based on the approach described in Tarantola (1987). This approach has since been adopted to solve for fluxes at the global scale (Bousquet et al., 1999; Gurney et al., 2003; Baker et al., 2006; Chevallier et al., 2010; Ciais et al., 2010), at the regional scale (Gerbig et al., 2003; Lauvaux et al., 2008; Broquet et al., 2013), and more recently at the city-scale (Bréon et al., 2015; Lauvaux et al., 2016). The inverse modelling framework used in this study is described in detail in Ziehn et al. (2014) and Nickless et al. (2015) and is based on the methodology outlined in Rodgers (2000), Enting (2002), and Tarantola (2005). This approach assumes that the atmospheric concentrations, $\boldsymbol{c}$, can be modelled based on the surface $CO_2$ fluxes, $\boldsymbol{s}$, (hereafter referred to as surface fluxes) based on the following linear relationship:

$$\boldsymbol{c}_{mod} = \mathbf{H}\boldsymbol{s} \tag{3.1}$$

where $\boldsymbol{c}_{mod}$ are the modelled concentrations at the measurement sites, and $\mathbf{H}$ is the sensitivity matrix, derived from the atmospheric transport model, which is driven by inputs derived from a regional climate model. The sensitivity matrix provides the sensitivities of modelled concentrations, $\boldsymbol{c}_{mod}$, to the surface fluxes ($\boldsymbol{s}$) (Enting, 2002; Tarantola, 2005). $\mathbf{H}$ maps the sources onto the observed concentrations and transforms the contribution of these sources from emission rates into $CO_2$ concentrations.

$\boldsymbol{c} - \boldsymbol{c}_{mod}$ represents the observation errors. These errors can be random or systematic, and can be split into measurement errors and modelling errors. Measurement errors in the $CO_2$ observation network, particularly those sites accredited by the

Global Atmospheric Watch, have errors that are typically negligible, usually below 0.2 ppm, and can be assumed to be random. Even if $\boldsymbol{s}$ were perfectly known, errors in $\boldsymbol{c}_{mod}$ would occur due to the errors in atmospheric transport model contained in $\mathbf{H}$, whose parameters are not constrained by the inversion. Modelling errors can occur due to an imperfectly parameterised transport model, and also due to representation discrepancies, where we use a point estimate to represent the concentration of a volume, and due to aggregation, as we homogenised patchy surface fluxes within each grid cell. In reality, the air will pass over only parts of the grid cell and collect information which we relate back to the whole grid cell. Tarantola (2005) shows that modelling errors can be accounted for in the inversion by adding these to the measurement errors represented by uncertainty covariance matrix of the observations, $\mathbf{C}_{\boldsymbol{c}}$.

If it is assumed that the observation errors and surface fluxes have unbiased Gaussian error distributions, the Bayesian cost function can be solved as follows (Enting et al.,, 1995; Rodgers, 2000; Enting, 2002; Tarantola, 2005):

$$J(\boldsymbol{s}) = \frac{1}{2}\left((\boldsymbol{c}_{mod}-\boldsymbol{c})^T\mathbf{C}_{\boldsymbol{c}}^{-1}(\boldsymbol{c}_{mod}-\boldsymbol{c}) + (\boldsymbol{s}-\boldsymbol{s}_0)^T\mathbf{C}_{\boldsymbol{s}_0}^{-1}(\boldsymbol{s}-\boldsymbol{s}_0)\right) \tag{3.2}$$

where $\boldsymbol{c}$ are the observed concentrations, $\mathbf{C}_{\boldsymbol{c}}$ is the uncertainty covariance matrix of observations, $\boldsymbol{s}_0$ is the vector of prior surface flux estimates, and $\mathbf{C}_{\boldsymbol{s}_0}$ is the prior uncertainty covariance matrix of the surface fluxes. In regional inversion problems, the sources are usually represented by a spatial temporal grid of surface fluxes. The number of sources solved for by the inversion are then equal to the number of spatial pixels multiplied by the number of periods for which the emissions are solved. For example, if weekly fluxes are solved for by the inversion, separated into day and night sources, and if the inversion is run over a month, there will be eight periods. Therefore the number of sources solved for by the inversion is equal to the number of pixels multiplied by eight. In our South African region the domain was divided into 50×25 spatial pixels and we solved for weekly fluxes, day and night separately, therefore eight periods per month. The total number of sources which would be solved for by the inversion are 10,000. The prior and posterior uncertainty covariance matrices of these sources had dimensions 10,000×10,000.

The solution for the posterior covariance matrix of the surface fluxes, which we will use to assess the uncertainty reduction of the different network designs, is:

$$\mathbf{C}_{\boldsymbol{s}} = \left(\mathbf{H}^T\mathbf{C}_{\boldsymbol{c}}^{-1}\mathbf{H} + \mathbf{C}_{\boldsymbol{s}_0}^{-1}\right)^{-1} \tag{3.3}$$

$$= \mathbf{C}_{\boldsymbol{s}_0} - \mathbf{C}_{\boldsymbol{s}_0}\mathbf{H}^T\left(\mathbf{H}\mathbf{C}_{\boldsymbol{s}_0}\mathbf{H}^T + \mathbf{C}_{\boldsymbol{c}}\right)^{-1}\mathbf{H}\mathbf{C}_{\boldsymbol{s}_0} \tag{3.4}$$

The solution of the posterior uncertainty covariance matrix of the sources does not depend on the measured concentrations at the site, only on the error covariance matrix of the modelled concentrations and the prior uncertainty estimates of the surface fluxes. This makes it possible, before any concentration measurements are obtained at the site, to assess to what extent a new site can contribute to the reduction in the total uncertainty of the aggregated surface flux estimate, relative to the total uncertainty in this estimate under the base network. In our original network design problem, the base network consisted of two background measurement sites located at Cape Point and Gobabeb. $\mathbf{C}_{\boldsymbol{s}}$ does depend on the transport matrix $\mathbf{H}$, and therefore depends on which stations are in the observation network.

The aggregation errors need to be added to the observation errors, as shown by Kaminski et al. (2001) and Tarantola (2005), and are dependent on the resolution at which the surface fluxes are solved. As shown in Nickless et al. (2015), to determine the aggregation error for each of the candidate measurement sites, the surface fluxes at a higher resolution of $0.6^\circ \times 0.6^\circ$ were used to represent the real, patchy surface fluxes, where these grid cells fit exactly into the grid cells of the surface solved for by the inversion. We could then use the method described in Kaminski et al. (2001) to approximate the aggregation error, where it was shown that the aggregation error $\mathbf{C}_{c,m}$ can be calculated as:

$$\mathbf{C}_{c,m} = \mathbf{H}\mathbf{P}_{-}\mathbf{C}_{s_{0h}}\mathbf{P}_{-}^{T}\mathbf{H}^{T}, \tag{3.5}$$

where $\mathbf{P}_{-} = \mathbf{I} - \mathbf{P}_{+}$ and $\mathbf{P}_{+}$ is the projection matrix which, if multiplied with the high resolution surface flux estimates, $\boldsymbol{s}_{0h}$, produces the lower resolution flux estimates, $\boldsymbol{s}_0$, in positions of the corresponding high resolution fluxes. The solution of $\mathbf{C}_{c,m}$ was obtained for each measurement site, and as a conservative approach, the maximum value of the diagonal was assigned as the aggregation error for that measurement site.

We assigned values of 4 ppm$^2$ as the diagonal elements of $\mathbf{C}_{\boldsymbol{c}}$. For the regional inversion performed by Wu et al. (2013), observation errors were determined to be between 2.9 and 3.6 ppm. We used the slightly lower uncertainty value of 2 ppm since our region occurs in the Southern Hemisphere where the variability in observed $CO_2$ concentrations is lower than in the Northern Hemisphere, and $CO_2$ fluxes are believed to be generally smaller as well. This value accounted for measurement error and errors in the atmospheric transport model. The aggregation errors determined using Equation 3.5 for each site were added to the diagonal elements. Therefore the observation errors were specific to each site.

The transport matrix, $\mathbf{H}$, is derived from a Lagrangian particle dispersion model. We have used the model developed by Uliasz (1994), which we refer to as LPDM. This model is run in backward mode for each of the potential measurement sites. A number of particles are released from the receptor point at regular intervals (every 20 seconds in this case) and tracked backwards in time. The particle counts at the surface and boundaries are recorded at each time step, where the surface is represented as a grid with a resolution of $1.2^\circ \times 1.2^\circ$ over the domain of southern Africa. The derivation of the conversion of particle counts to the influence functions which make up the elements of $\mathbf{H}$ is described in Ziehn et al. (2014) and follows Seibert and Frank (2004).

The elements of the prior uncertainty covariance matrix, $\mathbf{C}_{\boldsymbol{s}_0}$, were determined by the uncertainties in the fossil fuel emissions and natural biospheric fluxes for each surface flux grid cell. The fossil fuel uncertainties were determined from ten realisations of the fossil fuel fluxes from the Fossil Fuel Data Assimilation System (FFDAS) product (Rayner et al., 2010), which is produced at a resolution of $0.1^\circ \times 0.1^\circ$. The fluxes were first aggregated to the network design resolution of $1.2^\circ \times 1.2^\circ$, and then the variances calculated for the ten realisations for each grid cell. The uncertainty values for the bioshperic fluxes, or net ecosystem productivity (NEP), were estimated as the net primary productivity (NPP) as described in Nickless et al. (2015), similar to the approach of Chevallier et al. (2010). These estimates were derived from an assessment of the natural carbon sinks of South Africa (Nickless et al., 2015). The NPP estimates were aggregated to the resolution of $1.2^\circ \times 1.2^\circ$ and these used as the uncertainty estimates of the natural fluxes. The NPP estimates are high across most of the country during the month of January, which is when most of the country has its growing season and receives the most rainfall. Conversely, during the month of July the NPP estimates are small and the majority of activity is concentrated along the Western Cape coast, which receives winter rainfall. The total flux uncertainty is dominated by biospheric flux uncertainty in January, whereas in July it is dominated by fossil fuel flux uncertainty, which is concentrated within a few small regions, mainly near major cities and power stations, spread out across the country. Figure 3.1 provides the spatial distribution of the uncertainty prescribed to the NEP and fossil fuel prior fluxes.

Let $Y$ represent the sum of two surface fluxes, such that $Y = s_i + s_j$, where $s_i$ and $s_j$ are the surface fluxes in grid cells $i$ and $j$ respectively. The variance of Y is equal to

$$Var(Y) = C_{s_{ii}} + 2C_{s_{ij}} + C_{s_{jj}}. \tag{3.6}$$

If we sum over all surface fluxes, the variance of this total is the sum of all the elements of the covariance matrix. The overall uncertainty in surface fluxes was determined by summing over all the elements of $\mathbf{C_s}$ (cost function $J_{Ce}$ ) and then taking the square root, to obtain the uncertainty of the total flux estimate for South Africa expressed as a standard deviation:

$$J_{Ce} = \sqrt{\sum_{i=1}^{n}\sum_{j=1}^{n} C_{s_{ij}}} \tag{3.7}$$

The cost function used to assess the network members was based on the uncertainty reduction calculated as:

$$U_R = 1 - \frac{\hat{J}_{Ce}}{J_{Ce\,base}} \tag{3.8}$$

where $\hat{J}_{Ce}$ is the posterior standard deviation of the total flux estimate of the proposed network containing the additional five stations, and $J_{Ce\,base}$ the standard deviation estimate of the total estimate of the base network, which is determined from the posterior covariance matrix of the surface fluxes if only the existing Cape Point and Gobabeb stations are in the network. The use of the uncertainty reduction as a proportion of the prior uncertainty was used by Rayner (2004). Here the trace of $\mathbf{C_s}$ was used instead of the sum of the covariance elements to represent the total uncertainty. We performed a sensitivity analysis that compared these approaches, and found that the resulting network solutions were similar. A more generalised approach to optimal experimental design in inverse problems in provided in Haber et al. (2008), where they use the trace of the posterior covariance matrix, and show how this can be used to optimise measurement networks for inverse problems using alternative methods of regularisation.

The candidate stations and the existing background stations are displayed in Figure 3.2.

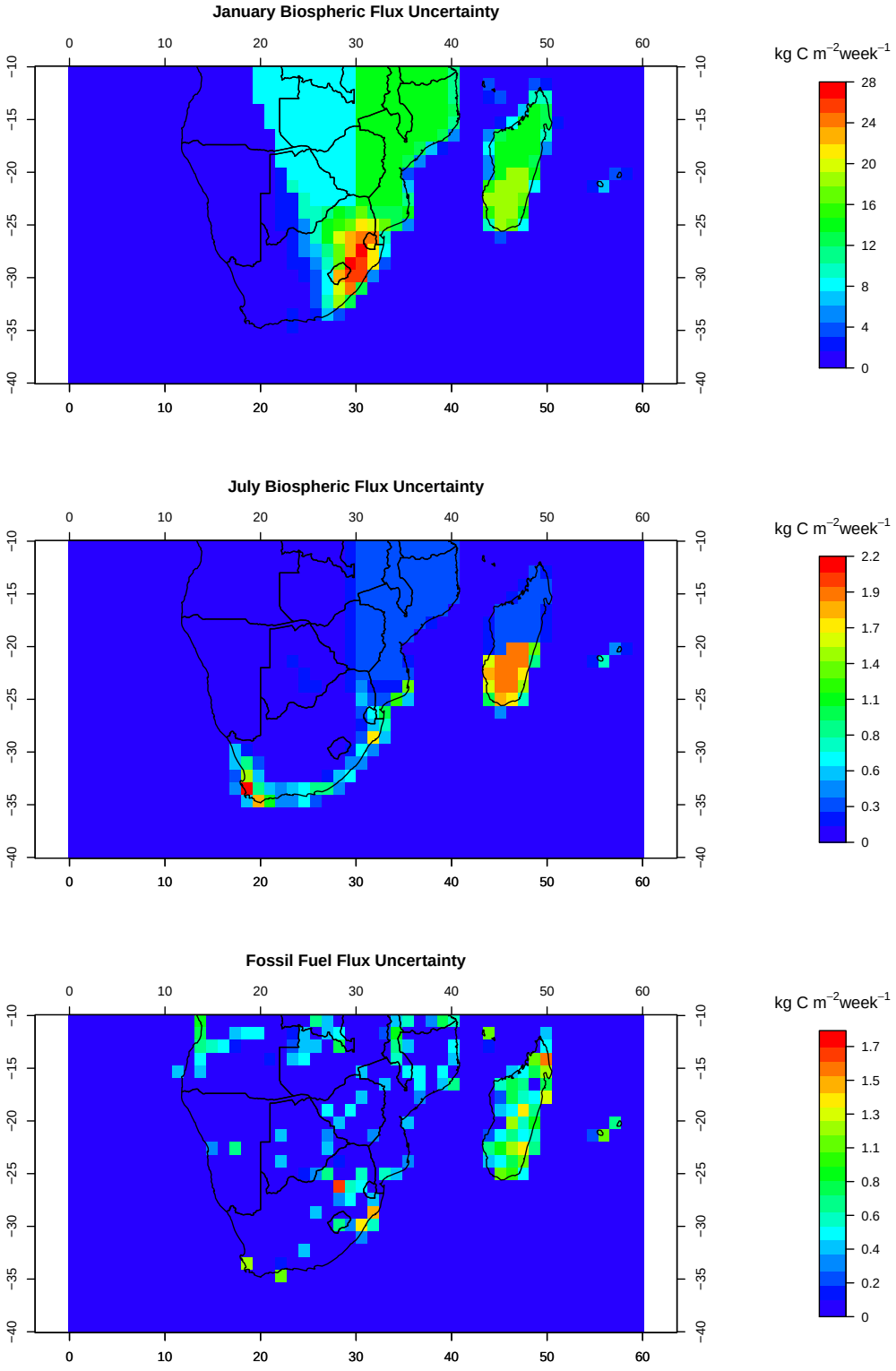


Figure 3.1: Prior uncertainty assigned to the net ecosystem productivity (NEP) fluxes in January and July, and the uncertainty in the fossil fuel fluxes, expressed as standard deviations (g C $m^{-2}$ $week^{-1}$)

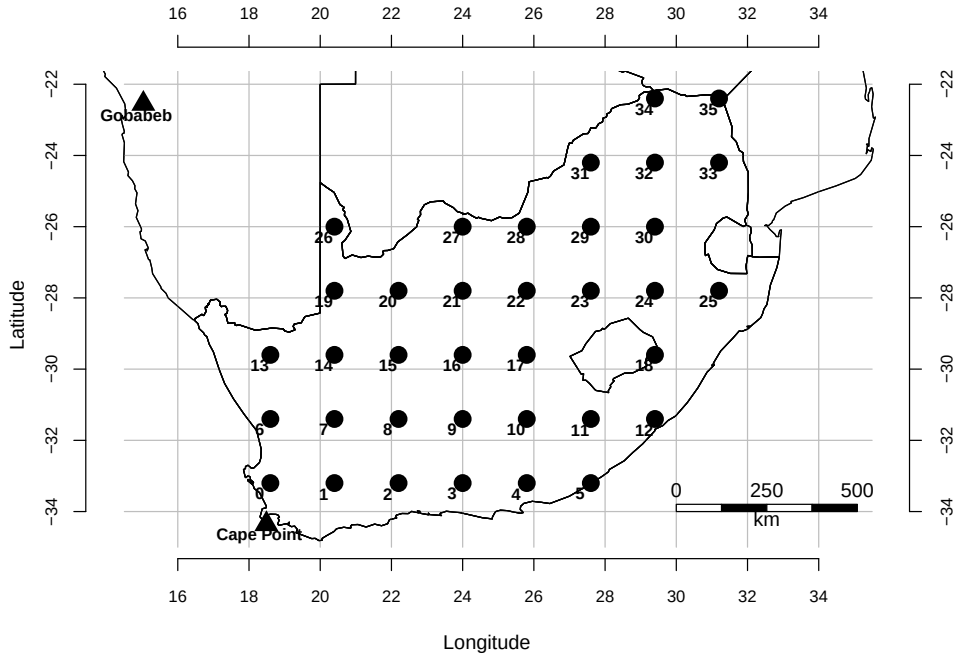


Figure 3.2: Location of candidate stations within South Africa together with the existing background stations at Cape Point and Gobabeb. Of these candidate stations, five locations are required for the placement of new monitoring sites for atmospheric $CO_2$ concentrations to solve the original network design problem.

## 3.2.2 Optimisation Routines

### 3.2.2.1 Incremental Optimisation

A description of the use of Incremental Optimisation (IO) to solve general optimisation problems is provided by Hartline and Sharp (2006). IO for $CO_2$ monitoring network design problems was proposed by Patra and Maksyutov (2002), where the addition of new stations to an existing measurement network was considered. The optimal network was thought of as a problem which consisted of several subproblems, where each was solved incrementally. Given an existing network, the first subproblem was to determine the first station to add to the network that would result in the greatest reduction in uncertainty. The candidate list of stations was derived from equally spaced locations within South Africa; a total of 36 stations (Figure 3.2). Adding each of the candidate stations in turn to the base network, the cost function was calculated, and the candidate station yielding the greatest uncertainty reduction was removed from the candidate list and added to the base network list. This procedure was repeated until the desired network size was reached. In this case the network size would be seven - two existing and five new stations.

The IO routine results in an evolution of the network solution, allowing the user to determine the best station to add to the network at each iteration, as well as the uncertainty reduction that each of the unselected stations would have had, providing a list of best alternatives. In addition, the IO routine is computationally inexpensive. This is an advantage due to the already high computational costs of solving for the posterior covariance matrix that would need to be calculated for each potential solution.

#### 3.2.2.2 Genetic Algorithm

The genetic algorithm (GA) draws on the concept of 'survival of the fittest' from evolutionary biology to determine the best solution for a numerical optimisation problem, and has a wide range of applications (Chambers, 2002). GA optimisation has been used to solve various network design problems, such as placement of wind turbines to maximise the power output (Grady et al., 2005) and the design of a telecommunications network to support the expected communications traffic between pairs of connections (Berry et al., 1999). For our optimisation problem the solution would be a list of stations to add to the existing network to best reduce the surface flux uncertainty. Each of the five stations in the network solution represents a parameter in the algorithm. The GA procedure carried out in this study is based on Rayner (2004).

The GA does not evolve a single solution, but rather a population of solutions. The population is made up of a number of potential five station solutions for the network problem. Each solution represents a member of the population. Through a process of culling, mutation and reproduction, population members are lost, evolved and replicated for the next iteration, all based on pseudo-random numbers generated from the uniform distribution. The algorithm begins by randomly generating a population of solution members of size N, where each solution consists of a list of five stations, based on the candidate list of stations; the same candidate list used by the IO. For this network design, candidate stations may appear only once in a solution. The first part of a GA iteration is the pairwise swap over of parameter values (i.e. stations) between two randomly selected population members, determined by whether a random uniform number is between zero and a pre-selected cross-over probability. Individual parameter values are also changed based on a random uniform number and the specified mutation probability. Based on a criterion for fitness, calculated as:

$$F = 1 - \frac{r - 0.5}{N} \tag{3.9}$$

where $r$ is the ordinal ranking of the member according to each member's cost function and $N$ is the population size, solutions are removed (or culled) from the population of solutions if a pseudo-random number generated from the uniform distribution for each of the population members is greater than $F$. The resulting probability of a member being culled is therefore 1 - $F$.

Once the culling procedure is completed, new members are added to the population through a process of reproduction until the population size is back to $N$. The current population members are repeated if a randomly generated number is below the member's fitness score. The probability of a member being replicated in the new generation is therefore equal to $F$. Sampling of the members is with replacement, so those population members with good fitness scores will have a better chance of appearing multiple times in the population of solutions. To ensure that the diversity of the solutions in the population is high enough to avoid the algorithm getting stuck at a local extrema, an additional process of mutation is applied to the population members. Here a random uniform number is generated for every parameter of each population member. If the value is below the mutation threshold, then the current value of the parameter is replaced from a randomly selected parameter from the candidate list of stations. We used the recommended mutation rate of 0.1 suggested by Rayner (2004). This concludes one iteration of the GA. The algorithm iterates until the pre-determined number of iterations is achieved.

Elitism is maintained, so that set of five candidate stations with the highest fitness is replicated unchanged into the next generation of population members at every iteration. Once the algorithm is complete, the member of the population with the best score is selected as the final solution.

### 3.2.3 Optimal Network Comparisons

For two representative months, January for summer and July for winter, the transport matrix, $\mathbf{H}$, was derived from the particle counts generated by LPDM, and the prior covariance matrices for weekly surface fluxes, $\mathbf{C}_{\boldsymbol{s}_0}$, for these periods were constructed. The IO routine was run to determine the optimal network for the two months separately. The optimisation was repeated, using the GA under different specifications of the number of iterations and the population size. Since the outcome of the algorithm has the potential to be inconsistent from run to run, due to the use of pseudo-random numbers, the algorithm was run five times for each configuration. The purpose of this was to demonstrate some of the variability in the GA solution set. The configurations considered were population sizes of 50 or 100 with either 50, 75 or 100 iterations.

These configurations therefore result in GAs with different numbers of evaluations. For example, a GA with 50 population members and 50 iterations would have 2,500 evaluations whereas a GA with 100 population members and 100 iterations would have 10,000 evaluations. We expected the solution set from the GA to stabilise as the number of evaluations increased. The time taken to run each of the algorithms was recorded in order to compare the efficiency of the algorithms.

The utility (or fitness) of a network of monitoring stations was assessed by means of the percentage uncertainty reduction in the total posterior flux estimate for the region relative to the uncertainty of the base network, as calculated from Equation 3.8. We expected the IO to obtained an inferior solution to the GA, and we wanted to assess how the IO solution compared in fitness to the best available GA solution. How similar two networks were in terms for their placement was assessed using the dissimilarity index (DI). How similar two network solutions were was of interest, because if two solutions had identical uncertainty reductions, but very different placement of stations, considerations such as the cost of establishing the network and the feasibility of the network in practice would need to be used to make a decision on which network would be implemented. The DI was calculated as the sum of the distance to the nearest neighbour in the compared network, over all the members in the pair of assessed networks.

$$DI = \sum_{i=1}^{5} \min_{j} \sqrt{\Delta x_{ij}^2 + \Delta y_{ij}^2} + \sum_{j=1}^{5} \min_{i} \sqrt{\Delta x_{ij}^2 + \Delta y_{ij}^2} \tag{3.10}$$

where i and j $\in$ [1,2,3,4,5], and $\Delta x_{ij}^2$ and $\Delta y_{ij}^2$ are the squared differences between the Cartesian coordinates of the $i^{th}$ station in the first network and the $j^{th}$ station in the second network. The first term in the DI calculation is the sum of the nearest neighbour distances between each site in the first network solution and its nearest neighbour in the second solution set (a sum of five nearest neighbour distances). The second term sums the nearest neighbour distances between each station in the second network solution and its nearest neighbour in the first network solution (a sum of five nearest neighbour distances). Therefore the DI is the sum of ten nearest neighbour distances when comparing two five-member networks.

In cases where the two networks compared were the same, the index results in a value of zero. Networks which did not contain exactly the same members would always have a DI of greater than zero. The index increases as the networks become more dissimilar in space. This provides a one-number measure of network similarity that can consistently be used for the network comparisons, provided each solution

consists of the same number of stations, and allows for an objective assessment of how different the positioning of sites are between two network solutions which may not be obvious to the eye. The index provides a measure of distance between solutions in terms of kilometres. The distribution characteristics of the DI if it were used to compare two randomly selected five-member networks are provided in Appendix A.

To assess the degree to which sites in a particular network solution were clumped together, we calculated the centroid of the spatial points from each network solution, and calculated the mean distance between each station in the solution and this centroid. The centroid provides additional information on where in South Africa the stations were concentrated. We measured the degree of clumping or clustering of stations in order to assess if the network solutions were concentrated over a particular region, or if the stations in the network solution were spread over the domain.

### 3.2.4 Additional Scenarios

Optimisations were performed for the original network problem, which required five additional stations to add to the existing background stations at Cape Point and Gobabeb. In this scenario it would be expected that the optimal solution would be one where the observation footprints of the towers are not overlapping, in order to view us much of the uncertainty across the country as possible. Both GA and IO should be able to achieve solutions which we would not expect to differ greatly, but as the optimisation problem was more complex than the original problem, the GA could potentially find solutions that were inaccessible through the IO.

We considered two additional hypothetical scenarios. In the first of these scenarios we considered the situation which may be in existence once the five new stations are established. The base network under this scenario had seven stations (two background stations and five new stations), and the purpose of the network design was to find a solution for the placement of five additional stations, to take the network to 12 stations. We used the best solution out of all available solutions from the original network problem for these five existing stations, and the optimisation routine was used to solve for the five-member network to add to this established network. Under these conditions, the new stations would more likely have observation footprints which were overlapping with those from the new elements and old elements of the network. The observation footprint of a site would depend on the prevailing atmospheric conditions around that site, described by the sensitivity matrix. Compared to the original network problem, which aimed to reduce the uncertainty of the total

flux estimate that was almost entirely unconstrained by the base network, the established network design problem had the objective of applying additional constraint to a network that already covered the main sources of uncertainty. Therefore, the aim of the established network design problem was to plug the holes in an existing network. The prior covariance matrix of the fluxes would be more complex under this scenario and we wanted to determine if the GA, which considers the global parameter solution, would be better suited than the IO to find an optimal solution under these circumstances, where assessing the additional stations simultaneously rather than sequentially could be an advantage.

The second hypothetical scenario was to adjust the original network problem so that the uncertainty reduction resulting from the network was optimised over a subregion of the country, rather than over the total land surface of South Africa. This was achieved by summing the variance and covariance terms of the posterior covariance matrix, $\mathbf{C}_{\boldsymbol{s}}$, for only those elements related to the subregion. The region we selected comprises a large grid on the eastern half of South Africa which includes the largest fossil fuel emitters and the largest biospheric sinks of $CO_2$. Under this scenario, the observation footprints of the measurement towers would be closer and may overlap in order to view the uncertainty over this subregion. The optimal network solution should be dependent on how much overlap (i.e. redundancy) can be afforded. A solution may require two sites close to each other in order to get a more comprehensive view of a source with large uncertainty. There would then be a trade-off between reducing the large uncertainty from this source and the lost opportunity to view elsewhere in the domain not already covered by the network. Stations did not necessarily need to be located within the subregion to reduce the subregion uncertainty. We wanted to assess if the GA would be better suited to optimising the overlap between observation footprints compared with the IO method to obtain a better uncertainty reduction in the overall flux in the subregion.

### 3.2.5 System configuration

The optimisation routines were carried out using Python version 2.7 on a desktop computer with a Linux operating system and a Intel Core i7-3770K processor running at 3.50 GHz with four cores and eight logical processors, and 16 gigabytes of RAM.

## 3.3 Results

### 3.3.1 Original Network Design Problem

Table 3.1 gives the uncertainty reduction results of the optimal network solutions under the different algorithm runs, as well as the mean distances to the centroid, DI's with the IO solution, and run times. The uncertainty reduction ranged between 76.5% and 78.8% in January, and between 42.9% and 43.3% in July. The IO, for both January and July, did not find the global maximum, but a local maximum with uncertainty reduction very close to the best GA solution, differing by an absolute amount of only 0.5% in January and 0.3% in July. As these are percentage uncertainty reductions, given all of the assumptions needed for the inversion solution, networks differing by 1%, or even up to 5%, in uncertainty reduction may be considered to have the same utility. The uncertainty reductions obtained by the different GA network solutions were very similar, a difference of only 0.4%. As expected, the consistency in the GA solutions increased as the number of evaluations increased. Comparing between months, the consistency of the GA solutions in July was much higher compared with the GA solutions in January.

The mean distance to the centroid will reduce as all sites are located nearer and nearer to a central point. As more sites are located far from the central point, this metric will increase. The mean distances to the centroid for the IO solution when compared with the best GA result were not the same for either January or July, indicating that the clumping of stations differed between the IO and GA solutions, with the best GA solutions having slightly higher values for the mean distance to the centroid indicating more spread in the placement of sites. The mean distance to the centroid was generally greater for January solutions compared with July solutions, indicating that stations were more spread out for the network solutions obtained for the winter month than for the summer month. We would expect this as the network would need to have stations concentrated on the eastern side of South Africa to cover both the high uncertainty in the biospheric fluxes occurring here during summer, and the large contribution of fossil fuel emissions. In the winter months the uncertainty would be mainly due to fossil fuel emissions, and therefore the network would need to view the cities such as Johannesburg, Pretoria and Durban, and also Cape Town to the south west of the country. Therefore sites would be spread out in order to reduce the fossil fuel emission uncertainty.

In January and July, the dissimilarity index for IO was greater than zero when compared with the best GA result, with a value of 772 km in January and 879 km

in July. For the current set of candidate sites, a comparison between two randomly generated networks would on average result in a dissimilarity index of 2763 km, with a standard deviation of 720 km, determined through simulation methods. A histogram showing the distribution of the mean dissimilarity index for two random networks is given in the appendix. The lower limit of the normal range (approximately the $2.5^{th}$ percentile) for the DI of randomly generated networks is 1350 km. The DI's obtained between the GA solutions and the IO solution were all below this value, which suggests that IO and GA solutions were more similar than two randomly selected solutions (Table 3.1). This provides evidence that both optimisation routines were aiming towards similar solutions.

The time taken to obtain a result ranged between 5 and 18 times longer under the GA compared with under the IO, with the largest run times associated with a population size of 100 and 100 iterations. Increasing the population size for the GA from 50 to 100 or increasing the iterations from 50 to 100 led to roughly doubling of the run time. Increasing both the number of iterations and population size to 100 resulted in a run time between 3.6 and 3.8 times longer than the initial GA setup. Therefore the computational cost of even the lowest configured GA is substantially larger compared with the IO routine.

The GA run under the initial setup of 50 iterations and 50 population members produced consistent network solutions for July but not for January, where all five of the July GA solutions were the same but only two of the five January solutions were the same. Greater inconsistencies were observed in solutions for January across the different GA configurations. In January the spatial distribution of fluxes, particularly biospheric fluxes, was far more dispersed across the whole of South Africa, and the prior uncertainties in the surface fluxes were much larger in January compared with July. This result is illustrated using the heat maps presented in Figures 3.3a and 3.3b. Much larger variability in the DI's is apparent when comparing GA solutions under fewer population members and iterations compared with GA solutions under larger population sizes or with greater number of iterations, as indicated by the lighter blocks in the heat map for January in the top right hand corner. This implies that for the month of January, the GA was converging towards a solution under larger population sizes and number of iterations. This convergence occurred more readily for July, where the heat map already showed lighter blocks compared with the initial setup just from increasing the iterations from 50 to 75. Across the different configurations of the GA the DI values for July were always lower compared with those for January (Figures 3.3a and 3.3b).

The best solution was not obtained under the cheapest GA configuration for either January or July. For the month of January when the number of iterations was increased to 75, two of the five GA runs converged to this solution, but when increased to 100 iterations, three of the five solutions converged to this solution. As expected, increasing the population size to 100 improved the chances of obtaining this best solution relative to the initial configuration, and this probability also increased as the number of iterations increased. But only two of the five solutions obtained the best solution when the population size and number of iterations were 100. Under this configuration the DI values between the network solutions were the lowest relative to comparisons within any of the other GA configurations (Figure 3.3a) Therefore, even when these two GA parameters were set relatively high, there was no guarantee of obtaining the best solution under the January scenario, although the differences between network solutions did decrease. In January the surface flux uncertainty was high, relative to July, and dispersed unevenly across South Africa, particularly concentrated in the northern and eastern parts of the country where the greatest biological activity takes place in Summer, but also where the large cities are located. Figures 3.4a and 3.4b provide the locations of all the sites from the different network solutions, together with the NPP surface fluxes (representative of the biospheric flux uncertainty) for January and July respectively. In January the sites of the different solutions are concentrated towards the central and eastern parts of the country, supporting the lower mean distances to the centroid obtained in January. Some sites are consistently selected, such as site 27 located at the border of South Africa and Zimbabwe, or site 11 located south of Lesotho. Other sites appear far less frequently, such as site 28 and site 10. Both these sites are located one step away from the most frequently selected sites, and therefore would be in a position to view much of the same uncertainty. In general, the network solutions have placed sites next to locations with the highest uncertainty in either fossil fuel or biogenic surface fluxes.

In July, the best GA solution was obtained by increasing either the number of iterations or the population size. By increasing the number of iterations to 75, four out of the five network solutions resulted in the best GA solution. Under the different configurations with iterations or population size greater than 50, between two and four of the network solutions converged to the best solution, with the maximum configuration resulting in four out of five network solutions as the best solution. Under the July scenario, the overall uncertainty in the surface fluxes was much lower compared with January, and the largest uncertainties were concentrated towards the

south west, where the greatest amount of biological activity would be taking place in winter and where the city of Cape Town is located, but also around the cities of Johannesburg and Pretoria in the central part of the country, and Durban to the south east. Figure 3.3b illustrates the network solutions for July. There was far less variability in the placement of stations compared with January. The stations were now split between those that view uncertainty around Cape Town and in the northern parts of the Western Cape province, where fossil fuel emission uncertainty and biogenic flux uncertainty are both high, and between those on the eastern side of the country, located near fossil fuel sources.

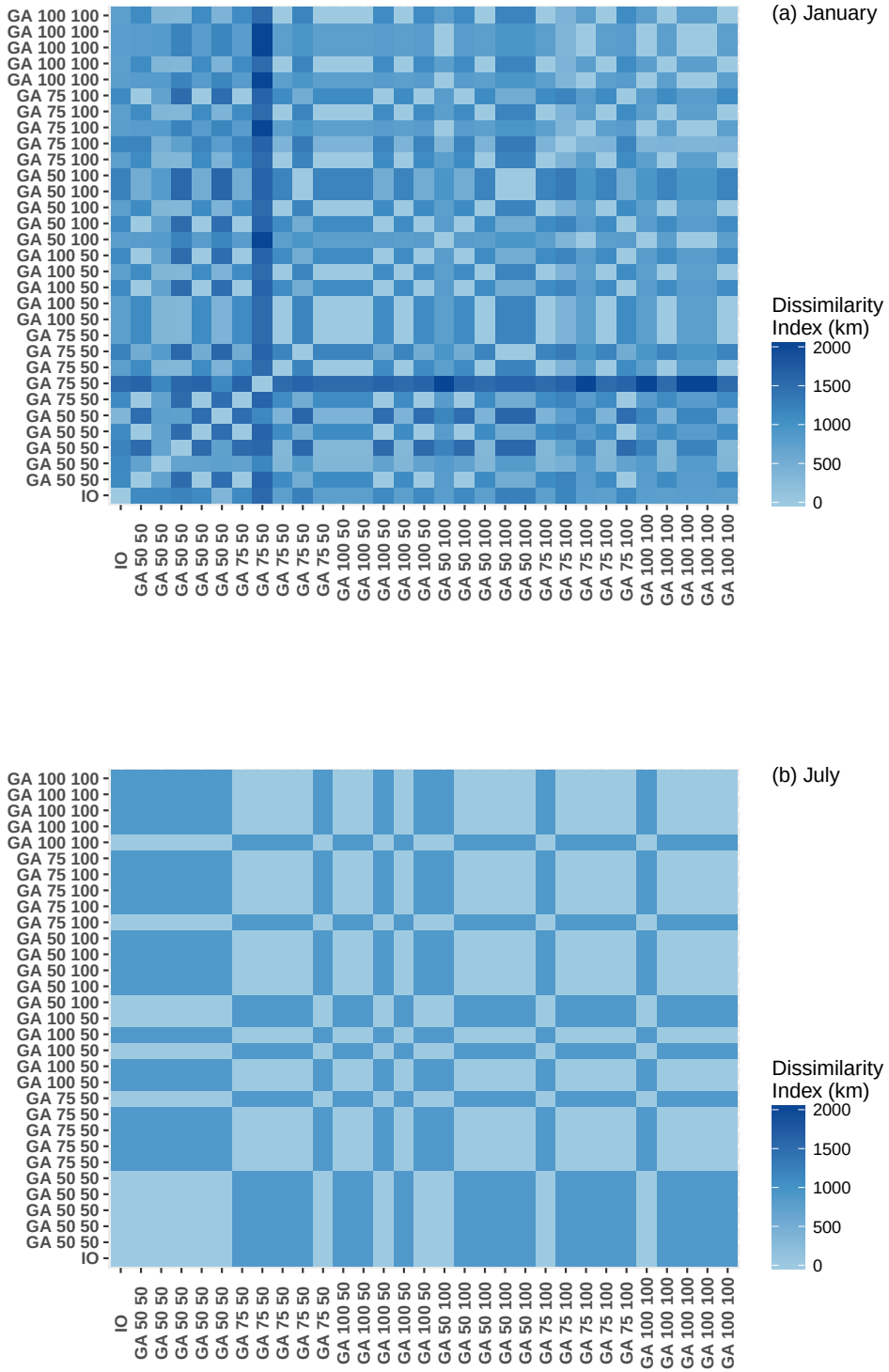


Figure 3.3: Heat maps displaying Dissimilarity Indices (DIs) for the January (top) and July (bottom) optimal network solutions. Network solutions which have similar placement of stations in space will have DIs closer to zero. The abbreviated names for the GA runs are the same as for Table 3.1.

Table 3.1: Table of uncertainty reductions achieved by each network in the original network design problem solving for five station locations, together with the network's centroid point, the mean distance to centroid, dissimilarity index, and running times. Results are presented for the IO result, and results under the GA with 50, 75, and 100 iterations together with 50 population members (GA 50 50, GA 75 50, GA 100 50), and with 50, 75 and 100 iterations together with 100 population members (GA 50 100, GA 75 100, GA 100 100)

| | January | | | | | July | | | | |
|---|---|---|---|---|---|---|---|---|---|---|
| Algorithm Specification | Uncertainty kt C week$^{-1}$ | Uncertainty reduction (%) (mean) | Centroid, mean distance to centroid (km) | DI with IO (km) | Run time (min) | Uncertainty kt C week$^{-1}$ | Uncertainty reduction (%) (mean) | Centroid, mean distance to centroid (km) | DI with IO (km) | Run time (min) |
| Prior | 2058.99 | | | | | 102.79 | | | | |
| IO | 447.21 | 78.28 | (27.6, -28.88), 303 | 0 | 14 | 58.66 | 42.933 | (24, -29.96), 502 | 0 | 12 |
| GA 50 50 | 438.09 | 78.723 | (27.6, -28.52), 310 | 1115 | 68 | 58.66 | 42.933 | (24, -29.96), 502 | 0 | 75 |
| GA 50 50 | 440.25 | 78.618 | (27.6, -28.88), 364 | 1132 | 68 | 58.66 | 42.933 | (24, -29.96), 502 | 0 | 74 |
| GA 50 50 | 459.35 | 77.69 | (26.88, -28.88), 363 | 1206 | 65 | 58.66 | 42.933 | (24, -29.96), 502 | 0 | 74 |
| GA 50 50 | 438.09 | 78.723 | (27.6, -28.52), 310 | 1115 | 73 | 58.66 | 42.933 | (24, -29.96), 502 | 0 | 78 |
| GA 50 50 | 442.42 | 78.513 (78.453) | (27.24, -29.24), 334 | 371 | 68 | 58.66 | 42.933 (42.933) | (24, -29.96), 502 | 0 | 78 |
| GA 75 50 | 438.09 | 78.723 | (27.6, -28.52), 310 | 1115 | 98 | 58.29 | 43.294 | (24.72, -29.6), 507 | 879 | 109 |
| GA 75 50 | 483.83 | 76.502 | (27.24, -28.52), 352 | 1542 | 97 | 58.29 | 43.294 | (24.72, -29.6), 507 | 879 | 109 |
| GA 75 50 | 436.23 | 78.813 | (27.24, -28.88), 357 | 772 | 105 | 58.29 | 43.294 | (24.72, -29.6), 507 | 879 | 110 |
| GA 75 50 | 438.66 | 78.696 | (27.24, -28.88), 326 | 1226 | 100 | 58.29 | 43.294 | (24.72, -29.6), 507 | 879 | 109 |
| GA 75 50 | 436.23 | 78.813 (78.309) | (27.24, -28.88), 357 | 772 | 99 | 58.66 | 42.933 (43.222) | (24, -29.96), 502 | 0 | 110 |
| GA 100 50 | 436.23 | 78.813 | (27.24, -28.88), 357 | 772 | 130 | 58.29 | 43.294 | (24.72, -29.6), 507 | 879 | 159 |
| GA 100 50 | 436.23 | 78.813 | (27.24, -28.88), 357 | 772 | 128 | 58.29 | 43.294 | (24.72, -29.6), 507 | 879 | 144 |
| GA 100 50 | 438.09 | 78.723 | (27.6, -28.52), 310 | 1115 | 133 | 58.66 | 42.933 | (24, -29.96), 502 | 0 | 144 |
| GA 100 50 | 436.23 | 78.813 | (27.24, -28.88), 357 | 772 | 130 | 58.29 | 43.294 | (24.72, -29.6), 507 | 879 | 144 |
| GA 100 50 | 438.09 | 78.723 (78.777) | (27.6, -28.52), 310 | 1115 | 133 | 58.66 | 42.933 (43.15) | (24, -29.96), 502 | 0 | 148 |
| GA 50 100 | 436.24 | 78.813 | (27.6, -28.16), 363 | 802 | 138 | 58.66 | 42.933 | (24, -29.96), 502 | 0 | 148 |
| GA 50 100 | 438.09 | 78.723 | (27.6, -28.52), 310 | 1115 | 132 | 58.29 | 43.294 | (24.72, -29.6), 507 | 879 | 147 |
| GA 50 100 | 436.23 | 78.813 | (27.24, -28.88), 357 | 772 | 105 | 58.29 | 43.294 | (24.72, -29.6), 507 | 879 | 146 |
| GA 50 100 | 438.66 | 78.696 | (27.24, -28.88), 326 | 1226 | 100 | 58.29 | 43.294 | (24.72, -29.6), 507 | 879 | 155 |
| GA 50 100 | 438.66 | 78.696 (78.748) | (27.24, -28.88), 326 | 1226 | 99 | 58.29 | 42.933 (43.15) | (24.72, -29.6), 507 | 879 | 170 |
| GA 75 100 | 436.23 | 78.813 | (27.24, -28.88), 357 | 772 | 189 | 58.66 | 42.933 | (24, -29.96), 502 | 0 | 223 |
| GA 75 100 | 437.06 | 78.773 | (27.24, -28.52), 396 | 1173 | 194 | 58.29 | 43.294 | (24.72, -29.6), 507 | 879 | 215 |
| GA 75 100 | 436.24 | 78.813 | (27.6, -28.16), 363 | 802 | 196 | 58.29 | 43.294 | (24.72, -29.6), 507 | 879 | 214 |
| GA 75 100 | 436.23 | 78.813 | (27.24, -28.88), 357 | 772 | 210 | 58.29 | 43.294 | (24.72, -29.6), 507 | 879 | 218 |
| GA 75 100 | 438.09 | 78.723 (78.787) | (27.6, -28.52), 310 | 1115 | 209 | 58.29 | 43.294 (43.222) | (24.72, -29.6), 507 | 879 | 233 |
| GA 100 100 | 436.24 | 78.813 | (27.6, -28.16), 363 | 802 | 252 | 58.66 | 42.933 | (24, -29.96), 502 | 0 | 280 |
| GA 100 100 | 436.23 | 78.813 | (27.24, -28.88), 357 | 772 | 254 | 58.29 | 43.294 | (24.72, -29.6), 507 | 879 | 284 |
| GA 100 100 | 436.24 | 78.813 | (27.6, -28.16), 363 | 802 | 257 | 58.29 | 43.294 | (24.72, -29.6), 507 | 879 | 282 |
| GA 100 100 | 436.24 | 78.813 | (27.6, -28.16), 363 | 802 | 254 | 58.29 | 43.294 | (24.72, -29.6), 507 | 879 | 286 |
| GA 100 100 | 436.23 | 78.813 (78.813) | (27.24, -28.88), 357 | 772 | 256 | 58.29 | 43.294 (43.222) | (24.72, -29.6), 507 | 879 | 287 |

### 3.3.2 Established Network Design Problem

In the established network scenario, the percentage uncertainty reduction achieved by each network solution was lower compared with the original network problem. In January the uncertainty reduction was approximately 78% for the original network problem, whereas for the established network solution, the reduction in the uncertainty remaining after a five-member network was established could only be improved by 50% (Table 3.2). Similarly in July, the original network solution was able to achieve an uncertainty reduction in the region of 43%, but once a network was established the remaining uncertainty in the total flux solution could only be reduced by 14%. This shows the diminishing returns of adding more stations to the network.

For the month of January the GA procedure was able to achieve a better solution by 3% compared to the solution obtained by IO. The GA configured with 50 iterations and 50 population members obtained the best solution as well as the worst solution with an uncertainty reduction of 45.2%. The IO solution reduced the uncertainty by 46.9%, whereas the best solution GA was able to obtain an uncertainty reduction of 49.9% (Table 3.2). This solution was obtained more reliably when the number of iterations and population size were at higher settings, with all GA configurations with 100 iterations obtaining the best solution. In July the GA always found a better solution compared with IO. The IO obtained a solution with 13.7% uncertainty reduction, whereas the solutions from the GA showed very little variation and all solutions with 14.2% uncertainty reduction. Figure 3.5 shows the cumulative influence of the surface sources on the concentration observations observed at the sites in the best solution for each month and for each of the scenarios. These maps show which sources (i.e. which of the surface pixels) are in view of the measurement sites in the best solution. As expected, the observation footprints of the measurement towers for the solutions under the established network design problem showed some overlap; more so than under the original network design problem (Figure 3.5). Under the established network design solutions, there is greater coverage of the coastal cities, such as Port Elizabeth and Durban.

The mean distances to the centroid and the map of the network solution show that more clustering of the stations towards a central point occurred in the January solutions than the July solution, with mean distances to the centroid of between 295 and 338 km in January verses 526 km on July, but the clustering in January was to a lesser extent compared with that of the original network problem which was between 303 and 357 km (Table 3.2 and Figure 3.6). The map of the January solutions

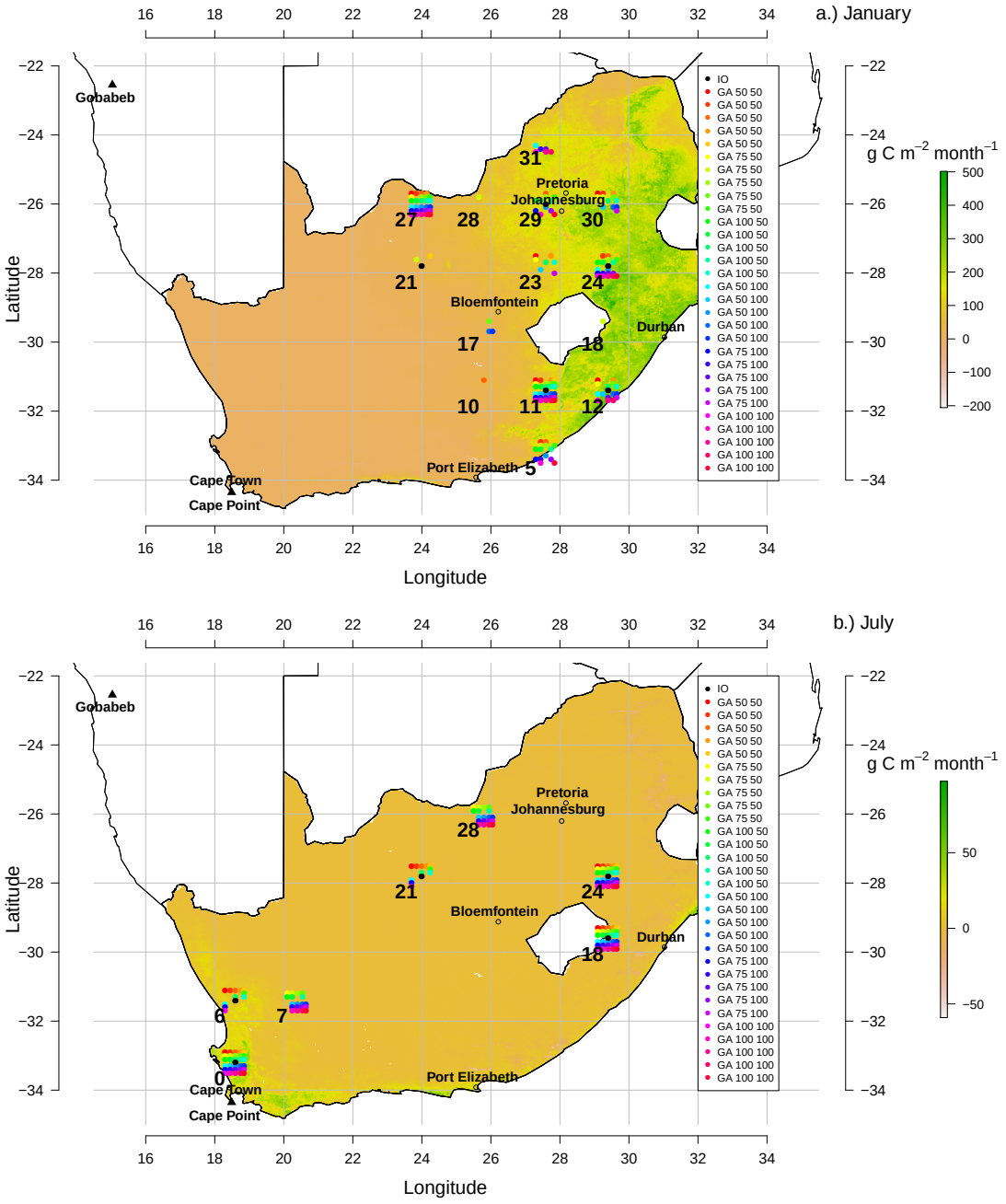


Figure 3.4: Maps of the optimal network locations for (a) January and (b) July from each of the algorithm runs, overlaid on the net primary productivity (NPP) (g C m$^{-2}$ month$^{-1}$). Code numbers for the GA solutions are the same as for Table 3.1. Numbers appearing on the maps are the station locations which have appeared in one or more network solutions. Black triangles - existing network stations of Cape Point and Gobabeb. Open circles - Major South African. Black closed circles - IO network solution. Coloured closed circles - GA solutions. Each colour represents a different GA solution. Points are laid out row by row, with the top row corresponding to the GA 50 50 and the bottom corresponding to the GA 100 100.

indicates that stations tended to be placed along the central vertical line of the country, between the area of lowest uncertainty and the area of highest uncertainty, with one station located near the largest cities (Johannesburg and Pretoria) and power generation sites (Figure 3.6). The July solutions also tended to place stations along a boundary, this time between areas of high winter biogenic activity in the Western Cape and low activity in the rest of the country, with two stations located near the cites of Johannesburg and Pretoria; one north and one south of these two cities (Figure 3.6).

The pattern of DI values revealed that there was much more consistency between the solutions from the GA compared with the original network design problem, with more dissimilarity occurring in January, when biospheric flux uncertainty was higher and more spread out across the eastern side of the country (Figure 3.7). The DI values for the July solutions show almost no variation between the network solutions, with GA solutions for iterations at 75 or above, or population size at 100, all resulting in the same network solution.

Run times to complete the optimisation routines were slightly higher compared with the original network problem, as the sensitivity matrix ($\mathbf{H}$) and observation error covariance matrix ($\mathbf{C_c}$) for the established scenario were larger in size due to a larger number of monitoring stations, and therefore larger number of hourly observations. The relative time differences to complete an optimisation between the IO and the different GA configurations remains similar to the original network problem.

In both January and July, under the established network scenario, the GA was able to find a better solution compared with the IO method, but the IO was within 3% of the uncertainty reduction achieved by any of the GA solutions. Only the GA at the lowest configuration had one solution with lower uncertainty reduction compared with the IO for the month of January. The improvement of the GA best solution over the IO was small; more so in July where the regions of high uncertainty were concentrated over small areas spread out across the domain. The spatial differences in these solutions were small, as evidenced by the small DI values.

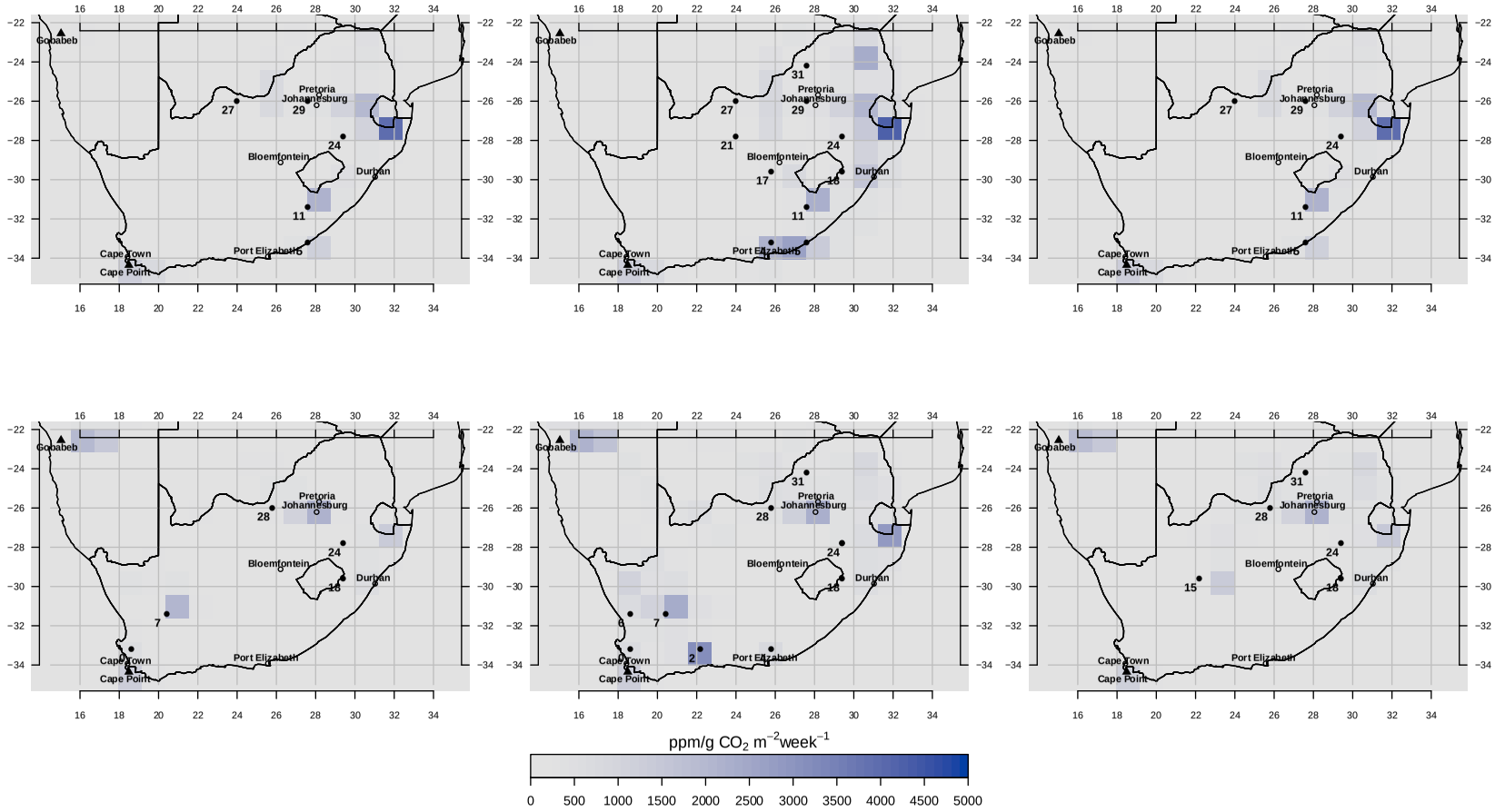


Figure 3.5: Cumulative sensitivities (ppm / g $CO_2$ m$^{-}$2 week$-$1 ) over all sites under the solution with highest uncertainty reduction for each scenario, where pixels with large sensitivities indicate areas likely viewed by more than one station. The top row shows the sensitivities for the best solution for January under the original network design problem (left), established network scenario (middle), and subregion scenario (right). The bottom row shows the sensitivities for July.

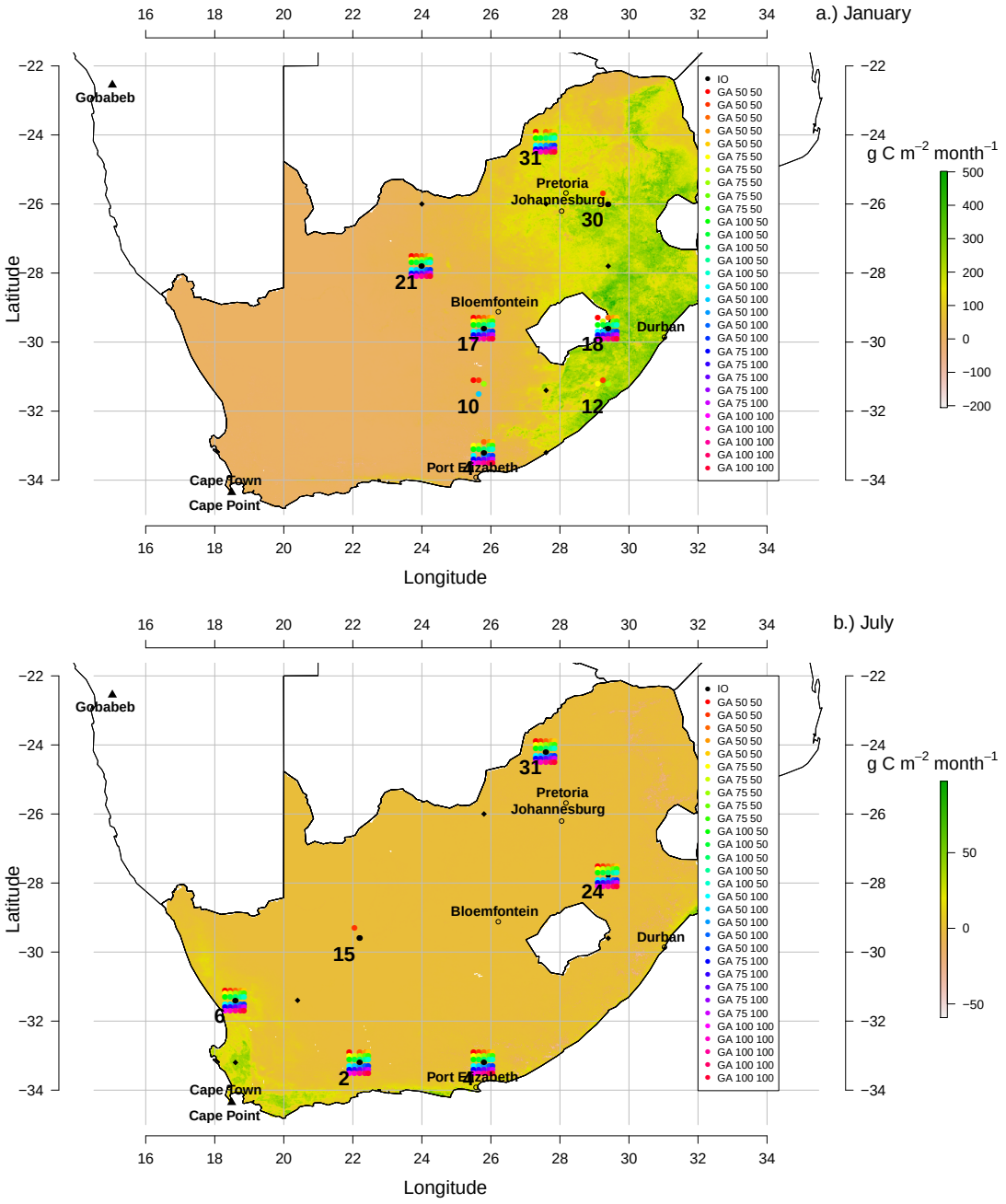


Figure 3.6: Optimal network locations for extended network case for (a) January and (b) July from each of the algorithm runs, overlaid on the net primary productivity (NPP) (g C m$^{-2}$ month$^{-1}$). Code numbers for the GA solutions are the same as for Table 3.2. Numbers appearing on the maps are the station locations which have appeared in one or more network solutions. Black triangles - existing network stations of Cape Point and Gobabeb. Open circles - Major South African. Black closed circles - IO network solution. Coloured closed circles - GA solutions. Each colour represents a different GA solution. Points are laid out row by row, with the top row corresponding to the GA 50 50 and the bottom corresponding to the GA 100 100.

Table 3.2: Table of uncertainty reductions achieved by each network, together with the network's centroid point, the mean distance to centroid, dissimilarity index, and running times. Results are presented for the IO result, and results under the GA with 50, 75, and 100 iterations together with 50 population members (GA 50 50, GA 75 50, GA 100 50), and with 50, 75 and 100 iterations together with 100 population members (GA 50 100, GA 75 100, GA 100 100), where solutions were generated under the assumption that a seven-member network already existed, which included Cape Point and Gobabeb and the best five-member solution from the original network design problem.

| | January | | | | | July | | | | |
|---|---|---|---|---|---|---|---|---|---|---|
| Algorithm Specification | Uncertainty kt C week$^{-1}$ | Uncertainty reduction (%) (mean) | Centroid, mean distance to centroid (km) | DI with IO (km) | Run time (min) | Uncertainty kt C week$^{-1}$ | Uncertainty reduction (%) (mean) | Centroid, mean distance to centroid (km) | DI with IO (km) | Run time (min) |
| Prior | 436.23 | | | | | 58.29 | | | | |
| IO | 231.42 | 46.949 | (26.88, -29.24), 315 | 0 | 15 | 50.3 | 13.701 | (23.28, -30.32), 427 | 0 | 14 |
| GA 50 50 | 219.61 | 49.657 | (26.52, -28.52), 305 | 941 | 96 | 49.99 | 14.238 | (24.72, -29.96), 526 | 839 | 98 |
| GA 50 50 | 239 | 45.212 | (26.88, -29.24), 295 | 802 | 93 | 50.02 | 14.178 | (24.72, -29.24), 490 | 775 | 99 |
| GA 50 50 | 218.41 | 49.932 | (26.52, -28.88), 338 | 541 | 91 | 49.99 | 14.238 | (24.72, -29.96), 526 | 839 | 98 |
| GA 50 50 | 218.41 | 49.932 | (26.52, -28.88), 338 | 541 | 91 | 49.99 | 14.238 | (24.72, -29.96), 526 | 839 | 97 |
| GA 50 50 | 218.41 | 49.932 (48.933) | (26.52, -28.88), 338 | 541 | 93 | 49.99 | 14.238 (14.226) | (24.72, -29.96), 526 | 839 | 98 |
| GA 75 50 | 228.37 | 47.649 | (26.52, -29.24), 352 | 941 | 133 | 49.99 | 14.238 | (24.72, -29.96), 526 | 839 | 138 |
| GA 75 50 | 218.41 | 49.932 | (26.52, -28.88), 338 | 541 | 133 | 49.99 | 14.238 | (24.72, -29.96), 526 | 839 | 133 |
| GA 75 50 | 227.95 | 47.745 | (26.52, -28.88), 319 | 1342 | 132 | 49.99 | 14.238 | (24.72, -29.96), 526 | 839 | 132 |
| GA 75 50 | 218.41 | 49.932 | (26.52, -28.88), 338 | 541 | 133 | 49.99 | 14.238 | (24.72, -29.96), 526 | 839 | 135 |
| GA 75 50 | 218.41 | 49.932 (49.038) | (26.52, -28.88), 338 | 541 | 133 | 49.99 | 14.238 (14.238) | (24.72, -29.96), 526 | 839 | 133 |
| GA 100 50 | 218.41 | 49.932 | (26.52, -28.88), 338 | 541 | 176 | 49.99 | 14.238 | (24.72, -29.96), 526 | 839 | 195 |
| GA 100 50 | 218.41 | 49.932 | (26.52, -28.88), 338 | 541 | 178 | 49.99 | 14.238 | (24.72, -29.96), 526 | 839 | 195 |
| GA 100 50 | 218.41 | 49.932 | (26.52, -28.88), 338 | 541 | 175 | 49.99 | 14.238 | (24.72, -29.96), 526 | 839 | 196 |
| GA 100 50 | 218.41 | 49.932 | (26.52, -28.88), 338 | 541 | 177 | 49.99 | 14.238 | (24.72, -29.96), 526 | 839 | 183 |
| GA 100 50 | 218.41 | 49.932 (49.932) | (26.52, -28.88), 338 | 541 | 176 | 49.99 | 14.238 (14.238) | (24.72, -29.96), 526 | 839 | 185 |
| GA 50 100 | 218.41 | 49.932 | (26.52, -28.88), 338 | 541 | 177 | 49.99 | 14.238 | (24.72, -29.96), 526 | 839 | 173 |
| GA 50 100 | 219.61 | 49.657 | (26.52, -28.52), 305 | 941 | 174 | 49.99 | 14.238 | (24.72, -29.96), 526 | 839 | 171 |
| GA 50 100 | 218.41 | 49.932 | (26.52, -28.88), 338 | 541 | 179 | 49.99 | 14.238 | (24.72, -29.96), 526 | 839 | 173 |
| GA 50 100 | 218.41 | 49.932 | (26.52, -28.88), 338 | 541 | 176 | 49.99 | 14.238 | (24.72, -29.96), 526 | 839 | 174 |
| GA 50 100 | 218.41 | 49.932 (49.877) | (26.52, -28.88), 338 | 541 | 175 | 49.99 | 14.238 (14.238) | (24.72, -29.96), 526 | 839 | 176 |
| GA 75 100 | 218.41 | 49.932 | (26.52, -28.88), 338 | 541 | 260 | 49.99 | 14.238 | (24.72, -29.96), 526 | 839 | 257 |
| GA 75 100 | 218.41 | 49.932 | (26.52, -28.88), 338 | 541 | 260 | 49.99 | 14.238 | (24.72, -29.96), 526 | 839 | 255 |
| GA 75 100 | 218.41 | 49.932 | (26.52, -28.88), 338 | 541 | 260 | 49.99 | 14.238 | (24.72, -29.96), 526 | 839 | 258 |
| GA 75 100 | 218.41 | 49.932 | (26.52, -28.88), 338 | 541 | 263 | 49.99 | 14.238 | (24.72, -29.96), 526 | 839 | 256 |
| GA 75 100 | 218.41 | 49.932 (49.932) | (26.52, -28.88), 338 | 541 | 260 | 49.99 | 14.238 (14.238) | (24.72, -29.96), 526 | 839 | 253 |
| GA 100 100 | 218.41 | 49.932 | (26.52, -28.88), 338 | 541 | 342 | 49.99 | 14.238 | (24.72, -29.96), 526 | 839 | 339 |
| GA 100 100 | 218.41 | 49.932 | (26.52, -28.88), 338 | 541 | 345 | 49.99 | 14.238 | (24.72, -29.96), 526 | 839 | 337 |
| GA 100 100 | 218.41 | 49.932 | (26.52, -28.88), 338 | 541 | 341 | 49.99 | 14.238 | (24.72, -29.96), 526 | 839 | 340 |
| GA 100 100 | 218.41 | 49.932 | (26.52, -28.88), 338 | 541 | 343 | 49.99 | 14.238 | (24.72, -29.96), 526 | 839 | 332 |
| GA 100 100 | 218.41 | 49.932 (49.932) | (26.52, -28.88), 338 | 541 | 342 | 49.99 | 14.238 (14.238) | (24.72, -29.96), 526 | 839 | 334 |

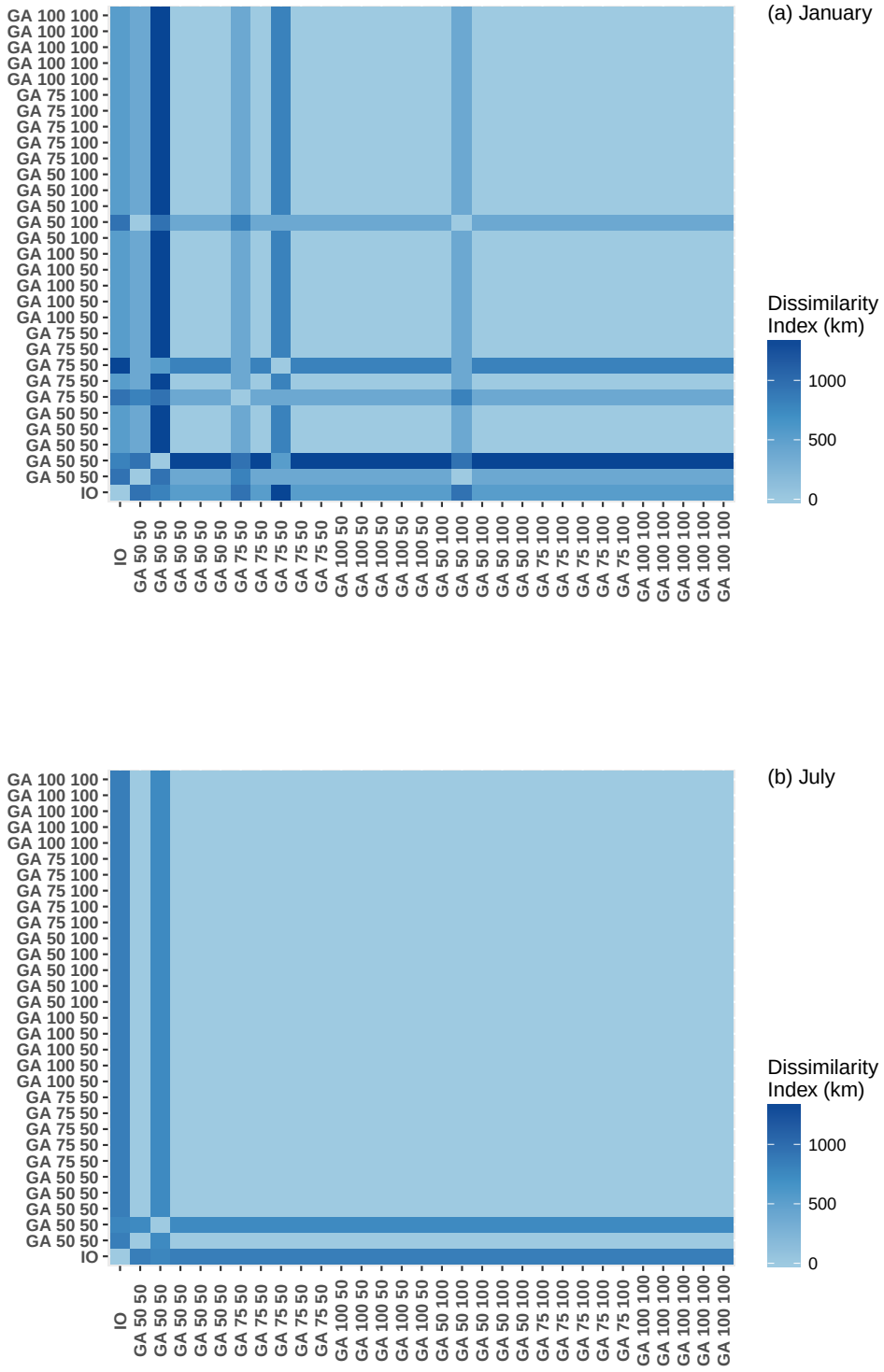


Figure 3.7: Heat maps displaying Dissimilarity Indices for the January (top) and July (bottom) optimal network solutions under the established network scenario. The abbreviated names for the GA runs are the same as for Table 3.2.

### 3.3.3 Subregion Design Problem

For the subregion scenario, the uncertainty reduction was based only on the uncertainty within a subregion located on the eastern side of South Africa. The background stations, both located on the western side of the domain, would provide very little information about this region. The uncertainty reduction achieved for the January solutions ranged between 78.6% and 79.1%, and in July ranged between 51.1% and 51.4% (Table 3.3). The IO had the lowest uncertainty reduction for both the January and July solutions, although very close to the maximum uncertainty reduction achieved, differing by only 0.5% in January and 0.3% in July. In January, when there were both large fossil fuel sources and a large amount of biospheric activity in the subregion, the GA was always able to obtain a better solution compared with the IO. The consistency in the GA solutions for July was achieved with fewer evaluations compared with January.

For the subregion scenario, footprints of the measurement towers showed more overlap compared with both the original network design problem and the established network design problem, with the highest cumulative sensitivity occurring in January (Figure 3.5). This occurred in a pixel over the north eastern edge of South Africa, close to the Swaziland border, where the biospheric flux uncertainty was high. In all the best network solutions, across both January and July, the optimisation algorithms aimed to reduce the uncertainty over this region. By restricting the uncertainty optimisation over a subregion which contained this pixel, the network solutions could include multiple sites which viewed this location in order to have more comprehensive information about this source and therefore to produce a large uncertainty reduction overall.

The mean distances to the centroid for the January solutions were similar to those obtained for the original network design, with stations scattered throughout the subregion, particularly close to the major cities in the region (Figure 3.8). Two stations were outside of the subregion close to the borders of the subregion, one to the west of the subregion, near the city of Johannesburg and areas of high fossil fuel activity, and one to the south near regions of high biospheric activity. In July the clustering was lower, and stations tended to be located near the cities in the subregion, with one station located in the central part of South Africa, outside of the subregion. The DI values were higher in January and showed diversity in the solutions between the different optimisation runs, whereas for July the DI values were smaller and showed that there were only two solution sets that were obtained from the GA

runs, where the best solution was obtained more reliably under either high number of iterations or high population size (Figure 3.9).

The run times for the optimisation procedures were very similar to those obtained for the original network design problem.

Table 3.3: Table of uncertainty reductions achieved by each network, together with the network's centroid point, the mean distance to centroid, dissimilarity index, and running times. Results are presented for the IO result, and results under the GA with 50, 75, and 100 iterations together with 50 population members (GA 50 50, GA 75 50, GA 100 50), and with 50, 75 and 100 iterations together with 100 population members (GA 50 100, GA 75 100, GA 100 100), where solutions were generated under the requirement that uncertainty needed to be reduced over the eastern subregion of South Africa

| | January | | | | | July | | | | |
|---|---|---|---|---|---|---|---|---|---|---|
| Algorithm Specification | Uncertainty kt C week$^{-1}$ | Uncertainty reduction (%) (mean) | Centroid, mean distance to centroid (km) | DI with IO (km) | Run time (min) | Uncertainty kt C week$^{-1}$ | Uncertainty reduction (%) (mean) | Centroid, mean distance to centroid (km) | DI with IO (km) | Run time (min) |
| Prior | 2052.21 | | | | | 83.5 | | | | |
| IO | 438.13 | 78.7 | (27.24, -28.52), 300 | 0 | 14 | 40.86 | 51.0661 | (27.24, -27.08), 284 | 0 | 16 |
| GA 50 50 | 435.76 | 78.8 | (27.24, -28.88), 326 | 891 | 68 | 40.56 | 51.4241 | (26.88, -27.44), 335 | 533 | 76 |
| GA 50 50 | 429.37 | 79.1 | (27.24, -28.88), 357 | 726 | 67 | 40.56 | 51.4241 | (26.88, -27.44), 335 | 533 | 75 |
| GA 50 50 | 435.76 | 78.8 | (27.24, -28.88), 326 | 891 | 68 | 40.86 | 51.0661 | (27.24, -27.08), 284 | 0 | 75 |
| GA 50 50 | 429.37 | 79.1 | (27.24, -28.88), 17 | 726 | 67 | 40.56 | 51.4241 | (26.88, -27.44), 335 | 533 | 75 |
| GA 50 50 | 431.48 | 79 (78.96) | (27.24, -28.52), 11 | 1127 | 68 | 40.56 | 51.4241 (51.3525) | (26.88, -27.44), 335 | 533 | 75 |
| GA 75 50 | 435.39 | 78.8 | (27.6, -28.52), 24 | 360 | 100 | 40.56 | 51.4241 | (26.88, -27.44), 335 | 533 | 109 |
| GA 75 50 | 435.39 | 78.8 | (27.6, -28.52), 24 | 360 | 99 | 40.86 | 51.0661 | (27.24, -27.08), 284 | 0 | 108 |
| GA 75 50 | 429.37 | 79.1 | (27.24, -28.88), 17 | 726 | 100 | 40.56 | 51.4241 | (26.88, -27.44), 335 | 533 | 109 |
| GA 75 50 | 433.75 | 78.9 | (27.6, -28.88), 17 | 1086 | 101 | 40.56 | 51.4241 | (26.88, -27.44), 335 | 533 | 109 |
| GA 75 50 | 429.37 | 79.1 (78.94) | (27.24, -28.88), 17 | 726 | 99 | 40.56 | 51.4241 (51.3525) | (26.88, -27.44), 335 | 533 | 110 |
| GA 100 50 | 429.37 | 79.1 | (27.24, -28.88), 17 | 726 | 129 | 40.56 | 51.4241 | (26.88, -27.44), 335 | 533 | 144 |
| GA 100 50 | 435.39 | 78.8 | (27.6, -28.52), 24 | 360 | 130 | 40.86 | 51.0661 | (27.24, -27.08), 284 | 0 | 146 |
| GA 100 50 | 435.06 | 78.8 | (27.6, -28.16), 17 | 755 | 133 | 40.56 | 51.4241 | (26.88, -27.44), 335 | 533 | 145 |
| GA 100 50 | 435.39 | 78.8 | (27.6, -28.52), 24 | 360 | 132 | 40.56 | 51.4241 | (26.88, -27.44), 335 | 533 | 147 |
| GA 100 50 | 435.39 | 78.8 (78.86) | (27.6, -28.52), 24 | 360 | 133 | 40.56 | 51.4241 (51.3525) | (26.88, -27.44), 335 | 533 | 158 |
| GA 50 100 | 429.37 | 79.1 | (27.24, -28.88), 17 | 726 | 137 | 40.56 | 51.4241 | (26.88, -27.44), 335 | 533 | 144 |
| GA 50 100 | 429.37 | 79.1 | (27.24, -28.88), 17 | 726 | 131 | 40.56 | 51.4241 | (26.88, -27.44), 335 | 533 | 147 |
| GA 50 100 | 435.39 | 78.8 | (27.6, -28.52), 24 | 360 | 132 | 40.56 | 51.4241 | (26.88, -27.44), 335 | 533 | 146 |
| GA 50 100 | 429.37 | 79.1 | (27.24, -28.88), 17 | 726 | 132 | 40.56 | 51.4241 | (26.88, -27.44), 335 | 533 | 146 |
| GA 50 100 | 429.37 | 79.1 (79.04) | (27.24, -28.88), 17 | 726 | 132 | 40.56 | 51.4241 (51.4241) | (26.88, -27.44), 335 | 533 | 145 |
| GA 75 100 | 429.37 | 79.1 | (27.24, -28.88), 17 | 726 | 194 | 40.56 | 51.4241 | (26.88, -27.44), 335 | 533 | 221 |
| GA 75 100 | 442.59 | 78.4 | (27.24, -28.52), 30 | 1272 | 195 | 40.56 | 51.4241 | (26.88, -27.44), 335 | 533 | 215 |
| GA 75 100 | 429.37 | 79.1 | (27.24, -28.88), 17 | 726 | 197 | 40.56 | 51.4241 | (26.88, -27.44), 335 | 533 | 215 |
| GA 75 100 | 435.39 | 78.8 | (27.6, -28.52), 24 | 360 | 198 | 40.56 | 51.4241 | (26.88, -27.44), 335 | 533 | 214 |
| GA 75 100 | 429.37 | 79.1 (78.9) | (27.24, -28.88), 17 | 726 | 197 | 40.56 | 51.4241 (51.4241) | (26.88, -27.44), 335 | 533 | 214 |
| GA 100 100 | 429.37 | 79.1 | (27.24, -28.88), 17 | 726 | 256 | 40.56 | 51.4241 | (26.88, -27.44), 335 | 533 | 282 |
| GA 100 100 | 435.39 | 78.8 | (27.6, -28.52), 24 | 360 | 255 | 40.56 | 51.4241 | (26.88, -27.44), 335 | 533 | 284 |
| GA 100 100 | 435.06 | 78.8 | (27.6, -28.16), 17 | 755 | 263 | 40.56 | 51.4241 | (26.88, -27.44), 335 | 533 | 287 |
| GA 100 100 | 429.37 | 79.1 | (27.24, -28.88), 17 | 726 | 254 | 40.56 | 51.4241 | (26.88, -27.44), 335 | 533 | 285 |
| GA 100 100 | 429.37 | 79.1 (78.98) | (27.24, -28.88), 17 | 726 | 258 | 40.56 | 51.4241 (51.4241) | (26.88, -27.44), 335 | 533 | 285 |

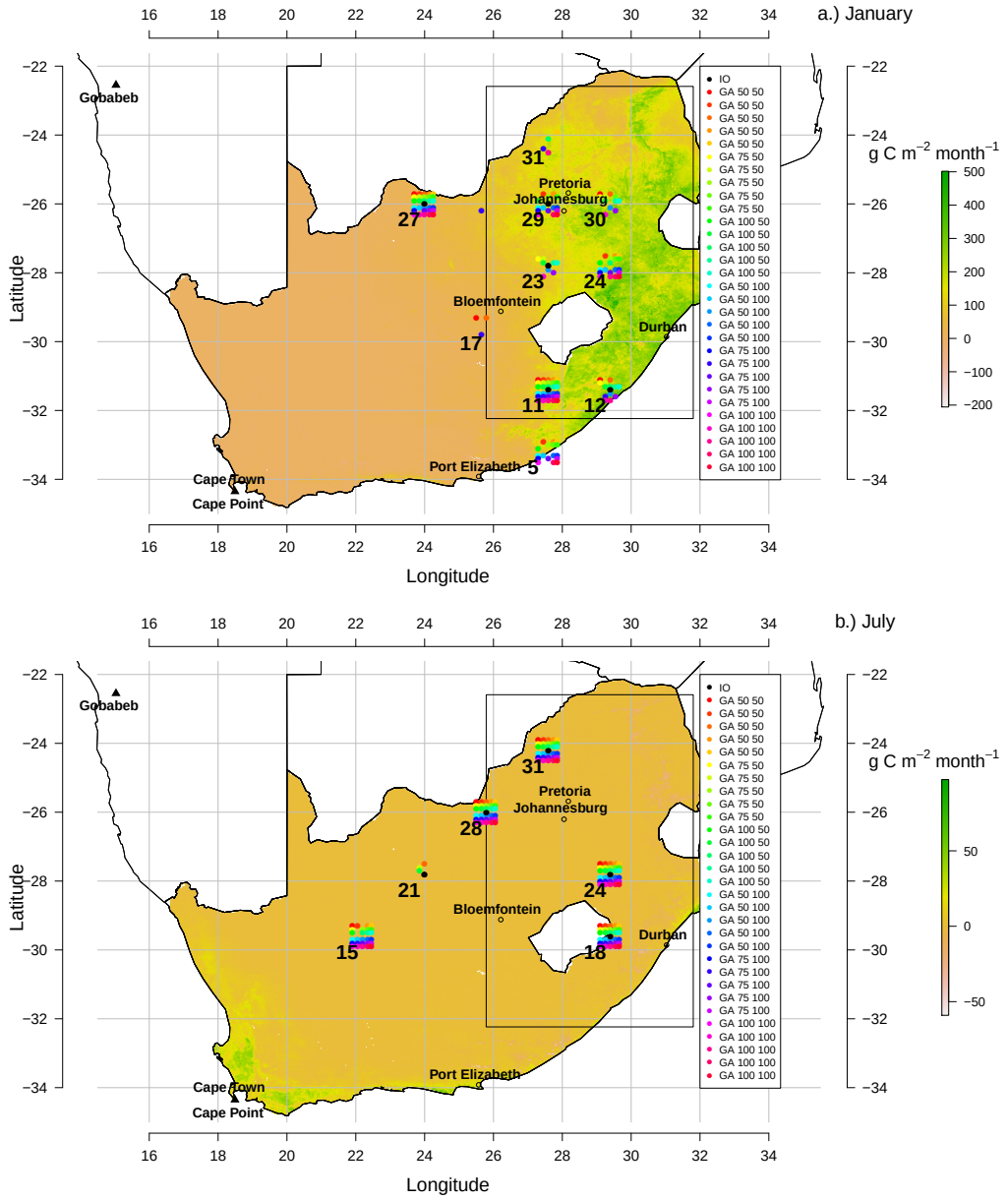


Figure 3.8: Optimal network locations for subregion case for (a) January and (b) July from each of the algorithm runs, overlaid on the net primary productivity (NPP) (g C m$^{-2}$ month$^{-1}$). Subregion is represented by the grid box. Code numbers for the GA runs are the same as for Table 3.3. Numbers appearing on the maps are the station locations which have appeared in one or more network solutions. Major South African - open circles. Black triangles - existing network. Black closed circles - IO network solution. Coloured closed circles - GA solutions. Each colour represents a different GA solution. Points are laid out row by row, with the top row corresponding to the GA 50 50 and the bottom corresponding to the GA 100 100.

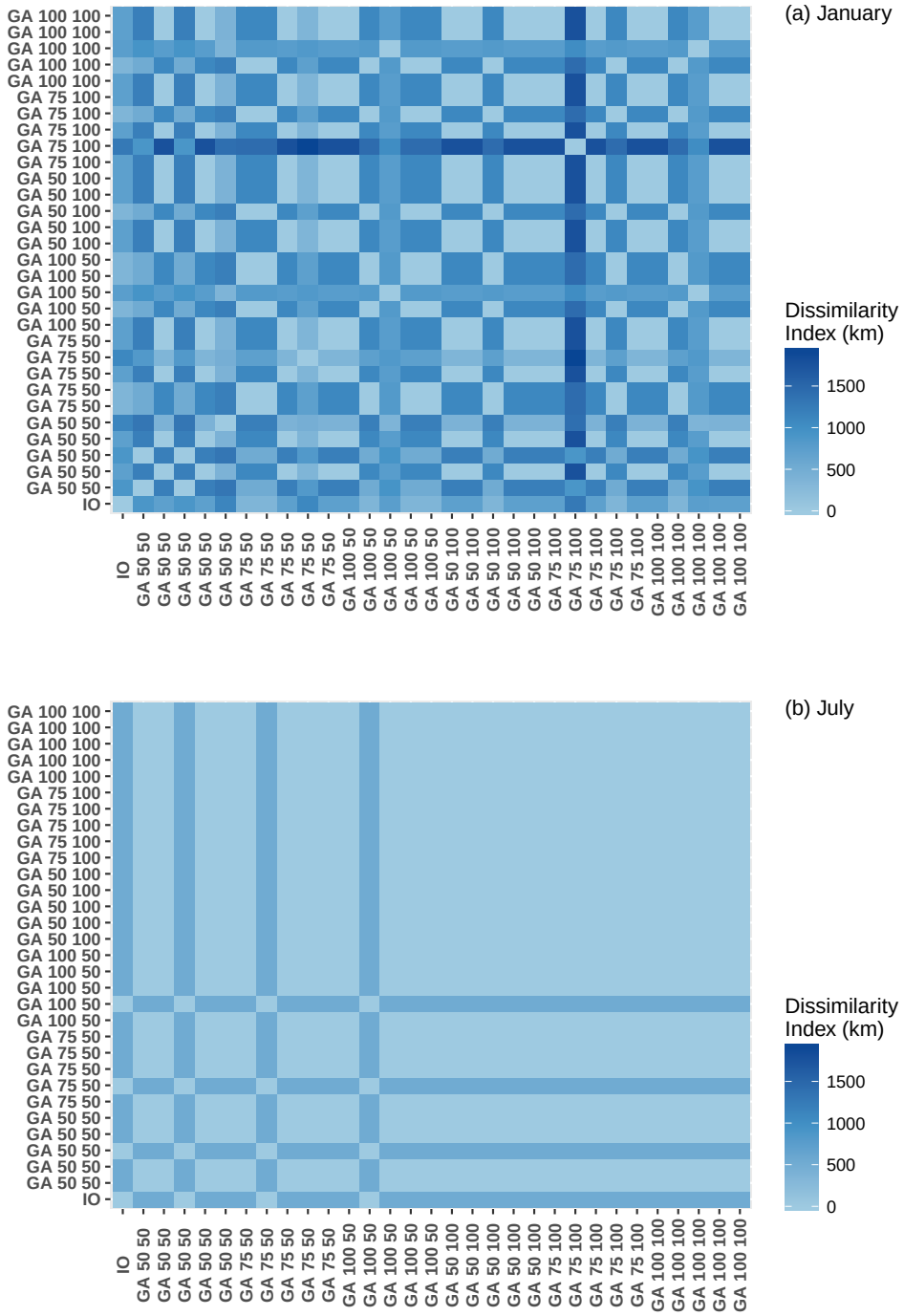


Figure 3.9: Heat maps displaying Dissimilarity Indices for the January (top) and July (bottom) optimal network solutions under the subregion scenario, requiring a solution to reduce the uncertainty in the eastern half of the country. The abbreviated names for the GA runs are the same as for Table 3.3.

## 3.4 Discussion and Conclusion

The results of this study show that although IO routine was not able to find the network with the global maximum uncertainty reduction, it found a network with uncertainty reduction only fractionally different from the best result obtained by means of the GA, at a much lower computational cost. Out of a five-member network solution, the IO differed by between one and two stations from the best GA solution. This occurred for the original network design problem, when solving for additional stations to an established network, and when solving for only a subregion of the domain. Moreover, the metrics for clustering of stations and dissimilarity showed that a very similar placement of stations would result. The advantage of the IO method over the GA method is that an evolution of results is obtained, which is useful for practical purposes. By identifying the station which on its own reduces the uncertainty by the most, it gives the decision makers the location of the site which should be prioritised. In addition, the running time for the IO is significantly shorter compared with the GA, which can play a role when computational resources are limited or when dealing with a larger or more complex domain, and where sensitivity tests need to be performed, for example using different configurations and estimates of the covariance matrices or using an alternative transport model. Therefore the IO algorithm is a viable alternative to the GA for optimal network design of atmospheric monitoring stations. In January, when the prior covariance matrix of the surface fluxes was more complex due to larger and more variable surface fluxes across a large proportion of the domain when compared with July, the difference in the uncertainty reduction between the best GA and IO solutions was also larger. In order to be confident of achieving the largest possible uncertainty reduction, the number of iterations and population size needed to be made large, and for the original network problem where the majority of the domain was unconstrained by the base network observations, there was still inconsistency between solutions in terms of placement. Fortunately, even if the GA settled on a sub-optimal solution, the fitness of this network was similar to the best available GA solution.

For the original network design problem, the GA was able to find the best solution, but not consistently, particularly for the month of January when the prior uncertainties of the fluxes were larger and more complex. In July, when the covariances were smaller and concentrated in small areas spread throughout the domain, the chances of the GA finding the best solution improved, resulting in greater consistency between runs. Increasing the number of iterations or population members did

not guarantee the best solution, but uncertainty reductions were always higher or the same compared with the IO result. Therefore if very small reductions in the uncertainty reduction are worth pursuing, such as in the case where the existing network is already well established, the GA routine is preferable. Under these circumstances a large amount of resources, relative to the IO routine, would be required in order to run the GA with sufficient iterations and population members. These specifications depend on the complexity of the prior covariance matrix, with a larger number of iterations and population members required to solve for networks under greater spatial variability in surface flux uncertainty. Therefore the number of iterations or population members should be tuned according to prior information available for a given network design problem.

We showed that even under more complicated scenarios, such as solving for additional stations to add to an established network or solving for the uncertainty in the fluxes of a subregion, the IO method was able to achieve a solution similar to the best GA solution, in terms of both location of stations and the uncertainty reduction achieved, but that the GA was always able to find a slightly better solution. The GA performed more consistently when the sources were concentrated within specific regions, such as around cities which occurred for the month of July. When the uncertainty resulting from the biospheric sources, which were more dispersed across the domain than the fossil fuel sources, had a dominant contribution to the overall uncertainty, such as for January in our case, the GA showed much more diversity in the network solutions, and a larger number of iterations and population members were required for convergence. The variability in the solutions was greater for the original network design problem than for the two additional scenarios, and the established network design for the month of July, where the gain in the uncertainty reduction was much lower and where the main sources of uncertainty were concentrated in a few places, showed the least amount of variability in the optimisation solutions.

The disadvantage of the GA procedure is that it does not supply the station which on its own results in the highest uncertainty reduction. This would require having to run the algorithm for a one station network. It also requires significantly more computational resources compared with the IO, without the guarantee of improvement over the IO. This implies that the user should not rely on a single run of the GA if the best solution is required, but rather have it run multiple times. Where computational resources are not limiting, the exact number of runs could be determined by the variability in the uncertainty reductions produced by multiple GA runs, where the number of evaluations of the GA can steadily be increased until the standard

error of the mean uncertainty reduction under the set number of evaluations is below a required level. This would further increase the computation resources required to obtain the final solution, but would give the user alternative network solutions and an indication of the most important stations, as these would repeatedly appear in the solutions. With the gain in the uncertainty reduction so small for the GA best solution over the IO solution under all scenarios, it would suggest that it would be more worthwhile to invest in the improvement of the prior covariance estimates than in implementing a complex and resource intensive optimisation algorithm for this network design application. The network solution itself and the computational resources required for convergence of the GA is dependent on the complexity of the uncertainty covariance matrix of the prior surface fluxes. The network solution, regardless of optimisation algorithm, is only as good as the information provided for the uncertainties in the prior fluxes.

The GA and IO show that more than one good solution exists for the network design. Pragmatic considerations should be taken into account so that the resulting network is feasible and cost effective. A network that is guaranteed to result in a reliable measurement record would be more valuable for constraining the overall flux uncertainty than one which has a slightly better assumed uncertainty reduction but more likely to have measurement gaps.

In this investigation we only considered the population size and number of iterations specified for the GA. We could also consider changing the probabilities assigned to cross-over and mutation. This could provide better ability of the GA solution to get away from local extrema. If we were to compare the specification of these parameters for the GA, we would need to ensure that the algorithms were compared under fair conditions (Črepinšek et al., 2014). If elitism is maintained, it would guarantee that the best solution always moves forward to the next iteration, which would ensure stability of the final solution. We recommend that the GA and its alternative parametrisations be used as part of a comprehensive sensitivity analysis when undertaking such an optimisation exercise.

We compared an evolutionary algorithm to a simple deterministic algorithm. An alternative deterministic algorithm to the IO is Decremental Optimisation (DO) (Curtis et al., 2004). DO starts with the maximal network, and eliminates sites from this network solution based on a fitness criterion, until the required network size is reached. Under the computational resources used for this analysis, DO would not have been possible as it would have resulted in a $\mathbf{H}$ approximately 7 times larger than for a five-member network, and a $\mathbf{C}_{\boldsymbol{c}}$ that was $7^2$ larger, which would have significantly

increased the memory requirement for a single inversion result. This type of optimisation may be possible under a system with larger memory resources to allow the large matrix multiplications and matrix inversions required.

We assumed that the observation errors and flux uncertainties followed a Gaussian distribution. This is common practice in the field $CO_2$ flux inversions, and has made the technique described in this paper possible. This optimisation problem could be extended to relax the assumption of Gaussian errors.

# Bibliography

Baker, D. F., Law, R. M., Gurney, K. R., Rayner, P., Peylin, P., Denning, A. S., Bourquet, P., Bruhwiler, L., Chen, Y., Ciais, P., Fung, I.Y., Heimann, M., John, J., Maki, T., Maksyutov, S., Masarie, K., Prather, M., Pak, B., Taguchi, S. and Zhu, Z.: TransCom 3 inversion intercomparison: Impact of transport model errors on the interannual variability of regional $CO_2$ fluxes, 1988–2003, Global Biogeochem. Cy., 20, GB1002, doi: 10.1029/2004GB002439, 2006.

Berry, L. T. M., Murtagh, B. A., McMahon, G., Sugden, S. and Welling, L.: An integrated GALP approach to communication network design, Telecommun. Syst., 12, 265–280, 1999.

Bousquet, P., Ciais, P., Peylin, P., Ramonet, M., and Monfray, P.: Inverse modeling of annual atmospheric $CO_2$ sources and sinks: 1. Method and control inversion, J. Geophys. Res., 104, 26161-26178, doi: 10.1029/1999JD900342, 1999.

Bréon, F. M., Broquet, G., Puygrenier, V., Chevallier, F., Xueref-Remy, I., Ramonet, M., Dieudonné, E., Lopez, M., Schmidt, M., Perrussel, O., and Ciais, P.: An attempt at estimating Paris area $CO_2$ emissions from atmospheric concentration measurements, Atmos. Chem. Phys., 15, 1707–1724, doi: 10.5194/acp-15-1707-2015, 2015.

Broquet, G., Chevallier, F., Bréon, F. -M., Kadygrov, M., Apadula, F., Hammer, S., Haszpra, L., Meinhardt, F., Morgui, J. A., Necki, J., Piacentino, S., Ramonet, M., Schmidt, M., Thompson, R. L., Vermeulen, A. T., Yver, C. and Ciais, P.: Regional inversion of $CO_2$ ecosystem fluxes from atmospheric measurements: reliability of the uncertainty estimates, Atmos. Chem. Phys., 13, 9039–9056, doi: 10.5194/acp-13-9039-2013, 2013.

Chambers, L.: The Practical Handbook of Genetic Algorithms: Applications, 2nd Edition, Chapman & Hall/CRC, 2001.

Chevallier, F., Ciais, P., Conway, T. J., Aalto, T., Anderson, B. E., Bousquet, P., Brunke, E. G., Ciattaglia, L., Esaki, Y., Fröhlich, M., Gomez, A., Gomez-Pelaez, A. J., Haszpra, L., Krummel, P. B., Langenfelds, R. L., Leuenberger, M., Machida, T., Maignan, F., Matsueda, H., Morgui, J. A., Mukai, H., Nakazawa, T., Peylin, P., Ramonet, M., Rivier, L., Sawa, Y., Schmidt, M., Steele, L. P., Vay, S. A., Vermeulen, A. T., Wofsy, S., and Worthy, D.: $CO_2$ surface fluxes at grid point scale estimated from a global 21 year reanalysis of atmospheric measurements, J. Geophys. Res., 115, D21307, doi: 10.1029/2010JD013887, 2010.

Ciais, P., Rayner, P., Chevallier, F., Bousquet, P., Logan, M., Peylin, P., and Ramonet, M.: Atmospheric inversions for estimating $CO_2$ fluxes: methods and perspectives, Climatic Change, 103, 69–92, 2010.

Črepinšek, M., Liu, S.-H. and Mernik, M.: Replication and comparison of computational experiments in applied evolutionary computing: Common pitfalls and guidelines to avoid them, Appl. Soft. Comput., 19, 161–170, 2014.

Crosson, E.:A cavity ring-down analyzer for measuring atmospheric levels of methane, carbon dioxide, and water vapor, Appl. Phys. B, 92, 403–408, doi:10.1007/s00340-008-3135-y, 2008.

Curtis, A., Michelini, A., Leslie, D. and Lomax, A.: A deterministic algorithm for experimental design applied to tomographic and microseismic monitoring surveys, Geophys. J. Int., 157, 595–606, doi: 10.1111/j.1365-246X.2004.02114.x, 2004.

Enting, I. G. and Mansbridge, J. V.: Latitudinal distribution of sources and sinks of $CO_2$: Results of an inversion study, Tellus B, 43, 156–170, 1991.

Enting, I. G., Trudinger, C. M. and Francey, R. J.: A synthesis inversion of the concentration and $\delta_1$3C of atmospheric $CO_2$, Tellus B, 47, 35–52, 1995.

Enting, I. G.: Inverse Problems in Atmospheric Constituent Transport, Cambridge Univ. Press, New York, 2002.

Gerbig, C., Lin, J. C., Wofsy, S. C., Daube, B. C., Andrews, A. E., Stephens, B. B., Bakwin, P. S. and Grainger, C. A.: Toward constraining regional-scale fluxes of $CO_2$ with atmospheric observations over a continent: 1. Observed spatial variability from airborne platforms, J. Geophys. Res., 108(D24), 4756, doi: 10.1029/2002JD003018, 2003.

Grady, S. A., Hussaini, M. Y. and Abdullah, M. M.: Placement of wind turbines using genetic algorithms, Renew. Energ., 30, 259–270, doi: 10.1016/j.renene.2004.05.007, 2005.

Gurney, K. R., Law, R. M., Denning, A. S., Rayner, P. J., Baker, D., Bousquet, P., Bruhwiler, L., Chen, Y., Ciais, P., Fan, S., Fung, I. Y., Gloor, M., Heimann, M., Higuchi, K., John, J., Kowalczyk, E., Maki, T., Maksyutov, S., Peylin, P., Prather, M., Pak, B. C., Sarmiento, J., Taguchi, S., Takahashi, T., and Yuen, C.: TransCom 3 $CO_2$ inversion intercomparison: 1. Annual mean control results and sensitivity to transport and prior flux information, Tellus B, 55, 555–579, 2003.

Haber, E., Horesh, L. and Tenorio, L.: Numerical methods for experimental design of large-scale linear ill-posed inverse problems, Inverse Probl., 24, 055012, doi: 10.1088/0266-5611/24/5/055012, 2008.

Hardt, M and Scherbaum, F.: The design of optimum networks for aftershock recordings, Geophys. J. Int., 117, 716–726, 1994.

Hartline, J. and Sharp, A.: An Incremental Model for Combinatorial Maximization Problems, in: Àlvarez, C. and Serna, M. (Eds.), Experimental Algorithms, 5th International Workshop, WEA 2006, pp. 716–726, 24–27 May, 2006.

Jackson, D. D.: The use of a priori data to resolve non-uniqueness in linear inversion, Geophys. J. R. astr. Soc., 57, 137–157, 1979.

Jackson, D. D and Matsu'ura, M.: A Bayesian approach to nonlinear inversion, J. Geophys. Res. 90 (B1), 581–591, 1985.

Kaminski, T., Rayner, P .J., Heimann, M., and Enting, I. G.: On aggregation errors in atmospheric transport inversions, J. Geophys. Res., 106, 4705–4715, 2001.

Kaminski, T. and Rayner, P .J.: Reviews and syntheses: guiding the evolution of the observing system for the carbon cycle through quantitative network design, Biogeosciences, 14, 4755-4766, doi: 10.5194/bg-14-4755-2017, 2017.

Lauvaux, T., Uliasz, M., Sarrat, C., Chevallier, F., Bousquet, P., Lac, C., Davis, K. J., Ciais, P., Denning, A. S., and Rayner, P. J.: Mesoscale inversion: first results from the CERES campaign with synthetic data, Atmos. Chem. Phys., 8, 3459–3471, doi: 10.5194/acp-8-3459-2008, 2008.

Lauvaux, T., Pannekoucke, O., Sarrat, C., Chevallier, F., Ciais, P., Noilhan, J., and Rayner, P. J.: Structure of the transport uncertainty in mesoscale inversions of $CO_2$ sources and sinks using ensemble model simulations, Biogeosciences, 6, 1089–1102, doi: 10.5194/bg-6-1089-2009, 2009.

Lauvaux, T., Schuh, A. E., Uliasz, M., Richardson, S., Miles, N., Andrews, A. E., Sweeney, C., Diaz, L. I., Martins, D., Shepson, P. B., and Davis, K. J.: Constraining the $CO_2$ budget of the corn belt: exploring uncertainties from the assumptions in a mesoscale inverse system, Atmos. Chem. Phys., 12, 337–354, doi: 10.5194/acp-12-337-2012, 2012.

Lauvaux, T., Miles, N. L., Deng, A. Richardson, S. J., Cambaliza, M. O., Davis, K. J., Gaudet, B., Gurney, K. R., Huang, J., O'Keefe, D., Song, Y., Karion, A., Oda, T., Patarasuk, R., Razlivanov, I., Sarmiento, D., Shepson, P., Sweeney, C., Turnbull, J., and Wu, K.: High-resolution atmospheric inversion of urban $CO_2$ emissions during the dormant season of the Indianapolis Flux Experiment (INFLUX), J. Geophys. Res. Atmos., 121, 5213–5236, doi: 10.1002/2015JD024473, 2016.

Nickless, A., Ziehn, T., Rayner, P. J., Scholes, R .J., and Engelbrecht, F.: Greenhouse gas network design using backward Lagrangian particle dispersion modelling – Part 2: Sensitivity analyses and South African test case, Atmos. Chem. Phys., 15, 2051–2069, doi: 10.5194/acp-15-2051-2015, 2015.

Patra, P. K. and Maksyutov, S.: Incremental approach to the optimal network design for $CO_2$ surface source inversion, Geophys. Res. Lett., 29, 1459, doi:10.1029/2001GL013943, 2001.

Rayner, P. J., Enting, I. G., Francey, R. J., and Langenfelds, R. L.: Reconstructing the recent carbon cycle from atmospheric $CO_2$, $\delta^{13}C$ and $O_2/N_2$ observations, Tellus B, 51, 213–232, 1999.

Rayner, P. J.: Optimizing $CO_2$ observing networks in the presence of model error: results from TransCom 3, Atmos. Chem. Phys., 4, 413–421, doi: 10.5194/acp-4-413-2004, 2004.

Rayner, P. J., Raupach, M. R., Paget, M., Peylin, P., and Koffi, E.: A new global gridded data set of $CO_2$ emissions from fossil fuel combustion: mehodology and evaluation, J. Geophys. Res., 115, D19306, doi: 10.1029/2009JD013439, 2010.

Rodgers, C. D.: Inverse Methods for Atmospheric Sounding: Theory and Practice, World Scientific, River Edge, N. J., 2000.

Seibert, P. and Frank, A.: Source-receptor matrix calculation with a Lagrangian particle dispersion model in backward mode, Atmos. Chem. Phys., 4, 51–63, doi: 10.5194/acp-4-51-2004, 2004.

Tarantola, A.: Inverse Problem Theory: Methods for Data Fitting and Model Parameter Estimation, Elsevier, Amsterdam, 1987.

Tarantola, A.: Inverse Problem Theory and Methods for Model Parameter Estimation, Society for Industrial and Applied Mathematics , Philadelphia, 1987.

Uliasz, M.: Lagrangian particle modeling in mesoscale applications, in: Environmental Modelling II, Computational Mechanics Publications, Southampton, UK, 71–102, 1994.

Wu, L., Bocquet, M., Chevallier, F., Lauvaux, T., and Davis, K.: Hyperparameter estimation for uncertainty quantification in mesoscale carbon dioxide inversions, Tellus B, 65, 20894, doi: 10.3402/tellusb.v65i0.20894, 2013.

Ziehn, T., Nickless, A., Rayner, P. J., Law, R. M., Roff, G., and Fraser, P.: Greenhouse gas network design using backward Lagrangian particle dispersion modelling – Part 1: Methodology and Australian test case, Atmos. Phys. Chem., 14, 9363–9378, doi: 10.5194/acp-14-9363-2014, 2014.

# Chapter 4

# Spatial and Temporal Disaggregation of Anthropogenic $CO_2$ Emissions from the City of Cape Town

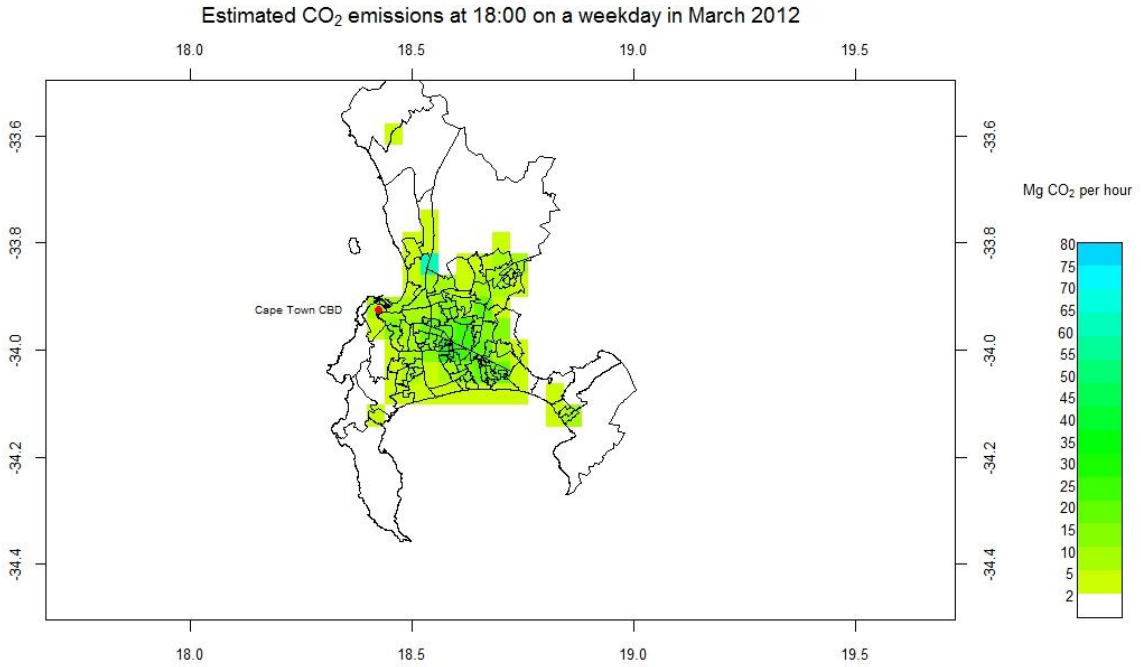

# Spatial and temporal disaggregation of anthropogenic $CO_2$ emissions from the City of Cape Town

**AUTHORS:**
Alecia Nickless[1,2]
Robert J. Scholes[2]
Ed Filby[3]

**AFFILIATIONS:**
[1]Department of Statistical Sciences, University of Cape Town, Cape Town, South Africa
[2]Global Change and Ecosystem Dynamics, Natural Resources and the Environment, Council for Scientific and Industrial Research, Pretoria, South Africa
[3]City of Cape Town, Air Quality Management, Cape Town, South Africa

**CORRESPONDENCE TO:**
Alecia Nickless

**EMAIL:**
alecia.nickless@phc.ox.ac.uk

**POSTAL ADDRESS:**
Global Change and Ecosystem Dynamics, Natural Resources and the Environment, Council for Scientific and Industrial Research, PO Box 395, Pretoria 0001, South Africa

**DATES:**
**Received:** 05 Nov. 2014
**Revised:** 10 Feb. 2015
**Accepted:** 15 Feb. 2015

**KEYWORDS:**
carbon dioxide inventory; emission factor; error propagation; mesoscale; interpolation

**HOW TO CITE:**
Nickless A, Scholes RJ, Filby E. Spatial and temporal disaggregation of anthropogenic $CO_2$ emissions from the City of Cape Town. S Afr J Sci. 2015;111(11/12), Art. #2014-0387, 8 pages. http://dx.doi.org/10.17159/sajs.2015/20140387



This paper describes the methodology used to spatially and temporally disaggregate carbon dioxide emission estimates for the City of Cape Town, to be used for a city-scale atmospheric inversion estimating carbon dioxide fluxes. Fossil fuel emissions were broken down into emissions from road transport, domestic emissions, industrial emissions, and airport and harbour emissions. Using spatially explicit information on vehicle counts, and an hourly scaling factor, vehicle emissions estimates were obtained for the city. Domestic emissions from fossil fuel burning were estimated from household fuel usage information and spatially disaggregated population data from the 2011 national census. Fuel usage data were used to derive industrial emissions from listed activities, which included emissions from power generation, and these were distributed spatially according to the source point locations. The emissions from the Cape Town harbour and the international airport were determined from vessel and aircraft count data, respectively. For each emission type, error estimates were determined through error propagation techniques. The total fossil fuel emission field for the city was obtained by summing the spatial layers for each emission type, accumulated for the period of interest. These results will be used in a city-scale inversion study, and this method implemented in the future for a national atmospheric inversion study.

## Introduction

Anthropogenic emissions are those emissions which are the result of human activities. Performing an inventory analysis is a method of quantifying these emissions based on human activity data. The basic equation is:

$$Emissions = AD \times EF \qquad \text{Equation 1}$$

where *AD* is the activity data and *EF* is the emissions factor, which converts the activity data into an emission.[1] For example, in the energy sector, in the case of carbon dioxide ($CO_2$) emissions, the amount of fuel consumed constitutes the activity data and the emission factor would then convert the activity data into the amount of $CO_2$ emitted per unit of fuel.

The Intergovernmental Panel on Climate Change (IPCC), at the invitation of the United Nations Framework Convention on Climate Change (UNFCCC) has produced a set of guidelines on how to conduct an inventory analysis for greenhouse gases, with the purpose of ensuring consistency and comparability between the greenhouse gas emissions reports of different countries. Under these guidelines, a national inventory consists of all the greenhouse gas emissions and removals which have taken place within the country's national jurisdiction. Inventory analyses are usually conducted at a national level because the activity data can easily be extracted from available national statistics.

In order to assess the magnitude of sources and sinks in a particular region within a country, a national inventory is not sufficient. The activity data need to be disaggregated between the regions which make up the country. For example, in the case of a mesoscale atmospheric inversion for $CO_2$, which aims to estimate fluxes based on high precision measurements of $CO_2$ concentrations and an atmospheric transport model, prior estimates are required for anthropogenic emissions. These estimates are required at the resolution of the source and sink regions which are used in the inversion exercise. An example of such a study is the fossil fuel emissions for the USA provided by the Vulcan project used by the Carbon Tracker inversion exercise.[2] This study was able to disaggregate the 2002 fossil fuel emissions for contiguous USA, based mainly on fuel usage data, at a 10 km $\times$ 10 km spatial resolution and a temporal resolution as high as a few hours. This project aimed to improve on its predecessor inventory which provided global spatial and temporal patterns of fossil fuel emissions, which used temporal resolutions of up to a month and spatial resolutions of one degree. The EDGAR (Emission Database for Global Atmospheric Research) is a global product on a $0.1° \times 0.1°$ grid, which calculates the total emissions of $CO_2$ and other species for each country, and distributes these total emissions spatially and temporally according to proxy data, such as population data or road transport network data.[3] A remote sensing based product also exists at the same spatial resolution, which calculates emissions based on night-time lights, population data, national fossil fuel data, and power plant location and statistics.[4,5] At a much more detailed level, taking into account information such as building locations and their dimensions, the Hestia project provides a bottom-up approach for quantifying fossil fuel emissions for a large city.[6] Our paper describes a bottom-up methodology approach which aims to make use of the available data for the City of Cape Town, but does so in the absence of the detailed building, road and population data which were available for Indianapolis during the Hestia project.

To determine the emissions from different source regions for a small mesoscale sub-national study, and to take advantage of hourly measurements of $CO_2$, it is necessary to use a method in which the data can be disaggregated into the different spatial subregions and at a time step which is congruent with the scope of the project. For a high spatial resolution study, this requires emissions inferred at high temporal scale as well, and so diurnal information on emissions from different sources is required. As explained by earlier studies,[2] data related to the consumption of fuel are lacking at these high-resolution spatiotemporal scales. In South Africa, data related to fuel consumption at individual institutions or sales at individual stations are not publically available, and

# Chapter 4

# Spatial and temporal disaggregation of anthropogenic $CO_2$ emissions from the City of Cape Town

## 4.1 Abstract

This paper describes the methodology used to spatially and temporally disaggregate carbon dioxide emission estimates for the City of Cape Town, to be used for a city-scale atmospheric inversion estimating carbon dioxide fluxes. Fossil fuel emissions were broken down into emissions from road transport, domestic emissions, industrial emissions, and airport and harbour emissions. Using spatially explicit information on vehicle counts, and an hourly scaling factor, vehicle emissions estimates were obtained for the City. Domestic emissions from fossil fuel burning were estimated from household fuel usage information and spatially disaggregated population data from the 2011 national census. Fuel usage data were used to derive industrial emissions from listed activities, which included emissions from power generation, and these were distributed spatially according to the source point locations. The emissions from the Cape Town harbour and the international airport were determined from vessel and aircraft count data respectively. For each emission type, error estimates were determined through error propagation techniques. The total fossil fuel emission field for the City was obtained by summing the spatial layers for each emission type, accumulated for the period of interest. These results will be used in a city-scale inversion study, and this method implemented in the future for a national atmospheric inversion study.

## 4.2 Introduction

Anthropogenic emissions are those emissions which are due to human activities. Performing an inventory analysis is a method of quantifying these emissions based on human activity data. The basic equation is

$$s_{0;ff} = AE \tag{4.1}$$

where $s_{0;ff}$ is the fossil fuel emission estimate, $A$ is the activity data and $E$ is the emissions factor, which converts the activity data into an emission (IPCC, 2006). For example, in the energy sector, in the case of carbon dioxide ($CO_2$) emissions, the amount of fuel consumed constitutes the activity data and the emission factor would then convert the activity data into the amount of $CO_2$ emitted per unit of fuel.

The IPCC (Intergovernmental Panel on Climate Change), under the invitation of the UNFCCC (United Nations Framework Convention on Climate Change) has produced a set of guidelines on how to conduct an inventory analysis for greenhouse gases, with the purpose of ensuring consistency and comparability between the greenhouse gas emissions reports of different countries. Under these guidelines, a national inventory consists of all the greenhouse gas emissions and removals which have taken place within the countrys national jurisdiction. Inventory analyses are usually conducted at the national level because the activity data can easily be extracted from available national statistics.

In order to assess the magnitude of sources and sinks in a particular region within a country, a national inventory will not be sufficient. The activity data will need to be disaggregated between the regions which make up the country. For example, in the case of a mesoscale atmospheric inversion for $CO_2$, which aims to estimate fluxes based on high precision measurements of $CO_2$ concentrations and an atmospheric transport model, prior estimates are required for anthropogenic emissions. These estimates are required at the resolution of the source and sink regions which are used in the inversion exercise. An example of such a study is the fossil fuel emissions for the United States provided by the Vulcan project used by the Carbon Tracker inversion exercise (Gurney et al., 2009). This study was able to disaggregate the 2002 fossil fuel emissions for contiguous U.S., based mainly on fuel usage data, at a 10 km $\times$ 10 km spatial resolution and a temporal resolution as high as a few hours. This project aimed to improve on its predecessor inventory which provided global spatial and temporal patterns of fossil fuel emissions, which used temporal resolutions of up to a month and spatial resolutions of one degree. The EDGAR (Emission Database for

Global Atmospheric Research) is a global product on a $0.1^\circ \times 0.1^\circ$ degree grid, which calculates the total emissions of $CO_2$ and other species for each country, and distributes these total emissions spatially and temporally according to proxy data, such as population data or road transport network data (Janssens-Maenhout et al., 2012). A remote sensing based product also exists at the same spatial resolution, which calculates emissions based on night-time lights, population data, national fossil fuel data, and power plant location and statistics (Rayner et al., 2010; Asefi-Najafabady et al., 2014). At a much more detailed level, taking into account information such as building locations and their dimensions, the Hestia project provides a bottom-up approach for quantifying fossil fuel emissions for a large city (Gurney et al., 2012). Our paper describes a bottom-up methodology approach which aims to make use of the available data for the City of Cape Town, but does so in the absence of the detailed building, road and population data which was available for Indianapolis during the Hestia project.

To determine the emissions from different source regions for a small mesoscale sub-national study, and to take advantage of hourly measurements of $CO_2$, it is necessary to use a method where the data can be disaggregated into the different spatial subregions and at a time step which is congruent with the scope of the project. For a high spatial resolution study, this requires emissions inferred at high temporal scale as well, and so diurnal information on emissions from different sources is required. As explained by earlier studies (Gurney et al., 2009), data related to the consumption of fuel is lacking at these high resolution spatiotemporal scales. In South Africa, data related to fuel consumption at individual institutions or sales at individual stations are not publicly available, and therefore special arrangements need to be made in order to access the data either with individual institutions or with the reporting agency.

This paper describes the methodology implemented to disaggregate anthropogenic emissions of $CO_2$ for a small domain, but high spatial resolution, atmospheric inversion study conducted for the City of Cape Town. At the time of the 2011 Census, the population of Cape Town was 3 740 025 (Statistics South Africa, 2011). A report of the energy usage of the City was compiled in 2011, which calculated the energy usage per sector of Cape Town, and calculated it to be 50% from transport, 18% from residential, 16% from commercial, 14% from industrial and 1% from government (City of Cape Town, 2011). But of the carbon emissions, only 27% of the carbon emissions are attributed to the transport sector due to the carbon intensive usage of coal for electricity generation which provides almost all of the energy to the residential and commercial sectors in South Africa (City of Cape Town, 2011). These two sectors

emit approximately 29 and 28% respectively of the total carbon emissions of Cape Town (City of Cape Town, 2015).

Koeberg, a nuclear power station near Cape Town and the only one in South Africa, provides 4.4% of the electricity requirements of the country (Eskom, 2013a). It feeds electricity directly to the grid, and therefore the reduction in carbon emissions due to nuclear power production, as opposed to coal intensive power production, is distributed throughout the grid, and the benefit is not just to the City of Cape Town. Therefore, the carbon emitted due to electricity generation for the City physically occurs where the coal fired power stations are located, which are mainly located in the North Eastern parts of South Africa. In this study we are concerned with the location of the emission sources, rather than who the emissions are attributed to. Therefore emissions due to electricity generation are all attributed to power stations, where these emissions are occurring in space. We assume all emissions from the commercial sector are due to electricity generation, and so are accounted for in the power station fuel usage information, and thus we do not consider the commercial sector separately.

## 4.3 Methods

### 4.3.1 Road Transport Vehicle Emissions

A model describing the amount of vehicles and vehicle kilometres travelled in an hour during peak hours on each section of road was obtained from the City of Cape Town town planners (modelled data from John Spotten, Head of Transport Modelling and System Analysis at the City of Cape Town (Spotten, 2012; Cambridge Environmental Research Consultants, 2012)), based on vehicle count data. No public information is available on vehicle composition for the city, so an average emission factor was used, calculated from available vehicle types supplied by the Greenhouse Gas Protocol guidelines for emissions calculations (Greenhouse Gas Protocol, 2005), based on the U.S. EPA published values, and by the Defra guidelines (DEFRA, 2013a), which therefore assumes an equal distribution of vehicles in each vehicles category. The average emission factor calculated was 347.01 g of $CO_2$ per vehicle kilometre, with a standard deviation of 239.64.

This emission factor converts vehicle kilometres into carbon dioxide emissions. The total number of vehicle kilometres travelled in a particular pixel was calculated by rasterising the line object data from the supplied shape file on vehicle kilometres provided by the City of Cape Town, so that the sum of vehicle kilometres over all lines

was equal to the sum of vehicle kilometres over all pixels. The proportion of vehicle kilometres allocated to a pixel was the same as the proportion of the length of the line which occurred inside the pixel. This was performed using the rgeos (Bivand et al., 2013) and raster (Hijmans, 2013) packages in R (R statistical software package).

In addition to the model describing the distribution of vehicle kilometres on Cape Town roads during peak hours, scaling factors were also provided to describe the traffic intensity at different times of the day, both over weekdays and weekends. These hourly scaling factors were used to transform the peak time weekday vehicle kilometres to match with a particular day of the week and time, so that a spatially explicit time series was created with an hourly time step from Monday through to Sunday (Figure 4.1).

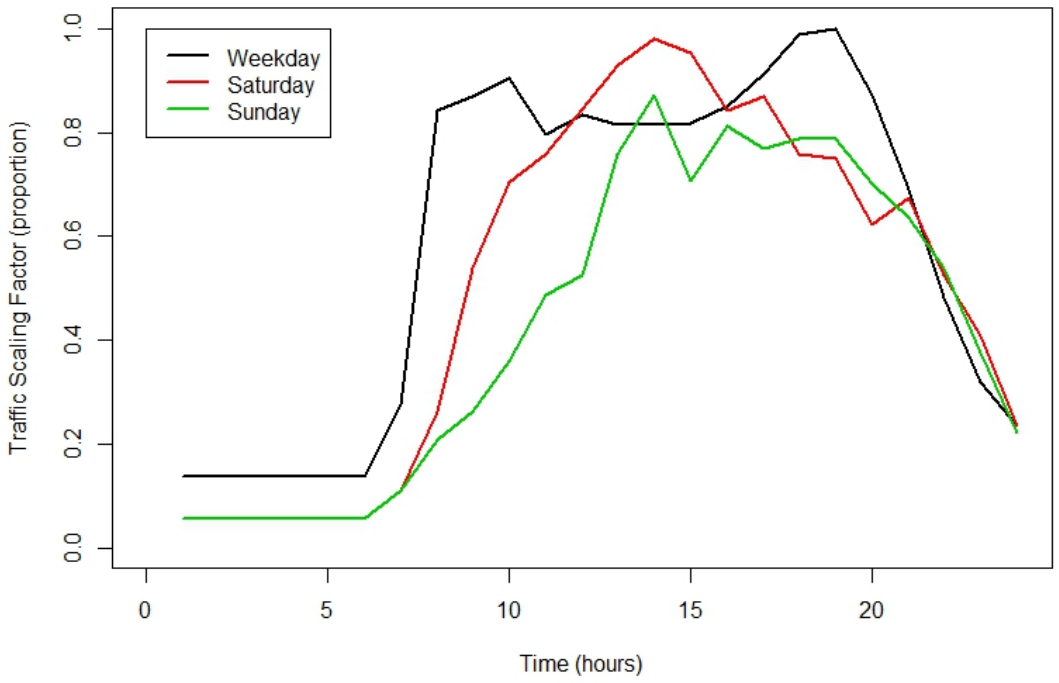


Figure 4.1: Plot of the scaling factors used to convert peak hour traffic hours on a weekday into traffic hours at different times of the day during the week, on Saturdays, and on Sundays. This information was obtained from the City of Cape Town city planners, estimated from vehicle count information.

### 4.3.2 Domestic Emissions

To obtain the emissions from domestic fossil fuel burning for lighting, cooking and heating, data on the number of households from the 2011 census and data on the

amount of residential fuel usage from the 2006 and 2009 Energy Digests (South African Department of Minerals and Energy, 2006; South African Department of Energy, 2009) were used. The average amount of fuel usage per household was obtained by dividing the total fuel usage across the whole country by the number of households reported in the 2011 South African census (14,450,161). The average amount of fuel used per household was multiplied by the number of households in each pixel, and this value was scaled according to the proportion of fuel used for cooking, lighting and heating, where 75% of the annual heating fuel usage was assumed to take place during the winter months (March to August). It was assumed that 75% of the annual energy consumed was used for heating, 20% for cooking and 5% for lighting.

The population of Cape Town was subdivided into the different wards of the City, and these data were recorded as a shape file containing polygons of the wards and the associated population and household count. Using a similar method as for the vehicle line data, the polygon information was rasterised into pixel data, so that the sum of the household counts over all the wards equalled the sum over all the pixels. The proportion of the household count which was assigned to each pixel was determined by the proportion of the polygon area located inside the pixel. This method can be extended to accommodate socio-economic data about the different wards used in our study, where the emissions from residential fossil fuel burning can be allocated based on income levels or electricity consumption since more affluent households will largely depend on electricity for heating, lighting and cooking. In order to understand the discrepancies in household fuel usage better, we have left this aspect for an future study.

### 4.3.3 Industrial Emissions from Listed Activities

Under South Africa's Air Quality Act, industry must obtain an emissions licence to perform listed activities, and reporting of activity data for the purpose of emissions calculations is mandatory (Presidency RSA, 2005). The dominant industrial activities listed include ceramic processes, hydrocarbon refining processes, iron and steel processes, Macadam processes for asphalt production, and waste incineration processes, as well as electricity generation at gas turbine power plants (Eskom, 2013b). The initial approach was based on the methodology from Gurney et al. (2009) for point source industrial emissions in the United States, where CO emissions were converted into $CO_2$ emissions based on the ratio between CO and $CO_2$ emissions factors for that industry. Due to the coarseness of the reported CO emissions, we were unable

to break the emissions down into different processes for which CO could be converted into $CO_2$ emission using the industry and process specific emission factors.

As an alternative, the reported fuel usage data for the top fuel users were converted directly into $CO_2$ emissions through multiplying this fuel usage date with the Defra greenhouse gas emission factors (DEFRA, 2013a). The fuel types that were considered include heavy fuel oil (HFO), coal, diesel, paraffin, and fuel gas which was divided into liquid petroleum gas and refinery fuel gas. In the case of gas fuels, which were recorded in units of $Nm^3$, the fuel usage was first converted into kWh, and then into $CO_2$ emissions, where the calorific values were obtained from Rayaprolu (2013) so that Defra emission factors could be used. The point data were then aggregated into the required raster format through summing the emissions from each source in a pixel. This analysis only took into account emissions from fuel combustion, but not process related emissions.

### 4.3.4 Airport and Harbour Emissions

Emissions from aircraft are normally separated into the landing/takeoff cycle (LTO) and the cruise phase of the flight. The LTO part of flights at the Cape Town International Airport is allocated to the Citys emissions, and divided evenly over the area which covers the airport. The South African Airports Company (ACSA) provides data on the number of aircraft movements, separated into domestic and international flights, for each month (Airports Company South Africa, 2013). The IPCC Guidelines provide emission factors per LTO (IPCC, 2000), separated into domestic and international flights. These emission factors were used to convert the monthly count of aircraft movements into $CO_2$ emissions.

The monthly emission was then divided equally between days, but emissions only allocated to the hours between 6:00am and 10:00pm, when most of the aircraft activity takes place at the airport. The average emission factor for the domestic fleet is reported to be 2,680 kg of $CO_2$ per LTO, and the average emission factor for the international fleet is 7,900 kg of $CO_2$ per LTO.

The National Ports Authority of South Africa (Transnet National Ports Authority, 2013) publishes statistics on the harbour activity at the Cape Town Port on a monthly basis. The U.K.s Defra published a report on 2010 shipping emissions in the U.K. (DEFRA, 2010), and this report was used as a guideline to obtain estimates of the average amount of time spent by a particular vessel type in port, the average power of the main engine (ME) and auxiliary engine (AE) of each vessel type, and the emission factors for each vessel type while at berth and performing manoeuvring activities in

Table 4.1: Estimates, per vessel type, of fuel types, the average ratio of the power output of the *AE* to the *ME*, the average number of hours spent in port, and the $CO_2$ emission factors for the *ME* and *AE*. Where RO is residual oil, MGO is Marine Gas Oil, and MDO is Marine Diesel Oil.

| **Engine Type** | **ME Fuel Type** | **AE Fuel Type** | **Average ratio of AE/ME power per vessel** | **Average number of hours in port** | **ME $CO_2$ emission factor (kg $CO_2$ per kWh)** | **AE $CO_2$ emission factor (kg $CO_2$ per kWh)** |
|---|---|---|---|---|---|---|
| Bulk Carrier | RO | MGO | 0.21 | 71.77 | 0.822 | 0.710 |
| Container Ship | RO | RO | 0.22 | 26.50 | 0.822 | 0.745 |
| General Cargo | RO | MGO | 0.33 | 40.01 | 0.822 | 0.710 |
| Passenger | MDO | MDO | 0.35 | 3.87 | 0.782 | 0.710 |
| Ro-Ro Cargo | RO | RO | 0.30 | 14.60 | 0.822 | 0.745 |
| Tanker | RO | MGO | 0.27 | 35.86 | 0.822 | 0.710 |
| Fishing | MGO | MGO | 0.64 | 65.31 | 0.782 | 0.710 |
| Others | MGO | MGO | 0.29 | 53.53 | 0.782 | 0.710 |

port. The guidelines provide the equation to convert the gross tonnage of a vessel into the total ME power as

$$ME\ Power = 6.608 \times Gross\ Tonnage^{0.7033} \tag{4.2}$$

as well as the estimated proportion of power of the AE relative to the ME for a particular vessel type. The emission formula used is as follows:

$$E_{inport} = T[(ME \times LF_{ME}) \times EF_{ME} + (AE \times LF_{AE}) \times EF_{AE}] \tag{4.3}$$

where $E$ is the emission, $T$ is the time in hours spent in port, *ME* is the power of the main engine, AE the power of the auxiliary engine, *LF* is the loading factor for a particular engine and *EF* is the emissions factor for a particular engine. At berth and while manoeuvring, vessels are expected to operate at 20% of the maximum continuous rating for the main engine operation and at 45% of the maximum continuous rating of the auxiliary engine (Table 4.1).

As for the airport emissions, the monthly estimates were divided between each day and each hour of the month, but no assumption was made regarding when the activity took place, so emissions were allocated to all hours of the day.

The monthly emission values from the airport or harbour were allocated to a polygon describing the shape of the airport or harbour respectively. The polygons were then rasterised using the same grid as for the previous emission fields. To obtain hourly emission estimates, the total emissions for the month were divided by

the number of days in the month, and then divided by 24 to get the hourly emission value. In the case of the airport emissions the daily emissions was divided by 16 instead, since it was assumed that the bulk of the aircraft activity took place from 6:00 until 22:00.

### 4.3.5 Uncertainty Analysis

Uncertainty estimates are required not only to show the reliability of the estimates, but the inverse modelling approach requires prior flux estimates as well as prior error estimates for the covariance matrix of the estimated fluxes.

As no information was available on the error of the vehicle counts model, the nature of the data was used to obtain the estimate of uncertainty. The model provides the mean number of vehicle kilometres over a unit distance, and therefore it is likely that the data will follow a Poisson process, which implies that the variance of the estimate should be equal to the mean, and therefore the standard deviation equal to the square root of the mean. The $CO_2$ emission is the product of this count in vehicle kilometres and the average $CO_2$ emission factor, which has a standard deviation of 239.64 g of $CO_2$ per kilometre. From error propagation laws, the error in the $CO_2$ emission estimate will then be

$$\delta CO_{2\ vehicle} = |CO_{2\ vehicle}| \times \sqrt{\frac{\delta CO_{2\ emission\ factor}}{CO_{2\ emission\ factor}}^2 + \frac{\delta vehicle\ km\ count}{vehicle\ km\ count}^2} \tag{4.4}$$

According to the Statistical Release of the 2011 South African census, the omission rate for the census questionnaire was approximately 15% (Statistics South Africa, 2011). The average fuel usage data per household was calculated by dividing the total annual amount of fuel sold by the number of households. No data was available for the difference between households in their fuel usage. Therefore to account for the missing source of uncertainty, the omission rate was elevated to 30%, double that of the omission rate, and this used as the estimate of the uncertainty in domestic emissions.

A report was published for the UK on the treatment of uncertainties of greenhouse gas emissions (DEFRA, 2013b), which provided estimates of activity data error and emission factor error under each fuel type for industrial sources. As the $CO_2$ emission at a particular point source is calculated as:

$$CO_2\ emission = fuel\ usage \times CO_2\ emission\ factor \tag{4.5}$$

error propagation techniques can be used to determine the uncertainty of the final estimate as:

$$\delta CO_{2\ industry} = |CO_{2\ industry}| \times \sqrt{\frac{\delta CO_{2\ emission\ factor}}{CO_{2\ emission\ factor}}^2 + \frac{\delta activity\ data}{fuel\ usage}^2} \tag{4.6}$$

where $\delta$ is the uncertainty value. The uncertainties provided are expressed as proportions of the amount of fuel use and of the size of the emission factor, therefore the uncertainty for the final $CO_2$ emission can be simplified to:

$$\delta CO_{2\ industry} = |CO_{2\ industry}| \times \sqrt{p^2_{activity\ data} + p^2_{CO_{2\ emission\ factor}}} \tag{4.7}$$

where $p_{activity\ data}$ and $p_{CO_{2\ emission\ factor}}$ are the proportions of error assumed for the reported fuel usage data and for the emission factor respectively for a given fuel type.

The aircraft count data is assumed to be without error, and therefore the error will be contained in the emission factors. The standard deviations of the emission factors of individual aircraft used to calculate the average emission factor for the domestic and international fleet were used to determine the uncertainty of the aircraft emissions. This was found to be 34% of the mean emission factor for the domestic fleet and 28% for the international fleet (IPCC, 2000).

As for the aircraft data, the counts of different ships in the harbour are assumed to be correct. Therefore the error is assumed to lie in the emission factors for the different vessel types. From the Defra UK shipping inventory guide (DEFRA, 2010), the assumed error for berth and manoeuvring activities in the port are assumed to be 20 and 30% respectively. Therefore to ensure a conservative estimate, the error is assumed to be 30% of the estimate.

### 4.3.6 Total Emissions

Once the layers for each emission source type is obtained, the total emissions for a particular hour or any particular period can be obtained by summing the raster layers, where the appropriate scalar manipulations have been performed, such as multiplying the vehicle emission layer by the appropriate scaling factor for the day of the week and time of day. In order to be able to obtain the error estimates for each pixel, the uncertainties will need to be expressed as variances instead of standard deviations, and then the variances for each of the source emission estimates in a pixel can be summed to obtain the total variance, which can then be converted back into a standard deviation by taking the square root.

### 4.3.7 Fossil Fuel Product Comparison

To determine if the emission estimated in this study are reasonable, the emissions for a weekday in March were compared with the EDGAR product (Janssens-Maenhout et al., 2012). The spatial distribution of the emissions were mapped for each of the products, and the total emission for the domain of Cape Town was calculated and compared between the two products.

## 4.4 Results

### 4.4.1 Road Transport Vehicle Emissions

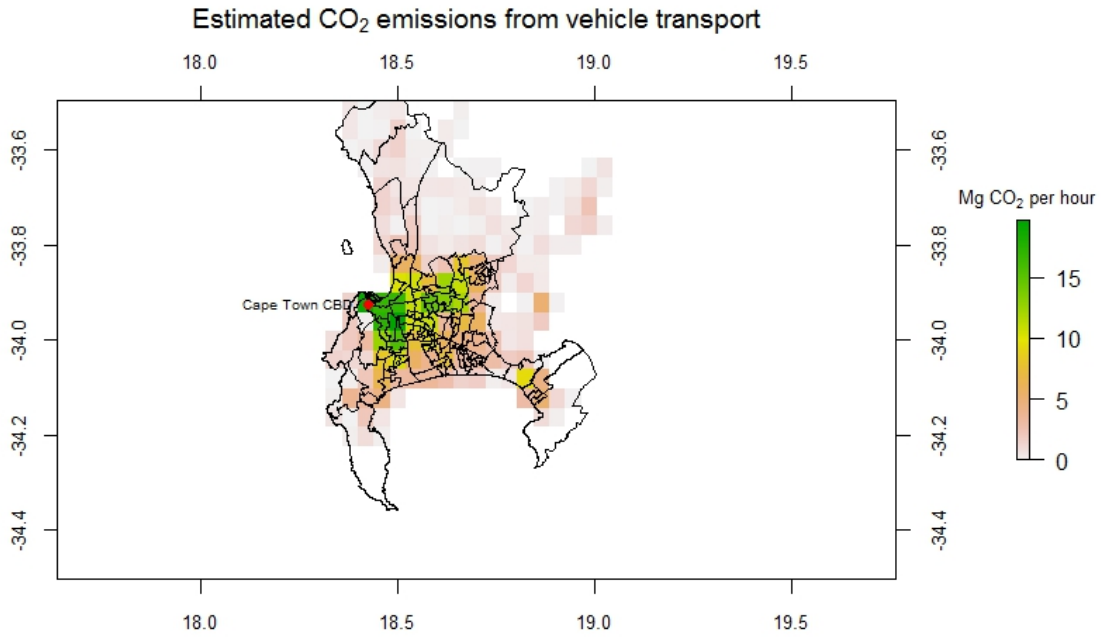


Figure 4.2: Map of rasterised vehicle emissions during peak hour traffic, produced from vehicle kilometre hours and an average emission factor.

The rasterised vehicle emissions during peak hour traffic show the concentration of emissions around the city centre of Cape Town and over the highway routes leading into the City from the suburban areas (Figure 4.2). Using the equation for the uncertainty in the emission estimates, the pixel with the largest emission estimate of 19.74 Mg $CO_2$ per hour has an error estimate of 16.45. This is 83% of the emission estimate. The error in the vehicle emissions would be expected to be large since there

is a great deal of uncertainty in the average emission factors, with factors ranging from 100.1 to 1,034.6 g of $CO_2$ per kilometre.

### 4.4.2 Domestic Emissions

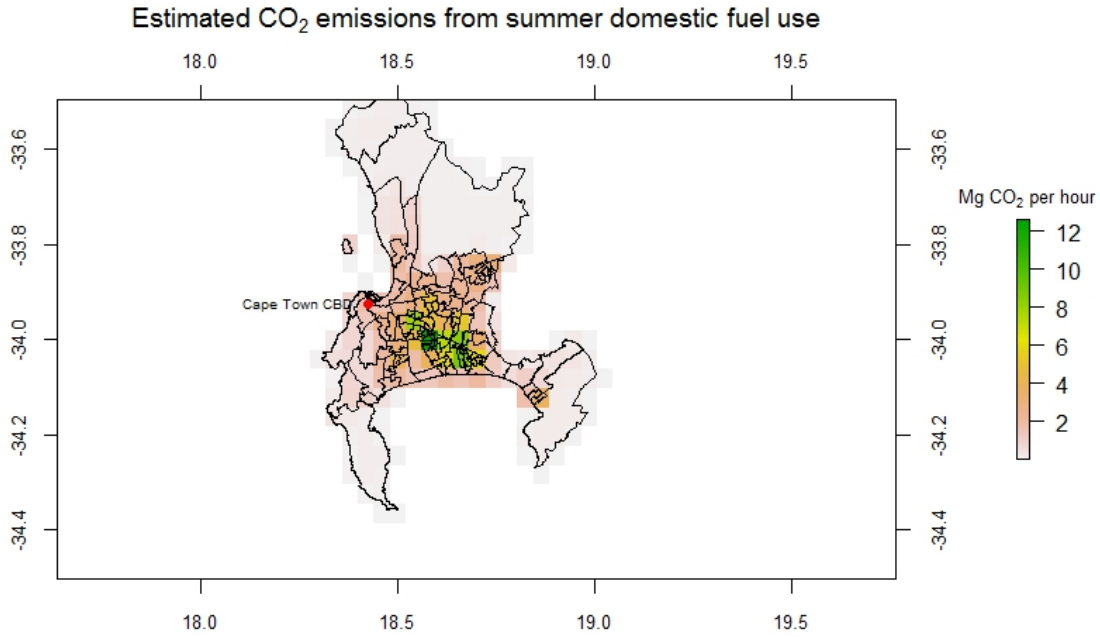


Figure 4.3: Map of rasterised emissions from domestic fuel use during the summer months.

The distribution of residential emissions from domestic fuel use is distributed over the suburban areas around Cape Town, as expected (Figures 4.3 and 4.4). Due to the assumption that more fuel was used for heating purposes in the winter months, the maximum levels of emissions during summer are approximately half of what is consumed during the winter months (Table 4.2). The largest emission estimate for a pixel was 27.7 Mg $CO_2$ per hour during the winter months. The error of the estimate, using the assumed 30% error rate, was 8.3 Mg $CO_2$ per hour.

### 4.4.3 Industrial Emissions from Scheduled Activities

The emissions due to industrial processes are distributed slightly away from the CBD towards the outskirts of the city centre, spreading outwards towards the city bound-

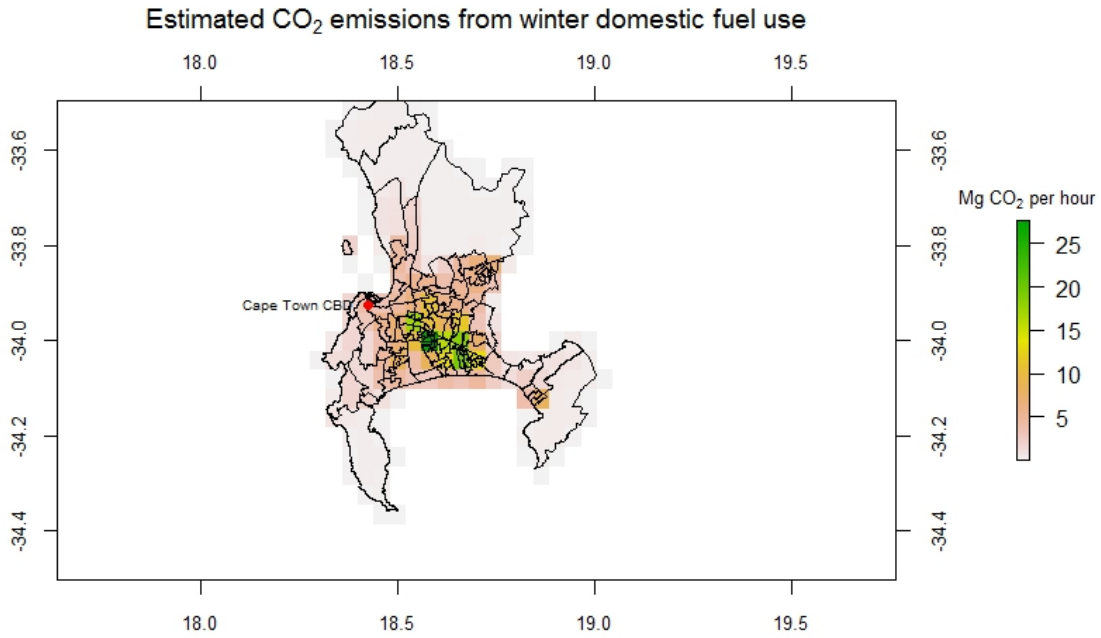


Figure 4.4: Map of rasterised emissions from domestic fuel use during the winter months.

aries (Figure 4.5). The largest per pixel emission 57 Mg $CO_2$ per hour, with an error value of 9, which is 16% of the mean value (Figure 4.6).

The advantage of obtaining the $CO_2$ emissions by using the fuel data compared to converting the CO emissions for different industries is that the error estimates are much smaller, as the fuel data has a much smaller associated error than estimated CO emissions for a particular industry. The disadvantage of the fuel data approach is that emissions from process related activities are ignored, which would be included if the total CO emissions were converted into $CO_2$ emissions. Both the fuel data and the CO emission data are difficult to access, and rely on accurate reporting from the industrial firms.

### 4.4.4 Airport and Harbour Emissions

The emissions from the aircraft at the airport are on average 10,890 Mg of $CO_2$ a month with higher emissions during the November to January months when air traffic increases into the City (Figure 4.7). The average hourly emission from aircraft at the airport is 15.1 Mg of $CO_2$. This analysis does not include the emissions from point

Table 4.2: Emission factors and fuel usage figures used to estimate the amount of $CO_2$ emissions per household (DEFRA, 2012). Total fuel usage figures were obtained from the 2009 energy digest published by the SA Department of Energy (South African Department of Energy, 2009) and estimates of households in South Africa and in the Cape Town area were obtained from the 2011 South African Census (Statistics South Africa, 2011).

| | **LPG** | **Paraffin** | **Wood** | **Coal** |
|---|---|---|---|---|
| **Emission Factor (DEFRA, 2012)** | 1,530.1 kg $CO_2$ kg $CO_2$ per kilolitre | 2,531.9 kg $CO_2$ per kilolitre | 77.38 kg of $CO_2$ per Mg | 2,448.7 kg of $CO_2$ per Mg |
| **Total amount used in Summer per household** | 4.758 $\times$ 10-3 kl | 9.683 $\times 10^{-3}$ kl | 2.465 $\times 10^{-1}$ Mg | 3.278 $\times 10^{-1}$ Mg |
| **Summer emission** of **$CO_2$ per household per hour** | 3.929 $\times 10^{-2}$ kg of $CO_2$ per hour | 1.347 $\times 10^{-1}$ kg of $CO_2$ per hour | 1.048 $\times 10^{-1}$ kg of $CO_2$ per hour | 4.410 kg of $CO_2$ per hour |
| **Total amount used in Winter per household** | 1.047 $\times 10^{-2}$ kl | 2.130 $\times 10^{-2}$ kl | 5.424 $\times 10^{-1}$ Mg | 7.212 $\times 10^{-1}$ Mg |
| **Winter emission of $CO_2$ per household per hour** | 8.551 $\times 10^{-2}$ kg of $CO_2$ per hour | 2.931 $\times 10^{-1}$ kg of $CO_2$ per hour | 2.281 $\times 10^{-1}$ kg of $CO_2$ per hour | 9.598 kg of $CO_2$ per hour |

sources or ground vehicles at the airport. This will require a count of each aircraft type arriving at the airport. The Defra guidelines for Aircraft emissions supply the average amount of time each ground unit spends in operation per LTO cycle for a particular aircraft type, and these estimates could be used to determine emissions from ground vehicles at the airport.

The total emissions from shipping vessels in the Cape Town harbour, at berth and during manoeuvring procedures, are on average 4,171.6 Mg of $CO_2$ per month (Figure 4.8), which is approximately 5.8 Mg of $CO_2$ per hour. Emissions take a dip during the mid-winter months, when the seas around Cape Town are particularly rough and storms are prevalent.

### 4.4.5 Total Emissions

To demonstrate the aggregation of the different source emission layers, the total emissions estimated for a weekday in March 2012 at 18:00 were obtained. The industrial

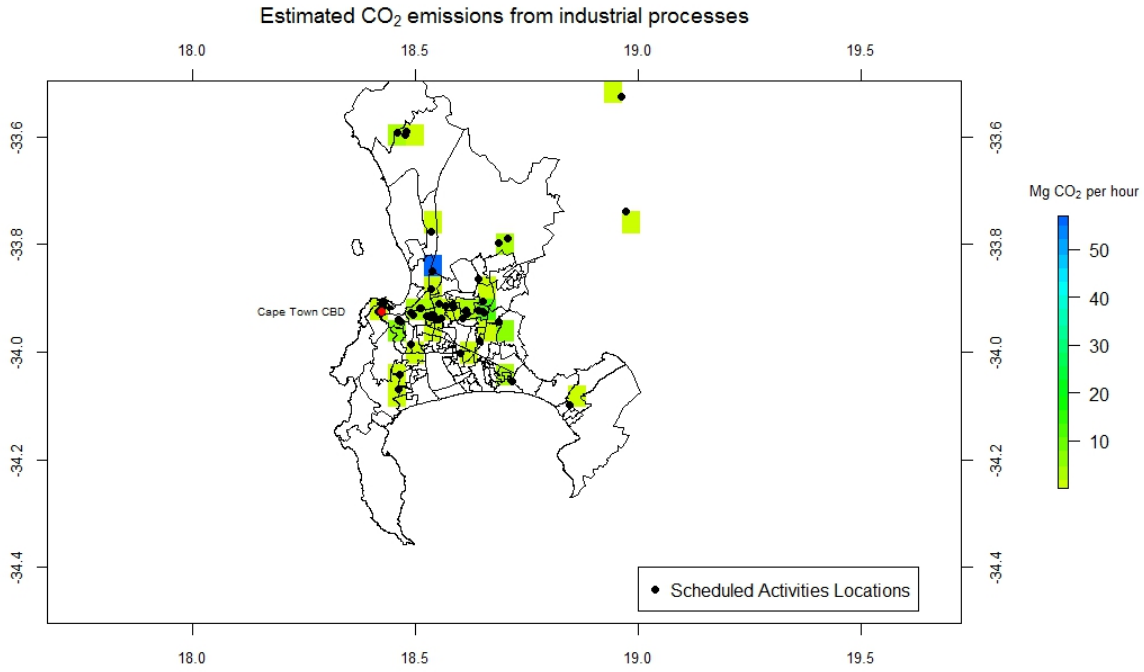


Figure 4.5: Map of rasterised emissions from industrial point sources.

emissions and power station emissions were assumed to take place at all times, so the same layer would be used regardless of which hour was of interest. Since March falls into the winter period, the winter domestic emission layer was used, and since the day falls during the week and at 18:00, no scaling was necessary for the vehicle emissions layer. The airport and harbour emissions for March 2012 were used. The monthly value was divided equally between all hours of the month for the harbour emissions and divided evenly between all days and the hours from 06:00 to 18:00 in the case of the airport emissions. These layers were summed and the resulting emission layer is mapped (Figure 4.9).

### 4.4.6 Fossil Fuel Product Comparison

A comparison with the EDGAR 0.1°×0.1° product over Cape Town reveals similar allocation of $CO_2$ emissions for different areas, but with the EDGAR product providing a more smoothed product (Figure 4.10). The total emissions calculated in this study are strongly influenced by the large point source industrial emitters. The total emission of $CO_2$ during a weekday in March over the full spatial domain of Cape Town was 9,252.883 kilotonnes. Calculated from the EDGAR data, which is

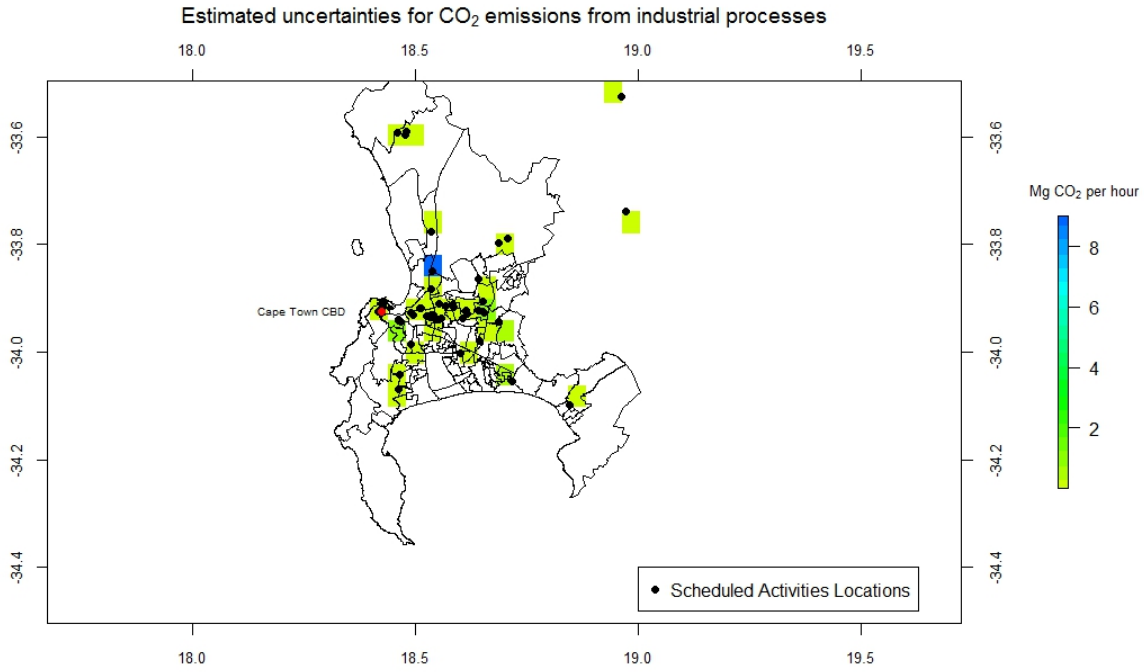


Figure 4.6: Uncertainties in the emissions from industrial point sources.

provided in kg $CO_2$ per $m^2$ per second, the total emission for the same area would be 7,574.559 kilotonnes. The EDGAR data is available until 2010, therefore there is a two year lag between the two products compared. The EDGAR data provided is also an average value for the year, and therefore it is not surprising that our study has a 22% higher estimate of $CO_2$ emissions, which was considered for a typical weekday in March 2012.

## 4.5 Discussion and Conclusions

The results for the City of Cape Town show that through the use of publicly available data and reported data on activity and population levels around the city, it is possible to obtain a spatially and temporally explicit inventory of emissions. The most challenging of the sectors is the industrial sector, where data at the required resolution is not always available at the required detail. These fossil fuel emission estimates are essential to run an atmospheric inversion for the City to obtain improved estimates of the total $CO_2$ fluxes occurring in and around the City.

These estimates can be improved by obtaining detailed fleet data for vehicle,

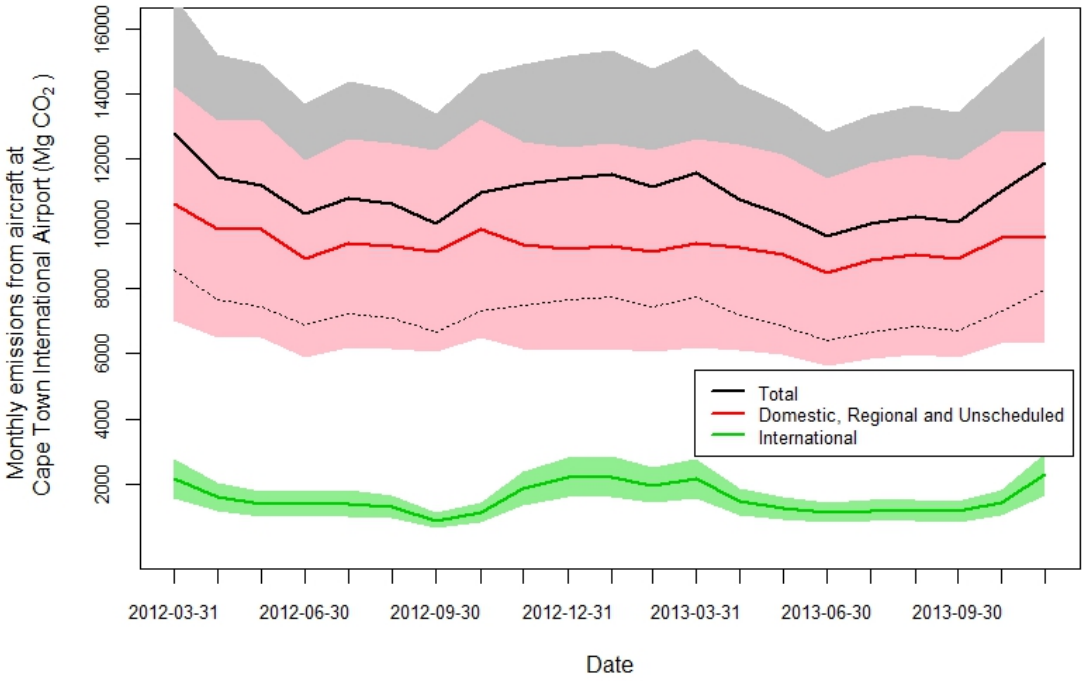


Figure 4.7: Monthly emissions from aircraft at the Cape Town International Airport, where the shaded region represents the level of uncertainty, with the dashed line representing the lower limit of the total emissions from the aircraft at the airport.

aircraft and shipping vessel movements, as the emission factors differ significantly between different fleet types. Domestic emissions estimates can be improved by using Cape Town specific surveys on the average fuel use quantities, and distinguishing this between different households depending on domicile type, as those homes with better amenities are less likely to rely on solid and liquid fuels for cooking, heating and lighting. The emissions from the power stations and industrial sources can be improved if more detailed fuel usage and specific process data were available for each facility included in the assessment. It may be useful for South Africa to publish a similar document as Defra publishes for the UK with South Africa specific emission factors to increase accuracy and so that emission estimates by different professionals can be standardised for South Africa. A comparison with alternative products has revealed that this approach provides reasonable estimates for $CO_2$ emissions.

The results obtained through this process will provide important inputs required for an atmospheric inversion study, relying on observations from a network of $CO_2$ measurement equipment placed around the city. A similar approach as described in this paper will be used to disaggregate the national emissions, to provide coarser

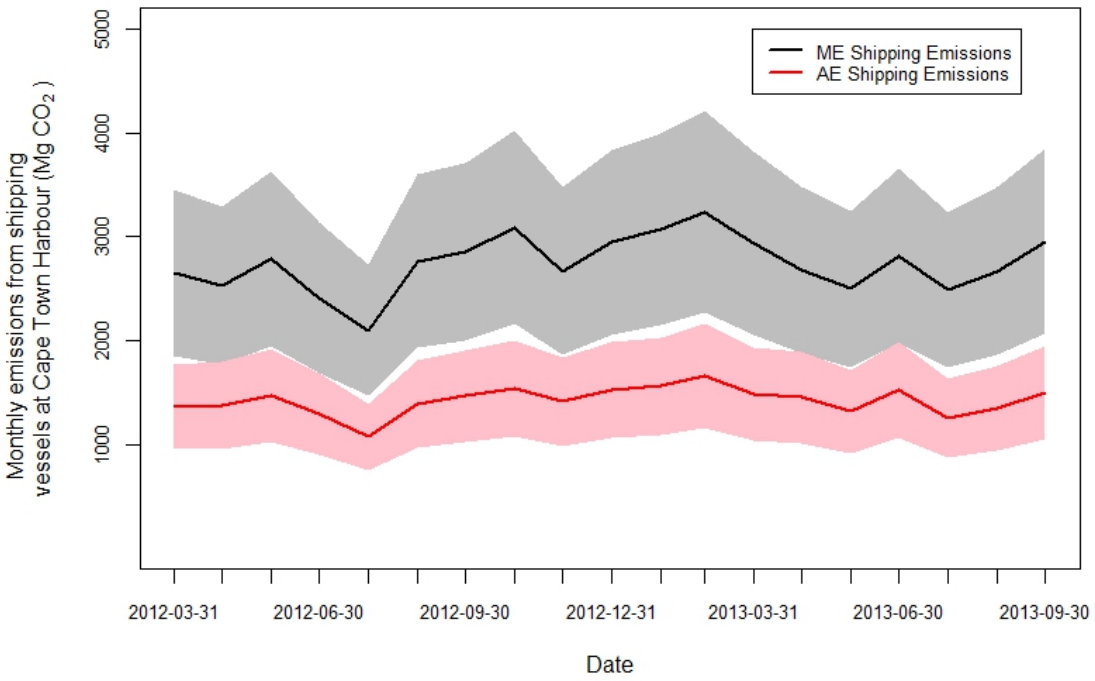


Figure 4.8: Monthly emissions from shipping vessels at the Cape Town Harbour, where the shaded region represents the region of uncertainty in the emission estimates. *ME* is main engine and *AE* is auxiliary engine.

estimates of $CO_2$ emission from fossil fuel combustion, which will then be used in a national inversion study. The best placement of new measurement sites for the observation of $CO_2$ sources and sinks at a national level has already been determined through an optimal network design (Nickless et al., 2015). Improving the knowledge of the South African $CO_2$ budget will help to reduce the uncertainty of the global estimates of sources and sinks, as southern Africa is normally a large source of error in global inversions, due to Africa's general under sampling of greenhouse gas concentration measurements (Denman et al., 2007).

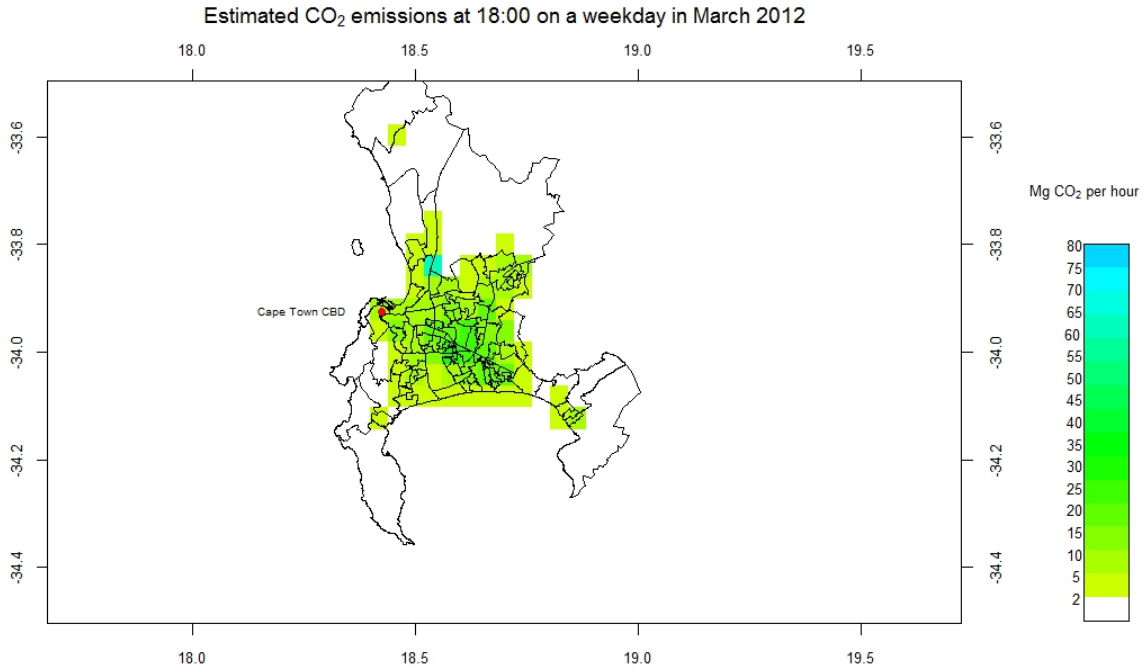


Figure 4.9: Aggregated emissions for the hour from 18:00 to 19:00 during a weekday in March 2012.

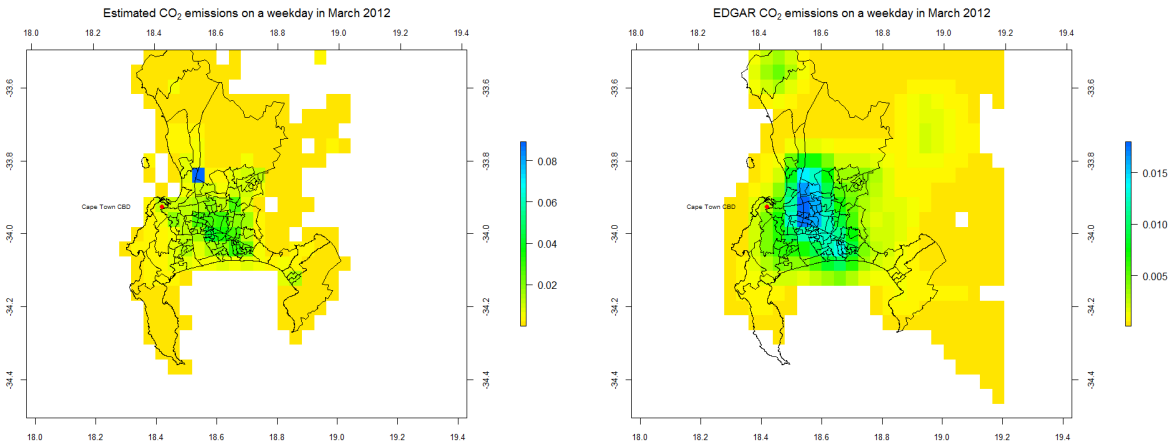


Figure 4.10: Comparison of emissions estimated from the spatial and temporal disaggregation approach (left) with EDGAR emission for the year 2010 (right) over the City of Cape Town. Emissions are presented as kg $CO_2$ per $m^2$ per day.

# Bibliography

Airports Company South Africa: Aircraft Statistics, http://www.acsa.co.za/uploads/AircraftStatistics/CPT_Arrival_AircraftsNOVEMBER2013.pdf, accessed 16 Jan 2014, 2013.

Bivand, R. and Rundel, C: Rgeos: Interface to Geometry Engine Open Sources (GEOS), R package version 0.3-2, http://CRAN.R-project.org/package=rgeos, 2013.

Asefi-Najafabady, S., Rayner, P. J., Gurney. K. R., McRobert, A., Song, ., Coltin K., Huang, J., Elvidge, C., and Baugh, K.: A multiyear, global gridded fossil fuel $CO_2$ emission data product: Evaluation and analysis of results, J. Geophys. Res., 119, doi: 10.1002/2013JD021296, 2014

Bivand, R. and Rundel, C: Rgeos: Interface to Geometry Engine Open Sources (GEOS), R package version 0.3-2, http://CRAN.R-project.org/package=rgeos, 2013.

Cambridge Environmental Research Consultants: Compilation of emissions inventory and preliminary air quality monitoring for Cape Town, City of Cape Town: Cape Town, 2012, Report number FM865/R5/12.

City of Cape Town: State of energy and energy futures report. Cape Town: City of Cape Town, http://www.capetown.gov.za/en/EnvironmentalResourceManagement/publications/Documents/State_of_Energy_+_Energy_Futures_Report_2011_revised_2012-01.pdf, 2011.

City of Cape Town: State of energy report 2015. Cape Town: City of Cape Town, https://africancityenergy.org/getfile.php?id=22&category=0, 2015.

UK Department for Environment, Food and Rural Affairs (Defra): UK ship emissions inventory. Final report. London: Crown, http://uk-air.defra.gov.uk/assets/

documents/reports/cat15/1012131459_21897_Final_Report_291110.pdf, 2010.

UK Department for Environment, Food and Rural Affairs (Defra): 2012 Guidelines to Defra / DECC's GHG Conversion Factors for Company Reporting, Crown: United Kingdom, PB 13773, https://www.gov.uk/government/uploads/system/uploads/attachment_data/file/519263/Emission_Factor_Methodology_Paper_-_2012.pdf, accessed 25 March 2014, 2012.

UK Department for Environment, Food and Rural Affairs (Defra): Government GHG conversion factors for company reporting: Methodology paper for emission factors, London: Crown, https://www.gov.uk/government/uploads/system/uploads/attachment_data/file/224437/pb13988-emission-factor-methodology-130719.pdf, 2013a.

UK Department for Environment, Food and Rural Affairs (Defra): Treatment of uncertainties for national estimates of greenhouse gas emissions, http://uk-air.defra.gov.uk/reports/empire/naei/ipcc/uncertainty/contents.html, 2013b.

Denman, K. L., Brasseur, G., Chidthaisong, A., Ciais, P., Cox, P. M., Dickinson, R. E., Hauglustaine, D., Heinze, C., Holland, E., Jacob, D., Lohmann, U., Ramachandran, S., da Silva Dias, P. L., Wofsy, S. C., and Zhang, X.: Couplings between changes in the climate system and biogeochemistry, in: Climate Change 2007: The Physical Science Basis. Contribution of Working Group I to the Fourth Assessment Report of the Intergovernmental Panel on Climate Change, edited by: Solomon, S., Qin, D., Manning, M., Chen, Z., Marquis, M., Averyt, K. B., Tignor, M., and Miller, H. L., Cambridge University Press, Cambridge, UK and New York, NY, USA, 499–587, 2007.

Eskom: Generating electricity at a nuclear power station fact sheet, revision 6, Generation Communication: South Africa, 2013a.

Eskom: Ankerling and Gourikwa gas turbine power stations fact sheet, revision 4, Generation Communication: South Africa, http://www.eskom.co.za/AboutElectricity/FactsFigures/Documents/GS_0003AnkerlGouriTechBrochRev4.pdf, accessed 14 January 2014, 2013b.

Greenhouse Gas Protocol: Calculating $CO_2$ emissions from mobile sources, version 1.3., http://www.ghgprotocol.org/files/ghgp/tools/CO$_2$-mobile.pdf, accessed 16 January 2014, 2005.

Gurney, K. R., Mendoza, D. L., Zhou, Y. Y., Fischer, M. L., Miller, C. C., Geethakumar, S., Du Can, S. D.: High resolution fossil fuel combustion $CO_2$ emission fluxes for the United States. Environ. Sci. Technol., 43 (14), 5535–5541, doi: 10.1021/es900806c, 2009.

Gurney, K. R., Razlivanov, I., Song, Y., Zhou, Y., Benes, B., and Abdul–Massih, M.: Quantification of fossil fuel $CO_2$ emissions on the building/street scale for a large U.S. city, Environ. Sci. Technol., 46, 12194–12202, doi: 10.1021/es3011282, 2012.

Hijmans, R.J.: Raster: Geographic data analysis and modelling, R package version 2.1-49, http://CRAN.R-project.org/package=raster, 2013

Intergovernmental Panel on Climate Change (IPCC): Good practice guidance and uncertainty management in national greenhouse gas inventories. Montreal: IPCC, 93–102, http://www.ipcc-nggip.iges.or.jp/public/gp/english/, 2000.

Intergovernmental Panel on Climate Change (IPCC): IPCC Guidelines for National Greenhouse Gas Inventories; Prepared by the National Greenhouse Gas Inventories Programme, Eggleston, H.S., Buendia, L., Miwa, K., Ngara, T., Tanabe, K., Eds.; IGES Japan. IPCC National Greenhouse Gas Inventories Programme Technical Support Unit, Institute for Global Environmental Strategies, 2108 -11, Kamiyamaguchi, Hayama, Kanagawa, Japan 2006, 240-0115, 2006.

IPCC: Climate Change 2014: Synthesis Report. Contribution of Working Groups I, II and III to the Fifth Assessment Report of the Intergovernmental Panel on Climate Change [Core Writing Team, Pachauri, R.K. and Meyer, L.A. (Eds.)]. IPCC, Geneva, Switzerland, 151 pp, 2014.

Janssens-Maenhout, G., Pagliari, V., Guizzardi, D., and Muntean, M.: Global emission inventories in the Emission Database for Global Atmospheric Research (EDGAR) Manual (I). Gridding: EDGAR emissions distribution on global gridmaps. Joint Research Centre, Luxembourg: European Union, 33 pp, doi: 10.2788/81454, 2012.

Nickless, A., Ziehn, T., Rayner, P. J., Scholes, R .J., and Engelbrecht, F.: Greenhouse gas network design using backward Lagrangian particle dispersion modelling – Part 2: Sensitivity analyses and South African test case, Atmos. Chem. Phys., 15, 2051–2069, doi: 10.5194/acp-15-2051-2015, 2015.

Presidency, Republic of South Africa: National Environment Management: Air Quality Act, 2004, Government Gazette: Cape Town, vol. 476, No.27318, 2005.

Rayner, P. J., Raupach, M. R., Paget, M., Peylin, P., and Koffi, E.: A new global gridded data set of $CO_2$ emissions from fossil fuel combustion: mehodology and evaluation, J. Geophys. Res., 115, D19306, doi: 10.1029/2009JD013439, 2010.

Rayaprolu K.: Boilers: a practical reference, Taylor and Francis: New York, pp. 181-183; ISBN: 978-1-4665-0053-2, 2013.

South African Department of Minerals and Energy, South Africa: Digest of South African Energy Statistics, ISBN: 0-9584376-4-5, http://www.energy.gov.za/files/media/explained/2006%20Digest%20PDF%20version.pdf, accessed 16 January 2014, 2006.

South African Department of Energy: Digest of South African energy statistics, Pretoria: Department of Energy. http://www.energy.gov.za/files/media/explained/2009%20Digest%20PDF%20version.pdf, accessed 16 January 2014, 2009.

Spotten. J.: Modelled vehicle counts for City of Cape Town Roads (personal communication), Transport Modelling and Systems Analysis: City of Cape Town, 2012.

Statistics South Africa: Census 2011 statistical release, P0301.4., Pretoria: Statistics South Africa, 2011.

Transnet National Ports Authority, South Africa: Summary of cargo handled at ports of South Africa, http://www.transnetnationalportsauthority.net/DoingBusinesswithUs/Pages/Port-Statistics.aspx, accessed 16 January 2014, 2013.

# Chapter 5

# Estimates of $CO_2$ Fluxes over the City of Cape Town, South Africa, through Bayesian Inverse Modelling

**Photos: Alecia Nickless and Ernst-Günther Brunke**

Atmos. Chem. Phys., 18, 4765–4801, 2018
https://doi.org/10.5194/acp-18-4765-2018


Atmospheric Chemistry and Physics
Open Access
EGU

# Estimates of $CO_2$ fluxes over the city of Cape Town, South Africa, through Bayesian inverse modelling

**Alecia Nickless[1,2], Peter J. Rayner[3], Francois Engelbrecht[4,5], Ernst-Günther Brunke[6], Birgit Erni[1,7], and Robert J. Scholes[8]**

[1]Department of Statistical Sciences, University of Cape Town, Cape Town, 7701, South Africa
[2]Nuffield Department of Primary Care Health Sciences, University of Oxford, Oxford, OX2 6GG, UK
[3]School of Earth Sciences, University of Melbourne, Melbourne, VIC 3010, Australia
[4]CSIR Natural Resources and the Environment – Climate Studies, Modelling and Environmental Health, P.O. Box 395, Pretoria, 0001, South Africa
[5]Unit for Environmental Sciences and Management, North-West University, Potchefstroom, 2520, South Africa
[6]South African Weather Service c/o CSIR, P.O. Box 320, Stellenbosch, 7599, South Africa
[7]Centre for Statistics in Ecology, the Environment and Conservation, University of Cape Town, Cape Town, 7701, South Africa
[8]Global Change Institute, University of the Witwatersrand, Johannesburg, 2050, South Africa

**Correspondence:** Alecia Nickless (alecia.nickless@phc.ox.ac.uk)

Received: 28 June 2017 – Discussion started: 25 July 2017
Revised: 25 February 2018 – Accepted: 7 March 2018 – Published: 9 April 2018

**Abstract.** We present a city-scale inversion over Cape Town, South Africa. Measurement sites for atmospheric $CO_2$ concentrations were installed at Robben Island and Hangklip lighthouses, located downwind and upwind of the metropolis. Prior estimates of the fossil fuel fluxes were obtained from a bespoke inventory analysis where emissions were spatially and temporally disaggregated and uncertainty estimates determined by means of error propagation techniques. Net ecosystem exchange (NEE) fluxes from biogenic processes were obtained from the land atmosphere exchange model CABLE (Community Atmosphere Biosphere Land Exchange). Uncertainty estimates were based on the estimates of net primary productivity. CABLE was dynamically coupled to the regional climate model CCAM (Conformal Cubic Atmospheric Model), which provided the climate inputs required to drive the Lagrangian particle dispersion model. The Bayesian inversion framework included a control vector where fossil fuel and NEE fluxes were solved for separately.

Due to the large prior uncertainty prescribed to the NEE fluxes, the current inversion framework was unable to adequately distinguish between the fossil fuel and NEE fluxes, but the inversion was able to obtain improved estimates of the total fluxes within pixels and across the domain. The median of the uncertainty reductions of the total weekly flux estimates for the inversion domain of Cape Town was 28 %, but reach as high as 50 %. At the pixel level, uncertainty reductions of the total weekly flux reached up to 98 %, but these large uncertainty reductions were for NEE-dominated pixels. Improved corrections to the fossil fuel fluxes would be possible if the uncertainty around the prior NEE fluxes could be reduced. In order for this inversion framework to be operationalised for monitoring, reporting, and verification (MRV) of emissions from Cape Town, the NEE component of the $CO_2$ budget needs to be better understood. Additional measurements of $\Delta^{14}C$ and $\delta^{13}C$ isotope measurements would be a beneficial component of an atmospheric monitoring programme aimed at MRV of $CO_2$ for any city which has significant biogenic influence, allowing improved separation of contributions from NEE and fossil fuel fluxes to the observed $CO_2$ concentration.

**Published by Copernicus Publications on behalf of the European Geosciences Union.**

# Chapter 5

# Estimates of $CO_2$ fluxes over the City of Cape Town, South Africa, through Bayesian inverse modelling

# Abstract

We present a city-scale inversion over Cape Town, South Africa. Measurement sites for atmospheric $CO_2$ concentrations were installed at Robben Island and Hangklip lighthouses, located downwind and upwind of the metropolis. Prior estimates of the fossil fuel fluxes were obtained from a bespoke inventory analysis where emissions were spatially and temporally disaggregated and uncertainty estimates determined by means of error propagation techniques. Net ecosystem exchange (NEE) fluxes from biogenic processes were obtained from the land atmosphere exchange model CABLE (Community Atmosphere Biosphere Land Exchange). Uncertainty estimates were based on the estimates of net primary productivity. CABLE was dynamically coupled to the regional climate model CCAM (Conformal Cubic Atmospheric Model), which provided the climate inputs required to drive the Lagrangian particle dispersion model. The Bayesian inversion framework included a control vector where fossil fuel and NEE fluxes were solved for separately.

Due to the large prior uncertainty prescribed to the NEE fluxes, the current inversion framework was unable to adequately distinguish between the fossil fuel and NEE fluxes, but the inversion was able to obtain improved estimates of the total fluxes within pixels and across the domain. The median of the uncertainty reductions of the total weekly flux estimates for the inversion domain of Cape Town was 28%, but reach as high as 50%. At the pixel level, uncertainty reductions of the total weekly flux reached up to 98%, but these large uncertainty reductions were for NEE-dominated pixels. Improved corrections to the fossil fuel fluxes would be possible if the uncertainty around the prior NEE fluxes could be reduced. In order for this inversion framework to be operationalised for monitoring, reporting and verification (MRV) of emissions from Cape Town, the NEE component of the $CO_2$ budget needs to be better understood. Additional measurements of $\Delta^{14}C$ and $\delta^{13}C$ isotope measurements would be a beneficial component of an atmospheric monitoring programme aimed at MRV

of $CO_2$ for any city which has significant biogenic influence, allowing improved separation of contributions from NEE and fossil fuel fluxes to the observed $CO_2$ concentration.

## 5.1 Introduction

Cities are under pressure to reduce their carbon dioxide emissions. In the last 10 years (2006 to 2015), the mean annual increase in carbon dioxide ($CO_2$) concentrations in the global atmosphere has been 2.11 ppm per year (Dlugokencky and Tans, 2016) (NOAA/ESRL 2016), a sharper rise in $CO_2$ emissions than the preceding decades (IPCC, 2014). Approximately 76% of current anthropogenic greenhouse gas emissions are comprised of $CO_2$ contributions (IPCC 2014). While cities cover a mere 2% of the global land surface area, they are responsible for 70% of anthropogenic greenhouse gas emissions (UN–Habitat, 2011), and between 71 and 76% of $CO_2$ emissions from global final energy use (Seto et al., 2014). Annual urban $CO_2$ emissions are more than double the net terrestrial or ocean carbon sinks (Le Quéré et al., 2013).

South Africa is the single largest emitter of $CO_2$ on the continent of Africa, and the 13th largest emitter in the world (Boden et al., 2011). South African cities are home to 63% of the present population (Statistics South Africa, 2011), and by 2030 this is predicted to be 71%. The population of Cape Town (CT) has been rising at 2.5% per annum over the past two decades, and currently is nearly 4 million (City of Cape Town, 2011). Cities are seen as having the greatest potential to provide solutions for emissions reduction and climate change mitigation (Seto et al., 2014; Wu et al., 2016). By reducing the $CO_2$ impact of cities, cities play a pivotal role in decreasing their own climate vulnerability. But there are also additional co-benefits which include improving air-quality, energy access, public health, city liveability, and developing the economy and job creation through advances in green technology (Seto et al., 2014).

Formal climate action plans are developed by governments and city managers whereby the roadmap for implementing greener policies is provided, such as encouraging and developing public transport which makes use of low emission technologies, mass and rapid transport systems, and building retrofits (Sugar and Kennedy, 2013; Erickson and Tempest, 2014). Many cities are taking it on themselves to respond to the climate crisis, reacting to limited international and national policy progress (Hutyra et al., 2014). But to determine if the plans implemented are having the anticipated effect of lowering $CO_2$ emissions, monitoring is required. Monitoring, reporting and verification (MRV) is a concept which is fundamental to most market and policy-based mechanisms in climate economics (Bellassen and Stephan, 2015). In order for emission reduction strategies to be properly implemented and assessed, an MRV approach should be adopted so that emission reduction claims can be validated

in a consistent and reliable manner. Currently, the primary source of this information for cities is by means of emissions inventories. This relies on the collection of activity data to provide an inventory of emissions from different sectors or specific point sources. These inventories are not perfect representations of $CO_2$ emissions. They are heavily dependent on accurate reporting, emission factors, and on assumptions regarding temporal or spatial disaggregation of emissions (Andres et al., 2012), where errors associated with these emission estimates increase with higher spatial and temporal resolutions (Andres et al., 2014). As the importance of these inventories increases due to the need to quantify emissions and assess emission targets, it has become necessary to verify the accuracy of these estimates (NRC, 2010). Adequate MRV implementation requires transparency, quality and comparability of information, with narrow uncertainty estimates (Wu et al., 2016). Currently, uncertainties associated with urban emissions far exceed emission reduction goals, and therefore verification remains challenging. The large amount of uncertainty is due to factors such as incomplete data, inconsistency in reporting between different institutions or facilities, fugitive emissions from point sources such as those caused by gas leaks, and methodology which is rarely checked against scientific standards and procedures (Hutyra et al., 2014). A way of verifying inventory data for a city, and reducing uncertainty of inventory estimates, is by means of the Bayesian atmospheric inversion technique. This method aims to take advantage of continuous measurement of $CO_2$ concentrations from a network of atmospheric monitoring sites located in and around a city. By attempting to model the $CO_2$ concentrations at these sites, the inversion is able to provide corrections to the inventory of $CO_2$ emissions from the city, so that the mismatch between the modelled and observed concentrations is reduced.

Several regional or mesoscale atmospheric inversions have been published (Lauvaux et al., 2008, 2009, 2012; Schuh et al., 2013), and more recently city-scale inversion studies have been conducted in Europe and North America (Strong et al., 2011; Duren and Miller, 2012; McKain et al., 2012; Brioude et al., 2013; Kort et al., 2013; Lauvaux et al., 2013; Bréon et al., 2015; Turnbull et al., 2015; Boon et al., 2016; Oda et al. , 2017). These top down approaches make use of an atmospheric transport model to relate observations of $CO_2$ concentrations in the atmosphere to the $CO_2$ fluxes from the domain of interest (Lauvaux et al., 2012). This method applies corrections to the inventory data, which enters the inversion calculation by means of the prior estimates. This paper reports the results for an atmospheric inversion for CT, South Africa.

Making use of point measurements of $CO_2$ concentrations means that the effects of all fluxes of $CO_2$ are observed as an aggregated total. It is challenging to separate

out these aggregated $CO_2$ fluxes into different components of the total $CO_2$ budget without additional measurements, such as $\Delta^{14}C$ (Turnbull et al., 2015) and $\delta^{13}C$ isotope measurements (Newman et al., 2016), or without high confidence in the spatial and temporal patterns of fluxes (Shiga et al., 2014). Even when additional measurements of $CO_2$ mole fractions are available, at the current point in time, background atmospheric conditions are not sufficiently characterised to use isotope tracers to discriminate between fossil fuel and biogenic fluxes (Turnbull et al., 2015). To conduct a Bayesian atmospheric inversion at the city-scale, a detailed $CO_2$ inventory analysis is required, where all the main contributors to the anthropogenic $CO_2$ budget are considered. Apart from their use in an atmospheric inversion, better understanding of the underlying processes at the urban scale and improved quantification of $CO_2$ emissions provides information contributing towards the policy decisions made by urban practitioners, helps to improve understanding of urban dynamics, and informs future scenarios (Hutyra et al., 2014). An example of this is the detailed street level inventory analysis undertaken in the Hestia project for U.S. cities Indianapolis, Los Angeles, Phoenix and Salt Lake City (Gurney et al., 2012; Davis et al., 2017). Preceding these inventories was the Vulcan inventory which covers the contiguous U.S. (Gurney et al., 2009). These detailed inventories have made possible atmospheric inversion exercises, as well as other top down methods for obtaining urban $CO_2$ flux estimates, for these cities (Strong et al., 2011; Brioude et al., 2013; Bréon et al., 2015; Lauvaux et al., 2016). Such a detailed inventory analysis is not available for any South African city, and therefore a detailed spatially and temporally disaggregated inventory analysis of direct $CO_2$ emissions was undertaken for CT specifically for the use of this atmospheric inversion exercise (Nickless et al., 2015a).

Atmospheric inversions have various sources of uncertainty, which include atmospheric transport modelling errors (particularly at night when the planetary boundary layer is shallow) (Geels et al., 2007); incorrect characterisation of prior flux estimates and their uncertainties (which includes errors in the inventory analysis) (Bréon et al., 2015; Lauvaux et al., 2016); atmospheric measurement errors (Gerbig et al., 2003); representation errors due to the comparison of a concentration measurement at a point with a modelled concentration representative of a surface grid box (Gerbig et al., 2003); and aggregation errors which occur as fluxes from various sources are coerced into homogeneous grid cells (Kaminski et al., 2001). In the case of cities, atmospheric transport modelling is further complicated by small-scale turbulence, highly heterogeneous surface characteristics, and urban heat island effects (Hutyra et al., 2014; Bréon et al., 2015).

Therefore, careful consideration of the atmospheric transport model (or models) is required for an atmospheric inversion. The atmospheric transport modelling in this study was provided by the Conformal Cubic Atmospheric Model (CCAM) (McGregor and Dix, 2008) at the resolution of 1 km×1 km. CCAM, at a slightly coarser resolution, has already been used for a regional network design study over South Africa, making use of a similar Bayesian inversion framework (Nickless et al., 2015b), and has been verified over South Africa and over the CT target region at a spatial resolution of up to 1 km×1 km (Roux, 2009; Engelbrecht et al., 2009, 2011).

High resolution inversions are required to quantify emissions down to the sector or point source level. Lauvaux et al. (2016) performed an ultra high resolution inversion where sector specific anthropogenic emissions were considered, but ignored biogenic fluxes. This was possible due to the selection of the dormant period for the inversion, when fluxes due the biosphere would have been at a minimum. When considering longer periods, or for cities in regions which may not have a dormant vegetation period, this assumption will not be valid, particularly for a medium-sized city, where natural processes can be a significant contributor to the carbon budget. Such would be the case for South African cities, such as CT and Johannesburg, where large national parks and other natural areas are located near or within city limits and within city vegetation growth is non-negligible. CT is also surrounded by a large agricultural sector consisting of vineyards and fruit orchards. Ironically, there are features of cities which allow for better plant growth. For example, the urban heat island effect leads to a longer growing season for plants, and reduced wind within cities leads to less plant stress resulting in better plant growth (Buyantuyev and Wu 2012). In addition, nitrogen deposition within cities leads to increased nutrient availability, and particularly in arid regions, cities cause augmented water availability for plants (Hutyra et al., 2014). If allowed growing space, plants can make a significant contribution to the carbon budget of a city.

Therefore, for a city like CT, biogenic fluxes cannot be ignored, and within atmospheric inversion studies are usually estimated by means of a land surface exchange model (Bréon et al., 2015; Staufer et al., 2016). Bréon et al. (2015) and Staufer et al. (2016) made use of the C-TESSEL land atmosphere scheme which is used in the ECMWF forecasting system. In this study we have made use of the CABLE (Community Atmosphere Biosphere Land Exchange) model to represent the biogenic $CO_2$ fluxes in the $CO_2$ budget (Kowalczyk et al., 2006). CABLE had the same spatial and temporal resolution as the meteorology. The average weekly fluxes for each pixel were calculated and used as the prior biogenic fluxes.

We present a Bayesian inversion framework used to obtain estimates of $CO_2$ fluxes over CT, and present the results of the reference atmospheric inversion for a sixteen month period from March 2012 until June 2013. The domain considered was a 100 km×100 km region with CT at the centre. The spatial resolution of the atmospheric transport model was set at 1 km×1 km, and the spatial resolution of the surface fluxes was made to match this resolution. Fluxes were solved for at a weekly time step, separately for day and night. Fossil fuel and biogenic fluxes were solved for separately, and fossil fuel fluxes separated into week and weekend fluxes.

## 5.2 Methods

### 5.2.1 Bayesian Inverse Modelling Approach

The Bayesian synthesis inversion method, as described by Tarantola (2005) and Enting (2002), was used to solve for the fluxes in this study. This method has been described for global inversions (Bousquet et al., 1999; Kaminski et al., 1999; Rayner et al., 1999; Gurney et al., 2002; Peylin et al., 2002; Gurney et al., 2003; Law et al., 2003; Baker et al., 2006; Rayner et al., 2008; Ciais et al., 2010), as well as for many of the recent city-scale inversions (Lauvaux et al., 2016; Bréon et al., 2015). The observed concentration ($c$) at a measurement station at a given time can be expressed as the sum of different contributions from the surface fluxes, from the domain boundaries, and from the initial concentration at the site. Concentrations at the measurement site can be modelled as:

$$\boldsymbol{c}_{mod} = \mathbf{H}\boldsymbol{s} \tag{5.1}$$

where $\boldsymbol{c}_{mod}$ are the modelled concentrations and $\boldsymbol{s}$ are various sources, where sources are any part of the domain which can provide a positive or negative contribution of $CO_2$. $\mathbf{H}$ is the Jacobian matrix representing the first derivative of the modelled concentration at the observational site and dated with respect to the coefficients of the source components (Enting, 2002). It provides the sensitivity of each observation to each of the unknown sources, where the sources can be either fluxes or concentrations of $CO_2$. Estimates of the unknown sources can be obtained by minimising the following cost-function with respect to $\boldsymbol{s}$:

$$J(\boldsymbol{s}) = \frac{1}{2}\left((\boldsymbol{c}_{mod} - \boldsymbol{c})^T \mathbf{C}_{\boldsymbol{c}}^{-1}(\boldsymbol{c}_{mod} - \boldsymbol{c}) + (\boldsymbol{s} - \boldsymbol{s}_0)^T \mathbf{C}_{\boldsymbol{s}_0}^{-1}(\boldsymbol{s} - \mathbf{s_0})\right) \tag{5.2}$$

where $\boldsymbol{s}$ is the control vector of unknown surface fluxes and boundary concentrations we wish to solve for, $\boldsymbol{s}_0$ is the vector of prior flux and boundary concentration estimates, $\mathbf{C}_{\boldsymbol{c}}$ is the uncertainty covariance matrix of the observations, and $\mathbf{C}_{\boldsymbol{s}_0}$ is the uncertainty covariance matrix of the fluxes and boundary concentrations (Tarantola, 2005).

The solution to this minimisation problem is:

$$\boldsymbol{s} = \mathbf{s_0} + \mathbf{C}_{\boldsymbol{s}_0}\mathbf{H}^T \left(\mathbf{H}\mathbf{C}_{\boldsymbol{s}_0}\mathbf{H}^T + \mathbf{C}_{\boldsymbol{c}}\right)^{-1} (\boldsymbol{c} - \mathbf{H}\boldsymbol{s}_0) \tag{5.3}$$

and the posterior covariance matrix can be determined as follows (Tarantola, 2005):

$$\begin{aligned} \mathbf{C_s} &= \left(\mathbf{H}^T\mathbf{C}_{\boldsymbol{c}}^{-1}\mathbf{H} + \mathbf{C}_{\boldsymbol{s}_0}^{-1}\right)^{-1} && (5.4)\\ &= \mathbf{C}_{\boldsymbol{s}_0} - \mathbf{C}_{\boldsymbol{s}_0}\mathbf{H}^T \left(\mathbf{H}\mathbf{C}_{\boldsymbol{s}_0}\mathbf{H}^T + \mathbf{C}_{\boldsymbol{c}}\right)^{-1} \mathbf{H}\mathbf{C}_{\boldsymbol{s}_0}. && (5.5) \end{aligned}$$

### 5.2.2 Control Vector - s

The control vector, $\boldsymbol{s}$, can be broken up into different components. The total $CO_2$ flux from a single surface pixel for a given week is made up of the following individual fluxes:

$$\boldsymbol{s}_{sf;\,i} = \boldsymbol{s}_{\mathit{ff\ week\ day};\,i} + \boldsymbol{s}_{\mathit{ff\ week\ night};\,i} + \boldsymbol{s}_{\mathit{ff\ weekend\ day};\,i} + \boldsymbol{s}_{\mathit{ff\ weekend\ night};\,i} \tag{5.6}$$

$$+\boldsymbol{s}_{\mathit{NEE\ day};\,i} + \boldsymbol{s}_{\mathit{NEE\ night};\,i} \tag{5.7}$$

where $\boldsymbol{s}_{sf;\,i}$ is the total weekly surface flux from the $i^{th}$ pixel, $\boldsymbol{s}_{\mathit{ff\ week\ day};\,i}$ is the total fossil fuel flux during the day during the working week, $\boldsymbol{s}_{\mathit{ff\ week\ night};\,i}$ is the total night-time fossil fuel flux during the working week, $\boldsymbol{s}_{\mathit{ff\ weekend\ day};\,i}$ is the total weekend daytime fossil fuel flux, $\boldsymbol{s}_{\mathit{ff\ weekend\ night};\,i}$ is the total weekend night-time fossil fuel flux, and $\boldsymbol{s}_{\mathit{NEE\ day};\,i}$ and $\boldsymbol{s}_{\mathit{NEE\ night};\,i}$ are the total day and night-time biogenic fluxes for the full week from the $i^{th}$ pixel. The inversion solves for each of these

separate fluxes. There are 101×101 = 10,201 surface pixels. Over the 16 month period from March 2012 to June 2013, separate monthly inversions are carried out for all months with sufficient valid concentration observations; a total of 13 inversions. Each monthly inversion solves for four weekly fluxes. Therefore a monthly inversion solves for 10,201×6×4 = 244,824 surface fluxes.

The mean day and night-time concentrations at each of the four domain boundaries for each week are the last components of the control vector. The inversion solves for 4×2×4 = 32 boundary concentrations (4 boundaries, day/night, 4 weeks). We solved for weekly concentrations at the boundaries as we expected these concentrations to show small changes on synoptic time scales, particularly inflow from the ocean boundaries. We avoided solving for too short a period so that the percentile filtering technique (see section 5.2.8) would never discard all measurements for a period. The maximum standard deviation in the hourly background $CO_2$ concentrations for a week was 0.8 ppm.

As a sensitivity analysis, presented in a companion paper, we examined two alternative compositions of the control vector. We considered solving for a mean weekly flux for each month. In this case for a surface pixel we solved for two biogenic mean weekly fluxes (day and night) and four fossil fuel mean weekly fluxes (day and night working week, day and night weekend). We also considered a separate inversion for each week. In this case only the concentration measurements for one week were used and the individual weekly fluxes (two biogenic and four fossil fuel) were solved for, and this was repeated for each of the four weeks in the month. The benefit of these two alternative control vectors is that the resulting dimensions of the $\mathbf{C}_{\boldsymbol{s}_0}$ matrix is much smaller compared with the reference case we present in this paper.

### 5.2.3 Concentration Measurements - c

Two $CO_2$ monitoring sites were established at Robben Island and Hangklip lighthouses. Due to the dominant wind directions in CT (Fawcett et al., 2007), either from the south or north west, the location of the Robben Island and Hangklip stations were well suited for observing contributions from the area of interest, particularly from CT. The Hangklip site observed mainly background air, but occasionally viewed the biogenic-influenced continental air. Robben Island often observed air with enhancements from CT. The location of these sites in relation to the domain are shown in Figure 5.1. The average wind speed and direction across the domain, as modelled by CCAM, are shown in the appendix (Appendix B.3).


Figure 5.1: Google Earth image of the domain, where Cape Town is located at the centre. The corner coordinates of the full domain are 33°29′42.00″ south 18°11′42.00″ east (top left), 33°29′42.00″ south 19°12′18.00″ east (top right), 34°30′18.00″ south 18°11′42.00″ east (bottom left), 34°30′18.00″ south 19°12′18.00″ east (bottom left). The locations of the measurement sites and the Cape Point GAW station background site are indicated together with images of these sites (Photo credits: Ernst Brunke and Alecia Nickless). CBD = central business district.

Each site was equipped with a Picarro Cavity Ring-down Spectroscopy (CRDS) (Picarro G2301) instrument. This instrument measures $CO_2$, methane $CH_4$, and water vapour ($H_2O$) simultaneously, every five seconds, producing a precision of better than 0.05 parts-per-million volume (ppmv) for $CO_2$, 0.07 parts-per-billion volume (ppbv) for $CH_4$, and 100 ppmv for $H_2O$. This instrument maintains high linearity, precision, and accuracy over changing environmental conditions, requiring only minimal calibration, and is recognised as one of the highest precision instruments for measurement of the top three greenhouse gases (Crosson, 2008).

The inlet of the measurement tube at each site was located at the top of the lighthouse, and had a Gelman filter to prevent contamination of the instrument through aerosols or water droplets. The inlet tube led to a VICI rotary valve which directed the sampled air stream to the Picarro instrument. Approximately every four days the rotary valve switched to a calibration line which allowed the flow of calibration gas through the instrument for a period of half an hour.

The Robben Island lighthouse is an 18 m tall circular masonry tower, and the height of the focal plane of the light is 47 m above the high water level. The location of the lighthouse is 33°48′52.20″ south and 18°22′29.25″ east. The Hangklip lighthouse is a 22 m tall concrete tower, where the focal plane of the light is 34 m above the high water level. It is located at 34°23′11.40″ south and 18°49′42.30″ east. It is located on the tip of False Bay, opposite to Cape Point.

### 5.2.4 System Meteorology

CCAM is the variable-resolution global atmospheric model developed by the Commonwealth Scientific and Industrial Research Organisation (CSIRO) (McGregor, 1996; McGregor and Dix, 2001; McGregor, 2005a,b; McGregor and Dix, 2008). It employs a semi-implicit semi-Lagrangian method to solve the hydrostatic primitive equations. The Geophysical Fluid Dynamics Laboratory (GFDL) parameterisations for long-wave and short-wave radiation are used (Lacis and Hansen, 1974; Schwarzkopf and Fels, 1991), with interactive cloud distributions determined by the liquid and ice-water scheme of Rotstayn (1997). Total-variation-diminishing vertical advection is applied to solve for the advective process in the vertical. A stability-dependent boundary layer scheme based on Monin Obukhov similarity theory is employed (McGregor, 1993), together with the non-local treatment of the boundary layer scheme as described in Holtslag and Boville (1993). A canopy scheme is included, as described by Kowalczyk et al. (1994), having 6 layers for soil temperatures and soil moisture (solving Richard's equation) and 3 layers for snow. The cumulus convection scheme uses a mass-flux

closure (McGregor, 2003), and includes downdrafts, entrainment and detrainment. Gravity wave drag is parameterised following Chouinard et al. (1986).

CCAM may be applied in stretched-grid mode to function as a regional climate model, thereby providing a flexible framework for downscaling reanalysis data or global circulation model simulations to high resolution over an area of interest. Stretched grids are obtained using the Schmidt (1977) transformation. A multiple-nudging approach was followed to downscale the 250 km resolution National Centres for Environmental Prediction (NCEP) reanalysis data (Kalnay et al., 1996) to a resolution of 60 km over southern Africa, 8 km over the south western Cape and subsequently to a 1 km resolution over the study area. The 8 km resolution domain stretched over an area of about $1300 \times 1300\,\mathrm{km}^2$, whilst the 1 km resolution domain centred over False Bay stretched over an area of about $160 \times 160\,\mathrm{km}^2$. Output was stored at a time resolution of 1 hour. CCAM was spectrally nudged with the synoptic-scale forcing reanalysis data at 6-hourly intervals for the period 1979-2013 using a scale-selective Gaussian filter (Thatcher and McGregor, 2009, 2010). This forcing was applied from 900 hPa higher up into the atmosphere. Sea-surface temperatures from the NCEP data set were used as lower boundary forcing.

To justify the use of CCAM to provide modelled winds and other climatological variables, we rely on previous studies which have used this model for atmospheric transport modelling in our target area (Whittlestone et al., 2009), and studies which have validated CCAM at various spatial resolutions (Engelbrecht et al., 2009; Roux, 2009; Engelbrecht et al., 2011, 2013, 2015). In particular, CCAM has been able to satisfactorily recreate present-day rainfall totals and the rainfall seasonal cycle, as well as circulation patterns over South Africa (Engelbrecht et al., 2009), and has been able to simulate with some success mid-tropospheric closed-lows and extreme rainfall events (Engelbrecht et al., 2015). CCAM has been validated over the Stellenbosch wine-producing area, which falls within the domain of this inversion, with respect to temperature, relative humidity and wind speed at six different stations within this region (Roux, 2009). Those stations located within the high-resolution focus area of the stretched-grid obtained root mean square errors of 0.64 $\mathrm{ms}^{-1}$ or lower and correlations close to 1 between the modelled and observed wind speeds. Validating the wind product from CCAM further in a rigorous manner is beyond the scope of this paper.

### 5.2.5 Jacobian Matrix - H

In order to generate the Jacobian matrix, **H**, for the inversion procedure, which maps the surface fluxes and boundary inflows to the concentrations observed at the receptor sites, a Lagrangian particle dispersion model (LPDM) was run in backward mode. An LPDM simulates the release of a large number of particles from arbitrary receptors and records the location of the particles at fixed time steps (Uliasz, 1993, 1994). The model implemented in this study was developed by Marek Uliasz (1993), which will be referred to as LPDM. LPDM is driven by the hourly three-dimensional fields of mean winds ($u$, $v$, $w$), potential temperature and turbulent kinetic energy (TKE), which were obtained from the CCAM model. When LPDM is run backward in time, in receptor-orientated mode, the particle counts can be used to generate **H** for a given receptor site, as described in Ziehn et al. (2014) and Nickless et al. (2015b) following Seibert and Frank (2004).

The Jacobian for a 4 week period during each month of the study was generated by allowing the LPDM model to run in backward mode over a full 2 month period. Particle counts were extracted for the 4 weeks of interest. Particles were released every 20 seconds and each particle's position was recorded at 1 minute intervals. Particles that were near the surface were allocated to a surface grid box, corresponding to the surface pixels of the atmospheric transport model, and the total particle count within each of these boxes was determined. These counts depended on the dimensions and position of the surface grid boxes. The particle counts were used to calculate the source–receptor ($s$–$r$) relationship. We followed Seibert and Frank (2004) to convert the particle counts into the elements of the Jacobian matrix. As described in Ziehn et al. (2014), we modified the approach of Seibert and Frank (2004) to account for the particle counts which were produced by our LPDM as opposed to the mass concentrations which were output by the atmospheric transport model in their study. The resulting $s$–$r$ relationship between the measurement site and source $i$ at time interval $n$, which provide the elements of the matrix **H**, is:

$$\frac{\partial \boldsymbol{c}_{sf}^{-}}{\partial \boldsymbol{s}_{in}} = \frac{\Delta T \mathrm{g}}{\Delta P} \overline{\left(\frac{N_{in}}{N_{tot}}\right)} \frac{44}{12} \times 10^3, \tag{5.8}$$

where $\boldsymbol{c}_{sf}^{-}$ is a volume mixing ratio (receptor) expressed in ppm and $\boldsymbol{s}_{in}$ is a mass flux density (source), $N_{in}$ the number of particles in the receptor surface grid from source pixel $i$ released at time interval $n$, $\Delta T$ is the length of the time interval, $\Delta P$ is the

pressure difference in the surface layer, g is the acceleration due to gravity, and $N_{tot}$ the total number of particles released during a given time interval.

In this inversion setup weekly fluxes of $CO_2$ were separated into day and night-time contributions, into fossil fuel and NEE contributions, and in the case of fossil fuels, into working week and weekend contributions. Therefore, to obtain the NEE contributions the particle count $N_{in}$ was the sum over one week ($\Delta T$=1 week (day/night)). For fossil fuel fluxes, the particle count was separated into the contribution from the working week and from the weekend, separately for day and night.

The surface layer height was set to 50 m which corresponds to approximately 595 Pa ($\Delta P$). If we assume well mixed conditions, then the $s$–$r$ relationship should be independent of the thickness of the surface layer, as long as the layer is not too deep, as the particle count will be adjusted proportional to the volume of the grid box. Under stable conditions, this may not be the case (Seibert and Frank, 2004). The spatial resolution of the surface flux grid boxes was set to be the same as that of the high-resolution subregion of the atmospheric transport model, resulting in a gridded domain consisting of 101×101 grid boxes (a resolution of approximately $0.01° \times 0.01°$ or 1 km×1 km).

The fluxes from the surface pixels are expressed in kg $CO_2 m^{-2}$ week$^{-1}$ and are transformed through $\mathbf{H}$ into contributions to the concentration at the measurement site in units of ppm. The inversion solves for the concentrations at the boundary of the domain. Ziehn et al. (2014) shows that the Jacobian which provides the sensitivities of observed concentrations to boundary concentrations can be calculated as:

$$\frac{\partial \bar{\boldsymbol{s}}_B}{\partial \boldsymbol{c}_b} = \frac{N_B}{N_{tot}} \tag{5.9}$$

where $\bar{\boldsymbol{s}}_B$ is the concentration at the domain boundary, $\boldsymbol{c}_b$ is the volume mixing ratio, $N_B$ is the number of particles from the specific domain boundary and $N_{tot}$ the total number of particles viewed at the receptor site from any of the domain boundaries. The contribution to the observed concentration at the receptor site can be written as:

$$\boldsymbol{c}_b = \mathbf{H}_B \boldsymbol{s}_B \tag{5.10}$$

where $\mathbf{H}_B$ is the Jacobian with respect to the domain boundary concentrations, $\boldsymbol{s}_B$ the domain boundary concentrations and $\boldsymbol{c}_b$ the contributions from the boundary to the

observed concentration at the measurement site in units of ppm. The row elements of $\mathbf{H}_B$ sum to one. Therefore the elements of $\boldsymbol{c}_b$ represent a weighted average of the concentrations at the domain boundaries, and provide a basis concentration to which the contributions from the surface fluxes are added. Each inversion solves for 4 weekly domain boundary concentrations for each cardinal direction, separated by day and night.

### 5.2.6 Inventory of Anthropogenic Emissions

An inventory analysis was conducted specifically for this atmospheric inversion exercise (Nickless et al., 2015a). The anthropogenic emissions were subdivided into those due to road transport, airport and harbour emissions, residential lighting and heating, and industrial point sources. Road transport emissions were derived from modelled values of vehicle kilometres for each section of the road network, modelled from observed vehicle count data. The vehicle kilometres were scaled for each hour of the day, and reported separately for working week days and weekend days. Therefore the vehicle emissions for day and night are distinctive for the week / weekend and day / night periods.

Airport emissions were derived from landing and takeoff cycles, as reported by Airports Company South Africa for each month. We used the IPCC reported average emission factors for domestic and international fleets (IPCC, 2000), and these were used to convert the airport activity data into emissions of $CO_2$. Emissions were expected to be concentrated between 6:00 and 22:00, and so the monthly emission was divided evenly between these hours. Harbour emissions were derived for port activity published by the South African Ports Authority for each month. Based on the gross tonnage of vessels which docked at the port during the month, emissions could be derived as described in DEFRA (2010). The monthly emissions were divided equally between all hours of the month, as it was assumed that harbour activities would be continuous.

Residential emissions for lighting and heating were derived from population count data obtained for each of the municipal wards in 2011 (Statistics South Africa, 2011). The population of CT was 3,740,025, as reported in the 2011 census (Statistics South Africa, 2011). The South African government reports on the fuel used for domestic heating and lighting (South African Department of Energy, 2009). This was divided between the total population, and then allocated to each ward depending on the population residing in that area. The fuel usage was scaled according to the proportion of fuel used for cooking, lighting and heating, where 75% of the annual heating fuel

usage was assumed to take place during the winter months (March to August). It was assumed that 75% of the annual energy consumed was used for heating, 20% for cooking and 5% for lighting.

CT provided monthly fuel usage by the largest industrial emitters. The reported fuel usage for the top fuel users were converted directly into $CO_2$ emissions by multiplying these figures with the Defra greenhouse gas emission factors (DEFRA, 2013a). The fuel types that were considered included heavy fuel oil, coal, diesel, paraffin and fuel gas which were divided into liquid petroleum gas and refinery fuel gas. As no information was available about when the activity was occurring at these facilities, the emissions were divided equally between all hours of the month.

Based on this inventory analysis, the percentage contribution of industrial point sources to the total fossil fuel emission for CT was 12.0%, 34.6% from vehicle road transport, 51.0% from the residential sector, and 2.4% from the airport and harbour transport. Residential emissions are a large contributor to the fossil fuel emission budget as well as one of the largest contributors to the uncertainties in the fossil fuel flux. This is due to the dependency that many people living in CT have on raw fossil fuel burning for heating and lighting. Emissions from power stations are a small component of the total fossil fuel flux from CT as the bulk of the direct emissions from power stations occur elsewhere in the country.

The total fossil fuel emissions for the domain were comparable with those from the EDGAR (Emission Database for Global Atmospheric Research) (v4.2) database (Nickless et al., 2015a). EDGAR is a global product on a $0.1^\circ \times 0.1^\circ$ grid, which provides the total anthropogenic emissions of $CO_2$ as estimated from proxy data such as population counts and information on the road transport network (Janssens-Maenhout et al., 2012). The total emissions estimated from our bespoke inventory analysis for 2012 were 22% higher relative to the emissions from EDGAR in 2010, where the emissions in our inventory tended to be concentrated over specific sources, such as oil refinery plants, whereas the EDGAR emissions were smoothed over the city region.

### 5.2.7 Biogenic Emissions

CCAM was dynamically coupled to the land surface model CABLE, which allows for feedbacks between land surface and climate processes, such as leaf area feedback on maximal canopy conductance and latent heat fluxes (Zhang et al., 2013). This type of coupling has successfully been implemented in CSIRO's national earth system modelling scheme (Australian Community Climate and Earth System Simulator or

ACCESS) and describes land-atmosphere exchanges of energy, carbon, and water using biogeochemical, vegetation-dynamic and disturbance processes (Law et al., 2012). Several studies have validated CABLE under different ecosystems and parameters using both global model simulations (e.g. Zhang et al. (2009); Wang et al. (2011)), and site level offline CABLE simulations (Exbrayat et al., 2013; Zhang et al., 2013).

The model produces hourly estimates of net ecosystem exchange (NEE), which were aggregated into weekly (day and night) flux estimates in units of kg $CO_2$ $m^{-2}\,week^{-1}$, and used as the prior estimate of biogenic fluxes over the land surface. The spatial resolution of these prior NEE fluxes were kept at a $0.01^\circ \times 0.01^\circ$ resolution.

In terms of natural vegetation, the target domain is dominated by the fynbos biome. This biome is biodiverse, with many endemic species, and covers a relatively small area in South Africa, but a significant area within the domain of the inversion. The fynbos biome is poorly represented by dynamic vegetation models (Moncrieff et al., 2015). The land atmosphere exchange model CABLE was selected to couple with CCAM due to its use and development in regions of Australia which share similar characteristics to the savanna biome in South Africa, which has a coverage of over 50%. Its ability to simulate respiration and photosynthesis in the fynbos region is largely untested. In addition to the natural vegetation, a large agricultural sector is within the proximity of CT, consisting predominantly of vineyards and fruit orchards. The CT region experiences a Mediterranean climate with winter rainfall. Consequently, summers are hot and dry and winters are mild and wet. Therefore significant NEE fluxes take place during both winter and summer periods. The NEE in this region is limited by the amount of water availability, whereas temperatures are usually sufficiently high enough not to limit plant production and respiration.

The $CO_2$ fluxes over the ocean were obtained from Gregor and Monteiro (2013). This study characterised the seasonal cycle of air-sea fluxes of $CO_2$ in the southern Benguela upwelling system off the South African west coast. A time series of $pCO_2$, derived from total alkalinity and dissolved inorganic carbon and scatterometer-based wind, was obtained from six monthly cross-shelf cruises in the St. Helena Bay region during 2010. Daily $CO_2$ fluxes were derived from these $pCO_2$. These fluxes were applied as prior estimates to the ocean surface grids within the domain. Therefore, an assumption was made that ocean $CO_2$ fluxes are relatively homogeneous in space near the south western coast of South Africa, but the inversion was given the ability to differentially adjust each of the ocean sources in the posterior estimates.

### 5.2.8 Domain Boundary Concentrations

The existence of the Cape Point Global Atmospheric Watch (GAW) station made CT an ideal candidate for a city-scale inversion exercise. The Cape Point station is located approximately 60 km south of CT within a nature reserve, situated on the southern-most tip of the Cape Peninsula at a latitude of 34°21′12.0″ south and longitude of 18°29′25.2″ east. The inlet is located on top of the 30 m measurement tower, which is located on a cliff 230 m above sea level. The station observes background measurements of $CO_2$ when observing maritime air advected directly from the south-western Atlantic Ocean. This is an extensive region stretching from 20° (sub-equatorial) to 80° (Antarctic region) (Brunke et al., 2004). Therefore, maritime measurements at Cape Point from the Southern Ocean are well representative of the background $CO_2$ signal influencing the Cape Peninsula. The background signal at Cape Point, obtained from a percentile filtering technique (Brunke et al., 2004), was used as the prior estimate of the concentrations at each of the four domain boundaries. The percentile filtering technique removes data influenced by the continent or anthropogenic emissions. Two 11-day moving percentiles, which are adjustable by tuneable factors, control the upper and lower threshold limits. This results in a subset of background measurements from Cape Point represented by a narrow concentration band contained within these limits. This filter, when applied to the Cape Point $CO_2$ measurements, selects approximately 75% of the data. The percentile-filtering technique has been shown to compare well with the more robust method of using contemporaneous radon ($^{222}Rn$) measurements to differentiate between marine and continental air.

This site provides a long term record of background $CO_2$ concentrations for the area. These continuous measurements of the background $CO_2$ levels meant that we were not dependent on the atmospheric transport model to produce estimates of $CO_2$ concentrations at the domain boundary, which are prone to large errors (Lauvaux et al., 2016). Due to the prevailing wind directions across the domain the "gradient approach" for solving for $CO_2$ was not appropriate. This gradient approach relies on the observed wind direction and wind speed to obtain a subset of the concentration measurements when the air flow is from one measurement site directly to another. The differential in the concentrations is modelled by the inversion (Lauvaux et al., 2013; Bréon et al., 2015; Staufer et al., 2016). Plots provided in the appendix (Appendix B.3) show the average wind speed and direction for the domain for each month. In general, the wind direction was not favourable to the gradient approach, and with only two measurement sites, would have left little information to constrain the surface

fluxes. When the wind is blowing from the south easterly direction, air from the Hangklip site curves northwards towards the interior and away from CT. When the Robben Island site is observing marine air on its way into the CT area from the Atlantic side, such as June 2013, the wind changes for the north westerly direction once it passes over CT to a more northerly direction, missing the Hangklip site.

The mean weekly background concentrations, separate for day and night, were determined from the percentile filtered measurements at the site, and were used as the prior domain boundary concentrations for each of the four cardinal directions. The inversion was then allowed to make small adjustments to these concentrations. The prior variance assigned to the boundary concentrations was equal to the variance of the measured hourly concentrations for that period. As the variability in the background $CO_2$ in the southern hemisphere is small, much smaller than for the northern hemisphere, this resulted in a tight constraint on the prior background $CO_2$ concentrations. Large adjustments by the inversion to the far-field domain boundary concentrations were not expected. The daytime weekly background concentrations are shown in Figure 5.2. The standard deviation in the hourly background $CO_2$ concentrations ranged between 0.32 and 0.90 ppm, with a mean of 0.62 ppm.

The boundaries of the domain were deliberately set to be far from the measurement sites so that contributions to the $CO_2$ concentration at a measurement site were dominated by the surface fluxes within the domain, rather than by the domain boundary concentrations.

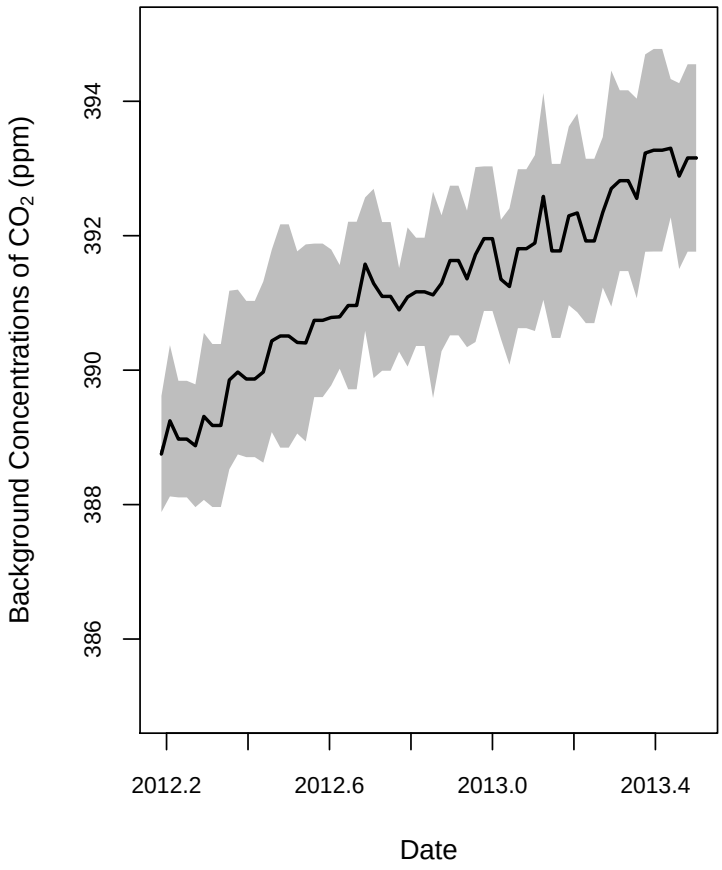


Figure 5.2: Weekly mean background concentrations of $CO_2$ (ppm) as measured at Cape Point GAW station, with 95% confidence interval represented by the grey shaded area. The mean concentrations are calculated from percentile filtered observations, extracting only those observations considered to be representative of background conditions.

### 5.2.9 Prior Covariance Matrix - $\mathbf{C_{s_0}}$

The uncertainty covariance matrix, $\mathbf{C}_{\boldsymbol{s}_0}$, of the prior fluxes and domain boundary concentrations $\mathbf{s_0}$ determines in part how much freedom the inversion has to adjust these fluxes based on the observed concentrations $\boldsymbol{c}$. If the off-diagonal prior covariance elements are significantly different from zero, then the estimate for a each flux will be more dependant on the prior estimates of the surrounding fluxes compared with an inversion where the covariances between the uncertainties in the prior fluxes were set to zero. On the other hand, if the prior variances are large, the inversion is able to make large adjustments to flux estimates to obtain better agreement between the observed and modelled concentrations. The next two subsections explain how the original estimates of the uncertainties in the fluxes and observation errors were determined. The uncertainties in the prior fluxes were scaled by an additional factor of 2 to ensure goodness-of-fit of the covariance structure (see Appendix B.2).

#### 5.2.9.1 Fossil Fuel Emissions

Error propagation techniques were used to estimate the uncertainties in the sector specific fossil fuel emissions. This was described in Nickless et al. (2015a). An industrial point source flux $s_{0;ff}$ was derived from the equation

$$s_{0;ff} = AE \tag{5.11}$$

where $A$ is the activity data, usually fuel usage, and $E$ is the process-specific emission factor. The uncertainty in the flux was estimated from

$$C_{s_{0;ff}} = |s_{0;ff}|^2 \times ((\frac{\delta A}{A})^2 + (\frac{\delta E}{E})^2) \tag{5.12}$$

where $C_{s_{0;ff}}$ is the uncertainty in the flux estimate expressed as a variance, $\delta A$ is the uncertainty in the activity data and $\delta E$ the uncertainty in the emission factor, expressed as standard deviations. DEFRA (2013b) provides estimates of uncertainty in the activity data and emission factors under various industrial processes for each fuel type.

For vehicle emissions, which relied on count data, Poisson errors were assumed, and propagated together with the uncertainty in the conversion factors for the different vehicle types. For airport and harbour emissions, vessel counts were assumed to be correct, and therefore the uncertainty in the emissions contained within the

emission factors for the different vessel types and activities. For aircraft, these errors are assumed to be 34% for the international fleet and 28% for the domestic fleet (IPCC, 2000). The error estimate for berth and manoeuvring activities of shipping vessels is reported to be between 20% and 30%, and therefore a conservative estimate of 30% was used (DEFRA, 2010). For domestic heating and lighting, the estimates relied on population census, which had a reported omission rate of 15%. There was no information available on the variability in fuel usage between households, and therefore the uncertainty in the domestic emissions was set at 30% as a relatively arbitrary, but conservative level. Domestic emissions due to fossil fuel burning was a large contributor to the overall fossil fuel flux of the domain. As the percentage uncertainty assigned to these fluxes was large, uncertainties in the domestic emissions was a significant contributor to the overall uncertainty in the fossil fuel fluxes.

After accounting for the scaling of the uncertainty estimates to improve goodness-of-fit of the covariance structure, the resulting uncertainty estimates (expressed as standard deviations) ranged between 6.7% to 71.7% of the prior fossil fuel emission estimate, with a median percentage of 34.9% to 38.4% depending on the month. These values are in general more conservative compared with uncertainties that were determined by Bréon et al. (2015) for the AirParif inventory, which were set at 20% throughout. The spatial distribution of the fossil fuel fluxes during the month of March 2012 are mapped in Figure 5.3. The daytime fossil fuel emissions have a mean of 0.006 kg $CO_2$ $m^{-2}$ $week^{-1}$ and go up to 3.4 kg $CO_2$ $m^{-2}$ $week^{-1}$. The mean went down to 0.004 kg $CO_2$ $m^{-2}$ $week^{-1}$ during the summer months, when domestic heating and lighting fuel usage is lower. The largest fossil fuel emission estimated was located towards the north of the city, and corresponded to a crude oil refinery. Most point estimates were located on the outskirts of the city, with a few located within the central peninsula area. The road network is apparent in the figure of the prior fossil fuel fluxes displaying the corresponding transport emissions, and clearly illustrates the large contribution that road transport makes to the overall $CO_2$ budget of CT.

Since we solved for weekly, rather than daily fluxes, we used a strong assumption that fossil fuel fluxes within the same week were 100% correlated. To allow the inversion to react to local conditions within a given week, no correlation was assumed between weekly fluxes. Since fossil fuel emissions were expected to be localised in space, we also assumed no spatial correlation between fossil fuel fluxes.

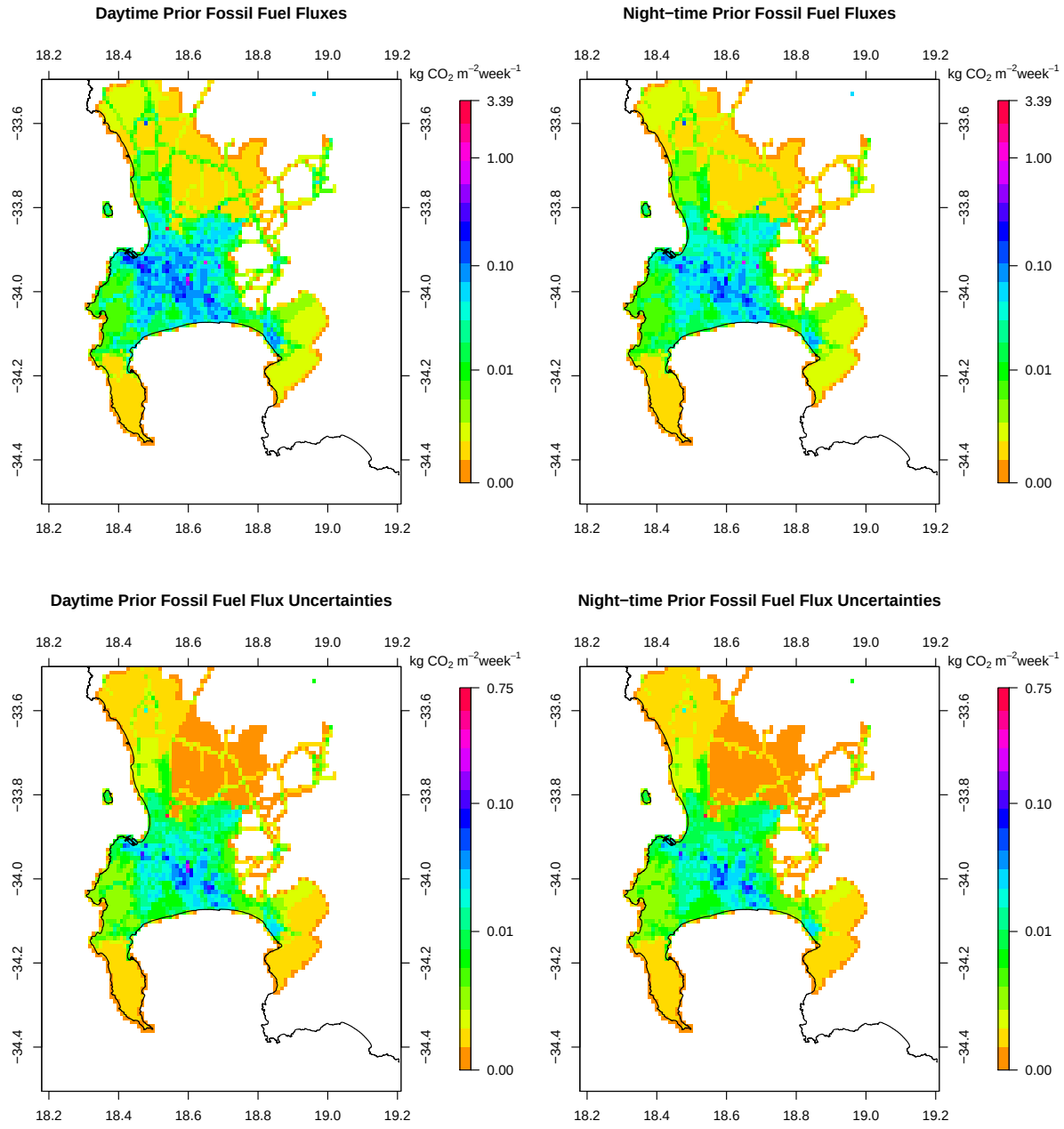


Figure 5.3: Prior estimates for day and night-time fossil fuel fluxes (kg $CO_2$ $m^{-2}\,week^{-1}$) and the corresponding uncertainties, expressed as standard deviations (kg $CO_2$ $m^{-2}\,week^{-1}$), for the month of March 2012. These estimates were derived from an inventory analysis for CT based on vehicle, aviation and shipping vessel count data, population census data, and fuel usage at industrial point sources. White indicates regions where the fossil fuel flux and its uncertainty are set to zero. These prior estimates are provided at a resolution of 1 km×1 km and the extent of the grid is between 34.5° and 33.5° south and between 18.2° and 19.2° east.

#### 5.2.9.2 Biogenic Fluxes

The uncertainty in the biogenic prior fluxes was set at the absolute value of the net primary productivity (NPP) as produced by CABLE. This is a large error relative to the prior estimate itself, but there is a great deal of uncertainty in both the productivity and respiration fluxes contributing to the NEE flux (Wang et al., 2011). The estimates of NEE are strongly dependent on the assumptions behind the model forms selected for different processes in the CABLE model. For example, the model forms used for the soil temperature-respiration function and the soil moisture-respiration function have large impacts on the NEE estimates, with resulting NEE estimates differing by over 100% compared with measurements from flux towers (Exbrayat et al., 2013). The approach of assigning either the productivity or respiration component of NEE as the uncertainty has been used by Chevallier et al. (2010). We avoided assigning a fixed proportional uncertainty to the NEE estimates as, particularly in semi-arid regions, such as those conditions found throughout South Africa, small NEE fluxes can occur as a result of both large productivity and respiration fluxes. In the CT situation, this would lead to unrealistically low estimates of the uncertainty in NEE fluxes. This is different to the approach used by Bréon et al. (2015), where an uncertainty level of 70% was assigned to biogenic fluxes, but in their case absolute NEE estimates were usually large in summer and expected to be small in winter.

To estimate covariances between the uncertainties in the NEE fluxes, we assumed an isotropic Balgovind correlation model as used in Wu et al. (2013). This helps to ensure positive-definiteness of the resulting covariance matrix. The off-diagonal covariance elements for $s_{NEE;i}$ and $s_{NEE;j}$ were calculated as:

$$C_{s_{0;NEE}}(s_{NEE;i}, s_{NEE;j}) = \sqrt{C_{s_{0;NEE}}(s_{NEE;i})}\sqrt{C_{s_{0;NEE}}(s_{NEE;j})}(1 + \frac{h}{L})exp(-\frac{h}{L}) \quad (5.13)$$

where $s_{NEE;i}$ and $s_{NEE;j}$ are NEE fluxes in pixels $i$ and $j$, $C_{s_{0;NEE}}(s_{NEE;i})$ and $C_{s_{0;NEE}}(s_{NEE;j})$ the corresponding variances in the NEE flux uncertainties in pixels $i$ and $j$, the characteristic correlation length $L$ was assumed to be 1 km, and $h$ is the spatial distance between pixels $i$ and $j$. As for the fossil fuel fluxes, no correlation was assumed between weekly biogenic fluxes, since the inversion setup is already assuming that biogenic fluxes within the same week were 100% correlated (i.e. constant over the week).

Figure 5.4 shows the spatial distribution of the NEE fluxes and their uncertainties for the month of March 2012. Day-time NEE fluxes ranged between -0.19 and 0.04 kg

$CO_2$ $m^{-2}$ $week^{-1}$, concentrated over areas such as the Cape Point Nature Reserve and Kogelberg Nature Reserve, located near the Hangklip lighthouse. At night the fluxes were between 0.0 and 0.06 kg $CO_2$ $m^{-2}$ $week^{-1}$. The uncertainties in the NEE daytime fluxes ranged between 0.00001 (over the ocean) and 0.30 kg $CO_2$ $m^{-2}$ $week^{-1}$, whereas at night the uncertainties ranged between between 0.000001 and 0.006 kg $CO_2$ $m^{-2}$ $week^{-1}$. Uncertainties were smaller at night because night-time biogenic activity was mainly driven by respiration, and consequently the flux estimates were smaller as well as their uncertainties. Over the full measurement period, the estimates of NEE fluxes ranged between -0.22 and 0.004 during the summer to -0.11 to 0.007 kg $CO_2$ $m^{-2}$ $week^{-1}$ during mid winter.

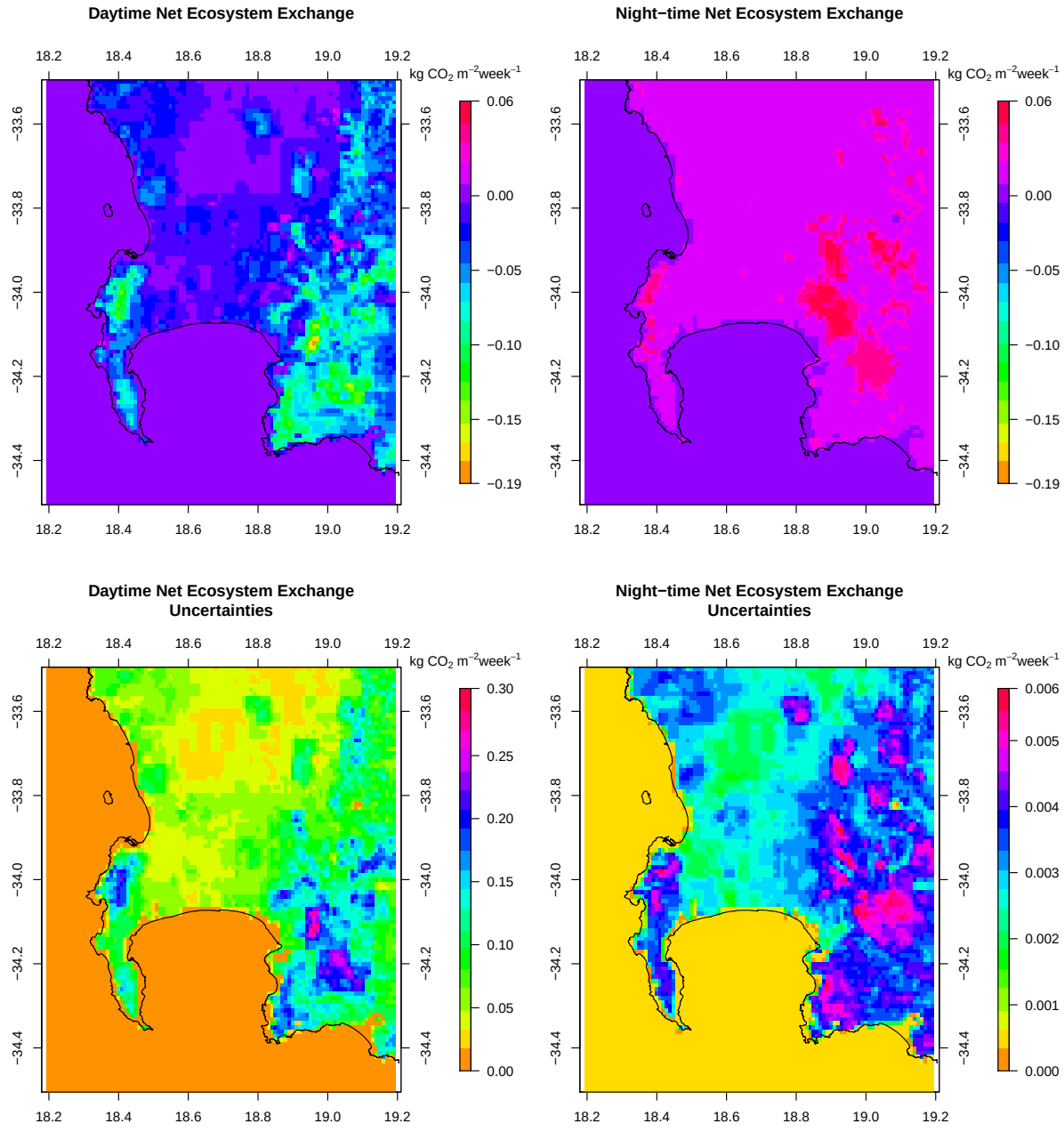


Figure 5.4: Prior estimates for day and night-time NEE fluxes (kg $CO_2$ $m^{-2}$ $week^{-1}$) and the corresponding uncertainties, expressed as standard deviations (kg $CO_2$ $m^{-2}$ $week^{-1}$), during the month of March 2012. The prior estimates were obtained from the CABLE land-atmosphere exchange model at a spatial resolution of 1 km×1 km. The extent of the grid is between 34.5° and 33.5° south and between 18.2° and 19.2° east.

### 5.2.10 Uncertainty Covariance Matrix of the Observations - $\mathbf{C}_c$

The uncertainties in the observations represented in $\mathbf{C_c}$ contain both the measurement error (which are known to be in the order of 0.3 ppm) (Bréon et al., 2015; Wu et al., 2016) and the error associated with modelling the concentrations. The modelling errors result from several sources, including errors within the atmospheric transport model and aggregation errors which are due to smoothing emission estimates from localised sources within the spatial grids (Kaminski et al., 2001).

Similar to the approach adopted in the optimal network design for South Africa (Nickless et al., 2015b), an error of 2 ppm during the day and 4 ppm at night was assigned to each observation, so that night-time observations carried less weight in the inversion. These values were assigned as baseline (i.e. minimum) errors, and accounted for measurement errors, atmospheric transport modelling errors, aggregation errors and representation errors.

These errors are smaller than those for city-scale inversions conducted in the Northern Hemisphere. We justify the use of these values in our application since we are dealing with a much smaller city compared with the megacity applications, such as Paris and Indianapolis. Measurements of background $CO_2$ have shown that $CO_2$ concentrations in the Southern Hemisphere have smaller standard deviations. For example, for the years 2012 to 2013 the standard deviation between the monthly $CO_2$ means for Mauna Loa GAW station in the Northern Hemisphere was 2.3 ppm (Tans and Keeling , 2016), whereas for the same time period at Cape Point the standard deviation between the monthly means was 1.6 ppm.

We accounted for additional sources of error in the atmospheric transport model. We took into consideration that errors in the modelled $CO_2$ concentrations due to the transport model would be larger when the wind speed was lower (Bréon et al., 2015), and this would be compounded at night when the planetary boundary layer height was lower and less stable (Feng et al., 2016). Additional error ranging between 0 and 1 ppm was added to the daytime uncertainty of 2 ppm, linearly scaled depending on the wind speed, with 0 ppm added when wind speeds were high ($20\,\mathrm{m\,s^{-1}}$) and 1 ppm added when the wind speed was close to zero. At night the additional uncertainty ranged between 0 and 4 ppm.

We also considered the standard deviation of the measured $CO_2$ concentrations during each hour. It would be expected that if there was a large amount of variability between the instantaneous measurements at the site, that the atmospheric transport model would be more likely to make errors during this period. The variance of the

observed $CO_2$ concentrations that contributed towards the mean estimate of the $CO_2$ concentration for that hour, was added to the overall uncertainty. Therefore each hour had a customised observation error dependant on the prevailing conditions at the measurement site. Therefore the total observation error for hour $k$, as a variance, is given as:

$$C_c(k,k) = {C_{c;base}}^2 + {C_{c;wind}}^2 + {C_{c;obs}}^2 \tag{5.14}$$

where $C_{c;base}$ is the baseline observation error of 2 ppm during the day and 4 ppm during the night, $C_{c;wind}$ is the additional error due to the wind speed conditions which ranged between 0 and 1, and $C_{c;obs}$ is the standard deviation of the observed concentrations within that hour. A time series of the customised observation errors is provided in Figure 5.5. The final observation errors could reach up to 10 or 15 ppm at night, reducing the weight of these measurements in the estimation of the prior fluxes.

Temporal correlation between the observation errors was accounted for in an analogous manner to which covariance terms were estimated for the NEE flux uncertainties. The characteristic correlation length $L$ was assumed to be 1 hour, and $h$ was the temporal distance between observations.

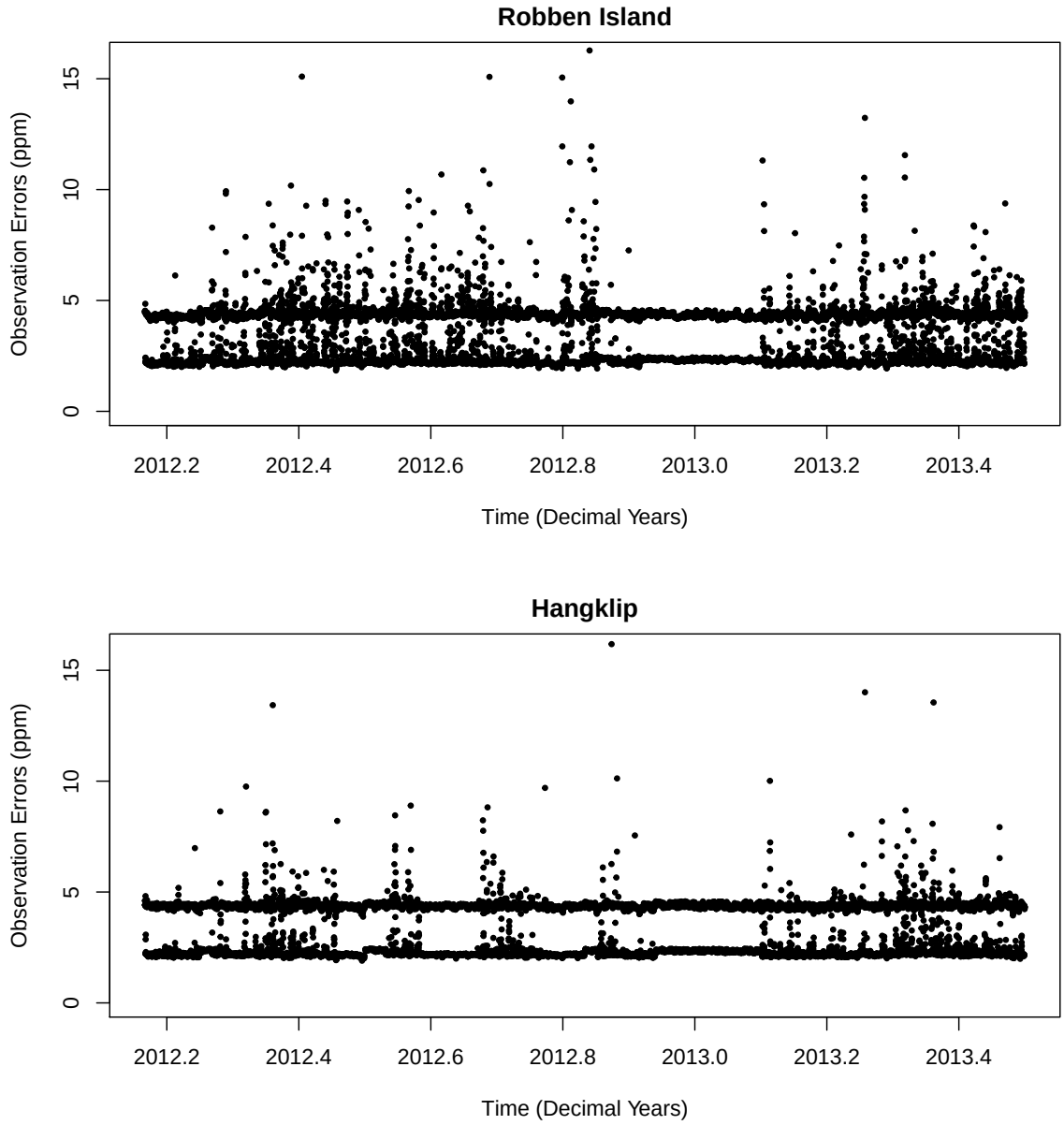


Figure 5.5: Time series of the customised observation errors (ppm) assigned to the $CO_2$ concentration measurement for each hour at the Robben Island and Hangklip measurement sites. The errors consist of a baseline error (set as 2 ppm during the day and 4 ppm at night), and additional atmospheric model errors based on prevailing wind speed and the variation in the instantaneous $CO_2$ observations within an hour. The two distinct sets of points for each site arises due to the night-time observation errors set to be larger than daytime observation errors.

### 5.2.11 Model Assessment

In order to assess the appropriateness of the uncertainty covariance matrices $\mathbf{C}_{\boldsymbol{c}}$ and $\mathbf{C}_{\boldsymbol{s}_0}$, the $\chi^2$ statistic, as described in Tarantola (2005) can be employed to determine the minimum value of the statistic:

$$\chi_1^2 = \frac{1}{\nu}(\mathbf{H}\boldsymbol{s}_0 - \boldsymbol{c})^T(\mathbf{H}\mathbf{C}_{\boldsymbol{s}_0}\mathbf{H}^T + \mathbf{C}_{\boldsymbol{c}})^{-1}(\mathbf{H}\boldsymbol{s}_0 - \boldsymbol{c}) \tag{5.15}$$

where $\nu$ is the dimension of the data space, in this case the length of observations in the inversion.

The squared residuals from the inversion (squared differences between observed and modelled concentrations) should follow the $\chi^2$ distribution with degrees of freedom equal to the number of observations (Michalak et al., 2005; Tarantola, 2005). Dividing this statistic by the degrees of freedom should yield a $\chi_1^2$ distribution. Values lower than one indicate that the uncertainty is too large, and values greater than one indicate that the uncertainty prescribed is lower than it should be. The error in the assignment of the uncertainty could be in either $\mathbf{C}_{\boldsymbol{c}}$ or $\mathbf{C}_{\boldsymbol{s}_0}$ (or both).

Sensitivity analyses carried out on the specification of the covariance matrices have indicated that these errors are most likely contained in $\mathbf{C}_{\boldsymbol{s}_0}$. These analyses are presented in a companion paper. In order to ensure the suitability of $\mathbf{C}_{\boldsymbol{s}_0}$, the prior variances were multiplied by a factor of two. This ensured that the $\chi_1^2$ statistic was close to a value of one for almost all months of the inversion. A single scaling factor was used to adjust all the prior flux variances. An alternative to a single value scaling factor will be considered in a subsequent paper.

Using the $\chi^2$ statistic to scale or estimate covariance parameters has been implemented by Lauvaux et al. (2016) and Michalak et al. (2005). Lauvaux et al. (2016) used the $\chi^2$ statistic to scale the elements of the observation error covariance matrix. An alternative to manually scaling the elements of either $\mathbf{C}_{\boldsymbol{s}_0}$ or $\mathbf{C}_{\boldsymbol{c}}$, is to use a hierarchical Bayes approach to estimate hyper-parameters for the covariance matrix, which are estimated based on the observed concentrations (Ganesan et al., 2014).

## 5.3 Results

In this paper we concentrate on the results of the reference inversion, as described in the previous section. We present sensitivity analyses elsewhere. Additional information on the distribution and time series of the observed concentrations at Robben Island, Hangklip and Cape Point over the 16 month period are provided in Appendix B.1. Information is also provided on the assessment of the goodness-of-fit of the prescribed covariance structures in Appendix B.2 to justify the use of the scaling factor of 2 to increase the original estimates of the uncertainties in the prior fluxes to get the $\chi^2$ statistic closer to one. The average wind speed and direction, supplied as monthly maps of the wind fields across the domain, as modelled by CCAM are provided in Appendix B.3.

### 5.3.1 Modelled Concentrations

The time series of the prior and posterior modelled concentrations at Robben Island were compared with the observed concentrations (Figures 5.6). The prior estimates tended to be in the correct range for $CO_2$ concentration measurements, but could be higher or lower compared with the observations by as much as 100 ppm. It is possible to test whether our assumed uncertainties in the prior fluxes are consistent with the misfit between the prior modelled concentrations and observations. Michalak et al. (2005) pointed out that the covariances of the differences between the prior simulation and observations is given by the matrix $\mathbf{H}\mathbf{C}_{\boldsymbol{s}_0}\mathbf{H}^T + \mathbf{C}_{\boldsymbol{c}}$. This matrix accounts for both the uncertainty in the prior fluxes and in the observations. The square root of the diagonal elements of this matrix had a similar distribution to the absolute mismatches between the observations and prior modelled concentrations, showing that the set-up is statistically consistent. The prior concentrations tended to spike at the same time as the observations, but these spikes were usually larger in the prior modelled concentrations.

As one would expect, the agreement between the posterior modelled concentrations and the observations was much stronger compared with the prior estimates. The posterior concentrations appeared to track the observed concentrations during localised "pollution" events. For example, in March to April 2012 all except one of the spikes in the observed $CO_2$ concentration was replicated in the posterior concentrations. The agreement can be assessed by means of the intraclass correlation coefficient (ICC) (Shrout and Fleiss, 1979), which is a stronger condition than correlation. Values close to zero indicate poor agreement while values close to one indicate

strong agreement. The ICC was low at 0.03 (95% CI: 0.01 to 0.06), but still significant, between the observed and prior modelled concentrations, but went up to 0.59 (95% CI: 0.57 to 0.61) between the observed and posterior modelled concentrations.

We define prior residuals as the difference between the observed and prior modelled concentrations, and posterior residuals as the difference between the observed and posterior modelled concentrations. A time series plot of the prior and posterior residuals given in Figure 5.6 indicates more clearly how large the misfits between the modelled and observed concentrations can get. The prior residuals could be large in either the positive or negative direction, up to 100 ppm and occasionally out by as much as 200 ppm. The posterior residuals were much closer to the zero line, with the highest deviation equal to 33 ppm. The bias in the prior modelled concentrations was -2.9 ppm. The standard deviation of the prior residuals was 21.4 ppm (interquartile range between -9.1 and 3.7 ppm), indicating a large amount of spread in the residuals. The bias in the posterior modelled concentrations went down to 0.5 ppm and the standard deviation of residuals reduced to 3.9 ppm (interquartile range -1.5 and 1.5 ppm), showing a significant reduction in the misfit compared with the prior modelled concentrations. Compared with the standard deviation of the observed concentrations, which was 5.02 ppm, the standard deviation of the posterior residuals was lower by 1.1 ppm, indicating that the uncertainty in the posterior estimates of the concentrations was well below the expected variability around the observed concentrations.

The time series of the observed, prior and posterior concentrations at Hangklip reveal a similar result compared with those for Robben Island (Figure 5.7). The prior estimates could be much larger or smaller compared with the observed concentrations. The posterior concentration estimates matched much more closely with the observed concentrations compared with those for Robben Island. The ICC between the observed and prior modelled concentrations was similar to Robben Island at 0.03 (95% CI: 0.003 to 0.05), but the agreement between the observed and posterior modelled concentrations was better with an ICC of 0.76 (95% CI: 0.75 to 0.77). The prior residuals at the Hangklip site tended to be less extreme compared with those for Robben Island, with a maximum deviation of 117 ppm in either direction (Figure 5.7). The summary statistics of the residuals indicate that the mean bias in the prior estimates was 2.4 ppm with standard deviation equal to 17.6 (interquartile range between -2.3 and 6.5 ppm). For the posterior residuals, the bias was reduced to 0.04 ppm with standard deviation equal to 2.46 (interquartile range -1.1 to 0.8), the standard deviation lower by 1.4 ppm compared with the standard deviation of the observed concentrations, which was 3.89 ppm.

The observed and modelled concentrations and their misfits are provided separately for day and night concentrations in Figures 5.6 and 5.7. There is no notable difference in the degree of misfit between day and night at either site. The large improvement in the representativeness of the posterior concentrations in relation to the observed concentrations at both sites lends confidence to the reference inversion's ability to adjust the estimates of the fluxes to better match the true fluxes in the region.

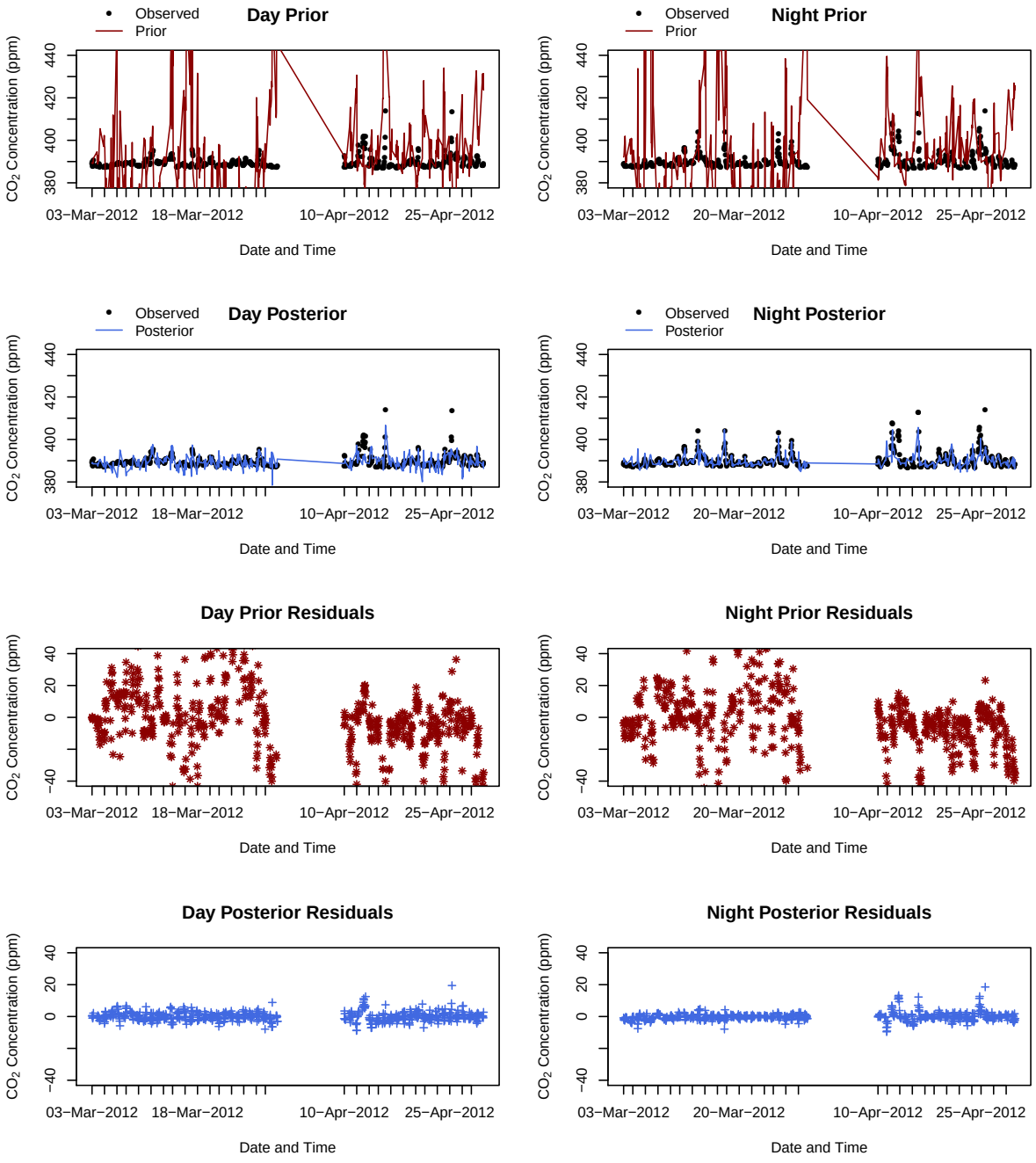


Figure 5.6: The top 4 panels provide a time series of the observed, prior and posterior modelled concentrations at the Robben Island site. The time series is separated into day and night-time periods. The residuals between the observed and prior/posterior modelled concentrations, defined as the difference between the observed and modelled concentrations, are provided in the lower panel 4 panels. The first two months are presented here and remainder of the time series is presented in Appendix B.4.

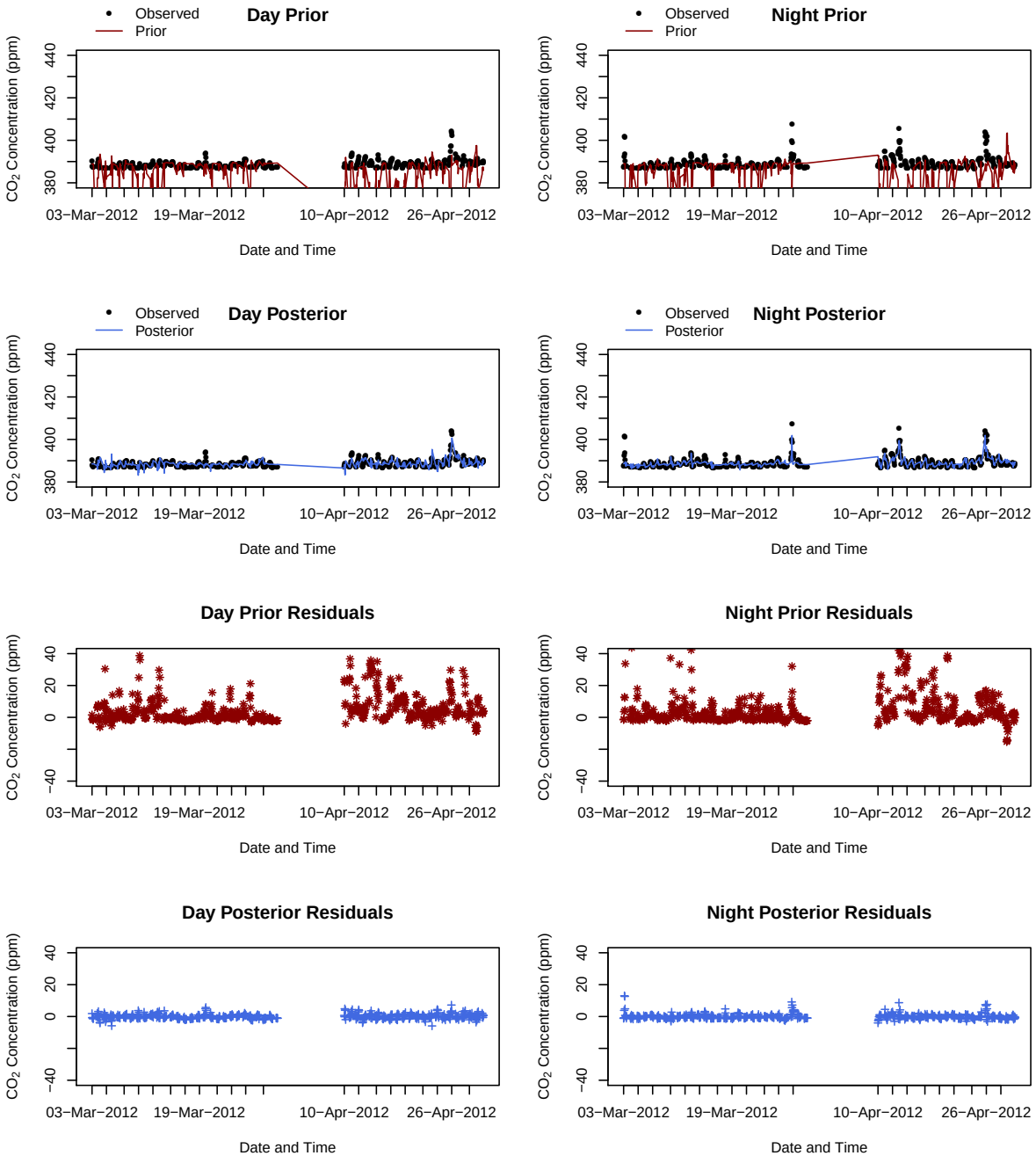


Figure 5.7: The top 4 panels provide a time series of the observed, prior and posterior modelled concentrations at the Hangklip site. The time series is separated into day and night-time periods. The residuals between the observed and prior/posterior modelled concentrations, defined as the difference between the observed and modelled concentrations, are provided in the lower panel 4 panels. The first two months are presented here and remainder of the time series is presented in Appendix B.4

The mean working week and weekend diurnal cycles in the observed, prior and posterior modelled concentrations are shown for each site and for each month in the appendix (Appendix B.5). Figure 5.8 provides the mean working week and weekend diurnal cycle over the full measurement period. For Robben Island, the mean concentrations for each hour indicate that the emissions are overestimated by the prior estimates. The posterior modelled concentrations are much closer to the observed concentrations, replicating the peak in concentrations to be between 8:00 and 9:00 in the morning and the trough in concentrations to occur between 15:00 and 18:00. Overall the cycle in the posterior concentrations is flatter compared with that of the observed concentrations. The observed concentrations during the week are usually slightly higher compared with those over the weekend. The posterior estimates show a smaller deviation between the week and weekend concentrations at each hour of the day, particularly around mid-morning, compared with the observed week and weekend concentrations.

The prior estimates for the Hangklip measurement show the opposite bias compared with Robben Island, with prior modelled concentrations lower at each hour compared with the observed concentrations. The posterior modelled concentrations for Hangklip overlap closely with the observed concentrations. When compared with Robben Island, there is slightly less separation between the working week and weekend concentrations at each hour. This should be expected as the concentrations observed at the Hangklip site are more dominated by biogenic sources compared with Robben Island. The closest fossil fuel sources are those from transport and domestic emissions. The main road through this area carries a large amount of commercial traffic during the week, and over the weekend the area is frequented by weekend residents and tourists, and therefore anthropogenic activity is not expected to be much lower over the weekend. The posterior concentrations show that the inversion was able to replicate the separation between the mean hourly working week and weekend concentrations shown by the observed concentrations for most hours of the day, particularly the difference between these concentrations occurring between the hours of 7:00 and 9:00.

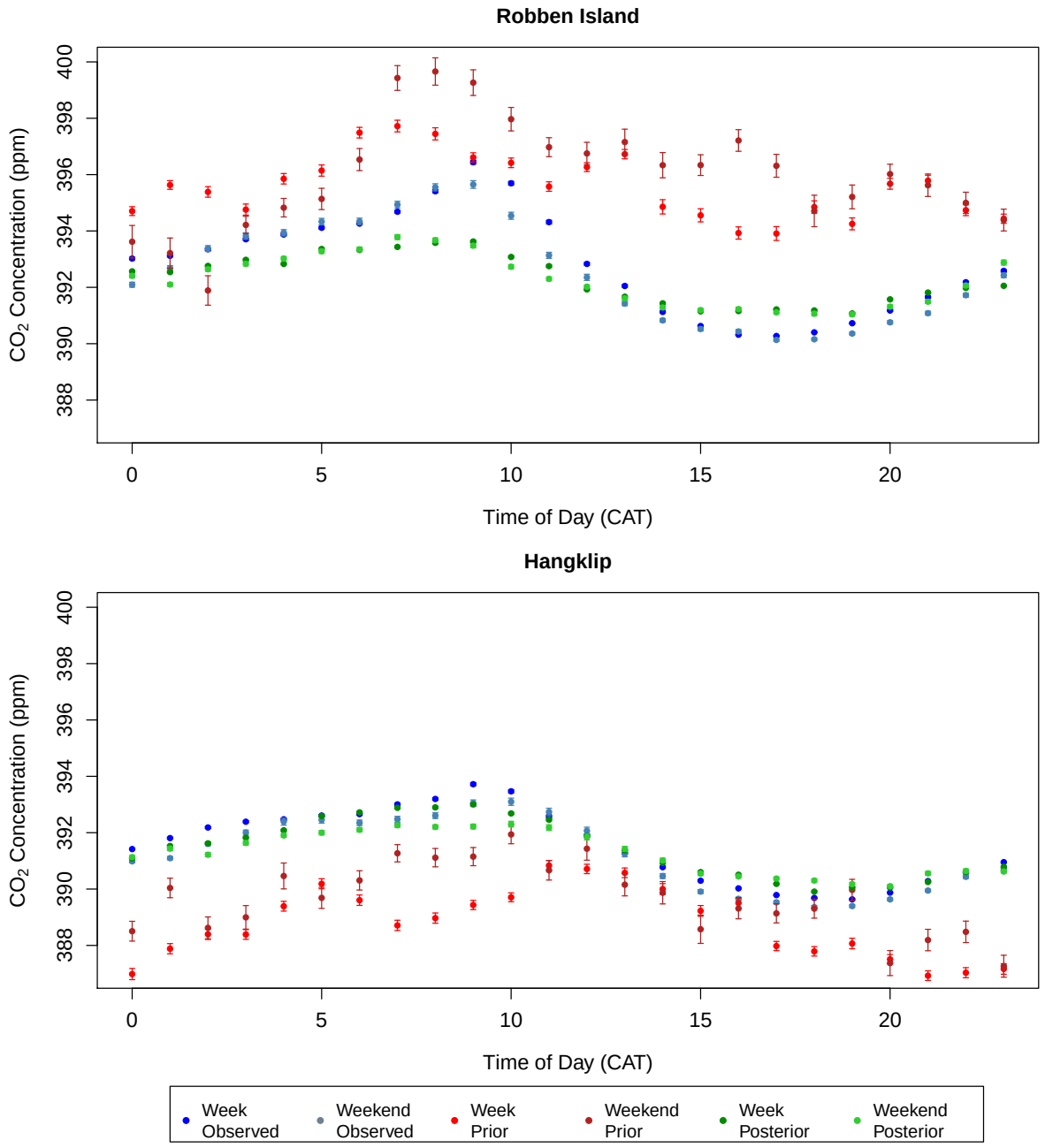


Figure 5.8: The hourly diurnal cycle (mean concentrations for each hour with 95% confidence interval) in the observed, prior and posterior modelled $CO_2$ concentrations (ppm) over the full measurement period from March 2012 until June 2013, separated by working week and weekend, and plotted separately for Robben Island (top) and Hangklip (bottom) measurement sites. The diurnal plots are separated into working week and weekend observed concentrations (blue and light blue), working week and weekend prior modelled concentrations (red and dark red), and working week and weekend posterior modelled concentrations (green and light green).

The contributions by the fossil fuel and NEE fluxes to the modelled concentrations were determined. These are displayed in Figures 5.9 and 5.10 for Robben Island and Hangklip respectively for March to June 2012. July 2012 to June 2013 are supplied in Appendix B.6. The prior contributions by these two fluxes were of similar magnitude at both sites, but with the fossil fuel fluxes increasing $CO_2$ concentrations and the NEE fluxes reducing the concentration. After the inversion, the contributions of the posterior NEE fluxes to the modelled concentrations were much more modified by the inversion compared with those from the posterior fossil fuel fluxes. Moreover, the adjustments made to the NEE fluxes resulted in the contributions to the $CO_2$ concentrations that were much more similar in magnitude to the fossil fuel fluxes, to the extent that the uptake of $CO_2$ due to biogenic processes cancelled out the contributions made by the fossil fuel fluxes.

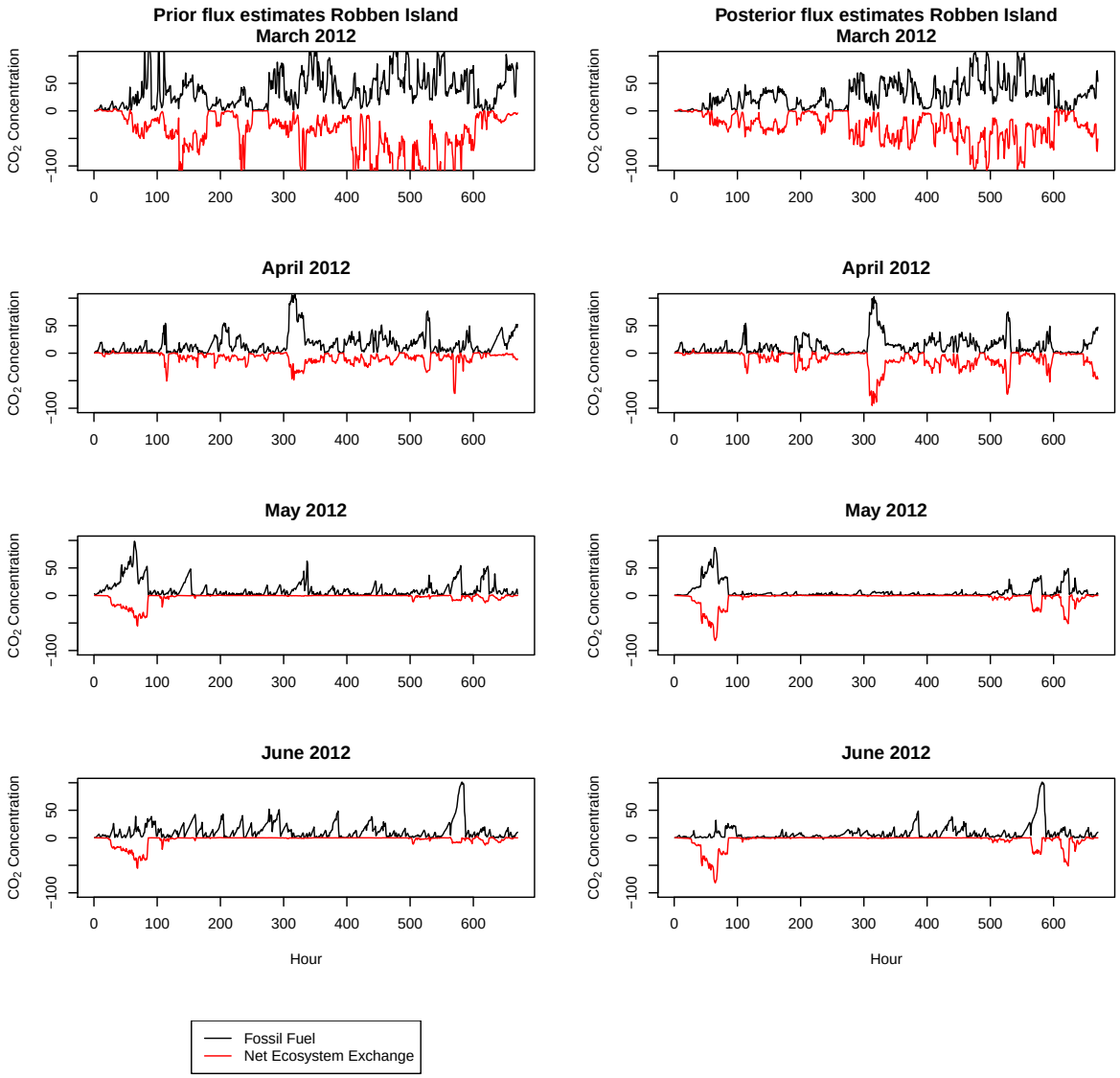


Figure 5.9: Prior and posterior contributions of the fossil fuel and NEE surface fluxes to the modelled $CO_2$ concentrations (ppm) at Robben Island from March 2012 until June 2012.

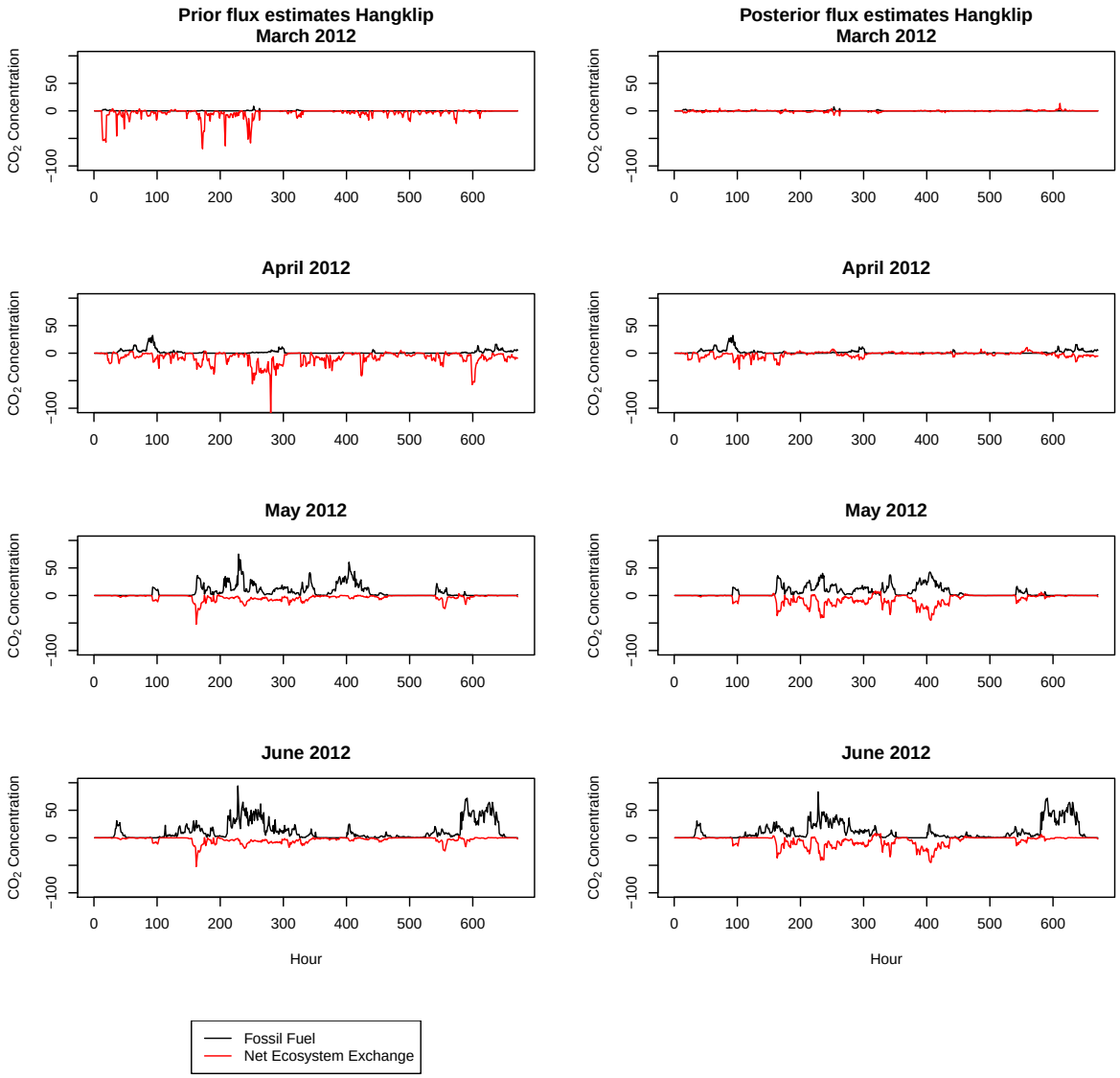


Figure 5.10: Prior and posterior contributions of the fossil fuel and NEE surface fluxes to the modelled $CO_2$ concentrations (ppm) at Hangklip from March 2012 until June 2012.

The inversion-corrected $CO_2$ concentrations at the domain boundary are obtained from the posterior source estimates. Therefore these concentrations are extracted from the solution of $\boldsymbol{s}$. Figure 5.11 provides a time series of the prior and posterior concentration estimates. The northern and eastern domain borders are terrestrial, whereas the ocean borders the south and west. For all four domain boundaries, across the total measurement period, the inversion has made only small innovations, with the posterior estimates remaining within the 95% confidence limits of the prior concentrations. Only the northern and eastern terrestrial boundaries showed some deviations from the priors between May and June 2012, and between March and April 2013. As these are the terrestrial boundaries of the domain, the concentrations here would be subject to influences from outside of the domain, and it would therefore be expected that the inversion would need to provide greater adjustments to these boundary concentrations. The ocean boundaries would be expected to have concentrations close to the background concentrations provided by the Cape Point measurement site.

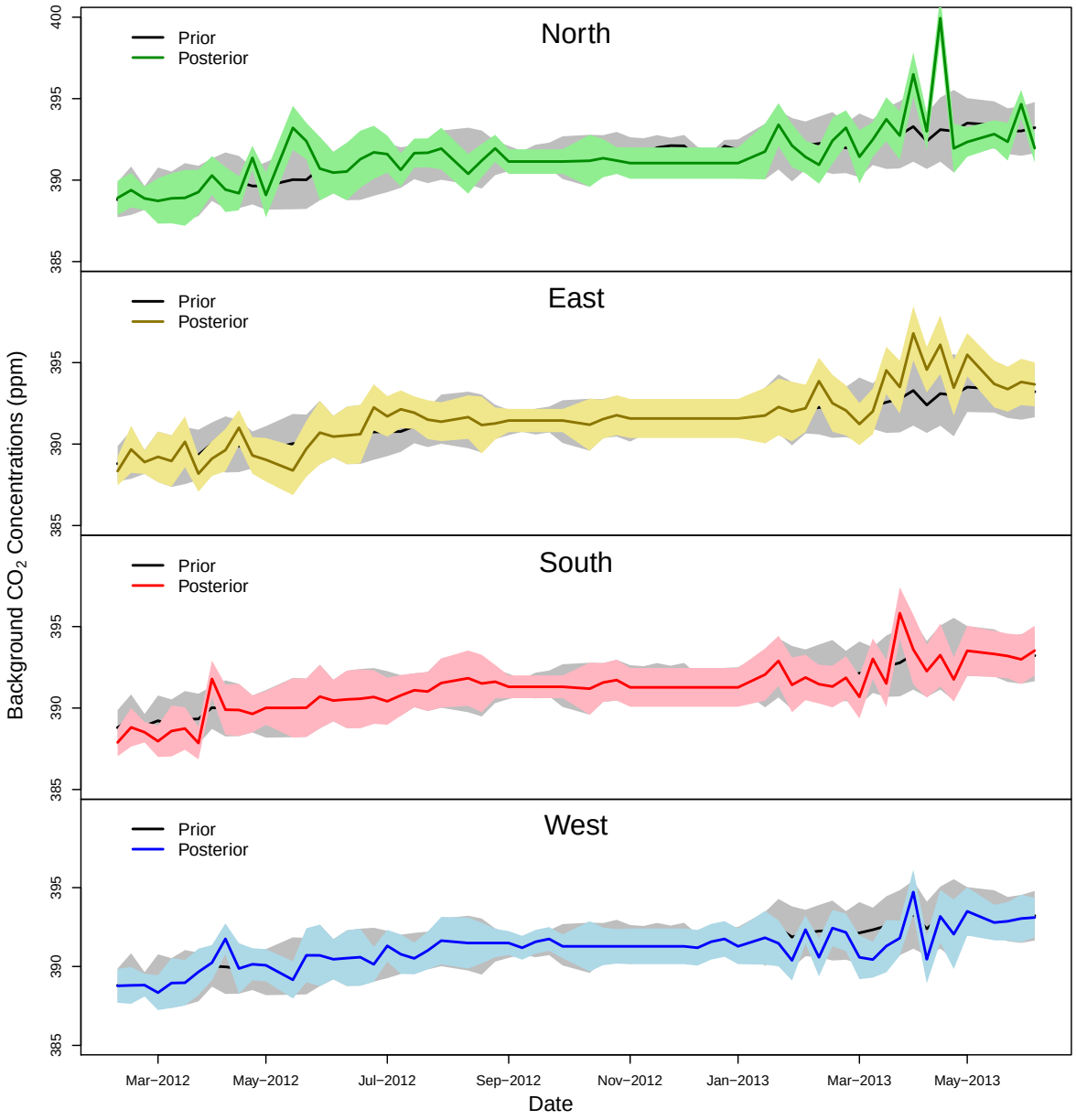


Figure 5.11: Time series with 95% confidence interval (represented by the shaded area) of the prior (black line) and posterior estimates of the $CO_2$ concentrations (ppm) at the domain boundaries (north - green, east - yellow, south - red, west - blue). The prior estimates are the same for each cardinal direction, and are obtained from the Cape Point percentile-filtered observations. The posterior estimates for the concentrations are solved for as additional unknowns in the reference inversion.

### 5.3.2 Weekly Flux Estimates

We refer to the difference between the prior and posterior flux estimates as the innovations. The impact of the inversion on the flux estimates can be assessed through the size and direction of these innovations and through the reduction in the flux uncertainties. Figure 5.12 shows the innovations in the total flux estimates for each pixel in kg $CO_2 m^{-2}$ $week^{-1}$ for the month of May 2012, as well as the percentage reduction in the flux uncertainty, the percentage reduction in the fossil fuel emissions and change in NEE fluxes. The mean total weekly flux of a pixel was obtained by first deriving the total flux from the six fossil fuel and NEE flux estimates for that week, and then taking the mean of the four weekly fluxes obtained for the month. The innovations for the total flux were calculated as the difference between the total prior and total posterior weekly fluxes. Positive innovations indicate that the prior fluxes were too far in the positive direction, and that the flux should be adjusted towards the negative direction, whereas negative innovations indicate that prior fluxes were too far in the negative direction and should be adjusted towards the positive direction. The uncertainties for the total flux in each pixel are represented by standard deviations which have been derived from the elements of the prior and posterior uncertainty covariance matrices of the fluxes. The figure displays the percentage uncertainty reduction within each pixel. The percentage reductions in the total fossil fuel flux are presented, rather than the absolute changes from the prior to posterior flux estimates in each pixel as these changes were small and the inversion generally resulted in a reduction in the fossil fuel flux estimate. The inversion had more freedom to make changes to the NEE estimates as the uncertainties prescribed were large relative to the prior NEE flux estimates, and therefore the absolute changes from prior to posterior are presented in kg $CO_2 m^{-2}$ $week^{-1}$.

May falls within the winter rainfall season of the Western Cape region. The innovations indicate that the total flux for the pixel over the petrol refinery, which had the largest prior flux estimate, was overestimated by the prior (9.43 kg $CO_2 m^{-2}$ $week^{-1}$) relative to the posterior estimate (6.62 kg $CO_2 m^{-2}$ $week^{-1}$) by an amount of 2.81 kg $CO_2 m^{-2}$ $week^{-1}$ (Fig. 5.12). Innovations were generally small ranging between -0.001 and 0.003 kg $CO_2 m^{-2}$ $week^{-1}$. The area around the natural reserves, such as Cape Point and Kogelberg Nature Reserves, had innovations by the inversion that were close to zero or slightly negative, indicating that the amount of carbon uptake (i.e. negative NEE flux) in these regions was overestimated by the CABLE model. The largest negative innovation by the inversion was -0.08 kg $CO_2 m^{-2}$ $week^{-1}$, from -0.03 up to 0.04 kg $CO_2 m^{-2}$ $week^{-1}$, over a pixel in the Cape Point Nature Reserve. The

prior flux indicated the pixel to be a slight carbon sink of $CO_2$ whereas the inversion adjusted the flux to be a slight $CO_2$ source. With respect to the rest of the domain, excluding the crude oil refinery, the most substantial innovations were made over the central business district (CBD) area to the south east of Robben Island. These innovations were positive, indicating that the fossil fuel fluxes were overestimated by the prior estimates.

The percentage change in the fossil fuel estimates, from prior to posterior, indicate the changes tended to be small, except on Robben Island itself, where percentage changes were up to 75% indicating that the emissions on the island were significantly reduced by the inversion (Fig. 5.12). There were a few pixels which had negative change, indicating that the inversion increased fossil fuel emissions, just north of the island. Located on the north eastern shore of Robben Island is a diesel-fuelled power generation plant, as well as desalination plant which is powered by this station. Increases in the fossil fuel fluxes may be due to emissions arising from these activities which have not been accounted for in the inventory analysis. In the inventory analysis there was no fuel information available for any industrial sources on Robben Island, but fossil fuel emissions were included due to domestic and transport activities, therefore these could have been adjusted by the inversion. The inventory analysis does not take into account explicitly the shipping routes going into CT harbour, or into Robben Island harbour, but rather all the emissions are concentrated within CT harbour, where the shipping information is available. This could also result in the inversion adjusting emissions on the island to deal with near shipping related emissions. There was a region in the Western Cape interior to the east of Robben Island which had slightly increased fossil fuel emissions. The inversion had the effect of mainly reducing fossil fuel emissions along the south east transect extending from Robben Island over the CBD towards Hangklip, or leaving the emission unchanged.

The inversion had a much larger impact on the terrestrial NEE fluxes (Fig. 5.12). This is unsurprising, as the relative uncertainties of the prior NEE fluxes were much larger compared with those of the prior fossil fuel fluxes. The area of the domain experiencing innovation from the inversion was also much more widespread compared with the innovations made to the fossil fuel fluxes. This is in part due to the correlation specified between the NEE fluxes of adjacent pixels, but not between their fossil fuel fluxes. The majority of the innovation over the domain was close to zero, between -0.02 and 0.02 kg $CO_2 m^{-2}$ $week^{-1}$, indicating that the inversion was making small absolute adjustments to the NEE flux estimates. Over the CBD region, the adjustments were the largest, up to 0.32 kg $CO_2 m^{-2}$ $week^{-1}$ and these differences

were positive indicating that the posterior fluxes were more in the negative direction and therefore the inversion was acting to reduce total emissions of $CO_2$ over the CBD region relative to the prior estimates, through changes to the NEE fluxes. The natural region around Cape Point and within the Kogelberg Nature Reserve north of Hangklip showed slight negative changes in the NEE fluxes, indicating that the uptake of $CO_2$ was reduced by the inversion making the total flux in these regions more positive towards the atmosphere.

In terms of the percentage standard deviation reduction (Fig. 5.12), the largest reductions occurred over the natural areas, particularly Cape Point to the south of Robben Island, where the posterior uncertainty over the area was significantly lower, by over 50%, compared with the prior uncertainties. Significant reductions are also shown over largely agricultural areas to the north of the CBD region. Over the CBD area itself, the reductions were present, reaching values of close to 60% over a few central CBD pixels, but generally smaller compared with the uncertainty reductions over natural areas in the domain which reached levels as high as 92%.

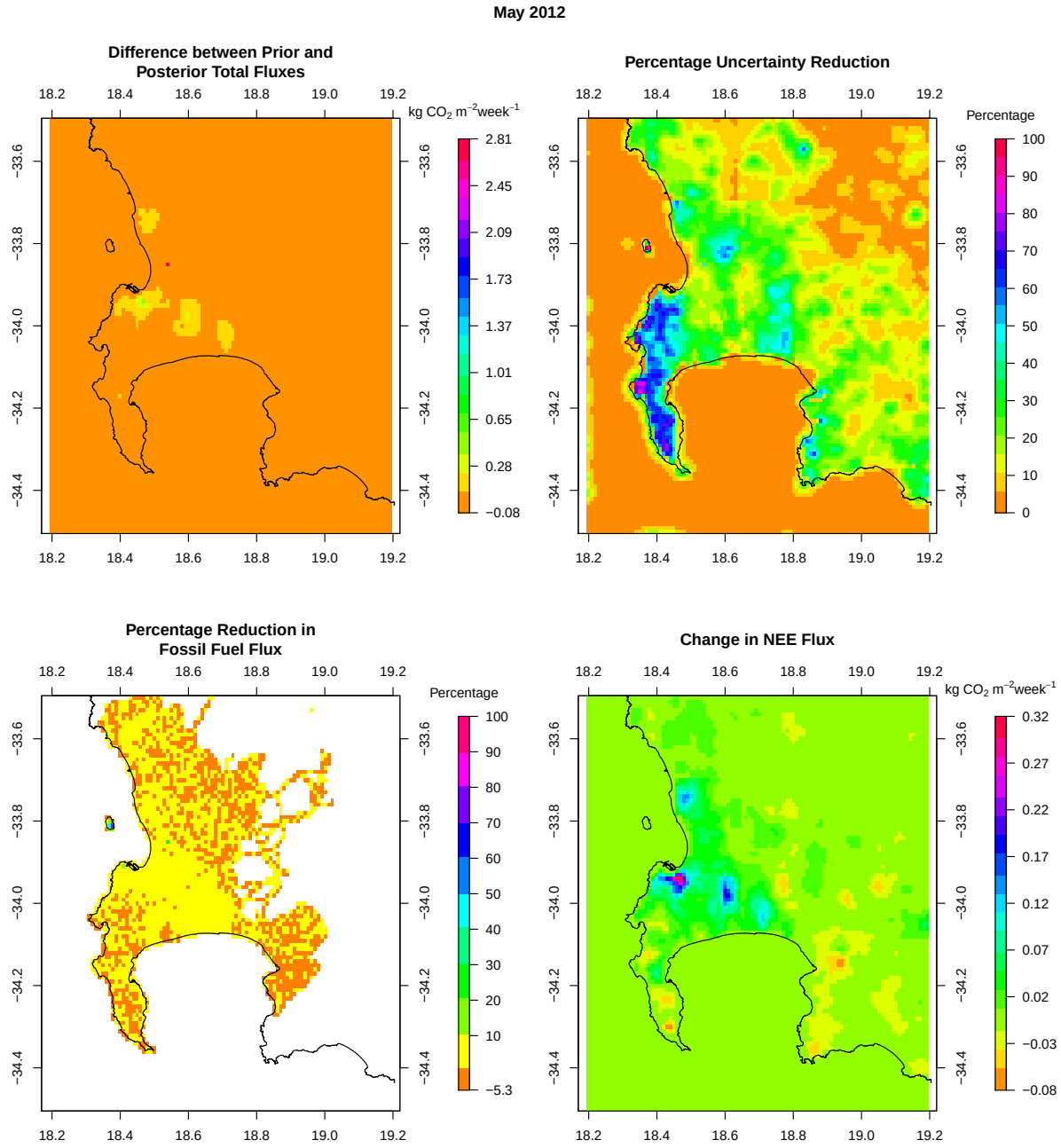


Figure 5.12: (Top left) Differences between the prior and posterior total flux estimates (kg $CO_2 m^{-2}$ $week^{-1}$) for May 2012 (prior - posterior). (Top right) Percentage reduction in the standard deviation of the flux estimate from prior to posterior. (Bottom left) Percentage reduction in the fossil fuel flux estimates from prior to posterior. (Bottom right) Differences in the biogenic flux estimates between prior and posterior estimates (prior - posterior) (kg $CO_2 m^{-2}$ $week^{-1}$), with negative values indicating posterior $CO_2$ fluxes were made more positive by the inversion compared with the prior estimates. Extent: between 34.5° and 33.5° south and between 18.2° and 19.2° east.

September is the beginning of the summer months in the Western Cape region, when temperatures start to rise, and the mean monthly rainfall reduces. The innovations across the region during this month were dominated by negative values with the majority ranging between -0.03 and -0.01 kg $CO_2 m^{-2}$ $week^{-1}$, indicating that the inversion increased emissions of $CO_2$ over the majority of the domain. The maximum increase in $CO_2$ fluxes of 0.2 kg $CO_2 m^{-2}$ $week^{-1}$ occurred over an agricultural region north east of the CBD region, from -0.10 up to 0.08 kg $CO_2 m^{-2}$ $week^{-1}$, where mainly vineyards are located (Fig. 5.13). The inversion increased the total fluxes by an amount close to 0.2 kg $CO_2 m^{-2}$ $week^{-1}$ over a further five areas. One of these areas, also over agricultural land, lies further inland to the east of the area with largest increase in $CO_2$ fluxes. Three more regions lie to the north, north east and east of the Hangklip site. These three regions are all within the Hottentots-Holland Mountain catchment area which is largely dominated by vineyard agriculture. The fifth area is located within the Kogelberg Nature Reserve near the Hangklip site. The maximum reduction of 2.1 kg $CO_2 m^{-2}$ $week^{-1}$ occurred over the crude oil refinery site, from 9.4 down to 7.2 kg $CO_2 m^{-2}$ $week^{-1}$ (Fig. 5.13). The inversion made small reductions to the fluxes near the CBD area of CT, or left the posterior fluxes to be similar to the priors.

Innovations made to the fossil fuel fluxes were mainly made on the transect of the city running between Robben Island and Hangklip, as well as to fossil fuel emissions on Robben Island itself, similar to the month of May. The maximum percentage adjustment to the fossil fuel fluxes was 51.1%, and the mean innovation close to zero, with almost all innovations positive, indicating that the posterior estimates were smaller relative to the priors. Robben Island itself showed a mix of positive and negative innovations, with posterior fluxes larger than the priors on the west of the island but smaller than the priors on the east of the island.

The effect of the inversion on the NEE fluxes was to make these fluxes more negative over the CBD region, and made $CO_2$ fluxes more positive relative to the priors over the Table Mountain region, over the agricultural area to the north of the CBD, and over the natural regions near Hangklip. The fluxes over the CBD were made more negative by up to 0.21 kg $CO_2 m^{-2}$ $week^{-1}$ through adjustments to the NEE fluxes. The areas to the north of the domain which had prior NEE estimates between -0.20 and -0.10 kg $CO_2 m^{-2}$ $week^{-1}$ were made more positive, with posterior estimates ranging between -0.10 and 0.10 kg $CO_2 m^{-2}$ $week^{-1}$, where the largest changes were over the vineyard agricultural areas. The natural area surrounding Hangklip site showed

negative innovations between the prior and posterior fluxes, indicating that the inversion adjusted the negative prior NEE fluxes by making these more positive. Therefore the CABLE model appears to have overestimated the amount of $CO_2$ uptake during this period.

Most reductions in the total flux uncertainty ranged between 2.3 and 18.6%, with a maximum reduction of 88.5% (Fig. 5.13). The largest uncertainty reductions induced by the inversion occurred over the natural areas bordering on the CBD, particularly over the Table Mountain National Park, as well as the natural areas surrounding the Hangklip site. The areas to the east of Robben Island over the Durbanville and Bellville townships, comprised of a mix of residential suburbs, vineyard agricultural areas and industrial areas, also showed reductions in the uncertainties of the fluxes.

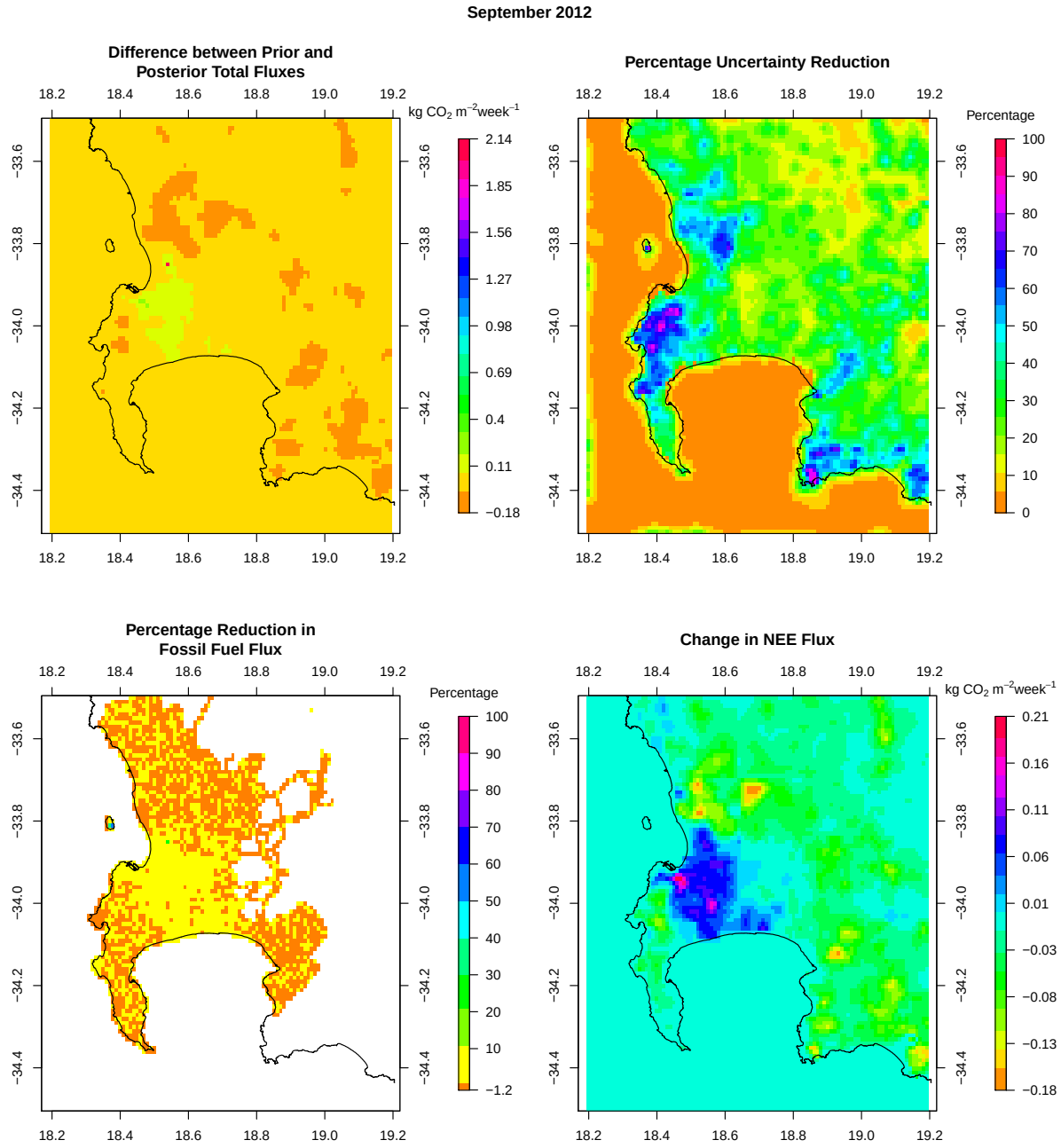


Figure 5.13: (Top left) Differences between the prior and posterior total flux estimates (kg $CO_2 m^{-2}$ $week^{-1}$) for September 2012 (prior - posterior). (Top right) Percentage reduction in the standard deviation of the flux estimate from prior to posterior. (Bottom left) Percentage reduction in the fossil fuel flux estimates from prior to posterior. (Bottom right) Differences in the biogenic flux estimates between prior and posterior estimates (prior - posterior) (kg $CO_2 m^{-2}$ $week^{-1}$), with negative values indicating posterior $CO_2$ fluxes were made more positive by the inversion compared with the prior estimates. Extent: between 34.5° and 33.5° south and between 18.2° and 19.2° east.

Figure 5.14 presents boxplots of the pixel-level weekly fluxes over the domain for each month, and the appendix (Appendix B.7) displays the spatial extent of the adjustments made to prior flux estimates by the inversion, as well as the uncertainty reductions, for each month. The limits of the range for the posterior pixel-level weekly fluxes are more negative compared with those of the prior estimates, indicating that for all the months, the inversion tended to reduce the emission of $CO_2$. This is also evident from the maps of differences in total flux estimates between the prior and posterior estimates. Specifically, the inversion tended to reduce the fossil fuel emissions, evident from the shift downwards in the distribution of the posterior pixel-level fossil fuel fluxes compared with the prior fluxes. The variability in the posterior fluxes across pixels was slightly reduced compared with the variability in the prior fluxes. The pixel-level NEE fluxes, although generally smaller in magnitude and range, were the most altered by the inversion, where these changes were related to the season in which the month fell. For most months, the overall mean in the NEE fluxes became more positive, indicating less uptake of $CO_2$ than predicted by the CABLE model. But for the months of June and July, which occur mid-winter, the mean NEE was made more negative. The minimum values were also at least twice the minimum value of the prior estimates for all months, and this is also evident from the maps of change in NEE from prior to posterior, which show that the inversion reduced the $CO_2$ flux towards the atmosphere over the CBD region by altering the NEE fluxes within those pixels.

For most months the percentage uncertainty reduction for the pixel-level total flux reached over 90% for at least some of the pixels, with a maximum uncertainty reduction over a pixel of 97.7% in March 2012. The lowest maximum reduction in the uncertainty of the total flux in a pixel in a month was 68.2% in June 2012.

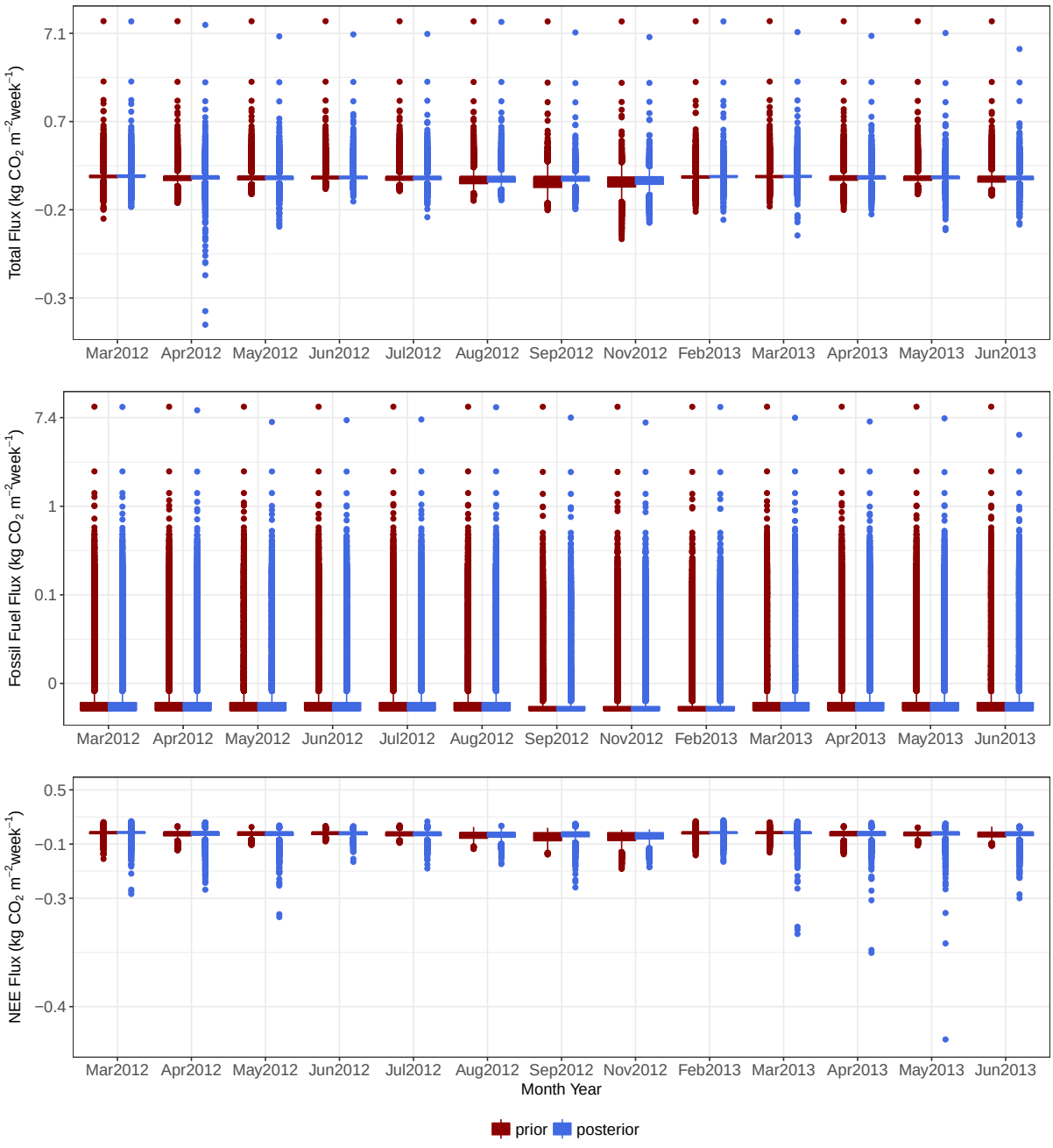


Figure 5.14: Boxplots of the pixel-level weekly prior and posterior flux estimates (kg $CO_2 m^{-2}$ $week^{-1}$) for each month. These plots present summary statistics calculated over all pixels in the domain of the pixel-level mean weekly fluxes. The y-axis is presented on a log scale.

An example pixel, located near the CBD sources, was selected in order to investigate posterior uncertainty spatial covariances in the fluxes resulting from the inversion. For a given week, the total $CO_2$ flux is composed of six sources: working week and weekend fossil fuel sources, both day and night, and the day and night biogenic sources; and each of these sources could have a non-zero covariance term between itself and the same source but from surrounding pixels, or with one of the other five sources from the same pixel or from surrounding pixels.

The posterior uncertainty covariances between the daytime working week flux of the selected pixel and other sources are only notably different from zero for working week daytime fossil fuel fluxes, working week night-time fossil fuel fluxes, and the daytime biogenic fluxes. The uncertainty covariances between the daytime working week fluxes reveal that non-zero covariances do not necessarily have to be close in proximity to the selected pixel, and negative and positive covariances can cluster in space. The uncertainty covariances with the night-time fossil fuel fluxes were larger than those during the day, but were limited to a few pixels close to the selected pixel. These covariances ranged between -0.15 and $0.09\,\mathrm{g}^2\ \mathrm{CO_2\,m^{-4}\,week^{-2}}$. The non-zero uncertainty covariances with NEE fluxes were larger (between -1.50 and $0.88\,\mathrm{g}^2\ \mathrm{CO_2\,m^{-4}\,week^{-2}}$) and fluctuated between patches of positive and negative values. Closer to the CBD area there was a distinct region of positive uncertainty covariance between the fossil fuel source of the selected pixel and the NEE fluxes from a region over the Table Mountain area and a negative covariance patch south of the CBD. The eastern terrestrial part of the domain had patches of positive and negative covariances. When converting these covariances are into correlations, correlations are small; no bigger than 0.001 in either direction.

The covariances between fossil fuel and NEE flux uncertainties are small because the uncertainties in the prior modelled concentrations that are attributed to the flux contributions ($\mathbf{HC}_{\boldsymbol{s}_0}\mathbf{H}^T$) are small relative to the uncertainties specified for the modelled concentration errors ($\mathbf{C}_{\boldsymbol{c}}$). This is not because our prior uncertainty is small but because the transport Jacobian only projects fluxes from individual pixels weakly into modelled concentrations. As the uncertainty in the modelled concentration errors is decreased, the size of the posterior off-diagonal covariance elements between the fossil fuel and NEE flux uncertainties from the same pixel increases. This can easily be confirmed through the use of a toy inversion system using typical values for $\mathbf{H}$, $\mathbf{C}_{\boldsymbol{s}_0}$ and $\mathbf{C}_{\boldsymbol{c}}$ from our inversion system. This is presented in Appendix B.8.

The sum of the covariances in the uncertainties between the selected fossil fuel flux and all other fluxes equals $-25.8\,\mathrm{g}^2\ \mathrm{CO_2\,m^{-4}\,week^{-2}}$. Therefore the covariances

associated with this pixel's fossil fuel flux would reduce the variance associated with the total pixel-level flux by 51.7, where the total uncertainty of the fossil fuel flux, as a variance, was $233.7\,\mathrm{g}^2\ \mathrm{CO}_2\,\mathrm{m}^{-4}\,\mathrm{week}^{-2}$.

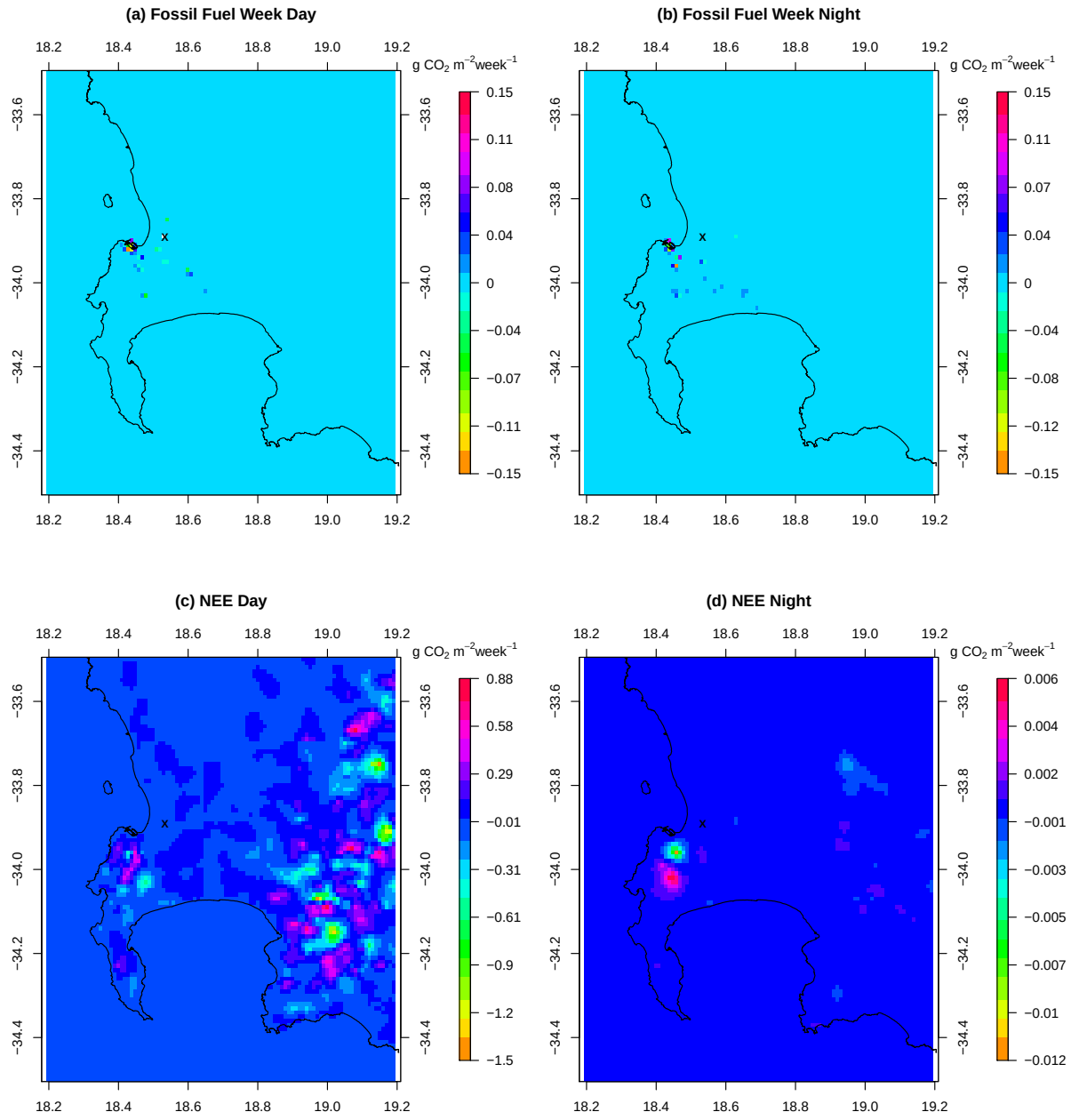


Figure 5.15: Posterior covariances ($g^2$ $CO_2\,m^{-4}\,week^{-2}$) between the uncertainty in the fossil fuel working week daytime flux during the first week of March 2012 in the selected pixel (marked by X) and (a) all other fossil fuel working week daytime fluxes; (b) fossil fuel working week night-time fluxes within this pixel and all other pixels; (c) NEE daytime fluxes within this pixel and all other pixels; (d) NEE night-time fluxes within this pixel and all other pixels. Extent: between 34.5° and 33.5° south and between 18.2° and 19.2° east.

### 5.3.3 Weekly Totals

Three time series plots of the total weekly estimates of $CO_2$ flux over the full spatial domain (i.e. all fluxes aggregated over all pixels) are presented in Figure 5.16. The total flux estimate for a week represents the sum of all the fossil fuel and NEE fluxes for that week. For the prior total flux uncertainties, the only non-zero covariances are those imposed between the uncertainties in NEE fluxes of neighbouring pixels. These positive covariance terms increase the total uncertainty. The uncertainties in the posterior total fluxes includes the posterior covariance terms between the uncertainties in the fossil fuel and NEE fluxes, which are generally negative and have the overall effect when summed of reducing the uncertainty in the total flux estimate.

Uncertainties in the prior total fossil fuel fluxes ranged between 1.3 and 1.5 kt $CO_2$ $week^{-1}$, whereas the posterior uncertainties ranged between 0.9 and 1.5 kt $CO_2$ $week^{-1}$. For the NEE fluxes the uncertainties ranged between 23.6 and 57.3 kt $CO_2$ $week^{-1}$ before the inversion and between 15.8 and 47.1 kt $CO_2$ $week^{-1}$ after the inversion. Uncertainties in the total fluxes were similar to those of the NEE fluxes, with prior uncertainties ranging between 23.6 and 57.3 and posterior uncertainties ranging between 15.8 and 47.1 kt $CO_2$ $week^{-1}$. The median percentage uncertainty reduction in the total weekly flux was 28.0 % and ranged between 2.3 and 50.5 %, with the largest reduction occurring in March 2012.

The posterior total estimate for the emission of $CO_2$ from the domain was within the confidence bounds of the prior total estimate for the majority of the period from March 2012 until June 2013. The confidence bounds of the posterior total estimates were narrower compared with those of the prior total estimates. Total prior flux estimates ranged between 139.5 and -386.8 kt $CO_2$ $week^{-1}$, with the maximum total during March 2013 and the minimum total flux occurring in November 2012. The posterior totals ranged between 149.5 and -375.1 kt $CO_2$ $week^{-1}$, with the maximum occurring in March 2013 and the minimum in October 2012. During the winter months, from March to July, the posterior fluxes fell within the uncertainty limits of the prior fluxes. The posterior total flux moved outside of the prior's confidence limits during August and September 2012, which was during the South African spring period. Posterior estimates were larger compared with the prior estimates. Data were missing during October 2012 and from December 2012 with January 2013, and therefore the estimates are completely overlapping during these periods. When observations were available during the summer months in November 2012 and February 2013 the posterior fluxes were more positive compared with the prior estimates.

The total prior fossil fuel flux was flat and close to 150 kt $CO_2$ $week^{-1}$ during the winter months, and close to 110 kt $CO_2$ $week^{-1}$ during the summer months. This stepped effect in the fossil fuel fluxes is due to the simple representation of the domestic emissions in the fossil fuel inventory. It is unlikely that fossil fuel emissions would have a sharp change between summer and winter. As a separate sensitivity analysis presented in a companion paper we adjusted the assumption of domestic emissions such that domestic emissions were distributed uniformly during the year. The inversion had the effect of reducing the total estimate, particularly during May 2012 and between March 2013 and June 2013, to a value of as low as 138 kt $CO_2$ $week^{-1}$ during the winter months and to a value of 107 kt $CO_2$ $week^{-1}$ during the summer months and early winter 2013. The posterior total fossil fluxes and confidence bounds for June 2013 were outside of those for the prior estimates for the full month. Compared with the total flux, the range of the total fossil fuel fluxes was much narrower (between 100 and 160 kt $CO_2$ $week^{-1}$), and the confidence bounds around the estimates were also narrower. This is not immediately apparent from the plot, but the range of the y-axis needed to be adjusted for the fossil fuel fluxes, otherwise it would appear as a thin line if plotted on the same range as the total fluxes.

Total prior NEE fluxes ranged between values close to zero and -494.9 kt $CO_2$ $week^{-1}$ and between zero and -483.1 kt $CO_2$ $week^{-1}$ for the posterior estimates. During the winter months posterior estimates were generally contained within the limits of the prior estimates, except for May 2012, where the total NEE flux was slightly lower compared with the prior. From August 2012 to September 2012, the posterior total NEE fluxes were well above the total prior estimates, indicating that the total uptake of $CO_2$ by the domain was reduced by the inversion during this period.

Comparisons of the NEE and fossil fuel fluxes to the total estimates show that the variability in the total flux estimates was driven by variability in the NEE fluxes, and differences between the posterior and prior total estimates were mainly driven by adjustments to the NEE fluxes induced by inversion. As would be expected, due to the large uncertainty around the NEE prior fluxes, the inversion was not strongly constrained by these priors, and therefore mainly adjusted the NEE fluxes, rather than the fossil fuel fluxes, so that the modelled concentrations better matched the observed concentrations. This is unsurprising as we provided no information regarding what proportion of the observed $CO_2$ concentration was attributable to fossil fuel contributions and what proportion was due to NEE fluxes.

Temperatures are at their highest between January and March. This is also the region's dry period. Both the prior and posterior NEE fluxes were most positive

during this period, with NEE fluxes close to zero. The posterior NEE fluxes were more positive than the prior fluxes during these periods, i.e. the posterior estimates indicated less uptake of $CO_2$ by biogenic processes compared with the prior estimates. The minimum temperatures occurred between July and October, and during this period the NEE estimates were negative, indicating $CO_2$ uptake. The peak in the uptake by biogenic processes occurred in September to early November. This was during the spring period, after the winter rainfall period, and when the temperatures in the region begin to increase. The posterior estimates were less negative than the prior NEE fluxes, indicating that the NEE fluxes estimated by CABLE may have overestimated the amount of $CO_2$ uptake.

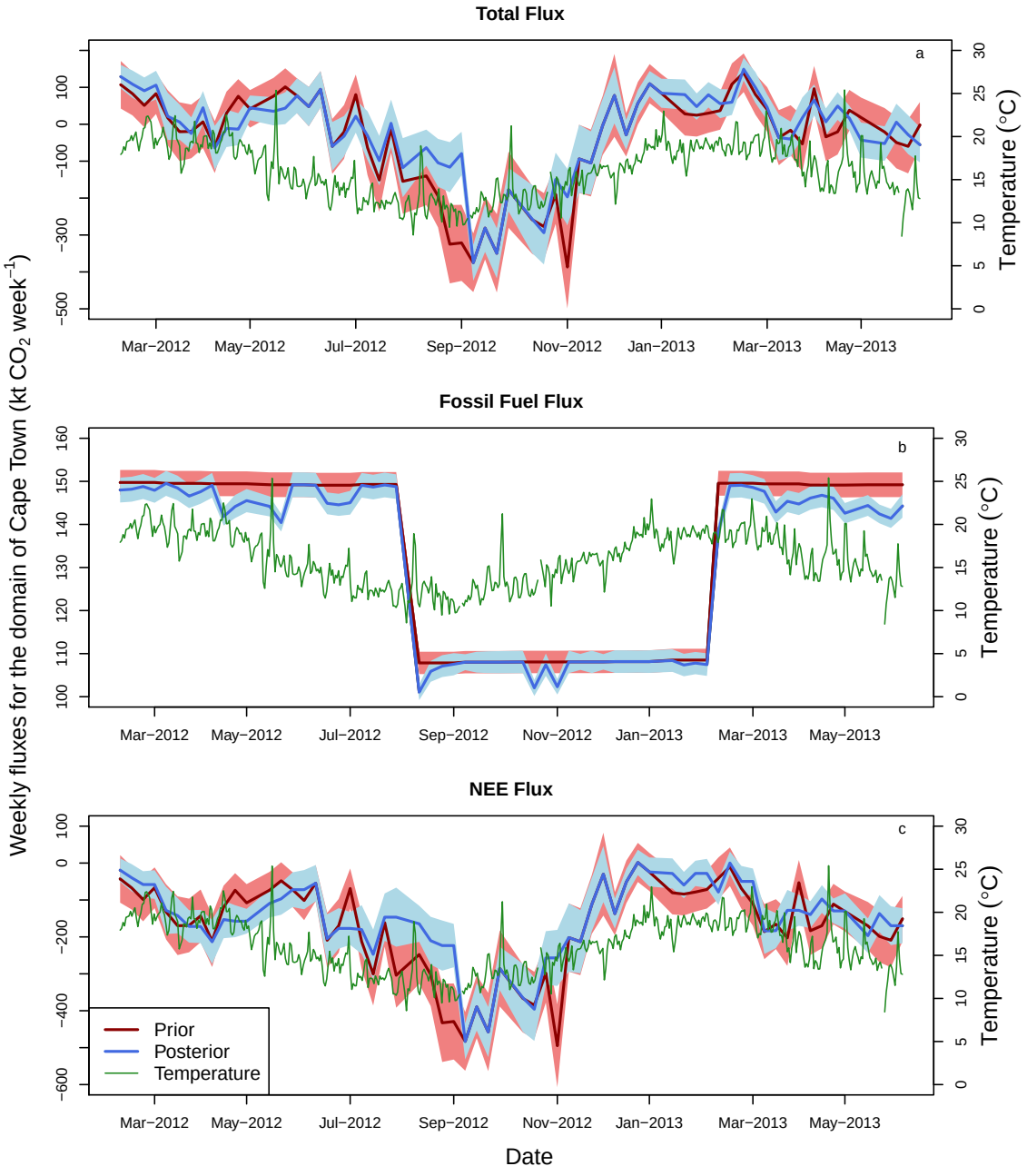


Figure 5.16: Prior (red) and posterior (blue) total weekly $CO_2$ flux estimates (kt $CO_2$ week$^{-1}$) (left-side axis) and uncertainty limits (shaded area), represented as a 95 % confidence interval, across the full domain of Cape Town, shown as (a) the total flux, (b) the fossil fuel flux, and (c) the NEE flux. The daily temperature (°C) as recorded at the Cape Point GAW station is provided by the lower green line (right-side axis).

## 5.4 Discussion

### 5.4.1 Inversion Innovation

The inversion was able to substantially improve the agreement between the prior and posterior modelled concentrations, with posterior modelled concentrations tracking most of the local events observed in the measurements. The most notable corrections to the pixel-level fluxes by the inversion were made to those with the largest industrial point sources, to pixels located on Robben Island where activities unaccounted for in the inventory were taking place, and to the areas dominated by NEE fluxes and located relatively close to the measurement sites. This evidence suggests that the inversion framework used here has had some success in capturing information regarding the $CO_2$ fluxes in the CT domain, and has applied reasonable corrections to the sources considered.

The inversion was able to reduce uncertainty of the total flux within a pixel by up to 97.7%, and was able to reduce the uncertainty in the total weekly flux over the whole domain by up to 50.5%. The largest innovation to a fossil fuel flux was applied to a pixel which contained an important point source in the domain - a crude oil refinery. This facility can process up to 100,000 barrels of crude oil per day. Unlike most industrial sources in the area which would be expected to have fairly consistent activity from day to day, activity at the crude oil refinery would depend on oil supply and on the global oil prices. During the period of March 2012 to June 2013, the global monthly oil price deviated between \$117.29 in March 2012 and \$90.73 in June 2012, ending on \$99.74 in June 2013 (World Bank commodity prices). In addition, the consumption of liquid petroleum gas and heavy furnace oils may have decreased during this period (City of Cape Town, 2015). As this is a source with a large amount of expected variability, it is unlikely that the inversion method with distant measurement sites will be able to adequately estimate the flux in this pixel. In order for this to occur, the measurement site would have to consistently view the source during periods of both high and low activity in order to provide an unbiased estimate. An inversion could be used to estimate this particular source if a ring of instruments were placed around the site in order to capture information from the site at all times, regardless of the prevailing wind direction, such as suggested for the Otway $CO_2$CRC carbon capture project (Cook, 2012).

Compared with the fossil fuel emissions, relative innovations to the NEE fluxes were much larger, due to the large uncertainty prescribed to these fluxes. The largest

innovations were made to natural areas near the CBD of CT, as well as to agricultural regions within the domain, particularly those close to the measurement sites. The prior estimates are dependent on the CABLE land-atmosphere interaction model and, although driven by the CCAM regional climate model, which in turn was driven by reliable reanalysed observations of the climate from NCEP, is still under ongoing development for use over South Africa. There is a great deal of uncertainty in its ability to simulate fluxes over the fynbos biome, as there is for most dynamic vegetation models (Moncrieff et al., 2015). In general, the inversion tended to increase the NEE fluxes so that the total flux was less negative compared with the priors, indicating that the amount of productivity estimated by CABLE may be overestimated.

### 5.4.2 Distinguishing Fossil Fuel and Biogenic Emissions

The spatial distribution and magnitude of the posterior fluxes and their uncertainties is strongly dependent on the prior spatial assignment of sources. In a city like CT, fossil fuel and NEE fluxes are usually co-occurring in the same pixel, with vegetation within the city representing a significant and large sink of $CO_2$. Under the current framework, if no fossil fuel source is prescribed to occur in a particular pixel, the inversion would only be able to adjust the NEE flux in this pixel, as the fossil fuel flux and its uncertainty are set to zero. If there is an unknown fossil fuel source in a pixel the inversion would lead to a better match between the modelled and observed concentrations, but a worse NEE flux estimate. Therefore the success of the inversion is largely dependent on how well the spatial extent of fossil fuel and biogenic sources are prescribed in the prior information.

In Bréon et al. (2015) NEE fluxes were aggregated to a larger grid size than the fossil fuel emissions. Effectively this means that perfect correlation was applied between the NEE fluxes for all pixels which fall within the same larger NEE pixel. By distinguishing the biogenic and fossil fuel sources in this way, it may allow the inversion to correctly allocate corrections between the fossil fuel and biogenic sources. We attempted to implement a similar idea by allowing correlation between NEE fluxes of neighbouring pixels and not prescribing correlations between fossil fuel sources. As the model tended to reduce fossil fuel emissions and increase NEE fluxes in the same pixel, it appears that the inversion is unlikely to adequately adjust the individual fluxes making up the total flux from a pixel. With the large coverage of vegetation within the domain, it is unlikely that a measurement network with only two sites could accurately estimate a given industrial point source, but there is still potential to monitor the overall city emissions, and assess the feasibility of inventory information.

This is evident from the large uncertainty reductions attained by the inversion for the total weekly flux estimates aggregated over the domain.

The posterior uncertainty of any linear combination of terms from the control vector of the fluxes (including the difference between two fluxes from the same pixel) will always be reduced or (at worst) left unchanged relative to the prior uncertainty of the same linear combination of elements (Jackson, 1979; Jackson and Matsu'ura, 1985). This means that although negative correlation between the flux components may be introduced through the inversion as observations are made of the sum of these components, the uncertainty in both the difference between fluxes from the same pixel and the total flux within a pixel will be reduced.

If we define the distinction between the fossil fuel flux and NEE flux within the same pixel $i$ as the variance of the difference between the fossil fuel and NEE fluxes $s_{f,i} - s_{NEE,i}$, this will be equal to the sum of the variances of these two fluxes minus twice the covariance between them: $C_{s(f,i;f,i)} + C_{s(NEE,i;NEE,i)} - 2 \times C_{s(f,i;NEE,i)}$ where $C_{s(f,i;NEE,i)}$ will be negative. Therefore although the posterior uncertainty of the difference in these fluxes will always be larger than the sum of the individual posterior flux uncertainties, it will be smaller than the prior uncertainty of this linear combination of terms. The ability of the inversion under the current framework to distinguish between NEE and fossil fuel fluxes is limited as the posterior uncertainties are still large, and therefore the uncertainty of $s_{f,i} - s_{NEE,i}$ is large.

On the other hand, when we aggregate these fluxes from the same pixel to get the total flux within a pixel $s_{f,i} + s_{NEE,i}$, the uncertainty of this term is equal to $C_{s(f,i;f,i)} + C_{s(NEE,i;NEE,i)} + 2 \times C_{s(f,i;NEE,i)}$ where $C_{s(f,i;NEE,i)}$ is negative. When we aggregate fluxes from the same pixel, the uncertainty of this total is smaller due to the both the smaller posterior uncertainties of the individual fluxes and also because the covariances are negative. This demonstrates that the value of the inversion is to reduce the uncertainty on each of the individual fluxes and to additionally reduce the uncertainty of the aggregation of the NEE and fossil fuel flux within the same pixel. In this case, the reduction in the uncertainty of the sum of fluxes within the same pixel is strongly dependent on the size of the uncertainty of the NEE flux, which is usually the larger uncertainty.

We have shown in the appendix (Appendix B.8) that if we reduce the uncertainty in the modelled concentrations, the negative off-diagonal covariance terms of $\mathbf{C_s}$ become larger in magnitude. To improve the ability of the inversion to estimate the total flux within a pixel, we need to improve the skill of the atmospheric transport model, and we need to reduce the uncertainty in the estimates of the

NEE. As it stands, with a large prior uncertainty in the estimation of the NEE fluxes from the CABLE model which remains a large posterior estimate after the inversion, the distinction between the fossil fuel and NEE flux from the same pixel, $C_{s(f,i;f,i)} + C_{s(NEE,i;NEE,i)} - 2 \times C_{s(f,i;NEE,i)}$, is not very different from the prior estimate, $C_{s_0(f,i;f,i)} + C_{s_0(NEE,i;NEE,i)}$.

### 5.4.3 Strengths and Limitations

This paper represents a first attempt at estimating $CO_2$ fluxes at the high resolution of 1 km by 1 km over CT, solving for individual fossil fuel, terrestrial and oceanic biogenic sources. A previous network design study for South Africa (Nickless et al., 2015b), which aggregated the NEE and fossil fuel fluxes up to a 15 km×15 km resolution, showed the aggregation errors could be high at the regional level. By avoiding this aggregation, and maintaining the 1 km by 1 km resolution of the atmospheric transport model throughout the inversion process, we attempted to minimise these aggregation errors. Maintaining this resolution is computationally expensive, but possible due to the relatively small domain size of 100 km by 100 km.

A limitation of this study is that human respiration was not explicitly accounted for. With a population of over three million, this flux could represent up to 26 kt $CO_2$ week$^{-1}$, if we attribute 1 kilogram $CO_2$ per day to each person (Bréon et al., 2015). This represents between a fifth to a quarter of the total fossil fuel flux estimated for the domain, and therefore is by no means a negligible quantity. Including this fossil fuel flux in the inventory information would most likely lead to confounding between the domestic emissions and the human respiration, as these two sources would have been calculated based on population data. Domestic emissions were heavily dependent on the assumption regarding how domestic heating emissions were distributed during the year. This had a large impact on the temporal profile of fossil fuel emissions, resulting in a lower average emission in summer compared with winter, which persisted in the posterior estimates of the fossil fuel fluxes. Consequently the prior uncertainties in the domestic emissions were larger compared with other fossil fuel sources. We have included sensitivity analyses on the specification of the fossil fuel emissions and their uncertainties in a companion paper.

This inversion was performed by solving for the total observed concentrations, rather than solving for the gradient in concentration measurements between two sites (Bréon et al., 2015). There are several reasons why the gradient method would not have been suitable in these circumstances. Firstly, we had the advantage of a background site which viewed background levels over 70% of the time. As our city is

located within the Southern Hemisphere, far less variability is expected between the hourly measurements or from week to week compared with the Northern Hemisphere, and we would expect the $CO_2$ concentration at the oceanic boundaries of our domain to be similar to background levels of $CO_2$. This was confirmed by the results of the inversion, which made almost no adjustments to the oceanic boundary concentrations, but made slightly larger adjustments to the boundary concentrations at the north and east terrestrial boundaries. This implies that the adjustments made by the inversion were largely due to the surface flux sources within the domain. In addition, there are no large expected sources located anywhere near the boundaries of the domain. The next major city in the proximity of CT is Port Elizabeth, which is over 600 km away. For this reason, it is unnecessary to solve for the gradients between the two sites, as we did not require the removal of unknown outside sources from the observation dataset. This allowed us to use the entire measurement record, which is an advantage as we only had two $CO_2$ measurement sites available.

Secondly, the gradient method would likely have performed poorly here, as the direction of travel of an air parcel between the two sites would not necessarily be in a straight line due to the topography of the site and demonstrated by the plot of the sensitivities at the two sites to the domain (Figure 5.17), as well as the modelled wind fields provided in Appendix B.3. Therefore extracting observations based on the prevailing wind speed and directions at the sites would have not represented true gradients in the $CO_2$ concentrations between the two measurements sites.

These sensitivities of the sites to the surface fluxes also reveal that the sites are often viewing oceanic sources (Figure 5.17). A limitation of this study is that a single time series of ocean biogenic emissions was used as the prior estimate for all oceanic pixels in the domain. The fluxes from the near-coastal oceanic pixels are likely to have significant spatial heterogeneity, although smaller compared with the terrestrial biogenic fluxes. A way of improving this would be to use the output of a model representing atmosphere-land-ocean biogeochemical exchanges to provide prior fluxes over both the land and ocean. The CSIR's Variable Resolution Earth System Model (VRESM) is such a model currently under development, which aims to couple CCAM, CABLE, and CSIR's Variable-Cubic Ocean Model (VCOM), and Pelagic Interactions Scheme for Carbon and Ecosystem Studies (PISCES) to model ocean transport and biogeochemistry (Engelbrecht et al., 2016). Due to the amount of shipping activity around the CT harbour and within the ocean domain viewed by the Robben Island site, the inventory analysis could be improved by the inclusion of information on

shipping routes so that the inversion can adjust fossil fuel fluxes in these ocean pixels as well.

The uncertainty in the NEE fluxes played an important role in the outcome of the inversion. If tighter uncertainty limits could be placed on the NEE flux estimates from the land-atmosphere exchange model, it would allow the inversion to better distinguish between the fossil fuel and NEE fluxes. This could be attained by validation work through eddy-covariance flux measurements over dominant vegetation types within the domain, for example. The use of a land-atmosphere exchange model well suited to the vegetation within the domain of a city-scale inversion is essential for improving the ability of the inversion to adjust the fossil fuel sources which are of foremost interest. The dependence on knowing the NEE fluxes well in order to estimate the fossil fuel fluxes could be reduced if there were additional measurements of $\Delta^{14}$C and $\delta^{13}$C isotope measurements at each of the sites, including at the background site (Turnbull et al., 2015; Newman et al., 2016).

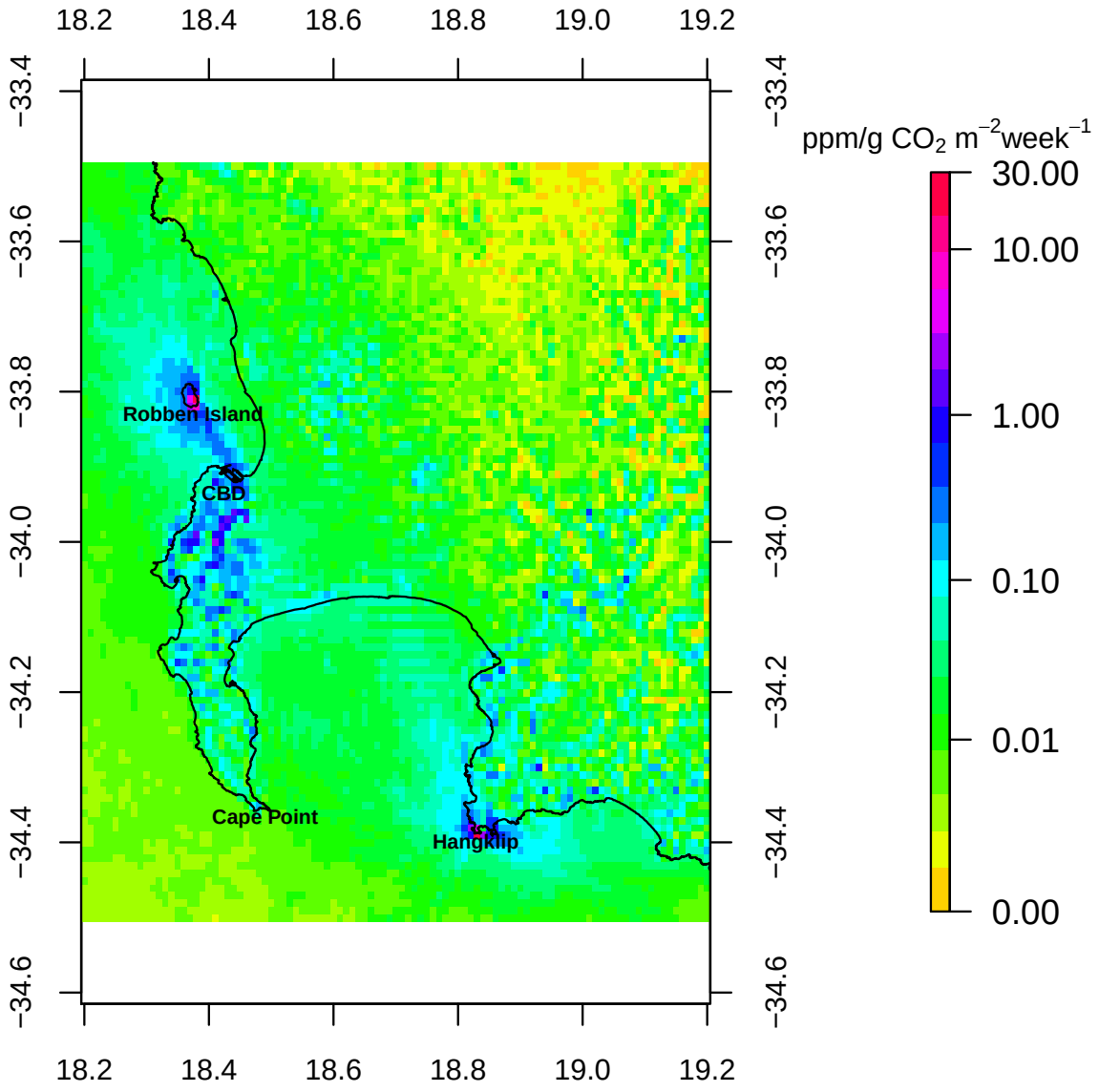


Figure 5.17: Mean weekly sensitivities (ppm $kg^{-1}$ $CO_2 m^{-2}$ $week^{-1}$) of the measurement sites at Robben Island and Hangklip to each surface source pixel, plotted on a log scale.

## 5.5 Conclusions

We have presented the results of a city-scale atmospheric inversion for Cape Town, South Africa. We have shown that the current inversion framework was able to reduce the misfit between the observed and modelled concentrations by making reasonable adjustments to the fossil fuel and NEE fluxes. We were able to reduce the total uncertainty in $CO_2$ weekly flux from the domain by up to 50%. We have demonstrated the ability of an inversion to obtain an improved estimate of an aggregated flux, even when the uncertainty in one component is large. To realistically use this framework for an operational inversion system for use in MRV, the uncertainty around the NEE estimates for Cape Town needs to be reduced. Further qualifying concentration observations according to the contributions from anthropogenic sources and those from the biosphere will help the inversion to disentangle the corrections to these two fluxes, and will reduce the dependency of the fossil fuel flux corrections on the uncertainty of the NEE flux estimates.

# Bibliography

Andres, R. J., Boden, T. A., Bréon, F. -M., Ciais, P., Davis, S., Erickson, D., Gregg, J. S., Jacobson, A., Marland, G., Miller, J., Oda, T., Olivier, J. G. J., Raupach, M. R., Rayner, P., and Treanton, K.: A synthesis of carbon dioxide emissions from fossil-fuel combustion, Biogeosciences, 9, 1845–1871, doi: 10.5194/bg-9-1845-2012, 2012.

Andres, R. J., Boden, T. A., and Higdon, D.: A new evaluation of the uncertainty associated with CDIAC estimates of fossil fuel carbon dioxide emission, Tellus B, 66, 23616, doi: 10.3402/tellusb.v66.23616, 2014.

Baker, D. F., Law, R. M., Gurney, K. R., Rayner, P., Peylin, P., Denning, A. S., Bourquet, P., Bruhwiler, L., Chen, Y., Ciais, P., Fung, I. Y., Heimann, M., John, J., Maki, T., Maksyutov, S., Masarie, K., Prather, M., Pak, B., Taguchi, S., Zhu, Z.: TransCom 3 inversion intercomparison: impact of transport model errors on the interannual variability of regional $CO_2$ fluxes, 1988–2003, Global Biogeochem. Cy., 20, GB1002, doi: 10.1029/2004GB002439, 2006.

Bellassen, V. and Stephan, N.: Accounting for carbon: Monitoring, reporting and verifying emissions in the climate economy, Cambridge University Press, Cambridge, UK, 2015.

Boden, T. A., Marland, G., and Andres, R. J.: Global, regional, and national fossil fuel $CO_2$ emissions, Carbon Dioxide Information Analysis Center, Oak Ridge National Laboratory, U.S. Department of Energy, Oak Ridge, Tenn., U.S.A., doi: 10.3334/CDIAC/00001_V2011, 2011.

Boon, A., Broquet, G., Clifford, D. J., Chevallier, F., Butterfield, D. M., Pison, I., Ramonet, M., Paris, J. -D., and Ciais, P.: Analysis of the potential of near-ground measurements of $CO_2$ and $CH_4$ in London, UK, for the monitoring of city-scale emissions using an atmospheric transport model, Atmos. Chem. Phys., 16, 6735–6756, doi:10.5194/acp-16-6735-2016, 2016.

Bousquet, P., Ciais, P., Peylin, P., Ramonet, M., and Monfray, P.: Inverse modeling of annual atmospheric $CO_2$ sources and sinks: 1. Method and control inversion, J. Geophys. Res., 104, 26161–26178, 1999.

Bréon, F. M., Broquet, G., Puygrenier, V., Chevallier, F., Xueref-Remy, I., Ramonet, M., Dieudonné, E., Lopez, M., Schmidt, M., Perrussel, O., and Ciais, P.: An attempt at estimating Paris area $CO_2$ emissions from atmospheric concentration measurements, Atmos. Chem. Phys., 15, 1707–1724, doi: 10.5194/acp-15-1707-2015, 2015.

Brioude, J., Angevine, W. M., Ahmadov, R., Kim, S. -W., Evan, S., McKeen, S. A., Hsie, E. -Y., Frost, G. J., Neuman, J. A., Pollack, I. B., Peischl, J., Ryerson, T. B., Holloway, J., Brown, S. S., Nowak, J. B., Roberts, J. M., Wofsy, S. C., Santoni, G. W., Oda, T., and Trainer, M.: Top-down estimate of surface flux in the Los Angeles Basin using a mesoscale inverse modeling technique: assessing anthropogenic emissions of CO, NOxand $CO_2$ and their impacts, Atmos. Chem. Phys., 13, 3661–3677, doi: 10.5194/acp-13-3661-2013, 2013.

Brunke, E. -G, Labuschagne, C., Parker, B., Scheel, H. E, and Wittlestone, S.: Baseline air mass selection at Cape Point,South Africa: application of $^{222}$Rn and other filter criteria to $CO_2$, Atmos. Environ., 38, 5693–5702, doi:10.1016/j.atmosenv.2004.04.024, 2004.

Carslaw, D. C. and Ropkins, K.: openair — an R package for air quality data analysis, Environ. Model. Softw., 27–28, 52–61, doi:10.1016/j.envsoft.2011.09.008, 2012.

Chevallier, F., Ciais, P., Conway, T. J., Aalto, T., Anderson, B. E., Bousquet, P., Brunke, E. G., Ciattaglia, L., Esaki, Y., Fröhlich, M., Gomez, A., Gomez-Pelaez, A. J., Haszpra, L., Krummel, P. B., Langenfelds, R. L., Leuenberger, M., Machida, T., Maignan, F., Matsueda, H., Morgui, J. A., Mukai, H., Nakazawa, T., Peylin, P., Ramonet, M., Rivier, L., Sawa, Y., Schmidt, M., Steele, L. P., Vay, S. A., Vermeulen, A. T., Wofsy, S., and Worthy, D.: $CO_2$ surface fluxes at grid point scale estimated from a global 21 year reanalysis of atmospheric measurements, J. Geophys. Res., 115, D21307, doi: 10.1029/2010JD013887, 2010.

Chouinard, C., Béland, M., McFarlane, N.: A simple gravity wave drag parameterization for use in medium-range weather forecast models, Atmos. Ocean, 24, 91–110, 1986.

Ciais, P., Rayner, P., Chevallier, F., Bousquet, P., Logan, M., Peylin, P., and Ramonet, M.: Atmospheric inversions for estimating $CO_2$ fluxes: methods and perspectives, Climatic Change, 103, 69–92, 2010.

City of Cape Town: State of energy and energy futures report. Cape Town: City of Cape Town, http://www.capetown.gov.za/en/EnvironmentalResourceManagement/publications/Documents/State_of_Energy_+_Energy_Futures_Report_2011_revised_2012-01.pdf, 2011.

City of Cape Town: State of energy report 2015. Cape Town: City of Cape Town, https://africancityenergy.org/getfile.php?id=22&category=0, 2015.

P. Cook (Ed.): Geologically storing carbon: The CO2CRC Otway Project: Learning from the Otway Project experience, CSIRO Press, Melbourne, p. 384, 2014.

Crosson, E.:A cavity ring-down analyzer for measuring atmospheric levels of methane, carbon dioxide, and water vapor, Appl. Phys. B, 92, 403–408, doi:10.1007/s00340-008-3135-y, 2008.

Davis, K. J., Deng, A., Lauvaux, T., Miles, N. L., Richardson, S. J., Sarmiento, D. P., Gurney, K. R., Hardesty, R. M., Bonin, T. A., Brewer, W. A., Lamb, B. K., Shepson, P. B., Harvey, R. M., Cambaliza, M. O., Sweeney, C., Turnbull, J. C., Whetstone, J., and Karion, A.: The Indianapolis Flux Experiment (INFLUX): A testbed for developing urban greenhouse gas emission measurements, Elem. Sci. Anth., 5:21, doi: 10.1525/elementa.188, 2017.

UK Department for Environment, Food and Rural Affairs (Defra): UK ship emissions inventory. Final report. London: Crown, http://uk-air.defra.gov.uk/assets/documents/reports/cat15/1012131459_21897_Final_Report_291110.pdf, 2010.

UK Department for Environment, Food and Rural Affairs (Defra): Government GHG conversion factors for company reporting: Methodology paper for emission factors, London: Crown, https://www.gov.uk/government/uploads/system/uploads/attachment_data/file/224437/pb13988-emission-factor-methodology-130719.pdf, 2013a.

UK Department for Environment, Food and Rural Affairs (Defra): Treatment of uncertainties for national estimates of greenhouse gas emissions, http://uk-air.

defra.gov.uk/reports/empire/naei/ipcc/uncertainty/contents.html, 2013b.

Dlugokencky, E. and Tans, P.: Trends in atmospheric carbon dioxide, National Oceanic and Atmospheric Administration, Earth System Research Laboratory (NOAA/ESRL), available at: https://www.esrl.noaa.gov/gmd/ccgg/trends/, last access: 29 September 2016, 2016.

Duren, R. M. and Miller, C. E.: Measuring the carbon emissions of megacities, Nat. Clim. Change, 2, 560–562, doi: 10.1038/nclimate1629, 2012.

Engelbrecht, F. A., McGregor, J. L. and Engelbrecht, C. J.: Dynamics of the conformal-cubic atmospheric model projected climate-change signal over southern Africa, Int. J. Climatol., 29, 1013-1033., doi: 10/1002/joc.1742.29., 2009.

Engelbrecht, F. A., Landman, W. A., Engelbrecht, C. J., Landman, S., Bopane, M. M., Roux, B., McGregor, J. L., and Thatcher, M.: Multi-scale climate modelling over Southern Africa using variable-resolution global model, Water Research Commission 40-Year Celebration Conference, Kempton Park, 31 August - 1 September 2011, doi: 10.4314/wsa.v37i5.2, 2011.

Engelbrecht, C. J., Engelbrecht, F. A. and Dyson, L. L.: High-resolution model-projected changes in mid-tropospheric closed-lows and extreme rainfall events over southern Africa. Int. J. Climatol., 33, 173–187, doi: 10/1002/joc.3420, 2013.

Engelbrecht, F., Adegoke, J., Bopape, M-J., Naidoo, M., Garland, R., Thatcher, M., McGregor, J., Katzfey, J., Werner, M., Ichoku, C. and Gatebe, C.: Projections of rapidly rising surface temperatures over Africa. Env. Res. Letters., 10(8), 085004, doi: 10.1088/1748-9326/10/8/085004, 2015.

Engelbrecht, F. A., McGregor, J. L., Thatcher, M., Garland, R., Sovara, M., Bopane, M. M., and van der Merwe, J.: The Variable-Resolution Earth System Model and its simulations of the Benguela upwelling system. The International Conference on Regional Climate CORDEX 2016, Stockholm, Sweden, 17–20 May 2016, 2016.

Enting, I. G.: Inverse Problems in Atmospheric Constituent Transport, Cambridge Univ. Press, New York, 2002.

Erickson, P. and Tempest, K.: Advancing climate ambition: Cities as partners in global climate action, Produced by Stockholm Environment Institute (SEI) in support of the UN Secretary-General's Special Envoy for Cities and Climate Change and C40, 2014.

Exbrayat, J. -F., Pitman, A. J. Abramowitz, G. and Wang, Y, -P.: Sensitivity of net ecosystem exchange and heterotrophic respiration to parameterization uncertainty, J. Geophys. Res. Atmos., 118, 16401651, doi:10.1029/2012JD018122, 2013.

Fawcett, R. A., Pitcher, G., Bernard, S., Cembella, A., and Kudela, R.: Contrasting wind patterns and toxigenic phytoplankton in the southern Benguela upwelling system, Mar. Ecol. Prog. Ser., 348, 19–31, doi: 10.3354/meps07027, 2007.

Feng, S., Lauvaux T., Newman, S., Rao, P., Ahmadov, R. Deng, A., Díaz-Isaac, L. I., Duren, R. M., Fischer, M. L., Gerbig, C., Gurney, K. R., Huang, J., Jeong, S., Li, Z., Miller, C. E., O'Keeffe, D., Patarasuk, R., Ser, S. P., Song, Y., Wong, K. W., and Yung, Y. L.: Los Angeles megacity: a high-resolution land–atmosphere modelling system for urban $CO_2$ emissions, Atmos. Chem. Phys., 16, 9019–9045, doi: 10.5194/acp-16-9019-2016, 2016.

Ganesan, A. L., Rigby, M., Zammit-Mangion, A., Manning, A. J., Prinn, R. G., Fraser, P. J., Harth, C. M., Kim, K. -R., Krummel, P. B., Li, S., Mühle, J., O'Doherty, S. J., Park, S., Salameh, P. K., Steele, L. P., and Weiss, R. F.: Characterization of uncertainties in atmospheric trace gas inversions using hierarchical Bayesian methods, Atmos. Chem. Phys., 14, 3855-3864, doi:10.5194/acp-14-3855-2014, 2014.

Geels, C., Gloor, M., Ciais, P., Bousquet, P., Peylin, P., Vermeulen, A. T., Dargaville, R., Aalto, T., Brandt, J., Christensen, J. H., Frohn, L. M., Haszpra, L., Karstens, U., Rödenbeck, C., Ramonet, M., Carboni, G., and Santaguida, R.: Comparing atmospheric transport models for future regional inversions over Europe Part 1: mapping the atmospheric $CO_2$ signals, Atmos. Chem. Phys., 7, 3461-3479, doi: 10.5194/acp-7-3461-2007, 2007.

Gerbig, C., Lin, J. C., Wofsy, S. C., Daube, B. C., Andrews, A. E., Stephens, B. B., Bakwin, P. S. and Grainger, C. A.: Toward constraining regional-scale fluxes of $CO_2$ with atmospheric observations over a continent: 1. Observed spatial variability from airborne platforms, J. Geophys. Res., 108(D24), 4756, doi: 10.1029/2002JD003018, 2003.

Gregor, L. and Monteiro P. M. S.: Is the southern Benguela a significant regional sink of CO2? S. Afr. J. Sci., 109(5/6), Art. #0094, 5 pages, doi: 10.1590/sajs.2013/20120094, 2013.

Gurney. K. R., Law, R. M., Denning, A. S., Rayner, P. J., Baker, D., Bousquet, P., Bruhwiler, L., Chen, Y., Ciais, P., Fan, S., Fung, I. Y., Gloor, M., Heimann, M., Higuchi, K., John, J., Maki, T., Maksyutov, S., Masarie, K., Peylin, P., Prather, M., Pak, B. C., Randerson, J., Sarmiento, J., Taguchi, S., Takahashi, T., and Yuen, C.: Towards robust regional estimates of $CO_2$ sources and sinks using atmospheric transport models, Nature, 405, 626–630, 2002.

Gurney, K. R., Law, R. M., Denning, A. S., Rayner, P. J., Baker, D., Bousquet, P., Bruhwiler, L., Chen, Y., Ciais, P., Fan, S., Fung, I. Y., Gloor, M., Heimann, M., Higuchi, K., John, J., Kowalczyk, E., Maki, T., Maksyutov, S., Peylin, P., Prather, M., Pak, B. C., Sarmiento, J., Taguchi, S., Takahashi, T., and Yuen, C.: TransCom 3 $CO_2$ inversion intercomparison: 1. Annual mean control results and sensitivity to transport and prior flux information, Tellus B, 55, 555–579, 2003.

Gurney, K. R., Mendoza, D. L., Zhou, Y. Y., Fischer, M. L., Miller, C. C., Geethakumar, S., Du Can, S. D.: High resolution fossil fuel combustion $CO_2$ emission fluxes for the United States. Environ. Sci. Technol., 43 (14), 5535–5541, doi: 10.1021/es900806c, 2009.

Gurney, K. R., Razlivanov, I., Song, Y., Zhou, Y., Benes, B., and Abdul–Massih, M.: Quantification of fossil fuel $CO_2$ emissions on the building/street scale for a large U.S. city, Environ. Sci. Technol., 46, 12194–12202, doi: 10.1021/es3011282, 2012.

Holtslag, A. A. M. and Boville, B. A.: Local versus non-local boundary layer diffusion in a global climate model, J. Clim., 6, 1825–1842, doi: 10.1175/1520-0442(1993)006¡1825:LVNBLD¿2.0.CO;2, 1993.

Hutyra, L., Duren, R., Gurney, K. R., Grimm, N., Kort, E. A., Larson, E., Shrestha, G.: Urbanization and the carbon cycle: Current capabilities and research outlook from the natural sciences perspective. Earth's Future, 2: 473–495. doi: 10.1002/2014EF000255, 2014.

Intergovernmental Panel on Climate Change (IPCC): Good practice guidance and uncertainty management in national greenhouse gas inventories. Montreal: IPCC, 93–102, http://www.ipcc-nggip.iges.or.jp/public/gp/english/, 2000.

IPCC: Climate Change 2014: Synthesis Report. Contribution of Working Groups I, II and III to the Fifth Assessment Report of the Intergovernmental Panel on Climate Change [Core Writing Team, Pachauri, R.K. and Meyer, L.A. (Eds.)]. IPCC, Geneva, Switzerland, 151 pp, 2014.

Jackson, D. D.: The use of a priori data to resolve non-uniqueness in linear inversion, Geophys. J. R. astr. Soc., 57, 137–157, 1979.

Jackson, D. D and Matsu'ura, M.: A Bayesian approach to nonlinear inversion, J. Geophys. Res. 90 (B1), 581–591, 1985.

Janssens-Maenhout, G., Pagliari, V., Guizzardi, D., and Muntean, M.: Global emission inventories in the Emission Database for Global Atmospheric Research (EDGAR) Manual (I). Gridding: EDGAR emissions distribution on global gridmaps. Joint Research Centre, Luxembourg: European Union, 33 pp, doi: 10.2788/81454, 2012.

Kalnay, E., Kanamitsu, M., Kistler, R., Collins, W., Deaven, D., Gandin, L., Iredell, M., Saha, S., White, G., Woollen, J., Zhu, Y., Chelliah, M., Ebisuzaki, W., Higgins, W., Janowiak, J., Mo, K., C., Ropelewski, C., Wang, J., Leetmaa, A., Reynolds R., Jenne, R., Joseph, D.: The NCEP/NCAR 40-year reanalysis project. Bull. Am. Meteorol. Soc., 77, 437–472, 1996.

Kaminski, T., Heimann, M., and Giering, R.: A coarse grid three dimensional global inverse model of the atmospheric transport, 2. Inversion of the transport of $CO_2$ in the 1980s, J. Geophys. Res., 104, 18555–18581, 1999.

Kaminski, T., Rayner, P .J., Heimann, M., and Enting, I. G.: On aggregation errors in atmospheric transport inversions, J. Geophys. Res., 106, 4705–4715, 2001.

Kort, E. A., Angevine, W. M., Duren, R., and Miller, C. E.: Surface observations for monitoring urban fossil fuel $CO_2$ emissions: minimum site location requirements for the Los Angeles megacity, J. Geophys. Res., 118, 1–8, doi: 10.1002/jgrd.50135, 2013.

Kowalczyk, E. A., Garratt, J. R. and Krummel, P. B.: Implementation of a soil-canopy scheme into the CSIRO GCM - regional aspects of the model response, CSIRO Div. Atmospheric Research, Melbourne, Australia, Tech Paper No. 32, 59 pp., 1994.

Kowalczyk, E. A., Wang, Y. P. and Law, R. M.: CSIRO Atmosphere Biosphere Land Exchange model for use in climate models and as an offline model, CSIRO Marine and Atmospheric Research technical paper xxV ISBN 1 921232 39 0, 2006.

Lacis, A. A. and Hansen, J. E.: A parameterization for the absorption of solar radiation in the earth's atmosphere, J. Atmos. Sci., 31, 118–133, doi: 10.1175/1520-0469(1974)031¡0118:APFTAO¿2.0.CO;2, 1974.

Landman, S., Engelbrecht, F. A, Dyson, L., Engelbrecht, C., J., and Landman, W., A.: A short-range ensemble prediction system for South Africa, Water SA, 38(5), 765–774, doi: 10.4314/wsa.v38i5.16, 2012.

Lauvaux, T., Uliasz, M., Sarrat, C., Chevallier, F., Bousquet, P., Lac, C., Davis, K. J., Ciais, P., Denning, A. S., and Rayner, P. J.: Mesoscale inversion: first results from the CERES campaign with synthetic data, Atmos. Chem. Phys., 8, 3459–3471, doi: 10.5194/acp-8-3459-2008, 2008.

Lauvaux, T., Pannekoucke, O., Sarrat, C., Chevallier, F., Ciais, P., Noilhan, J., and Rayner, P. J.: Structure of the transport uncertainty in mesoscale inversions of CO2 sources and sinks using ensemble model simulations, Biogeosciences, 6, 1089–1102, doi: 10.5194/bg-6-1089-2009, 2009.

Lauvaux, T., Schuh, A. E., Uliasz, M., Richardson, S., Miles, N., Andrews, A. E., Sweeney, C., Diaz, L. I., Martins, D., Shepson, P. B., and Davis, K. J.: Constraining the $CO_2$ budget of the corn belt: exploring uncertainties from the assumptions in a mesoscale inverse system, Atmos. Chem. Phys., 12, 337–354, doi: 10.5194/acp-12-337-2012, 2012.

Lauvaux, T., Miles, N. L., Richardson, S. J., Deng, A., Stauffer, D. R., Davis, K. J., Jacobson, G., Rella, C., Calonder, G. -P., and DeCola, P. L.: Urban emissions of $CO_2$ from Davos, Switzerland: the first real-time monitoring system using atmospheric inversion technique, J. Appl. Meteorol. Climatol., 52, 2654–2668, doi: 10.1175/JAMC-D-13-038.1, 2013.

Lauvaux, T., Miles, N. L., Deng, A. Richardson, S. J., Cambaliza, M. O., Davis, K. J., Gaudet, B., Gurney, K. R., Huang, J., O'Keefe, D., Song, Y., Karion, A., Oda, T., Patarasuk, R., Razlivanov, I., Sarmiento, D., Shepson, P., Sweeney, C., Turnbull, J., and Wu, K.: High-resolution atmospheric inversion of urban $CO_2$ emissions during the dormant season of the Indianapolis Flux Experiment (INFLUX), J. Geophys. Res. Atmos., 121, 5213–5236, doi: 10.1002/2015JD024473, 2016.

Law, R. M., Chen, Y., Gurney, K. R., and Transcom 3 Modellers: TransCom 3 $CO_2$ inversion intercomparison: 2. Sensitivity of annual mean results to data choices, Tellus B, 55, 580–595, 2003.

Law, R. M., Raupach, M. R., Abramowitz, G., Dharssi, I., Haverd, V.,Pitman, A. J.,Renzullo, L., Van Dijk, A. and Wang, Y. -P.: The Community Atmosphere Biosphere Land Exchange (CABLE) model Roadmap for 2012-2017, CAWCR Technical Report No. 057, 2012.

Le Quéré, C., Andres, R. J., Boden, T. A., Conway, T., Houghton, R. A., House, J. I., Marland, G., Peters, G. P., van der Werf, G. R., Ahlström, A., Andrew, R. M., Bopp, L., Canadell, J. G., Ciais, P., Doney, S. C., Enright, C., Friedlingstein, P., Huntingford, C., Jain, A. K., Jourdain, C., Kato, E., Keeling, R. F., Klein Goldewijk, K., Levis, S., Levy, P., Lomas, M., Poulter, B., Raupach, M. R., Schwinger, J., Sitch, S., Stocker, B. D.,Viovy, N., Zaehle, S., and Zeng, N.: The global carbon budget 1959–2011, Earth Syst. Sci. Data, 5, 165–185, doi: 10.5194/essd-5-165-2013 2013.

McGregor, J. L., Gordon, H. B., Watterson, I. G., Dix, M. R., and Rotstayn, L. D.: The CSIRO 9-level atmospheric general circulation model, CSIRO Div. Atmospheric Research Tech, Paper No. 26, 89 pp., 1993.

McGregor, J. L.: Semi-Lagrangian advection on conformal-cubic grids. Mon. Weather Rev., 124, 1311–1322, doi: 10.1175/1520-0493(1996)124¡1311:SLAOCC¿2.0.CO;2, 1996.

McGregor, J. L. and Dix, M. R.: The CSIRO conformal-cubic atmospheric GCM, in: IUTAM Symposium on Advances in Mathematical Modelling of Atmosphere and Ocean Dynamics, Limerick, Ireland, 2–7 July 2000, edited by: Hodnett, P. F., Kluwer, Dordrecht, 197–202, 2001.

McGregor, J. L.: A new convection scheme using a simple closure, in: Current issues in the parameterization of convection, BMRC, Melbourne, Australia, Research Report 93, 33-36, 2003.

McGregor, J. L.: Geostrophic adjustment for reversibly staggered grids. Mon. Weather Rev., 133, 1119–1128, doi: 10.1175/MWR2908.1, 2005a.

McGregor, J. L.: C-CAM: Geometric aspects and dynamical formulation. CSIRO Atmospheric Research Technical Paper, No 70, 41, 2005b.

McGregor, J. L. and Dix, M. R.: An updated description of the Conformal-Cubic Atmospheric Model, in: High Resolution Numerical Modelling of the Atmosphere and Ocean, edited by: Hamilton, K. and Ohfuchi, W., Springer, New York, USA, 51–76, 2008.

McKain, K., Wofsy, S. C., Nehrkorn, T., Eluszkiewicz, J., Ehleringer, J. R., and Stephens, B. B.: Assessment of ground-based atmospheric observations for verification of greenhouse gas emissions from an urban region, Proc. Natl. Acad. Sci. U. S. A., 109(22), 8423–8428, doi: 10.1073/pnas.1116645109, 2012.

Michalak, A. M., Hirsch, A., Bruhwiler, L., Gurney, K. R., Peters, W., and Tans, P. P.: Maximum likelihood estimation of covariance parameters for Bayesian atmospheric trace gas surface flux inversions, J. Geophys. Res., 110, D24107, doi: 10.1029/2005JD005970, 2005.

Moncrieff, G.R., Scheiter,S. Slingsby, J. A. and Higgins, S. I.: Understanding global change impacts on South African biomes using Dynamic Vegetation Models, S. Afr. J. Bot., 101, 16–23, doi: 10.1016/j.sajb.2015.02.004, 2015.

Newman, S., Xu, X., Gurney, K. R., Hsu, Y. K., Li, K. F., Jiang, X., Keeling, R., Feng, S., O'Keefe, D., Patarasuk, R., Wong, K. W., Rao, P., Fischer, M. L., and Yung, Y. L.: Toward consistency between trends in bottom-up $CO_2$ emissions and top-down atmospheric measurements in the Los Angeles megacity, Atmos. Chem. Phys., 16, 3843–3863, doi: 10.5194/acp-16-3843-2016, 2016.

Nickless, A., Scholes, R. J. and Filby, E.: Spatial and temporal disaggregation of anthropogenic $CO_2$ emissions from the City of Cape Town, S. Afr. J. Sci., 111(11/12), Art. $\#2014 - 0387$, 8 pages, doi: 10.17159/sajs.2015/20140387, 2015a.

Nickless, A., Ziehn, T., Rayner, P. J., Scholes, R .J., and Engelbrecht, F.: Greenhouse gas network design using backward Lagrangian particle dispersion modelling – Part 2: Sensitivity analyses and South African test case, Atmos. Chem. Phys., 15, 2051–2069, doi: 10.5194/acp-15-2051-2015, 2015b.

NRC (Committee on Methods for Estimating Greenhouse Gas Emissions): Verifying greenhouse gas emissions: methods to support international climate agreements (9780309152112), The National Academies Press, Washington, D.C., 2010.

Oda, T., Lauvaux, T., Lu, D., Rao, P., Miles, N. L., Richardson, S. J. and Gurney, K. R.: On the impact of granularity of space-based urban $CO_2$ emissions in urban atmospheric inversions: A case study for Indianapolis, IN, Elem Sci Anth, 5, 28, doi: 10.1525/elementa.146, 2017.

Peylin, P., Baker, D., Sarmiento, J., Ciais, P., and Bousquet, P.: Influence of transport uncertainty on annual mean and seasonal inversions of atmospheric $CO_2$ data, J. Geophys. Res., 107, 4385, doi: 10.1029/2001JD000857, 2002.

Rayner, P. J., Enting, I. G., Francey, R. J., and Langenfelds, R. L.: Reconstructing the recent carbon cycle from atmospheric $CO_2$, $\delta^{13}C$ and $O_2/N_2$ observations, Tellus B, 51, 213–232, 1999.

Rayner, P. J., Law, R. M, Allison, C. E., Francey, R. J., Trudinger, C. M., Pickett-Heaps, C.: Interannual variability of the global carbon cycle (1992-2005) inferred by inversion of atmospheric $CO_2$ and $\delta^{13}C$ measurements, Global Biogeochem. Cy., 22, GB3008, doi: 10.1029/2007GB003068, 2008.

Rotstayn, L. D.: A physically based scheme for the treatment of stratiform clouds and precipitation in large-scale models. I: Description and evaluation of the microphysical processes, Q. J. R. Meteorol. Soc., 123, 1227–1282, 1997.

Roux, B.: Ultra high-resolution climate simulations over the Stellenbosch wine producing region using a variable-resolution model, MSc Thesis, Faculty of Natural and Agricultural Sciences, University of Pretoria, South Africa, 106 pp., 2009.

Schmidt, F.: Variable fine mesh in spectral global model, Beitr. Phys. Atmos., 50, 211–217, 1977.

Schuh, A. E., Lauvaux, T., West, T. O., Denning, A. S., Davis, K., J., Miles, N., Richardson, S., Uliasz, M., Lokupitiya, E., Cooley, D., Andrews, A., and Ogle, S.: Evaluating atmospheric $CO_2$ inversions at multiple scales over a highly inventoried agricultural landscape, Glob. Change Biol., 19, 1424–1439, doi: 10.1111/gcb.12141, 2013.

Schwarzkopf, M. D. and Fels, S. B.: The simplified exchange method revisited: An accurate, rapid method for computation of infrared cooling rates and fluxes, J. Geophys. Res., 96, 9075–9096, 1991.

Shiga, Y. P., Michalak, A. M., Gourdji, S. M., Mueller, K. L., and Yadav, V.: Detecting fossil fuel emissions patterns from subcontinental regions using North American in situ $CO_2$ measurements, Geophys. Res. Lett., 41(12), 4381–4388, doi: 10.1002/2014GL059684, 2014.

Shrout, P. E. and Fleiss, J. L.: Intraclass correlations: uses in assessing rater reliability, Psychol. Bull., 2, 420–428, 1979.

Seibert, P. and Frank, A.: Source-receptor matrix calculation with a Lagrangian particle dispersion model in backward mode, Atmos. Chem. Phys., 4, 51–63, doi: 10.5194/acp-4-51-2004, 2004.

South African Department of Energy: Digest of South African energy statistics, Pretoria: Department of Energy. `http://www.energy.gov.za/files/media/explained/2009%20Digest%20PDF%20version.pdf`, 2009.

Statistics South Africa: Census 2011 statistical release, P0301.4., Pretoria: Statistics South Africa, 2011.

Staufer, J., Broquet, G., Bréon, F. -M., Puygrenier, V., Chevallier, F., Xueref-Rémy, I., Dieudonné, E., Lopez, M., Schmidt, M., Ramonet, M., Perrussel, O., Lac, C., Wu, L., and Ciais, P.: The first 1-year-long estimate of the Paris region fossil fuel CO2 emissions based on atmospheric inversion, Atmos. Chem. Phys., 16, 14703–14726, doi: 10.5194/acp-16-14703-2016, 2016.

Strong, C., Stwertka, C., Bowling, D. R., Stephens, B. B. and Ehleringer, J. R.: Urban carbon dioxide cycles within the Salt Lake Valley: A multiple-box model validated by observations, J. Geophys. Res., 116, D15307, doi: 10.1029/2011JD015693, 2011.

Seto, K. C., Dhakal, S., Bigio, A., Blanco, H., Delgado, G. C., Dewar, D., Huang, L., Inaba, A., Kansal, A., Lwasa, S., McMahon, J. E., Müller, D. B., Murakami, J., Nagendra, H., and Ramaswami, A.: Human settlements, infrastructure and spatial planning, in: Climate Change 2014: Mitigation of Climate Change. Contribution of Working Group III to the Fifth Assessment Report of the Intergovernmental Panel on Climate Change, edited by: Edenhofer, O., Pichs-Madruga, R., Sokona, Y., Farahani, E., Kadner, S., Seyboth, K., Adler, A., Baum, I., Brunner, S., Eickemeier, P., Kriemann, B., Savolainen, J., Schlömer, S., von Stechow, C., Zwickel, T., and Minx, J. C., Cambridge, United Kingdom and New York, NY, USA, 2014.

Sugar, L. and Kennedy, C.: A low carbon infrastructure plan for Toronto, Canada, Can. J. Civ. Eng., 40, 86–96, doi: 10.1139/cjce-2011-0523, 2013.

Tans, P. and Keeling, R.: Mauna Loa $CO_2$ monthly mean data, NOAA/ESRL `www.esrl.noaa.gov/gmd/ccgg/trends/` and Scripps Institution of Oceanography `scrippsco2.ucsd.edu/`, 2016.

Tarantola, A.: Inverse Problem Theory and Methods for Model Parameter Estimation, Society for Industrial and Applied Mathematics, Philadelphia, 2005.

Thatcher, M. and McGregor, J. L.: Using a scale-selective filter for dynamical downscaling with the conformal cubic atmospheric model, Mon. Weather Rev., 137, 1742–1752, 2009.

Thatcher, M. and McGregor, J. L.: A technique for dynamically downscaling daily-averaged GCM datasets over Australia using the Conformal Cubic Atmospheric Model, Mon. Weather Rev., 139, 79–95, 2010.

Turnbull, J. C., Sweeney, C., Karion, A., Newberger, T., Lehman, S. J., Tans, P. P., Davis, K. J., Lauvaux, T., Miles, N. L., Richardson, S. J., Cambaliza, M. O., Shepson, P. B., Gurney, K., and Patarasuk, P.: Toward quantification and source sector identification of fossil fuel $CO_2$ emissions from an urban area: Results from the INFLUX experiment, J. Geophys. Res. Atmos., 120, 292–312, doi: 10.1002/2014JD022555, 2015.

Uliasz, M.: The atmospheric mesoscale dispersion modeling system, J. Appl. Meteorol., 31, 139–149, 1993.

Uliasz, M.: Lagrangian particle modeling in mesoscale applications, in: Environmental Modelling II, Computational Mechanics Publications, Southampton, UK, 71–102, 1994.

UN–Habitat: Cities and climate change: global report on human settlements 2011, Earthscan, United Nations Human Settlements Programme (UN–Habitat), 2011.

Wang, Y, P., Kowalczyk, E., Leuning, R., Abramowitz, G., Raupach, M. R., Pak, B., van Gorsel, E. and Luhar, A.: Diagnosing errors in a land surface model (CABLE) in the time and frequency domains, J. Geophys. Res., 116, G01034, doi: 10.1029/2010JG001385, 2011.

Whittlestone, S., Kowalczyk, E., Brunke, E. G., and Labuschagne, C.: Source Regions for $CO_2$ at Cape Point Assessed by Modelling 222Rn and Meteorological Data, Technical Report for the South African Weather Service, Pretoria, South Africa, 2009.

Wu, L., Bocquet, M., Chevallier, F., Lauvaux, T., and Davis, K.: Hyperparameter estimation for uncertainty quantification in mesoscale carbon dioxide inversions, Tellus B, 65, 20894, doi: 10.3402/tellusb.v65i0.20894, 2013.

Wu, L., Broquet, G., Ciais, P., Bellassen, V., Vogel, F., Chevallier, F., Xueref-Remy, I., and Wang, Y.: What would dense atmospheric observation networks bring to the quantification of city $CO_2$ emissions?, Atmos. Chem. Phys., 16, 7743–7771, doi: 10.5194/acp-16-7743-2016, 2016.

Zhang, L., Zhang, H. and Li, Y.: Surface energy, water and carbon cycle in China simulated by the Australian community land surface model (CABLE), Theor. Appl. Climatol.,96(3),375–394, doi:10.1007/s00704-008-0047-z, 2009.

Zhang, H ., Pak, .B., Wang, Y. P., Zhou, X., Zhang, Y. and Zhang, L.: Evaluating surface water cycles simulated by the Australian community land surface model (CABLE) across different spatial and temporal domains. J. Hydrometeor, 14, 1119–1138, 2013.

Ziehn, T., Nickless, A., Rayner, P. J., Law, R. M., Roff, G., and Fraser, P.: Greenhouse gas network design using backward Lagrangian particle dispersion modelling – Part 1: Methodology and Australian test case, Atmos. Phys. Chem., 14, 9363–9378, doi: 10.5194/acp-14-9363-2014, 2014.

# Chapter 6

# An Atmospheric Inversion over the City of Cape Town: Sensitivity Analyses

**Photo: Alecia Nickless**

Atmos. Chem. Phys. Discuss., https://doi.org/10.5194/acp-2018-535
Manuscript under review for journal Atmos. Chem. Phys.
Discussion started: 26 June 2018


Atmospheric Chemistry and Physics Discussions

# An atmospheric inversion over the city of Cape Town: sensitivity analyses

Alecia Nickless[1,2], Peter J. Rayner[3], Robert J. Scholes[4], Francois Engelbrecht[5], and Birgit Erni[1,6]

[1]Department of Statistical Sciences, University of Cape Town, Cape Town, 7701, South Africa
[2]Nuffield Department of Primary Care Health Sciences, University of Oxford, Oxford, OX2 6GG, UK
[3]School of Earth Sciences, University of Melbourne, Melbourne, VIC 3010, Australia
[4]Global Change Institute, University of the Witwatersrand, Johannesburg, 2050, South Africa
[5]Climate Studies and Modelling and Environmental Health, CSIR, Pretoria, 0005, South Africa
[6]The Centre for Statistics in Ecology, the Environment and Conservation, University of Cape Town, Cape Town, 7701, South Africa

**Correspondence:** Alecia Nickless alecia.nickless@phc.ox.ac.uk

**Abstract.** We present sixteen different sensitivity tests applied to the Cape Town atmospheric Bayesian inversion analysis from March 2012 until June 2013. The reference inversion made use of a fossil fuel inventory analysis and estimates of biogenic fluxes from CABLE (Community Atmosphere Biosphere Land Exchange model). Changing the prior information product and the assumptions behind the uncertainties in the biogenic fluxes had the largest impact on the inversion results in terms of the spatial distribution of the fluxes, the size of the aggregated fluxes, and the uncertainty reduction achieved. A carbon assessment product of natural carbon fluxes, used in place of CABLE, and the Open-source Data Inventory for Anthropogenic $CO_2$ product, in place of the fossil fuel inventory, resulted in prior estimates that were more positive on average than the reference configuration. The use of different prior flux products to inform separate inversions provided better constraint on the posterior fluxes compared with a single inversion. For the Cape Town inversion we showed that, where our reference inversion had aggregated prior flux estimates that were made more positive by the inversion, suggesting that the CABLE was overestimating the amount of $CO_2$ uptake by the biota, when the alternative prior information was used, fluxes were made more negative by the inversion. As the posterior estimates were tending towards the same point, we could deduce that the best estimate was located somewhere between these two posterior fluxes. We could therefore restrict the best posterior flux estimate to be bounded between the solutions of these separate inversions.

The assumed error correlation length for NEE fluxes played a major role in the spatial distribution of the posterior fluxes and in the size of the aggregated flux estimates, where ignoring these correlations led to posterior estimates more similar to the priors compared with the reference inversion. Apart from changing the prior flux products, making changes to the error correlation length in the NEE fluxes resulted in the greatest contribution to variability in the aggregated flux estimates between different inversions. Those cases where the prior information or NEE error correlations were altered resulted in greater variability between the aggregated fluxes of different inversions compared with the uncertainty around the posterior fluxes of the reference inversion.

# Chapter 6

# An atmospheric inversion over the City of Cape Town: Sensitivity analyses

# Abstract

We present sixteen different sensitivity tests applied to the Cape Town atmospheric Bayesian inversion analysis from March 2012 until June 2013. The reference inversion made use of a fossil fuel inventory analysis and estimates of biogenic fluxes from CABLE (Community Atmosphere Biosphere Land Exchange model). Changing the prior information product and the assumptions behind the uncertainties in the biogenic fluxes had the largest impact on the inversion results in terms of the spatial distribution of the fluxes, the size of the aggregated fluxes, and the uncertainty reduction achieved. A carbon assessment product of natural carbon fluxes, used in place of CABLE, and the Open-source Data Inventory for Anthropogenic $CO_2$ product, in place of the fossil fuel inventory, resulted in prior estimates that were more positive on average than the reference configuration. The use of different prior flux products to inform separate inversions provided better constraint on the posterior fluxes compared with a single inversion. For the Cape Town inversion we showed that, where our reference inversion had aggregated prior flux estimates that were made more positive by the inversion, suggesting that the CABLE was overestimating the amount of $CO_2$ uptake by the biota, when the alternative prior information was used, fluxes were made more negative by the inversion. As the posterior estimates were tending towards the same point, we could deduce that the best estimate was located somewhere between these two posterior fluxes. We could therefore restrict the best posterior flux estimate to be bounded between the solutions of these separate inversions.

The assumed error correlation length for NEE fluxes played a major role in the spatial distribution of the posterior fluxes and in the size of the aggregated flux estimates, where ignoring these correlations led to posterior estimates more similar to the priors compared with the reference inversion. Apart from changing the prior flux products, making changes to the error correlation length in the NEE fluxes resulted in the greatest

contribution to variability in the aggregated flux estimates between different inversions. Those cases where the prior information or NEE error correlations were altered resulted in greater variability between the aggregated fluxes of different inversions compared with the uncertainty around the posterior fluxes of the reference inversion.

Solving for four separate weekly inversions resulted in similar estimates for the weekly fluxes compared with the single monthly inversion, while reducing computation time by up to 75 %. Solving for a mean weekly flux within a monthly inversion did result in differences in the aggregated fluxes compared with the reference inversion, but these differences were mainly during periods with data gaps. The uncertainty reduction from this inversion was almost double that of the reference inversion (47.2% versus 25.6%). Taking advantage of more observations to solve for one flux, such as allowing the inversion to solve for separate slow and fast components of the fossil fuel and NEE fluxes, as well as taking advantage of expected error correlation between fluxes of homogeneous biota, would reduce the uncertainty around the posterior fluxes. The sensitivity tests demonstrate that going one step further and assigning a probability distribution to these parameters, for example in a hierarchical Bayes approach, would lead to more useful estimates of the posterior fluxes and their uncertainties.

## 6.1 Introduction

Atmospheric inversion, where estimates of $CO_2$ fluxes can be derived from measurements of $CO_2$ concentrations at a point location, is a useful tool for monitoring, reporting and verification (MRV) of $CO_2$ emissions from cities (Bellassen and Stephan, 2015; Wu et al., 2016; Lauvaux et al., 2016; Oda et al. , 2017a). Estimates of city-level $CO_2$ emissions are usually obtained using bottom-up techniques, which require some knowledge of what activities produce $CO_2$ emissions and the fuel usage of these activities. Ascertaining the uncertainty in these inventory-based estimates is not trivial, and these uncertainties increase as the spatio-temporal resolution of these estimates is increased (Turnbull et al., 2011). The inversion solves for both the anthropogenic and biogenic contributions, usually expressed as fluxes of $CO_2$. This approach attempts to correct prior estimates of these fluxes such that the misfit between the observed and modelled concentrations at the measurement sites is minimised. Therefore, if an inventory analysis of fossil fuel emissions from the city is used as the prior information, the inversion will provide corrections to these emissions.

Inversions used for investigating city-level emissions are carried out at kilometric resolutions (Bréon et al., 2015; Lauvaux et al., 2016). Such an inversion was carried out for the city of Cape Town, South Africa (Nickless et al., 2018). As is required for all atmospheric inversions, decisions need to be made regarding what prior information should be used; for which unknown $CO_2$ fluxes will the inversion solve; and what the structure of the covariance matrices will be (Bréon et al., 2015; Lauvaux et al., 2016; Staufer et al., 2016; Oda et al. , 2017a). Sensitivity tests on the impact of these decisions are necessary, and provide information on the robustness of the inversion results. This paper presents the results of sensitivity tests applied to these decisions for the Cape Town inversion.

The prior information required for an atmospheric inversion are the initial estimates of the unknown fluxes. For a city-level inversion, this means initial estimates of the gridded fossil fuel emissions, at the spatio-temporal scale at which the inversion is to be performed. The inversion described in Nickless et al. (2018) made use of a bespoke inventory analysis carried out for the purpose of the inversion (Nickless et al., 2015a). Information on the uncertainty in these prior fluxes is also required. The uncertainties applied to the estimates of the fossil fuel fluxes for Cape Town were based on error propagation techniques. The uncertainties in the emission factors and activity data were combined to obtain an overall uncertainty in the flux estimate (Nickless et al., 2015a).

The observed concentration data, as measured at atmospheric monitoring sites and which are the data used by an atmospheric inversion, are as a result of aggregated fluxes from all sources of $CO_2$ along the path of the air flow. Sources refer to anything which may have a positive (i.e. emit) or negative (i.e. uptake) contribution to the overall $CO_2$ concentration. Even if biogenic fluxes are not necessarily of interest in the city-level inversion, they need to be accounted for in the model as these fluxes will be inducing changes to the observed $CO_2$ concentration. For the Cape Town inversion, net ecosystem exchange (NEE) fluxes were obtained from the land atmosphere exchange model CABLE (Community Atmosphere Biosphere Land Exchange) (Nickless et al., 2018). This model was dynamically coupled to the regional climate model, CCAM (Conformal Cubic Atmospheric Model), from which climatic variables, required for the atmospheric transport model, were obtained. Uncertainties in the prior fluxes were specified to be large due to the large amount of variation in modelling ecosystem productivity and respiration from the fynbos biome by dynamic vegetation models (Moncrieff et al., 2015). Fynbos is the dominant naturally occurring vegetation type in the area. Cape Town city is also surrounded by large agricultural areas, particularly vineyards. The uncertainties in the prior NEE fluxes were set at the estimate of net primary productivity (NPP). NEE = NPP + Rh, where Rh is the heterotrophic respiration. Therefore NEE is a balance of two large fluxes, which are both non-trivial to model (Archibald et al., 2009). The uncertainty in set as the productivity component of the NEE flux as the error in the estimate of NEE can be as large as either the productivity or respiration component. Therefore, for the Cape Town inversion, the uncertainty was much larger than the accompanying NEE estimate. We emphasize these details, as the sensitivty analyses will demonstrate the importance of the approach adopted for assigning uncertainties and error correlations to these natural fluxes.

Using the inversion described in Nickless et al. (2018) as the reference inversion, we carried out sensitivity analyses which considered alternative products for the prior information. For the prior fossil fuel fluxes, we substituted the estimates from the bespoke inventory analysis with those from the ODIAC (Open-source Data Inventory for Anthropogenic $CO_2$) product (Oda and Maksyutov, 2011; Lauvaux et al., 2016; Oda et al. , 2017a,b). For the biogenic fluxes, we performed a test where the CABLE estimates were replaced with those from a carbon assessment study (Scholes et al., 2013). The carbon assessment study aimed to map terrestrial carbon stocks for South Africa and provided estimates of NPP and NEE at a spatial resolution of 1 km $\times$ 1 km, and was used for a previous optimal measurement network design study for South

Africa (Nickless et al., 2015b). Sensitivity tests were performed where the original products were used for the prior fossil fuel and NEE fluxes, but the uncertainties prescribed to these fluxes were either individually doubled or halved, which therefore changed the relative contribution of each flux to the uncertainty in the total prior flux.

The structure of the uncertainty covariance matrices for the observations and for the prior fluxes can have a significant effect on the resulting flux estimates from the inversion, as well as on the spatial distribution of these fluxes (Lauvaux et al., 2016). We investigated the impact of the prescribed off-diagonal covariances in these prior covariance matrices. In the reference inversion we allowed a small correlation length of one hour between observation errors. For the prior NEE uncertainty estimates, a correlation length of one kilometre was specified for NEE fluxes from the same week. No spatial correlation was specified between fossil fuel flux uncertainties as many of the larger sources from the inventory analysis were point sources. As we did not solve for fossil fuel fluxes from different sectors separately, we decided it would be better to keep fossil fuel flux uncertainties uncorrelated. This would avoid implausible correlations between uncertainties; for example, between a large industrial source and a residential source. As sensitivity tests, we removed each of these correlations from the prescribed uncertainty covariance matrices; individually as well as the case where the uncertainty covariance matrices for both the observations and for the prior fluxes were specified as diagonal matrices.

We were interested in the composition of the control vector, which contains the unknown surface fluxes and domain boundary concentrations. For the reference inversion we carried out thirteen monthly inversions which solved for weekly fluxes from each of the 101 $\times$ 101 surface pixels. The weekly fluxes consisted of working week and weekend fossil fuel fluxes, and NEE fluxes for the full week; each separated into day and night fluxes. Each monthly inversion solved for four sets (i.e. a period of four weeks) of these six distinct weekly fluxes from each pixel. We tested whether solving for an average of each of these weekly fluxes over the course of the month would achieve similar results compared with the reference inversion. We also compared the reference inversion with the approach of carrying out separate inversions for each week. Therefore instead of performing 13 monthly inversions, we performed 13 $\times$ 4 weekly inversions; four inversions per month. Each of these cases requires considerably less computational resources to perform an individual inversion. If either of these alternative control vectors provides sufficiently similar results to the reference case, this would provide a more efficient means of conducting the inversion.

This would allow more alternative configurations of other components of the inversion framework to be tested in the same period of time.

The Cape Town inversion differs from recent city-scale inversions carried out over mega cities (Bréon et al., 2015; Staufer et al., 2016) due to the high integration of natural areas in the city borders of Cape Town. Natural fluxes are an important contributor to the $CO_2$ budget of the region. For example, Table Mountain National Park is located directly adjacent to the city bowl. In fact the city wraps around the base of the mountain. This national park covers an area of 221 $km^2$. For this reason, the gradient method, which relies on the difference between pairs of measurement sites when the wind is blowing from one site, over the target region, to the second site, would not be appropriate given locations of our two measurement sites. In our case, if the air travelled between the two sites, it would pass directly over Table Mountain National Park, and therefore the gradient method would not have the desired effect of diminishing the impact of biogenic fluxes along the transect between the two sites. In addition, the wind fields showed that air did not travel in a straight path between our two sites (Nickless et al., 2018).

We adopted the approach usually used from regional inversions, where the inversion modelled the concentrations at the measurement sites (Lauvaux et al., 2012). Instead of subtracting the background $CO_2$ concentration from the measurements, which would have arrived from one of the domain boundaries, we solved for the concentrations at the boundary and therefore included these in the control vector, similar to the approach of Lauvaux et al. (2016). We kept tight constraints on what these concentrations could be, and used the background measurements obtained from Cape Point as prior estimates of these concentrations. We were able to do this as there are no large anthropogenic sources near the boundary of the domain. We showed in the reference inversion that the variation in the total $CO_2$ was largely driven by the variation in the NEE flux. In these sensitivity analyses we investigate the impact of reduced uncertainty assigned to the prior NEE estimates.

The purpose of this paper is to present the results of these sensitivity tests in comparison with the Cape Town reference inversion. Based on these tests, conclusions can be drawn on how well the reference inversion was specified, and which components could be improved with highest priority to give the greatest improvement in the estimation of the posterior fluxes. Section 6.2 briefly introduces the Bayesian inversion framework. Details of the reference inversion can be found in Nickless et al. (2018). This is followed by a description of the alternative prior information products. The details of the sensitivity analysis are provided. The results of the sensitivity analyses

are provided in section 6.3, followed by discussion of these results in section 6.4, and conclusions in section 5.

## 6.2 Methods

Characterisations of the two observational sites installed at Robben Island and Hangklip lighthouses, and the background monitoring site at Cape Point, are provided in (Nickless et al., 2018). Measurements of $CO_2$ concentrations were obtained between March 2012 and June 2013 by means of a Picarro Cavity Ring-down Spectroscopy (CRDS) (Picarro G2301) instrument. Sufficient data for 13 of the 16 months were available to perform monthly inversions. Robben Island site viewed predominantly air influenced by the Cape Town city bowl whereas Hangklip viewed air influenced by biogenic fluxes from nearby fynbos vegetation and agricultural areas.

In the next section we describe the Bayesian inverse modelling framework and the details of the reference Cape Town inversion (referred to in short-hand as inversion **Ref**). In sections 6.2.3 to 6.2.6 we describe the alterations we considered to the reference inversion, and how we compared the results between different inversions.

### 6.2.1 Bayesian inverse modelling framework and the reference inversion

Nickless et al. (2018) used the Bayesian inverse modelling framework to model $CO_2$ hourly concentrations at Robben Island and Hangklip measurement sites. This approach solves for the unknown sources, as defined in the control vector, $\boldsymbol{s}$, using the Bayesian least squares solution as described in Tarantola (2005),

$$\boldsymbol{s} = \boldsymbol{s}_0 + \mathbf{C}_{\boldsymbol{s}_0}\mathbf{H}^T\left(\mathbf{H}\mathbf{C}_{\boldsymbol{s}_0}\mathbf{H}^T + \mathbf{C}_{\boldsymbol{c}}\right)^{-1}\left(\boldsymbol{c} - \mathbf{H}\boldsymbol{s}_0\right) \tag{6.1}$$

and the solution for the posterior error covariance matrix for the sources, $\mathbf{C}_{\boldsymbol{s}}$,

$$\begin{aligned} \mathbf{C}_{\boldsymbol{s}} &= \left(\mathbf{H}^T\mathbf{C}_{\boldsymbol{c}}^{-1}\mathbf{H} + \mathbf{C}_{\boldsymbol{s}_0}^{-1}\right)^{-1} && (6.2)\\ &= \mathbf{C}_{\boldsymbol{s}_0} - \mathbf{C}_{\boldsymbol{s}_0}\mathbf{H}^T\left(\mathbf{H}\mathbf{C}_{\boldsymbol{s}_0}\mathbf{H}^T + \mathbf{C}_{\boldsymbol{c}}\right)^{-1}\mathbf{H}\mathbf{C}_{\boldsymbol{s}_0} && (6.3)\end{aligned}$$

where $\boldsymbol{c}$ is the vector of $CO_2$ concentration measurements from Robben Island and

Hangklip measurement sites, $\boldsymbol{s}_0$ is the vector of prior estimates of these sources, $\mathbf{C}_{\boldsymbol{c}}$ the error covariance matrix of $\boldsymbol{c}$, and $\mathbf{C}_{\boldsymbol{s}_0}$ the prior uncertainty covariance matrix of $\boldsymbol{s}_0$. $\mathbf{H}$ is the Jacobian matrix representing the first derivative of the modelled concentration, $\boldsymbol{c}_{mod}$, at the observational site and dated with respect to the elements of $\boldsymbol{s}$. $\mathbf{H}$ projects the elements of $\boldsymbol{s}$ into the observation space of $\boldsymbol{c}$:

$$\boldsymbol{c}_{mod} = \mathbf{H}\boldsymbol{s}. \tag{6.4}$$

The sources, $\boldsymbol{s}$, consisted of gridded surface fluxes contained within the domain and concentrations of $CO_2$ at the boundary. The spatial resolution of inversion was set at 1 km by 1 km and the extent of the domain was between 34.5° and 33.5° south and between 18.2° and 19.2° east.

Separate monthly inversions were performed. $\boldsymbol{s}$ contained six surface fluxes from each of the 101×101 surface pixels for each of the four weeks. The surface fluxes included working week and weekend fossil fuel fluxes and weekly NEE fluxes, each separated into day and night fluxes. Therefore a monthly inversion solves for 10,201×6×4 = 244,824 surface fluxes. The boundaries were considered as the edge of the domain at each cardinal direction (north, east, south, and west). The boundary concentrations in $\boldsymbol{s}$ consisted of four average weekly concentrations at the four boundaries, separated into day and night averages, therefore 32 boundary concentrations.

The observed $CO_2$ concentrations, $\boldsymbol{c}$, consisted of hourly averaged concentrations derived from the instantaneous measurements obtained at Robben Island and Hangklip. As the parameters of the atmospheric transport model are not constrained by the inversion, the resulting errors in the modelled concentrations can be added to the measurement errors contained in $\mathbf{C}_{\boldsymbol{c}}$ (Tarantola, 2005). The diagonal elements of the observation error covariance matrix, $\mathbf{C}_{\boldsymbol{c}}$, consisted of daytime error variances of 4 $\text{ppm}^2$ and night-time errors of 16 $\text{ppm}^2$. Night-time errors in modelled concentrations are set higher at night than during the day as the planetary boundary layer (PBL) is lower at night (Feng et al., 2016; Lauvaux et al., 2016). The PBL is characterised by continuous turbulence, whereas turbulence is lacking above this layer, and its height changes in response to thermal stratification. It has significant impact on weather, climate, and the hydrologic cycle (Zhang et al., 2014). These error variances accounted for measurement errors, atmospheric transport modelling errors, representation errors and aggregation errors. As described in Nickless et al. (2018), to account for meteorological conditions, these error variances were inflated by up

to 1 ppm$^2$ during day and 4 ppm$^2$ at night depending on the wind speed, with still conditions leading to the maximum error inflation. An additional inflation factor was added equal to the observed variance of the instantaneous $CO_2$ concentration measurements made within the hour. These additional inflations represented periods when the atmospheric transport model would have been most likely to misrepresent the atmospheric transport.

The off-diagonal elements of $\mathbf{C_c}$ were calculated, based on the Balgovind correlation model as used in Wu et al. (2013), as:

$$C_c(c_i, c_j) = \sqrt{C_c(c_i)}\sqrt{C_c(c_j)}(1 + \frac{h}{L})exp(-\frac{h}{L}) \tag{6.5}$$

where $c_i$ and $c_j$ are the average concentrations during hours $i$ and $j$, $C_c(c_i)$ and $C_c(c_j)$ the corresponding error variances for the concentrations in hours $i$ and $j$, the characteristic correlation length $L$ was assumed to be 1 hour, and $h$ is the length in time between observations $i$ and $j$. The impact of this, albeit short, correlation length was assessed in a sensitivity test where no correlation between the observation errors was assumed. No consensus has yet been reached on how these correlations between model errors in the concentrations should be treated (Lauvaux et al., 2016).

We used the regional climate model CCAM, run in variable-resolution mode with Cape Town at its centre and driven by NCEP (National Centres for Environmental Prediction) reanalysis data, to produce three-dimensional fields of mean winds ($u$, $v$, $w$), potential temperature and turbulent kinetic energy (TKE) (McGregor and Dix, 2001; Roux, 2009; Engelbrecht et al., 2013). The model produced hourly estimates on a 1 km × 1 km spatial grid, which extended from between 34.5° and 33.5° south and between 18.2° and 19.2° east. These variables were used to drive a Lagrangian particle dispersion model (LPDM) (Uliasz, 1994). LPDM simulates atmospheric transport by releasing particles from the observational sites and tracking these particles backward in time. These particle counts can be used to derive the elements of the Jacobian matrix $\mathbf{H}$ as originally described by Seibert and Frank (2004) and subsequently used in several inversion studies (Lauvaux et al., 2012; Wu et al., 2013; Ziehn et al., 2014; Nickless et al., 2015b; Lauvaux et al., 2016; Nickless et al., 2018; Oda et al. , 2017a). The details of this as pertaining to the Cape Town reference inversion are described in Nickless et al. (2018). The number of rows in $\mathbf{H}$ are equal to the number of hourly concentrations assimilated into the inversion and the number of columns is equal to the number of sources solved for in the control vector, $\boldsymbol{s}$.

The prior fossil fuel fluxes were estimated from a bespoke inventory analysis carried out for Cape Town. Details are provided in Nickless et al. (2015a) and Nickless et al. (2018). The inventory analysis includes fossil fuel emissions from industrial point sources, road vehicle transport emissions, airport and harbour emissions, and residential emissions. Residential emissions were based on the assumed use of raw fossil fuels for heating, lighting and cooking. The largest point source was a crude oil refinery located north east of the central business district (CBD).

Uncertainties in these fossil fuel estimates were derived based on error propagation techniques (Nickless et al., 2015a). In the next section we present a comparison between the uncertainties assigned in the reference inversion with those assigned to the inversion using the ODIAC fossil fuel fluxes (see Figure 6.2). The largest uncertainties, as a percentage of the fossil fuel flux estimate, were for those associated with residential emissions, which were spatially distributed according to the 2011 population census. These uncertainties were set at 60% of the domestic emissions estimate. Point sources had relatively smaller uncertainties, as these estimates were based on reported fuel usage data, which was assumed to be accurate, but in absolute terms these uncertainties were large contributors to the total fossil fuel flux uncertainty. Fossil fuel emissions from all sources were summed to provide a total fossil fuel flux for the working week and weekend, separately for day and night. No correlation was assumed between uncertainties in the fossil fuel sources. This was to avoid creating unlikely correlations between fluxes from different sources. We assumed no correlation in time between fossil fuel fluxes as we were already solving for weekly averaged fluxes, which effectively assumes 100% correlation between fluxes in the same week.

Prior estimates of the NEE fluxes were obtained from the land atmosphere exchange model CABLE (Kowalczyk et al., 2006). The model produced hourly estimates of NEE, which were aggregated into weekly (day and night) flux estimates in units of kg $CO_2$ $m^{-2}$ $week^{-1}$, and used as the prior estimates of terrestrial biogenic fluxes. The spatial resolution of these prior NEE fluxes were kept at a 1 km $\times$ 1 km resolution. We selected CABLE to produce our NEE estimates as CCAM had been dynamically coupled to this land surface model, which allowed for feedbacks between land surface and climate processes, such as leaf area feedback on maximal canopy conductance and latent heat fluxes (Zhang et al., 2013).

The $CO_2$ fluxes over the ocean were obtained from a study that characterised the seasonal cycle of air-sea fluxes of $CO_2$ in the southern Benguela upwelling system off the South African west coast (Gregor and Monteiro, 2013). Daily $CO_2$ fluxes were derived from measurements of $pCO_2$. These daily fluxes were used to derive

weekly flux estimates, which were averaged over a monthly period, and applied as prior estimates to the ocean surface grids within the domain.

As the fynbos biome, which covers a large proportion of the terrestrial surface in our domain, is poorly represented by dynamic vegetation models (Moncrieff et al., 2015), the uncertainties assigned to the NEE estimates were large. Previous studies, for example, have shown that the model forms used for the soil temperature-respiration function and the soil moisture-respiration function have large impacts on the NEE estimates, with resulting NEE estimates differing by over 100% compared with eddy-covariance measurements (Exbrayat et al., 2013). We assigned the value of the NPP associated with the terrestrial NEE estimate as the uncertainty value. For the ocean fluxes, the standard deviations in the daily $CO_2$ fluxes from Gregor and Monteiro (2013) were assigned as the uncertainties. As the uncertainties in NEE estimates were likely to be related, spatial error correlations between NEE fluxes were incorporated in the off-diagonal elements of $\mathbf{C}_{\boldsymbol{s}_0}$. The off-diagonal elements were calculated in an analogous manner to those for $\mathbf{C}_{\boldsymbol{c}}$, where $C_{s_{0;NEE}}(s_{NEE;i})$ and $C_{s_{0;NEE}}(s_{NEE;j})$ were the corresponding variances in the NEE flux uncertainty matrix for pixels $i$ and $j$, the characteristic correlation length $L$ was assumed to be 1 km, and $h$ was the spatial distance between pixels $i$ and $j$. Non-zero error covariances were allowed between NEE estimates from the same week. We assumed no error correlation between fossil fuel and NEE fluxes.

Sections 6.2.2 to 6.2.5 describe alterations made to the reference inversion for the purpose of sensitivity analyses.

### 6.2.2 Alternative biogenic flux product

As part of a project which aimed to assess the carbon sinks of South Africa (DEA, 2015), a report together with monthly 1 km × 1 km estimates of terrestrial carbon stocks and fluxes were produced (Scholes et al., 2013). To estimate these fluxes, a distinction was made between carbon stocks in natural to semi-natural areas and those on transformed land, such as annually-cropped cultivated land, plantation forests, and urban areas (which was based on the IPCC 2006 value for closed urban forests). We used these estimates of NEE and NPP in place of those from CABLE (inversion **Carbon Assess**).

To estimate gross primary productivity (GPP), ten years (2001 to 2010) of monthly climatologies (temperature, rainfall, relative humidity) and satellite products for photosynthetically active radiation (PAR) and fraction of absorbed photosynthetically

active radiation (FAPAR) were assimilated. Autotrophic respiration (Ra) was calculated based on the inputs for temperature, above-ground biomass, below-ground biomass and FAPAR. NPP could then be calculated as NPP = GPP - Ra. The hetrotrophic component (Rh) of Ecosystem respiration (Re) was based on estimates of soil organic carbon stocks and above-ground litter. The basic calculation to obtain NEE was NEE = GPP - Re, and additional losses of $CO_2$ through biomass burning, and export and import fluxes from harvest and trade-related activities were accounted for.

To disaggregate the monthly products into day and night fluxes, it was assumed that all GPP took place during the day, and that half of Re occurred during the day and half at night. Therefore the weekly NEE and NPP estimates used for the prior information in the inversion were based on the GPP and respiration products from the assessment. The GPP flux for the year in the fynbos biome was estimated to be 521 g $CO_2$ $m^{-1}year^{-1}$ with a standard deviation of 492 g $CO_2$ $m^{-1}year^{-1}$. Therefore, as for the CABLE estimates used in the reference inversion, we assign uncertainties to the prior NEE estimates equal to the NPP estimate. A map of the prior daytime NEE fluxes in May 2012 from the CABLE and carbon assessment products is provided in Figure 6.1.

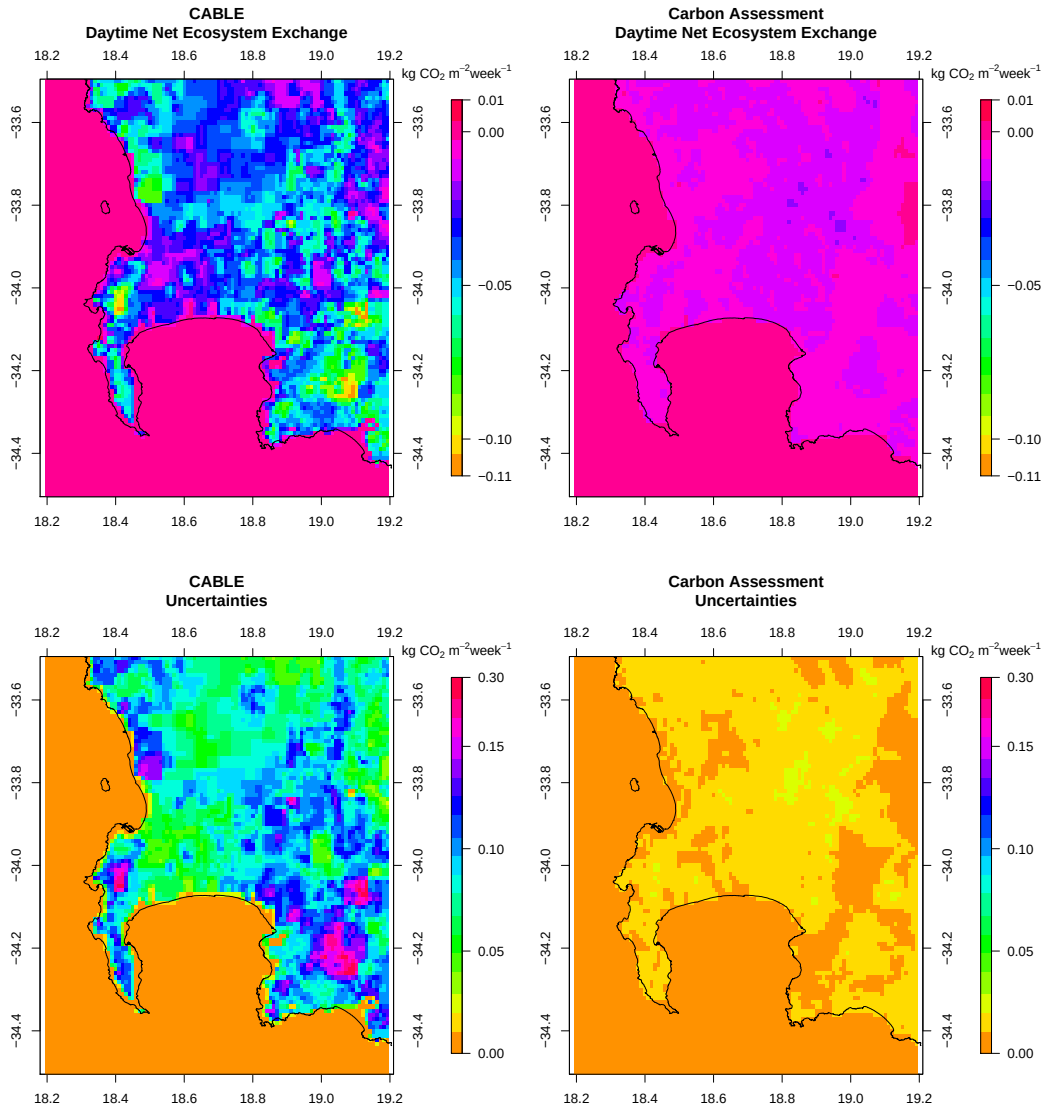


Figure 6.1: Spatial distribution of the prior daytime NEE fluxes produced by CABLE (top left) and the carbon assessment product (top right) in May 2012, as well as the uncertainty estimates assigned to these fluxes (bottom row).

### 6.2.3 Alternative fossil fuel emissions product

As an alternative to the inventory analysis of the fossil fuel fluxes, we used current estimates of anthropogenic fossil fuel emissions from the 1 km × 1 km ODIAC product for the years 2012 and 2013 (ODIAC2017) (Oda and Maksyutov, 2011; Lauvaux et al., 2016; Oda et al. , 2017a,b) (inversion **ODIAC**). The product provides monthly emissions of $CO_2$ in kt of carbon. The original ODIAC product (Oda and Maksyutov, 2011) made use of global energy consumption statistics and distributed the emissions from these activities based on known point source emitters, such as power plants, and on a global nightlight distribution satellite product. Emissions from point sources, such as those from power plants, were estimated separately from the diffuse emissions, for example those due to transport. These emissions were disaggregated onto to a 1 km × 1 km grid. The updated product has further disaggregated the diffuse emissions to a 30 m × 30 m grid by making use of global road network data, a satellite product on surface imperviousness, and population census data (Oda et al. , 2017a,b). This 30 m × 30 m diffuse emission product together with the point source emission product were aggregated back up to the 1 km × 1 km grid. An inversion carried out for Indianapolis, IN, making use of the updated ODIAC product has shown it to produce similar corrections to the fluxes as those from the inversion making use of the Hestia inventory product (Oda et al. , 2017a). The Hestia product is a fine-grained - down to the street/building level - bottom-up $CO_2$ emission product which makes use of information from building energy simulation models, traffic data, power production reporting, and pollution reporting (Gurney et al., 2012). This product is available for a few cities in the United States, including Indianapolis.

The monthly estimates were re-scaled according to the day of the week and to the hour of day using scaling factors for South Africa as estimated by Nassar et al. (2013). These estimates were re-aggregated into day and night working week and weekend fossil fuel fluxes in units of kg $CO_2 m^{-2}\,week^{-1}$. These estimates for the fossil fuel fluxes were used as prior estimates for the inversion in place of the inventory-based estimates used for the reference inversion. The daytime fossil fuel fluxes produced by the inventory analysis and the ODIAC product are provided in Figure 6.2.

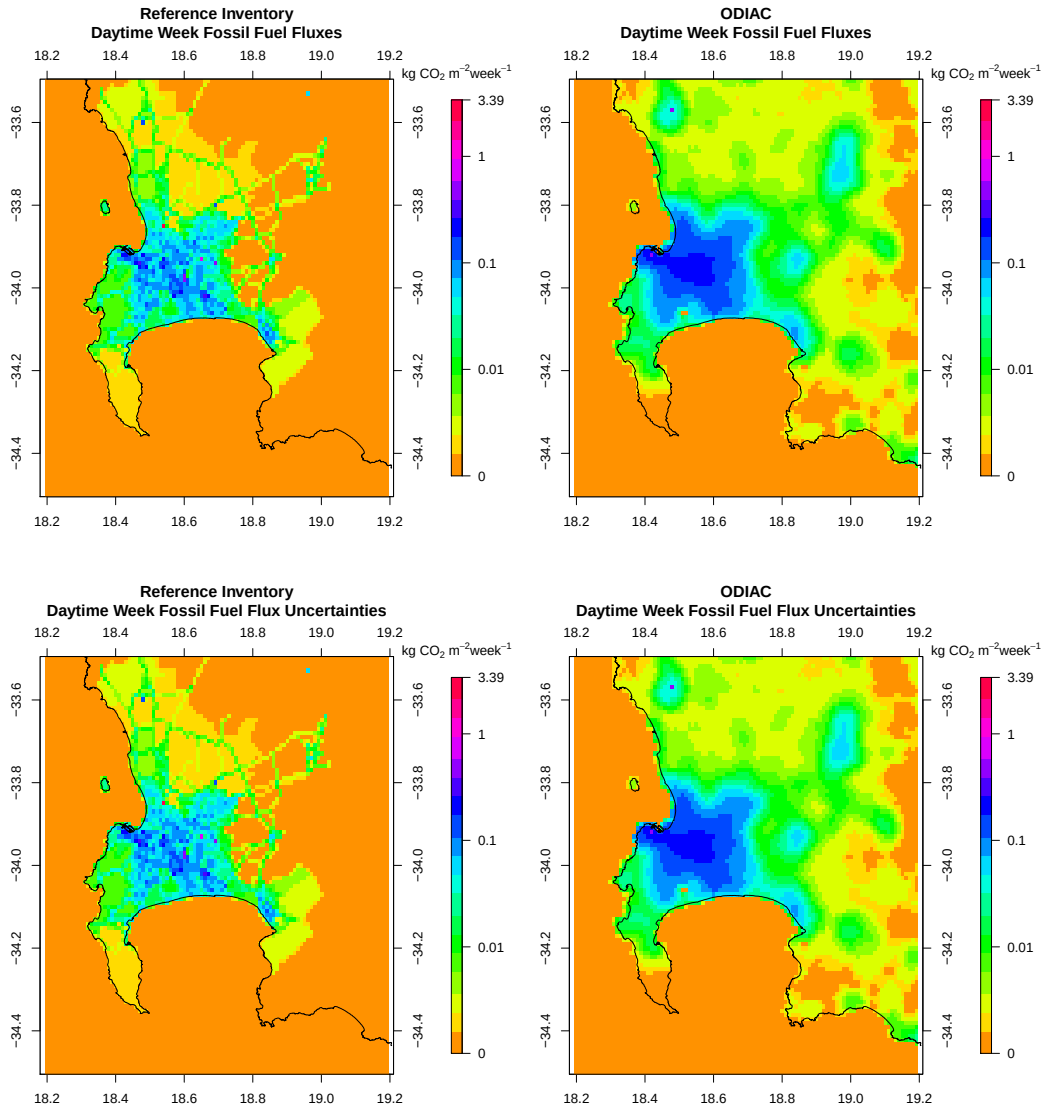


Figure 6.2: Spatial distribution of the prior fossil fuel fluxes produced from the Cape Town inventory analysis (top left) and the ODIAC fossil fuel product (top right) in May 2012, as well as the uncertainty estimates assigned to these fluxes (bottom row).

### 6.2.4 Alternative covariance structures

The specification of the prior uncertainty covariance structures have been shown to have a significant impact on the pixel-level flux estimates, the total flux estimate for the domain, and on the spatial distribution of the fluxes (Wu et al., 2013; Lauvaux et al., 2016). For example, in the Indianapolis inversion, assuming correlation lengths of 4 or 12 km in the prior uncertainty covariance matrix of the fluxes resulted in total flux estimates for the city that were 17 and 25% larger than the total flux estimate assuming no correlation (Lauvaux et al., 2016). The effect of changing the correlation length had a larger impact on the total flux estimate than changing the prior emission product from Hestia to ODIAC.

To assess the sensitivity of the posterior flux estimates, their uncertainties, and their distribution in space to the specification of the covariance matrix, we considered inversions where the non-zero off-diagonal elements of $\mathbf{C}_{\boldsymbol{s}_0}$ and $\mathbf{C}_{\boldsymbol{c}}$ were set to zero. We considered an inversion which assumed no temporal error correlation in the specification of $\mathbf{C}_{\boldsymbol{c}}$ (inversion **NEE Corr**), an inversion where no spatial error correlation was assumed for $\mathbf{C}_{\boldsymbol{s}_0}$ (inversion **Obs Corr**), and an inversion which assumed no error correlations in the specification of $\mathbf{C}_{\boldsymbol{s}_0}$ and $\mathbf{C}_{\boldsymbol{c}}$ (inversion **No Corr**).

We also considered inversions where the prior fossil fuel flux uncertainty was doubled (inversion **Double FF**) and where it was halved (inversion **Half FF**), and similarly for the NEE flux uncertainties (inversions **Double NEE** and **Half NEE**). By doubling or halving the uncertainty of the fossil fuel or NEE component of the total flux, we changed the relative uncertainty contribution of each of these had to the total uncertainty when compared with the reference inversion.

Due to the large impact that the estimation of the domestic fossil fuel emissions had on the temporal profile of the total fossil fuel fluxes, we considered a modification of the estimated domestic emissions in the inventory product. In the reference inversion 75% of the domestic emissions from heating were assumed to take place during the six winter months. We tested the impact of this assumption by altering the domestic emissions so that they were distributed uniformly through time, but still spatially distributed according to the population size. This changes the prior estimates of the fossil fuel fluxes and their distribution through time, as well as their uncertainties, which were set at 60% of the domestic emission estimate (inversion **Domestic Homogenised**).

Due to the large uncertainty in the modelling of NEE (Zhang et al., 2013; Moncrieff et al., 2015), particularly over the fynbos biome, we considered that perhaps the average of the NEE estimates from CABLE over the domain may be a more reliable

representation of the true flux compared with the pixel-level estimates. Therefore we averaged the NEE and NPP estimates from CABLE over the inversion domain and assigned this average NEE, and NPP for its uncertainty, as the prior biogenic flux estimates (inversion **NEE Homogenised**).

We considered an inversion where the uncertainties in $\mathbf{C_c}$ were set at 2 ppm for the day and 4 ppm at night (inversion **Simp Obs Error**). In this case all the errors in the modelled concentrations are contained within these values, and we disregard the climatic conditions under which the measurements were taken. We tested the impact of increasing the night-time uncertainty in the observation errors to 10 ppm (inversion **Simp Obs with Large Night**). We further simplified $\mathbf{C_c}$ by performing an inversion which disregarded the temporal correlation which was assumed for the reference inversion (inversion **Simp Obs No Corr**).

### 6.2.5 Alternative control vectors

In the reference inversion the total $CO_2$ flux from a single surface pixel for given week was made up of the following individual fluxes:

$$\boldsymbol{s}_{sf;\,i} = \boldsymbol{s}_{ff\ week\ day;\,i} + \boldsymbol{s}_{ff\ week\ night;\,i} + \boldsymbol{s}_{ff\ weekend\ day;\,i} + \boldsymbol{s}_{ff\ weekend\ night;\,i} \tag{6.6}$$

$$+\boldsymbol{s}_{NEE\ day;\,i} + \boldsymbol{s}_{NEE\ night;\,i} \tag{6.7}$$

where $\boldsymbol{s}_{sf;\,i}$ is the total weekly surface flux from the $i^{th}$ pixel, $\boldsymbol{s}_{ff\ week\ day;\,i}$ is the fossil fuel flux during the day during the working week, $\boldsymbol{s}_{ff\ week\ night;\,i}$ is the night-time fossil fuel flux during the working week, $\boldsymbol{s}_{ff\ weekend\ day;\,i}$ is the weekend daytime fossil fuel flux, $\boldsymbol{s}_{ff\ weekend\ night;\,i}$ is the weekend night-time fossil fuel flux, and $\boldsymbol{s}_{NEE\ day;\,i}$ and $\boldsymbol{s}_{NEE\ night;\,i}$ are the day and night-time NEE fluxes for the full week from the $i^{th}$ pixel. The inversion solved for each of these fluxes separately and for each of the four weeks in the monthly inversion. Therefore a monthly inversion solved for $10{,}201 \times 6 \times 4 = 244{,}824$ surface fluxes. The mean day and night-time concentrations at each of the four domain boundaries for each week were the final components of the control vector. The inversion solved for $4 \times 2 \times 4 = 32$ boundary concentrations.

As a sensitivity analysis we examined two alternative approaches to the control vector. If we assumed that neither the NEE nor fossil fuel flux would change very much from week to week, an option would be to solve for the mean of the six individual fluxes over the four weeks in a given month. We therefore considered a sensitivity test where the inversion solved for one average day and one average night NEE flux

within each pixel, and four fossil fuel mean weekly fluxes (day and night working week, day and night weekend) (inversion **Mean Month**). We also considered performing a separate inversion for each week; i.e. four separate weekly inversions in place of each of the monthly inversions (inversion **Week**). In this case only the concentration measurements for one week were used and the individual weekly fluxes (two NEE and four fossil fuel) were solved for, and this was repeated for each of the four weeks in the month. The benefit of these two alternative control vectors is that for each individual inversion the resulting $\mathbf{C}_{\boldsymbol{s}_0}$ matrix is much smaller compared with the reference case.

When solving for only one week, or a mean weekly flux for a particular month, the number of surface sources reduced to 10,201×6 = 61,206. Solving for individual weeks required 4×2 additional boundary concentrations to be added to the control vector, and when solving for the mean weekly flux for the month, we allowed the boundary concentrations to differ for each week, and therefore we still solved for the 32 boundary concentrations as in the reference case. Therefore the $\mathbf{C}_{\boldsymbol{s}_0}$ for these two alternative control vectors is 16 times smaller than that of the reference inversion.

The benefit of these two alternative approaches is a substantial reduction (at least 75% reduction) in the time taken to perform the inversion. If the results are similar to that of the reference inversion, this type of saving in the computational time and resources would allow more components of the inversion to be tested in a shorter period of time.

### 6.2.6 Sensitivity analysis approach

The sensitivity tests were divided into those which assessed alternative products for the prior information; those which assessed an alteration to the structure of the uncertainty covariance matrices; those which assess an alteration to the relative uncertainty specified in $\mathbf{C}_{\boldsymbol{s}_0}$; those which assessed a homogenisation of a component of the prior information; those which considered a simplified version of $\mathbf{C}_{\boldsymbol{c}}$; and those which solved for an alternative control vector. A summary of the sensitivity tests are presented in Table 6.1.

The modelled concentrations from each inversion were compared with the observations by assessing the bias and standard deviation of the prior and posterior modelled concentration residuals. Residuals in the prior modelled concentrations were calculated as:

$$\boldsymbol{c}_{res\,prior} = \boldsymbol{c} - \boldsymbol{c}_{mod\,prior}. \tag{6.8}$$

Residuals in the posterior modelled concentrations were calculated as:

$$\boldsymbol{c}_{res\,post} = \boldsymbol{c} - \boldsymbol{c}_{mod\,post}. \tag{6.9}$$

where $\boldsymbol{c}_{mod\,prior}$ are the $CO_2$ concentrations modelled from $\boldsymbol{s}_0$ and $\boldsymbol{c}_{mod\,post}$ are the $CO_2$ concentrations modelled from the posterior estimate of $\boldsymbol{s}$, and $\boldsymbol{c}_{res\,prior}$ and $\boldsymbol{c}_{res\,post}$ are the respective residuals in the modelled concentrations. The bias, calculated as the mean of these residuals, and standard deviation of these residuals were provided for each inversion. We plotted the time series of the observed and modelled concentrations to assess the skill of the inversion to reproduce the observed concentrations, particularly "local events", which were periods of larger than normal spikes in the observed concentration signal.

The posterior fluxes from each inversion were compared with those of the reference inversion in a number of ways. The posterior flux estimates and their spatial distribution were assessed for each inversion by mapping the mean total weekly flux within each pixel for two months (May and September 2012). We calculated the total flux over the domain, and plotted these weekly total fluxes over time together with the uncertainty bounds. We also considered the total flux over the domain for each month. These total flux estimates are the nett flux resulting from the fossil fuel and NEE flux estimates solved for by the inversion. The inversion induces negative correlations between the fossil fuel and NEE flux components from the same week and pixel. When the total flux is considered in a particular pixel, the uncertainty for the total flux will be lower than the sum of the uncertainties for the individual components due to the negative covariance terms. The size of these negative covariances will depend on the prior information specified in the inversion framework. The total estimate gives an indication of the central tendency which we can compare between inversions, and allows us to assess, for example, if the inversion is predicting the region to be a nett source or a nett sink. The uncertainties of these posterior total estimates allow us to assess the confidence we can place around these totals, and how this compares to the estimate itself.

In order to assess the goodness-of-fit of the prior uncertainty covariance matrices $\mathbf{C}_{\boldsymbol{c}}$ and $\mathbf{C}_{\boldsymbol{s}_0}$, the $\chi^2$ statistic, as described in Tarantola (2005), was calculated:

$$\chi_1^2 = \frac{1}{\nu}(\mathbf{H}\boldsymbol{s}_0 - \boldsymbol{c})^T(\mathbf{H}\mathbf{C}_{\boldsymbol{s}_0}\mathbf{H}^T + \mathbf{C}_{\boldsymbol{c}})^{-1}(\mathbf{H}\boldsymbol{s}_0 - \boldsymbol{c}) \tag{6.10}$$

where $\nu$ is the dimension of the data space, which is the number of observations used in the inversion.

The squared concentration residuals from the inversion should follow the $\chi^2$ distribution with degrees of freedom equal to the number of observations (Michalak et al., 2005; Tarantola, 2005). Dividing this statistic by the degrees of freedom should yield a $\chi^2_1$ distribution. We compared these statistics between the different inversions to assess the suitability of the uncertainties prescribed to the prior fluxes.

Table 6.1: Description of sensitivity tests performed on the Cape Town inversion. Only those aspects which are changed for the sensitivity test are indicated. Other fields are the same as those for the reference inversion.

| Sensitivity test abbreviation | Prior NEE product | Prior Fossil fuel product | NEE error correlations | Observation error correlations | Fossil fuel uncertainties | NEE uncertainties | Observation errors | Control vectors |
|---|---|---|---|---|---|---|---|---|
| **Ref** | CABLE | Cape Town Inventory | Balgovind 1 km | Balgovind 1 hr | Cape Town Inventory Errors | CABLE NPP | 2 ppm (day); 4 ppm (night) with wind condition and measurement variance inflation | Six individual weekly fluxes |
| **Carbon Assess** | Carbon Assessment Product | | | | | Carbon Assessment NPP | | |
| **ODIAC** | | ODIAC | | | ODIAC Estimates $\times 100\,\%$ | | | |
| **NEE Corr** | | | | No observation error correlation | | | | |
| **Obs Corr** | | | No NEE error correlation | | | | | |
| **No Corr** | | | No NEE error correlation | No observation error correlation | | | | |
| **Double FF** | | | | | Cape Town Inventory Errors$\times 2$ | | | |
| **Half FF** | | | | | Cape Town Inventory Errors$\times \frac{1}{2}$ | | | |
| **Double NEE** | | | | | | CABLE NPP$\times 2$ | | |
| **Half NEE** | | | | | | CABLE NPP$\times \frac{1}{2}$ | | |
| **Domestic Homogenised** | | Cape Town Inventory with domestic emissions homogenised over the year | | | Cape Town Inventory Errors domestic emissions homogenised | | | |
| **NEE Homogenised** | Averaged CABLE weekly estimates over all pixels | | | | | Averages CABLE NPP weekly estimates over all pixels | | |
| **Simp Obs Error** | | | | | | | 2 ppm (day); 4 ppm (night) | |
| **Simp Obs with Large Night** | | | | | | | 2 ppm (day); 10 ppm (night) | |
| **Simp Obs No Corr** | | | | No observation error correlation | | | 2 ppm (day); 4 ppm (night) | |
| **Mean Month** | | | | | | | | Six average weekly fluxes for each month |
| **Week** | | | | | | | | Separate weekly inversions |

## 6.3 Results

The results of the reference inversion (**Ref**) are explained in detail in Nickless et al. (2018). The following sections compare the sensitivity tests to **Ref** with respect to the modelled concentrations, pixel-level weekly flux estimates, and aggregated fluxes over each week, month and over the full measurement period. When we refer to the total pixel-level weekly flux, this is the sum of the four weekly fossil fuel fluxes (week / weekend; day / night) and the two NEE fluxes (day and night) within that pixel. The uncertainty of this total flux is obtained by first obtaining the sum of all the error variance and covariance terms of these six fluxes, and then taking the square root of this total variance term. The aggregated total weekly flux is the sum of all these total fluxes over the full inversion domain for the week in question. The total uncertainty of this aggregated total flux is derived in the same way as for the pixel-level total weekly flux, but now summing over all variance and covariance terms applicable to that week for all pixels in the domain.

Aggregated fluxes are often of interest. For example, we may wish to report the total flux for a region from year to year. As we did not have a contiguous measurement period covering all seasons or over a full year period, which is often reported in these city-scale inversions, we instead aggregated over weekly and monthly periods. The purposes of this is to illustrate how weekly fluxes estimated within the same monthly inversion may differ, and the differences in aggregated fluxes between different inversions at different times of the year. These aggregated monthly fluxes are calculated in the same way as the aggregated weekly flux.

The biases in the prior and posterior modelled concentrations, together with the standard deviation of the residuals, are provided in Table 6.2. We supply the time series of the modelled concentrations for each inversion and at both sites in the Appendix C.1, and the total period average diurnal concentration plots in Appendix C.2. We provide time series plots of the aggregated weekly fluxes and their uncertainty bounds (Appendix C.3) and a table of the aggregated monthly fluxes over the full domain for each month (Appendix C.4). We also supply maps of the prior and posterior modelled fluxes, together with the uncertainty reduction in each pixel, in the supplementary material for the months of May (early winter) and September (spring / early summer) 2012 (Appendix C.5). For the main paper we provide a table of the aggregated fluxes over the full inversion period, together with the uncertainty reduction in the aggregated flux estimate and the mean $\chi^2$ statistic which provides an assessment of the appropriateness of the prior covariance matrices (Table 6.3).

Table 6.2: Bias (ppm) in the prior and posterior modelled concentrations together with the standard deviation of the modelled concentration residuals at the Hangklip and Robben Island measurement sites for the period March 2012 to June 2013. NEE = Net Ecosystem Exchange, FF = Fossil Fuel

| **Hangklip** | | | | | | |
|---|---|---|---|---|---|---|
| | **Ref** | **Carbon Assess** | **ODIAC** | **NEE Corr** | **Obs Corr** | **No Corr** |
| **Prior Bias (sd)** | 2.4 ( 17.6) | -4.8 (12.4) | -6.1 (27.8) | 2.4 (17.6) | 2.4 (17.6) | 2.4 (17.6) |
| **Posterior Bias (sd)** | 0.0 (2.5) | -0.4 (4.2) | -0.1 (2.1) | 0.0 (2.5) | 0.0 (2.9) | 0.0 (2.9) |
| | **Double FF** | **Half FF** | **Double NEE** | **Half NEE** | **Domestic Homogenised** | **NEE Homogenised** |
| **Prior Bias (sd)** | 2.4 (17.6) | 2.4 (17.6) | 2.4 (17.6) | 2.4 (17.6) | 3.2 (16.3) | 2.1 (13.2) |
| **Posterior Bias (sd)** | 0.0 ( 2.3) | 0.1 (2.6) | 0.0 (2.0) | 0.1 (3.0) | 0.1 (2.4) | 0.0 (2.1) |
| | **Simp Obs Error** | **Simp Obs with Large Night** | **Simp Obs No Corr** | **Mean Month** | **Week** | |
| **Prior Bias (sd)** | 2.4 (17.6) | 2.4 (17.6) | 2.4 (17.6) | 2.5 (17.7) | 1.2 (15.6) | |
| **Posterior Bias (sd)** | -0.1 (2.3) | -0.1 (2.3) | 0.0 (2.9) | 0.0 (2.5) | -0.1 (2.9) | |
| **Robben Island** | | | | | | |
| | **Ref** | **Carbon Assess** | **ODIAC** | **NEE Corr** | **Obs Corr** | **No Corr** |
| **Prior Bias (sd)** | -2.9 (21.4) | -12.6 (20.1) | -17.1 (43.7) | -2.9 (21.4) | -2.9 (21.4) | -2.9 (21.4) |
| **Posterior Bias (sd)** | 0.5 (3.9) | 0.3 (5.2) | 0.6 (3.6) | 0.5 (3.7) | 0.5 (4.2) | 0.5 (3.9) |
| | **Double FF** | **Half FF** | **Double NEE** | **Half NEE** | **Domestic Homogenised** | **NEE Homogenised** |
| **Prior Bias (sd)** | -2.9 (21.4) | -2.9 (21.4) | -2.9 (21.4) | -2.9 (21.4) | -1.0 (20.2) | -6.4 (19.8) |
| **Posterior Bias (sd)** | 0.5 (3.6) | 0.3 (4.2) | 0.4 (3.5) | 0.6 (4.3) | 0.5 (3.9) | 0.4 (3.1) |
| | **Simp Obs Error** | **Simp Obs with Large Night** | **Simp Obs No Corr** | **Mean Month** | **Week** | |
| **Prior Bias (sd)** | -2.9 (21.4) | -2.9 (21.4) | -2.9 (21.4) | -3.5 (20.6) | -4.2 (18.5) | |
| **Posterior Bias (sd)** | 0.1 (3.6) | 0.1 ( 3.4) | 0.0 (4.5) | 0.6 (4.0) | 0.5 (4.3) | |

[1]

[1]The sd alongside the bias refers to the standard deviation of the residuals of the modelled concentrations in units of ppm. Ref = Reference Inversion; Carbon Assess = Carbon Assessment Inversion; ODIAC = ODIAC fossil fuel inversion; NEE Corr = Correlation for NEE flux uncertainties only; Obs Corr = Correlation for observation errors only; No Corr = No correlation specified in prior covariance matrices; Double FF = Double fossil fuel uncertainties; Half FF = Half fossil fuel uncertainties; Double NEE = Double NEE uncertainties; Half NEE = Half NEE uncertainties; Domestic Homogenised = Domestic emission homogenised over the year; NEE Homogenised = NEE fluxes averaged over the domain; Simp Obs Error = Simple specification of observation error covariance matrix; Simp Obs with Large Night = Simple observation error covariance matrix with larger night-time error; Simp Obs No Corr = Simple observation error covariance matrix with no correlation; Mean Month = Inversion solving for mean weekly fluxes over the month; Week = Separate inversions for each week.

Table 6.3: Prior and posterior total flux estimates of each inversion over the thirteen four-week periods for which observation data were available from March 2012 to June 2013, with uncertainties and the reduction in uncertainty with respect to the prior uncertainty. Total fluxes are expressed as kt $CO_2$. The mean $\chi^2$ statistic is provided over the thirteen inversion periods. NEE = Net Ecosystem Exchange, FF = Fossil Fuel

| | **Ref** | **Carbon Assess** | **ODIAC** | **NEE Corr** | **Obs Corr** | **No Corr** |
|---|---|---|---|---|---|---|
| **Prior Flux (sd)** | -1336 (254) | 5181 (32) | 7635 (256) | -1336 (254) | -1336 (63) | -1336 (63) |
| **Posterior Flux (sd)** | -317 (189) | 4045 (28) | 5787 (195) | -310 (189) | -1281 (59) | -1287 (59) |
| **Uncertainty Reduction** | 25.6% | 11.9% | 23.6% | 25.6% | 7.5% | 7.5% |
| **Mean $\chi^2$ Statistic** | 1.48 (0.55) | 4.13 (1.24) | 1.25 (0.49) | 1.49 (0.54) | 2.10 (0.78) | 2.12 (0.79) |
| | **Double FF** | **Half FF** | **Double NEE** | **Half NEE** | **Domestic Homogenised** | **NEE Homogenised** |
| **Prior Flux (sd)** | -1336 (255) | -1336 (254) | -1336 (508) | -1336 (128) | -1916 (254) | -1328 (126) |
| **Posterior Flux (sd)** | -151 (190) | -423 (189) | -316 (365) | -337 (100) | -624 (189) | -1707 (106) |
| **Uncertainty Reduction** | 25.4% | 25.7% | 28.2% | 21.9% | 25.6% | 15.8% |
| **Mean $\chi^2$ Statistic** | 1.21 (0.50) | 1.86 (0.63) | 1.03 (0.47) | 2.22 (0.69) | 1.41 (0.49) | 1.17 (0.47) |
| | **Simp Obs Error** | **Simp Obs with Large Night** | **Simp Obs No Corr** | **Mean Month** | **Week** | |
| **Prior Flux (sd)** | -1336 (254) | -1336 (254) | -1336 (254) | -1336 (126) | -1220 (251) | |
| **Posterior Flux (sd)** | -325 (188) | -579 (192) | -338 (188) | 662 (66) | -687 (186) | |
| **Uncertainty Reduction** | 26.1% | 24.4% | 26.1% | 47.2% | 25.8% | |
| **Mean $\chi^2$ Statistic** | 2.17 (1.04) | 1.88 (0.92) | 2.25 (1.13) | 1.43 (0.55) | 1.54 (0.56) | |

[2]Prior and Posterior Flux refer to the total flux from the domain over the thirteen four-week periods. The sd of the fluxes refers to the uncertainty in the total flux estimate. The sd of the $\chi^2$ statistic refers to the standard deviation between the $\chi^2$ statistics of the thirteen four-week period $\chi^2$ Statistics. Ref = Reference Inversion; Carbon Assess = Carbon Assessment Inversion; ODIAC = ODIAC fossil fuel inversion; NEE Corr = Correlation for NEE fluxes only; Obs Corr = Correlation for observation errors only; No Corr = No correlation specified in prior covariance matrices; Double FF = Double fossil fuel uncertainties; Half FF = Half fossil fuel uncertainties; Double NEE = Double NEE uncertainties; Half NEE = Half NEE uncertainties; Domestic Homogenised = Domestic emission homogenised over the year; NEE Homogenised = NEE fluxes averaged over the domain; Simp Obs Error = Simple specification of observation error covariance matrix; Simp Obs with Large Night = Simple observation error covariance matrix with larger night-time error; Simp Obs No Corr = Simple observation error covariance matrix with no correlation; Mean Month = Inversion solving for mean weekly fluxes over the month; Week = Separate inversions for each week.

### 6.3.1 Alternative prior information products

The prior biases for both the inversion making use of the carbon assessment for prior NEE flux estimates and uncertainties (which we denote with the emboldened shorthand **Carbon Assess**), and the ODIAC fossil fuel inversion (**ODIAC**) were larger in magnitude and more negative than that of the reference inversion (**Ref**). This indicates that the prior modelled concentrations of $CO_2$ from these two inversions were larger on average compared with the observations. The standard deviation in these residuals was larger compared with **Ref** (Table 6.2). A plot of the modelled concentrations shows that for all three inversions, the prior modelled concentrations only weakly followed the observed concentrations, with modelled concentrations at the Robben Island site too large, and too small at the Hangklip site (Figures 6.3 and 6.4). In the case of the **Carbon Assess** inversion the prior modelled concentrations were not underestimated as much as those from **Ref** at the Hangklip site. The $\chi^2$ statistics indicated that the inversion framework specified for the **Carbon Assess** inversion had uncertainties that were too small (Table 6.3). For **ODIAC**, the $\chi^2$ statistics were slightly closer to one than those for **Ref**.

The prior total weekly fluxes were notably different compared with **Ref** (Figure 6.5). The carbon assessment product for NEE fluxes resulted in prior total weekly flux estimates that were always positive and which showed little variation over the year compared with the reference prior. The uncertainty bands were much narrower for the carbon assessment total flux estimates. The resulting posterior weekly fluxes were very similar to the priors.

The ODIAC product for fossil fuel fluxes resulted in prior total weekly fluxes that had a similar pattern of weekly fluxes over time as those obtained by **Ref** (Figure 6.5), with more positive fluxes between March and June 2012 and March and June 2013, and negative or near-zero total weekly fluxes between August 2012 and February 2013. These summer-time negative fluxes were not as negative as those obtained by **Ref**.

Considering the aggregated flux for each month over the inversion domain, the **Carbon Assess** inversion had larger prior fluxes for every month compared with **Ref**, particularly during the summer months. During these months the discrepancy between the reference and carbon assessment prior aggregated fluxes was between 699 and 1386 kt $CO_2$ for a four week period (Appendix C.4). The inversion reduced these fluxes. The resulting posterior fluxes were still larger than the reference posterior fluxes by between 400 and 1000 kt $CO_2$ for this same period. The ODIAC prior fluxes were always larger than the reference priors, but consistently for all months by

an amount of approximately 690 kt $CO_2$. The posterior aggregated fluxes were still larger than those for **Ref**, but the difference was reduced to 469 kt $CO_2$ on average.

Whereas the aggregated total prior fluxes from **Ref** were generally made more positive by the inversion, there were some months when the total fluxes were made more negative, notably during the winter months. In the case of the **Carbon Assess** inversion, fluxes were made more negative by the inversion for all months. The resulting posterior total fluxes were positive for all months. For **ODIAC**, the posterior fluxes were more negative than their priors, indicating that compared with the reference, the positive fluxes from the fossil fuel sources were specified too large. August and September 2012 were the only months when **ODIAC** made the total posterior fluxes larger than the priors, which agrees with the direction in which **Ref** adjusted the posterior total fluxes.

The aggregated total fluxes of these alternative prior product inversions over the thirteen inversion periods are larger than for **Ref** (Table 6.3). The uncertainty of the aggregated total flux for **Carbon Assess** was smaller relative to **Ref**, whereas **ODIAC** obtained similar uncertainties in the aggregated total flux. The corrections made by the inversion made the aggregated total flux of **Ref** less negative and closer to zero. When these two alternative prior products were used, the inversion corrected the prior fluxes to be less positive, also attempting to make these fluxes closer to zero. The uncertainty reduction achieved over the full inversion period was 25.6% for **Ref** and 23.6% for **ODIAC**, but only 11.9% for **Carbon Assess**. This smaller uncertainty reduction is due to prior biospheric flux estimates from the carbon assessment product being close to zero, with corresponding small NPP fluxes, and therefore error correlations much smaller in comparison with **Ref**. The error correlations play an important role in determining the uncertainty reduction achievable by the inversion.

The spatial distribution of the prior and posterior fluxes for May 2012 are provided in Figure 6.6. **Carbon Assess** has prior total flux estimates that are notably closer to zero and less negative compared with **Ref** across both May and September 2012 (provided in Appendix C.5). **Ref** was able to change the spatial distribution of these negative fluxes somewhat, but still maintained these negative fluxes in the posterior estimates. The posterior fluxes of **Carbon Assess** were largely left unchanged, with September 2012 having the most notable adjustments with a small area of negative fluxes created to the east of the oil refinery pixel, to the north of the Cape Town metropolitan area.

The map of the ODIAC prior fluxes is distinctly different to those of **Ref** (Figure 6.6). The reference inventory limited the fossil fuel fluxes to a few specific pixels, with

a small number of pixels over point sources with large positive fluxes. The ODIAC product smoothed the fluxes over the Cape Town metropolitan area, covering a larger area with positive fluxes compared with the reference case, and having only three pixels with distinctly larger fluxes than the rest of the region. Although the ODIAC priors do not show any of the very large positive fluxes of the reference, the area of positive flux resulting from the fossil fuel fluxes is focused on the same general area as **Ref**.

With regards to the uncertainty reduction (Figure 6.6), **Ref** was able to obtain higher reductions than either of these test cases. The spatial pattern of uncertainty reduction was similar between **ODIAC** and **Ref**, whereas for **Carbon Assess** many of the pixels in the domain showed no uncertainty reduction.

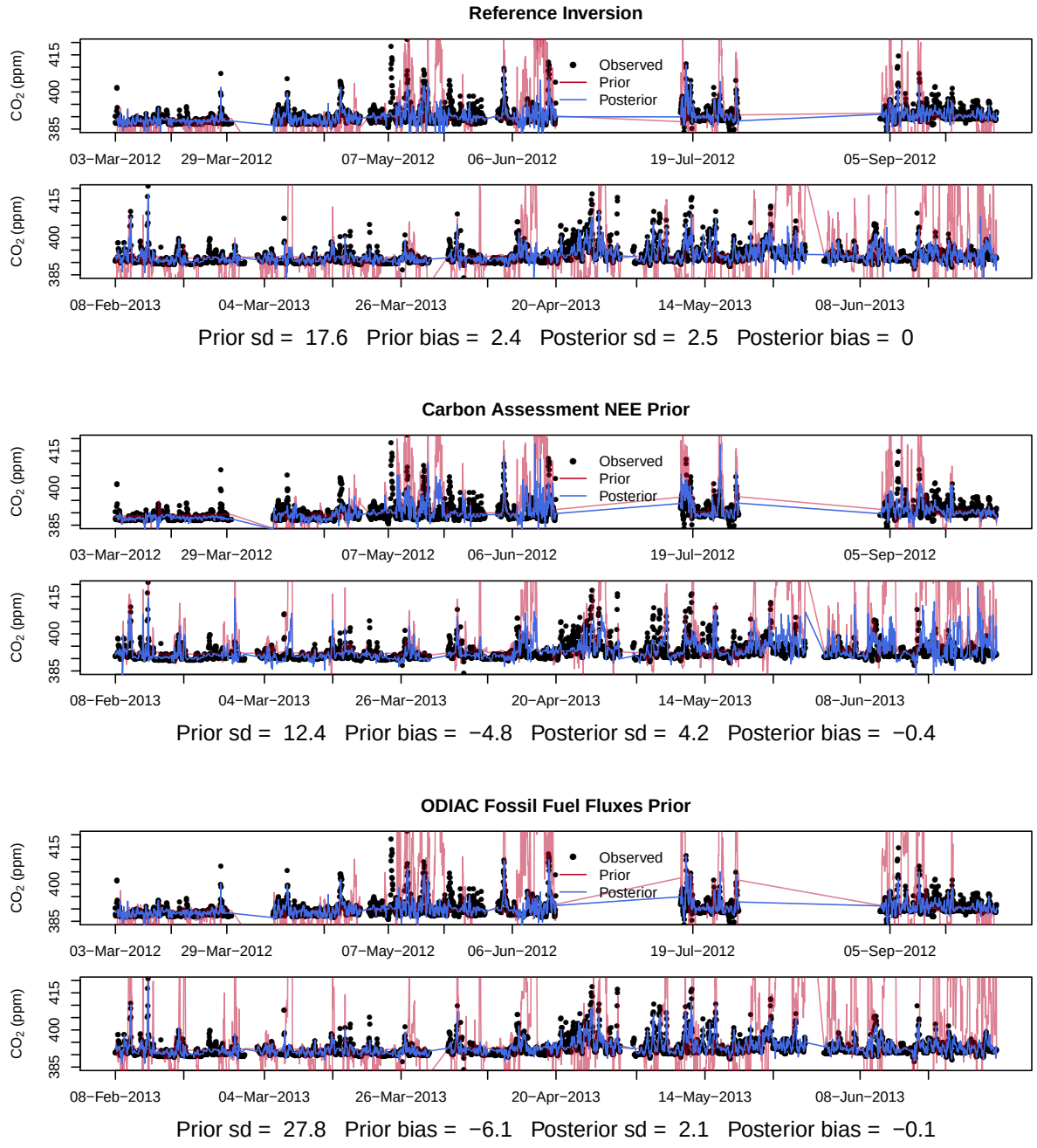


Figure 6.3: Prior and posterior modelled concentrations for the Hangklip site over the full inversion period from March 2012 until June 2013 for the reference inversion (top), carbon assessment inversion (middle), and ODIAC fossil fuel flux product inversion (bottom).

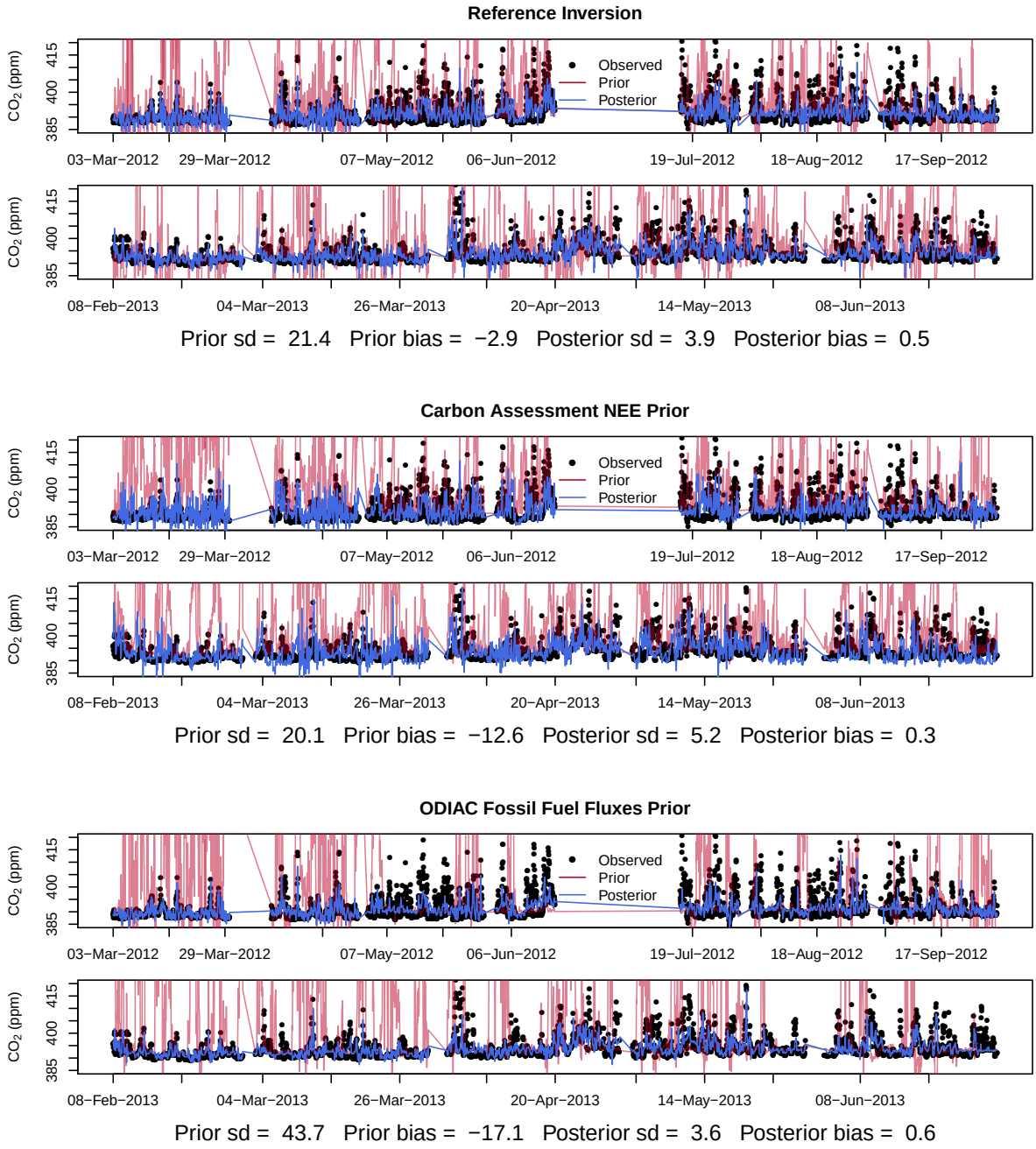


Figure 6.4: Prior and posterior modelled concentrations for the Robben Island site over the full inversion period from March 2012 until June 2013 for the reference inversion (top), carbon assessment inversion (middle), and ODIAC fossil fuel flux product inversion (bottom).

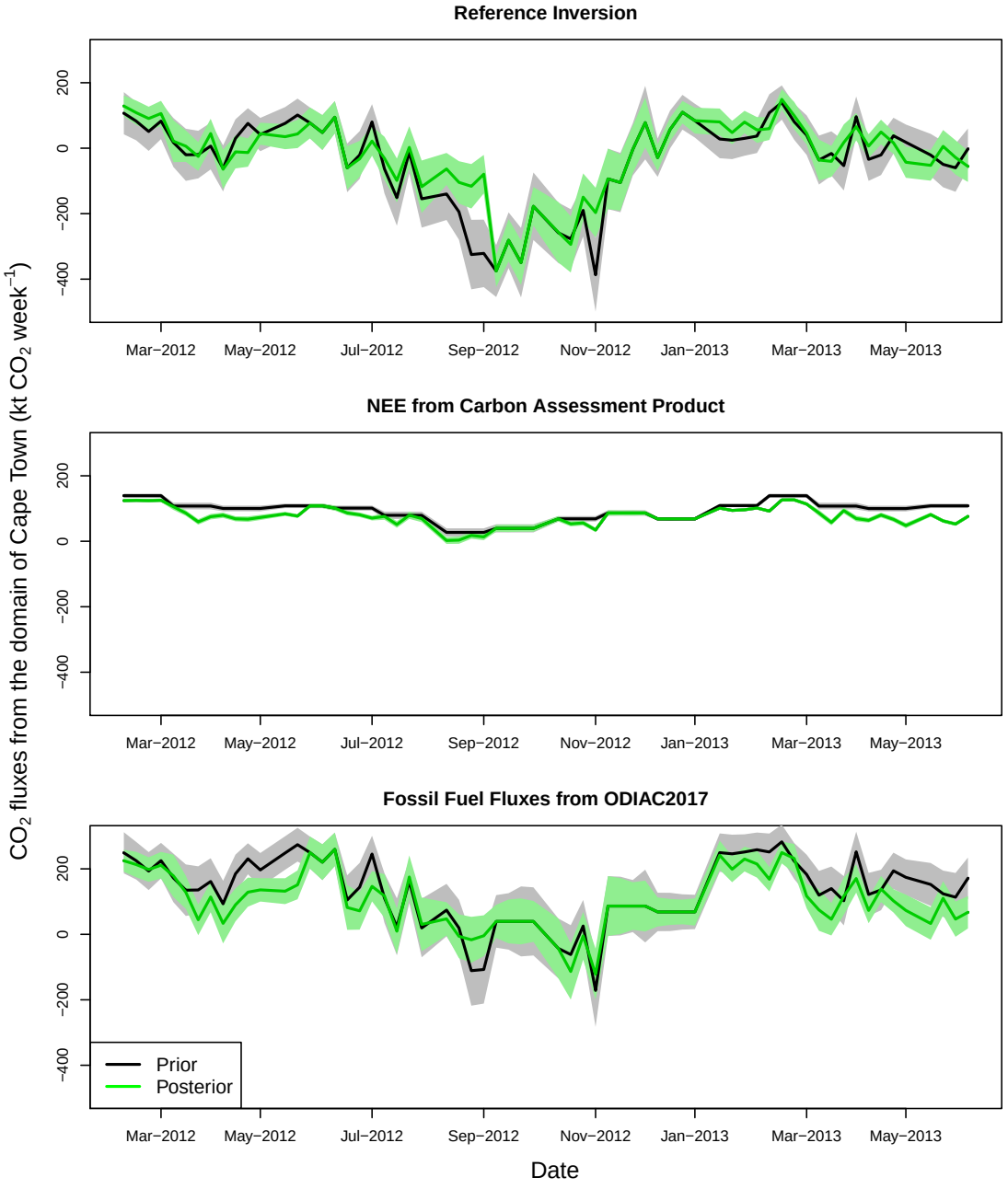


Figure 6.5: Prior and posterior aggregated weekly fluxes over the inversion domain from March 2012 to June 2013 for the reference, carbon assessment and ODIAC inversions.

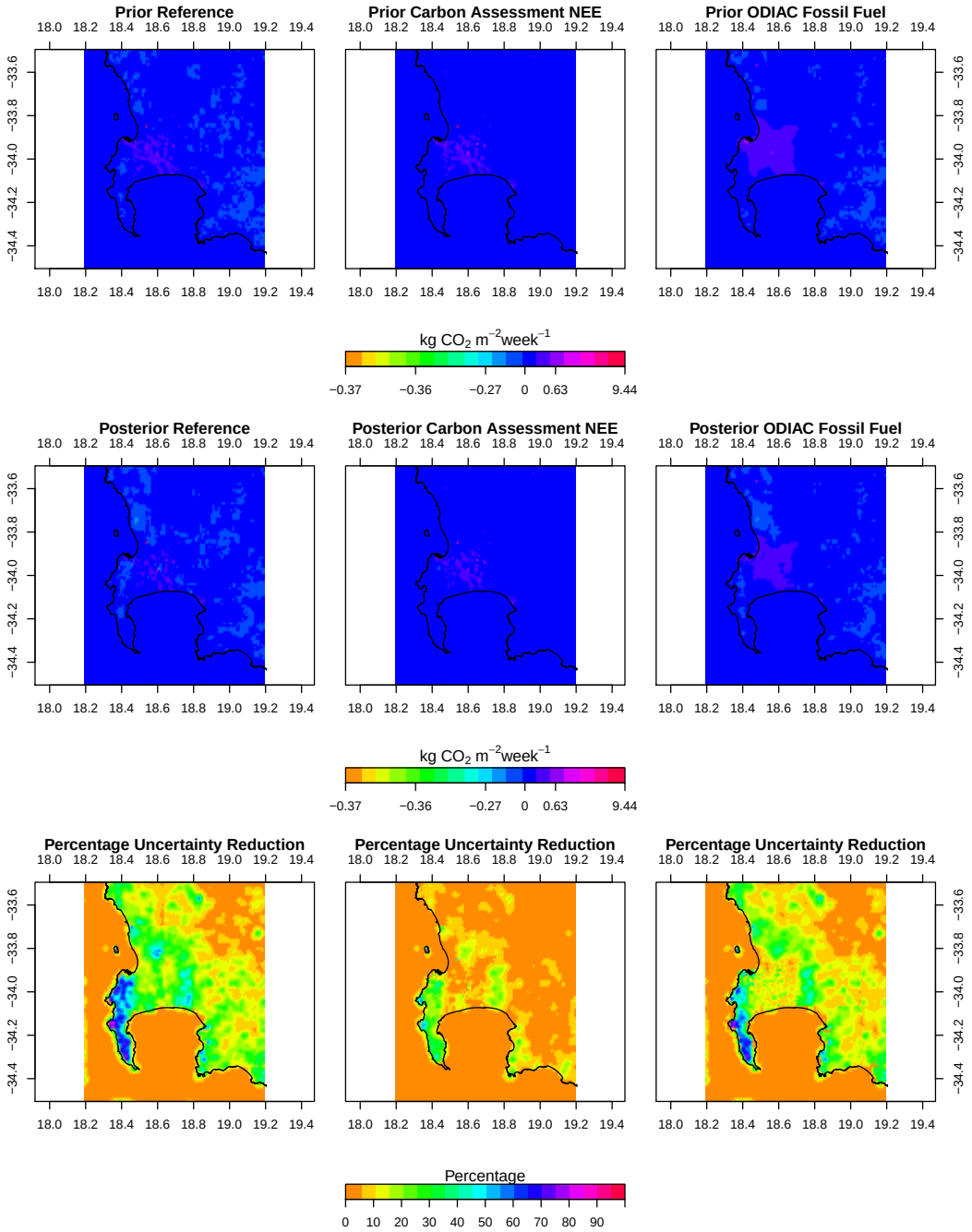


Figure 6.6: Spatial distribution of the prior (top row) and posterior (middle row) total weekly fluxes in May 2012 for the reference (left column), carbon assessment (middle column) and ODIAC (right column) inversions, as well as the uncertainty reduction achieved at the pixel-level relative to the prior uncertainty (bottom row).

### 6.3.2 Uncertainty covariance matrix structure: $\mathbf{C}_{s_0}$ and $\mathbf{C}_c$

**Ref** accounted for correlation between the uncertainties in pixel-level NEE fluxes in space, as well as for temporal correlation in observation errors. The correlation lengths were made small in **Ref**. In this group of sensitivity tests, we assessed how the inversion results would be affected if we systematically ignored these sources of correlation.

In terms of the prior and posterior modelled concentrations achieved by these inversions, the bias and standard deviation in the model concentration residuals were similar (Table 6.2). The posterior modelled concentrations from those inversions which ignored NEE flux uncertainty (inversions **Obs Corr** and **No Corr**) had higher standard deviations in their residuals. The $\chi^2$ statistics indicated that the inversion ignoring the observation error correlations (**NEE Corr**) had similar goodness-of-fit for the prior uncertainty covariance matrices as **Ref**, but that the two inversions that ignored the spatial correlation between NEE flux uncertainties had poorer goodness-of-fit (Table 6.3). The $\chi^2$ statistics for these latter two inversions were as high as 3.3, as for the inversion in July. In comparison, the removal of the temporal correlation in the observation errors had only a small penalty in the $\chi^2$ statistic.

In **Ref**, the positive covariances specified between neighbouring NEE flux uncertainties led to large prior and posterior uncertainty around the aggregated weekly fluxes. For the test cases with observation error correlation only or no correlation at all, the uncertainty bounds around the prior and posterior aggregated fluxes are indistinguishable from **Ref**. If these positive covariances are removed from $\mathbf{C}_{\boldsymbol{s}_0}$ then the uncertainty around the aggregated total flux was much smaller.

When aggregating over a month, ignoring NEE flux uncertainty correlations made a large difference to the aggregated monthly flux as well as to its uncertainty. The posterior aggregated fluxes for each month were similar to the priors in these two test cases, and the uncertainty reduction was very small. For **Ref** and **NEE Corr**, the uncertainty reduction in the monthly aggregated flux was on average 26.6% whereas for the **Obs Corr** and **No Corr** the uncertainty reduction was on average only 7.6%. Aggregating over the full period leads to estimates of -317 and -310 kt $CO_2$ for **Ref** and **NEE Corr**, whereas **Obs Corr** and **No Corr** had posterior estimates of -1281 and -1287 kt $CO_2$, close to the prior aggregated fluxes (Table 6.3).

The spatial distribution of the posterior fluxes were similar for **Ref** and **NEE Corr**. The spatial distribution changed when these NEE covariances were removed. The adjustments made to the pixel-level fluxes in these inversions were small and limited to only a few pixels, whereas in **Ref** adjustments were made to larger areas

of the domain. The uncertainty reduction achieved by **Obs Corr** and **No Corr** was small and confined to only a few pixels, with a much larger proportion of the domain showing no uncertainty reduction in comparison with **Ref** (Figure 6.7).

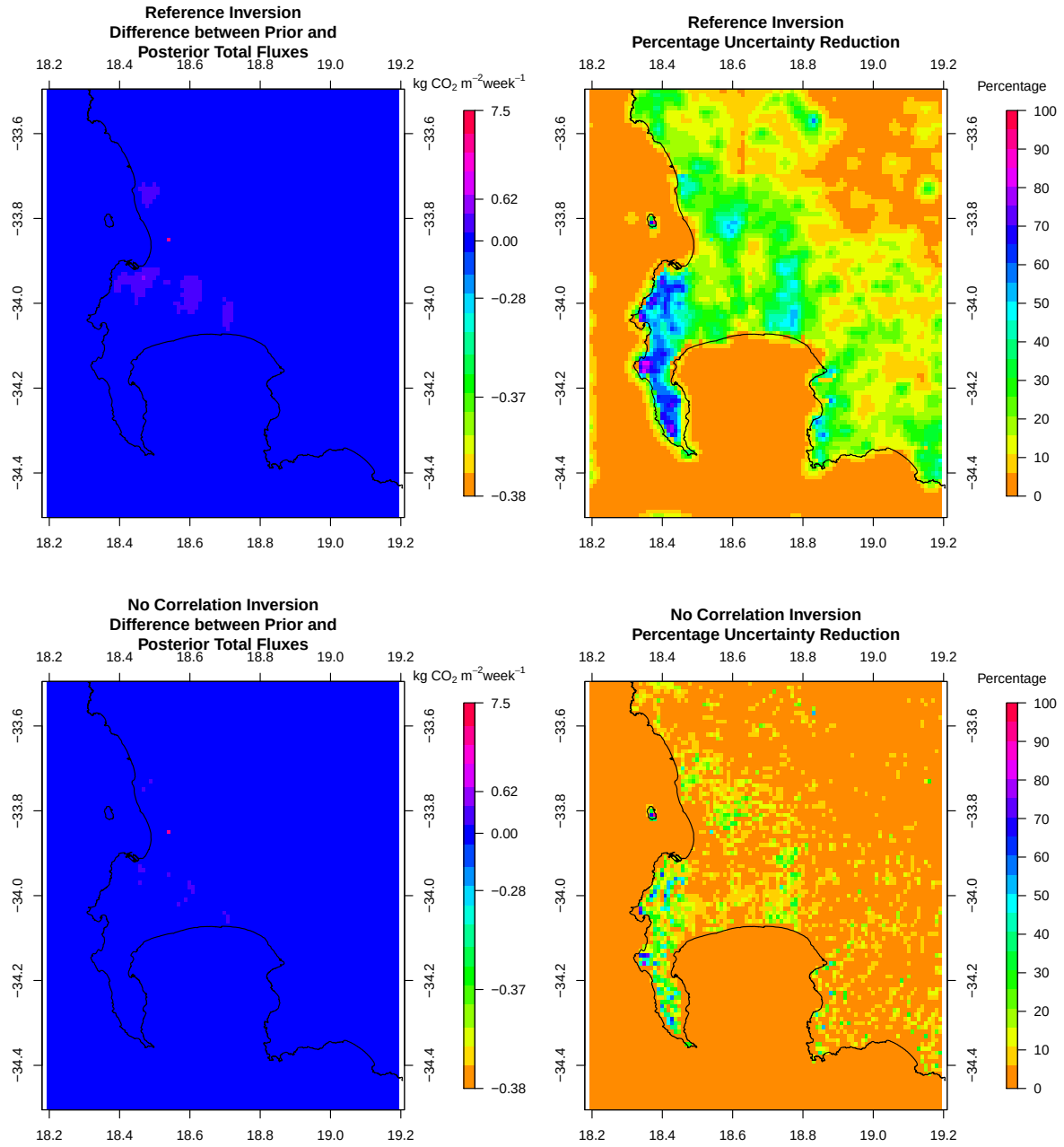


Figure 6.7: Spatial distribution in the adjustments made by the inversion to the prior fluxes in May 2012 for the reference inversion (top left), and no correlation inversion (bottom left), as well as the uncertainty reduction achieved at the pixel-level relative to the prior uncertainty (right).

### 6.3.3 Relative uncertainty in $C_{s_0}$

In this group of sensitivity tests we assessed how the relative contribution of the uncertainty in the fossil fuel and NEE fluxes affected the inversion results. We considered doubling and halving these uncertainties with respect to **Ref** uncertainties. The impact on the modelled concentrations was small. Biases were similar to **Ref** at both sites, and the standard deviation in the residuals of the modelled concentrations were similar (Table 6.2). The $\chi^2$ statistics were larger when the uncertainties were halved, particularly the uncertainties in the NEE fluxes (inversion **Half NEE**), indicating that insufficient uncertainty had been assigned to either the fluxes or observations, whereas doubling the uncertainties led to $\chi^2$ statistics closer to one (Table 6.3).

The pattern in prior and posterior aggregated fluxes was similar between **Ref** and these test cases. The uncertainty around the weekly aggregated fluxes was strongly dependent on the NEE uncertainty (Table 6.8) (inversions **Double NEE** and **Half NEE**), whereas it was not noticeably different if the uncertainty in the fossil fuel fluxes was either double or halved (inversions **Double FF** and **Half FF**).

In this group of sensitivity tests, the differences in the aggregated monthly fluxes was more pronounced between months within the same inversion than between inversions performed for the same month. All inversions corrected the prior aggregated fluxes to a similar degree and in the same direction. Doubling the uncertainty in the fossil fuel fluxes led to posterior aggregated fluxes that were consistently larger for all months compared with **Ref**, whereas halving this uncertainty led to smaller posterior fluxes. Doubling and halving the uncertainty in the NEE fluxes led to posterior flux estimates that were similar on average to those of **Ref** but with greater variability in this difference between the reference and test inversion posterior estimates from month to month compared with the fossil fuel test inversions.

**Double NEE** obtained the largest uncertainty reduction, but the resulting posterior uncertainty was larger than for **Ref**. Halving the NEE uncertainty led to smaller relative uncertainty reductions for the aggregated monthly fluxes, and therefore posterior uncertainties that were similar in magnitude to the prior uncertainties. The uncertainties in the posterior aggregated monthly fluxes were similar between **Ref**, **Double FF**, and **Half FF**. It was always higher for **Double NEE**, and lower for **Half NEE**. The resulting uncertainty in the posterior aggregated flux for **Half NEE** was more similar to **Ref** than **Double NEE**. The aggregated flux over the full inversion period shows that, whereas this estimate was close to the result for **Ref** in the case of the two NEE uncertainty cases (316 and 337 kt $CO_2$), the aggregated flux was more positive when the fossil fuel uncertainty was doubled (-151 kt $CO_2$) and

more negative when the fossil fuel flux was halved (-423 kt $CO_2$) (Table 6.3). On the other hand, changing the relative uncertainty of the fossil fuel fluxes had no impact on the uncertainty in the posterior flux estimate, whereas doubling or halving the uncertainty in the NEE fluxes led to roughly doubling or halving the uncertainty in the posterior aggregated flux.

The spatial distributions of the posterior fluxes were similar between the inversions in this group of sensitivity tests. A notable feature in the September 2012 posterior fluxes is, when NEE uncertainty was doubled, the inversion was able to reduce the aggregated flux with respect to the priors, by creating a region of negative flux in an area close to the oil refinery point source to the north of the CBD region (Appendix C.5 Figure C.59).

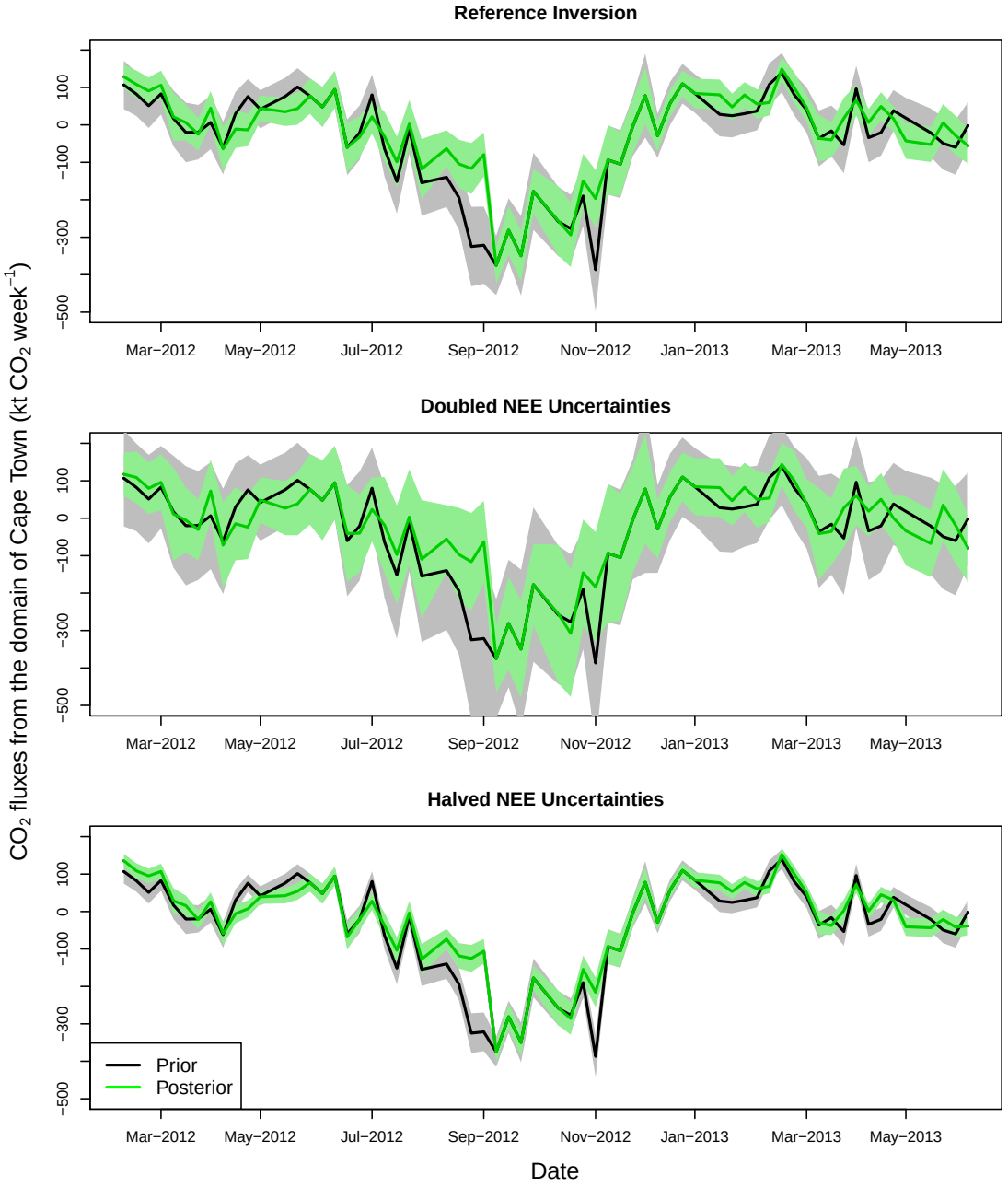


Figure 6.8: Prior and posterior aggregated weekly fluxes over the inversion domain from March 2012 to June 2013 for the reference inversion and the doubled and halved NEE uncertainty test cases.

### 6.3.4 Homogenised prior information

In this group of sensitivity tests we looked at the impact on the inversion results of assuming that the domestic emissions were constant through time (**Domestic Homogenised**), and of assuming a spatially homogeneous biogenic flux over the inversion domain within each month (**NEE Homogenised**). The prior modelled concentrations from these two test cases were biased to a similar degree as **Ref**. Homogenising the NEE flux over space led to smaller standard deviations in the prior residuals. The most noticeable difference in the bias was for the Robben Island site, where the modelled concentrations under the homogenised NEE prior were biased by -6 ppm compared with the -3 ppm of **Ref**, indicating that prior fluxes around Robben Island (generally from the Cape Town central business district area and the Table Mountain National Park area adjacent to this region) were too positive (Table 6.2). The $\chi^2$ statistics indicated that the inversion framework for these homogenised prior test cases is more suitable than the reference case (Table 6.3). For the **NEE Homogenised** priors, the statistic was close to one for most months.

The prior and posterior modelled concentrations for **Domestic Homogenised** are similar to those of **Ref**. In the case of **NEE Homogenised**, the time series shows better agreement between the prior modelled and observed concentrations at the Hangklip site, but worse agreement with respect to **Ref** at the Robben Island site (Figure 6.9).

There was no notable difference in the prior and posterior weekly aggregated flux between **Domestic Homogenised** and **Ref**. Smoothing NEE over space resulted in less extreme prior NEE and NPP estimates, and therefore the uncertainty around the NEE estimates was smaller than for **Ref**, leading to smaller uncertainties around the aggregated flux (Figure 6.10). The general pattern in the aggregated weekly fluxes over the course of the inversion period was similar to **Ref**.

Compared to other groups of sensitivity tests performed here, the aggregated monthly fluxes were not very different between the reference and test cases. For **Domestic Homogenised**, the adjustments made to the prior fluxes by the inversion were generally in the same direction and to the same degree as for **Ref**. The adjustments made by **NEE Homogenised** were not always in the same direction. The resulting posterior fluxes from **NEE Homogenised** were generally more negative than those of **Ref**. This is illustrated in the posterior aggregated fluxes for the inversion period (Table 6.3.

Differences between the prior and posterior fluxes were small for **Ref** and these changes are consistent with those obtained by **Domestic Homogenised**. In May

2012, which would have had a smaller domestic emissions specified than in **Ref**, the differences between the prior and posterior fluxes were limited to very few pixels, mainly near the Cape Town CBD area. In September 2012, when the domestic emissions would have been larger than those for **Ref**, the adjustments made by the inversion were more widespread.

When NEE was smoothed over the domain with each month, the adjustments made to the prior fluxes were very small in comparison to **Ref**. Changes were restricted to a few pixels in the CBD region and close to the measurement sites. The uncertainty reduction was concentrated in the regions around the measurement sites and reached over 90% in these areas. Over the Table Mountain National Park, which had some of the highest uncertainty reductions in **Ref**, uncertainty reduction was limited to between 20 to 30% and almost no adjustment to these prior fluxes were made by the inversion (Figure 6.11).

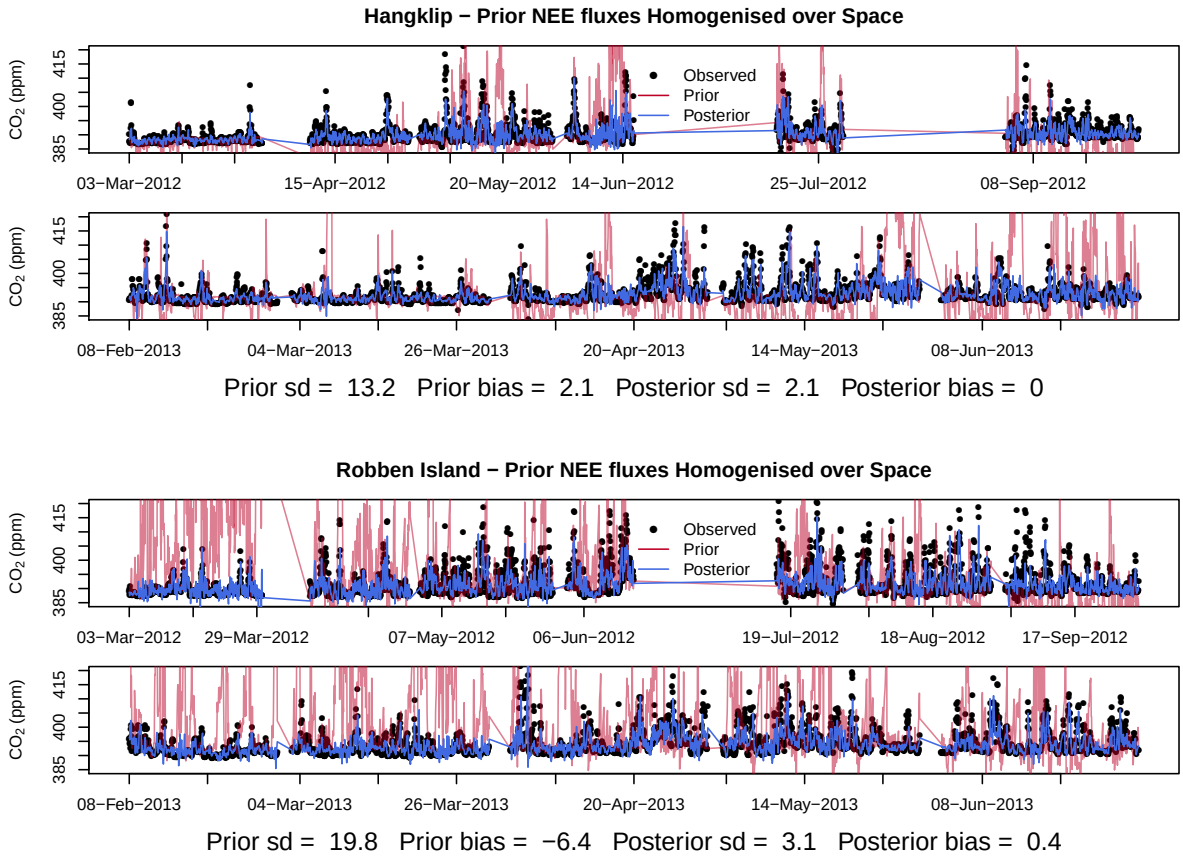


Figure 6.9: Prior and posterior modelled concentrations when the homogenised NEE prior was used for the Hangklip and Robben Island sites over the full inversion period from March 2012 until June 2013.

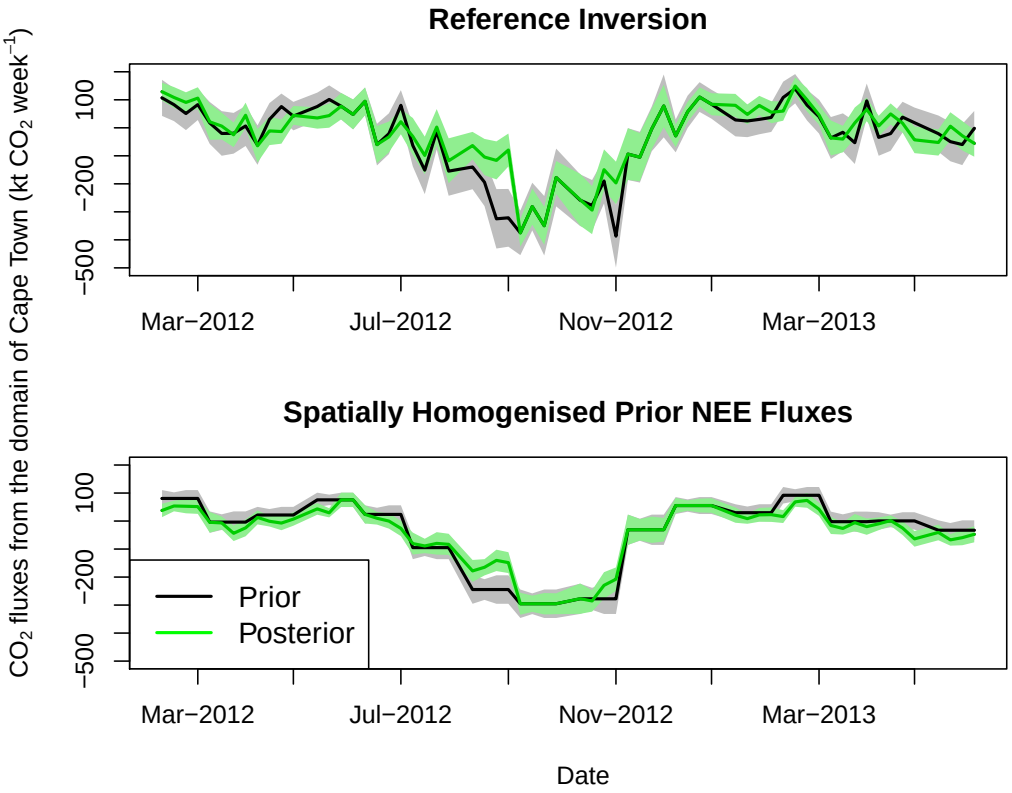


Figure 6.10: Prior and posterior aggregated weekly fluxes over the inversion domain from March 2012 to June 2013 for the reference inversion and homogenised NEE prior test case.

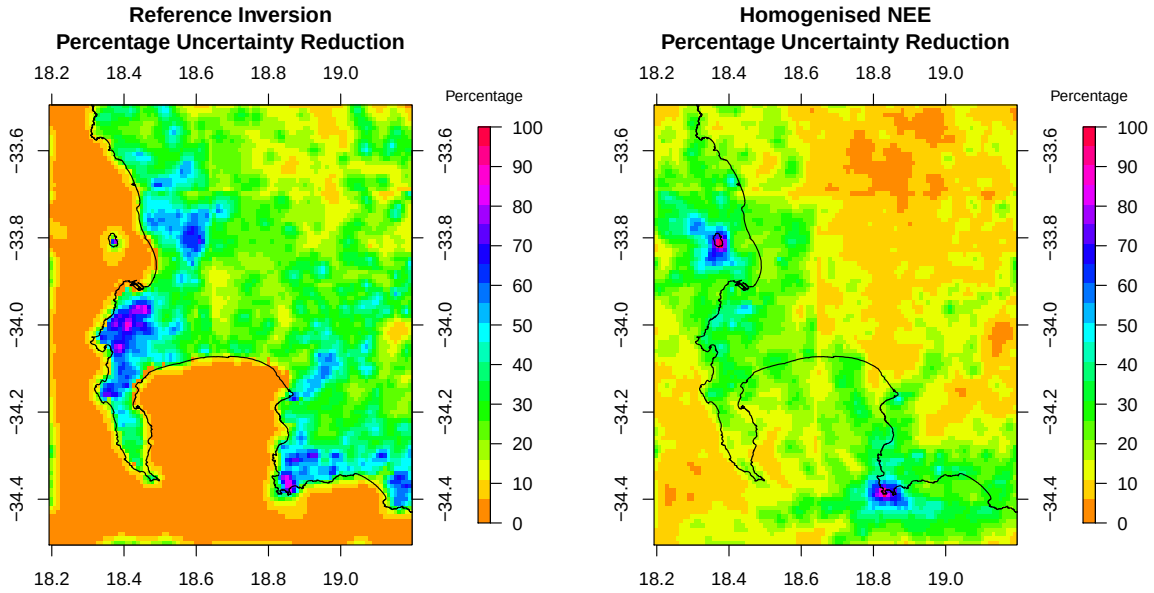


Figure 6.11: Spatial distribution of the pixel-level uncertainty reductions achieved by the reference inversion and homogenised NEE prior test case for September 2012.

### 6.3.5 Simplified $\mathbf{C}_c$

In this group of sensitivity tests, the specification of $\mathbf{C_c}$ was simplified to a single uncertainty value of 2 ppm during the day or 4 ppm at night (**Simp Obs Error**), or up to 10 ppm for the night-time observations (**Simp Obs with Large Night**). These test cases had uncertainties in the observation errors that were lower than for **Ref**. Removing the correlation assumed in **Ref** was also considered (**Simp Obs No Corr**). The $\chi^2$ statistics indicated that simplifying the $\mathbf{C_c}$ with smaller errors reduced the goodness-of-fit of the prior uncertainty covariance matrices (Table 6.3).

The impact on the modelled concentrations was very small, with biases in the prior and posterior modelled concentrations closes to those obtained by **Ref** (Table 6.2). The bias for the Robben Island modelled concentrations was slightly reduced compared with **Ref** in all three of the simple observation error test cases.

The posterior aggregated weekly fluxes of the simple observation error cases and their uncertainties were indistinguishable from those of **Ref**. The posterior fluxes, both the spatial distribution in these fluxes and the aggregated fluxes, were similar between all three test cases and when compared with **Ref**. The uncertainty reduction was slightly larger under the simplified (i.e. smaller) observation error covariance matrix, but the spatial distribution in the uncertainty reduction was the same. Increasing the night-time observation errors to account for greater uncertainty in the atmospheric transport at night led to an aggregated flux estimate over the full measurement period that was more negative than for **Ref**, but with a similar uncertainty in the posterior aggregated flux (Table 6.3). The aggregated fluxes for this test case were consistently more negative across all months compared with **Ref**. Removing the correlation between observation errors had little impact on the inversion results.

### 6.3.6 Alternative control vectors

Performing separate weekly inversions (**Week**) or solving for a mean weekly flux for the month (**Mean Month**) led to inversions that required less computational resources and time, which meant these inversions could be completed for the full inversion period faster than **Ref**.

The time series in the posterior modelled concentrations, and the bias and standard deviation in the posterior modelled concentrations were similar between **Ref** and the two alternative control vector inversions (Table 6.2). The $\chi^2$ statistics were similar for these three inversions.

**Ref** and **Week** had similar aggregated weekly fluxes (Appendix C.3). For **Mean Month**, the weekly aggregated fluxes were forced to be the same within each month, but the general pattern over time was similar to **Ref**. For most months the posterior weekly flux was above or below the prior weekly flux to the same degree as **Ref**, but the estimates, as expected, were smoother over time.

The monthly aggregated fluxes were generally very close to those from **Ref** except for August, September and November 2012 (Appendix C.4). These are the summer months, and there was a great deal of variation in the aggregated fluxes from week to week from the results of **Ref** in these months. **Mean Month** generally had aggregated fluxes that were closer to zero than **Ref** or **Week**. This had a large impact on the aggregated flux over the full measurement period, due to these less negative posterior aggregated fluxes during the summer months. The aggregated flux for **Mean Month** was 662 kt $CO_2$ compared with the -317 kt $CO_2$ of **Ref** (Table 6.3). **Week** had an aggregated flux of -687 kt $CO_2$. This discrepancy is partly due to some weeks with missing observations. In **Ref** these fluxes would have been adjusted by the available observations for neighbouring weeks, but were completely unconstrained by the observations in **Week**. For those months when all measurements were available, the aggregated totals were similar between **Ref** and **Week**. The uncertainty reduction in the aggregated estimates was almost double for **Mean Month** compared with **Ref** and **Week**.

The spatial distribution of the posterior fluxes was very similar for **Ref** and **Week**, but was distinctly different for **Mean Month**. Notably, the area around the oil refinery pixel was adjusted to negative fluxes for the month of September (Figure 6.12). Other areas were made closer to zero compared with **Ref**. For the month of May the posterior fluxes in the CBD were distributed differently and a new area of relatively large negative fluxes was created north west of the oil refinery pixel (refer to Appendix C.5 Figure C.72). The uncertainty reductions at the pixel-level were large for the **Mean Month** compared with **Ref**, with areas of large uncertainty reduction much more widespread. In particular, the areas of uncertainty reduction above 90% that were restricted to the area over Table Mountain National Park in **Ref** were now extended over the CBD area.

Consequently the aggregated fluxes had uncertainty reduction that were twice as large as those for **Ref**, and uncertainties in the aggregated fluxes that were much smaller. For the aggregated flux over the full period, the posterior uncertainty was 66 kt $CO_2$ for t**Mean Month**, compared with the uncertainty of 189 and 186 kt $CO_2$ from **Ref** and **Week** respectively (Table 6.3).

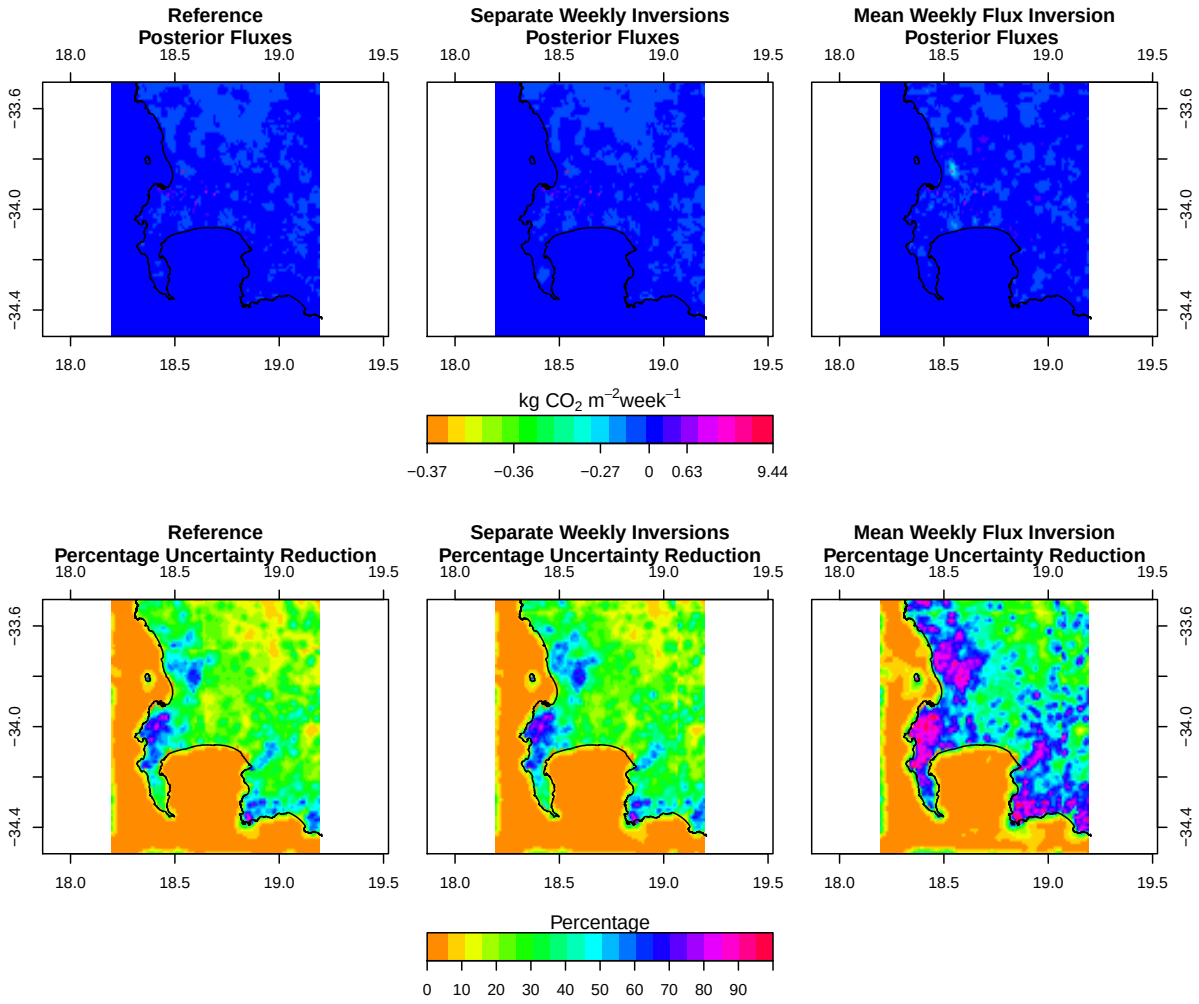


Figure 6.12: Spatial distribution of the pixel-level uncertainty reductions achieved by the reference inversion and homogenised NEE prior test case for September 2012.

## 6.4 Discussion

### 6.4.1 Alternative prior information products

As Robben Island is dominated by fossil fuel influence from the Cape Town metropolitan area, and Hangklip by biogenic sources from natural and agricultural areas in its vicinity, the discrepancy in the modelled concentrations relative to the observations suggests that the fossil fuel fluxes provided by the prior products are too large in magnitude, and the NEE estimates from CABLE estimate too much carbon uptake by the biota around the Hangklip site. In the case of the carbon assessment inversion, the bias in the prior modelled concentrations was positive compared with the negative bias of the reference inversion, indicating that the carbon assessment product was underestimating the uptake by the biota. As the carbon assessment product was much more homogeneous over space than CABLE, and could not react to local climate conditions, the uncertainty prescribed by using the NPP estimates is most likely too small. This is evident from the $\chi^2$ statistic for the carbon assessment inversion, which is on average 4.1 (Table 6.3). This is related to the degrees of freedom of the signal (DFS) (Chevallier et al., 2007), which describes the amount of independent information provided by the observations. This quantity is determined by how far the optimal flux solution is from the prior estimates, and how large the flux uncertainties and prior uncertainty correlations are specified. Increasing the uncertainties and the positive uncertainty correlations leads to a smaller DFS. The large value of 4.1 is an indication that for the carbon assessment inversion framework, the uncertainties were not made large enough, and so the DFS for the carbon assessment inversion were much larger than was realistic.

The comparison of inversion results using different prior products provides useful information regarding which direction the true flux estimates are likely to be. A pixel within the CBD limits had similar fossil fuel flux estimates from the ODIAC product compared with the reference inventory product. The ODIAC product extended the fossil fuel fluxes much further a field from the CBD region than the reference inventory. This led to aggregated estimates that were much larger under the ODIAC inversion than the reference inversion. The inversion attempted to reduce the aggregated flux, indicating that compared with the reference inventory, the ODIAC prior was most likely overestimating the amount of fossil fuel emissions from Cape Town. It can therefore be deduced that the true fossil fuel flux lies somewhere between the reference inventory and ODIAC fossil fuel flux estimates.

### 6.4.2 Uncertainty covariance matrix structure: $\mathbf{C}_{s_0}$ and $\mathbf{C}_c$

From the analysis of the reference inversion (Nickless et al., 2018), the $\chi^2$ statistics indicated that the reference inversion could be improved by small increases to the uncertainty specified in $\mathbf{C}_{\boldsymbol{s}_0}$, either through accounting for a larger correlation length or increasing the pixel-level uncertainties. Removal of the observation error correlations had a very small impact on the goodness-of-fit statistics, or on the posterior flux estimates and uncertainty reduction achieved by the inversion. To ensure that our reference inversion did not deviate too far from conventions for city-scale inversions where observation error correlations are ignored, we assigned a very short error correlation length to the observations of one hour. If we had assigned a longer length, such as 6 hours, this may have had more of an effect on the inversion. Lauvaux et al. (2009) have shown that observation errors up to 24 hours apart may be strongly correlated. The specification of the most suitable observation error length is still under investigation.

The impact of the inversion on the posterior fluxes and their uncertainties strongly depended on the specification of the correlation between the uncertainties in the NEE fluxes. In particular, the aggregated fluxes were distinctly different between the reference and test cases ignoring covariances between NEE flux uncertainties, which tended to have aggregated fluxes closer to the priors and uncertainty reductions achieved by the inversion that were much lower (7.6% compared with 26.6% on average by the reference inversion). This indicates that advantage should be taken of knowledge related to the correlation induced by homogeneity of biogenic productivity in subregions of the domain. If this correlation is correctly specified in $\mathbf{C}_{\boldsymbol{s}_0}$, then the inversion is able to make larger adjustments to the prior fluxes and achieve a larger uncertainty reduction in these fluxes.

### 6.4.3 Relative uncertainty in $\mathbf{C}_{s_0}$

Specification of the uncertainties in the prior flux estimates is one of the most challenging tasks in an atmospheric inversion exercise. There is little consensus on the correct approach to follow, and it is difficult to ensure that the most important sources of uncertainty are accounted for. The $\chi^2$ statistics indicated that for this Cape Town application, further increasing either the uncertainty in the fossil fuel fluxes or in the NEE fluxes led to statistics closer to one. Increasing the fossil fuel flux or NEE uncertainty led to a lower number of DFS. The degree to which the inversion is constrained by the prior fluxes is inversely related to the specified prior uncertainty. If either the

uncertainty in the fossil fuel fluxes or in the NEE fluxes was increased, this led to aggregated flux estimates that were more positive as the inversion was apparently attempting to compensate for the overestimation of the NEE uptake by the CABLE model. When the uncertainties were made smaller, the degree to which the inversion could increase the fluxes was restricted, and the resulting aggregated fluxes were more negative compared with the reference inversion.

These sensitivity results illustrate how dependent the uncertainty bounds around the posterior estimates are on the uncertainties specified for the prior fluxes. The inversion relies on the correctness of the uncertainty estimates assigned to the prior fluxes. The posterior uncertainties reflect the reduction in uncertainty achieved by the inversion given that the prior uncertainties are accurate. This motivates for the hierarchical Bayesian approach where a distribution is assigned to the uncertainty estimates. It can be shown that in the absence of observation error, doubling or halving the prior uncertainty in the fluxes results in a respective doubling or halving of the posterior uncertainty (see Appendix C.6). Therefore it us unsurprising that if a prior uncertainty is made larger with respect to a reference inversion specification, that the posterior uncertainty of this inversion will be larger than the posterior uncertainty of the reference.

This set of sensitivity tests demonstrated that if we wish to ensure that the uncertainty bounds around the posterior fluxes are within a prespecified margin, say 10% of the aggregated flux estimate, then we have to ensure that prior uncertainty that we begin with is sufficiently small. Assuming no large shifts in the mean estimate, it can be shown that if we wish to obtain an uncertainty estimate that is within 10% of the aggregated flux estimate, and we are able to reduce the uncertainty by 25% through the inversion, then the prior uncertainty estimate would need to be within 13.3% of the prior aggregated flux estimate.

### 6.4.4 Homogenised prior information

Applying a spatially homogenised prior for NEE resulted in aggregated prior fluxes with smaller uncertainties, but in aggregated posterior fluxes that were quite different to those of the reference inversion. As the uncertainty was smaller, the degree to which the inversion could adjust these priors was diminished. An alternative sensitivity test could use the mean NEE flux as the prior for all pixels, but the maximum NPP as the uncertainty across all pixels. This would have allowed the inversion to adjust the fluxes by a much larger degree allowing us to determine how much the inversion

wanted to adjust the prior fluxes. Comparing the results to the reference inversion did illustrate that CABLE was most likely over-estimating the amount of $CO_2$ uptake.

Smoothing the domestic emissions over time had less of an effect on the inversion, with corrections to the prior estimates generally of the same magnitude and in the same direction, and with similar uncertainty reductions.

### 6.4.5 Simplified $\mathbf{C}_c$

Simplifying the $\mathbf{C_c}$ had very little impact on the inversion results. Increasing the night-time observation errors caused the aggregated flux to be more negative. Assigning an uncertainty in the night-time modelled concentrations of 10 ppm effectively led to the inversion ignoring most of the information available at night, leaving the posterior night-time fluxes (which are mostly affected by the night-time observations) to be similar to their prior estimates. If the inversion is tending to make large corrections to the daytime fluxes, and is now unable to make large corrections to the night-time fluxes, it implies that the aggregated fluxes will be more in error than if the inversion could be constrained by the observations - provided the constraint is good. The analysis of the misfits in the modelled concentrations from the reference inversion ((Nickless et al., 2018)) demonstrated that the errors in the day and night-time atmospheric transport modelling were not very different, and therefore it is unlikely that assigning errors as large as 10 ppm to all the night-time observations is necessary. The analysis of the errors in the modelled concentrations between day and night for the reference inversion provided confidence that the approach of increasing the errors only when conditions indicated that errors were more likely led model errors that were similar to those obtained during the day (Nickless et al., 2018).

### 6.4.6 Alternative control vectors

The separate weekly inversions obtained similar results to those of the reference inversion. Therefore, if necessary, for example due to computational costs, the separate weekly inversions could have been performed in place of the monthly inversions used in the reference case. In addition to the reduction in computation resources required, this allows additional features of the inversion to be tested more easily.

The large uncertainty reduction achieved by the mean weekly flux inversion is expected as a mean weekly flux estimate over four weeks has four times as many observations to constrain this estimate than if separately weekly fluxes are solved for. The estimates from the inversion solving for a mean weekly flux were consistent

with those from the reference inversion, except in the summer months. During these months observations were often missing, and therefore smaller discrepancies may have been observed if data continuity during these periods was similar to the rest of the inversion study period.

An alternative control vector, which could improve on all three of the alternative control vectors used in this study, would be to solve for separate components of fossil fuel and NEE fluxes. For example, if fossil fuel fluxes were split into those fluxes from sectors which change slowly and those which change more quickly, the inversion could solve for a mean weekly flux over the month for the slow fluxes, and for sectors with faster changes, the inversion could solve for individual weekly fluxes. This would allow greater uncertainty reductions for those fluxes for which a mean weekly flux could be solved, which would in turn reduce the overall uncertainty in the aggregated fossil fuel flux. The NEE flux could also potentially be split into a slow and fast component. The fast component responds to local climate conditions and this component could be tightly constrained by the available climate data. The inversion could solve for the slower component which is much harder to model, and to which we could assign larger uncertainties than we would need to for the fast component. As this is the slower component, we could solve for a mean weekly flux over the month, which would allow greater uncertainty reduction.

### 6.4.7 Inversion sensitivity

If we consider the aggregated flux over the full measurement period presented in Table 3, the variability between flux estimates across those inversions which used the reference control vector is 2024 kt $CO_2$. This is largely driven by the inversions using different prior products, and this uncertainty drops to 487 if these two inversions are removed, and drops further to 393 if the inversions with the transformed prior information are removed. This represents the variability in the aggregated flux estimate across all inversions which used the same prior information products. If we compare this to the uncertainty in the aggregated fluxes, which is approximately 185 kt $CO_2$, it shows that variability between posterior flux estimates from different inversion frameworks is still very large when compared with the uncertainty we expect around the posterior flux estimates. If the inversions with no error correlation between biospheric fluxes are removed, then the variability between inversions drops to 113 kt $CO_2$ - now below the expected uncertainty around the posterior flux from a single inversion. All the inversions that we removed from the estimate of variability were those which had a large influence on the error correlations of the NEE fluxes, either because they were

specifically manipulated or because they were affected by the choice of prior product. This demonstrates the important role error correlations in the prior fluxes have on the posterior flux estimates obtained from an inversion.

Exceptions are the inversions which changed the prior estimates of the fossil fuel fluxes. These fluxes were not assigned error correlations. Those inversions which altered the prior estimates of the fossil fuel fluxes also had variable aggregated fluxes compared with the reference inversion. This is due to the inversion having limited ability to make large changes to the fossil fuel fluxes. The ensemble of posterior fluxes obtained from inversions with alternative prior fluxes allowed us to determine in which direction the inversion was attempting to adjust these fluxes, and provided us with an interval in which we could deduce the best estimate of the aggregated flux would lie. Changing the control vector also had a large influence on the aggregated flux, but this was largely due to periods with low data completeness.

## 6.5 Conclusions

Sensitivity tests have shown that to improve the inversion results for the Cape Town inversion, two important advancements should be made to the inversion framework. Firstly the NEE estimates need to be improved. The results from the reference inversion and from these sensitivity tests clearly indicate that CABLE is generally overestimating the amount of $CO_2$ uptake in the domain. Where there is more confidence in the estimation of the biogenic fluxes, either from CABLE for an alternative land-atmosphere exchange model, these reduced uncertainties should be incorporated into the prior information, rather than applying a blanket uncertainty equal to the NPP as done for the reference inversion. For example, over agricultural areas, where the biogenic fluxes may be more reliably modelled, uncertainties may be substantially reduced.

Solving for mean weekly fluxes over a month produced much larger uncertainty reductions. Using an alternative control vector which solves for separate components of the fossil fuel and NEE fluxes that can be split into slow and fast components could take advantage of the larger uncertainty reduction achieved from solving for a mean weekly flux for each month. This could potentially allow the inversion to better distinguish between NEE and fossil fuel fluxes, allowing the inversion to apply corrections to the correct flux, and at the same time obtain aggregated flux estimates with smaller uncertainties than those obtained for the reference inversion. The estimates

of the aggregated fluxes was shown to be more reliable in the reference inversion than those for the individual fossil fuel and NEE fluxes (Nickless et al., 2018).

The posterior uncertainties are highly dependent on the prior uncertainties. This was shown across several sensitivity tests, including the inversions which used alternative priors, inversions that used homogenised priors and inversions that adjusted the relative uncertainties of the prior fossil fuel and NEE fluxes. Of more concern is the large impact that the correlation assumed for the NEE fluxes had on the aggregated flux estimates and on the spatial distribution of the posterior fluxes. This has been observed in previous inversions (Lauvaux et al., 2016). Of all the specifications made, the correlation lengths are the most arbitrary, but can redefine the posterior flux estimates. The sensitivity tests suggested that correlations between observation errors were of less importance to the inversion result.

Approaches which attempt to solve for the uncertainties rather than relying on prior estimates may provide better estimates of the true uncertainty bounds around the inversion posterior flux estimates. Ganesan et al. (2014) and Wu et al. (2013) propose an hierarchical Bayesian approach to solve for hyper-parameters of the inversion, including the covariance terms, which could reduce the dependency of inversion results on expert opinion estimates of uncertainty.

These sensitivity analyses did not consider alternative atmospheric transport models. Sensitivity tests on previous city-scale inversions have shown this to be an important source of variation between inversion results (Lauvaux et al., 2016; Staufer et al., 2016). Future work on the Cape Town inversion will consider multiple atmospheric transport models, such as the WRF (Weather Research and Forecasting model coupled with Chemistry) regional climate model.

If enough of these sensitivity tests can be performed, and probability distribution around the posterior fluxes can be determined, which may provide better uncertainty limits around these estimates. The ability of running more inversions in a shorter period of time if a more efficient control vector is chosen would make running many more inversion specifications for such an exercise possible. Assigning probability distributions to these parameters that we test underpins the hierarchical Bayesian approach in Ganesan et al. (2014).

# Bibliography

Archibald, S. A., Kirton, A., van der Merwe, M. R., Scholes, R. J., Williams, C. A., and Hanan, N.: Drivers of inter-annual variability in Net Ecosystem Exchange in a semi-arid savanna ecosystem, South Africa, Biogeosciences, 6, 251-266, doi: 10.5194/bg-6-251-2009, 2009.

Bellassen, V. and Stephan, N.: Accounting for carbon: Monitoring, reporting and verifying emissions in the climate economy, Cambridge University Press, Cambridge, UK, 2015.

Bréon, F. M., Broquet, G., Puygrenier, V., Chevallier, F., Xueref-Remy, I., Ramonet, M., Dieudonné, E., Lopez, M., Schmidt, M., Perrussel, O., and Ciais, P.: An attempt at estimating Paris area $CO_2$ emissions from atmospheric concentration measurements, Atmos. Chem. Phys., 15, 1707–1724, doi: 10.5194/acp-15-1707-2015, 2015.

Chevallier, F., F.-M. Bréon, P. J. Rayner (2007), The contribution of the Orbiting Carbon Observatory to the estimation of $CO_2$ sources and sinks: Theoretical study in a variational data assimilation framework, J. Geophys. Res., 112, D09307, doi:10.1029/2006JD007375, 2007.

Department of Environmental Affairs (South Africa): South African National Terrestrial Carbon Sink Assessment, Department of Environmental Affairs, Pretoria, South Africa, 2015.

Engelbrecht, C. J., Engelbrecht, F. A. and Dyson, L. L.: High-resolution model-projected changes in mid-tropospheric closed-lows and extreme rainfall events over southern Africa. Int. J. Climatol., 33, 173–187, doi: 10/1002/joc.3420, 2013.

Exbrayat, J. -F., Pitman, A. J. Abramowitz, G. and Wang, Y, -P.: Sensitivity of net ecosystem exchange and heterotrophic respiration to parameterization uncertainty, J. Geophys. Res. Atmos., 118, 16401651, doi:10.1029/2012JD018122, 2013.

Feng, S., Lauvaux T., Newman, S., Rao, P., Ahmadov, R. Deng, A., Díaz-Isaac, L. I., Duren, R. M., Fischer, M. L., Gerbig, C., Gurney, K. R., Huang, J., Jeong, S., Li, Z., Miller, C. E., O'Keeffe, D., Patarasuk, R., Ser, S. P., Song, Y., Wong, K. W., and Yung, Y. L.: Los Angeles megacity: a high-resolution land–atmosphere modelling system for urban $CO_2$ emissions, Atmos. Chem. Phys., 16, 9019–9045, doi: 10.5194/acp-16-9019-2016, 2016.

Ganesan, A. L., Rigby, M., Zammit-Mangion, A., Manning, A. J., Prinn, R. G., Fraser, P. J., Harth, C. M., Kim, K. -R., Krummel, P. B., Li, S., Mühle, J., O'Doherty, S. J., Park, S., Salameh, P. K., Steele, L. P., and Weiss, R. F.: Characterization of uncertainties in atmospheric trace gas inversions using hierarchical Bayesian methods, Atmos. Chem. Phys., 14, 3855-3864, doi:10.5194/acp-14-3855-2014, 2014.

Gregor, L. and Monteiro P. M. S.: Is the southern Benguela a significant regional sink of CO2? S. Afr. J. Sci., 109(5/6), Art. #0094, 5 pages, doi: 10.1590/sajs.2013/20120094, 2013.

Gurney, K. R., Razlivanov, I., Song, Y., Zhou, Y., Benes, B., and Abdul–Massih, M.: Quantification of fossil fuel $CO_2$ emissions on the building/street scale for a large U.S. city, Environ. Sci. Technol., 46, 12194–12202, doi: 10.1021/es3011282, 2012.

Kowalczyk, E. A., Wang, Y. P. and Law, R. M.: CSIRO Atmosphere Biosphere Land Exchange model for use in climate models and as an offline model, CSIRO Marine and Atmospheric Research technical paper xxV ISBN 1 921232 39 0, 2006.

Lauvaux, T., Pannekoucke, O., Sarrat, C., Chevallier, F., Ciais, P., Noilhan, J., and Rayner, P. J.: Structure of the transport uncertainty in mesoscale inversions of $CO_2$ sources and sinks using ensemble model simulations, Biogeosciences, 6, 1089-1102, doi: 10.5194/bg-6-1089-2009, 2009.

Lauvaux, T., Schuh, A. E., Uliasz, M., Richardson, S., Miles, N., Andrews, A. E., Sweeney, C., Diaz, L. I., Martins, D., Shepson, P. B., and Davis, K. J.: Constraining the $CO_2$ budget of the corn belt: exploring uncertainties from the assumptions in a mesoscale inverse system, Atmos. Chem. Phys., 12, 337–354, doi: 10.5194/acp-12-337-2012, 2012.

Lauvaux, T., Miles, N. L., Deng, A. Richardson, S. J., Cambaliza, M. O., Davis, K. J., Gaudet, B., Gurney, K. R., Huang, J., O'Keefe, D., Song, Y., Karion, A., Oda, T.,

Patarasuk, R., Razlivanov, I., Sarmiento, D., Shepson, P., Sweeney, C., Turnbull, J., and Wu, K.: High-resolution atmospheric inversion of urban $CO_2$ emissions during the dormant season of the Indianapolis Flux Experiment (INFLUX), J. Geophys. Res. Atmos., 121, 5213–5236, doi: 10.1002/2015JD024473, 2016.

McGregor, J. L. and Dix, M. R.: The CSIRO conformal-cubic atmospheric GCM, in: IUTAM Symposium on Advances in Mathematical Modelling of Atmosphere and Ocean Dynamics, Limerick, Ireland, 2–7 July 2000, edited by: Hodnett, P. F., Kluwer, Dordrecht, 197–202, 2001.

Michalak, A. M., Hirsch, A., Bruhwiler, L., Gurney, K. R., Peters, W., and Tans, P. P.: Maximum likelihood estimation of covariance parameters for Bayesian atmospheric trace gas surface flux inversions, J. Geophys. Res., 110, D24107, doi: 10.1029/2005JD005970, 2005.

Moncrieff, G.R., Scheiter,S. Slingsby, J. A. and Higgins, S. I.: Understanding global change impacts on South African biomes using Dynamic Vegetation Models, S. Afr. J. Bot., 101, 16–23, doi: 10.1016/j.sajb.2015.02.004, 2015.

Nassar, R.,Napier-Linton, L., Gurney, K. R., Andres, R. J., Oda, T., Vogel, F. R. and Deng, F.: Improving the temporal and spatial distribution of $CO_2$ emissions from global fossil fuel emission data sets, J. Geophys. Res. Atmos.,118, 917-933, doi: 10.1029/2012JD018196, 2013.

Nickless, A., Scholes, R. J. and Filby, E.: Spatial and temporal disaggregation of anthropogenic $CO_2$ emissions from the City of Cape Town, S. Afr. J. Sci., 111(11/12), Art. $\#2014 - 0387$, 8 pages, doi: 10.17159/sajs.2015/20140387, 2015.

Nickless, A., Ziehn, T., Rayner, P. J., Scholes, R .J., and Engelbrecht, F.: Greenhouse gas network design using backward Lagrangian particle dispersion modelling – Part 2: Sensitivity analyses and South African test case, Atmos. Chem. Phys., 15, 2051–2069, doi: 10.5194/acp-15-2051-2015, 2015.

Nickless, A., Rayner, P. J., Engelbrecht, F., Brunke, E.-G., Erni, B., and Scholes, R. J.: Estimates of $CO_2$ fluxes over the city of Cape Town, South Africa, through Bayesian inverse modelling, Atmos. Chem. Phys., 18, 4765-4801, doi: 10.5194/acp-18-4765-2018, 2018.

Oda, T. and Maksyutov, S.: A very high-resolution (1 km×1 km) global fossil fuel $CO_2$ emission inventory derived using a point source database and satellite observations of nighttime lights, Atmos. Chem. Phys., 11, 543-556, doi:10.5194/acp-11-543-2011, 2011.

Oda, T., Lauvaux, T., Lu, D., Rao, P., Miles, N. L., Richardson, S. J. and Gurney, K. R.: On the impact of granularity of space-based urban $CO_2$ emissions in urban atmospheric inversions: A case study for Indianapolis, IN, Elem Sci Anth, 5, 28, doi: 10.1525/elementa.146, 2017.

Oda, T., Maksyutov, S., and Andres, R. J.: The Open-source Data Inventory for Anthropogenic Carbon dioxide ($CO_2$), version 2016 (ODIAC2016): A global, monthly fossil-fuel $CO_2$ gridded emission data product for tracer transport simulations and surface flux inversions, Earth Syst. Sci. Data Discuss., doi: 10.5194/essd-2017-76, in review, 2017.

Roux, B.: Ultra high-resolution climate simulations over the Stellenbosch wine producing region using a variable-resolution model, MSc Thesis, Faculty of Natural and Agricultural Sciences, University of Pretoria, South Africa, 106 pp., 2009.

Scholes, R. J., von Maltitz, G. P., Archibald, S. A., Wessels, K., van Zyl, T., Swanepoel, D., and Steenkamp, K.: National Carbon Sink Assessment for South Africa: First Estimate of Terrestrial Stocks and Fluxes, CSIR Technical Report, Pretoria, South Africa, CSIR/NRE/GC/ER/2013/0056/B, 2013.

Seibert, P. and Frank, A.: Source-receptor matrix calculation with a Lagrangian particle dispersion model in backward mode, Atmos. Chem. Phys., 4, 51–63, doi: 10.5194/acp-4-51-2004, 2004.

Staufer, J., Broquet, G., Bréon, F. -M., Puygrenier, V., Chevallier, F., Xueref-Rémy, I., Dieudonné, E., Lopez, M., Schmidt, M., Ramonet, M., Perrussel, O., Lac, C., Wu, L., and Ciais, P.: The first 1-year-long estimate of the Paris region fossil fuel CO2 emissions based on atmospheric inversion, Atmos. Chem. Phys., 16, 14703–14726, doi: 10.5194/acp-16-14703-2016, 2016.

Tarantola, A.: Inverse Problem Theory and Methods for Model Parameter Estimation, Society for Industrial and Applied Mathematics, Philadelphia, 2005.

Turnbull, J. C., Karion, A., Fischer, M. L., Faloona, I., Guilderson, T., Lehman, S. J., Miller, B. R., Miller, J. B., Montzka, S., Sherwood, T., Saripalli, S., Sweeney, C., and Tans, P. P.: Assessment of fossil fuel carbon dioxide and other anthropogenic trace gas emissions from airborne measurements over Sacramento, California in spring 2009, Atmos. Chem. Phys., 11, 705-721, doi: 10.5194/acp-11-705-2011, 2011.

Uliasz, M.: Lagrangian particle modeling in mesoscale applications, in: Environmental Modelling II, Computational Mechanics Publications, Southampton, UK, 71–102, 1994.

Wu, L., Bocquet, M., Chevallier, F., Lauvaux, T., and Davis, K.: Hyperparameter estimation for uncertainty quantification in mesoscale carbon dioxide inversions, Tellus B, 65, 20894, doi: 10.3402/tellusb.v65i0.20894, 2013.

Wu, L., Broquet, G., Ciais, P., Bellassen, V., Vogel, F., Chevallier, F., Xueref-Remy, I., and Wang, Y.: What would dense atmospheric observation networks bring to the quantification of city $CO_2$ emissions?, Atmos. Chem. Phys., 16, 7743–7771, doi: 10.5194/acp-16-7743-2016, 2016.

Zhang, H., Pak, .B., Wang, Y. P., Zhou, X., Zhang, Y. and Zhang, L.: Evaluating surface water cycles simulated by the Australian community land surface model (CABLE) across different spatial and temporal domains. J. Hydrometeor, 14, 1119–1138, 2013.

Zhang, Y., Gao, Z., Li, D., Li, Y., Zhang, N., Zhao, X., and Chen, J.: On the computation of planetary boundary-layer height using the bulk Richardson number method, Geosci. Model Dev., 7, 2599–2611, doi: 10.5194/gmd-7-2599-2014, 2014.

Ziehn, T., Nickless, A., Rayner, P. J., Law, R. M., Roff, G., and Fraser, P.: Greenhouse gas network design using backward Lagrangian particle dispersion modelling – Part 1: Methodology and Australian test case, Atmos. Phys. Chem., 14, 9363–9378, doi: 10.5194/acp-14-9363-2014, 2014.

# Chapter 7

# Conclusions

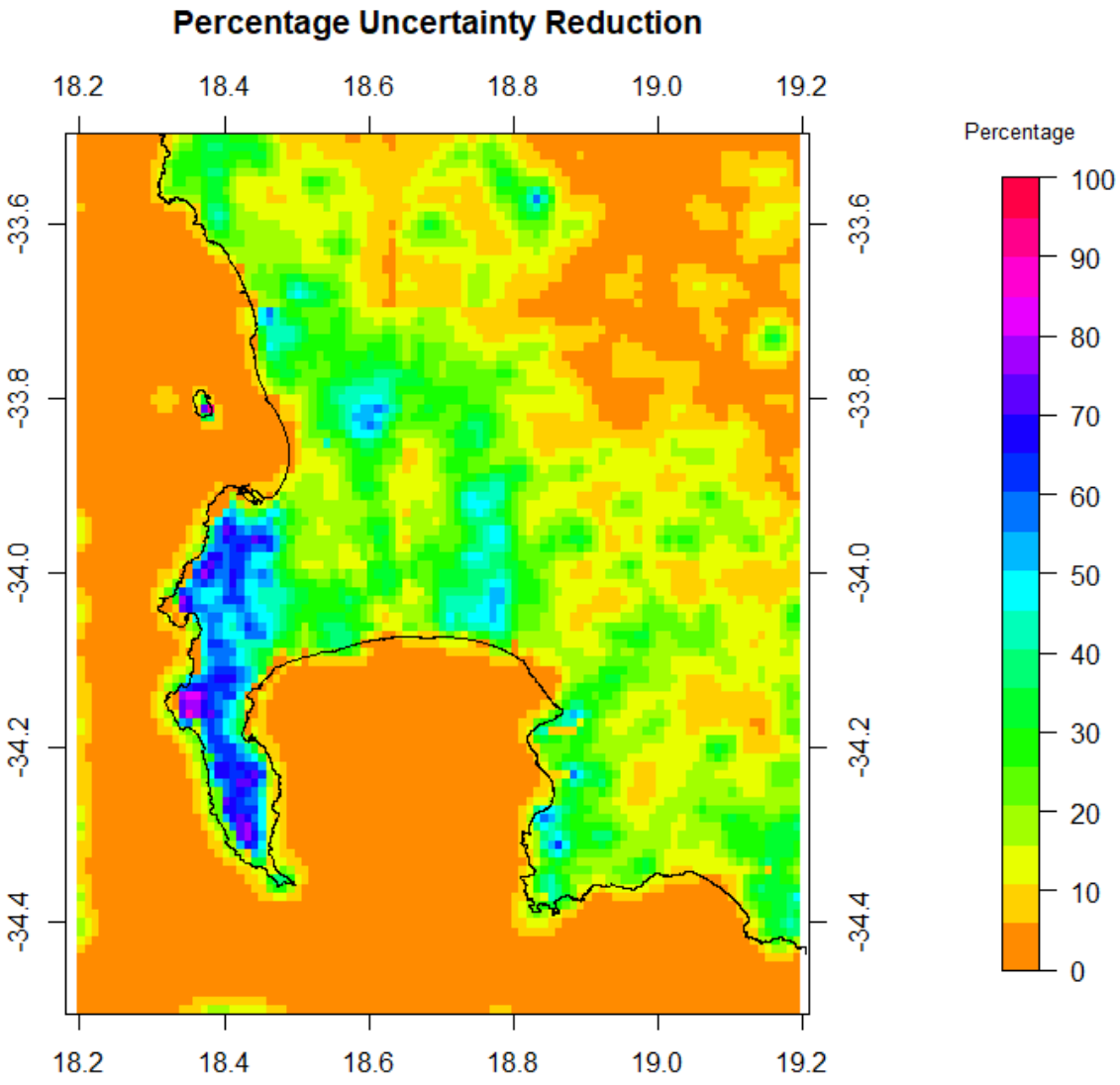

# Chapter 7

# Conclusions

## 7.1 Optimal Observation Network

The optimal network design, under various sensitivity tests, placed stations near the central interior, close to the industrial heart of South Africa, and in areas to the east of South Africa, where some of the largest biogenic fluxes occur, particularly over the summer months. This was consistent with the network design of Lauvaux et al. (2012) which showed that sites could only provide constraint for those fluxes located within a hundred kilometres from the tower. The uncertainty reduction ranged between 76.5% and 78.8% in January, and between 42.9% and 43.3% in July. Three locations were common across most of the network solutions. These three sites played an important role in reducing the uncertainty in the fluxes, under the assumed prior fluxes and uncertainties prescribed in this study. These sites were located near areas with existing infrastructure available for measurements, such as the Welgegund atmospheric monitoring site of the North West University and Helsinki University collaboration, therefore there is potential for deployment of measurement equipment to these locations. As these sites had previous measurements or have current measurement of atmospheric constituents, it would imply that the solution for the network design problem agrees with previous assessments of where might be good locations to make atmospheric observations of trace gases in South Africa.

Network solutions were sensitive to the spatial resolution of the prior fluxes, which is shown in other network design studies (e.g. Lauvaux et al. (2012); Kaminski and Rayner (2017)). Depending on the coarseness of the spatial resolution, our sensitivity tests showed that sites that were prone to large aggregation errors could be excluded from the optimal design, even if they were in view of important sourced of $CO_2$ fluxes. The difference between January (South African summer) and July (South African winter) indicated that the biogenic fluxes played an important role in the placement

of stations in this network design problem. If biogenic fluxes could be estimated with greater confidence, then the contribution of the total uncertainty would shift towards the fossil fuel fluxes, and the network design would then favour placing constraint on these fluxes.

Spatial error correlations had a very large impact on the placement of stations. The specification of these error correlations is not trivial and no consensus exists on the best way of making decisions on what these should be in the context of a Bayesian inverse modelling framework, where the posterior estimates and their uncertainties are largely driven by these expert-based estimates of the fluxes and their uncertainties (Chevallier et al., 2006; Lauvaux et al., 2012).

The error structure is potentially complex due to the existence of anthropogenic point sources in close proximity to large, but dispersed, biogenic fluxes. The large number of $CO_2$ sources and the overlapping nature of anthropogenic and biospheric sources could lead to difficulty in accurately placing stations to optimise the uncertainty reduction in the fluxes, simply by looking at where these sources are and the average wind fields. It is also important to incorporate information such as aggregation error, which can be done in the context of an optimal network design using the Bayesian inversion framework, as these errors could have a large impact on the placement of stations dues to large anticipated errors in modelled concentrations at particular sites. Two optimisation procedures that have previously been used for optimising the placement of observation sites were compared: the genetic algorithm (GA) and incremental optimisation (IO). Both are methods for optimising non-linear models, where a model refers to an algorithm, in this case for uncertainty reduction, which produces a quantity as a function of inputs (Rayner, 2004). There were no large differences in the placement or uncertainty reduction achieved by the GA, which may require considerable resources depending on the size of the sensitivity and covariance matrices in the inversion, compared with the resources required by the IO routine. As the spatial resolution of the prior fluxes and the complexity in the biogenic fluxes increased, the number of iterations and population members required for a stable solution from the GA increased. The comparison of the GA with IO revealed that even under more complex network design problems than that of establishing a new network for constraining terrestrial fluxes from South African, the IO solution was still competitive with that of an optimally parametrised GA.

## 7.2 Fossil Fuel Inventory Analysis

The aggregated Cape Town fossil fuel fluxes were dominated by a few industrial sources, such as the oil refinery north of the central business district (CBD). The spatial distribution was largely determined by the vehicle and domestic emissions. When compared to products such as EDGAR (Emission Database for Global Atmospheric Research) (Janssens-Maenhout et al., 2012) or ODIAC (Open-source Data Inventory for Anthropogenic $CO_2$) (Oda and Maksyutov, 2011; Lauvaux et al., 2016; Oda et al. , 2017a,b), the spatial distribution largely agreed, although these products had a smoother distribution of fluxes across the city, and a greater spatial extent compared with the inventory analysis performed for this study. The aggregated fossil fuel fluxes were larger than when compared with EDGAR 2010, but smaller when compared with the ODIAC product.

The uncertainty analysis of the fossil fuel fluxes from different sectors were based on expert guidelines, where possible, but these may be based on limited evidence. We did not account for uncertainty due to missing fossil fuel sources. An increase in the fossil fuel uncertainty to account for this, and an allowance for fossil fuel fluxes to occur where none were present in the inventory, would allow the inversion more ability to make changes to the prior fossil fuel fluxes in accordance with the observations, rather than relying on changing the biogenic fluxes to obtain smaller misfits between the modelled and observed concentrations.

The domestic emissions played an important role in determining the temporal distribution of the fossil fuel fluxes. This component of the inventory analysis could have been improved by survey information on domestic fuel use, and from better distinction between domiciles, so that the domestic emissions could be more realistically allocated across space, rather than assuming all households had the same fuel use.

## 7.3 Cape Town $CO_2$ Fluxes

This paper represents a first attempt at estimating $CO_2$ fluxes at the high resolution of 1 km by 1 km over Cape Town, solving for individual fossil fuel, terrestrial and oceanic biogenic sources. The inversion was able to reduce uncertainty of the total flux within a pixel by up to 97.7%, and was able to reduce the uncertainty in the total weekly flux over the whole domain by up to 50.5%. The largest innovation to a fossil fuel flux was applied to the pixel with the largest point-source fossil fuel flux of the oil-refinery. In the main Cape Town inversion, and in the sensitivity tests,

the inversion attempted to make this flux less positive by reducing fossil fuel flux in this pixel and by creating areas of more negative fluxes around this pixel. This indicates that either the prior fossil fuel flux is over-estimated, or the atmospheric transport model is not correctly indicating sensitivity to this flux at the measurement site. It is unlikely that an atmospheric observation network with only two sites will be able to successfully constrain a point industrial source. Compared with the fossil fuel emissions, relative innovations to the NEE fluxes were much larger, due to the large uncertainty prescribed to these fluxes. The largest innovations were made to natural areas near the CBD of Cape Town, as well as to agricultural regions within the domain, particularly those close to the measurement sites.

The results of the inversion over Cape Town demonstrated the ability of the Bayesian inverse modelling approach to take advantage of aggregating fluxes. The inversion creates negative covariances in the posterior uncertainty covariance matrix for those fluxes that are viewed simultaneously at the atmospheric measurement site. When we sum these fluxes, the effect of these negative covariances is to reduce the uncertainty of the aggregated flux - over and above the uncertainty reduction achieved by the inversion for the individual fluxes.

## 7.4 Biogenic Fluxes

The prior estimates are dependent on the CABLE land-atmosphere exchange model and, although driven by the CCAM regional climate model, which in turn was driven by reliable reanalysed observations of the climate from NCEP, is still under ongoing development for use over South Africa. There is a great deal of uncertainty in its ability to simulate fluxes over the fynbos biome, as there is for most dynamic vegetation models (Moncrieff et al., 2015). In general, the inversion tended to increase the NEE fluxes so that the total flux was less negative compared with the priors, indicating that the amount of productivity estimated by CABLE may be too large.

As for the network design, the posterior flux estimates for the Cape Town inversion were largely determined by the specification of the biogenic fluxes, their uncertainties and the error correlations. This has been observed in previous inversions (Lauvaux et al., 2016). These prior specifications impacted the aggregated flux as well as the spatial distribution of the fluxes. To obtain estimates of $CO_2$ fluxes for South Africa through inverse modelling, at the regional or city-scale level, better estimates of biogenic fluxes are required. Therefore investment of time and resources in developing and validating land-atmosphere exchange models should be a priority if this

approach is to be used for monitoring, reporting and verification (MRV) of fossil fuel emissions. Therefore development work on modelling schemes such as the Variable Resolution Earth System Model (VRESM) of the CSIR (Council for Scientific and Industrial Research), which aims to couple CCAM, CABLE, CSIR's Variable-Cubic Ocean Model (VCOM), and Pelagic Interactions Scheme for Carbon and Ecosystem Studies (PISCES) (Engelbrecht et al., 2016), is important. Better parametrisation and validation of each of component is critical to ensure that, not only are the different models successfully coupled, but that they are accurately representing the biosphere. The dependence on more accurate and precise estimates of NEE fluxes to estimate the fossil fuel fluxes could be reduced if there were additional measurements of $\Delta^{14}$C and $\delta^{13}$C isotope measurements at each of the sites, including at the background site (Turnbull et al., 2015; Newman et al., 2016).

The sensitivity tests showed that solving for mean weekly fluxes produced much larger uncertainty reductions than those solving for four separate weekly fluxes. Using an alternative control vector which solved for mean weekly fluxes for NEE, but separate weekly fluxes for fossil fuel emissions, could take advantage of this uncertainty reduction. This could potentially allow the inversion to better distinguish between NEE and fossil fuel fluxes, allowing the inversion to apply corrections to the correct flux, and at the same time obtain aggregated flux estimates with smaller uncertainties than those obtained for the reference inversion. Removal of the biogenic error correlations reduced the inversions ability to make corrections to the unknown fluxes, leaving he posterior estimates very similar to the priors. Therefore accurately estimating these error correlations can enhance the inversion's ability to spread corrections to the unknown fluxes. Poor estimates of the error correlation lengths will lead to corrections to fluxes where they are not applicable.

## 7.5 Future Work

This work shows the importance of the biospheric fluxes in deciding where to locate stations, and in solving for the fossil fuel fluxes from a city. This provides an opportunity to further our understanding of carbon processes in diversity-rich biomes, such as the fynbos, by obtaining more measurements of fluxes in these landscapes, for example using eddy covariance measurements, which can help to challenge our current models for productivity in these regions and their responses to climate inputs. This could potentially be carried out in an integrated project which incorporates atmospheric measurements of $CO_2$ concentrations, and allows the eddy-covariance data

to inform the estimates of the fluxes and their uncertainties in at least part of the footprint used in an atmospheric inversion exercise. Using eddy-covariance data as a comparison to inversion estimates of fluxes has happened for large-scale mesoscale inversions (e.g. Chevallier et al. (2012); Dolman et al. (2012); Kountouris et al. (2015); Molina et al. (2015)), but making use of eddy-covariance measurements has been less used for city-scale inversions (e.g. Davis et al. (2013)), and there is still work to be done in order to assimilate these measurements as part of the data in an atmospheric inversion, rather than as a comparator to the inversion results.

The solution to the posterior uncertainty covariance matrix clearly shows that these uncertainties are highly dependent on the prior uncertainties. This was reflected across several sensitivity tests, including the inversions which used alternative priors, inversions that used homogenised priors and inversions that adjusted the relative uncertainties of the prior fossil fuel and NEE fluxes. Of most concern is the large impact that the error correlation assumed for the NEE fluxes had on the aggregated flux estimates and on the spatial distribution of the posterior fluxes. These error correlations impact on the posterior uncertainties, which is why they have a large impact on the network design solution as well. This has been observed in previous inversions (Lauvaux et al., 2016) and network designs (Lauvaux et al., 2012a). Of all the specifications made, the correlation lengths are the most arbitrary, but can redefine the posterior flux estimates.

Approaches which attempt to solve for the uncertainties rather than relying on prior estimates may provide better estimates of the true uncertainty bounds around the inversion posterior flux estimates. Ganesan et al. (2014) and Wu et al. (2013) propose an hierarchical Bayesian approach to solve for hyper-parameters of the inversion, including the covariance terms, which could reduce the dependency of inversion results on expert opinion estimates of uncertainty. If enough sensitivity tests can be performed, a probability distribution around the posterior fluxes can be determined, which may provide better limits of uncertainty around the flux estimates. The ability of running more inversions in a shorter period of time if a more efficient control vector is chosen would make running many more inversion specifications for such an exercise possible. Assigning probability distributions to the parameters of the inversion framework that are tested underpins the hierarchical Bayesian approach in Wu et al. (2013) and Ganesan et al. (2014). Estimating ensemble posterior fluxes and their uncertainties from inversions under different specifications has been suggested by Lauvaux et al. (2016), which is a type of meta-analysis approach.

Sensitivity tests on previous city-scale inversions have shown that the atmospheric model can have a significant impact on the inversion results (Lauvaux et al., 2016; Staufer et al., 2016), and on optimal network designs (Kaminski and Rayner, 2017). For both the network design and the Cape Town inversion, no sensitivity tests were performed on the atmospheric transport model or on the regional climate model. The analysis of the aggregation error, just one component of the total observation error, for the network design in Chapter 2 revealed that these errors could be large for many sites across South Africa, particularly those close to both large biospheric sources and fossil fuel emissions. Further work is needed in order to assess how well inversion results agree if alternative regional climate models or Lagrangian particle dispersion models, such as FLEXPART or STILT, are used in comparison with our CCAM/LPDM set up. It is also possible to include perturbations in the regional climate model which are still physically consistent, and assess the sensitivity of the inversion to the perturbations (e.g. Lauvaux et al. (2009)). Future work on the Cape Town inversion will consider alternative regional climate models, such as the WRF (Weather Research and Forecasting model coupled with Chemistry) regional climate model. WRF is a potential comparator to CCAM as this model has been used for several mesoscale and city-scale inversions (Lauvaux et al., 2012b; Lauvaux et al., 2016; Oda et al. , 2017a).

# Bibliography

Chevallier, F., Viovy, N., Reichstein, M., and Ciais, P.: On the assignment of prior errors in Bayesian inversions of $CO_2$ surface fluxes. Geophys. Res. Lett., 33, LL13802, doi: 10.1029/2006GL026496, 2006.

Chevallier, F., Wang, T., Ciais, P., Maignan, F., Bocquet, M., Arain, M. A., Cescatti, A., Chen, J., Dolman, A. J., Law, B. E., Margolis, H. A., Montagnani, L., and Moors, E. J.: What eddy-covariance measurements tell us about prior land flux errors in $CO_2$-flux inversion schemes, Global Biogeochem. Cy., 26, GB1021, doi: 10.1029/2010GB003974, 2012.

Davis, K. J., Deng, A., Lauvaux, T., Miles, N. L., Richardson, S. J., Sarmiento, D. P., Gurney, K. R., Hardesty, R. M., Bonin, T. A., Brewer, W. A., Lamb, B. K., Shepson, P. B., Harvey, R. M., Cambaliza, M. O., Sweeney, C., Turnbull, J. C., Whetstone, J., and Karion, A.: The Indianapolis Flux Experiment (INFLUX): A test-bed for developing urban greenhouse gas emission measurements, Elem. Sci. Anth., 5, 21, doi: 10.1525/elementa.188, 2013.

Dolman, A. J., Shvidenko, A., Schepaschenko, D., Ciais, P., Tchebakova, N., Chen, T., van der Molen, M. K., Belelli Marchesini, L., Maximov, T. C., Maksyutov, S., and Schulze, E.-D.: An estimate of the terrestrial carbon budget of Russia using inventory-based, eddy covariance and inversion methods, Biogeosciences, 9, 5323–5340, doi: 10.5194/bg-9-5323-2012, 2012.

Engelbrecht, F. A., McGregor, J. L., Thatcher, M., Garland, R., Sovara, M., Bopane, M. M., and van der Merwe, J.: The Variable-Resolution Earth System Model and its simulations of the Benguela upwelling system. The International Conference on Regional Climate CORDEX 2016, Stockholm, Sweden, 17–20 May 2016, 2016.

Ganesan, A. L., Rigby, M., Zammit-Mangion, A., Manning, A. J., Prinn, R. G., Fraser, P. J., Harth, C. M., Kim, K. -R., Krummel, P. B., Li, S., Mühle, J.,

O'Doherty, S. J., Park, S., Salameh, P. K., Steele, L. P., and Weiss, R. F.: Characterization of uncertainties in atmospheric trace gas inversions using hierarchical Bayesian methods, Atmos. Chem. Phys., 14, 3855-3864, doi:10.5194/acp-14-3855-2014, 2014.

Janssens-Maenhout, G., Pagliari, V., Guizzardi, D., and Muntean, M.: Global emission inventories in the Emission Database for Global Atmospheric Research (EDGAR) Manual (I). Gridding: EDGAR emissions distribution on global gridmaps. Joint Research Centre, Luxembourg: European Union, 33 pp, doi: 10.2788/81454, 2012.

Kaminski, T. and Rayner, P .J.: Reviews and syntheses: guiding the evolution of the observing system for the carbon cycle through quantitative network design, Biogeosciences, 14, 4755-4766, doi: 10.5194/bg-14-4755-2017, 2017.

Kountouris, P., Gerbig, C., Totsche, K.-U., Dolman, A. J., Meesters, A. G. C. A., Broquet, G., Maignan, F., Gioli, B., Montagnani, L., and Helfter, C.: An objective prior error quantification for regional atmospheric inverse applications, Biogeosciences, 12, 7403–7421, doi: 10.5194/bg-12-7403-2015, 2015.

Lauvaux, T., Pannekoucke, O., Sarrat, C., Chevallier, F., Ciais, P., Noilhan, J., and Rayner, P. J.: Structure of the transport uncertainty in mesoscale inversions of $CO_2$ sources and sinks using ensemble model simulations, Biogeosciences, 6, 1089–1102, doi: 10.5194/bg-6-1089-2009, 2009.

Lauvaux, T., Schuh, A. E., Bouquet, M., Wu, L., Richardson, S., Miles, N., and Davis, K. J.: Network design for mesoscale inversions of $CO_2$ sources and sinks, Tellus, 64B, doi:10.3402/tellusb.v64i0.17980, 2012a.

Lauvaux, T., Schuh, A. E., Uliasz, M., Richardson, S., Miles, N., Andrews, A. E., Sweeney, C., Diaz, L. I., Martins, D., Shepson, P. B., and Davis, K. J.: Constraining the $CO_2$ budget of the corn belt: exploring uncertainties from the assumptions in a mesoscale inverse system, Atmos. Chem. Phys., 12, 337–354, doi: 10.5194/acp-12-337-2012, 2012b.

Lauvaux, T., Miles, N. L., Deng, A. Richardson, S. J., Cambaliza, M. O., Davis, K. J., Gaudet, B., Gurney, K. R., Huang, J., O'Keefe, D., Song, Y., Karion, A., Oda, T., Patarasuk, R., Razlivanov, I., Sarmiento, D., Shepson, P., Sweeney, C., Turnbull, J., and Wu, K.: High-resolution atmospheric inversion of urban $CO_2$ emissions during

the dormant season of the Indianapolis Flux Experiment (INFLUX), J. Geophys. Res. Atmos., 121, 5213–5236, doi: 10.1002/2015JD024473, 2016.

Molina, L., Broquet, G., Imbach, P., Chevallier, F., Poulter, B., Bonal, D., Burban, B., Ramonet, M., Gatti, L. V., Wofsy, S. C., Munger, J. W., Dlugokencky, E., and Ciais, P.: On the ability of a global atmospheric inversion to constrain variations of $CO_2$ fluxes over Amazonia, Atmos. Chem. Phys., 15, 8423-8438, doi: 10.5194/acp-15-8423-2015, 2015.

Moncrieff, G.R., Scheiter,S. Slingsby, J. A. and Higgins, S. I.: Understanding global change impacts on South African biomes using Dynamic Vegetation Models, S. Afr. J. Bot., 101, 16–23, doi: 10.1016/j.sajb.2015.02.004, 2015.

Newman, S., Xu, X., Gurney, K. R., Hsu, Y. K., Li, K. F., Jiang, X., Keeling, R., Feng, S., O'Keefe, D., Patarasuk, R., Wong, K. W., Rao, P., Fischer, M. L., and Yung, Y. L.: Toward consistency between trends in bottom-up $CO_2$ emissions and top-down atmospheric measurements in the Los Angeles megacity, Atmos. Chem. Phys., 16, 3843–3863, doi: 10.5194/acp-16-3843-2016, 2016.

Oda, T. and Maksyutov, S.: A very high-resolution (1 km×1 km) global fossil fuel CO2 emission inventory derived using a point source database and satellite observations of nighttime lights, Atmos. Chem. Phys., 11, 543-556, doi:10.5194/acp-11-543-2011, 2011.

Oda, T., Lauvaux, T., Lu, D., Rao, P., Miles, N. L., Richardson, S. J. and Gurney, K. R.: On the impact of granularity of space-based urban $CO_2$ emissions in urban atmospheric inversions: A case study for Indianapolis, IN, Elem Sci Anth, 5, 28, doi: 10.1525/elementa.146, 2017a.

Oda, T., Maksyutov, S., and Andres, R. J.: The Open-source Data Inventory for Anthropogenic Carbon dioxide ($CO_2$), version 2016 (ODIAC2016): A global, monthly fossil-fuel $CO_2$ gridded emission data product for tracer transport simulations and surface flux inversions, Earth Syst. Sci. Data Discuss., doi: 10.5194/essd-2017-76, in review, 2017b.

Rayner, P. J.: Optimizing $CO_2$ observing networks in the presence of model error: results from TransCom 3, Atmos. Chem. Phys., 4, 413–421, doi: 10.5194/acp-4-413-2004, 2004.

Staufer, J., Broquet, G., Bréon, F. -M., Puygrenier, V., Chevallier, F., Xueref-Rémy, I., Dieudonné, E., Lopez, M., Schmidt, M., Ramonet, M., Perrussel, O., Lac, C., Wu, L., and Ciais, P.: The first 1-year-long estimate of the Paris region fossil fuel CO2 emissions based on atmospheric inversion, Atmos. Chem. Phys., 16, 14703–14726, doi: 10.5194/acp-16-14703-2016, 2016.

Turnbull, J. C., Sweeney, C., Karion, A., Newberger, T., Lehman, S. J., Tans, P. P., Davis, K. J., Lauvaux, T., Miles, N. L., Richardson, S. J., Cambaliza, M. O., Shepson, P. B., Gurney, K., and Patarasuk, P.: Toward quantification and source sector identification of fossil fuel $CO_2$ emissions from an urban area: Results from the INFLUX experiment, J. Geophys. Res. Atmos., 120, 292–312, doi: 10.1002/2014JD022555, 2015.

Wu, L., Bocquet, M., Chevallier, F., Lauvaux, T., and Davis, K.: Hyperparameter estimation for uncertainty quantification in mesoscale carbon dioxide inversions, Tellus B, 65, 20894, doi: 10.3402/tellusb.v65i0.20894, 2013.

# Appendix A

# Appendix - Chapter 3

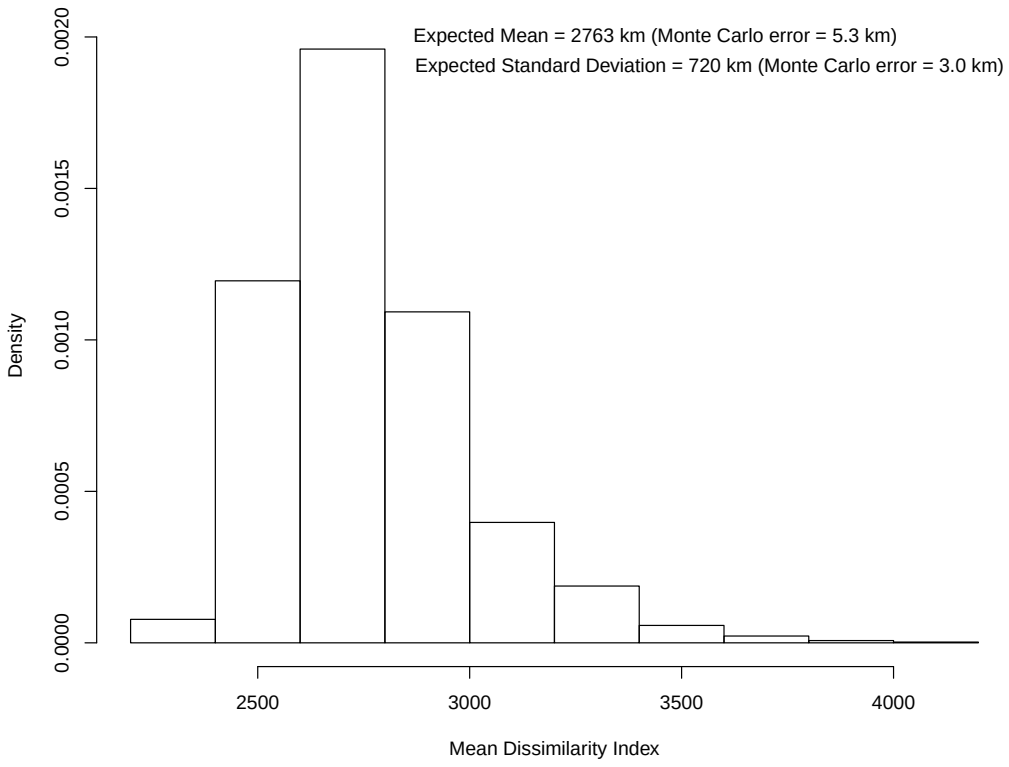


Figure A.1: Histogram showing the distribution of the means for the dissimilarity index arising for 2000 generated pairs of network members. The expected mean and standard deviation for the dissimilarity index, together with Monte Carlo errors, are provided.

As the dissimilarity index (DI) was likely to have a non-normal distribution, the distribution characteristics were determined via simulation. The DI was calculated

between every pair of randomly generated five-member networks within the domain, where 2000 of these five-member networks were randomly sampled from the set of available stations. For each simulation of 2000 network solutions, the mean, variance, minimum and maximum of the DI's was determined. These distribution characteristics should be invariant to the number of randomly generated solutions, which represents a large pool of potential network solutions. This was repeated 2000 times (the bootstrap sample size). The distribution of the mean DI's is plotted in Figure A.1, and the expected mean and standard deviation, as determined from the empirical summary statistics of the bootstrap samples, together with Monte Carlo error estimates are provided.

# Appendix B

# Supplementary Material - Chapter 5

## B.1 $CO_2$ Measurements

A single calibration standard was kept at each site, and run periodically in order to assess whether any drift occurred in the $CO_2$ measurements over time, to determine if the calibration coefficients required any adjustment. At Robben Island the measurements of the calibration standard were (mean ± (standard deviation)) 386.89 ppm (± 0.014) in November, 385.67 ppm (± 0.012) in February 2013, and 385.73 ppm (± 0.012) in June 2013. This indicates that the instrument was making stable measurements during the sixteen month campaign. The slightly higher reading in November 2012 occurred when the weather was wet, and there was more moisture contamination from the previous ambient measurements prior to calibration. At Hangklip the instrument measured the calibration standard at 378.26 ppm (± 0.009) in November 2012 and at 378.16 ppm (± 0.022) in June 2013, indicating no evidence of drift over the measurement period.

In addition to each site's calibration standard, a travelling reference standard was also measured at close proximity in time at all three sites, including Cape Point. This standard consisted of clean air collected at the Cape Point site. The results of two of these calibration measurements are presented in Table B.1. By comparing calibration measurements with Cape Point inter-site differences are ensured to be negligible, and also links the Robben Island and Hangklip sites into the greater GAW network. The instruments at Cape Point are routinely calibrated with standards shared around the GAW network, which maintains high levels of quality control. Differences were found to be small between sites, and between calibration periods using the same standard in June 2012 and June 2013.

Table B.1: Mean and standard deviation of $CO_2$ measurements (ppm) during calibration phase using a travelling $CO_2$ standard (June 2012 and June 2013) traceable to several Cape Point $CO_2$ laboratory standards. These in turn are linked to primary $CO_2$ standards maintained at the NOAA calibration laboratory in Boulder, USA.

| FA01830 | Site | | | |
|---|---|---|---|---|
| Date | Cape Point | Robben Island | Hangklip | Maximum inter-site difference |
| June 2012 | 452.77 (0.03) | 452.88 (0.02) | 452.89 (0.03) | 0.12 |
| June 2013 | 452.28 (0.03) | 452.86 (0.02) | 452.60 (0.03) | 0.58 |
| June 2012 - June 2013 | 0.49 | 0.02 | 0.29 | |

The observed hourly $CO_2$ concentrations at the Robben Island and Hangklip sites are presented in Figure B.1, together with the hourly measurements at Cape Point and the measured daily temperature at this site. There is no clear correlation between the peaks in $CO_2$ and daily temperature. From March 2012 until June 2013, the mean $CO_2$ concentration observed at Robben Island was 391.3 ppm ($\pm$ 5.02), usually ranging between 389.5 and 394.2 ppm, with a minimum of 382.4 ppm and a maximum of 445.0 ppm. The measurements at Hangklip had a similar mean of 390.6 ppm ($\pm$ 3.89), usually ranging between 389.5 and 391.4 ppm with a minimum of 380.4 ppm and a maximum of 430.6 ppm. The Cape Point measurements have a narrower range of 382.9 to 412.3 ppm, with a mean of 392.1 ppm, indicating less influence from local sources and sinks.

The mean diurnal cycle for each month is presented in Figure B.2. Across all months, the diurnal cycle of $CO_2$ concentrations at Cape Point are relatively flat compared with Robben Island and Hangklip. In November 2012 and February 2013 the diurnal cycle for both measurement sites was the most flat. This is the summer period, when temperatures are high and the Western Cape experiences the lowest amount of rain. The amplitude of the diurnal cycle at both sites increased from April, reaching a maximum amplitude in June and July. This is during the winter rainfall period in the Western Cape. Temperatures are mild and much of the vegetation growth occurs during this period. The diurnal cycle of the Hangklip site dipped below both Cape Point and Robben Island, indicating that this site is more affected by local sinks of $CO_2$. Robben Island consistently had the highest peaks in $CO_2$ concentrations across all months, indicating that this site was the most affected by local sources, which is what we expected.

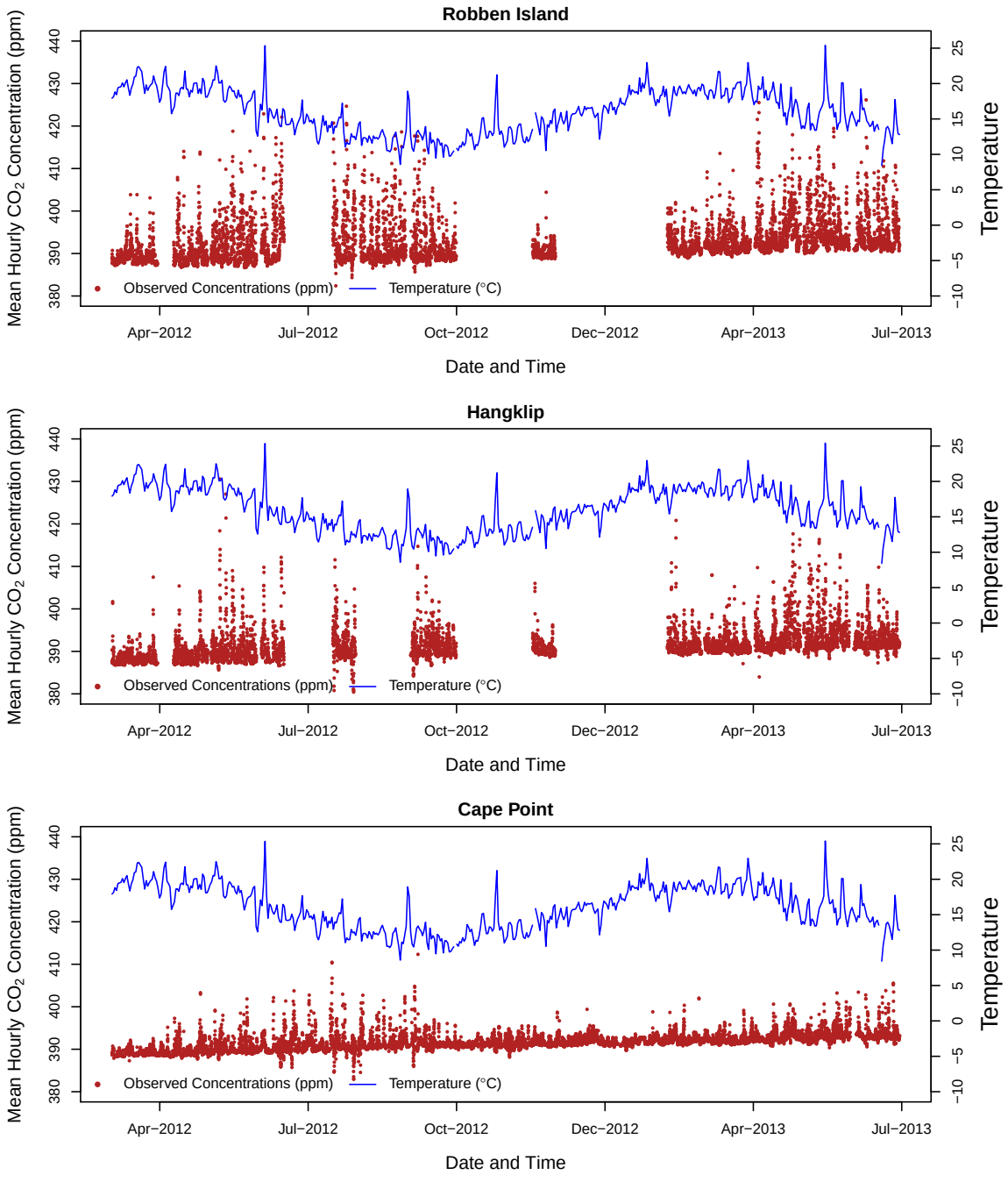


Figure B.1: Observed hourly $CO_2$ concentrations (ppm) (left-side axis) at the Robben Island (top closed red circles) and Hangklip (bottom closed black circles) measurement sites. The blue line appearing at the bottom of each plot is the $CO_2$ concentration measurements at Cape Point station (ppm) and the green line at the top of each plot is the mean daily temperature (°C) as measured at the Cape Point station, which is represented by the right-side axis.

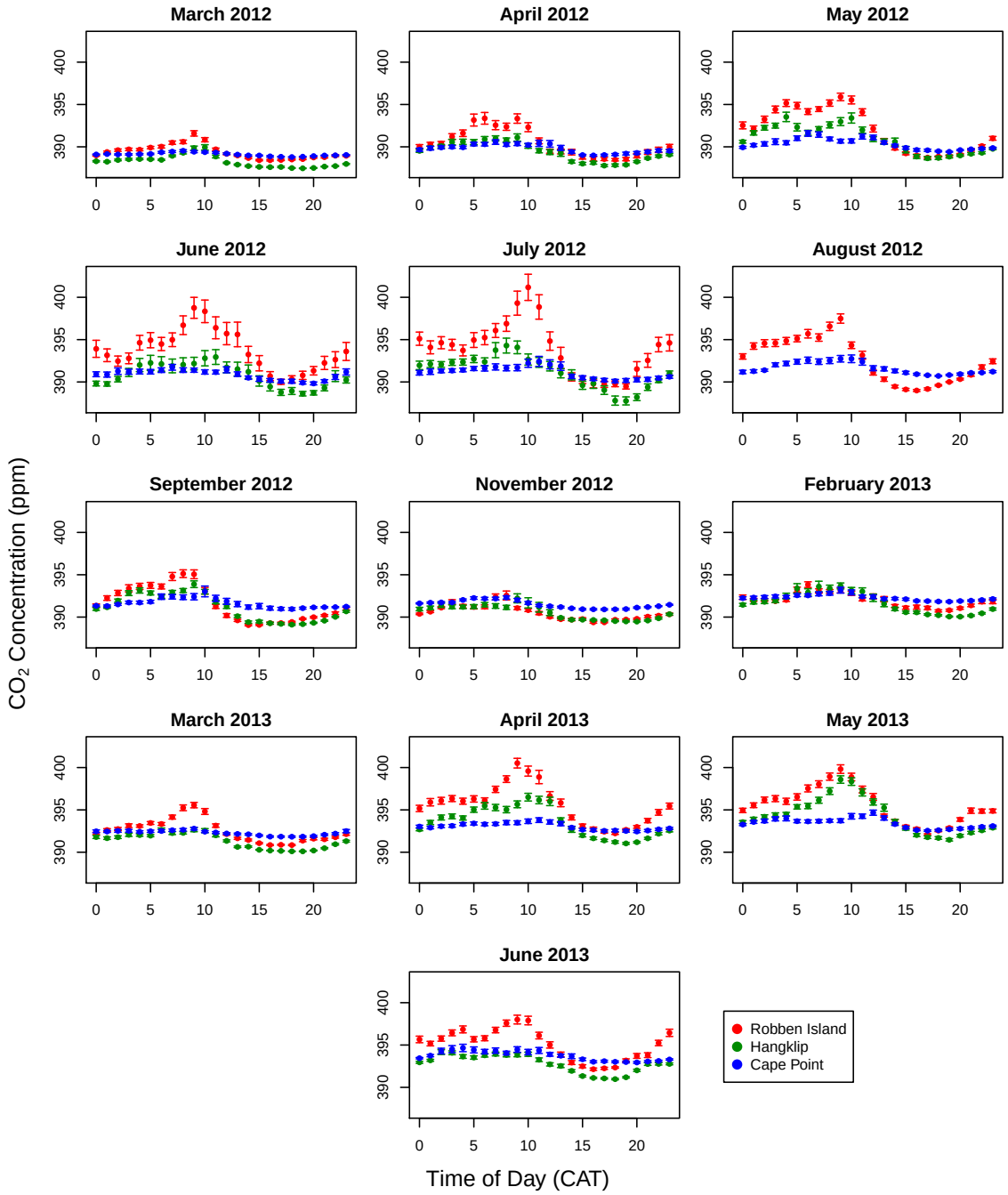


Figure B.2: Diurnal cycle of the observed $CO_2$ concentrations (ppm) for each month and at each site with 95% confidence intervals, where the standard error is calculated over all measurements available for that hour of the day during that particular month. Cape Point is the generally flat diurnal cycle in blue, Robben Island with the generally larger daytime $CO_2$ concentrations in red, and Hangklip with the generally lower afternoon $CO_2$ concentrations in black.

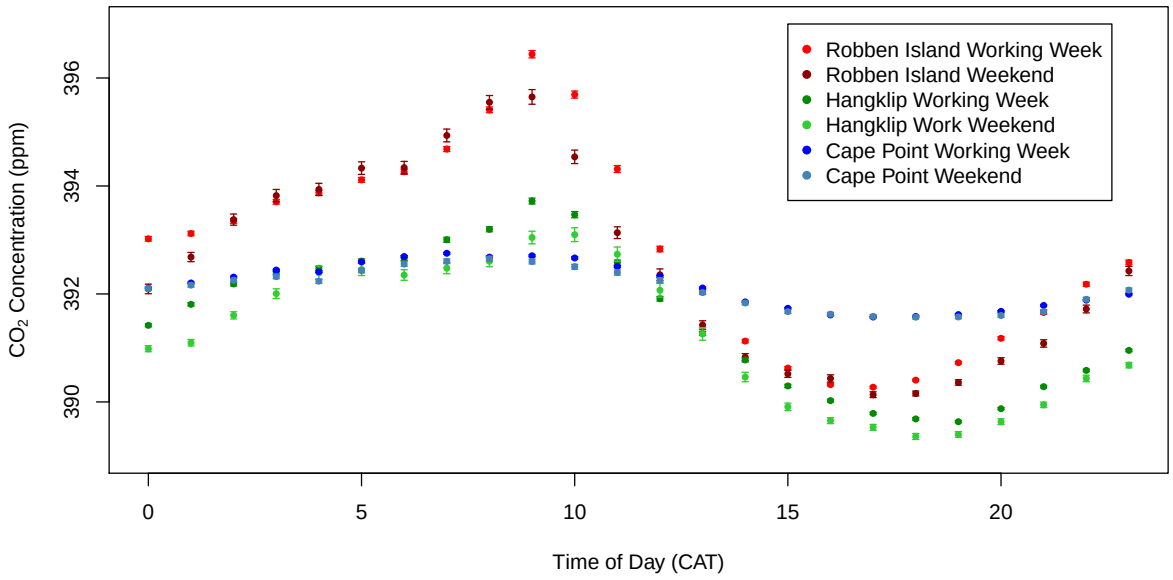


Figure B.3: Diurnal cycle of the observed $CO_2$ concentrations (ppm) over the full measurement period from March 2012 until June 2013 at each site with 95% confidence intervals, where the standard error is calculated over all measurements available for that hour of the day during the entire measurement period, separated by site (Cape Point - blue and light blue, Robben Island - red and dark red, Hangklip - black and grey) and by working week (brighter colour) and weekend (duller colour).

The mean diurnal cycle over the whole measurement period is presented in Figure B.3, separated by site and by working week and weekend. The background site, Cape Point, shows no discernible difference between the mean concentrations over the week and weekend, whereas Robben Island and Hangklip sites measure concentrations during the working week which tend to be larger across most of the day. Both the early morning and afternoon means show a clear tendency for these sites to have larger concentrations during the working week compared with the same time of day over the weekend, which can only be due to anthropogenic influences. This supports the separation of fossil fuel fluxes into working week and weekend contributions.

Table B.2: The number of days with available $CO_2$ measurement data for each month (out of a possible four week period considered) and overall percentage available data out of 16 four-week periods for each site.

| Site | Year / Month | | | | | | | | | | | | | | | | Overall Percentage |
|---|---|---|---|---|---|---|---|---|---|---|---|---|---|---|---|---|---|
| | 2012 | | | | | | | | | | 2013 | | | | | | |
| | 3 | 4 | 5 | 6 | 7 | 8 | 9 | 10 | 11 | 12 | 1 | 2 | 3 | 4 | 5 | 6 | |
| Robben Island | 28 | 21 | 28 | 14 | 14 | 28 | 28 | 0 | 14 | 0 | 0 | 21 | 28 | 28 | 28 | 28 | 68.75 |
| Hangklip | 28 | 21 | 28 | 14 | 14 | 0 | 28 | 0 | 14 | 0 | 0 | 21 | 28 | 28 | 28 | 28 | 62.50 |
| Combined | 56 | 42 | 56 | 28 | 28 | 28 | 56 | 0 | 28 | 0 | 0 | 42 | 56 | 56 | 56 | 56 | 65.63 |

Table B.2 provides the measured $CO_2$ concentration availability at each site. Robben Island had slightly higher data availability compared with Hangklip, with a 65.6% data availability overall for the sixteen month measurement campaign. Each site was equipped with a Hauwei USB modem connected to a 3G network, and were set to submit data to an email address on a regular basis. Through these emails or through connecting remotely to the instruments, instrumentation problems could be detected. Most of the down-time at the sites was attributed to either pump failure, or occasionally the instrument software had failed and there was no available person to restart the instrument due to limited access to these sites. Robben Island lighthouse is manned, and therefore it was possible to request the lighthouse keeper to restart the instrument when frozen, but more regular than expected pump problems required visits to the site to replace the offending device. This entailed making arrangements for unplanned voyages to Robben Island, which could take some time to arrange. Hangklip is unmanned, and the site has strict access control, therefore problems at this site tended to take slightly longer to remedy. The final four months considered in this study had the best continuity of data availability.

## B.2 Model Assessment

To determine if the prescribed prior covariance parameters were consistent with the model assumptions, the sum of the squared normalised residuals was compared against the $\chi^2$ distribution. For most months the standardised statistic was close to one, but in the case of June and July 2012, this statistic was above 2. We did not scale the variances independently for each month, and therefore the single scaling factor of 2 for the prior flux variances was not large enough for all months. The statistic remained below 2.5 for all months, and had a minimum of 0.68 for the month of November 2012. The mean of the statistic over all months was 1.48. A subsequent study will assess an alternative approach to determine prior flux uncertainties, which would guarantee compliance of the sum of the squared normalised residuals to follow the $\chi^2$ distribution.

Table B.3: Sum of the squared normalised residuals for each month, which should approximate a $\chi^2$ distribution with one degree of freedom.

| Month | $\chi^2$ statistic | Percentage available data |
|---|---|---|
| Mar2012 | 1.006 | 100% |
| Apr2012 | 1.089 | 75% |
| May2012 | 1.959 | 100% |
| Jun2012 | 2.473 | 50% |
| Jul2012 | 2.170 | 50% |
| Aug2012 | 1.586 | 50% |
| Sep2012 | 1.028 | 100% |
| Nov2012 | 0.678 | 50% |
| Feb2012 | 0.938 | 75% |
| Mar2013 | 1.048 | 100% |
| Apr2013 | 1.776 | 100% |
| May2013 | 1.829 | 100% |
| Jun2013 | 1.706 | 100% |

## B.3 Modelled Wind

Figure B.4 provides the average wind speed and direction for the domain for each month, as modelled by CCAM. The plots were created using the R package rasterVis (Lamigueiro, 2016).

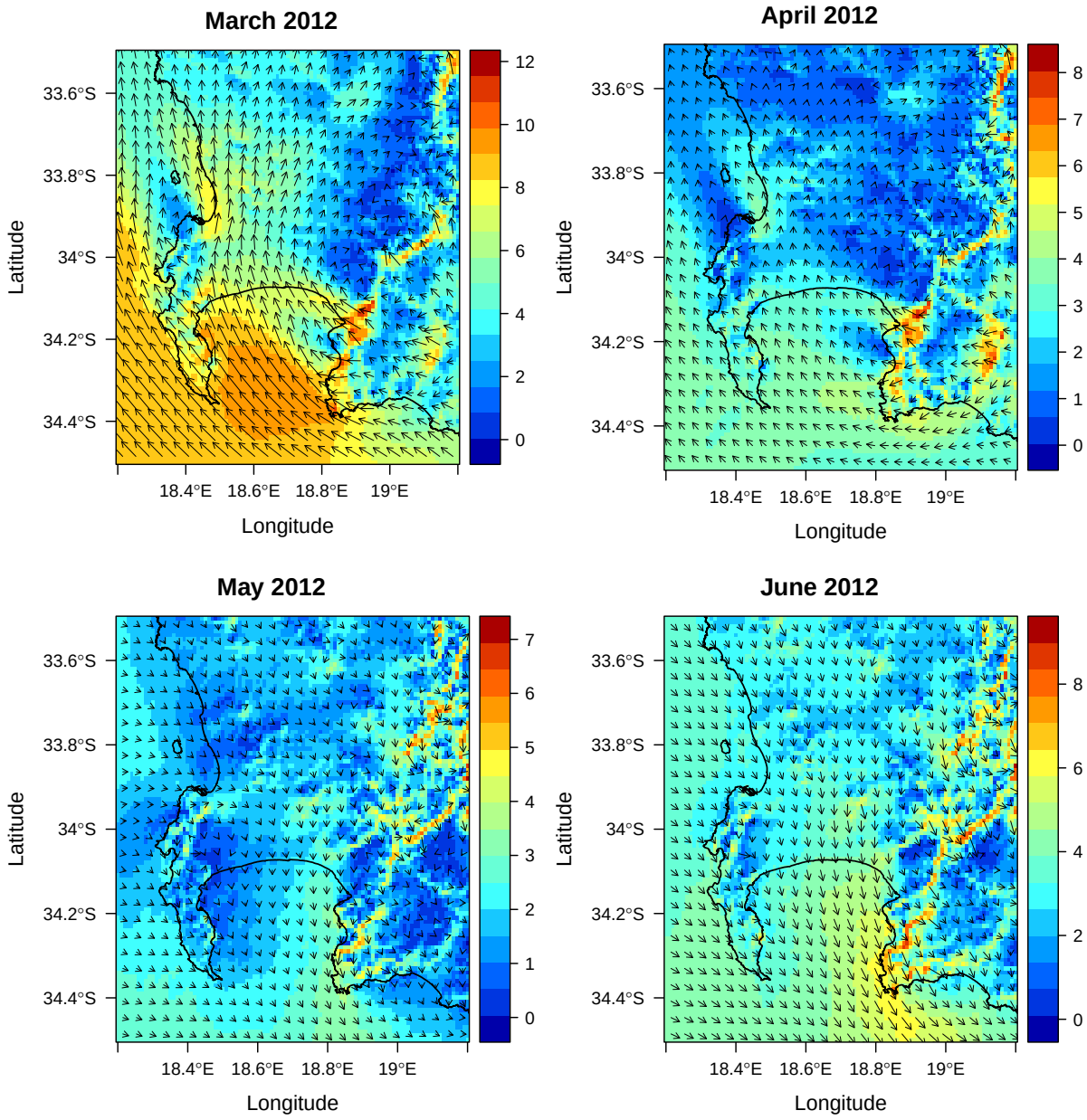

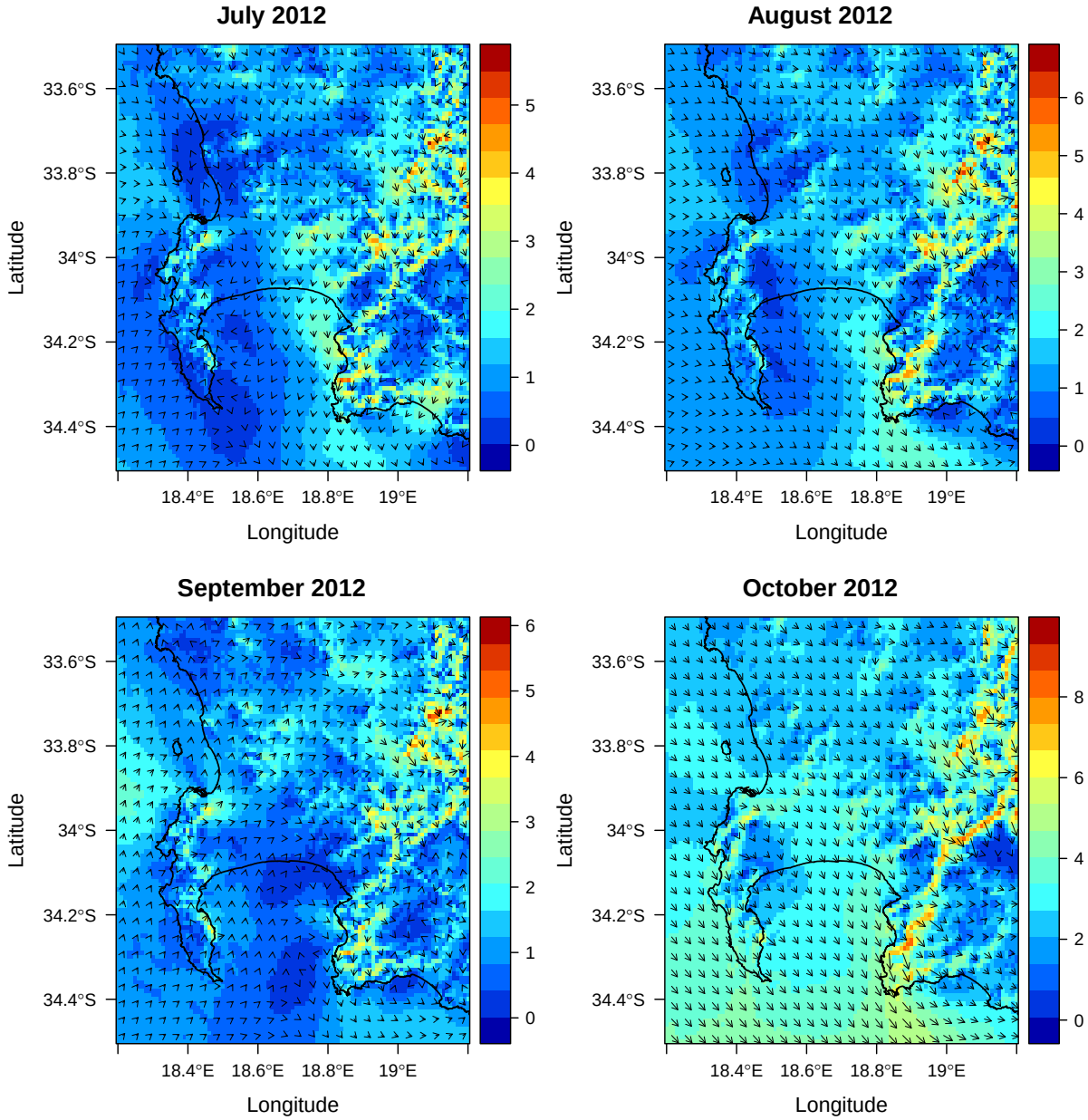
July 2012
August 2012
September 2012
October 2012
Latitude
Longitude
33.6°S
33.8°S
34°S
34.2°S
34.4°S
18.4°E
18.6°E
18.8°E
19°E

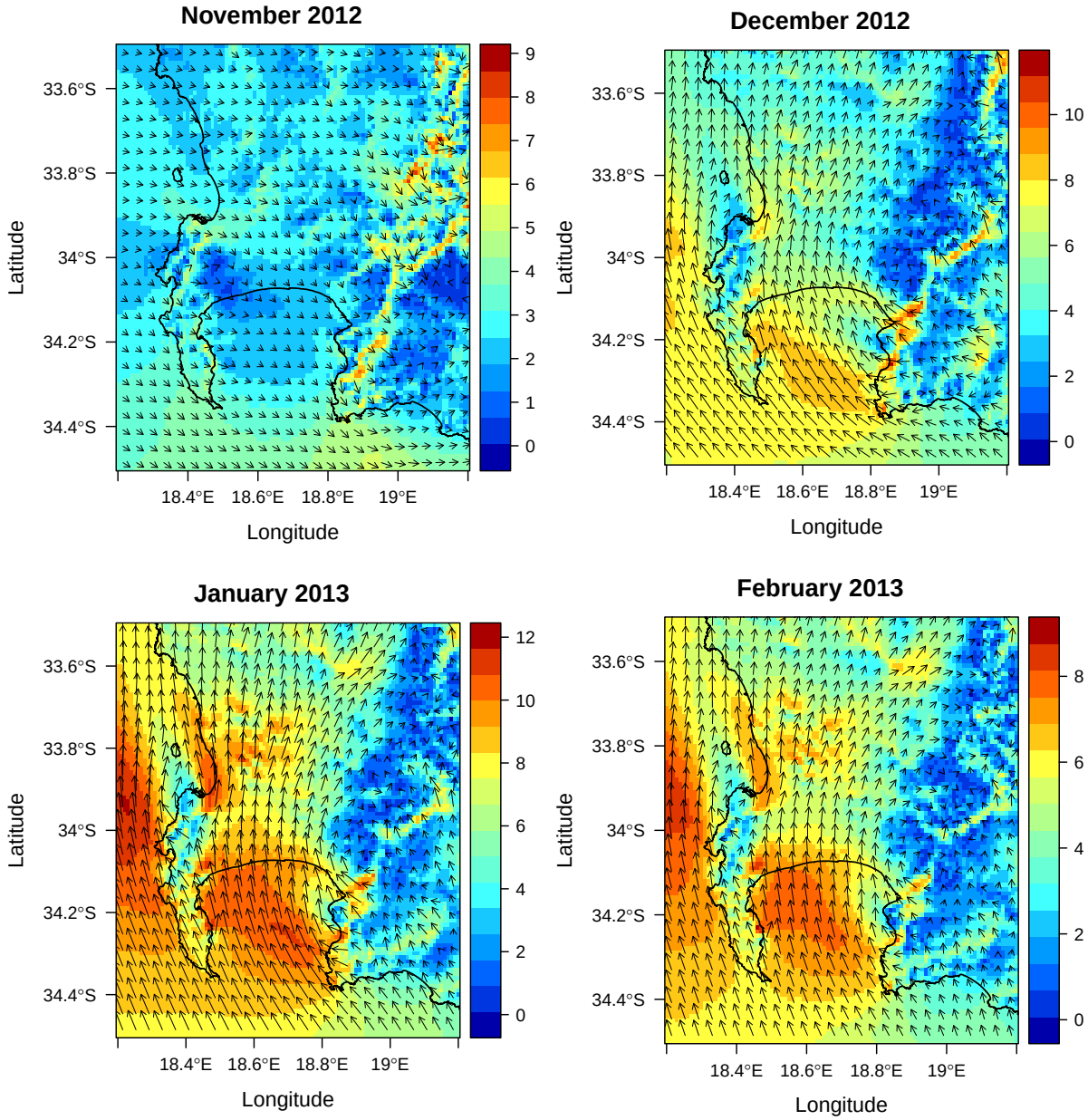
November 2012
December 2012
January 2013
February 2013
Latitude
Longitude
33.6°S
33.8°S
34°S
34.2°S
34.4°S
18.4°E
18.6°E
18.8°E
19°E

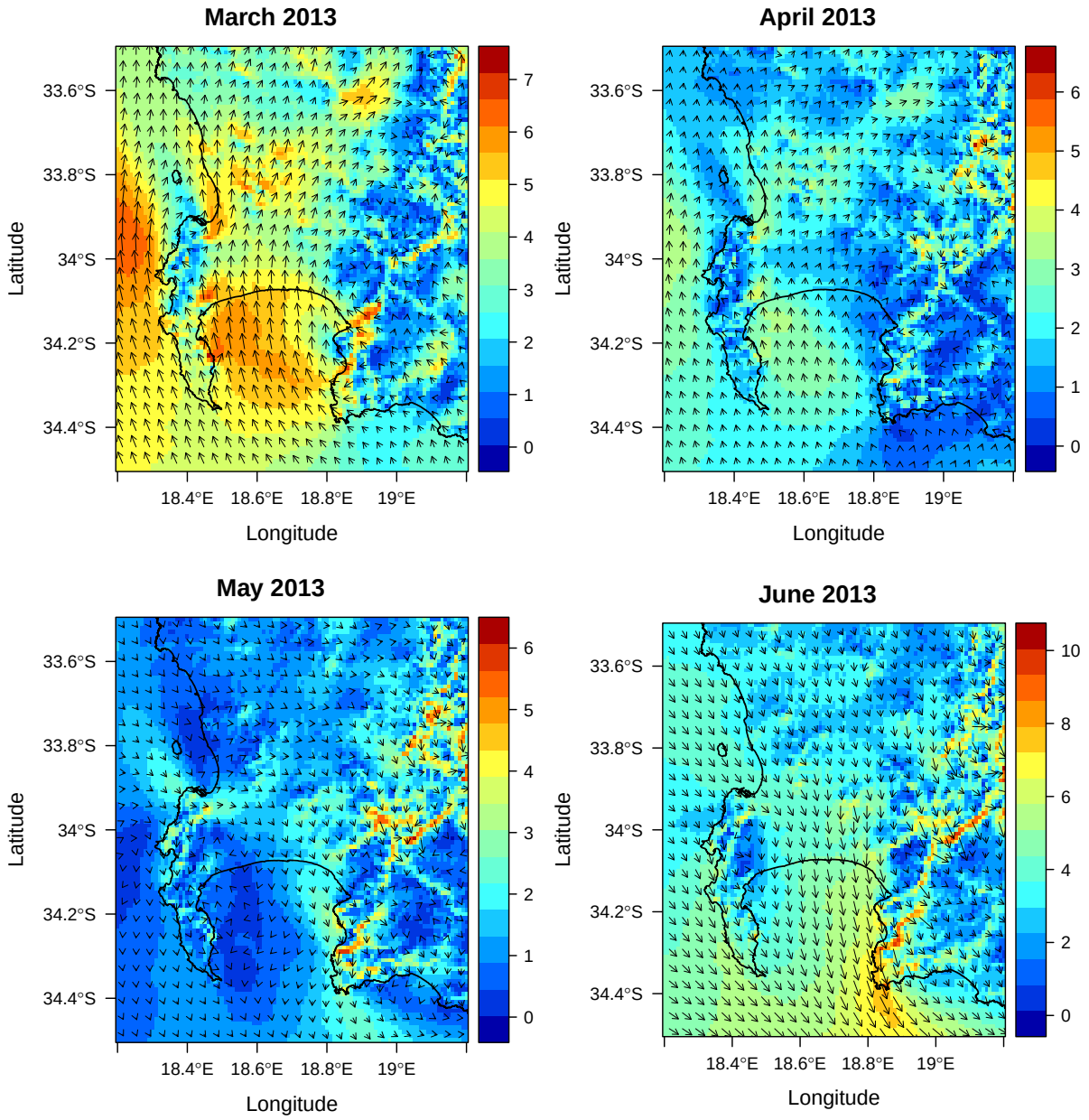


Figure B.4: Mean modelled wind speed and direction in the Cape Town domain for each month. The colourbar represents the mean wind speed (m/s).

## B.4 Modelled Concentrations

The time series for the modelled concentrations is discussed in Section 3.1 of the main paper.

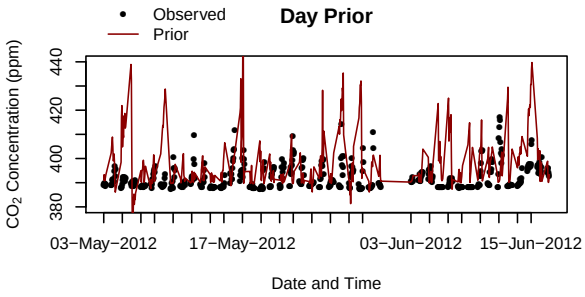
Observed
Prior
Day Prior
CO2 Concentration (ppm)
380
400
420
440
03−May−2012
17−May−2012
03−Jun−2012
15−Jun−2012
Date and Time

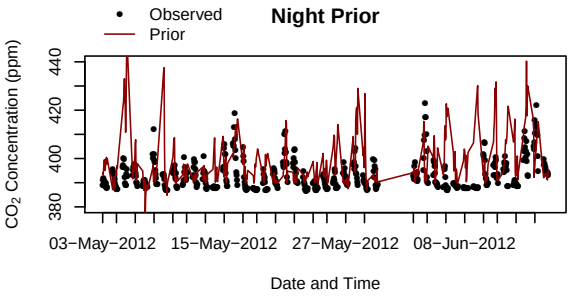
Observed
Prior
Night Prior
CO2 Concentration (ppm)
380
400
420
440
03−May−2012
15−May−2012
27−May−2012
08−Jun−2012
Date and Time

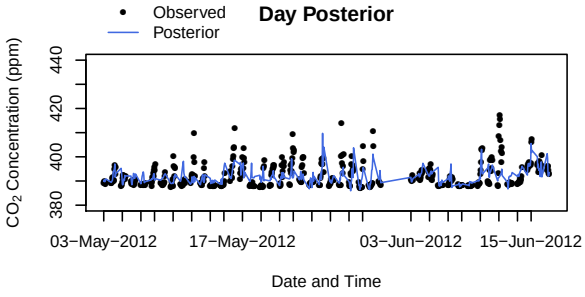
Observed
Posterior
Day Posterior
CO2 Concentration (ppm)
380
400
420
440
03−May−2012
17−May−2012
03−Jun−2012
15−Jun−2012
Date and Time

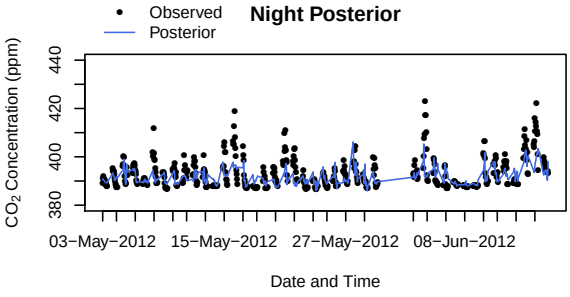
Observed
Posterior
Night Posterior
CO2 Concentration (ppm)
380
400
420
440
03−May−2012
15−May−2012
27−May−2012
08−Jun−2012
Date and Time

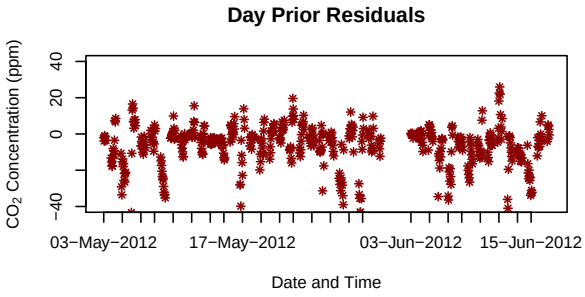
Day Prior Residuals
CO2 Concentration (ppm)
−40
0
20
40
03−May−2012
17−May−2012
03−Jun−2012
15−Jun−2012
Date and Time

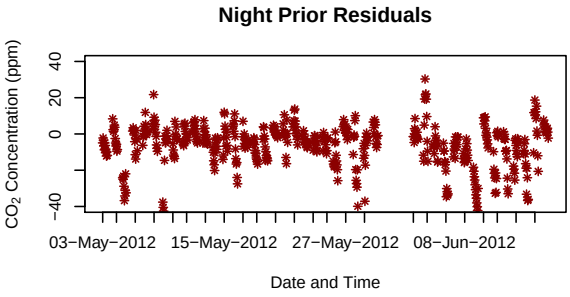
Night Prior Residuals
CO2 Concentration (ppm)
−40
0
20
40
03−May−2012
15−May−2012
27−May−2012
08−Jun−2012
Date and Time

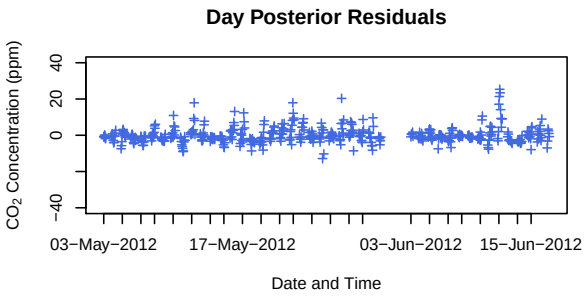
Day Posterior Residuals
CO2 Concentration (ppm)
−40
0
20
40
03−May−2012
17−May−2012
03−Jun−2012
15−Jun−2012
Date and Time

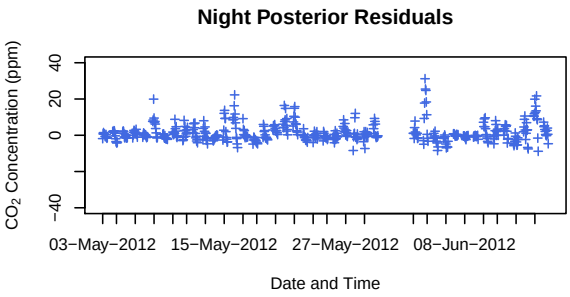
Night Posterior Residuals
CO2 Concentration (ppm)
−40
0
20
40
03−May−2012
15−May−2012
27−May−2012
08−Jun−2012
Date and Time

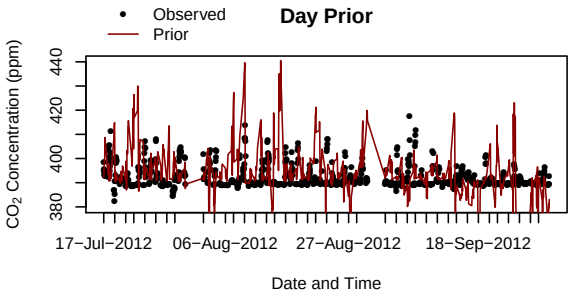
Observed
Prior
Day Prior
CO2 Concentration (ppm)
380
400
420
440
17−Jul−2012
06−Aug−2012
27−Aug−2012
18−Sep−2012
Date and Time

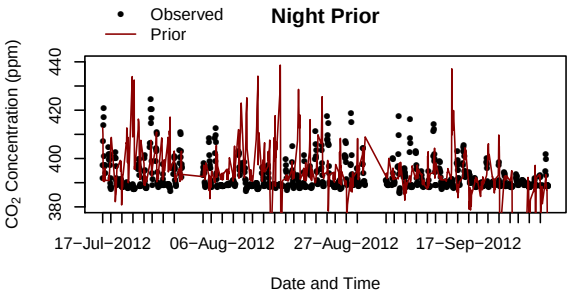
Observed
Prior
Night Prior
CO2 Concentration (ppm)
380
400
420
440
17−Jul−2012
06−Aug−2012
27−Aug−2012
17−Sep−2012
Date and Time

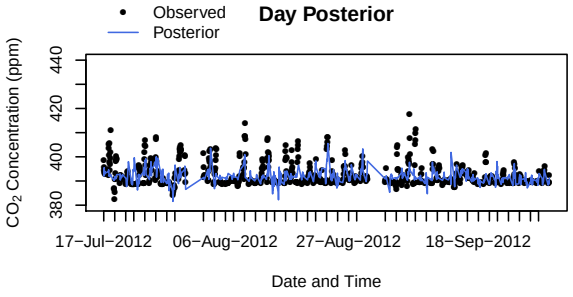
Observed
Posterior
Day Posterior
CO2 Concentration (ppm)
380
400
420
440
17−Jul−2012
06−Aug−2012
27−Aug−2012
18−Sep−2012
Date and Time

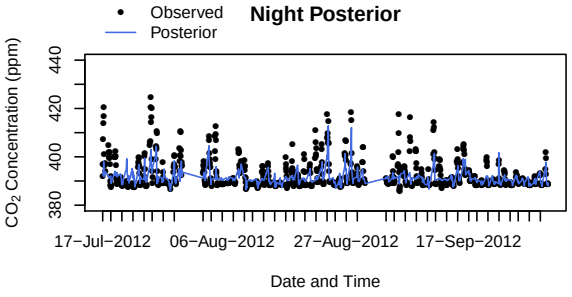
Observed
Posterior
Night Posterior
CO2 Concentration (ppm)
380
400
420
440
17−Jul−2012
06−Aug−2012
27−Aug−2012
17−Sep−2012
Date and Time

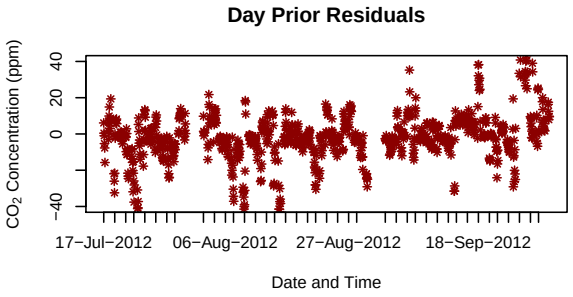
Day Prior Residuals
CO2 Concentration (ppm)
−40
0
20
40
17−Jul−2012
06−Aug−2012
27−Aug−2012
18−Sep−2012
Date and Time

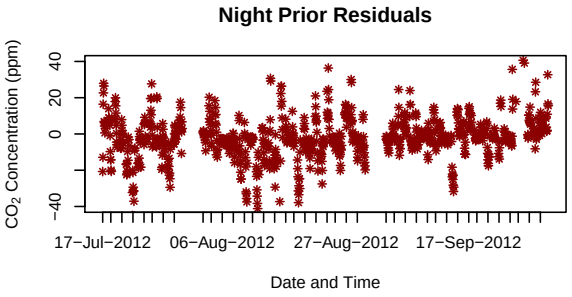
Night Prior Residuals
CO2 Concentration (ppm)
−40
0
20
40
17−Jul−2012
06−Aug−2012
27−Aug−2012
17−Sep−2012
Date and Time

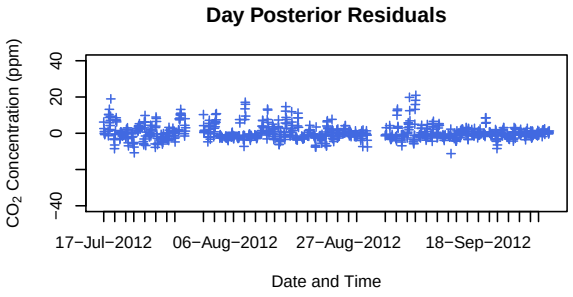
Day Posterior Residuals
CO2 Concentration (ppm)
−40
0
20
40
17−Jul−2012
06−Aug−2012
27−Aug−2012
18−Sep−2012
Date and Time

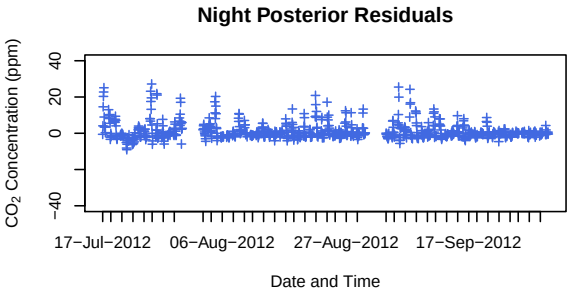
Night Posterior Residuals
CO2 Concentration (ppm)
−40
0
20
40
17−Jul−2012
06−Aug−2012
27−Aug−2012
17−Sep−2012
Date and Time

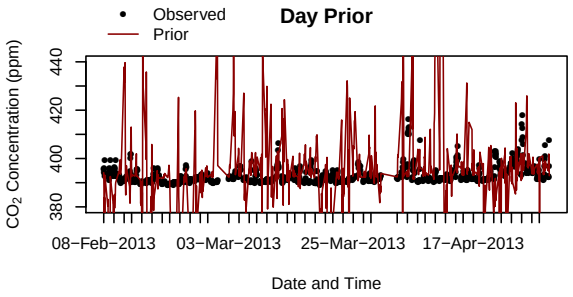
Observed
Prior
Day Prior
CO2 Concentration (ppm)
380
400
420
440
08−Feb−2013
03−Mar−2013
25−Mar−2013
17−Apr−2013
Date and Time

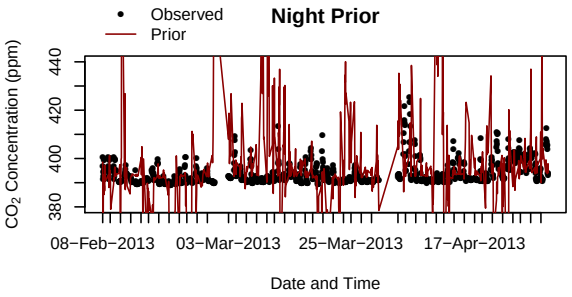
Observed
Prior
Night Prior
CO2 Concentration (ppm)
380
400
420
440
08−Feb−2013
03−Mar−2013
25−Mar−2013
17−Apr−2013
Date and Time

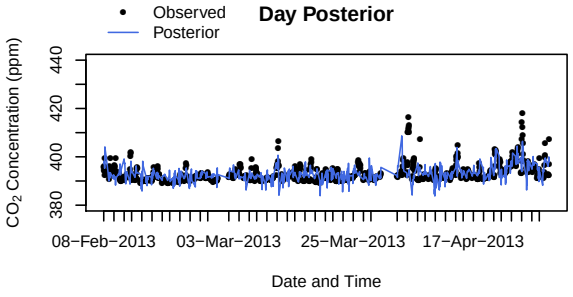
Observed
Posterior
Day Posterior
CO2 Concentration (ppm)
380
400
420
440
08−Feb−2013
03−Mar−2013
25−Mar−2013
17−Apr−2013
Date and Time

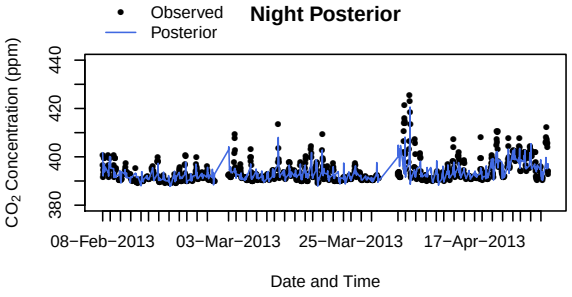
Observed
Posterior
Night Posterior
CO2 Concentration (ppm)
380
400
420
440
08−Feb−2013
03−Mar−2013
25−Mar−2013
17−Apr−2013
Date and Time

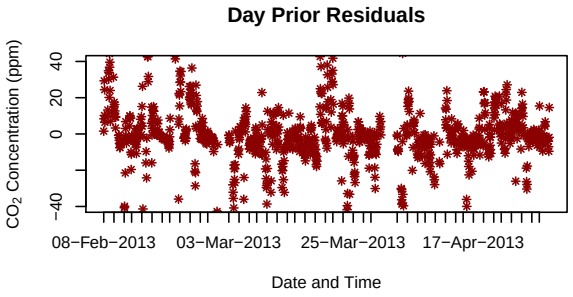
Day Prior Residuals
CO2 Concentration (ppm)
−40
0
20
40
08−Feb−2013
03−Mar−2013
25−Mar−2013
17−Apr−2013
Date and Time

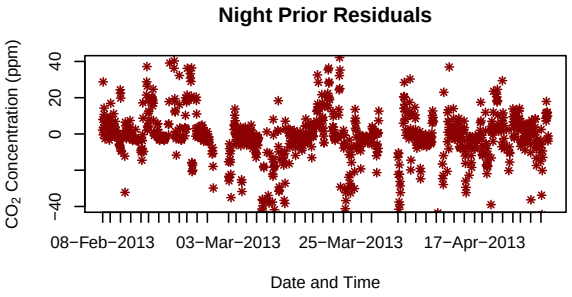
Night Prior Residuals
CO2 Concentration (ppm)
−40
0
20
40
08−Feb−2013
03−Mar−2013
25−Mar−2013
17−Apr−2013
Date and Time

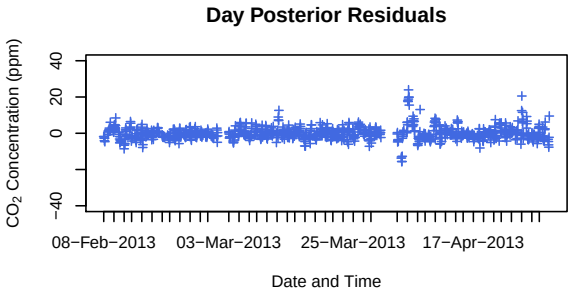
Day Posterior Residuals
CO2 Concentration (ppm)
−40
0
20
40
08−Feb−2013
03−Mar−2013
25−Mar−2013
17−Apr−2013
Date and Time

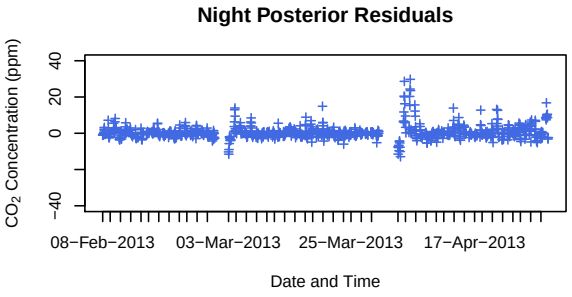
Night Posterior Residuals
CO2 Concentration (ppm)
−40
0
20
40
08−Feb−2013
03−Mar−2013
25−Mar−2013
17−Apr−2013
Date and Time

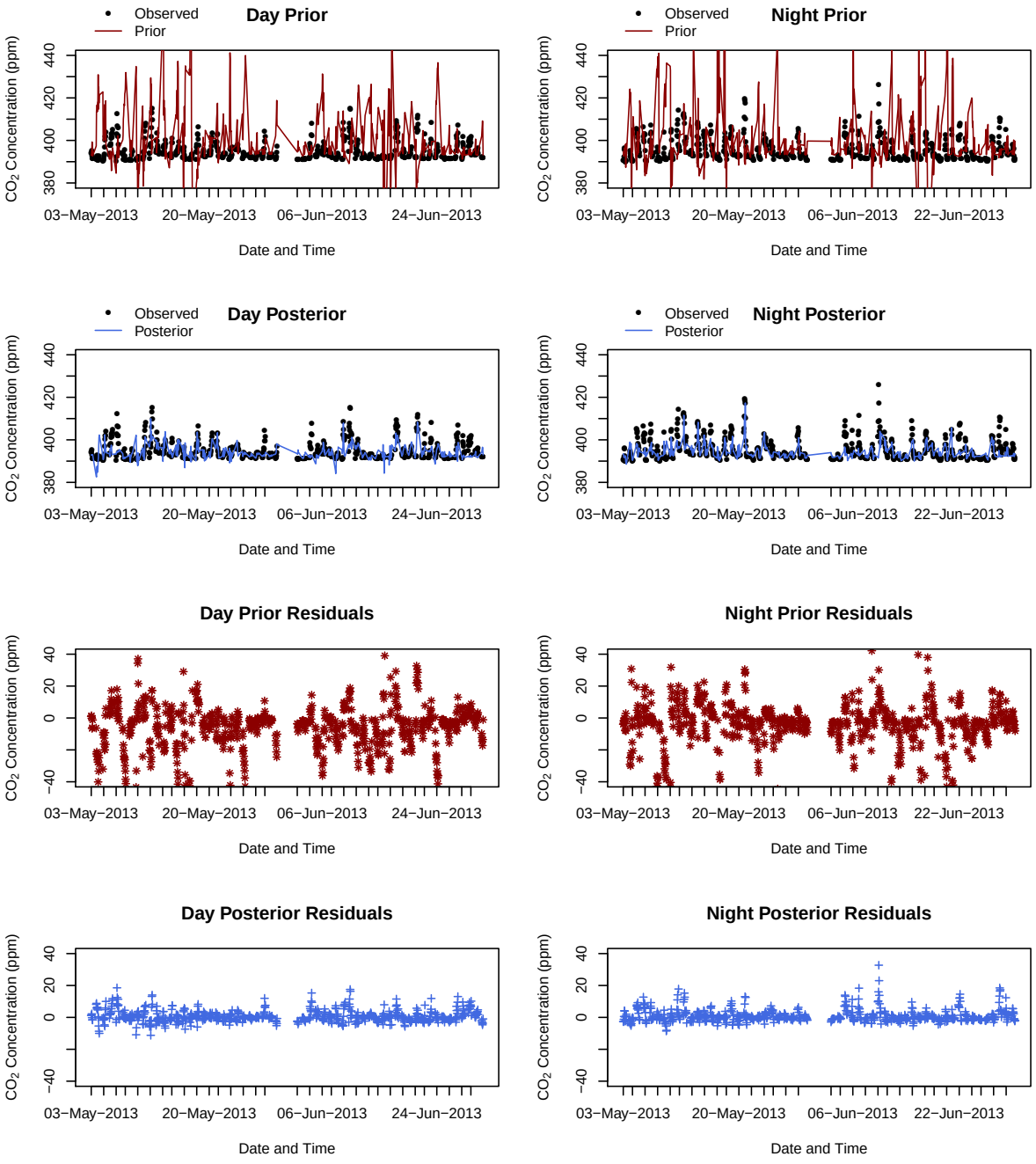


Figure B.5: The top 4 panels provide a time series of the observed, prior and posterior modelled concentrations at the Robben Island site. The time series is separated into day and night-time periods. The residuals between the modelled and observed concentrations, defined as the difference between the observed and modelled concentrations, are provided in the lower panel 4 panels. The first 2 months are presented in the main paper in section 3.1.

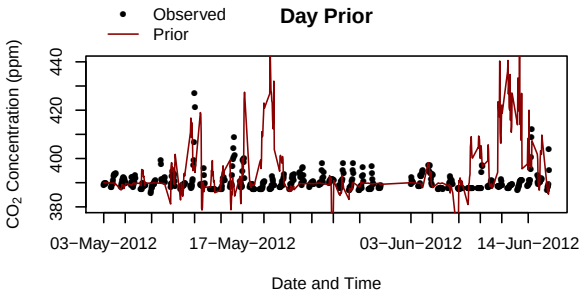
Observed
Prior
Day Prior
CO2 Concentration (ppm)
380
400
420
440
03−May−2012
17−May−2012
03−Jun−2012
14−Jun−2012
Date and Time

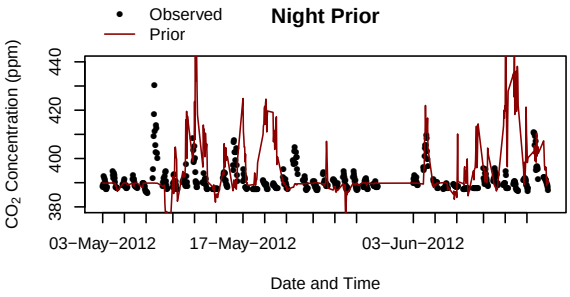
Observed
Prior
Night Prior
CO2 Concentration (ppm)
380
400
420
440
03−May−2012
17−May−2012
03−Jun−2012
Date and Time

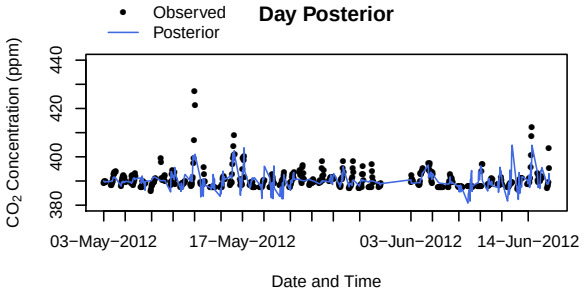
Observed
Posterior
Day Posterior
CO2 Concentration (ppm)
380
400
420
440
03−May−2012
17−May−2012
03−Jun−2012
14−Jun−2012
Date and Time

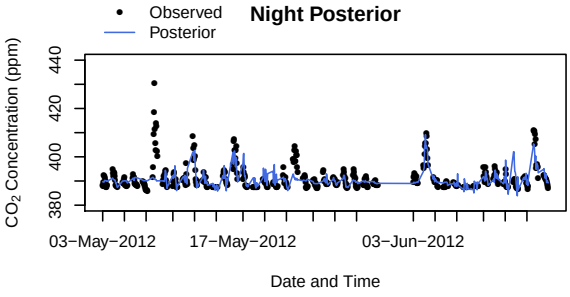
Observed
Posterior
Night Posterior
CO2 Concentration (ppm)
380
400
420
440
03−May−2012
17−May−2012
03−Jun−2012
Date and Time

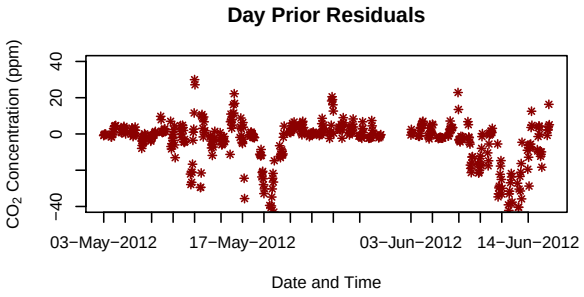
Day Prior Residuals
CO2 Concentration (ppm)
−40
0
20
40
03−May−2012
17−May−2012
03−Jun−2012
14−Jun−2012
Date and Time

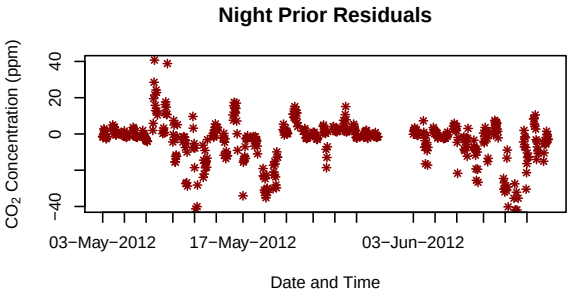
Night Prior Residuals
CO2 Concentration (ppm)
−40
0
20
40
03−May−2012
17−May−2012
03−Jun−2012
Date and Time

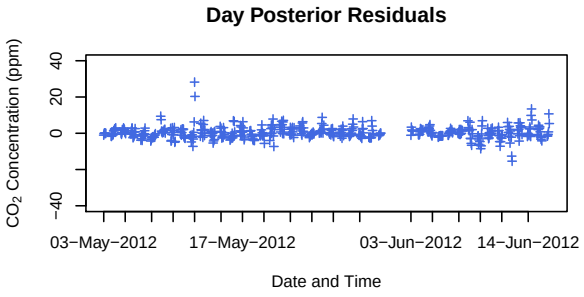
Day Posterior Residuals
CO2 Concentration (ppm)
−40
0
20
40
03−May−2012
17−May−2012
03−Jun−2012
14−Jun−2012
Date and Time

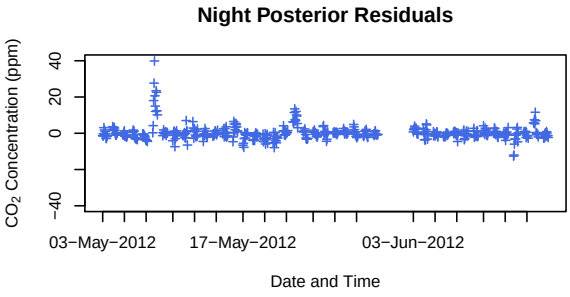
Night Posterior Residuals
CO2 Concentration (ppm)
−40
0
20
40
03−May−2012
17−May−2012
03−Jun−2012
Date and Time

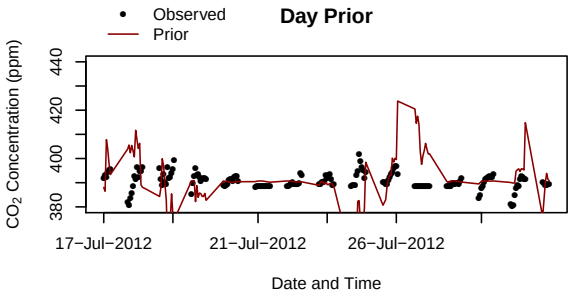
Observed
Prior
Day Prior
CO2 Concentration (ppm)
380
400
420
440
17−Jul−2012
21−Jul−2012
26−Jul−2012
Date and Time

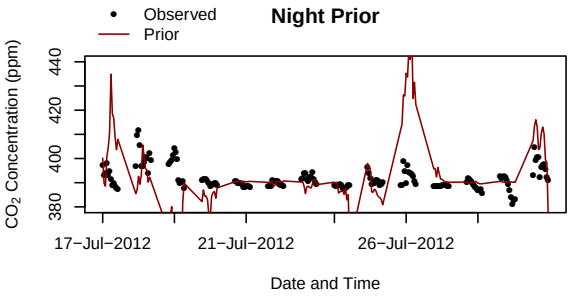
Observed
Prior
Night Prior
CO2 Concentration (ppm)
380
400
420
440
17−Jul−2012
21−Jul−2012
26−Jul−2012
Date and Time

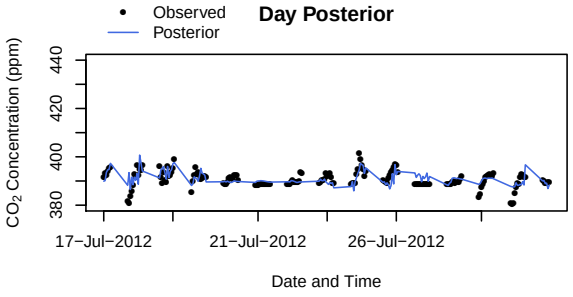
Observed
Posterior
Day Posterior
CO2 Concentration (ppm)
380
400
420
440
17−Jul−2012
21−Jul−2012
26−Jul−2012
Date and Time

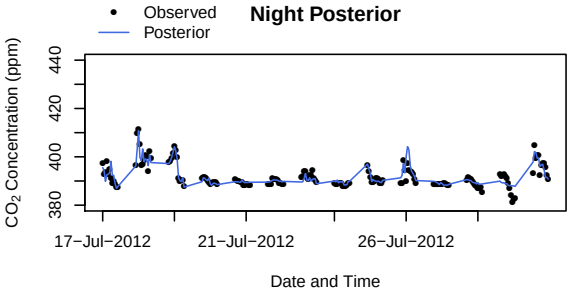
Observed
Posterior
Night Posterior
CO2 Concentration (ppm)
380
400
420
440
17−Jul−2012
21−Jul−2012
26−Jul−2012
Date and Time

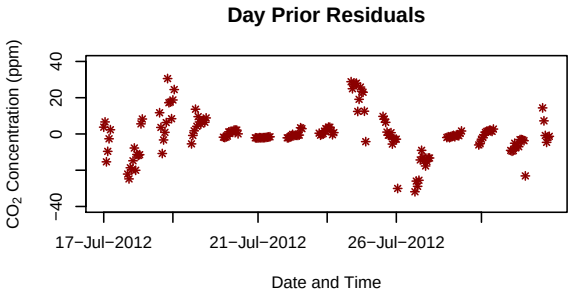
Day Prior Residuals
CO2 Concentration (ppm)
−40
0
20
40
17−Jul−2012
21−Jul−2012
26−Jul−2012
Date and Time

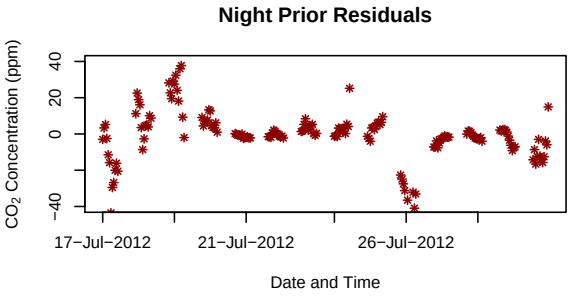
Night Prior Residuals
CO2 Concentration (ppm)
−40
0
20
40
17−Jul−2012
21−Jul−2012
26−Jul−2012
Date and Time

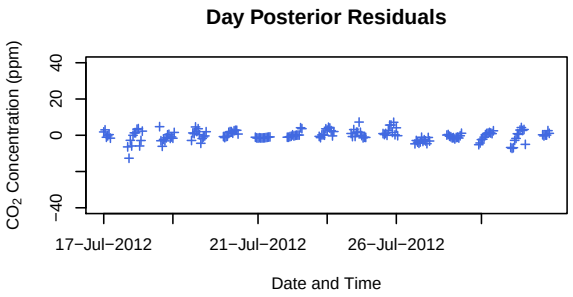
Day Posterior Residuals
CO2 Concentration (ppm)
−40
0
20
40
17−Jul−2012
21−Jul−2012
26−Jul−2012
Date and Time

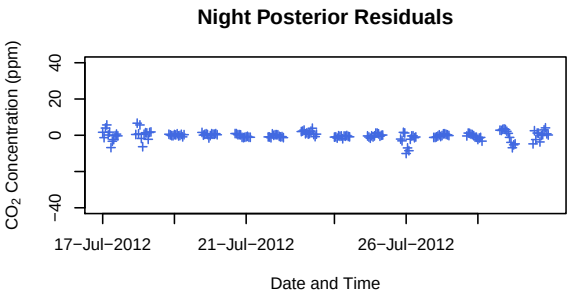
Night Posterior Residuals
CO2 Concentration (ppm)
−40
0
20
40
17−Jul−2012
21−Jul−2012
26−Jul−2012
Date and Time

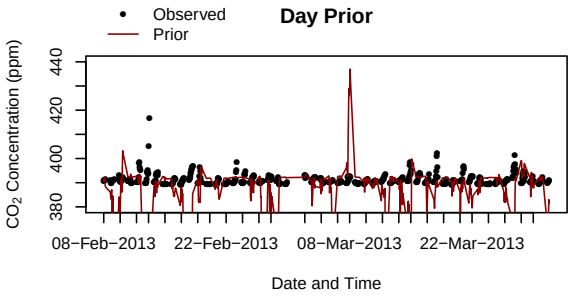
Observed
Prior
Day Prior
CO2 Concentration (ppm)
380
400
420
440
08−Feb−2013
22−Feb−2013
08−Mar−2013
22−Mar−2013
Date and Time

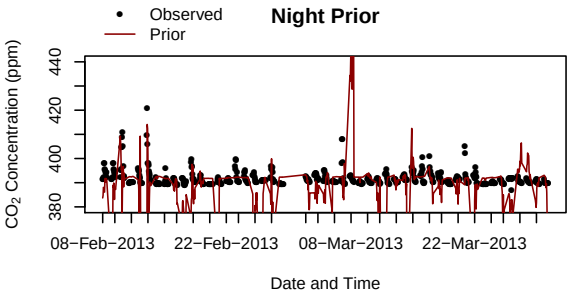
Observed
Prior
Night Prior
CO2 Concentration (ppm)
380
400
420
440
08−Feb−2013
22−Feb−2013
08−Mar−2013
22−Mar−2013
Date and Time

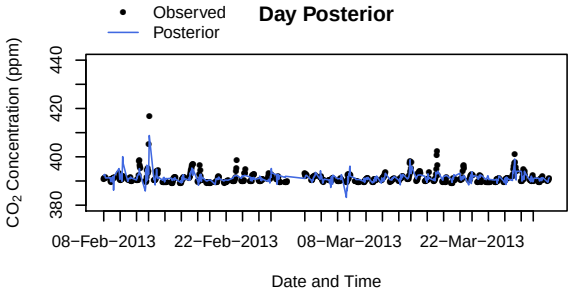
Observed
Posterior
Day Posterior
CO2 Concentration (ppm)
380
400
420
440
08−Feb−2013
22−Feb−2013
08−Mar−2013
22−Mar−2013
Date and Time

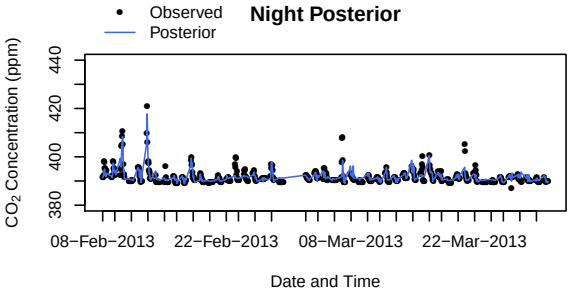
Observed
Posterior
Night Posterior
CO2 Concentration (ppm)
380
400
420
440
08−Feb−2013
22−Feb−2013
08−Mar−2013
22−Mar−2013
Date and Time

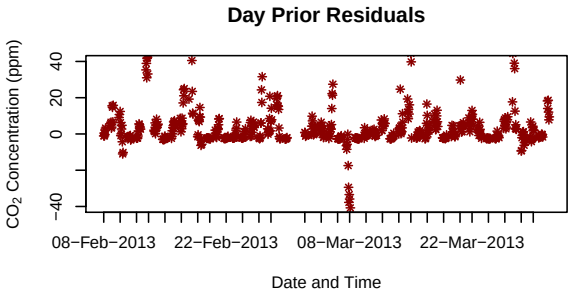
Day Prior Residuals
CO2 Concentration (ppm)
−40
0
20
40
08−Feb−2013
22−Feb−2013
08−Mar−2013
22−Mar−2013
Date and Time

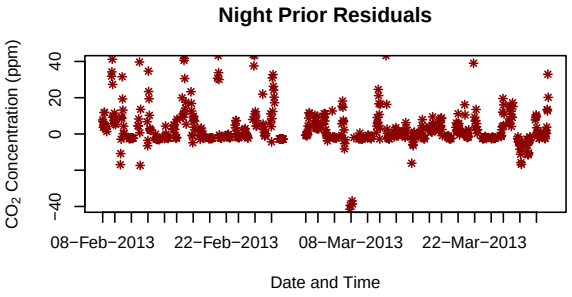
Night Prior Residuals
CO2 Concentration (ppm)
−40
0
20
40
08−Feb−2013
22−Feb−2013
08−Mar−2013
22−Mar−2013
Date and Time

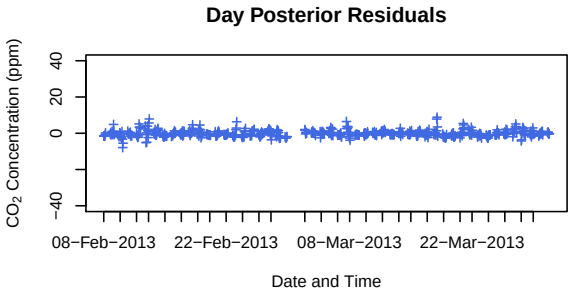
Day Posterior Residuals
CO2 Concentration (ppm)
−40
0
20
40
08−Feb−2013
22−Feb−2013
08−Mar−2013
22−Mar−2013
Date and Time

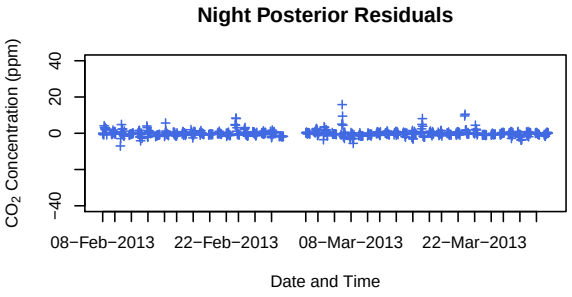
Night Posterior Residuals
CO2 Concentration (ppm)
−40
0
20
40
08−Feb−2013
22−Feb−2013
08−Mar−2013
22−Mar−2013
Date and Time

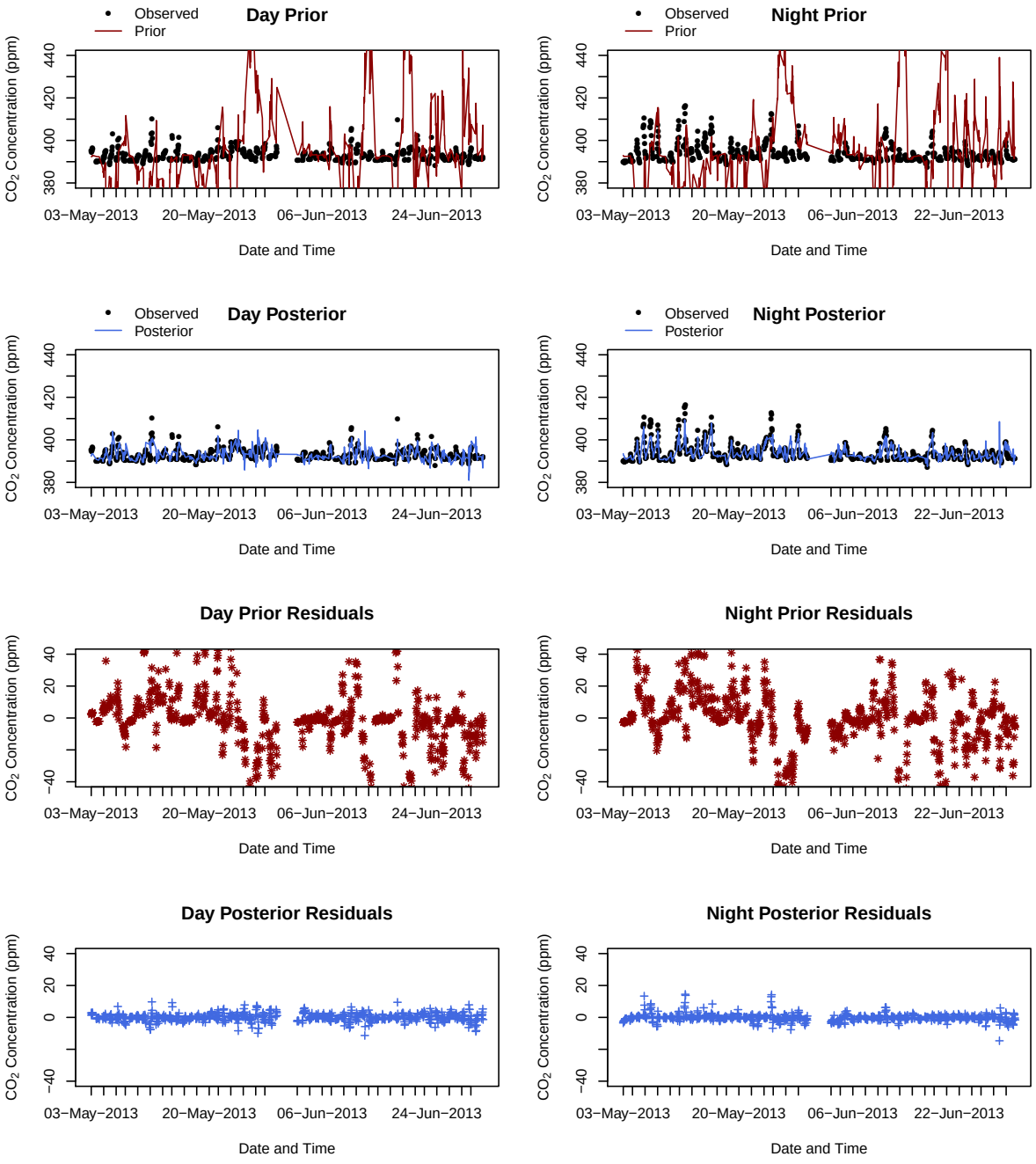


Figure B.6: The top 4 panels provide a time series of the observed, prior and posterior modelled concentrations at the Hangklip site. The time series is separated into day and night-time periods. The residuals between the modelled and observed concentrations, defined as the difference between the observed and modelled concentrations, are provided in the lower panel 4 panels. The first 2 months are presented in the main paper in section 3.1.

## B.5 Diurnal Cycle

The observed, prior and posterior modelled diurnal cycle, separated into working week and weekend $CO_2$ concentrations, are provided for each site and for each month in Figures B.7 and B.8. For all months, the diurnal cycle of the posterior modelled concentrations is relatively flat in comparison with the observed diurnal cycle, and usually sits at a higher mean level in the case of Robben Island, and at a lower mean level in the case of Hangklip. Compared with the prior modelled concentrations, the posterior diurnal cycle matches better with the observed concentrations in terms of the peaks and troughs of the cycle and in terms of the mean level of the concentrations at each hour, although the posterior cycle still appears relatively flat in comparison to the observed cycle.

April 2013 at the Robben Island site provides an example where the prior modelled concentrations had working week concentrations that were above those for the weekend during the early morning hours, whereas the observed concentrations showed the opposite situation. After the inversion, the posterior estimates had mean concentrations for the weekend that were above those for the working week during the early morning hours, matching better with the observed diurnal cycle.

Therefore the inversion does show an ability to improve estimates of the diurnal cycle, despite only separating the sources into day and night sources over a week period, and further separating the fossil fuel sources into weekend and week sources.

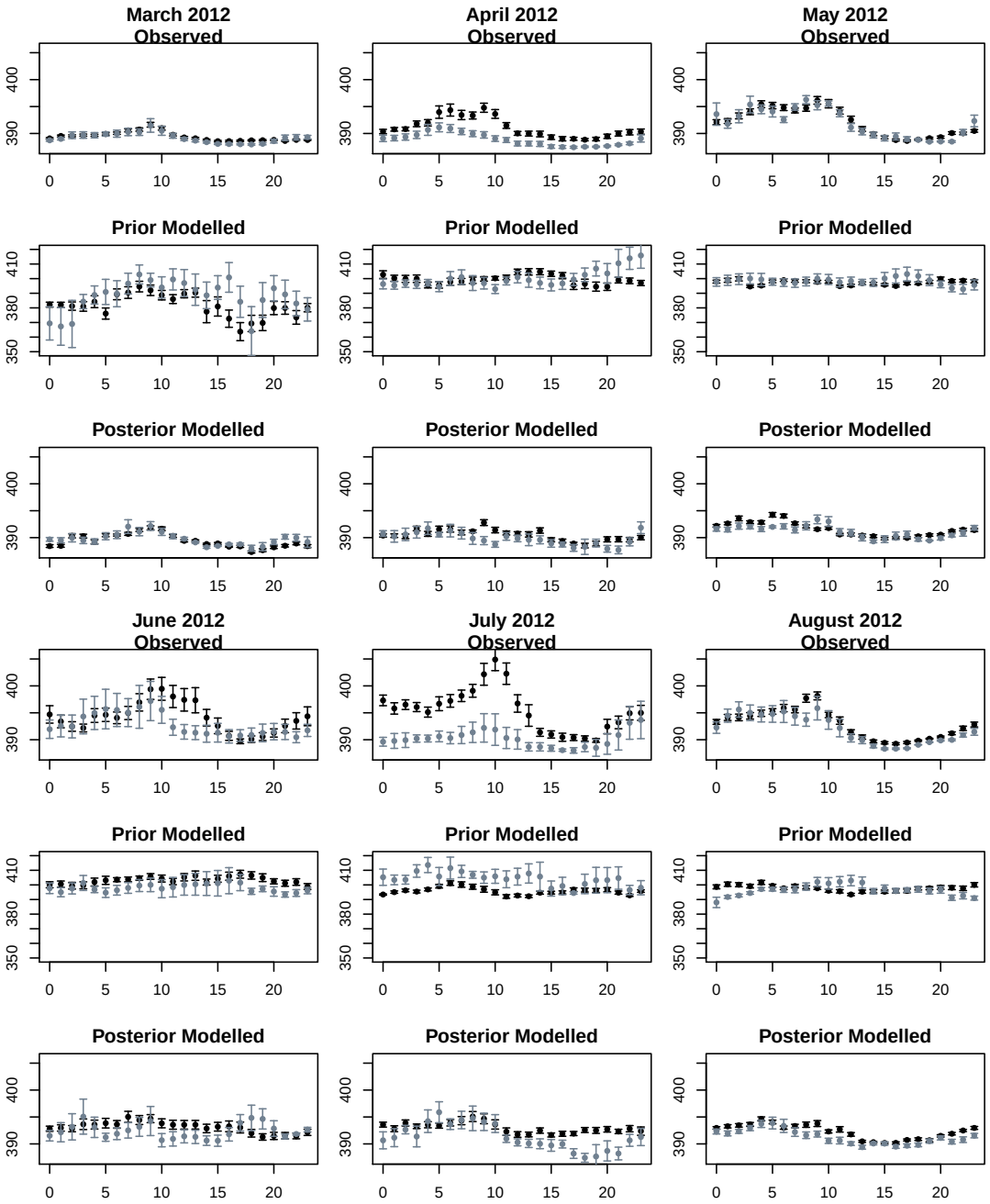
March 2012
Observed
April 2012
Observed
May 2012
Observed
Prior Modelled
Prior Modelled
Prior Modelled
Posterior Modelled
Posterior Modelled
Posterior Modelled
June 2012
Observed
July 2012
Observed
August 2012
Observed
Prior Modelled
Prior Modelled
Prior Modelled
Posterior Modelled
Posterior Modelled
Posterior Modelled

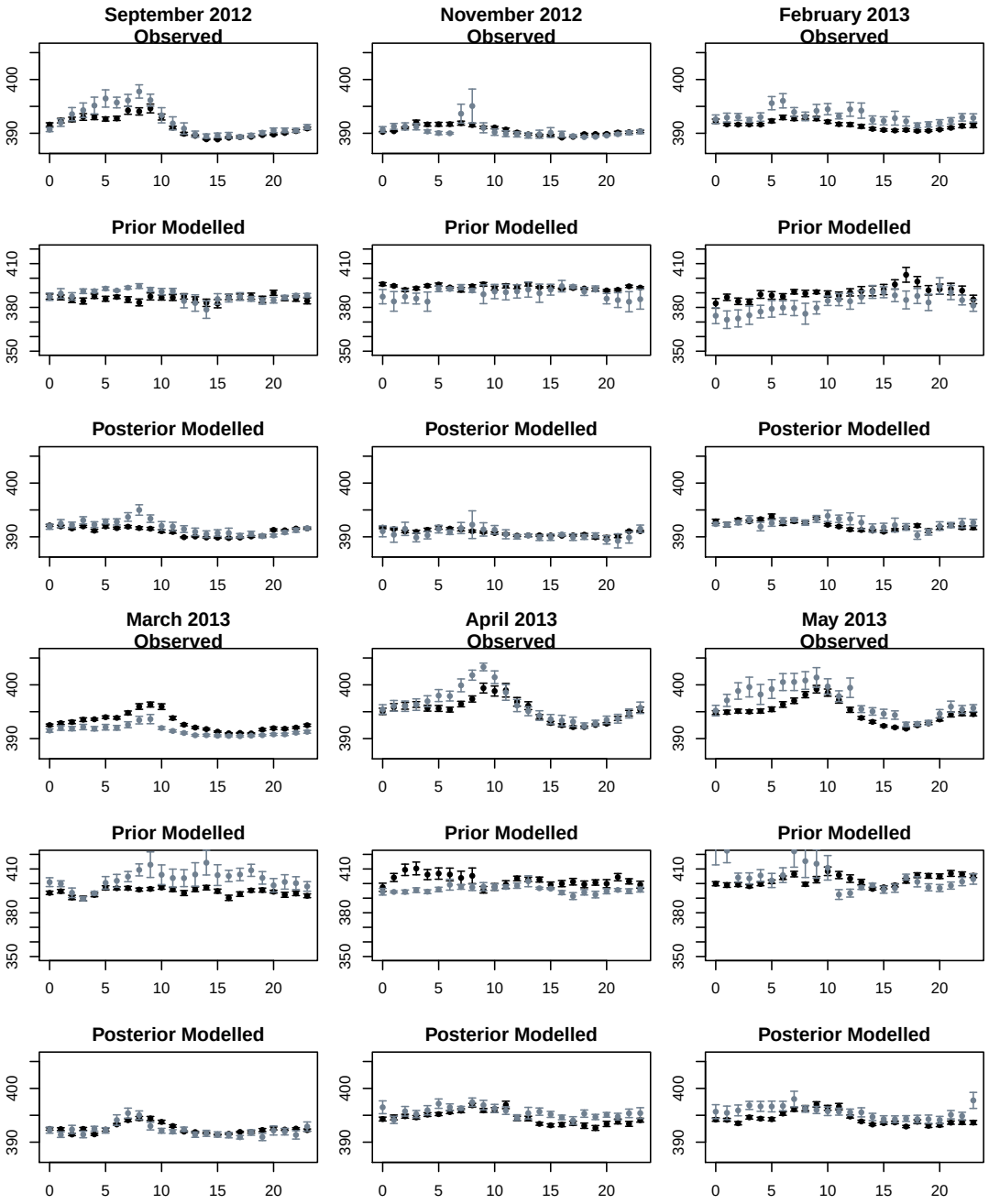
September 2012
Observed
November 2012
Observed
February 2013
Observed
Prior Modelled
Prior Modelled
Prior Modelled
Posterior Modelled
Posterior Modelled
Posterior Modelled
March 2013
Observed
April 2013
Observed
May 2013
Observed
Prior Modelled
Prior Modelled
Prior Modelled
Posterior Modelled
Posterior Modelled
Posterior Modelled
390
400
410
380
350
0
5
10
15
20

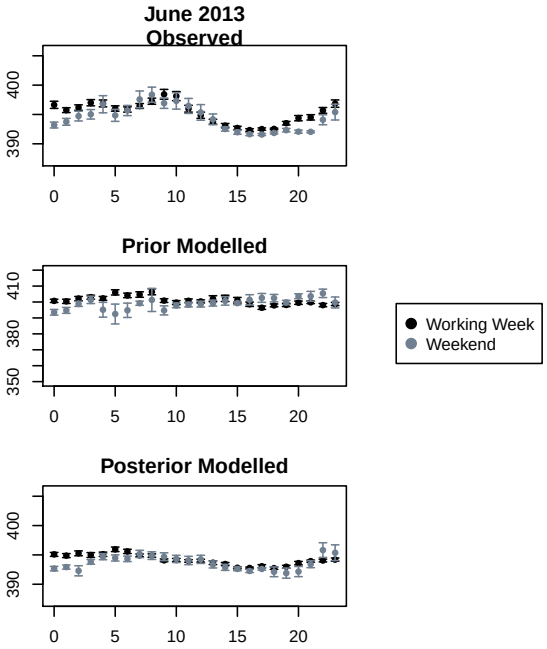


Figure B.7: Diurnal cycle of the observed, prior modelled and posterior modelled $CO_2$ concentrations (ppm) at Robben Island, separated into working week (black) and weekend concentrations (grey), for each month with 95% confidence intervals, where the standard error is calculated over all measurements available for that hour of the day during that particular month.

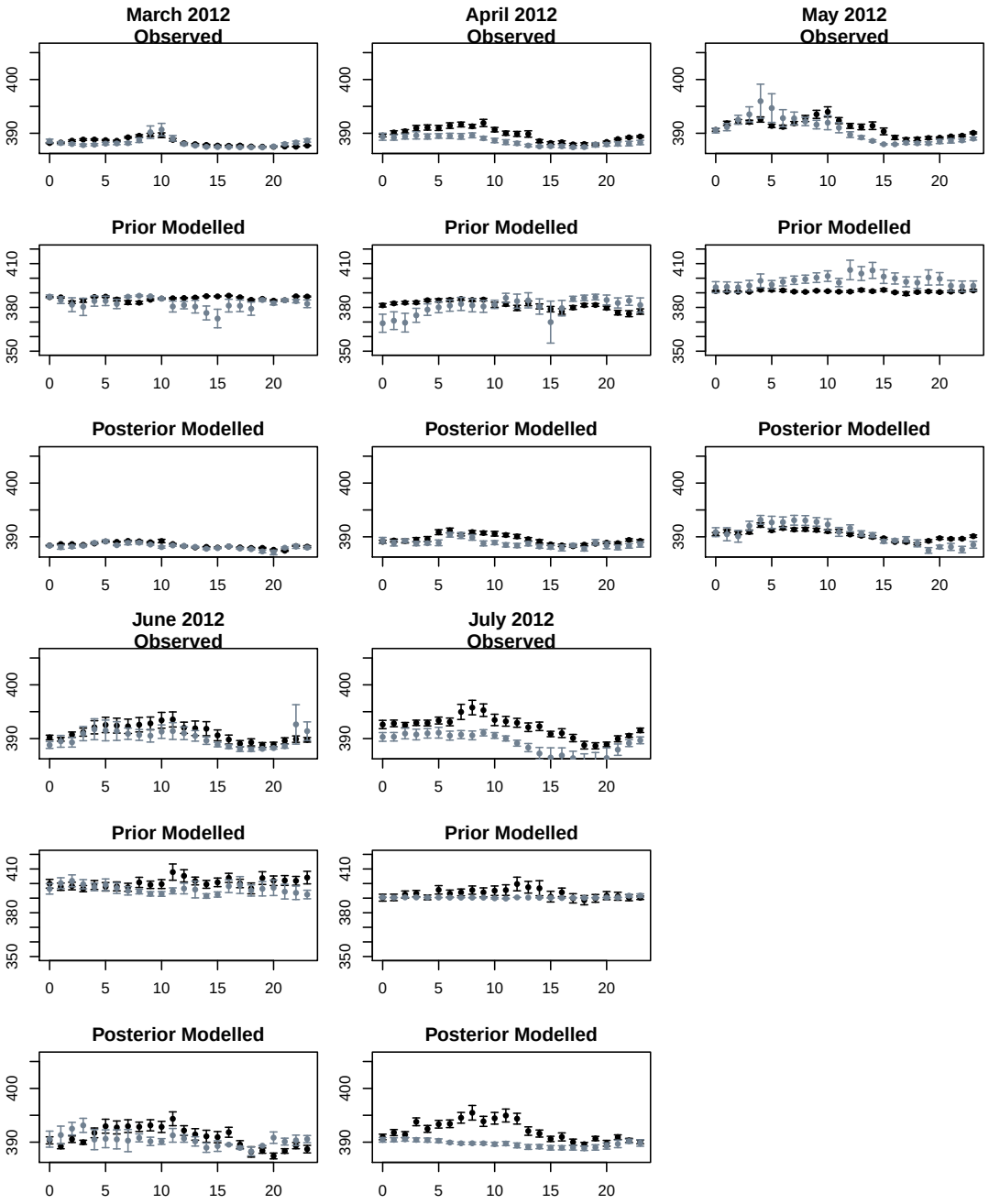
March 2012
Observed
April 2012
Observed
May 2012
Observed
Prior Modelled
Prior Modelled
Prior Modelled
Posterior Modelled
Posterior Modelled
Posterior Modelled
June 2012
Observed
July 2012
Observed
Prior Modelled
Prior Modelled
Posterior Modelled
Posterior Modelled
390
400
350
380
410
0
5
10
15
20

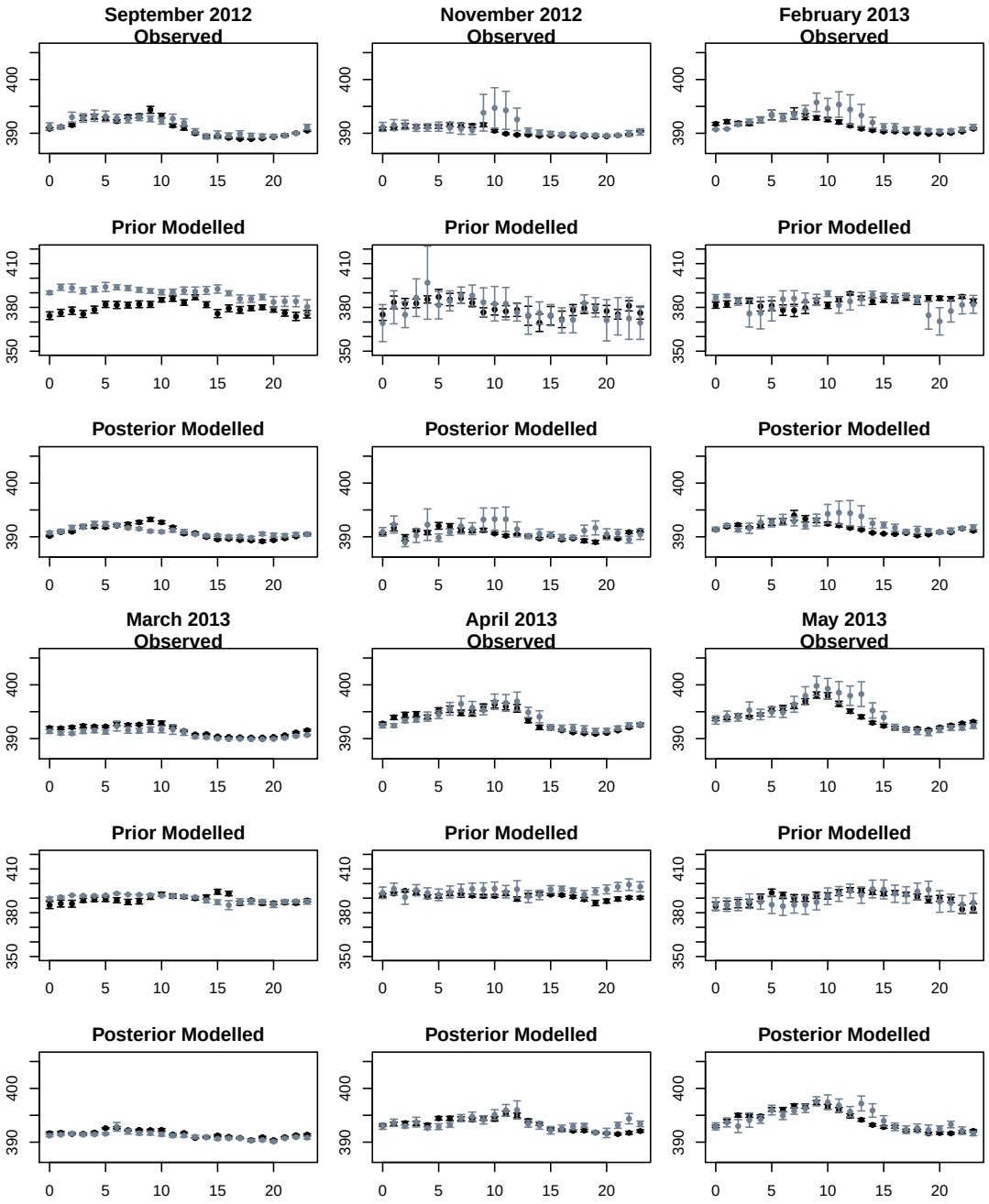
September 2012
Observed
November 2012
Observed
February 2013
Observed
Prior Modelled
Prior Modelled
Prior Modelled
Posterior Modelled
Posterior Modelled
Posterior Modelled
March 2013
Observed
April 2013
Observed
May 2013
Observed
Prior Modelled
Prior Modelled
Prior Modelled
Posterior Modelled
Posterior Modelled
Posterior Modelled
350
380
390
400
410
0
5
10
15
20

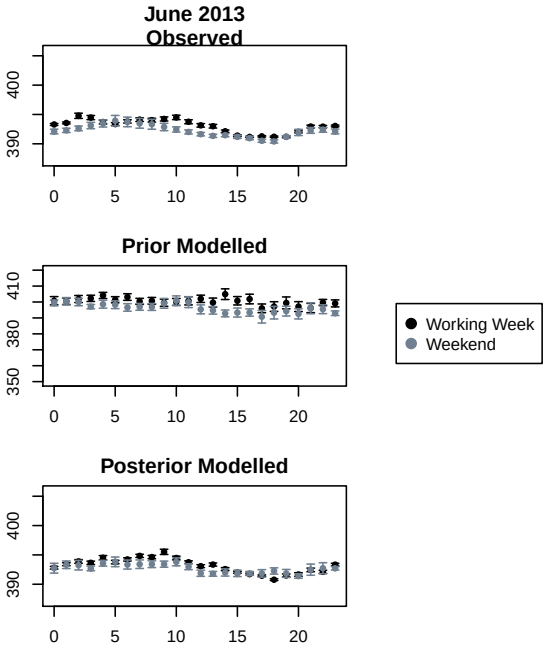


Figure B.8: Diurnal cycle of the observed, prior modelled and posterior modelled $CO_2$ concentrations (ppm) at Hangklip, separated into working week (black) and weekend concentrations (grey), for each month with 95% confidence intervals, where the standard error is calculated over all measurements available for that hour of the day during that particular month.

## B.6 Fossil Fuel and NEE Contributions

The contributions of the fossil fuel and NEE fluxes to the modelled concentrations are provided for Robben Island and Hangklip for the months July 2012 to June 2013. As for March 2012 to June 2012, the posterior estimates of the NEE fluxes are increased in such a way that the uptake of $CO_2$ cancels out the emission of $CO_2$ due to fossil fuel sources. Little adjustment is made to the contribution from the fossil fuel fluxes to the modelled concentration by the inversion.

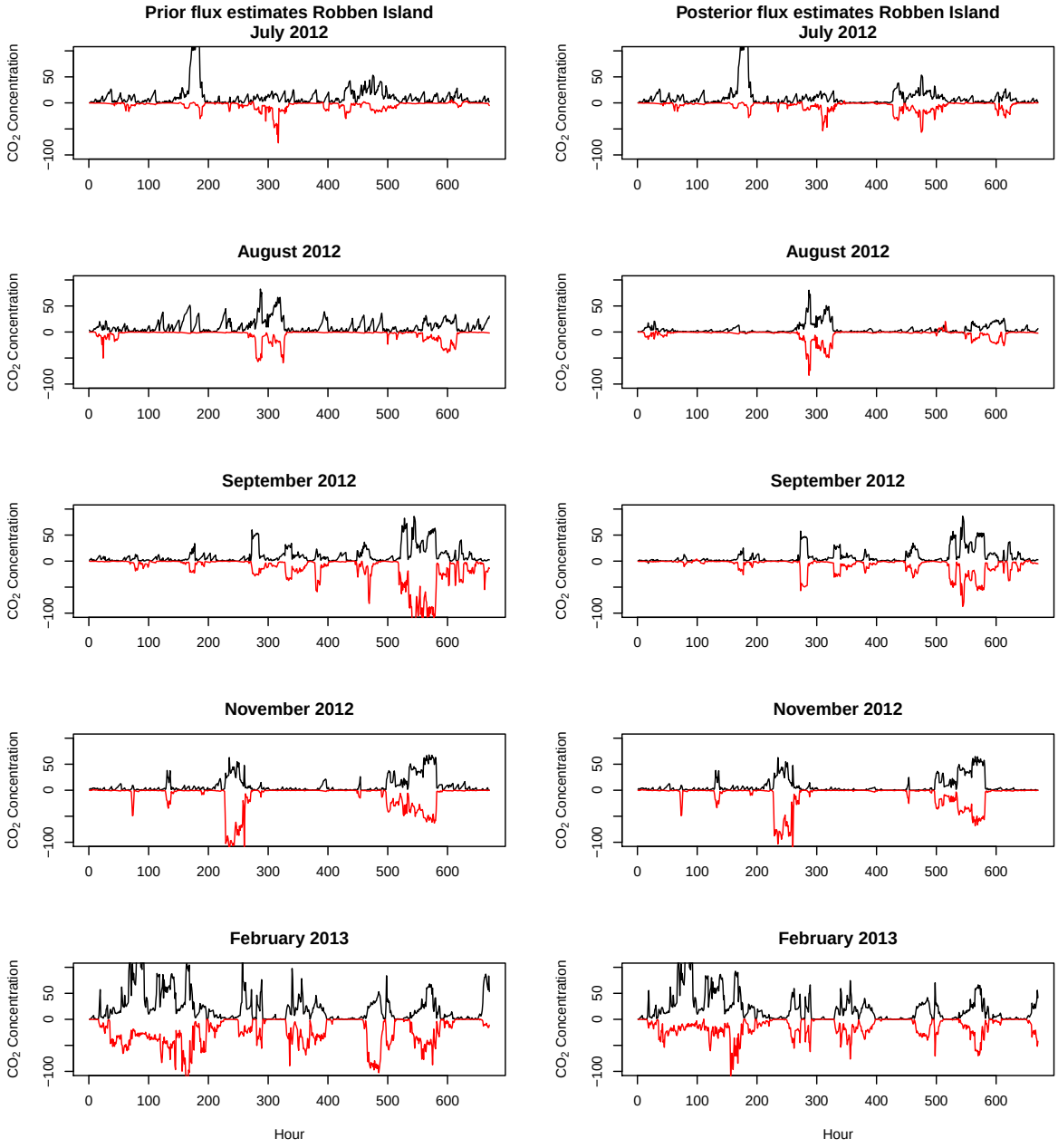
Prior flux estimates Robben Island
July 2012
Posterior flux estimates Robben Island
July 2012
August 2012
September 2012
November 2012
February 2013
CO2 Concentration
Hour

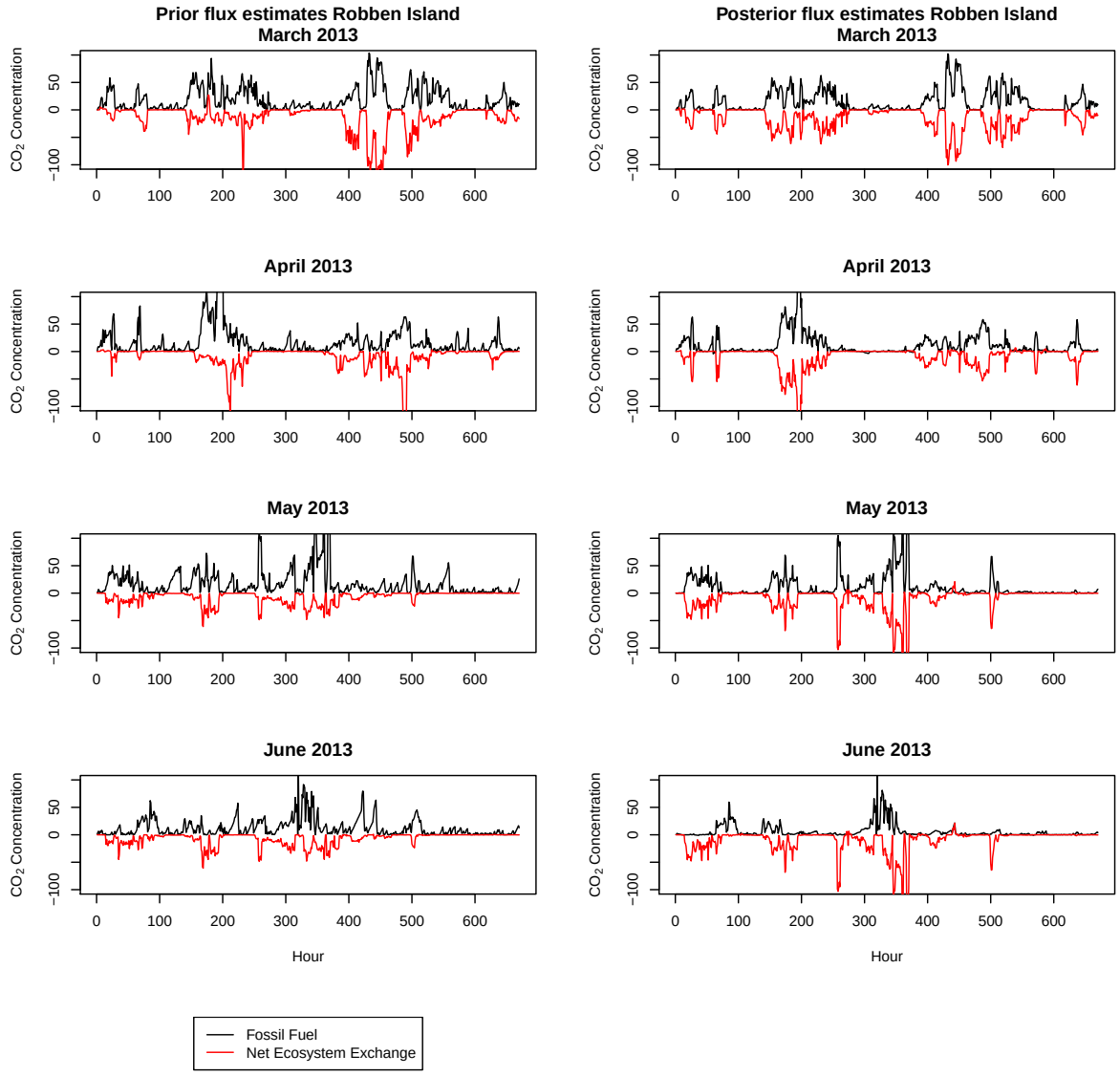


Figure B.9: Contribution of the fossil fuel and NEE surface fluxes to the modelled $CO_2$ concentrations (ppm) at Robben Island.

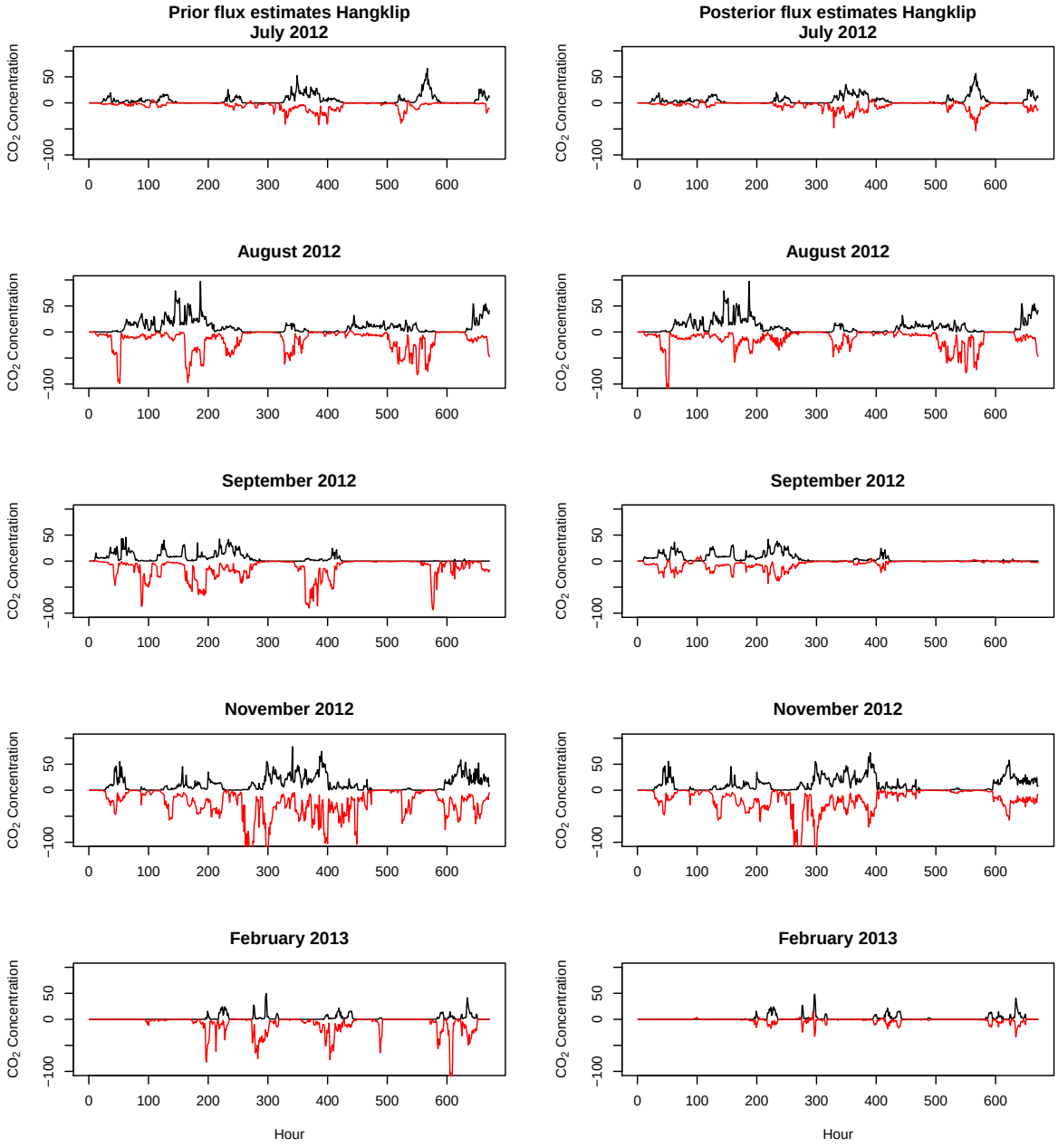
Prior flux estimates Hangklip
July 2012
Posterior flux estimates Hangklip
July 2012
August 2012
August 2012
September 2012
September 2012
November 2012
November 2012
February 2013
February 2013
CO2 Concentration
−100
0
50
0
100
200
300
400
500
600
Hour

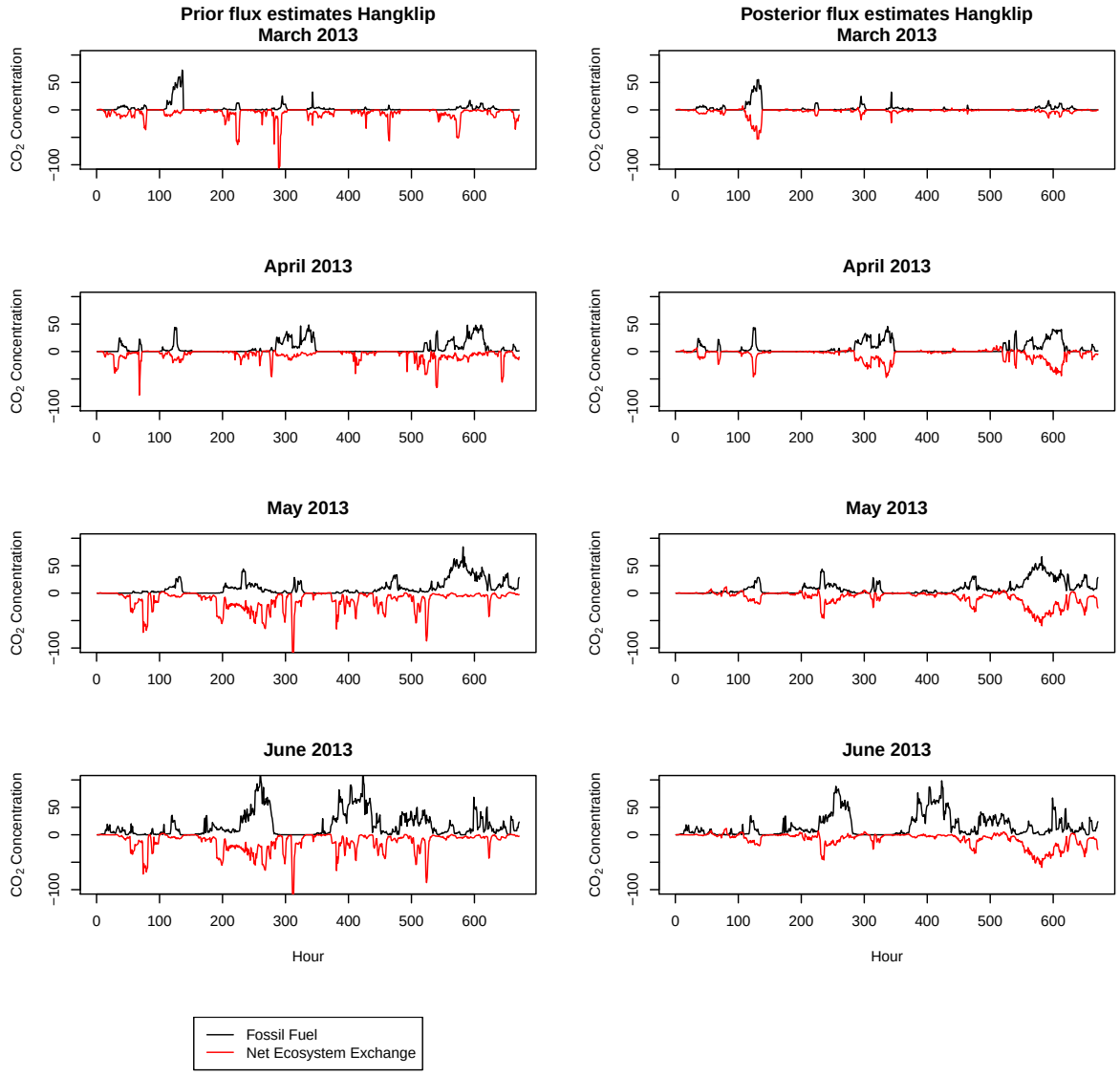


Figure B.10: Contribution of the fossil fuel and NEE surface fluxes to the modelled $CO_2$ concentrations (ppm) at Hangklip.

## B.7 Weekly Flux Estimates

Section 5.3.2 provides a summary of the estimates presented here for the pixel-level weekly fluxes over the full domain for each month.

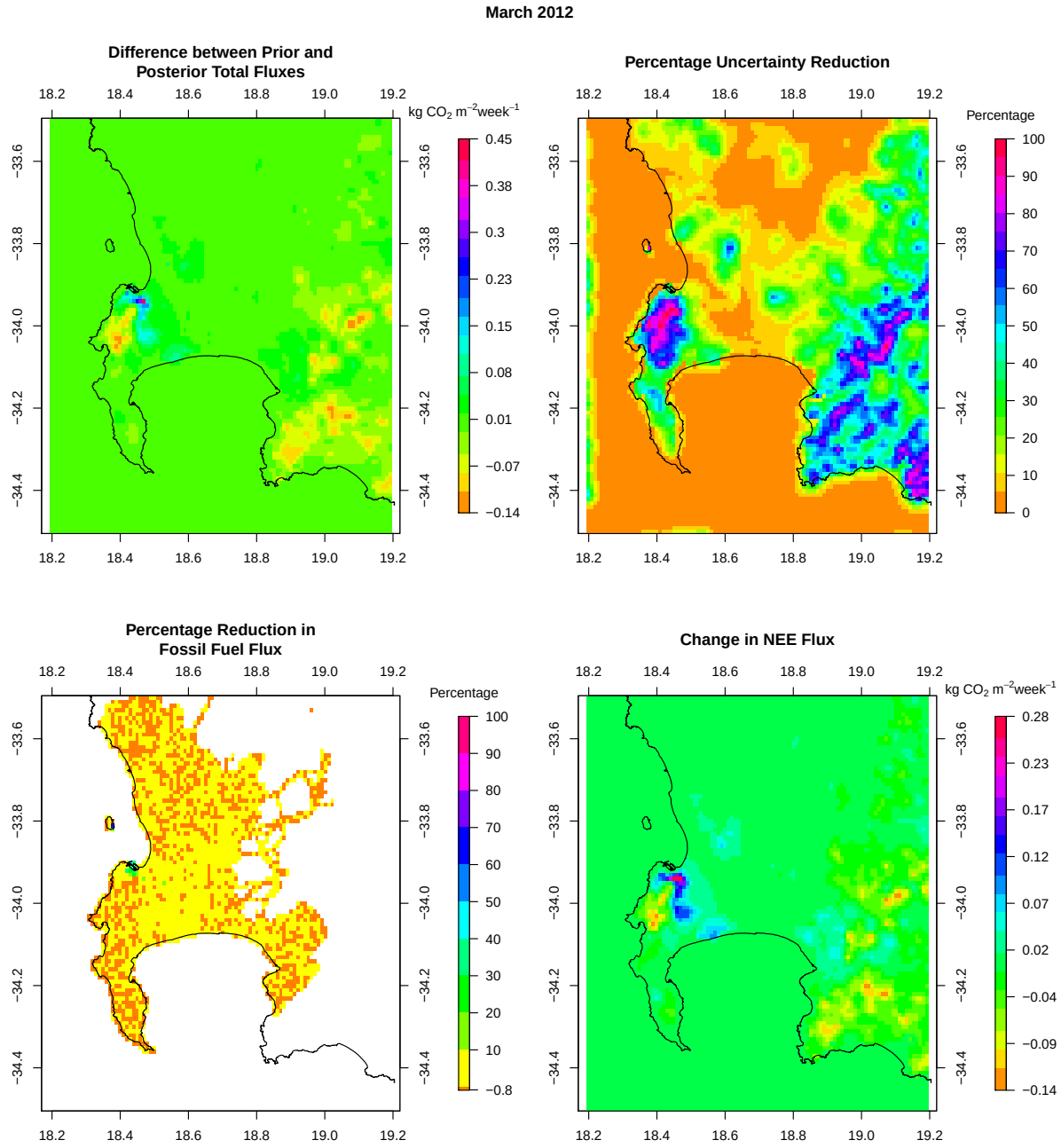


Figure B.11: (Top left) Differences between the prior and posterior total flux estimates (kg $CO_2 m^{-2}$ $week^{-1}$) for March 2012 (prior - posterior). (Top right) Percentage reduction in the standard deviation of the flux estimate from prior to posterior. (Bottom left) Percentage reduction in the fossil fuel flux estimates from prior to posterior. (Bottom right) Differences in the biogenic flux estimates between prior and posterior estimates (prior - posterior) (kg $CO_2 m^{-2}$ $week^{-1}$), with negative values indicating posterior $CO_2$ fluxes were make more positive by the inversion compared with the prior estimates. Extent: between 34.5° and 33.5° south and between 18.2° and 19.2° east.

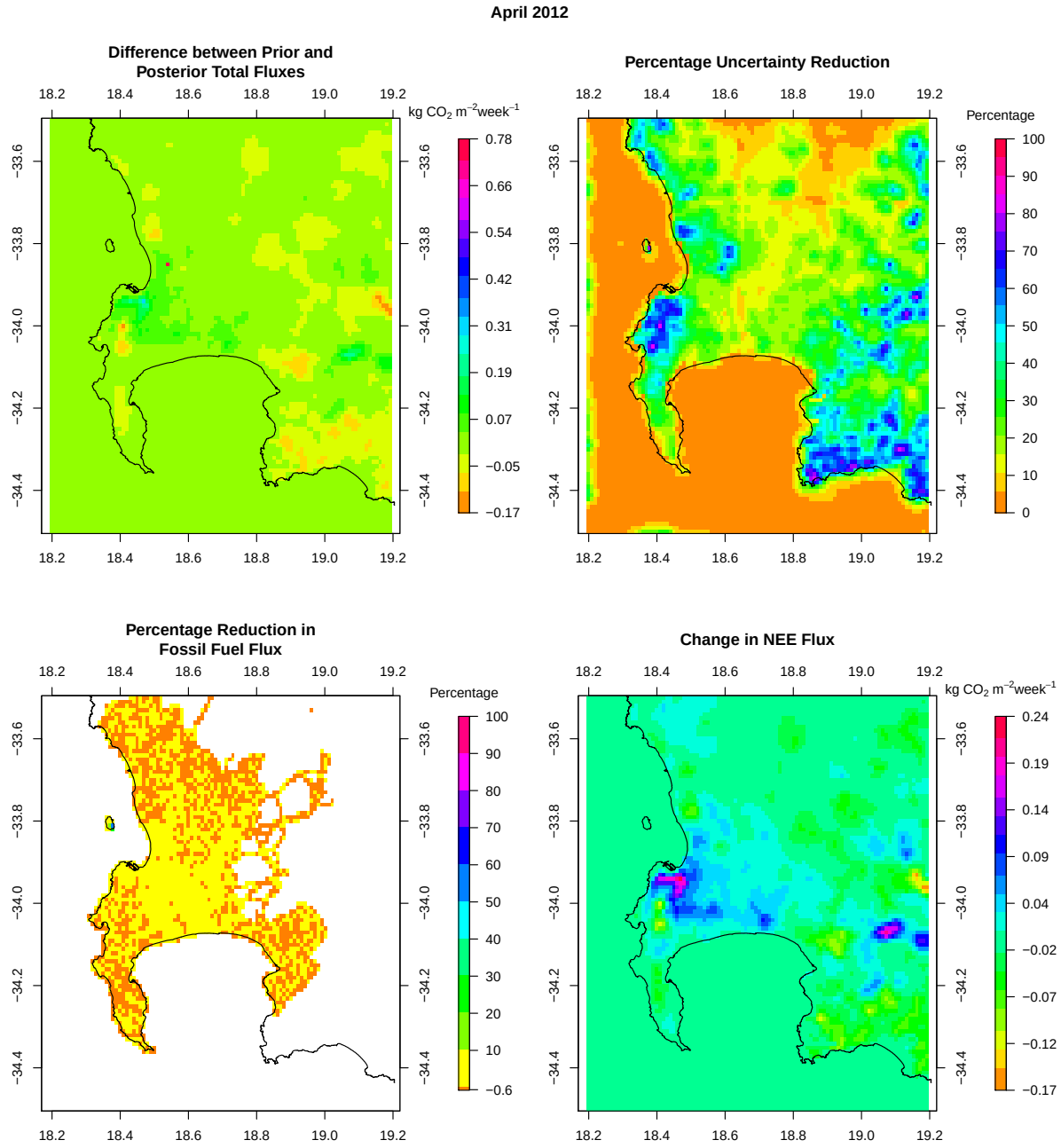


Figure B.12: (Top left) Differences between the prior and posterior total flux estimates (kg $CO_2 m^{-2}$ $week^{-1}$) for April 2012 (prior - posterior). (Top right) Percentage reduction in the standard deviation of the flux estimate from prior to posterior. (Bottom left) Percentage reduction in the fossil fuel flux estimates from prior to posterior. (Bottom right) Differences in the biogenic flux estimates between prior and posterior estimates (prior - posterior) (kg $CO_2 m^{-2}$ $week^{-1}$), with negative values indicating posterior $CO_2$ fluxes were make more positive by the inversion compared with the prior estimates. Extent: between 34.5° and 33.5° south and between 18.2° and 19.2° east.

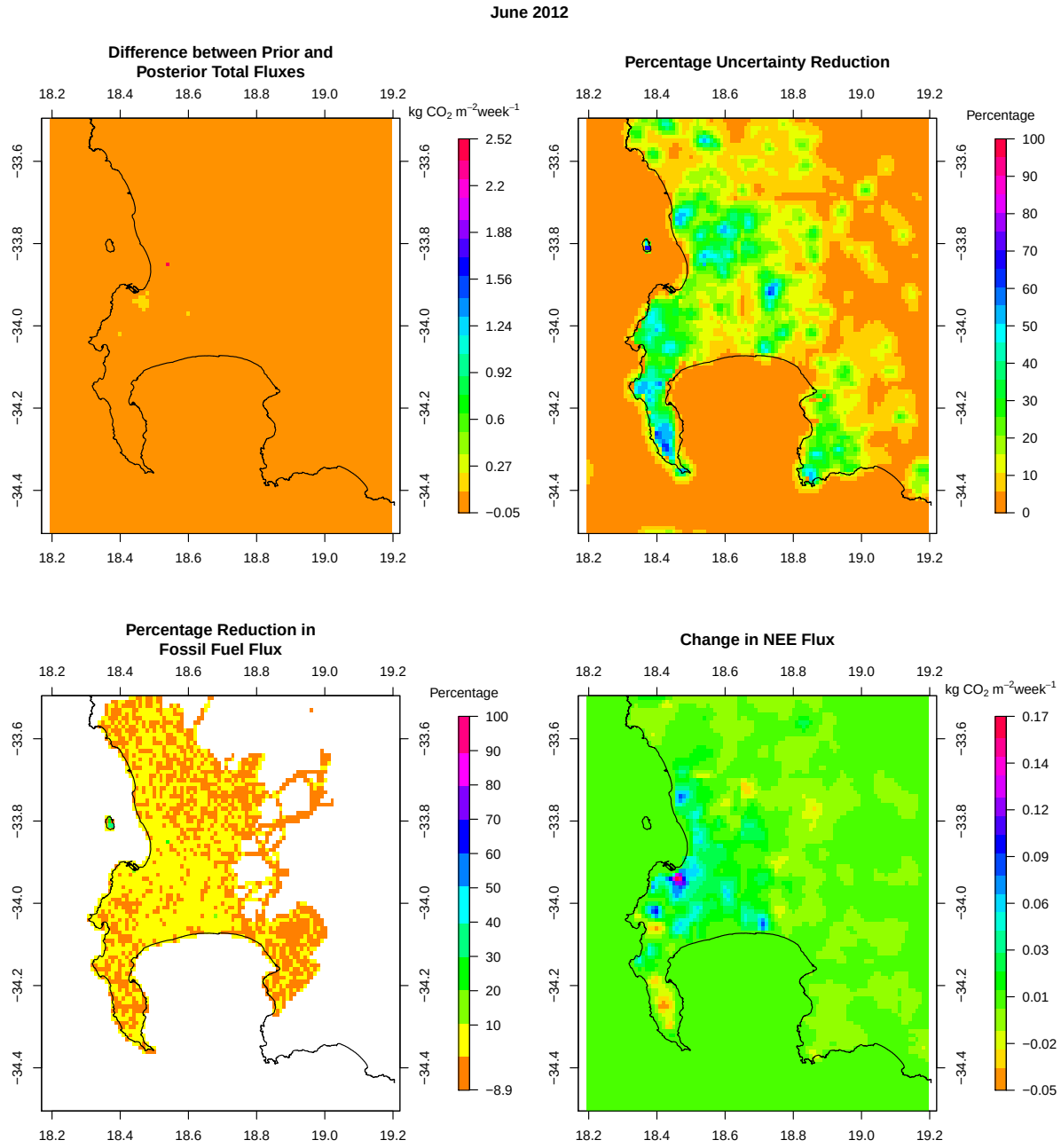


Figure B.13: (Top left) Differences between the prior and posterior total flux estimates (kg $CO_2 m^{-2}$ $week^{-1}$) for June 2012 (prior - posterior). (Top right) Percentage reduction in the standard deviation of the flux estimate from prior to posterior. (Bottom left) Percentage reduction in the fossil fuel flux estimates from prior to posterior. (Bottom right) Differences in the biogenic flux estimates between prior and posterior estimates (prior - posterior) (kg $CO_2 m^{-2}$ $week^{-1}$), with negative values indicating posterior $CO_2$ fluxes were make more positive by the inversion compared with the prior estimates. Extent: between 34.5° and 33.5° south and between 18.2° and 19.2° east.

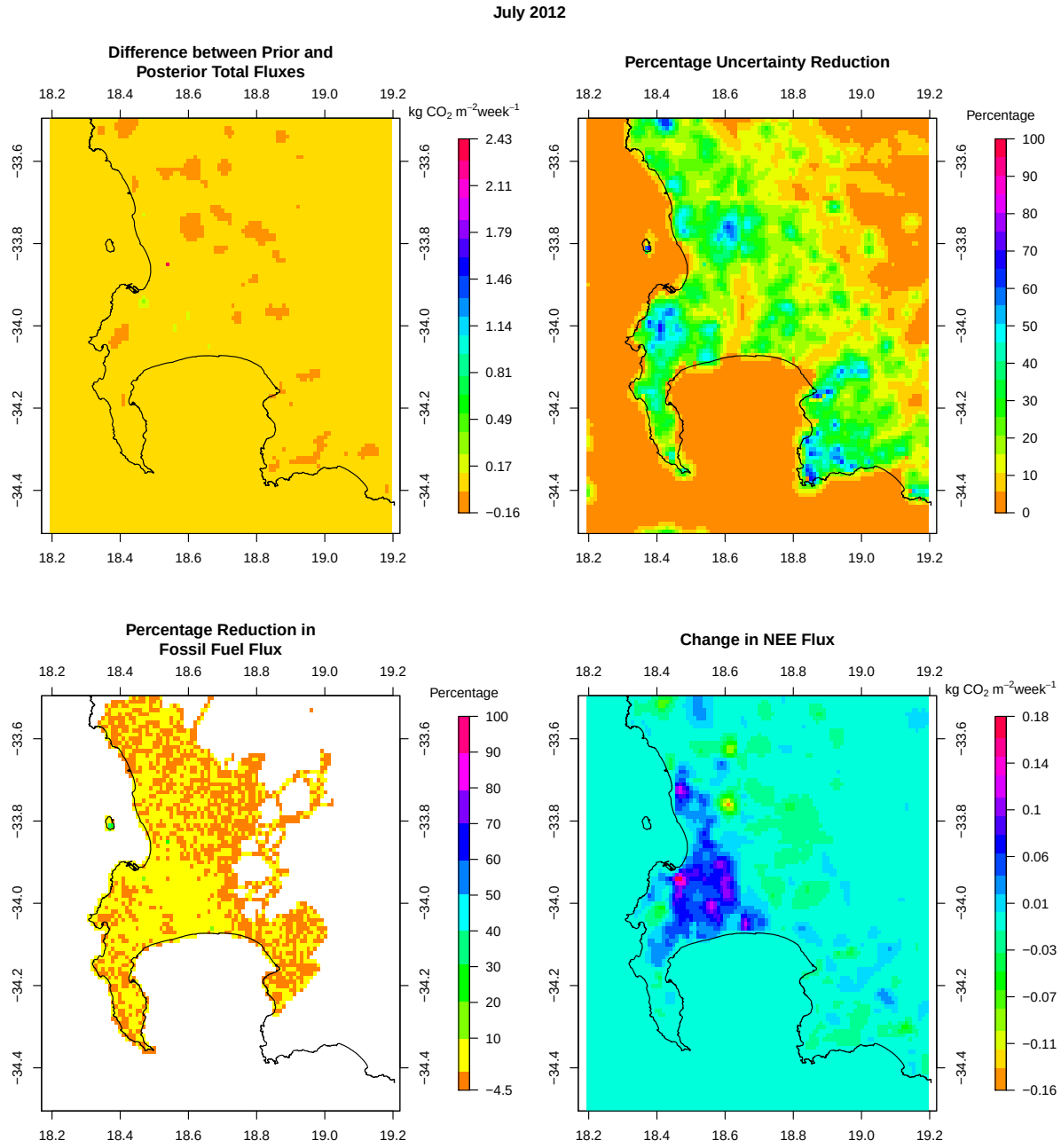


Figure B.14: (Top left) Differences between the prior and posterior total flux estimates (kg $CO_2 m^{-2}$ $week^{-1}$) for July 2012 (prior - posterior). (Top right) Percentage reduction in the standard deviation of the flux estimate from prior to posterior. (Bottom left) Percentage reduction in the fossil fuel flux estimates from prior to posterior. (Bottom right) Differences in the biogenic flux estimates between prior and posterior estimates (prior - posterior) (kg $CO_2 m^{-2}$ $week^{-1}$), with negative values indicating posterior $CO_2$ fluxes were make more positive by the inversion compared with the prior estimates. Extent: between 34.5° and 33.5° south and between 18.2° and 19.2° east.

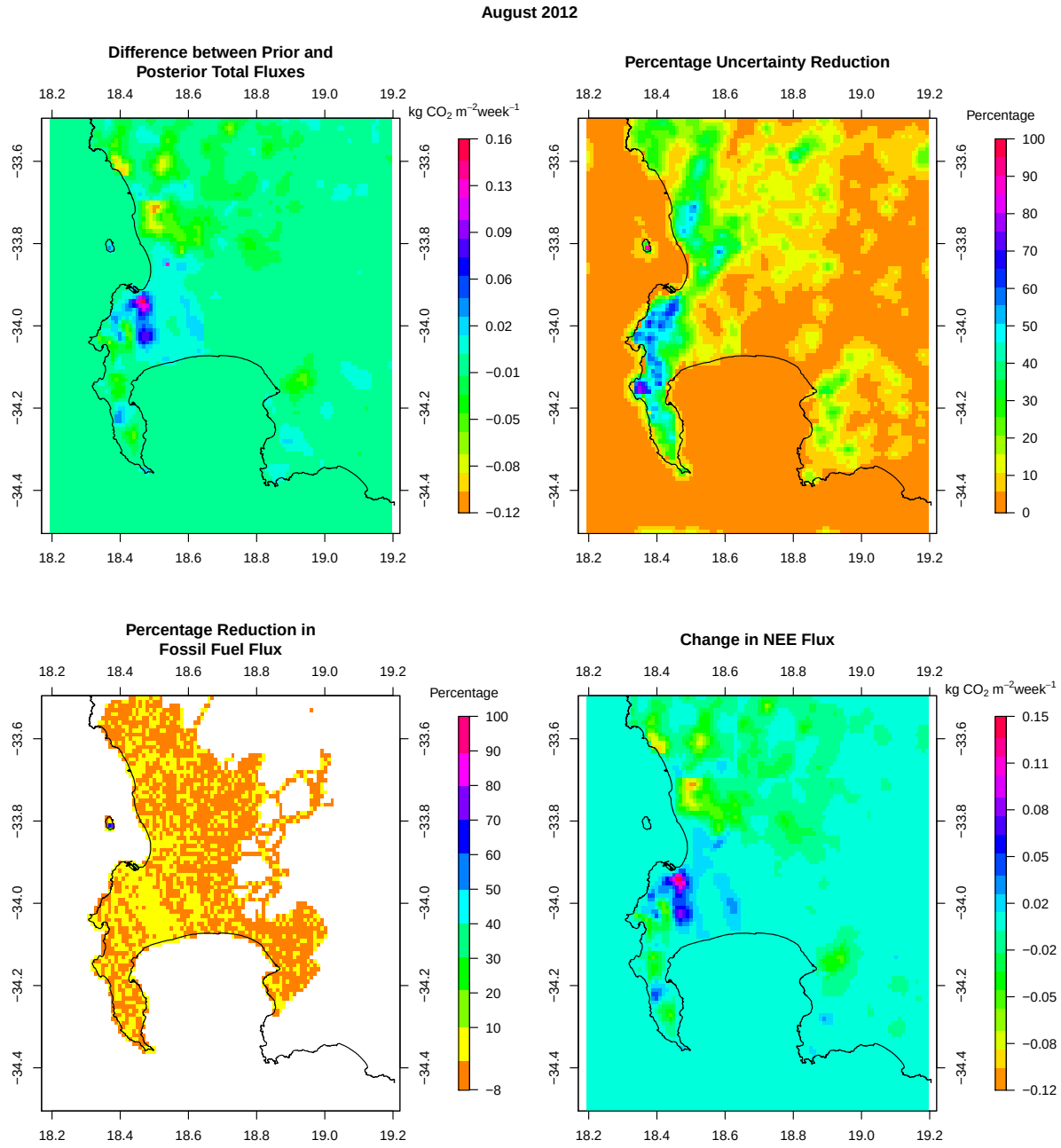


Figure B.15: (Top left) Differences between the prior and posterior total flux estimates (kg $CO_2 m^{-2}$ $week^{-1}$) for August 2012 (prior - posterior). (Top right) Percentage reduction in the standard deviation of the flux estimate from prior to posterior. (Bottom left) Percentage reduction in the fossil fuel flux estimates from prior to posterior. (Bottom right) Differences in the biogenic flux estimates between prior and posterior estimates (prior - posterior) (kg $CO_2 m^{-2}$ $week^{-1}$), with negative values indicating posterior $CO_2$ fluxes were make more positive by the inversion compared with the prior estimates. Extent: between 34.5° and 33.5° south and between 18.2° and 19.2° east.

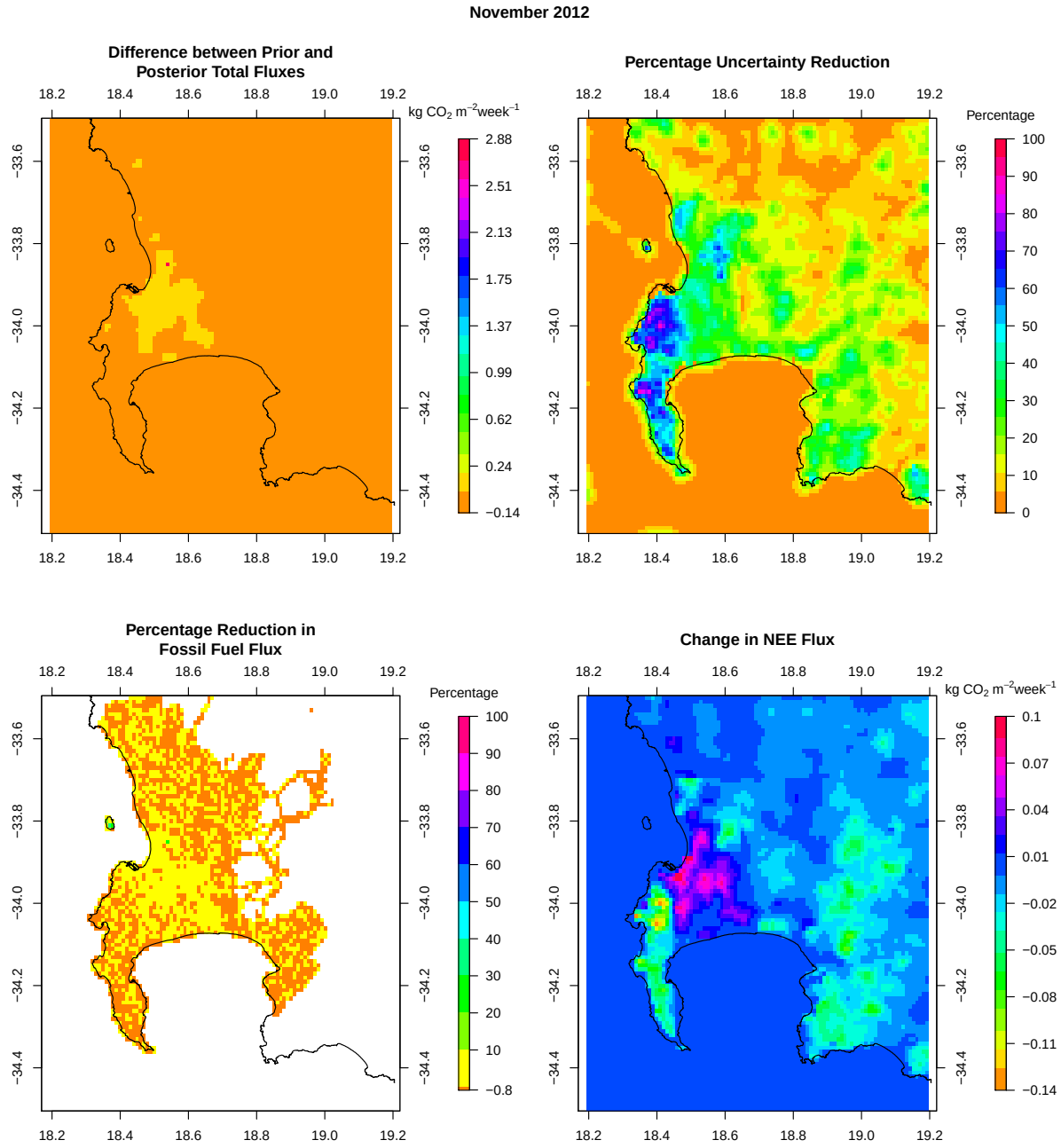


Figure B.16: (Top left) Differences between the prior and posterior total flux estimates (kg $CO_2 m^{-2}$ $week^{-1}$) for November 2012 (prior - posterior). (Top right) Percentage reduction in the standard deviation of the flux estimate from prior to posterior. (Bottom left) Percentage reduction in the fossil fuel flux estimates from prior to posterior. (Bottom right) Differences in the biogenic flux estimates between prior and posterior estimates (prior - posterior) (kg $CO_2 m^{-2}$ $week^{-1}$), with negative values indicating posterior $CO_2$ fluxes were make more positive by the inversion compared with the prior estimates. Extent: between 34.5° and 33.5° south and between 18.2° and 19.2° east.

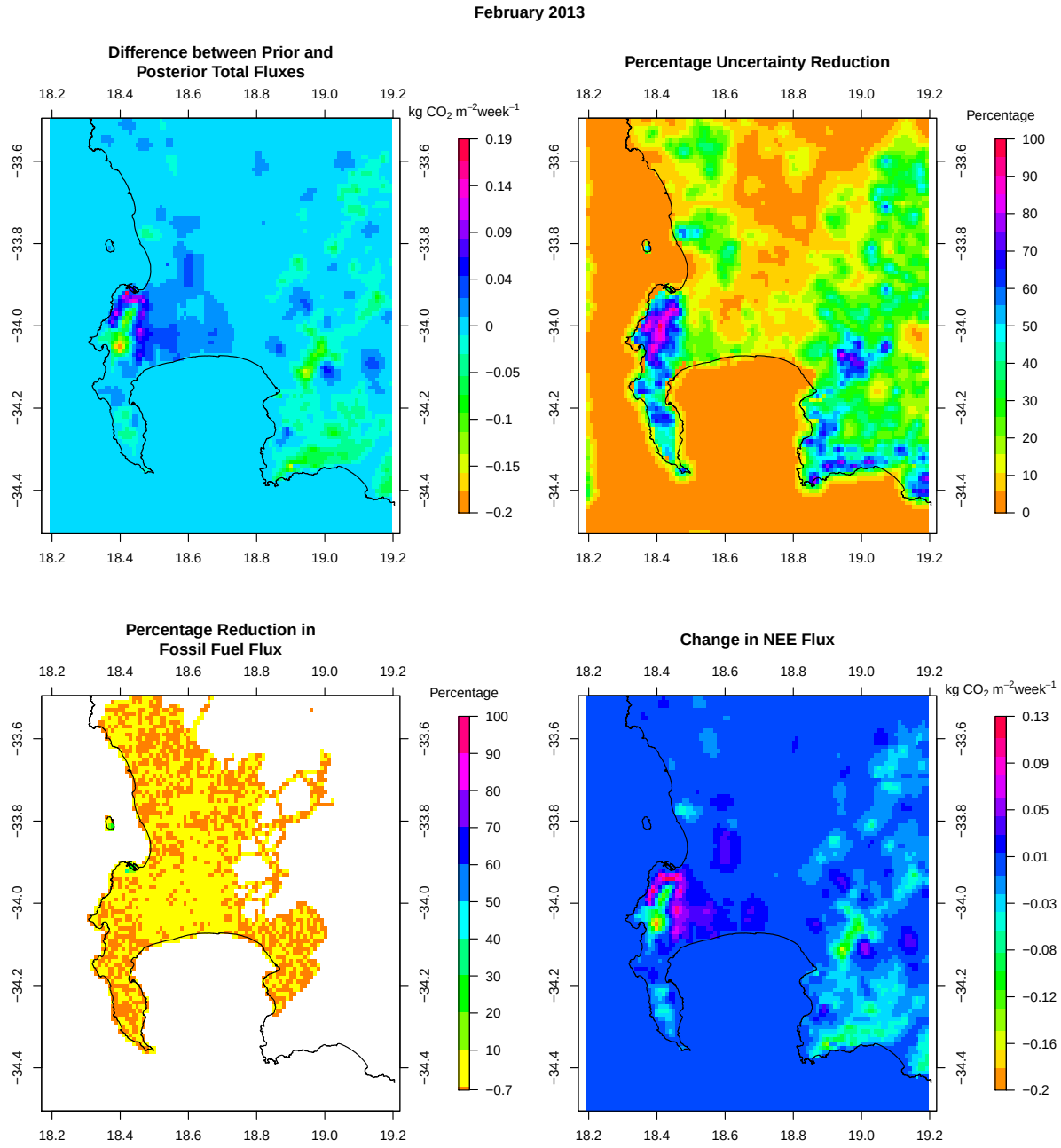


Figure B.17: (Top left) Differences between the prior and posterior total flux estimates (kg $CO_2 m^{-2}$ $week^{-1}$) for February 2013 (prior - posterior). (Top right) Percentage reduction in the standard deviation of the flux estimate from prior to posterior. (Bottom left) Percentage reduction in the fossil fuel flux estimates from prior to posterior. (Bottom right) Differences in the biogenic flux estimates between prior and posterior estimates (prior - posterior) (kg $CO_2 m^{-2}$ $week^{-1}$), with negative values indicating posterior $CO_2$ fluxes were make more positive by the inversion compared with the prior estimates. Extent: between 34.5° and 33.5° south and between 18.2° and 19.2° east.

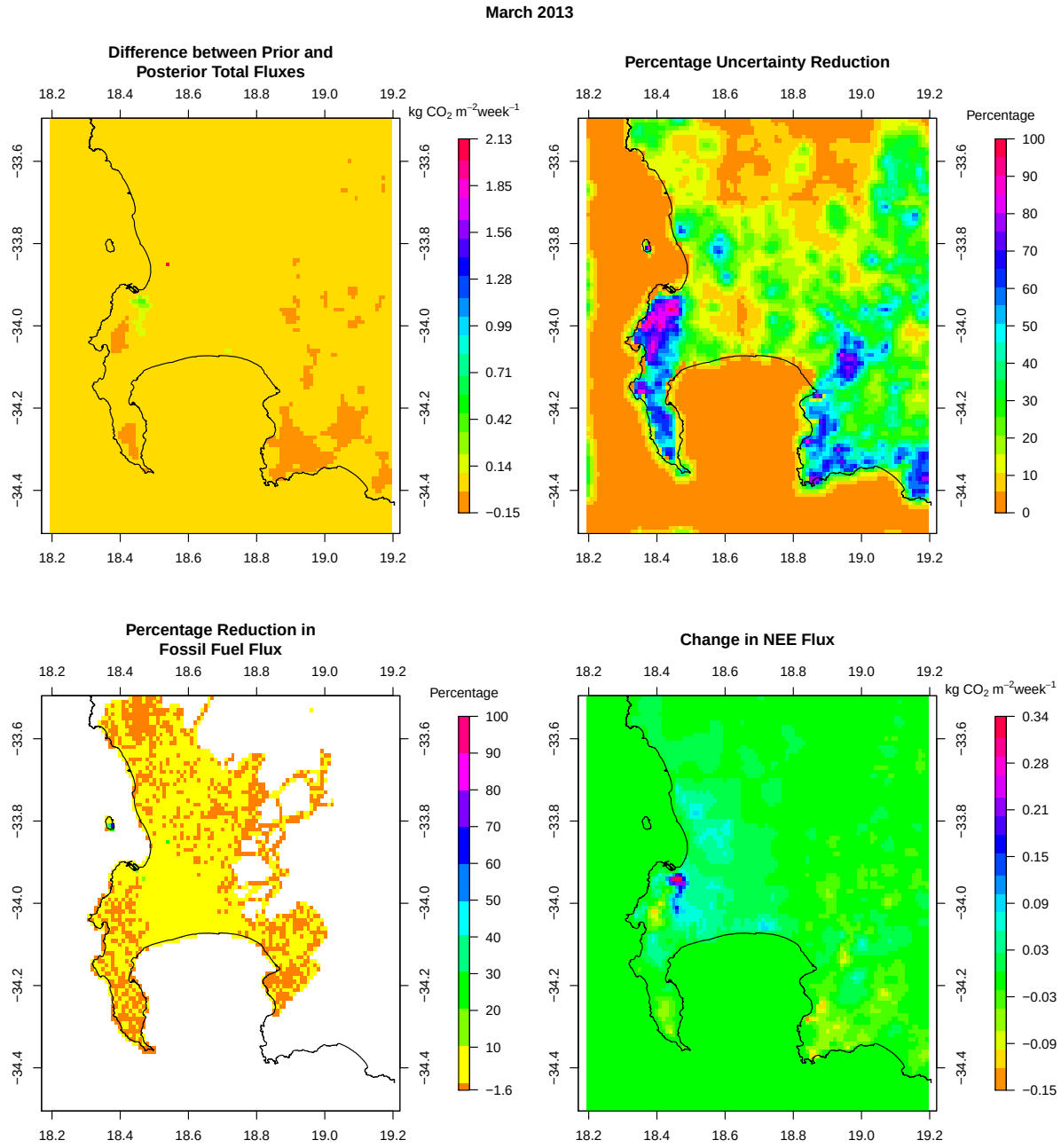


Figure B.18: (Top left) Differences between the prior and posterior total flux estimates (kg $CO_2 m^{-2}$ $week^{-1}$) for March 2013 (prior - posterior). (Top right) Percentage reduction in the standard deviation of the flux estimate from prior to posterior. (Bottom left) Percentage reduction in the fossil fuel flux estimates from prior to posterior. (Bottom right) Differences in the biogenic flux estimates between prior and posterior estimates (prior - posterior) (kg $CO_2 m^{-2}$ $week^{-1}$), with negative values indicating posterior $CO_2$ fluxes were make more positive by the inversion compared with the prior estimates. Extent: between 34.5° and 33.5° south and between 18.2° and 19.2° east.

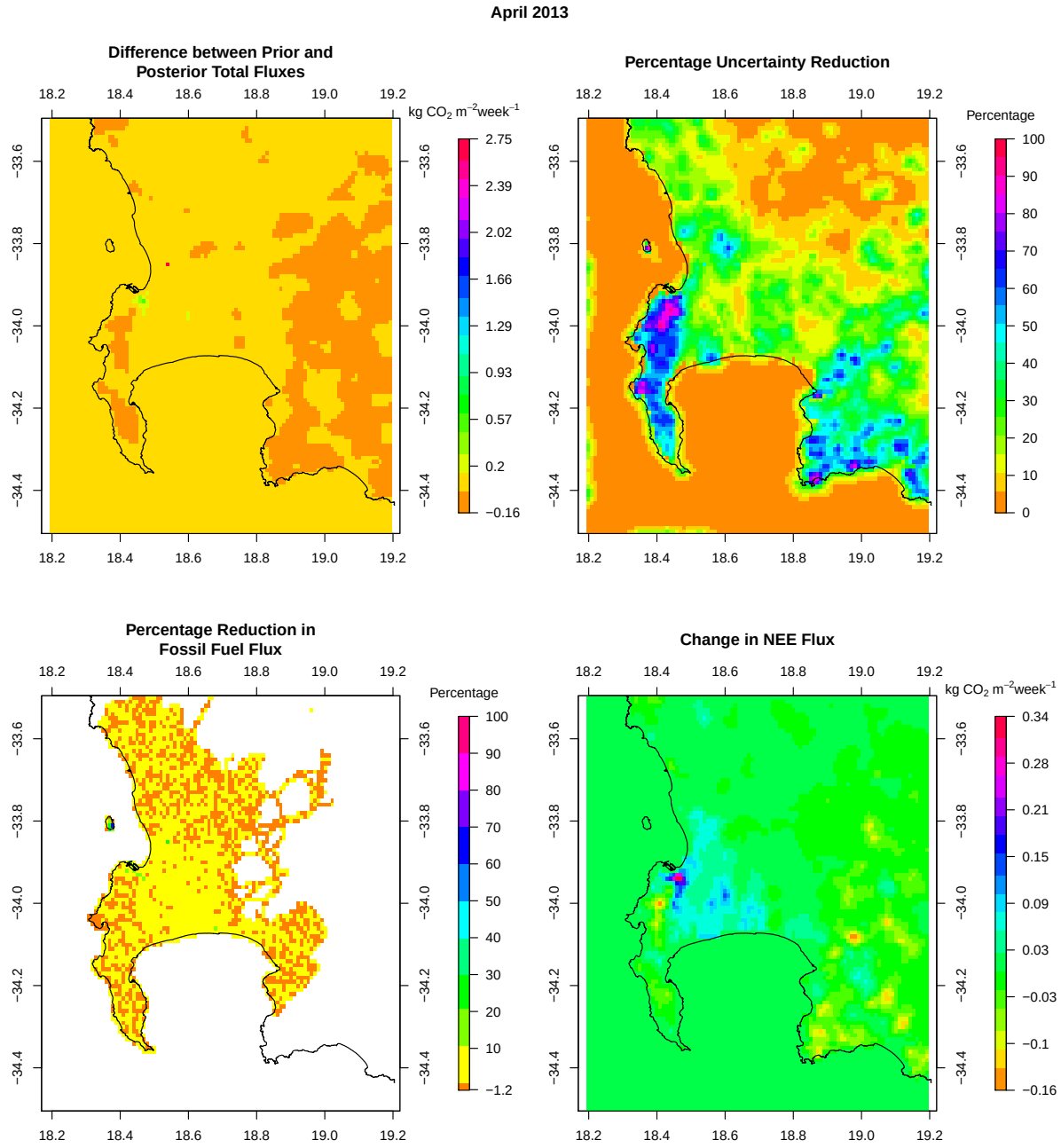


Figure B.19: (Top left) Differences between the prior and posterior total flux estimates (kg $CO_2 m^{-2}$ week$^{-1}$) for April 2013 (prior - posterior). (Top right) Percentage reduction in the standard deviation of the flux estimate from prior to posterior. (Bottom left) Percentage reduction in the fossil fuel flux estimates from prior to posterior. (Bottom right) Differences in the biogenic flux estimates between prior and posterior estimates (prior - posterior) (kg $CO_2 m^{-2}$ week$^{-1}$), with negative values indicating posterior $CO_2$ fluxes were make more positive by the inversion compared with the prior estimates. Extent: between 34.5° and 33.5° south and between 18.2° and 19.2° east.

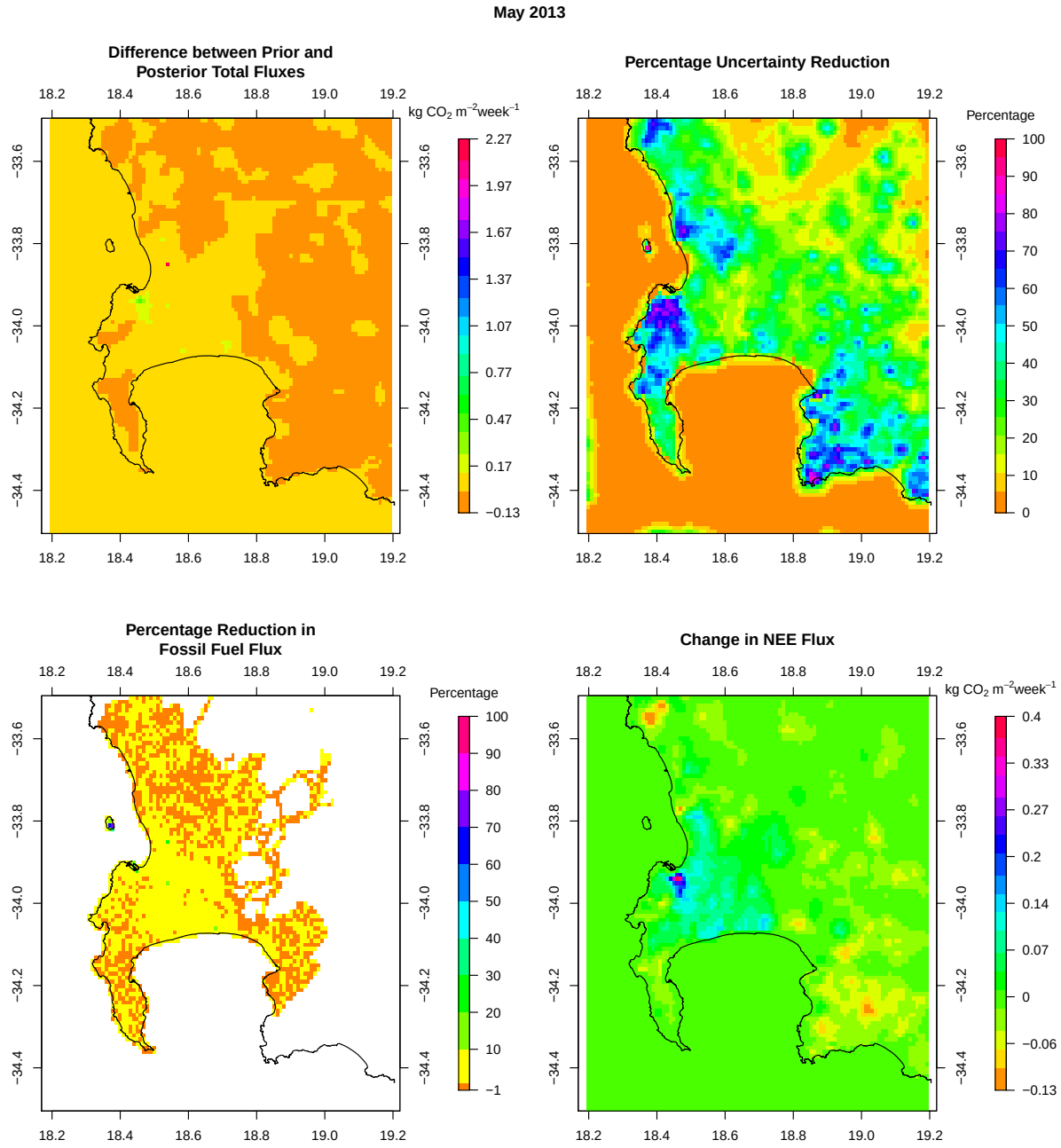


Figure B.20: (Top left) Differences between the prior and posterior total flux estimates (kg $CO_2 m^{-2}$ week$^{-1}$) for May 2013 (prior - posterior). (Top right) Percentage reduction in the standard deviation of the flux estimate from prior to posterior. (Bottom left) Percentage reduction in the fossil fuel flux estimates from prior to posterior. (Bottom right) Differences in the biogenic flux estimates between prior and posterior estimates (prior - posterior) (kg $CO_2 m^{-2}$ week$^{-1}$), with negative values indicating posterior $CO_2$ fluxes were make more positive by the inversion compared with the prior estimates. Extent: between 34.5° and 33.5° south and between 18.2° and 19.2° east.

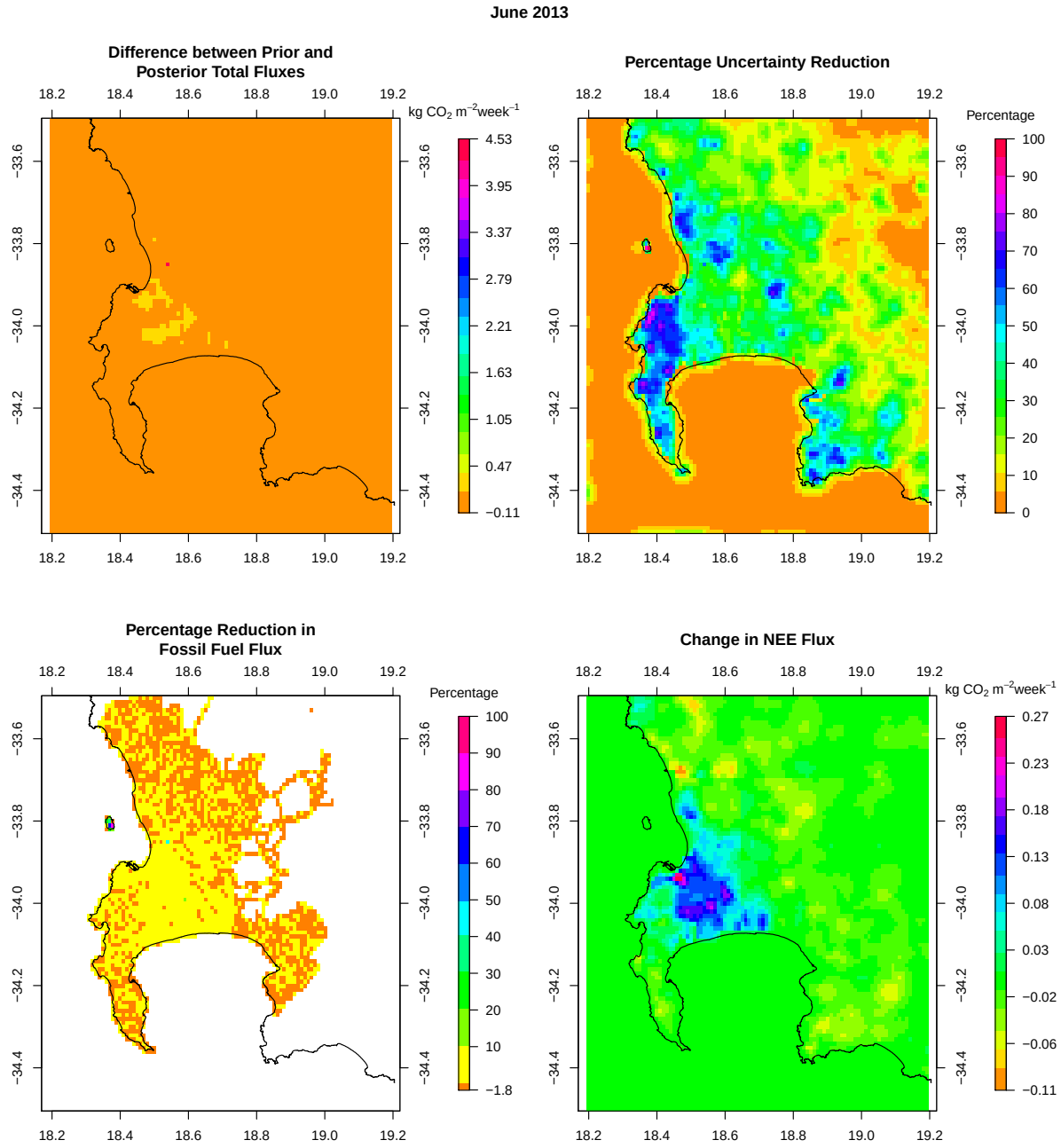


Figure B.21: (Top left) Differences between the prior and posterior total flux estimates (kg $CO_2 m^{-2}$ $week^{-1}$) for June 2013 (prior - posterior). (Top right) Percentage reduction in the standard deviation of the flux estimate from prior to posterior. (Bottom left) Percentage reduction in the fossil fuel flux estimates from prior to posterior. (Bottom right) Differences in the biogenic flux estimates between prior and posterior estimates (prior - posterior) (kg $CO_2 m^{-2}$ $week^{-1}$), with negative values indicating posterior $CO_2$ fluxes were make more positive by the inversion compared with the prior estimates. Extent: between 34.5° and 33.5° south and between 18.2° and 19.2° east.

## B.8 Toy Inversion

Let us consider an hourly measurement at a single site, with a fossil fuel flux daytime source, a fossil fuel flux night-time source, an NEE flux from the same location, and an NEE flux from a neighbouring pixel. We wish to solve for these four fluxes and the covariance matrix of the uncertainties in these fluxes. Selecting some of the most extreme values for the uncertainties and for the sensitivities for the current inversion framework we could get the following:

$$\mathbf{H} = \quad (0.0, 0.0126, 0.00902, 0.0032); \quad \mathbf{C}_{\boldsymbol{s}_0} = \quad \begin{pmatrix} 233 & 0 & 0 & 0 \\ 0 & 78 & 0 & 0 \\ 0 & 0 & 1578 & 1220 \\ 0 & 0 & 1220 & 1578 \end{pmatrix}; \quad \mathbf{C}_{\boldsymbol{c}} = 4$$

Solving for the posterior covariance matrix of the flux uncertainties using:

$$\begin{aligned} \mathbf{C}_{\boldsymbol{s}} &= \left(\mathbf{H}^T \mathbf{C}_{\boldsymbol{c}}^{-1} \mathbf{H} + \mathbf{C}_{\boldsymbol{s}_0}^{-1}\right)^{-1} && \text{(B.1)} \\ &= \mathbf{C}_{\boldsymbol{s}_0} - \mathbf{C}_{\boldsymbol{s}_0} \mathbf{H}^T \left(\mathbf{H} \mathbf{C}_{\boldsymbol{s}_0} \mathbf{H}^T + \mathbf{C}_{\boldsymbol{c}}\right)^{-1} \mathbf{H} \mathbf{C}_{\boldsymbol{s}_0}. && \text{(B.2)} \end{aligned}$$

gives

$$\mathbf{C}_{\boldsymbol{s}} = \quad \begin{pmatrix} 233 & 0 & 0 & 0 \\ 0 & 77.8 & -4.2 & -3.7 \\ 0 & -4.2 & 1500.2 & 1151.1 \\ 0 & -3.7 & 1151.1 & 1517.0 \end{pmatrix}; \quad \rho_{\mathbf{matrix}} = \quad \begin{pmatrix} 1 & 0 & 0 & 0 \\ 0 & 1 & -0.01 & -0.01 \\ 0 & -0.01 & 1 & 0.76 \\ 0 & -0.01 & 0.76 & 1 \end{pmatrix};$$

Although the sensitivity of the concentration measurement to the fossil fuel and NEE fluxes are not that different, the posterior covariances are small because the transport Jacobian only projects fluxes from individual pixels weakly into modelled concentrations. The uncertainties in the prior modelled concentrations that are attributed to the flux contributions ($\mathbf{H}\mathbf{C}_{\boldsymbol{s}_0}\mathbf{H}^T$) are small relative to the uncertainties specified for the modelled concentration errors ($\mathbf{C}_{\boldsymbol{c}}$). If we reduce the elements of $\mathbf{C}_{\boldsymbol{c}}$ then the posterior covariances increase. For example, If $\mathbf{C}_{\boldsymbol{c}} = 1$ then

$$\mathbf{C}_{\boldsymbol{s}} = \quad \begin{pmatrix} 233 & 0 & 0 & 0 \\ 0 & 77.2 & -14.5 & -12.9 \\ 0 & -14.5 & 1310.0 & 982.8 \\ 0 & -12.9 & 982.8 & 1368.0 \end{pmatrix}; \quad \rho_{\mathbf{matrix}} = \quad \begin{pmatrix} 1 & 0 & 0 & 0 \\ 0 & 1 & -0.04 & -0.04 \\ 0 & -0.04 & 1 & 0.73 \\ 0 & -0.04 & 0.73 & 1 \end{pmatrix};$$

# Bibliography

Lamigueiro, O., P.: Visualization methods for raster data, ver. 0.41. http://oscarperpinan.github.io/rastervis

# Appendix C

# Supplementary Material - Chapter 6

## C.1 Observed versus Modelled Concentrations

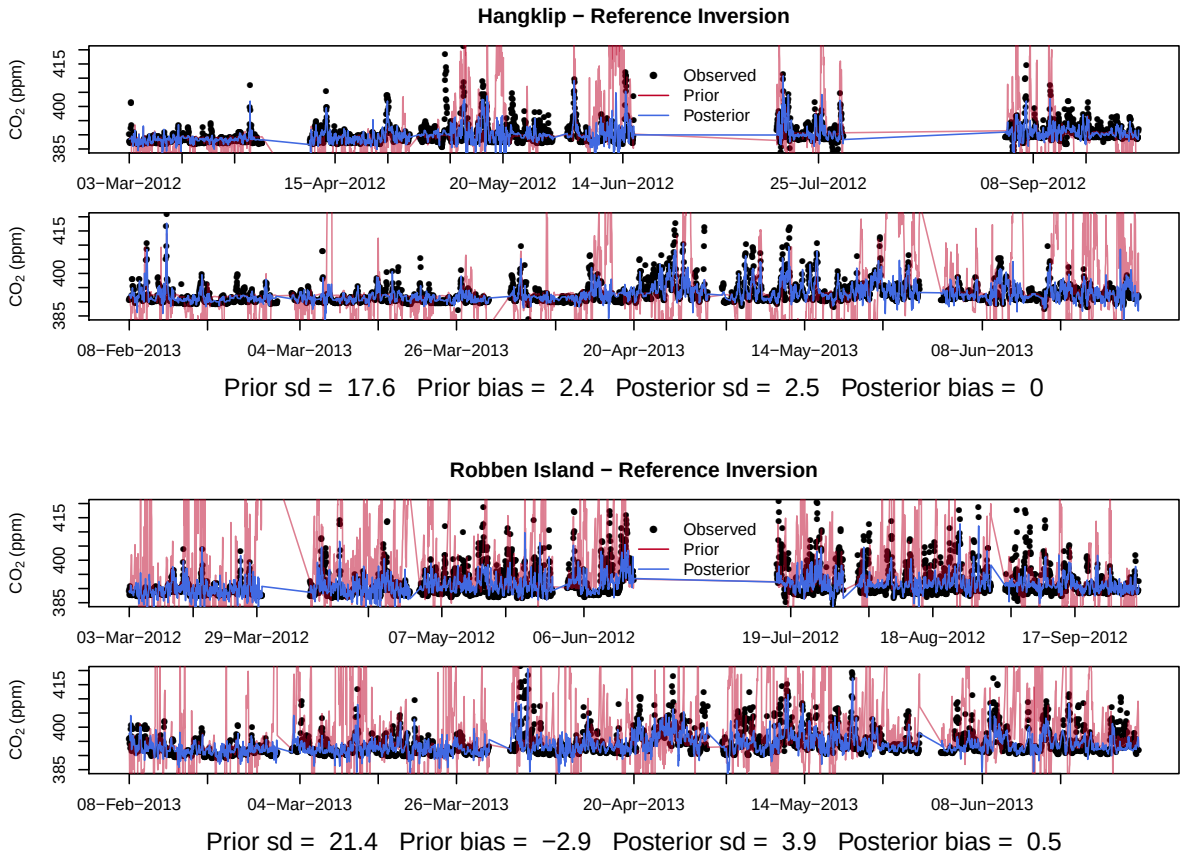


Figure C.1: Prior and posterior modelled concentrations at Hangklip and Robben Island sites under the reference inversion over the full inversion period from March 2012 until June 2013.

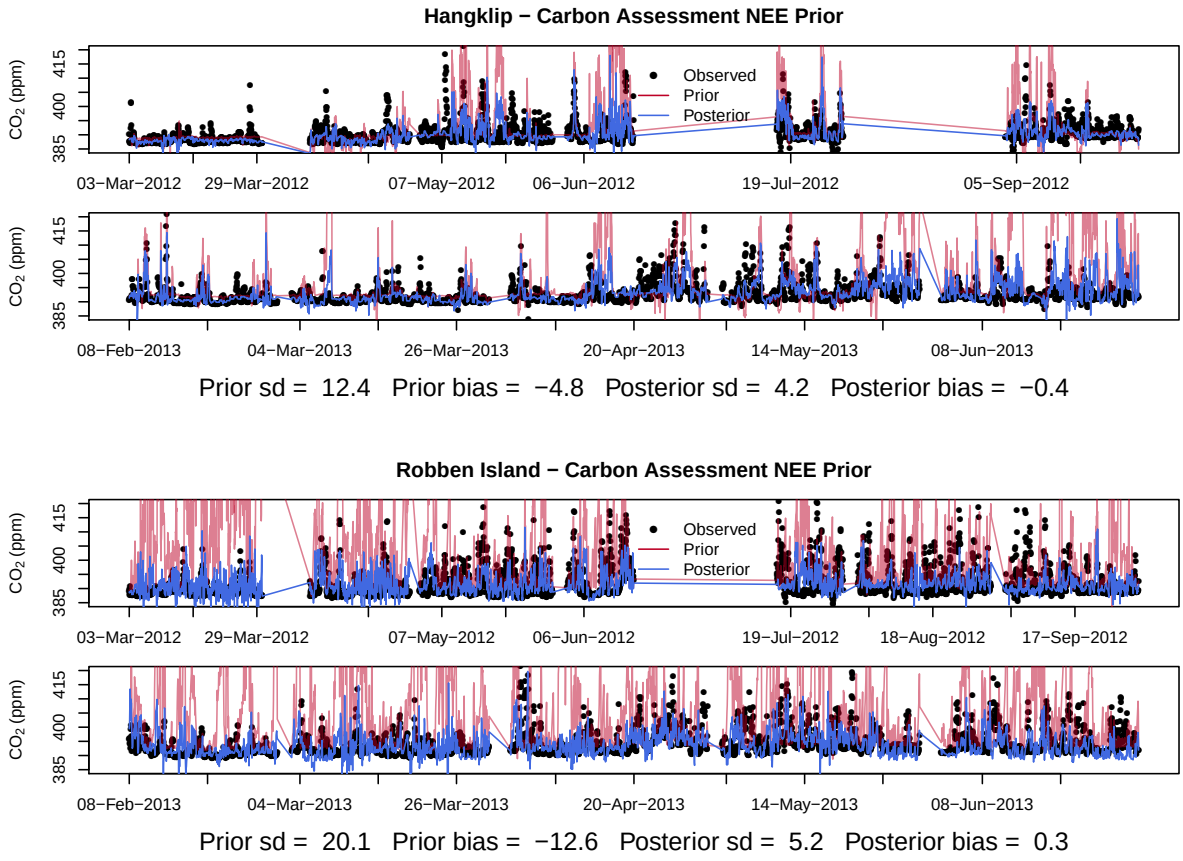


Figure C.2: Prior and posterior modelled concentrations at Hangklip and Robben Island sites under the inversion using the carbon assessment product for the NEE prior over the full inversion period from March 2012 until June 2013.

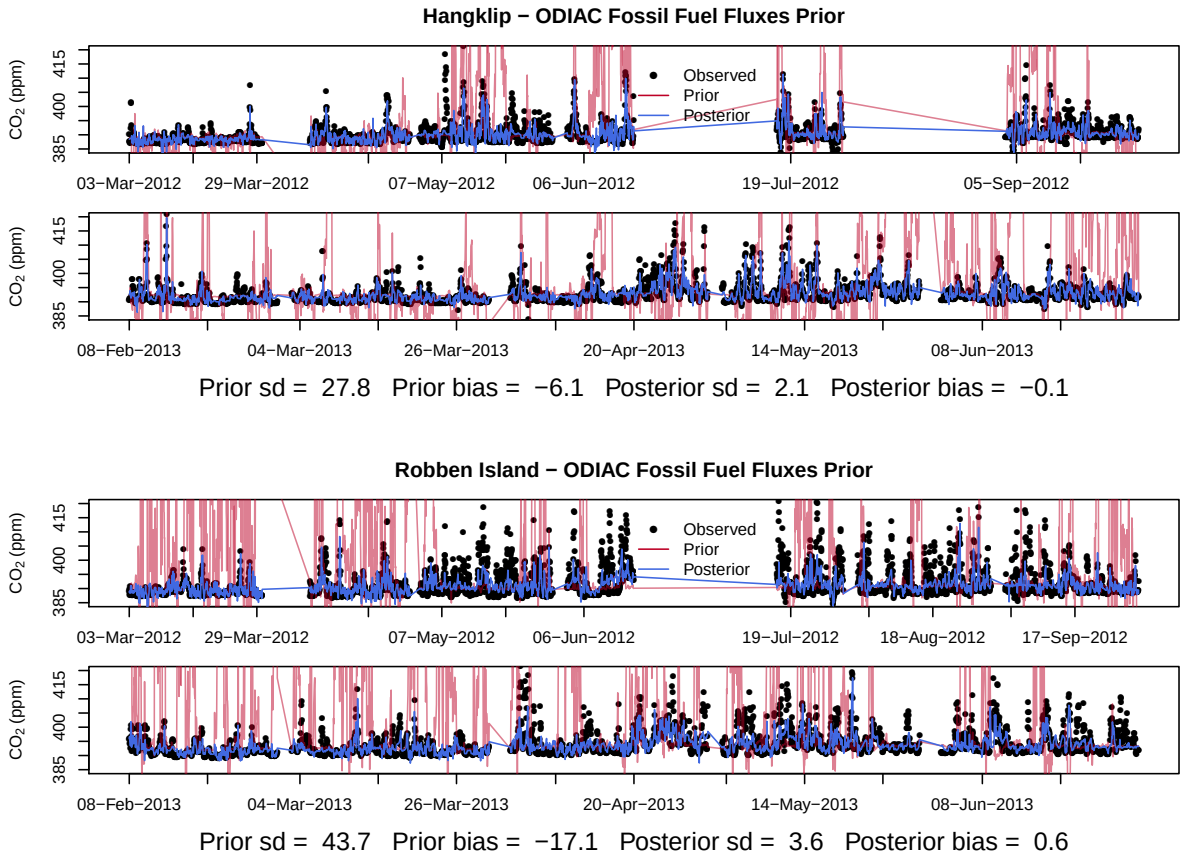


Figure C.3: Prior and posterior modelled concentrations at Hangklip and Robben Island sites under the inversion using the ODIAC fossil fuel emission product for the fossil fuel flux prior over the full inversion period from March 2012 until June 2013.

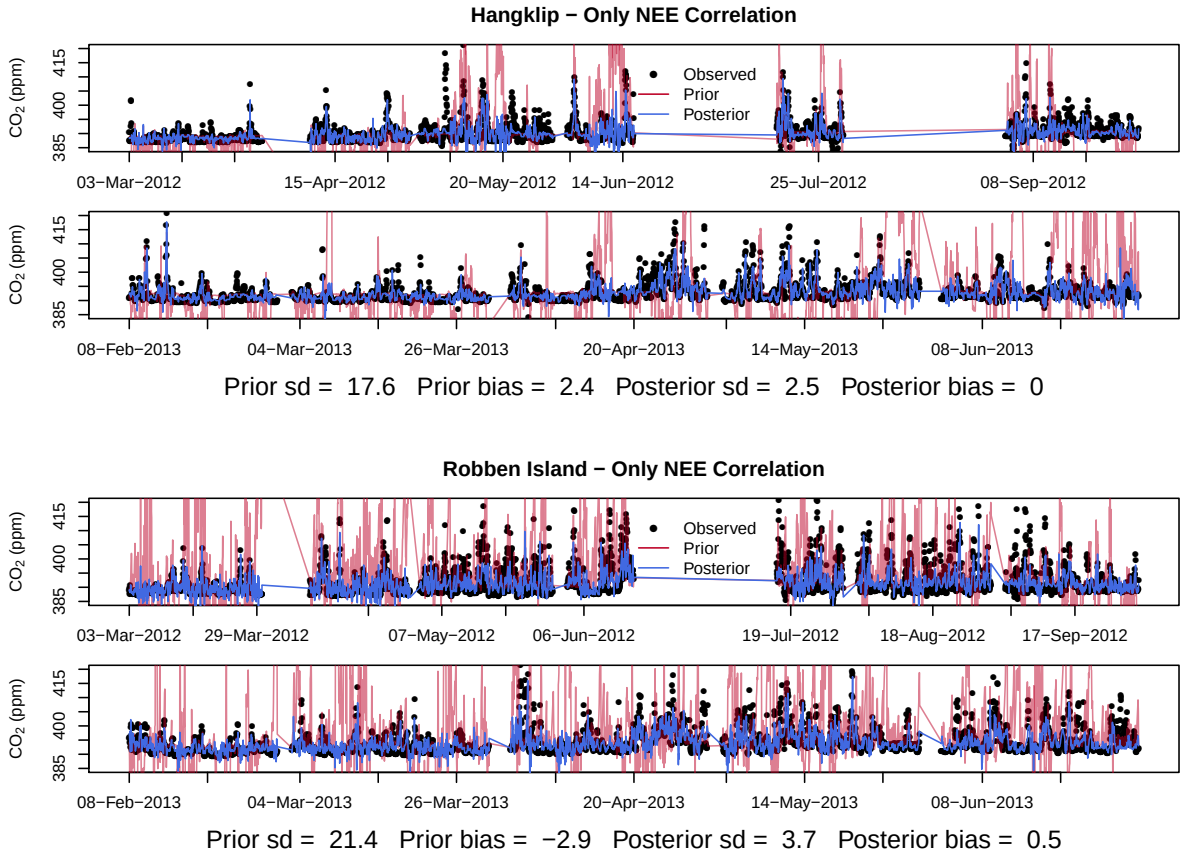


Figure C.4: Prior and posterior modelled concentrations at Hangklip and Robben Island sites under the inversion with only correlation accounted for between the uncertainties in the NEE fluxes over the full inversion period from March 2012 until June 2013.

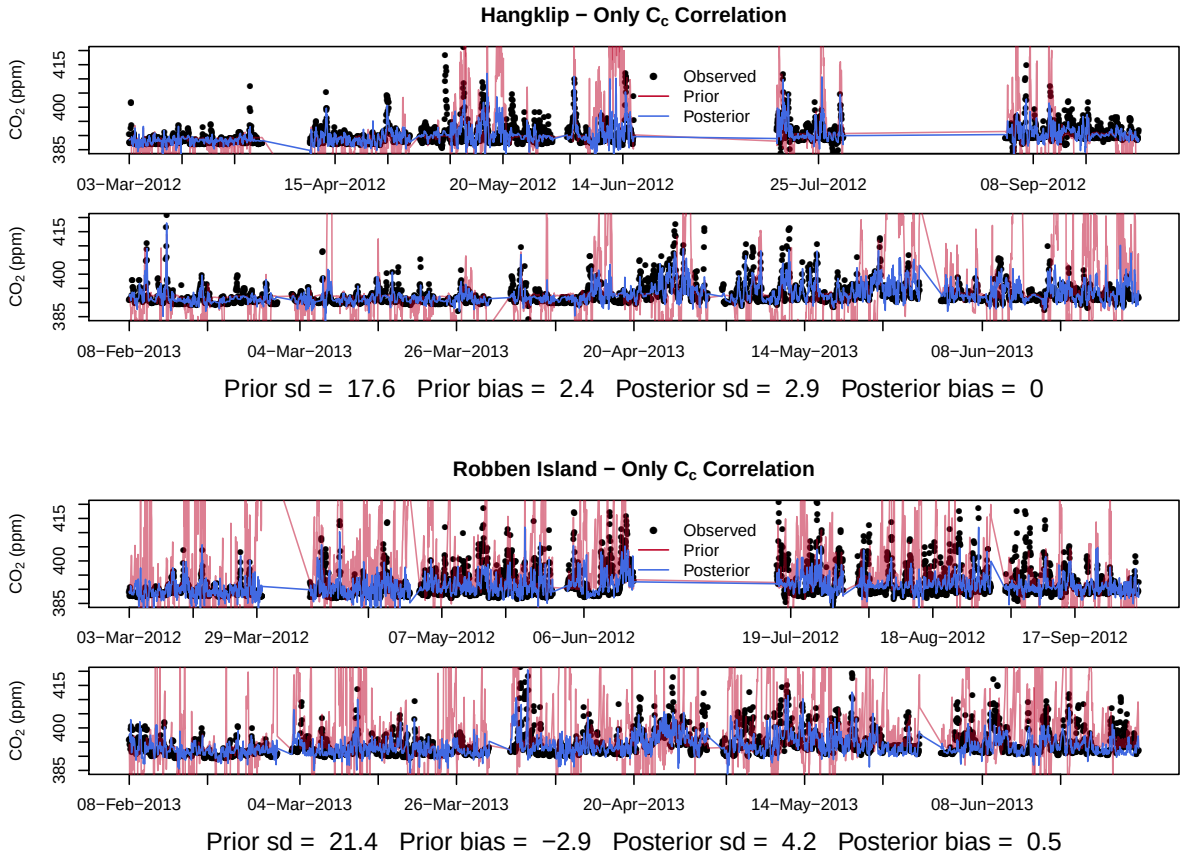


Figure C.5: Prior and posterior modelled concentrations at Hangklip and Robben Island sites under the inversion with only correlation accounted between the observation errors and ignoring correlations between the uncertainties in the NEE fluxes over the full inversion period from March 2012 until June 2013.

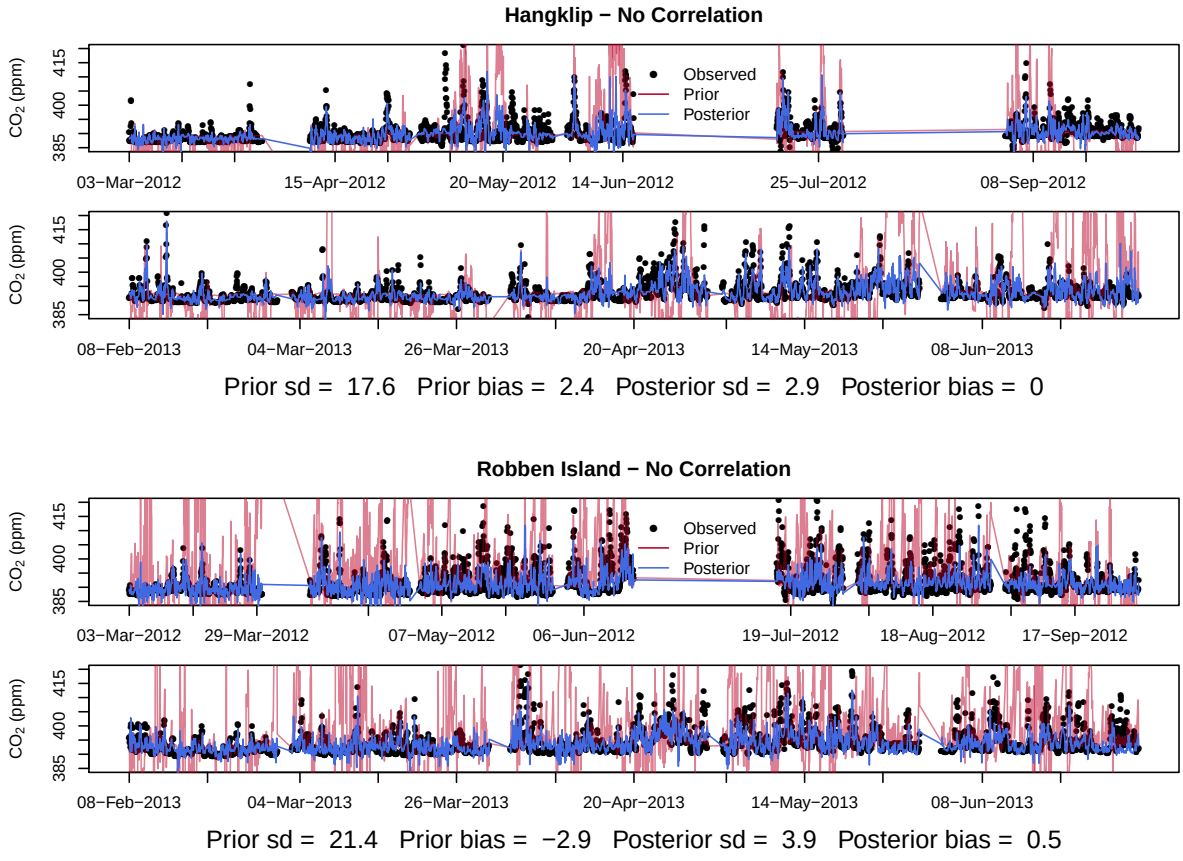


Figure C.6: Prior and posterior modelled concentrations at Hangklip and Robben Island sites under the inversion which ignored correlations between the observation errors and correlations between the uncertainties in the NEE fluxes over the full inversion period from March 2012 until June 2013.

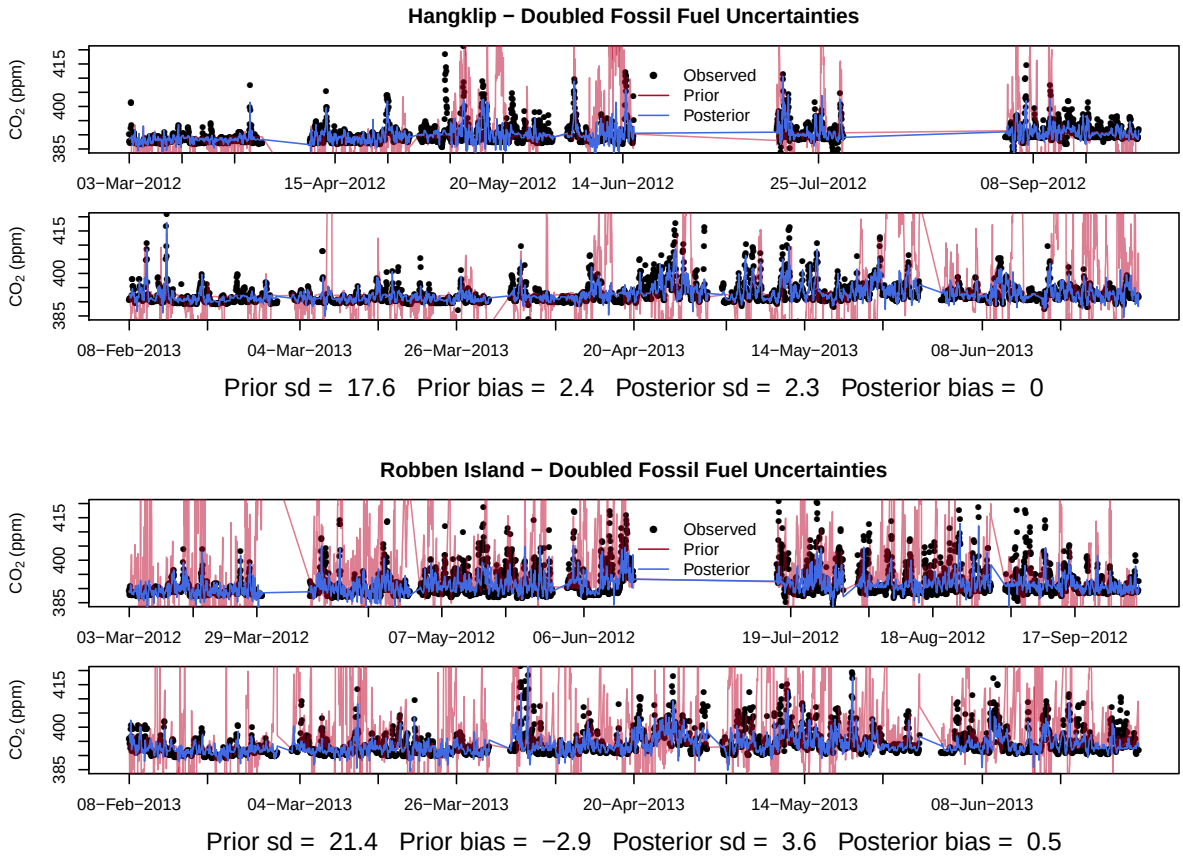


Figure C.7: Prior and posterior modelled concentrations at Hangklip and Robben Island sites under the inversion where uncertainties in the fossil fuel fluxes were doubled over the full inversion period from March 2012 until June 2013.

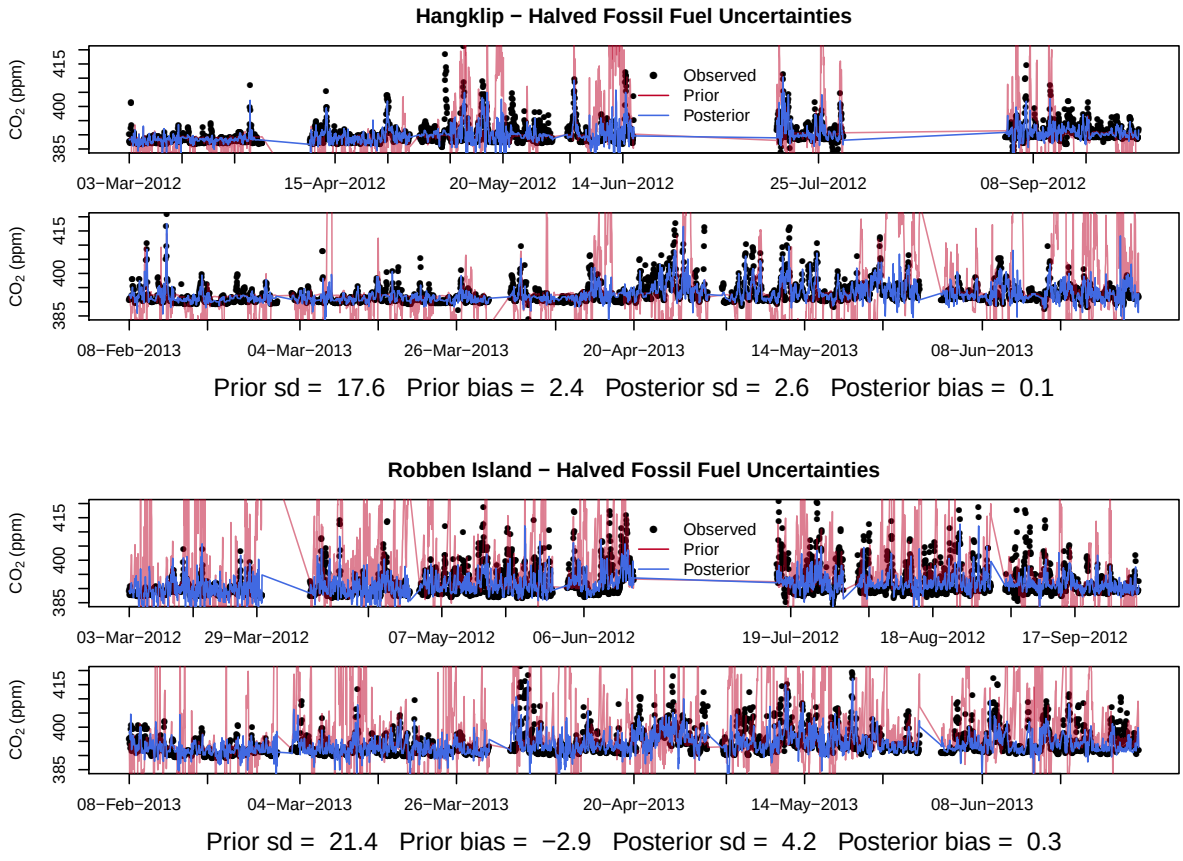


Figure C.8: Prior and posterior modelled concentrations at Hangklip and Robben Island sites under the inversion where uncertainties in the fossil fuel fluxes were halved over the full inversion period from March 2012 until June 2013.

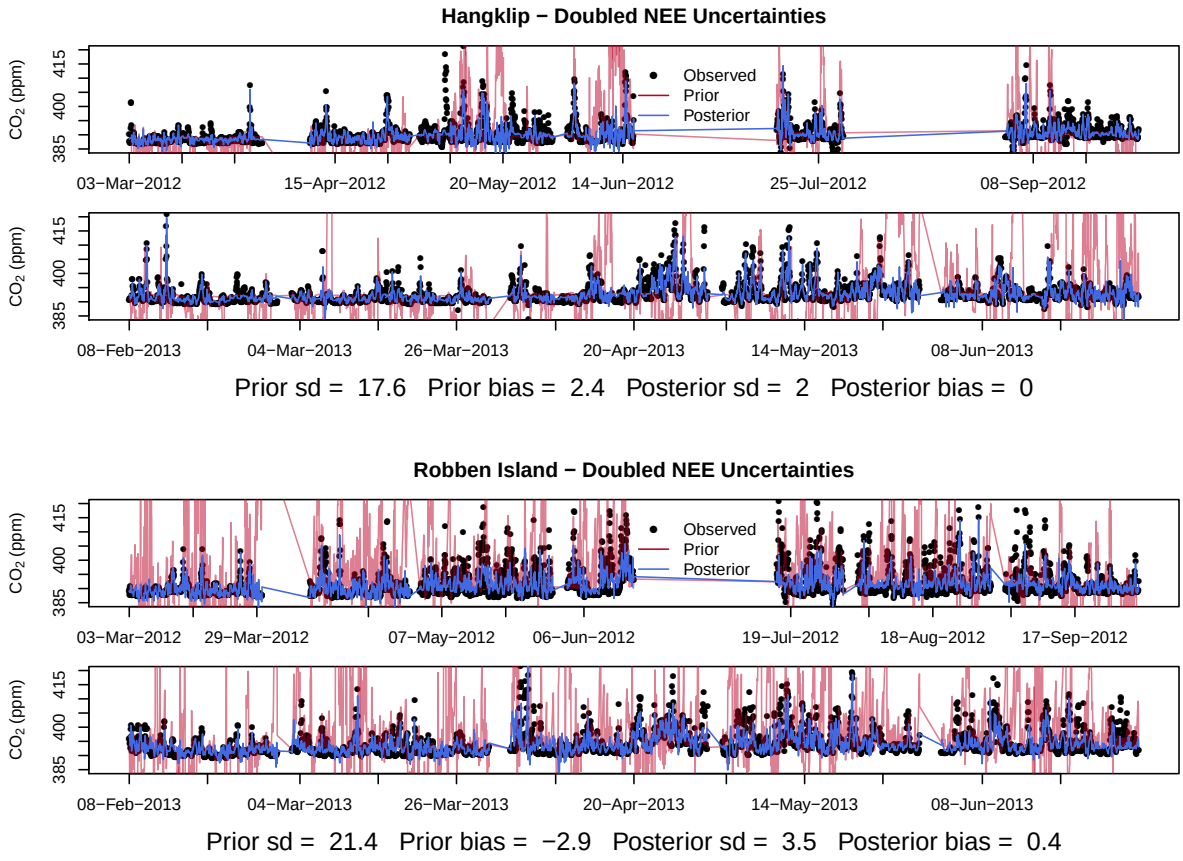


Figure C.9: Prior and posterior modelled concentrations at Hangklip and Robben Island sites under the inversion where uncertainties in the NEE fluxes were doubled over the full inversion period from March 2012 until June 2013.

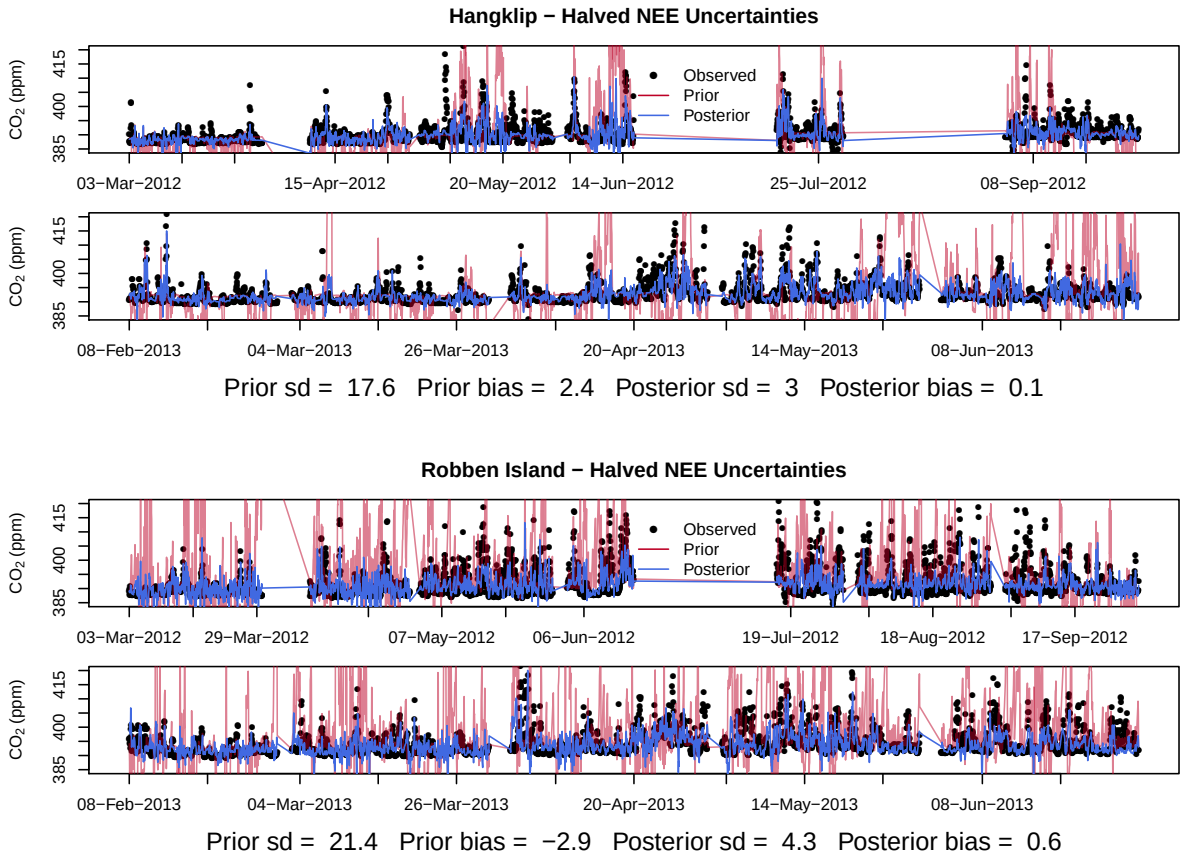


Figure C.10: Prior and posterior modelled concentrations at Hangklip and Robben Island sites under the inversion where uncertainties in the NEE fluxes were halved over the full inversion period from March 2012 until June 2013.

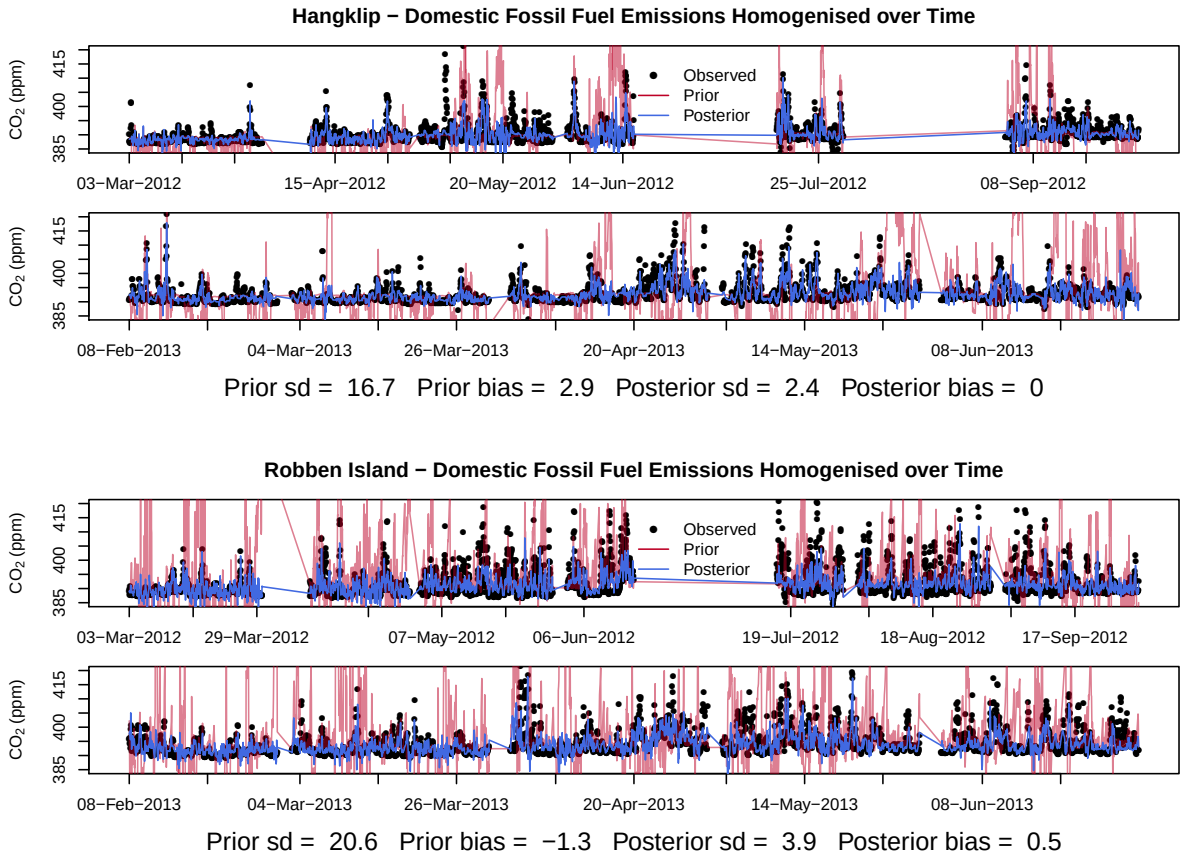


Figure C.11: Prior and posterior modelled concentrations at Hangklip and Robben Island sites when the temporally homogenised domestic fossil fuel fluxes prior was used over the full inversion period from March 2012 until June 2013.

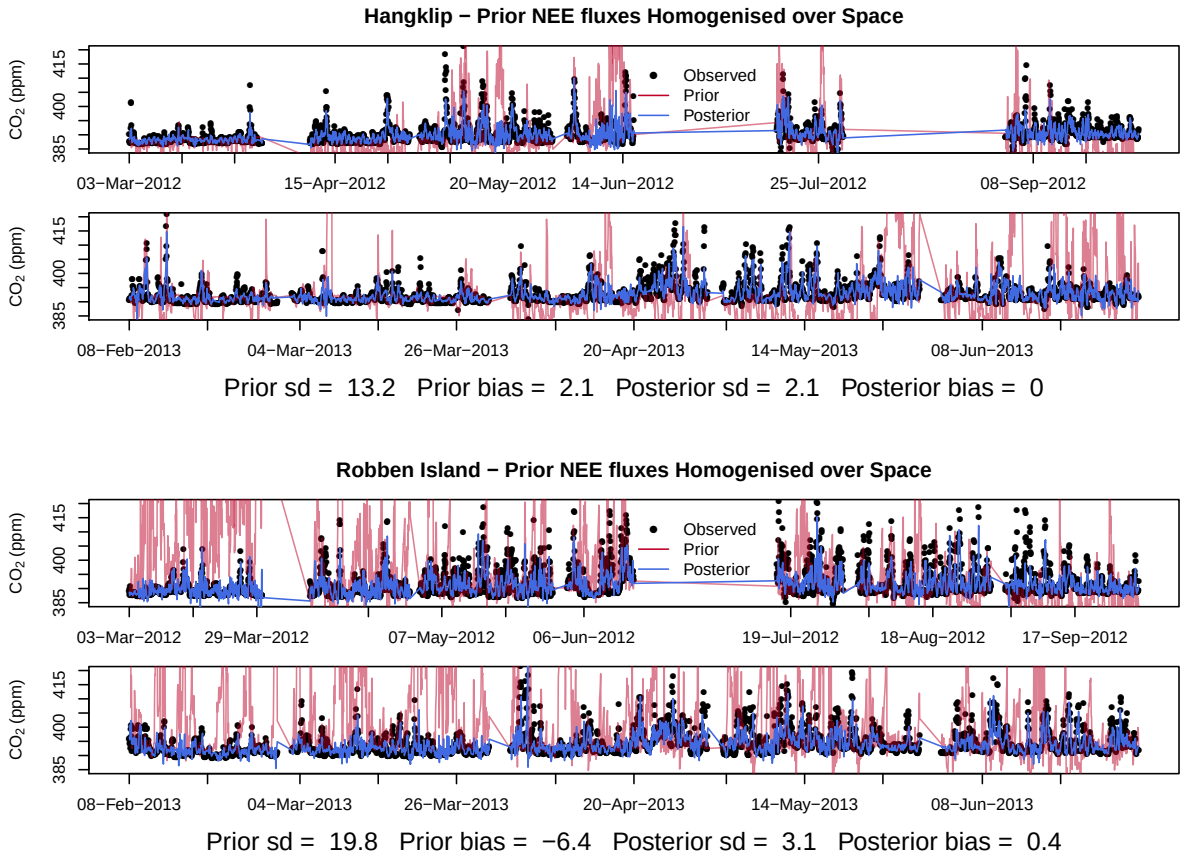


Figure C.12: Prior and posterior modelled concentrations at Hangklip and Robben Island sites when the spatially homogenised NEE fluxes prior was used over the full inversion period from March 2012 until June 2013.

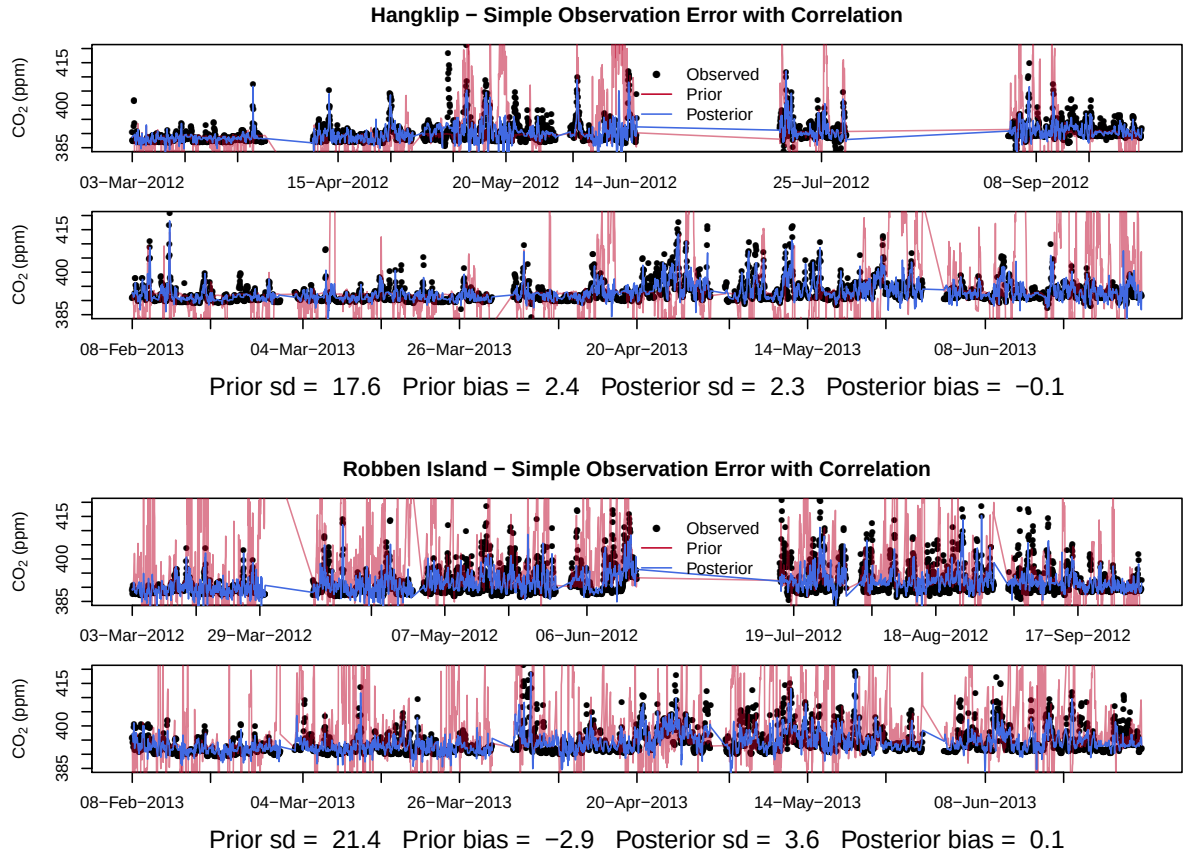


Figure C.13: Prior and posterior modelled concentrations at Hangklip and Robben Island sites under the inversion where uncertainties in the observation errors were estimated to be 2 ppm during the day and 4 ppm at night over the full inversion period from March 2012 until June 2013.

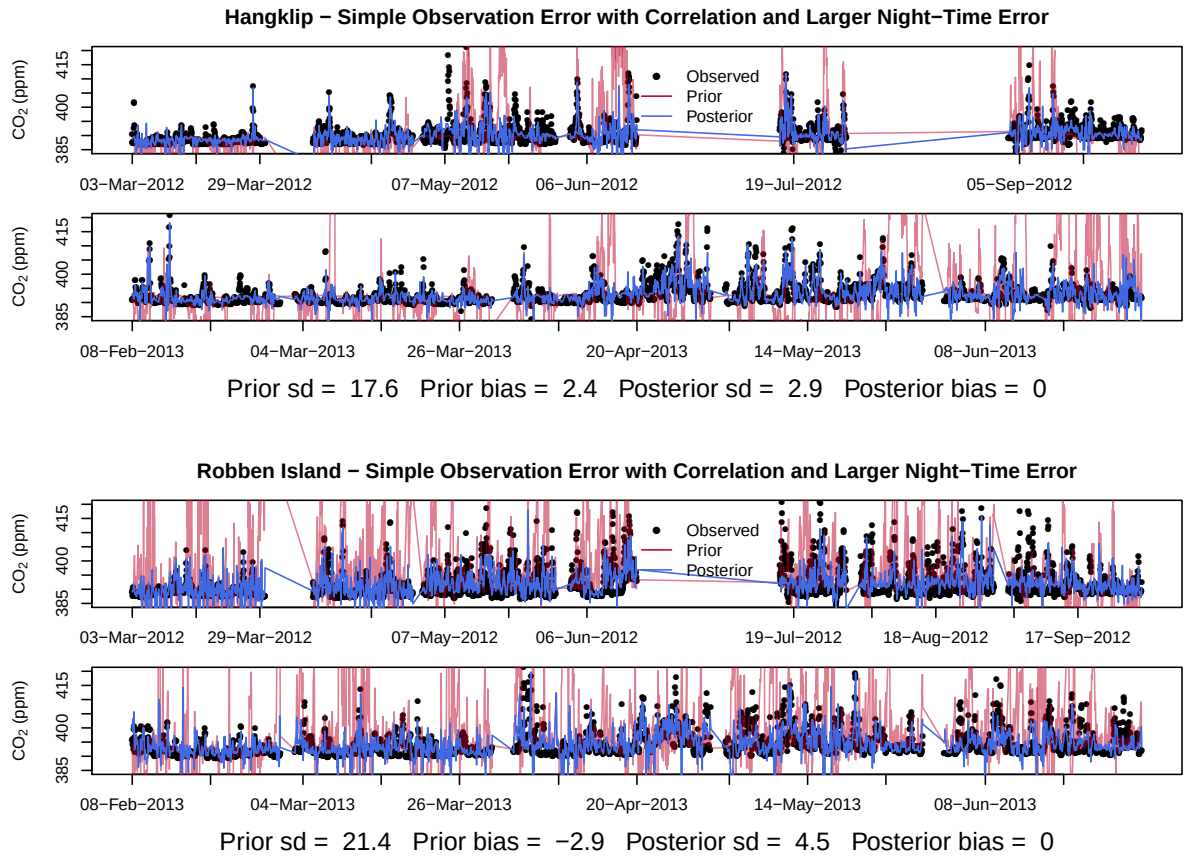


Figure C.14: Prior and posterior modelled concentrations at Hangklip and Robben Island sites under the inversion where uncertainties in the observation errors were estimated to be 2 ppm during the day and 10 ppm at night over the full inversion period from March 2012 until June 2013.

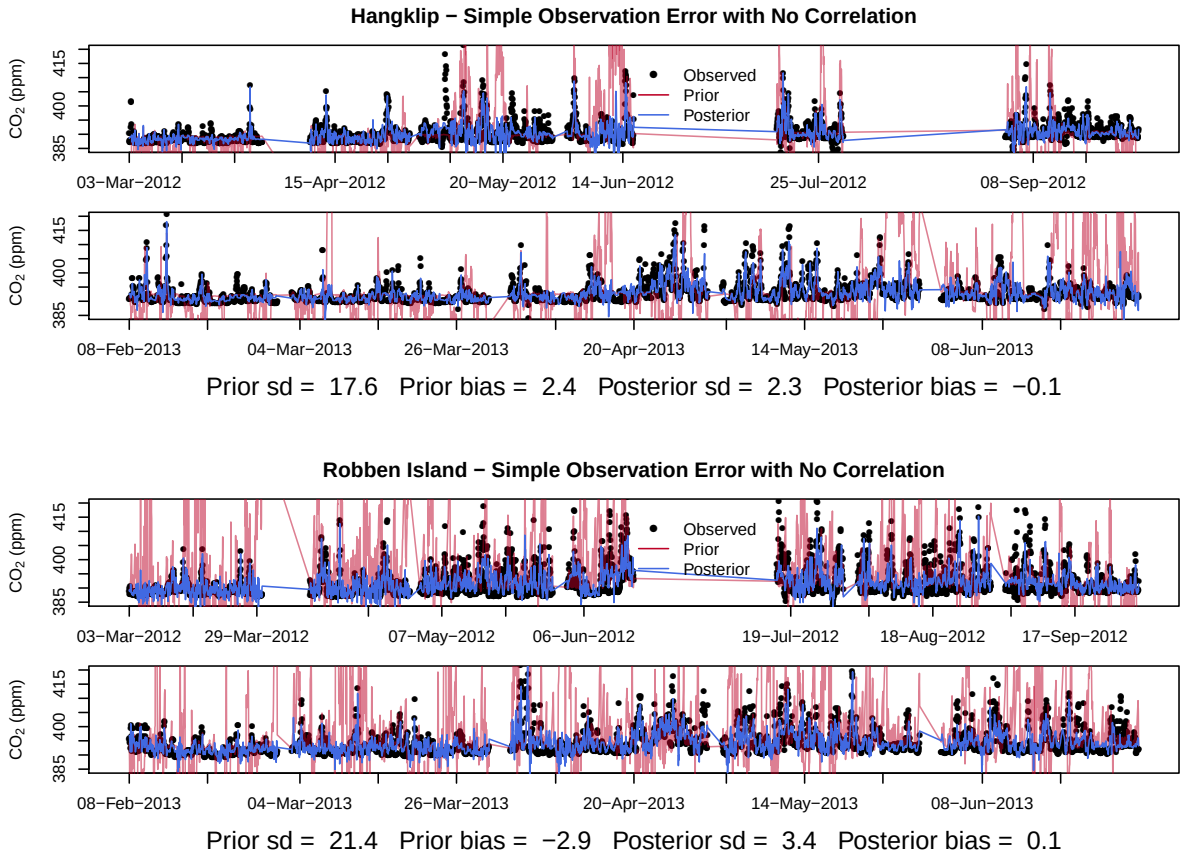


Figure C.15: Prior and posterior modelled concentrations at Hangklip and Robben Island sites under the inversion where uncertainties in the observation errors were estimated to be 2 ppm during the day and 4 ppm at night, and no correlation was specified between the observation errors, over the full inversion period from March 2012 until June 2013.

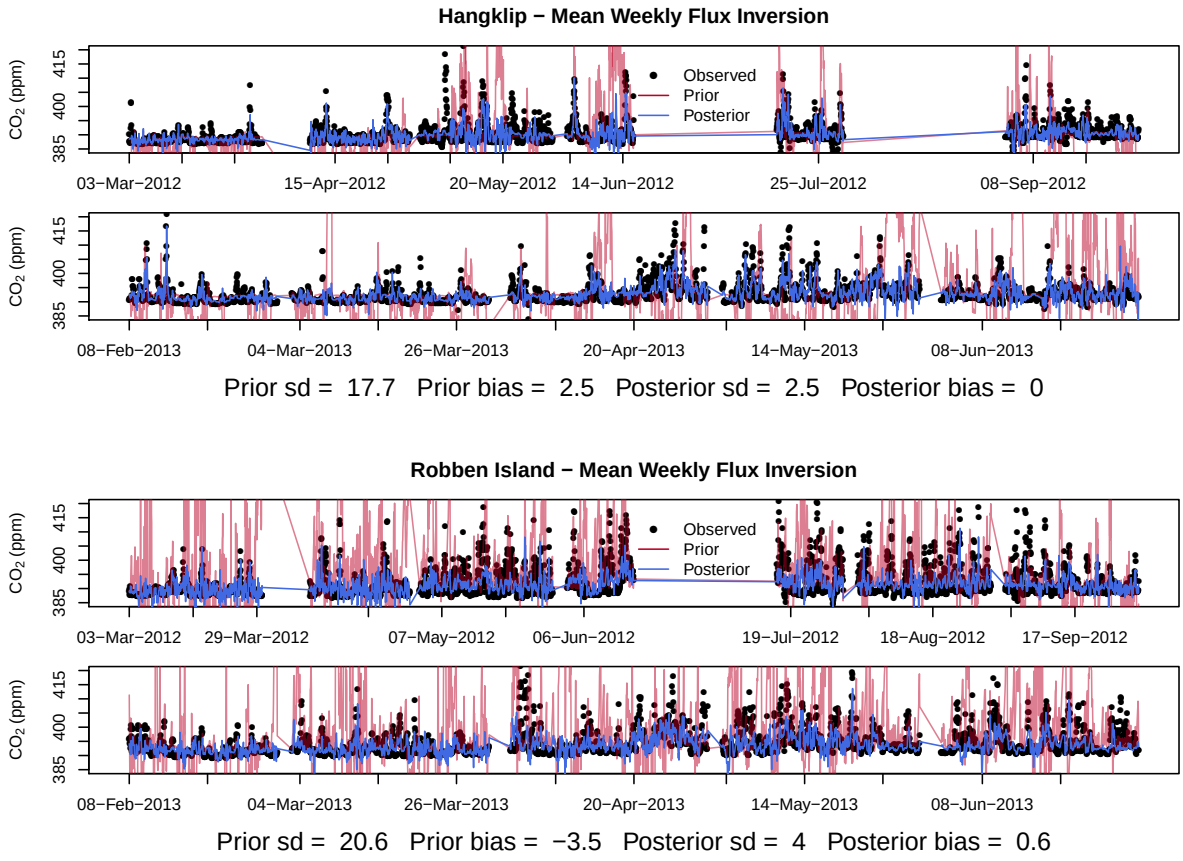


Figure C.16: Prior and posterior modelled concentrations at Hangklip and Robben Island sites under the inversion which solved for the mean weekly flux over the full inversion period from March 2012 until June 2013.

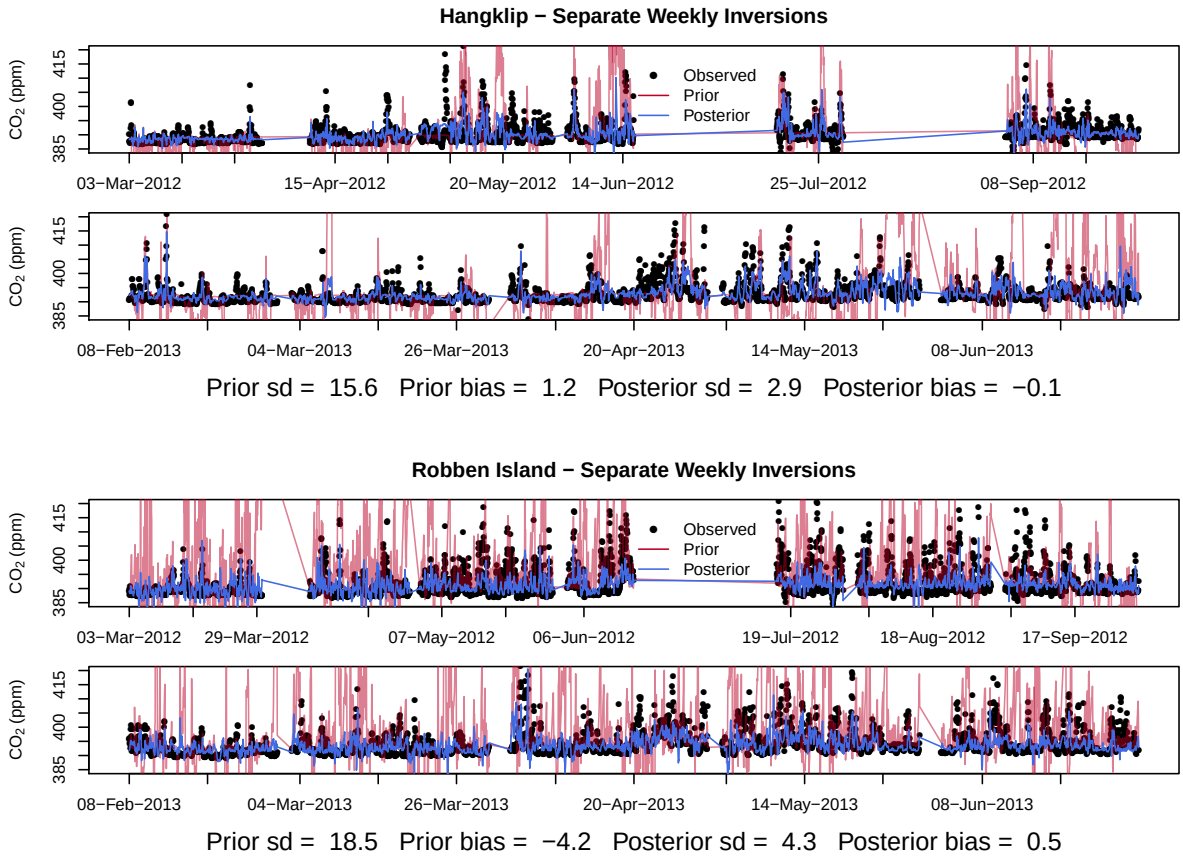


Figure C.17: Prior and posterior modelled concentrations at Hangklip and Robben Island sites under separate weekly inversions over the full inversion period from March 2012 until June 2013.

## C.2 Diurnal Concentration Plots

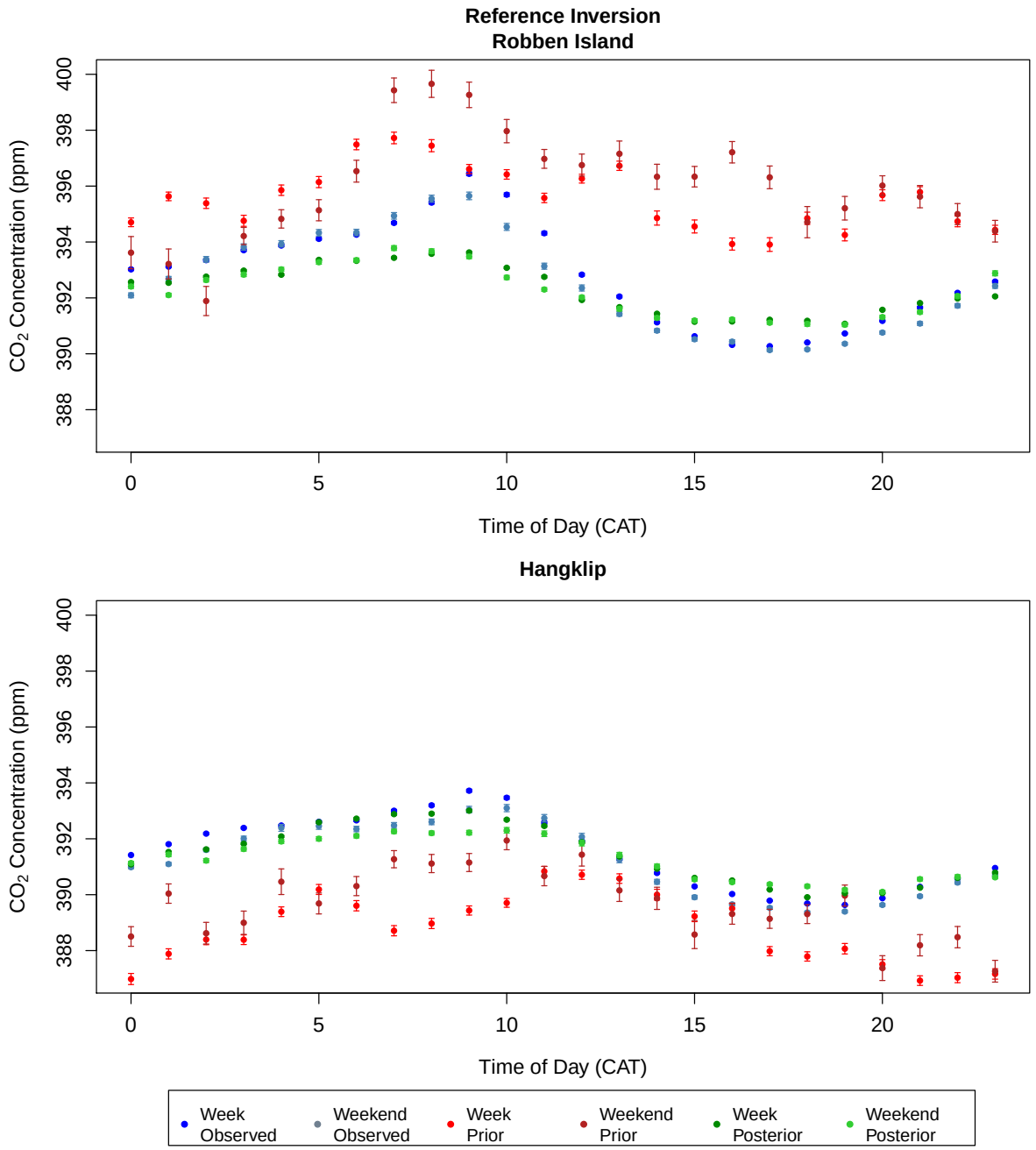


Figure C.18: The hourly diurnal cycle (mean concentrations for each hour with 95% confidence interval) in the observed, prior and posterior modelled $CO_2$ concentrations (ppm) over the full measurement period from March 2012 until June 2013, separated by working week and weekend, and plotted separately for Robben Island (top) and Hangklip (bottom) measurement sites for the reference inversion. The diurnal plots are separated into working week and weekend observed concentrations (blue and light blue), working week and weekend prior modelled concentrations (red and dark red), and working week and weekend posterior modelled concentrations (green and light green).

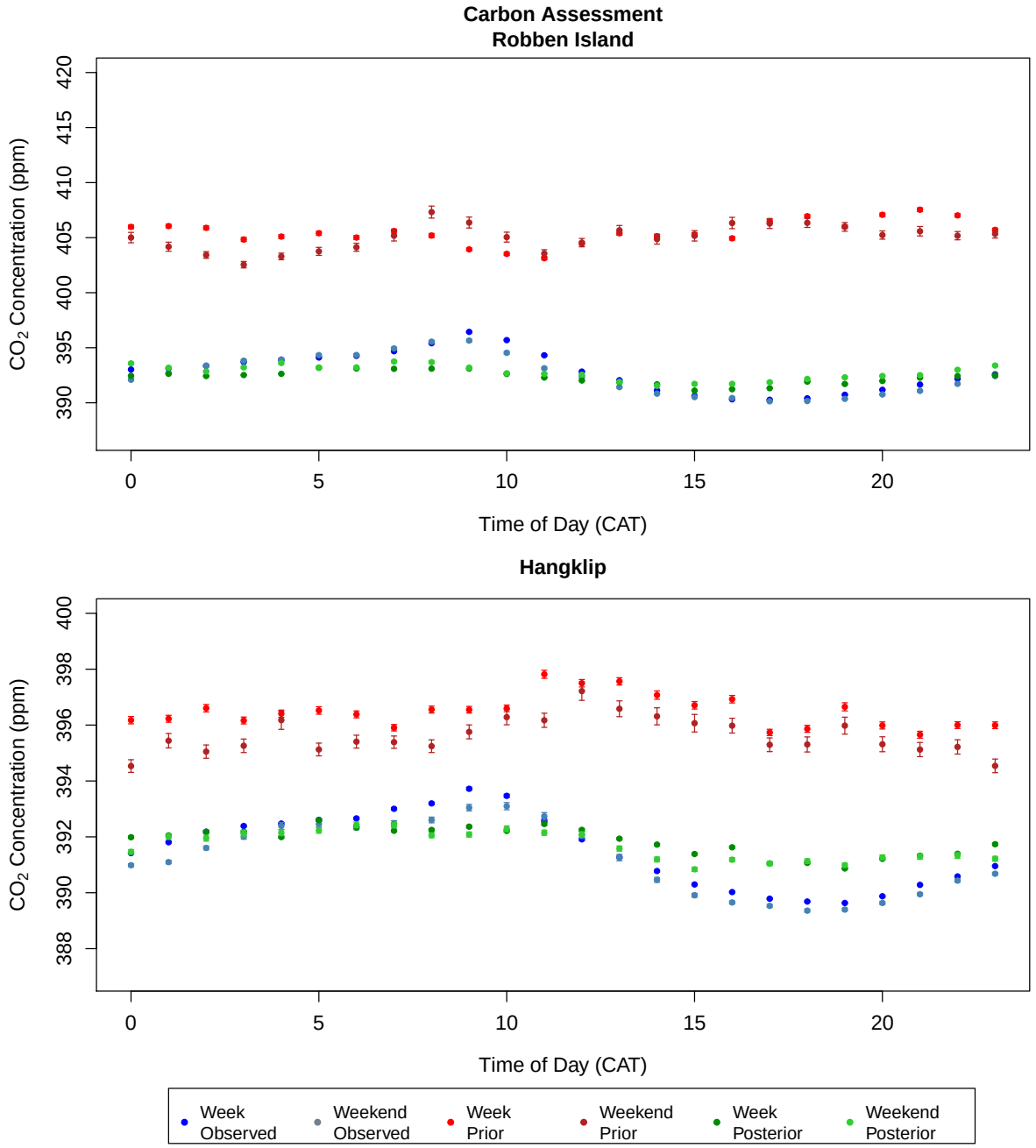


Figure C.19: The hourly diurnal cycle (mean concentrations for each hour with 95% confidence interval) in the observed, prior and posterior modelled $CO_2$ concentrations (ppm) over the full measurement period from March 2012 until June 2013, separated by working week and weekend, and plotted separately for Robben Island (top) and Hangklip (bottom) measurement sites for the inversion using the carbon assessment product for the NEE prior flux estimates. The diurnal plots are separated into working week and weekend observed concentrations (blue and light blue), working week and weekend prior modelled concentrations (red and dark red), and working week and weekend posterior modelled concentrations (green and light green).

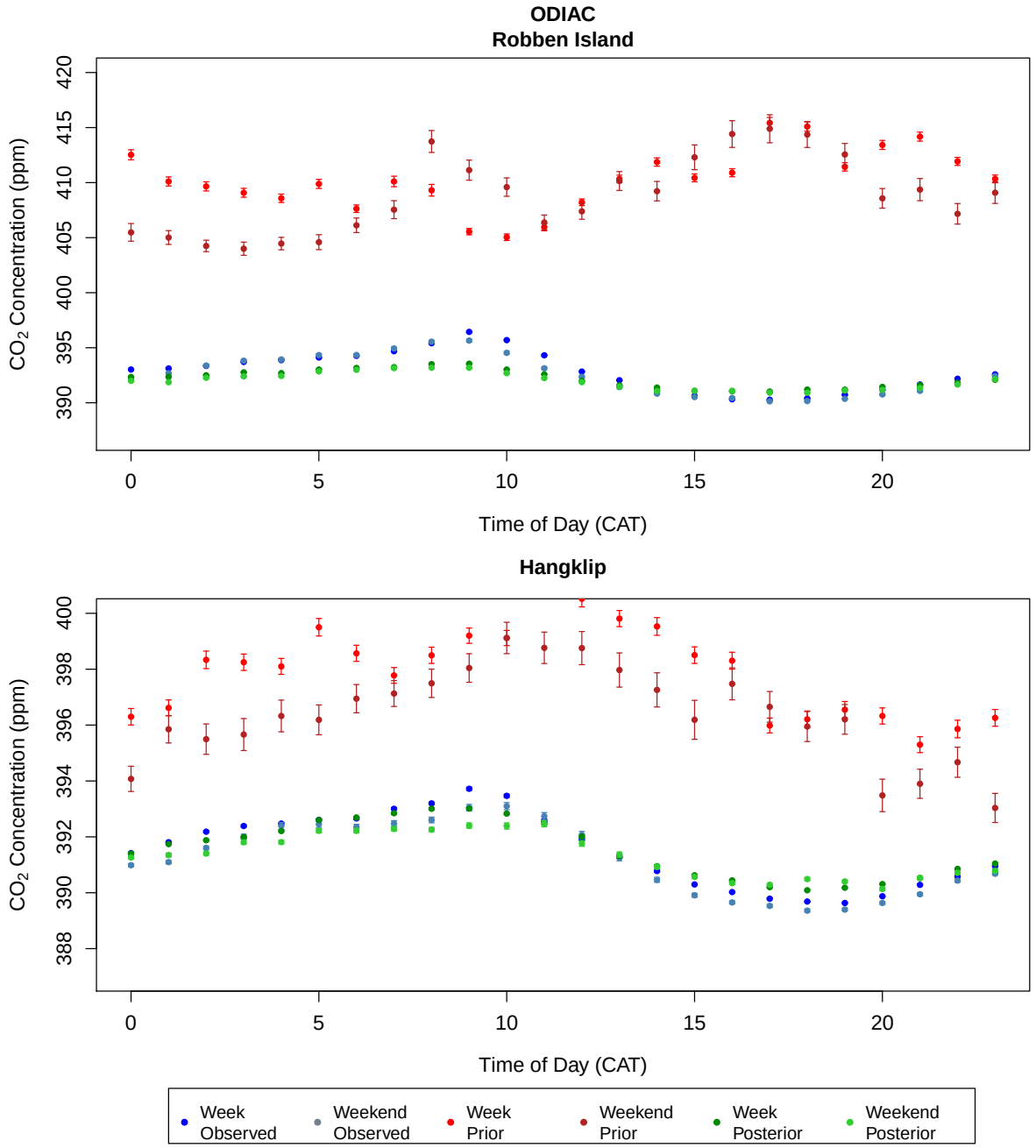


Figure C.20: The hourly diurnal cycle (mean concentrations for each hour with 95% confidence interval) in the observed, prior and posterior modelled $CO_2$ concentrations (ppm) over the full measurement period from March 2012 until June 2013, separated by working week and weekend, and plotted separately for Robben Island (top) and Hangklip (bottom) measurement sites for the inversion using the ODIAC product for the fossil fuel flux prior estimates. The diurnal plots are separated into working week and weekend observed concentrations (blue and light blue), working week and weekend prior modelled concentrations (red and dark red), and working week and weekend posterior modelled concentrations (green and light green).

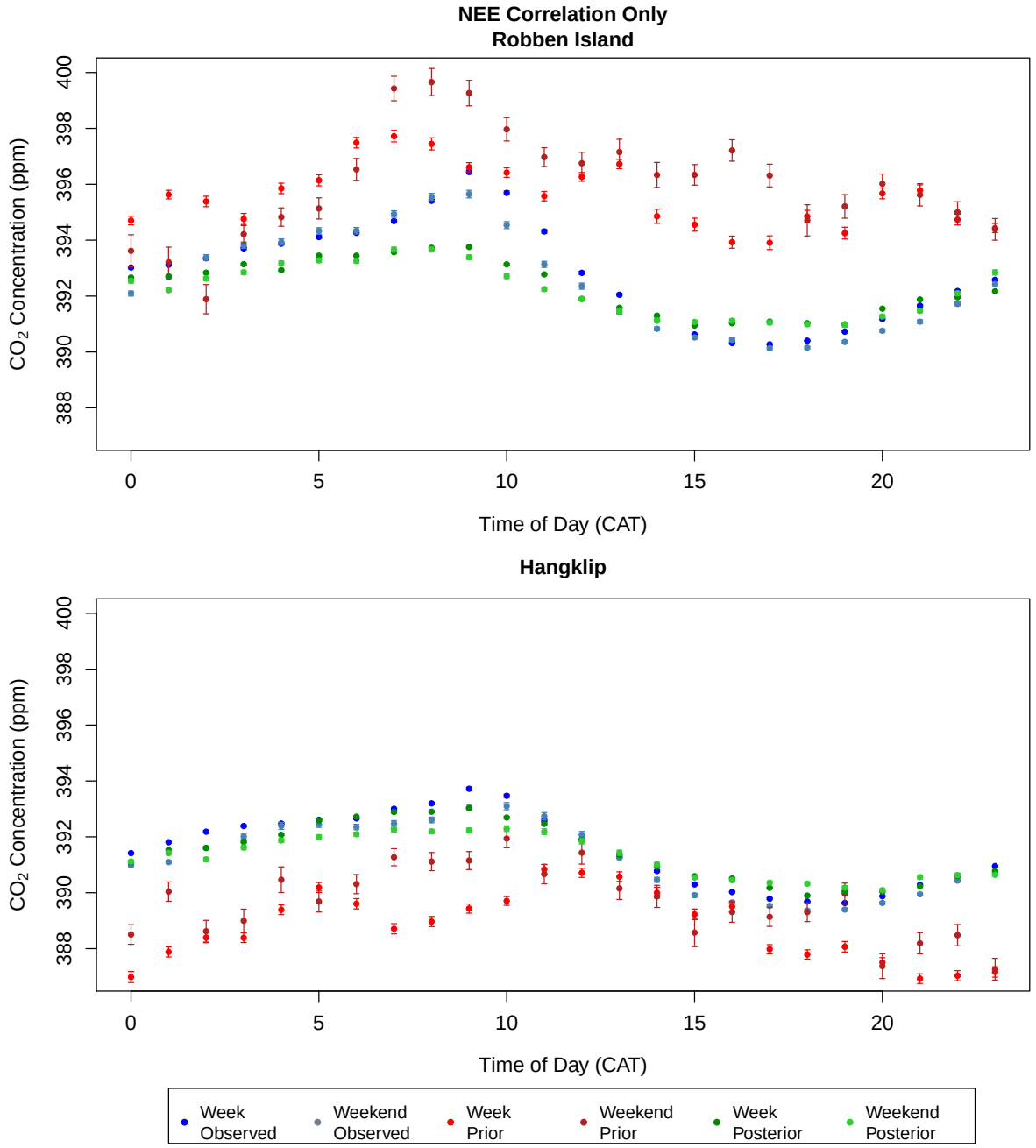


Figure C.21: The hourly diurnal cycle (mean concentrations for each hour with 95% confidence interval) in the observed, prior and posterior modelled $CO_2$ concentrations (ppm) over the full measurement period from March 2012 until June 2013, separated by working week and weekend, and plotted separately for Robben Island (top) and Hangklip (bottom) measurement sites for the inversion accounting for only correlation between the NEE flux uncertainties. The diurnal plots are separated into working week and weekend observed concentrations (blue and light blue), working week and weekend prior modelled concentrations (red and dark red), and working week and weekend posterior modelled concentrations (green and light green).

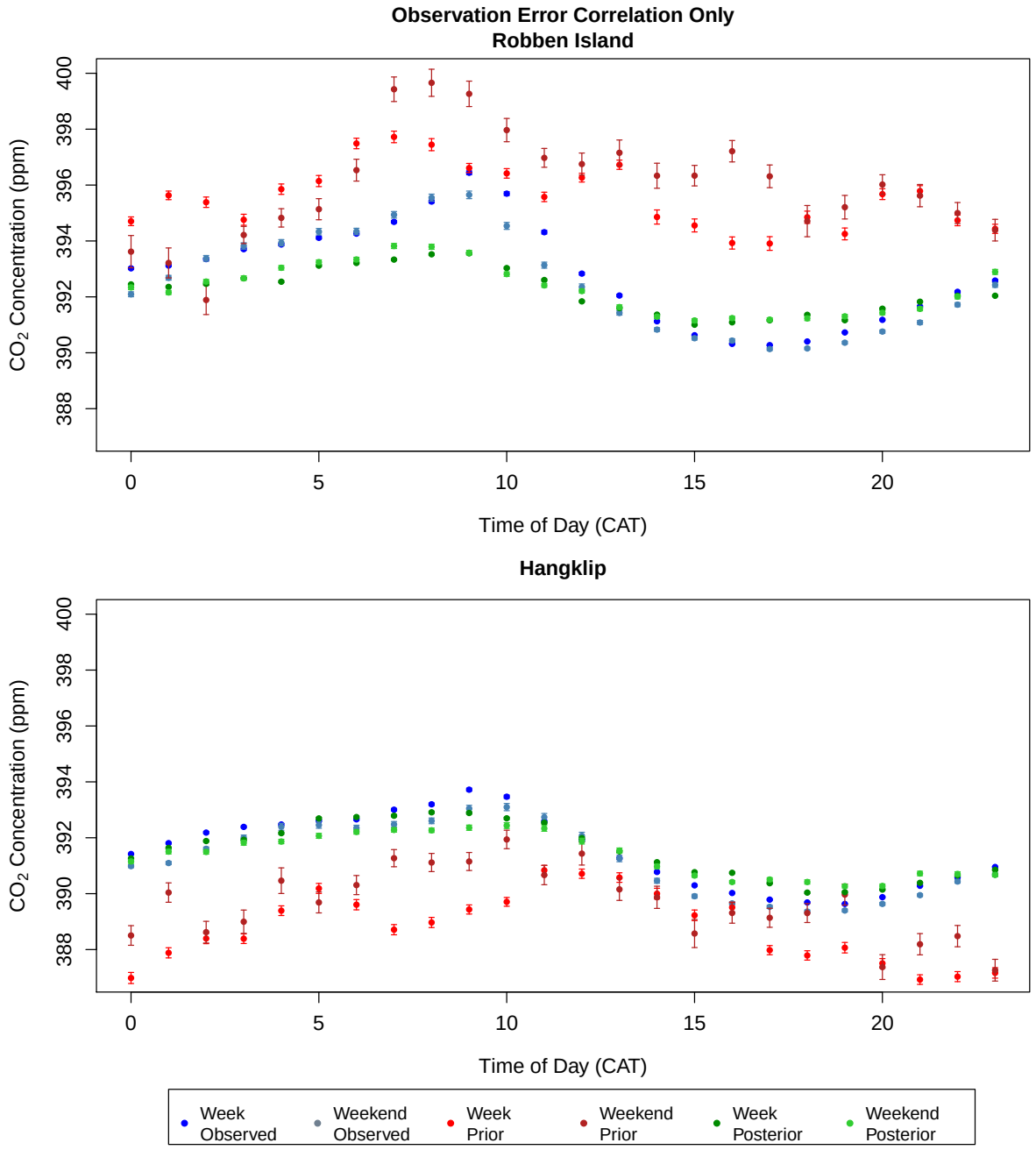


Figure C.22: The hourly diurnal cycle (mean concentrations for each hour with 95% confidence interval) in the observed, prior and posterior modelled $CO_2$ concentrations (ppm) over the full measurement period from March 2012 until June 2013, separated by working week and weekend, and plotted separately for Robben Island (top) and Hangklip (bottom) measurement sites for the inversion accounting for only correlation between the observation errors with no correlation specified between the NEE flux uncertainties. The diurnal plots are separated into working week and weekend observed concentrations (blue and light blue), working week and weekend prior modelled concentrations (red and dark red), and working week and weekend posterior modelled concentrations (green and light green).

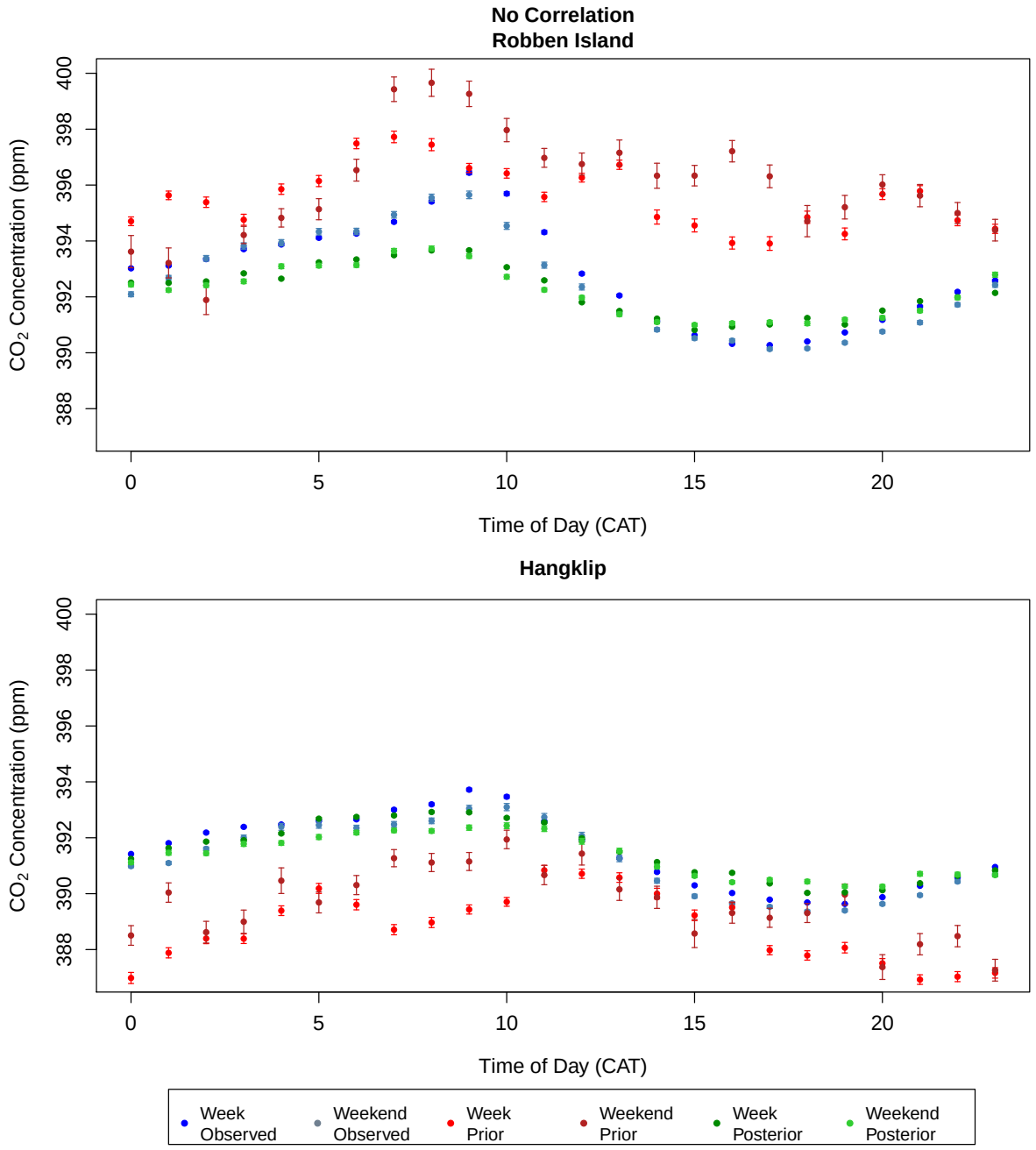


Figure C.23: The hourly diurnal cycle (mean concentrations for each hour with 95% confidence interval) in the observed, prior and posterior modelled $CO_2$ concentrations (ppm) over the full measurement period from March 2012 until June 2013, separated by working week and weekend, and plotted separately for Robben Island (top) and Hangklip (bottom) measurement sites for the inversion specifying no correlation between the observation errors and no correlation between the NEE flux uncertainties. The diurnal plots are separated into working week and weekend observed concentrations (blue and light blue), working week and weekend prior modelled concentrations (red and dark red), and working week and weekend posterior modelled concentrations (green and light green).

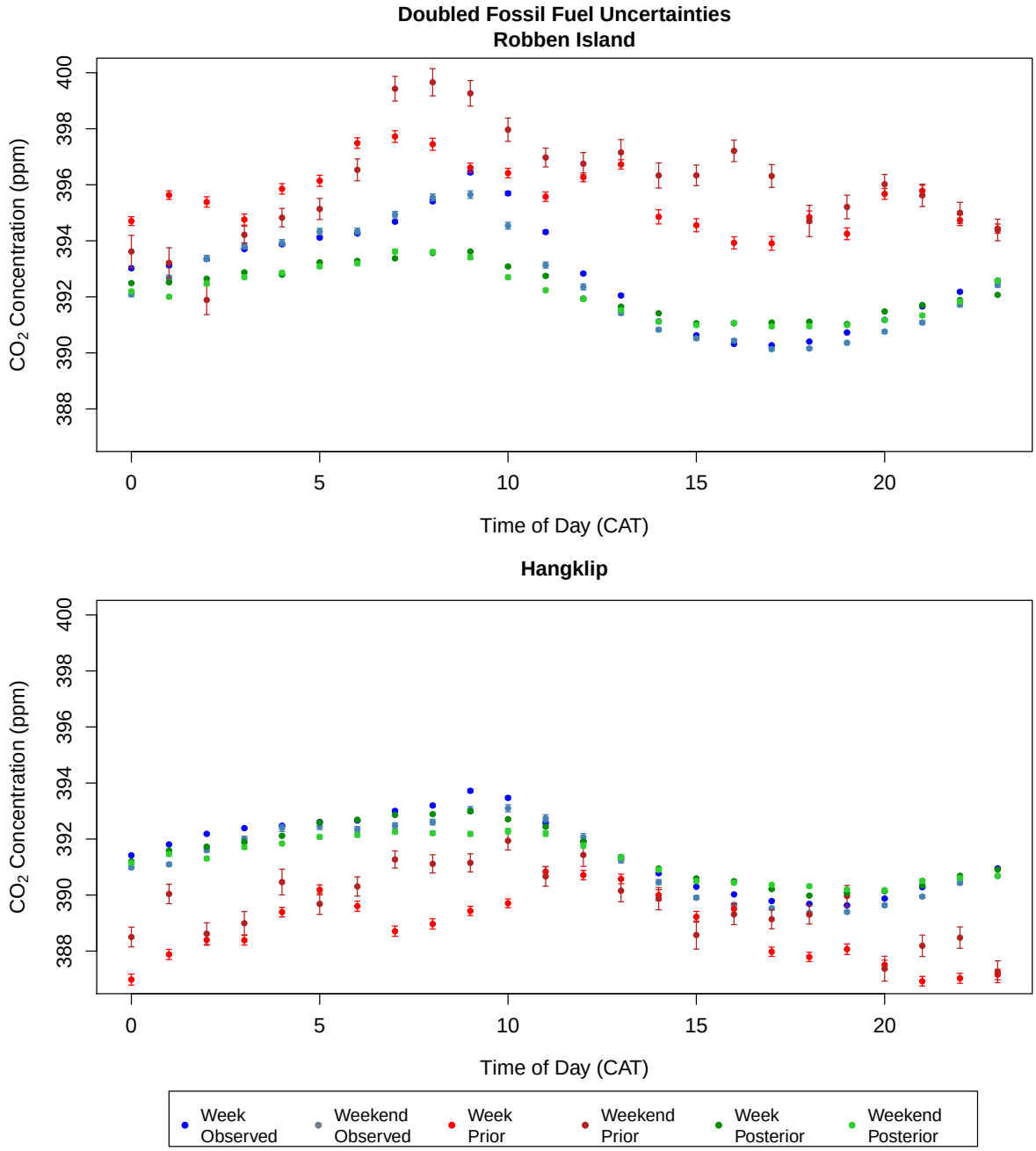


Figure C.24: The hourly diurnal cycle (mean concentrations for each hour with 95% confidence interval) in the observed, prior and posterior modelled $CO_2$ concentrations (ppm) over the full measurement period from March 2012 until June 2013, separated by working week and weekend, and plotted separately for Robben Island (top) and Hangklip (bottom) measurement sites for the inversion with doubled fossil fuel flux uncertainties. The diurnal plots are separated into working week and weekend observed concentrations (blue and light blue), working week and weekend prior modelled concentrations (red and dark red), and working week and weekend posterior modelled concentrations (green and light green).

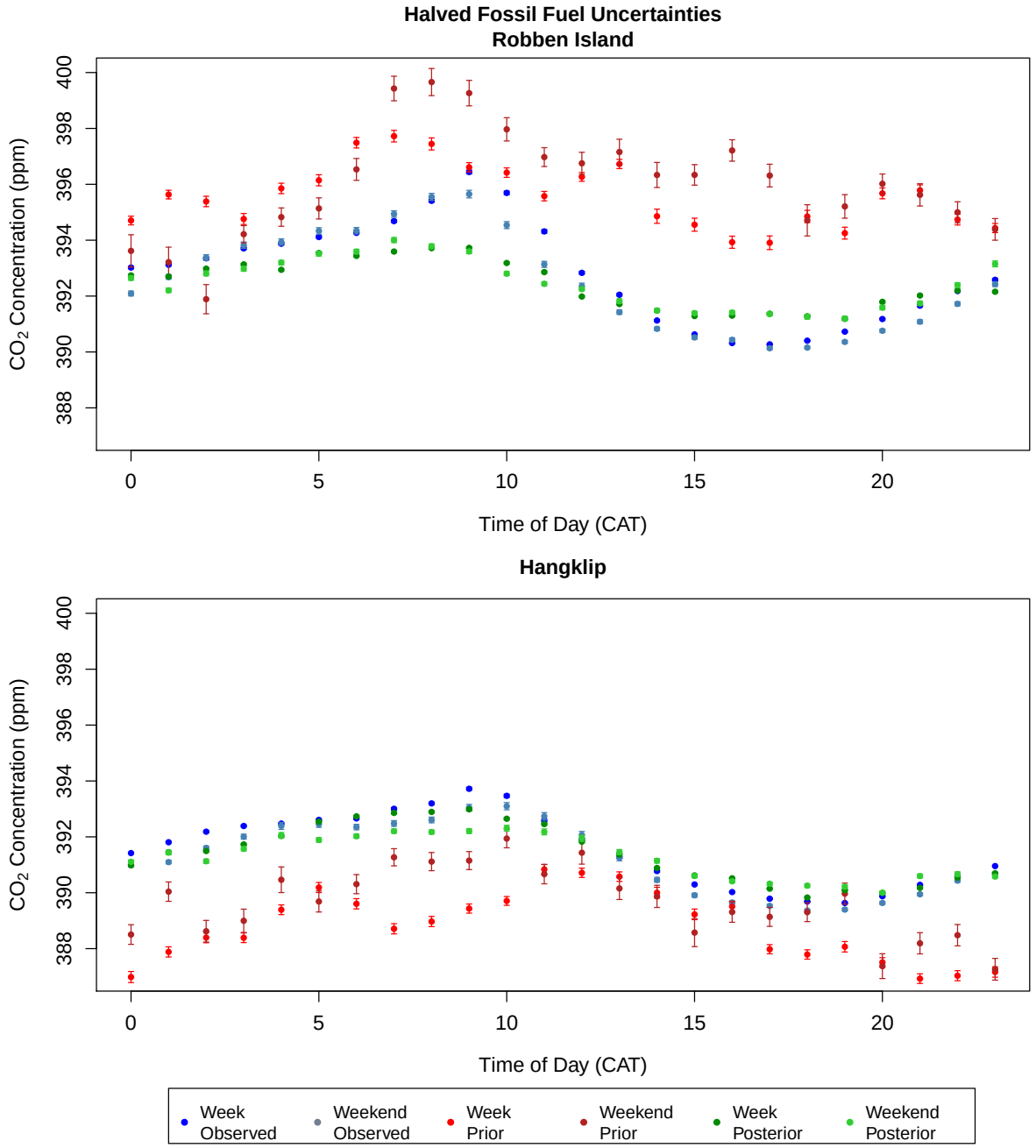


Figure C.25: The hourly diurnal cycle (mean concentrations for each hour with 95% confidence interval) in the observed, prior and posterior modelled $CO_2$ concentrations (ppm) over the full measurement period from March 2012 until June 2013, separated by working week and weekend, and plotted separately for Robben Island (top) and Hangklip (bottom) measurement sites for the inversion with halved fossil fuel flux uncertainties. The diurnal plots are separated into working week and weekend observed concentrations (blue and light blue), working week and weekend prior modelled concentrations (red and dark red), and working week and weekend posterior modelled concentrations (green and light green).

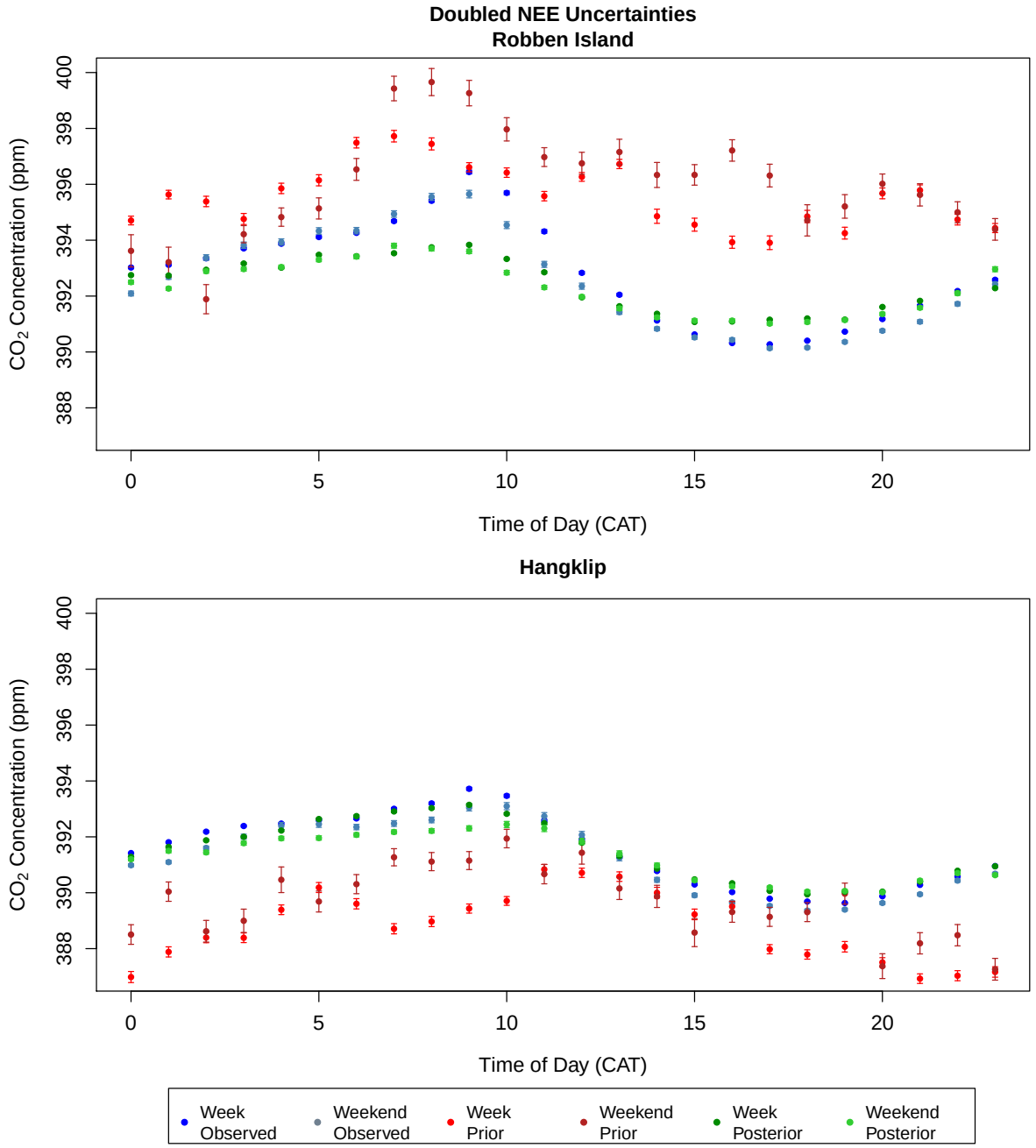


Figure C.26: The hourly diurnal cycle (mean concentrations for each hour with 95% confidence interval) in the observed, prior and posterior modelled $CO_2$ concentrations (ppm) over the full measurement period from March 2012 until June 2013, separated by working week and weekend, and plotted separately for Robben Island (top) and Hangklip (bottom) measurement sites for the inversion with doubled NEE flux uncertainties. The diurnal plots are separated into working week and weekend observed concentrations (blue and light blue), working week and weekend prior modelled concentrations (red and dark red), and working week and weekend posterior modelled concentrations (green and light green).

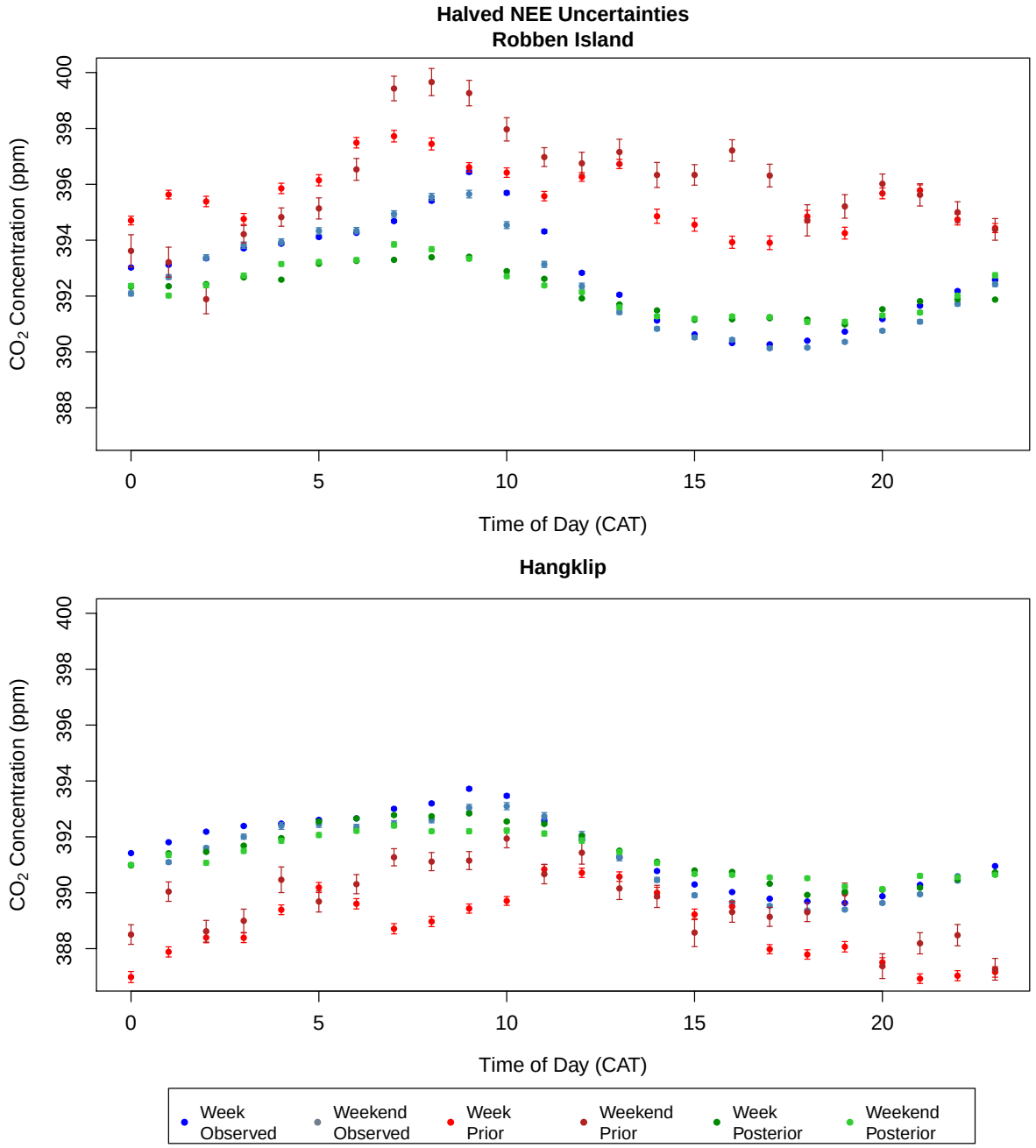


Figure C.27: The hourly diurnal cycle (mean concentrations for each hour with 95% confidence interval) in the observed, prior and posterior modelled $CO_2$ concentrations (ppm) over the full measurement period from March 2012 until June 2013, separated by working week and weekend, and plotted separately for Robben Island (top) and Hangklip (bottom) measurement sites for the inversion with halved NEE flux uncertainties. The diurnal plots are separated into working week and weekend observed concentrations (blue and light blue), working week and weekend prior modelled concentrations (red and dark red), and working week and weekend posterior modelled concentrations (green and light green).

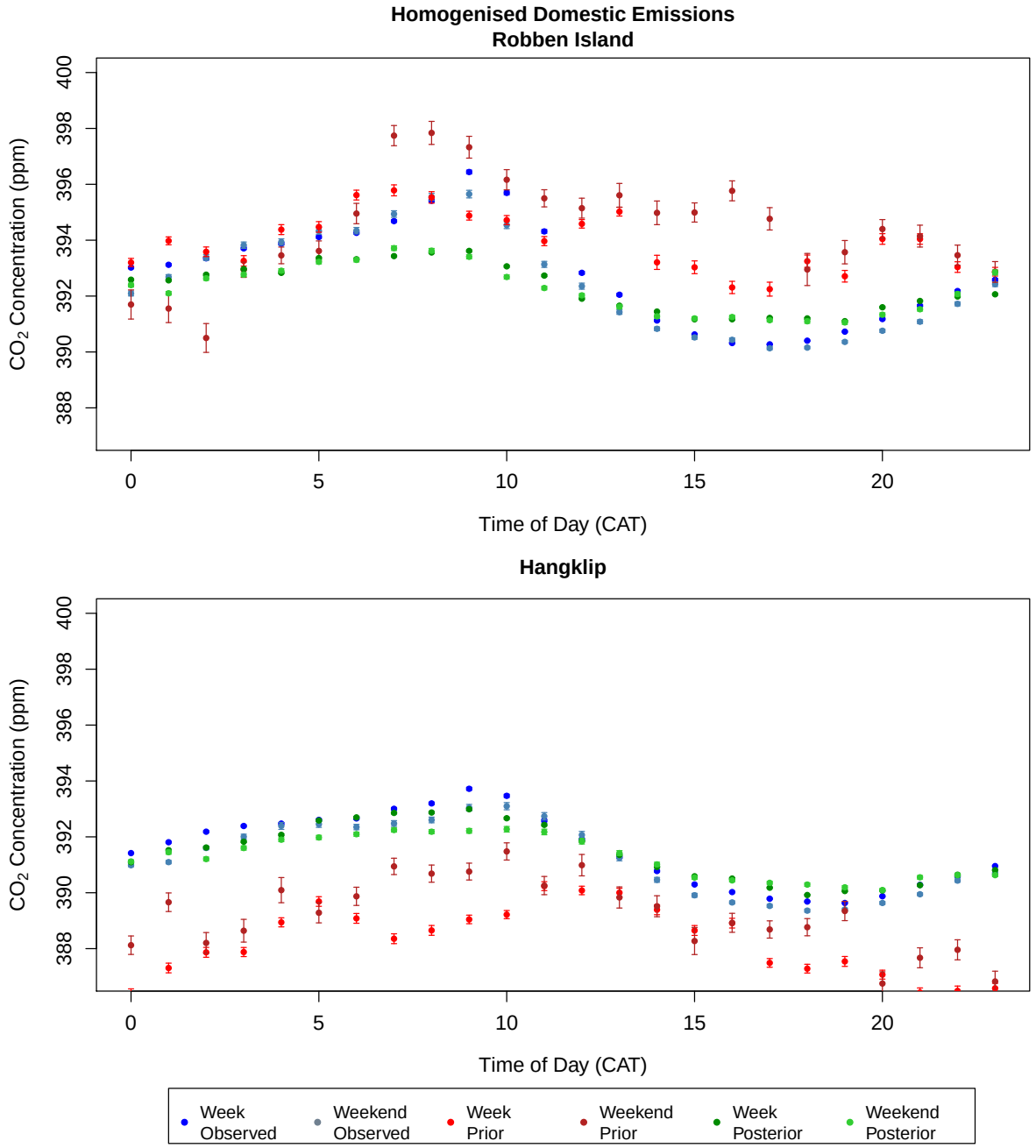


Figure C.28: The hourly diurnal cycle (mean concentrations for each hour with 95% confidence interval) in the observed, prior and posterior modelled $CO_2$ concentrations (ppm) over the full measurement period from March 2012 until June 2013, separated by working week and weekend, and plotted separately for Robben Island (top) and Hangklip (bottom) measurement sites for the inversion with temporally homogenised domestic fossil fuel prior fluxes. The diurnal plots are separated into working week and weekend observed concentrations (blue and light blue), working week and weekend prior modelled concentrations (red and dark red), and working week and weekend posterior modelled concentrations (green and light green).

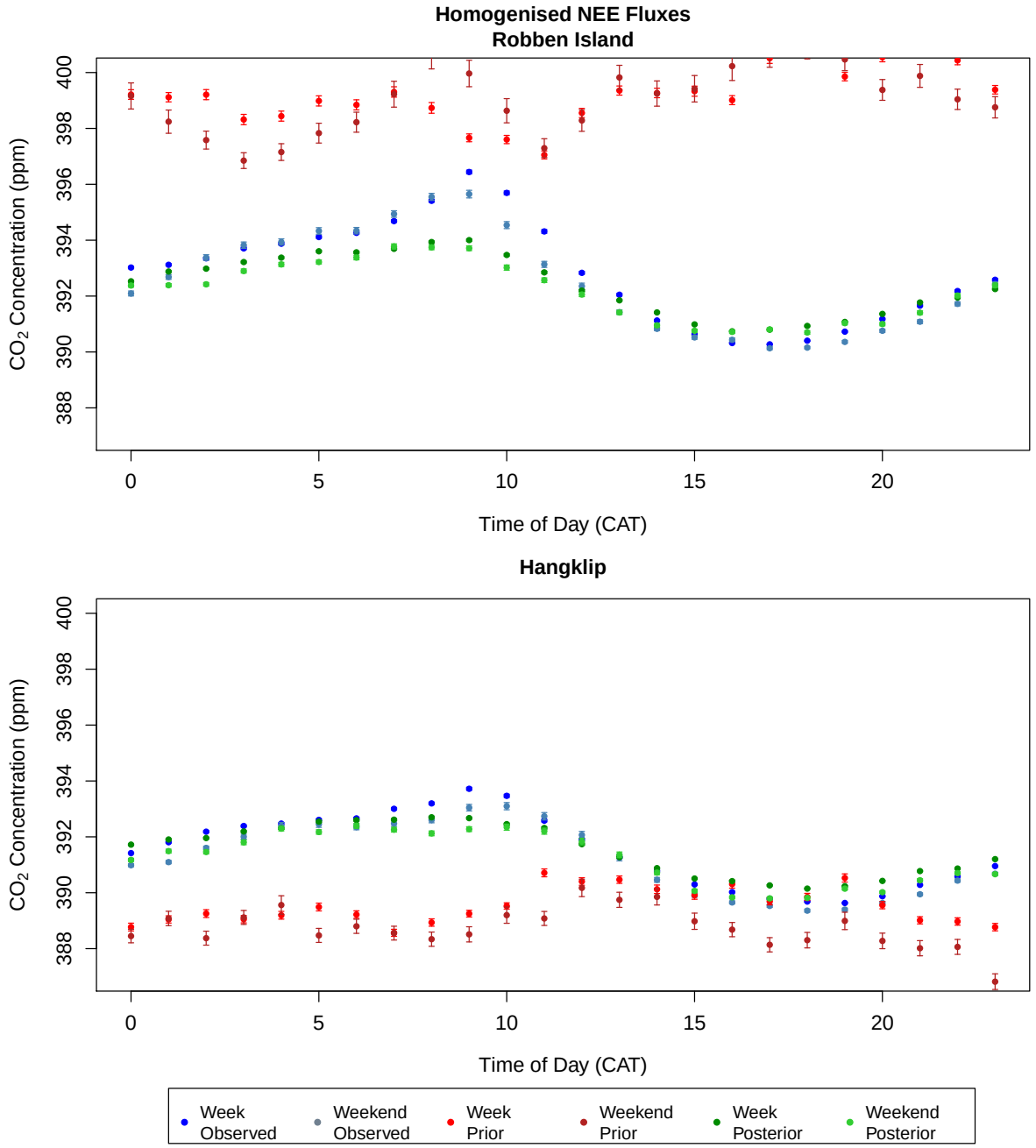


Figure C.29: The hourly diurnal cycle (mean concentrations for each hour with 95% confidence interval) in the observed, prior and posterior modelled $CO_2$ concentrations (ppm) over the full measurement period from March 2012 until June 2013, separated by working week and weekend, and plotted separately for Robben Island (top) and Hangklip (bottom) measurement sites for the inversion with spatially homogenised NEE prior fluxes. The diurnal plots are separated into working week and weekend observed concentrations (blue and light blue), working week and weekend prior modelled concentrations (red and dark red), and working week and weekend posterior modelled concentrations (green and light green).

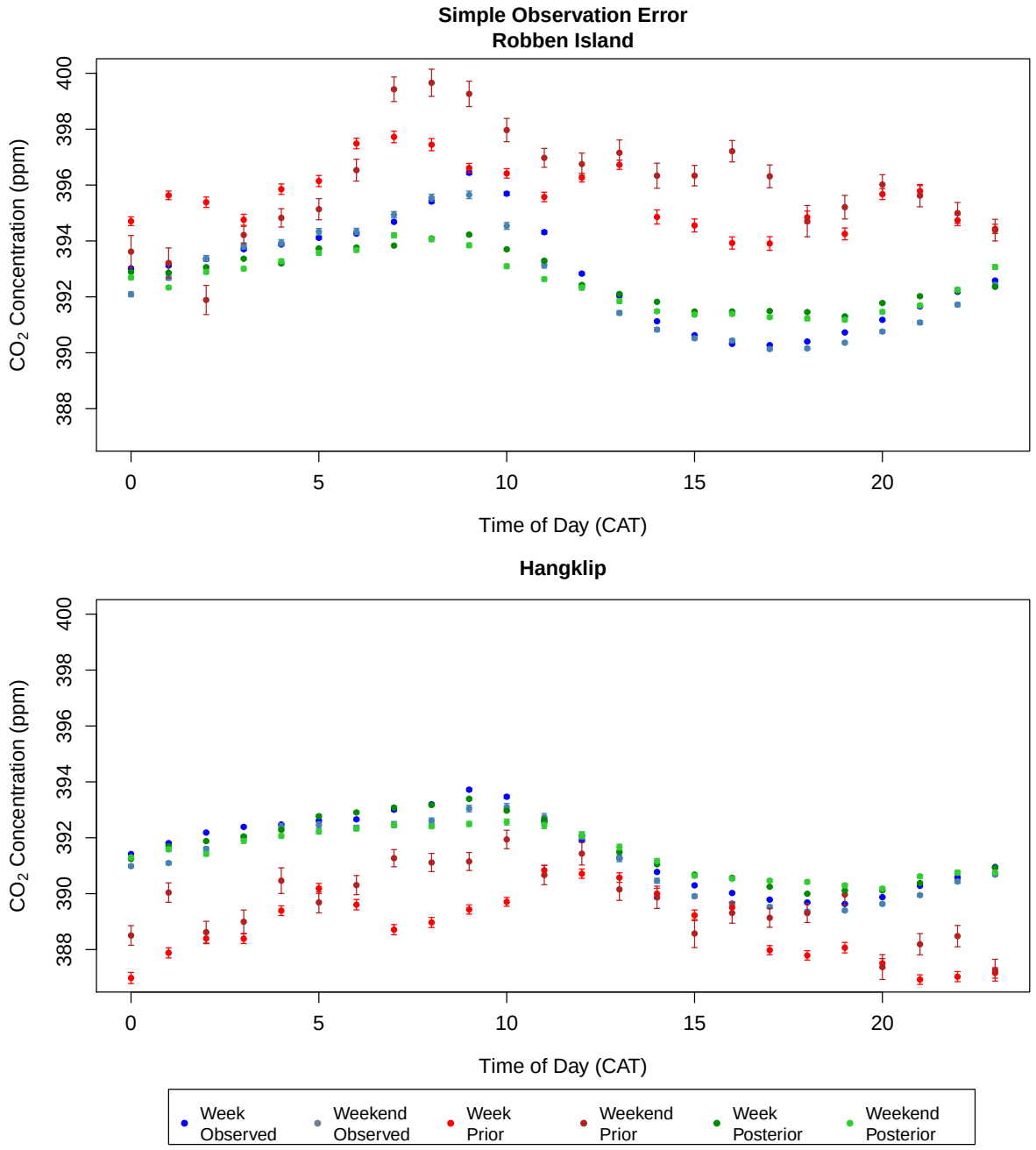


Figure C.30: The hourly diurnal cycle (mean concentrations for each hour with 95% confidence interval) in the observed, prior and posterior modelled $CO_2$ concentrations (ppm) over the full measurement period from March 2012 until June 2013, separated by working week and weekend, and plotted separately for Robben Island (top) and Hangklip (bottom) measurement sites for the inversion specifying uncertainties of 2 ppm and 4 ppm for the day and night-time observation errors. The diurnal plots are separated into working week and weekend observed concentrations (blue and light blue), working week and weekend prior modelled concentrations (red and dark red), and working week and weekend posterior modelled concentrations (green and light green).

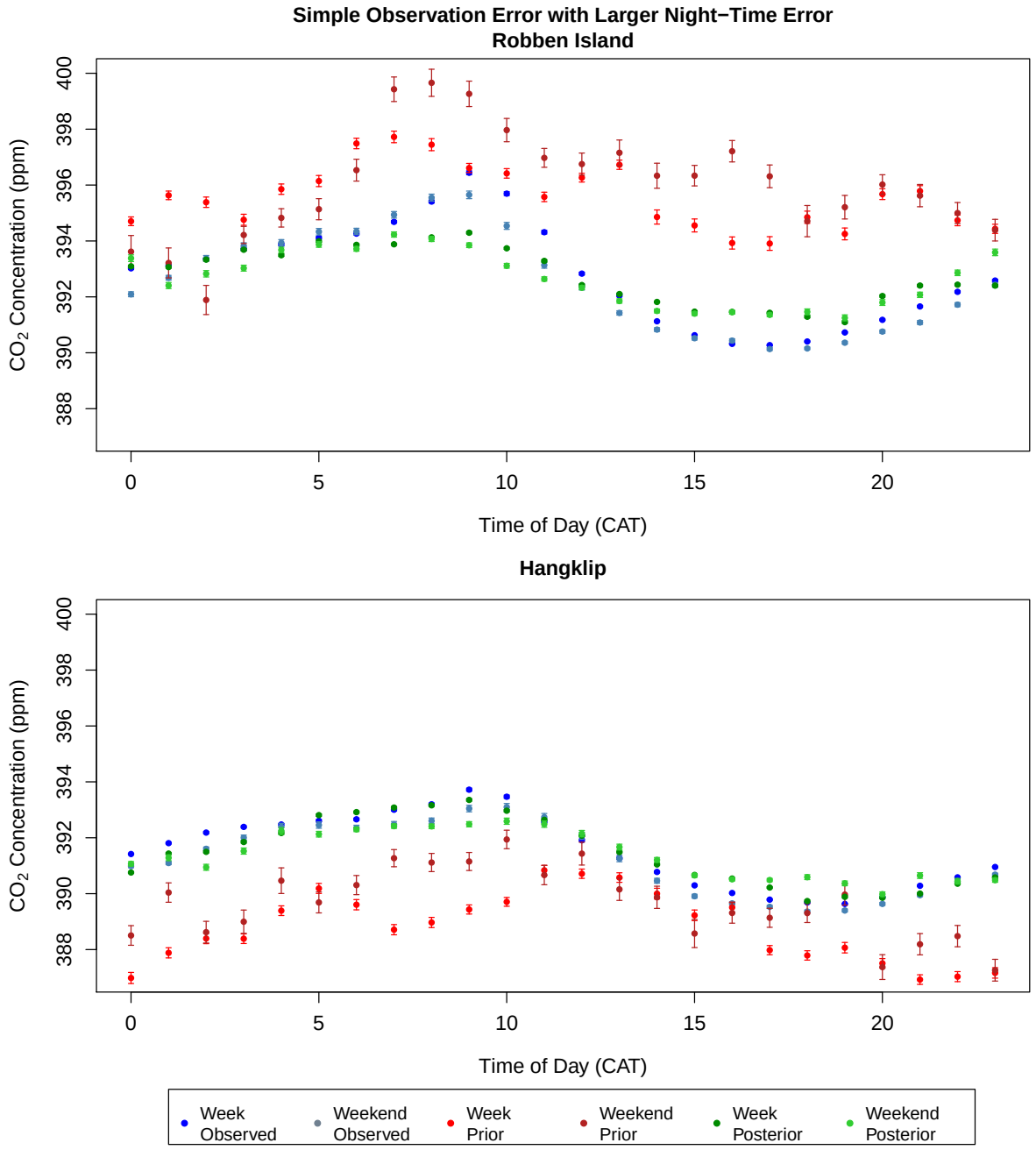


Figure C.31: The hourly diurnal cycle (mean concentrations for each hour with 95% confidence interval) in the observed, prior and posterior modelled $CO_2$ concentrations (ppm) over the full measurement period from March 2012 until June 2013, separated by working week and weekend, and plotted separately for Robben Island (top) and Hangklip (bottom) measurement sites for the inversion specifying uncertainties of 2 ppm and 10 ppm for the day and night-time observation errors. The diurnal plots are separated into working week and weekend observed concentrations (blue and light blue), working week and weekend prior modelled concentrations (red and dark red), and working week and weekend posterior modelled concentrations (green and light green).

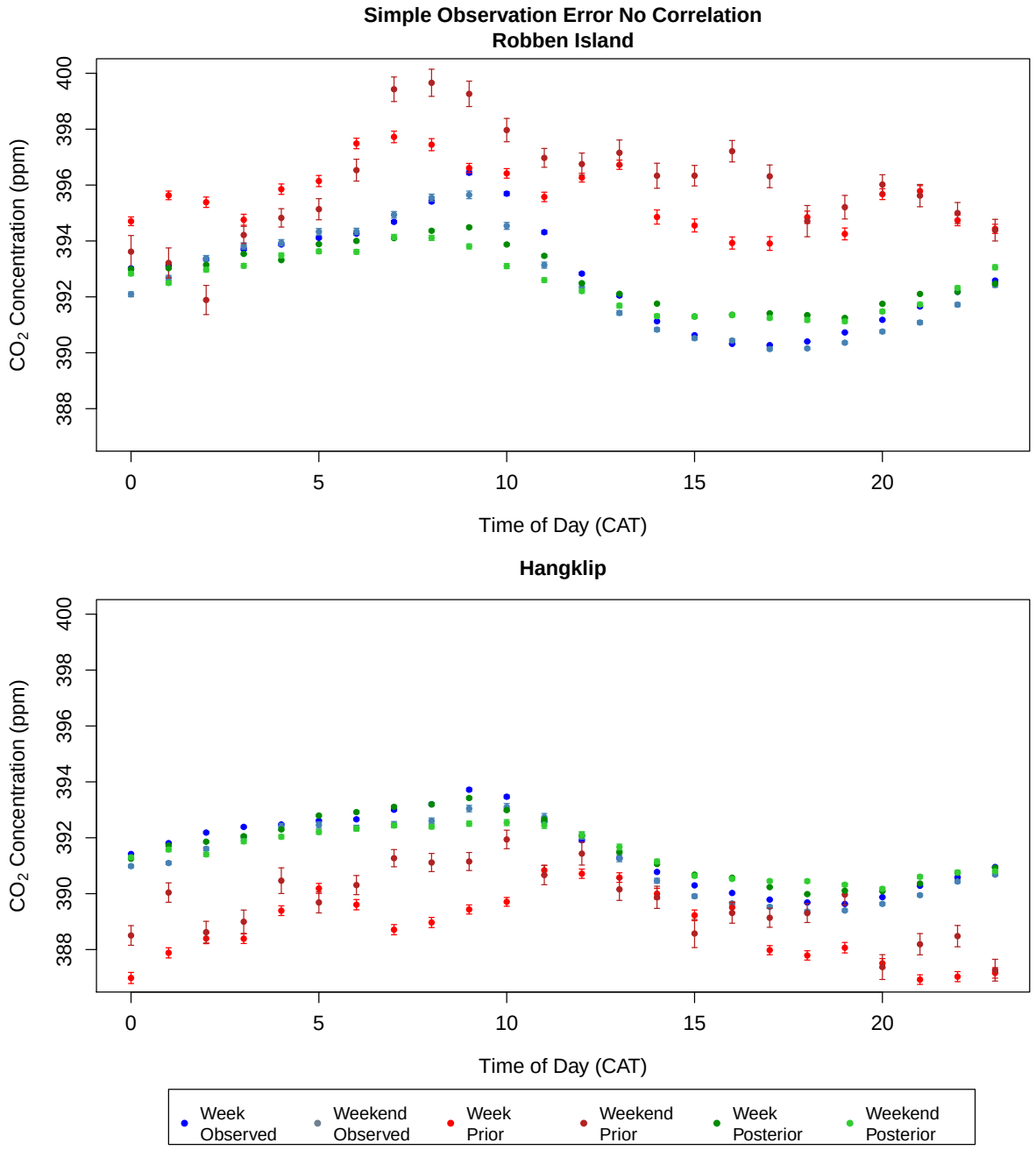


Figure C.32: The hourly diurnal cycle (mean concentrations for each hour with 95% confidence interval) in the observed, prior and posterior modelled $CO_2$ concentrations (ppm) over the full measurement period from March 2012 until June 2013, separated by working week and weekend, and plotted separately for Robben Island (top) and Hangklip (bottom) measurement sites for the inversion specifying uncertainties of 2 ppm and 4 ppm for the day and night-time observation errors with no correlation. The diurnal plots are separated into working week and weekend observed concentrations (blue and light blue), working week and weekend prior modelled concentrations (red and dark red), and working week and weekend posterior modelled concentrations (green and light green).

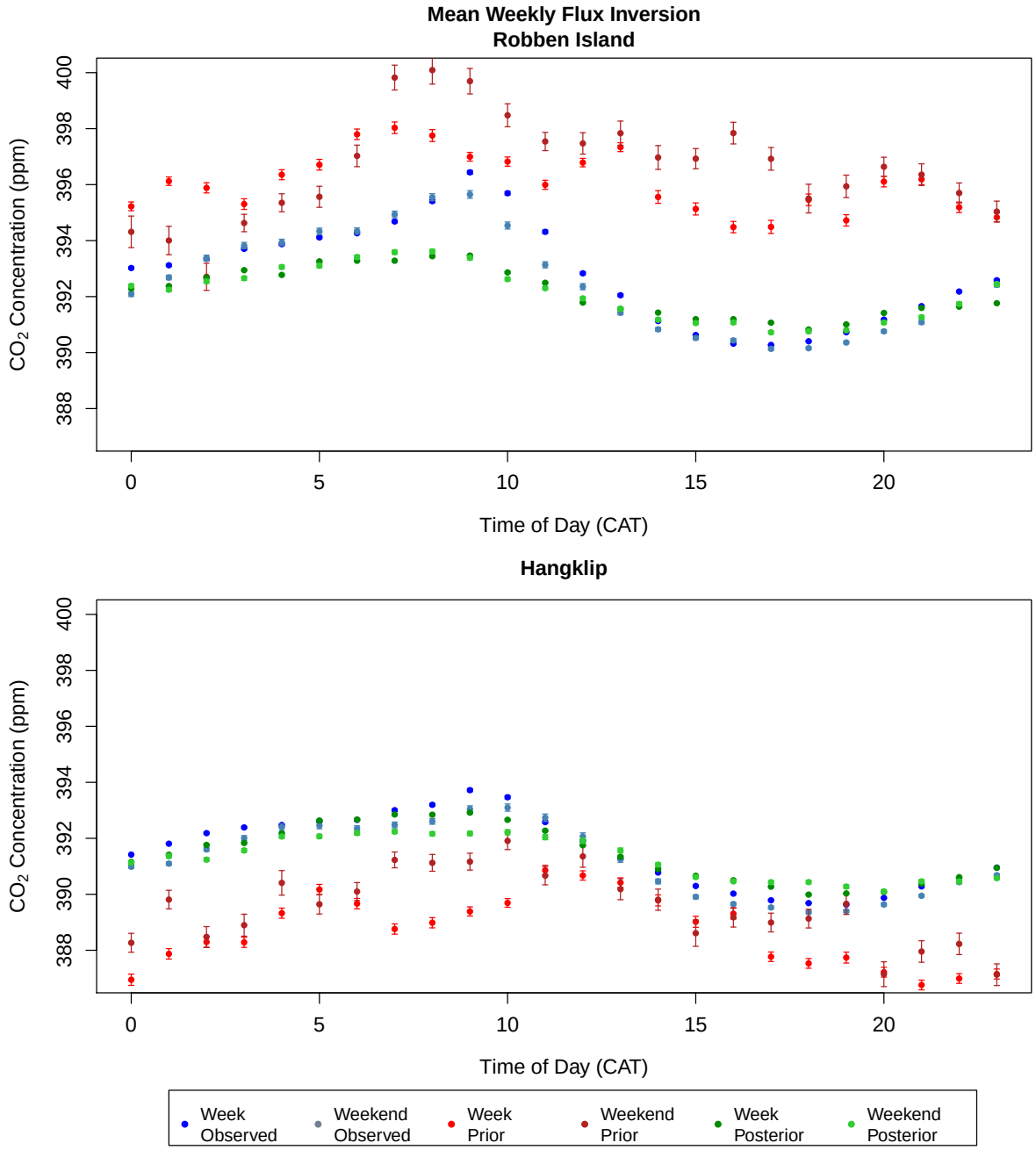


Figure C.33: The hourly diurnal cycle (mean concentrations for each hour with 95% confidence interval) in the observed, prior and posterior modelled $CO_2$ concentrations (ppm) over the full measurement period from March 2012 until June 2013, separated by working week and weekend, and plotted separately for Robben Island (top) and Hangklip (bottom) measurement sites for the inversion solving for the mean weekly flux. The diurnal plots are separated into working week and weekend observed concentrations (blue and light blue), working week and weekend prior modelled concentrations (red and dark red), and working week and weekend posterior modelled concentrations (green and light green).

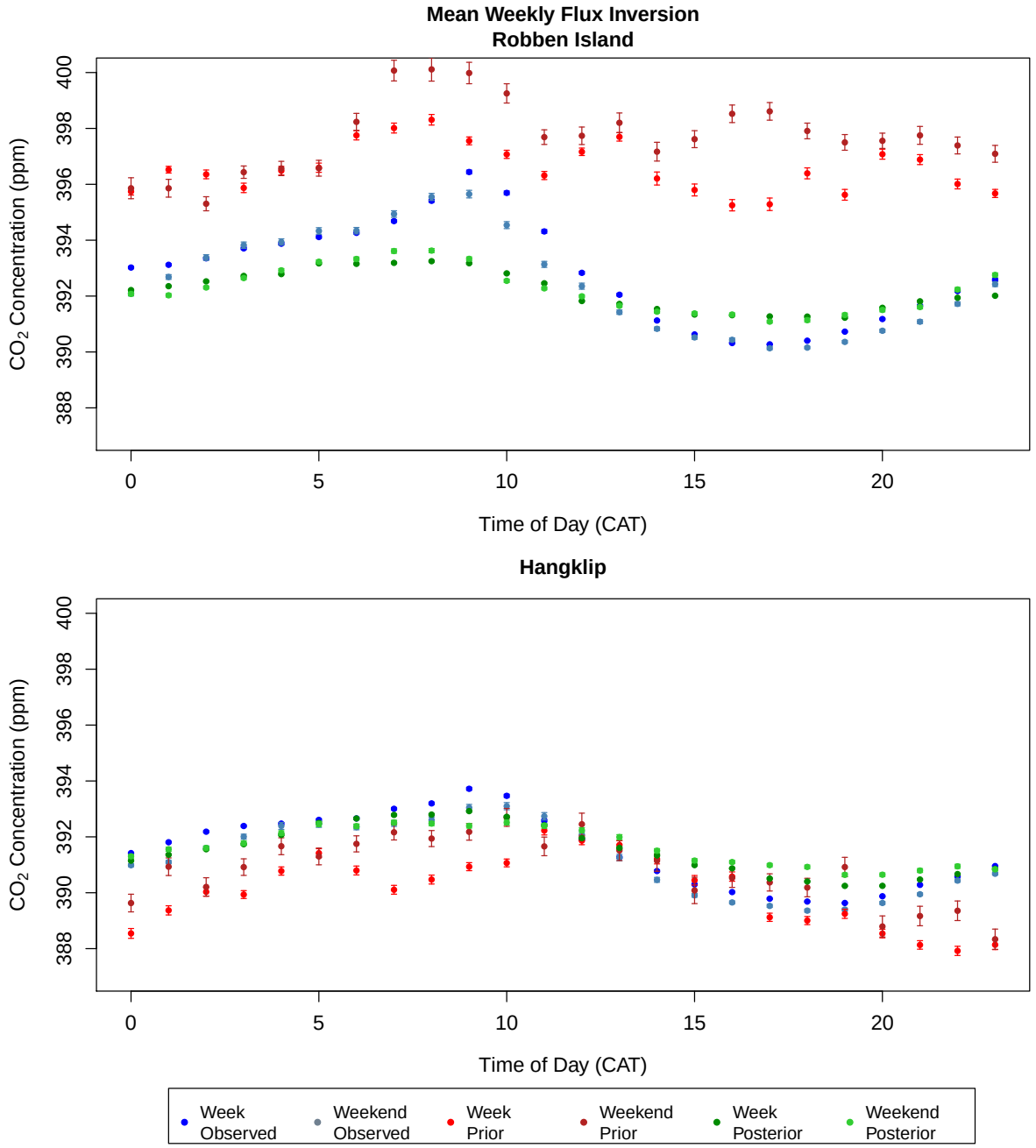


Figure C.34: The hourly diurnal cycle (mean concentrations for each hour with 95% confidence interval) in the observed, prior and posterior modelled $CO_2$ concentrations (ppm) over the full measurement period from March 2012 until June 2013, separated by working week and weekend, and plotted separately for Robben Island (top) and Hangklip (bottom) measurement sites for the separate weekly inversions. The diurnal plots are separated into working week and weekend observed concentrations (blue and light blue), working week and weekend prior modelled concentrations (red and dark red), and working week and weekend posterior modelled concentrations (green and light green).

## C.3 Weekly Aggregated Fluxes

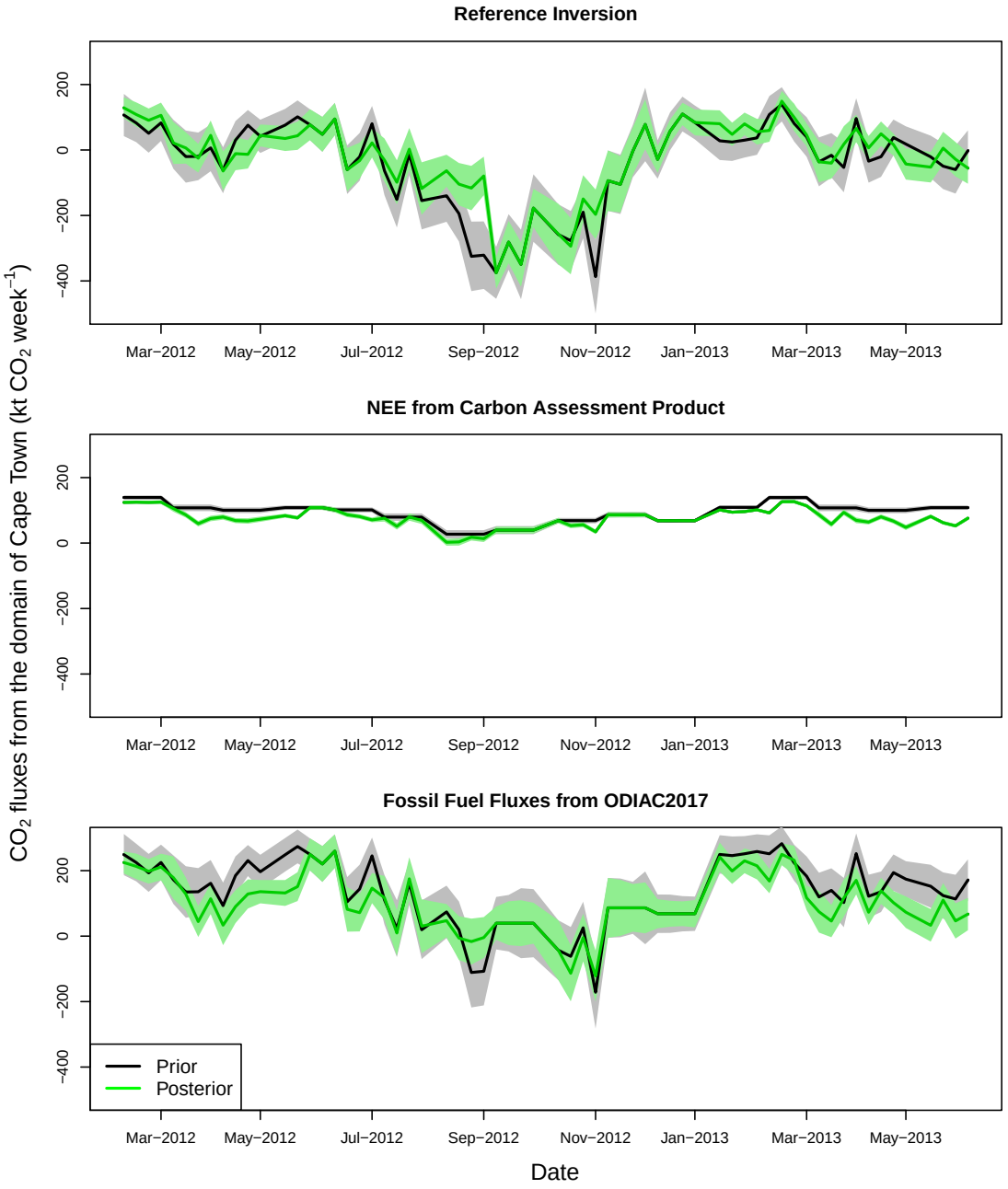


Figure C.35: Prior and posterior aggregated weekly fluxes over the inversion domain from March 2012 to June 2013 for the reference inversion (top) and the inversions making use of the carbon assessment product for the prior NEE fluxes (middle)and the ODIAC fossil fuel product for prior fossil fuel fluxes (bottom).

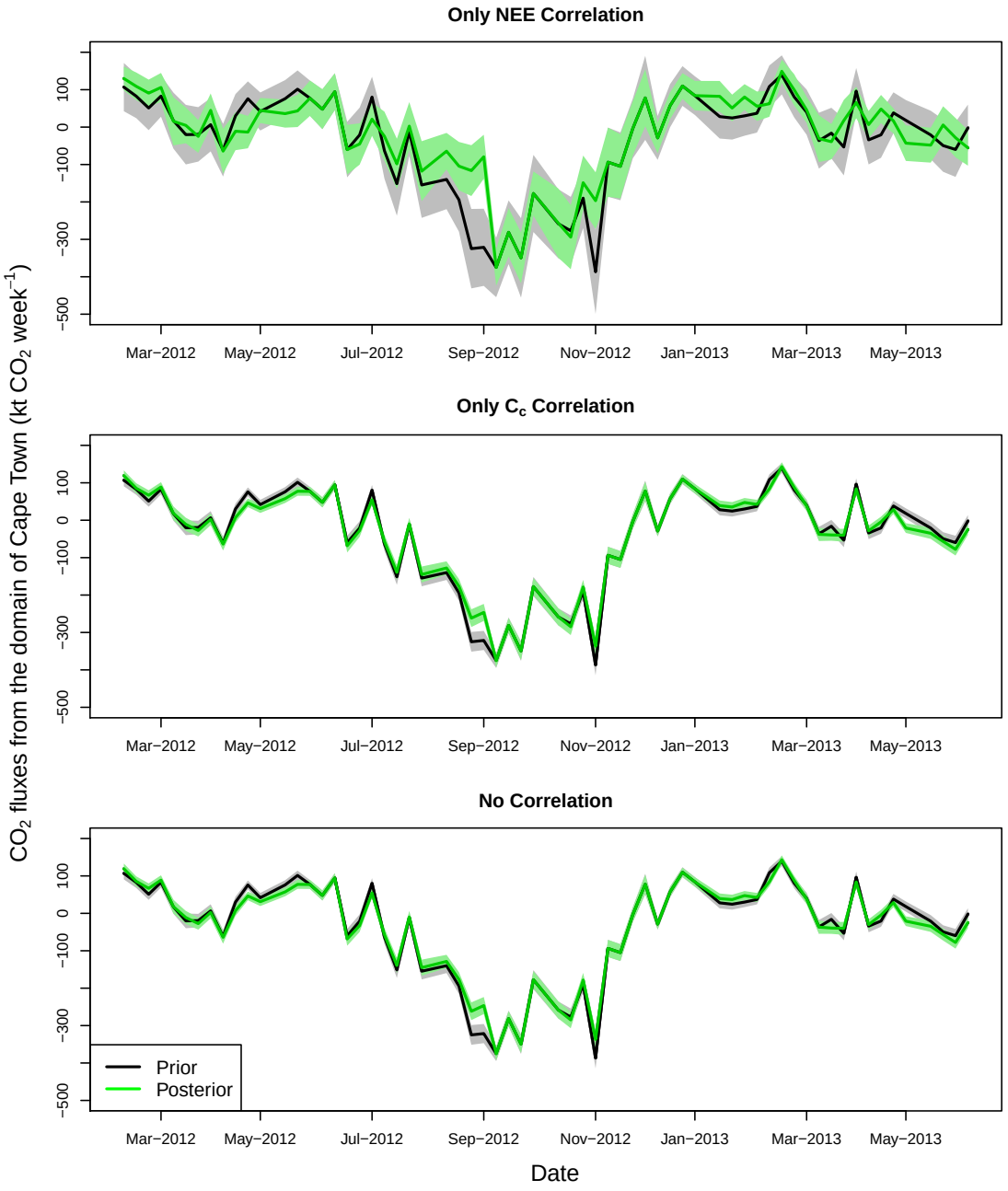


Figure C.36: Prior and posterior aggregated weekly fluxes over the inversion domain from March 2012 to June 2013 for the inversion accounting for only correlation between NEE flux uncertainties (top) the inversion accounting for only correlation between the observation errors (middle) and the inversion with no correlation in the prior uncertainty covariance matrices (bottom).

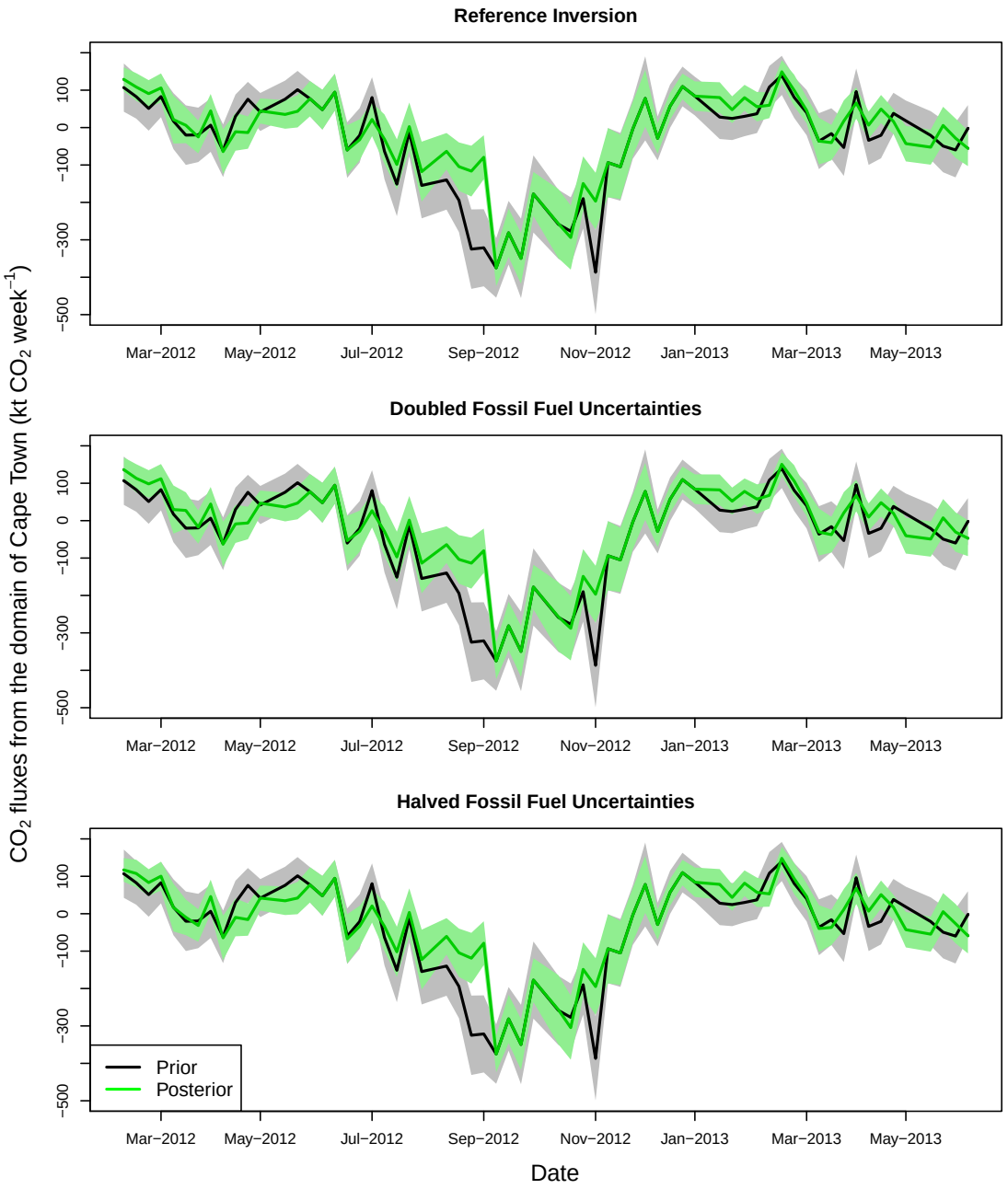


Figure C.37: Prior and posterior aggregated weekly fluxes over the inversion domain from March 2012 to June 2013 for the reference inversion (top) and the inversions doubling (middle) and halving (bottom) the uncertainty in the fossil fuel fluxes.

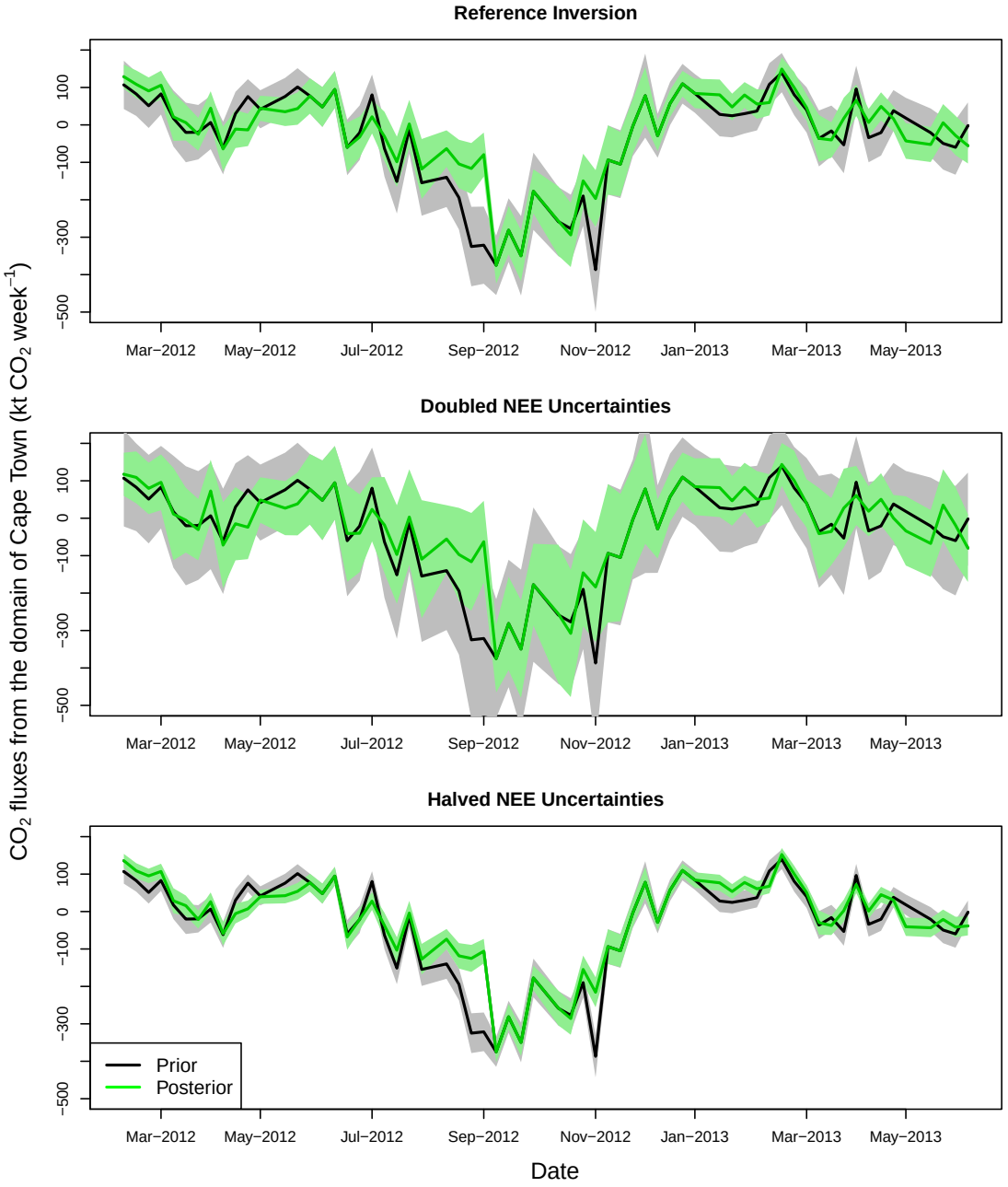


Figure C.38: Prior and posterior aggregated weekly fluxes over the inversion domain from March 2012 to June 2013 for the reference inversion (top) and the inversions doubling (middle) and halving (bottom) the uncertainty in the NEE fluxes.

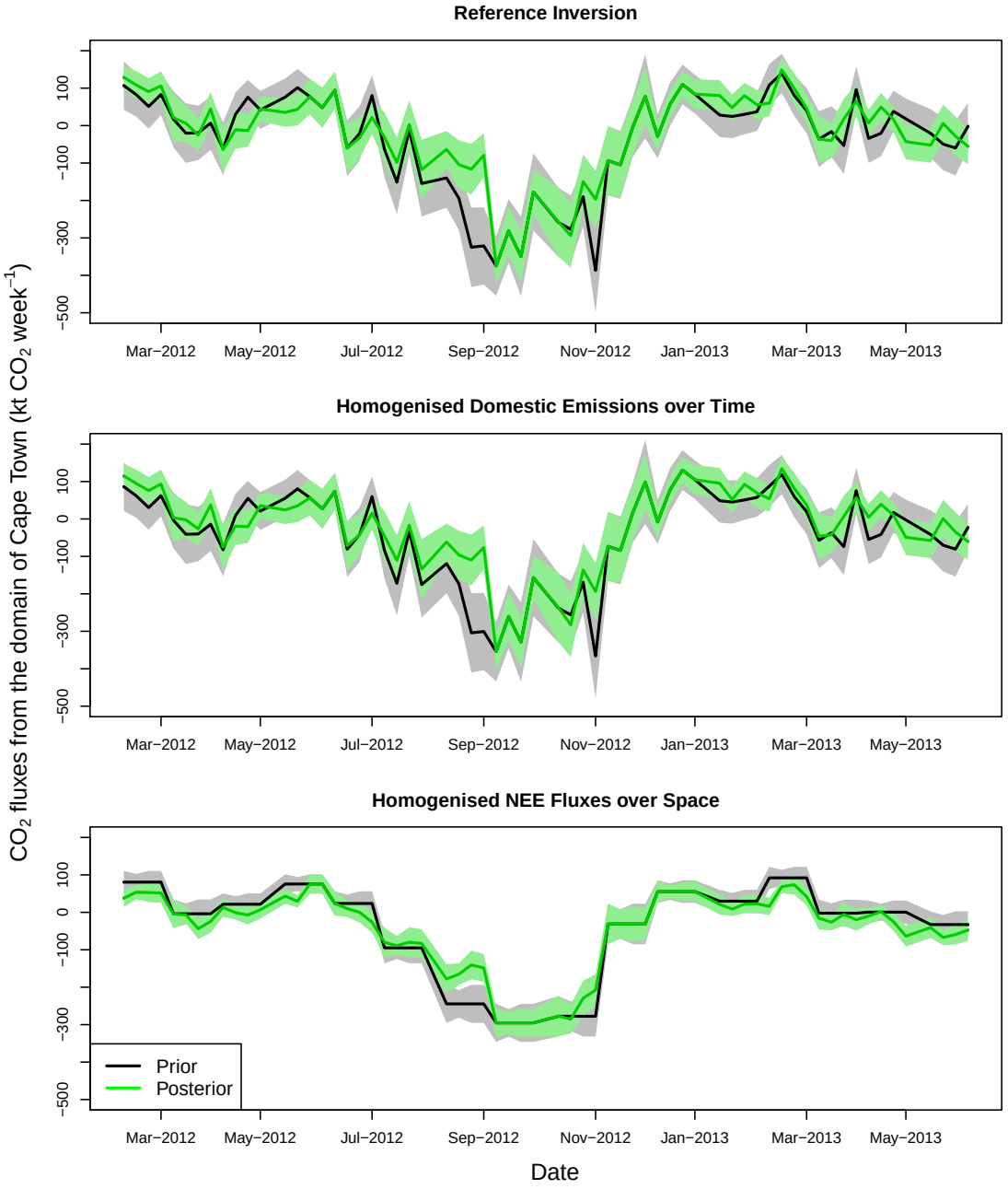


Figure C.39: Prior and posterior aggregated weekly fluxes over the inversion domain from March 2012 to June 2013 for the reference inversion (top) and the inversions making use of the temporally homogenised domestic fossil fuel prior (middle) and spatially homogenised NEE flux prior (bottom).

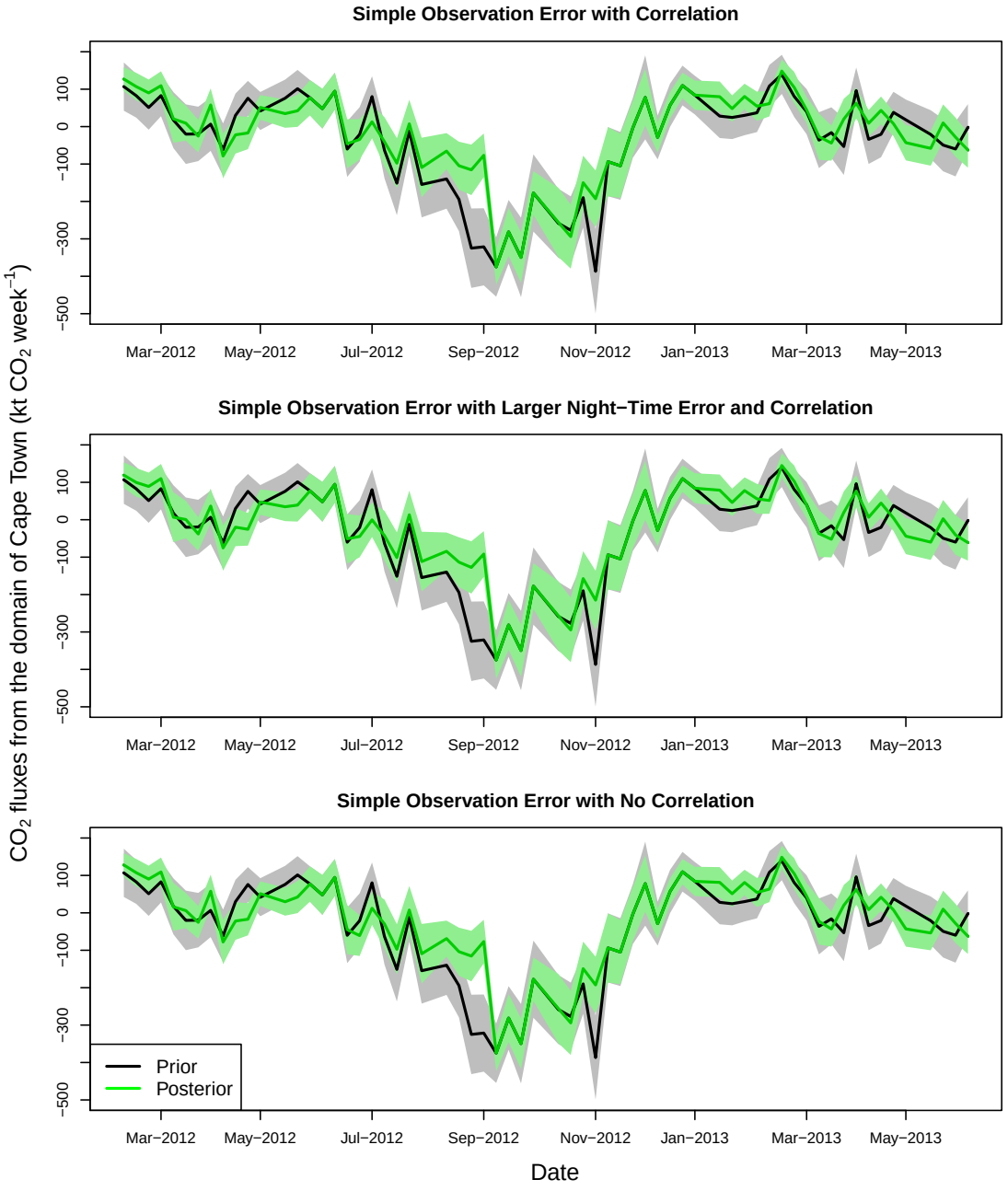


Figure C.40: Prior and posterior aggregated weekly fluxes over the inversion domain from March 2012 to June 2013 for the inversion specifying uncertainties of 2 ppm and 4 ppm for the day and night-time observation errors (top), the inversion specifying uncertainties of 2 ppm and 10 ppm for the day and night-time observation errors (middle), and the inversion specifying uncertainties of 2 ppm and 4 ppm for the day and night-time observation errors with no correlation between observation errors (bottom).

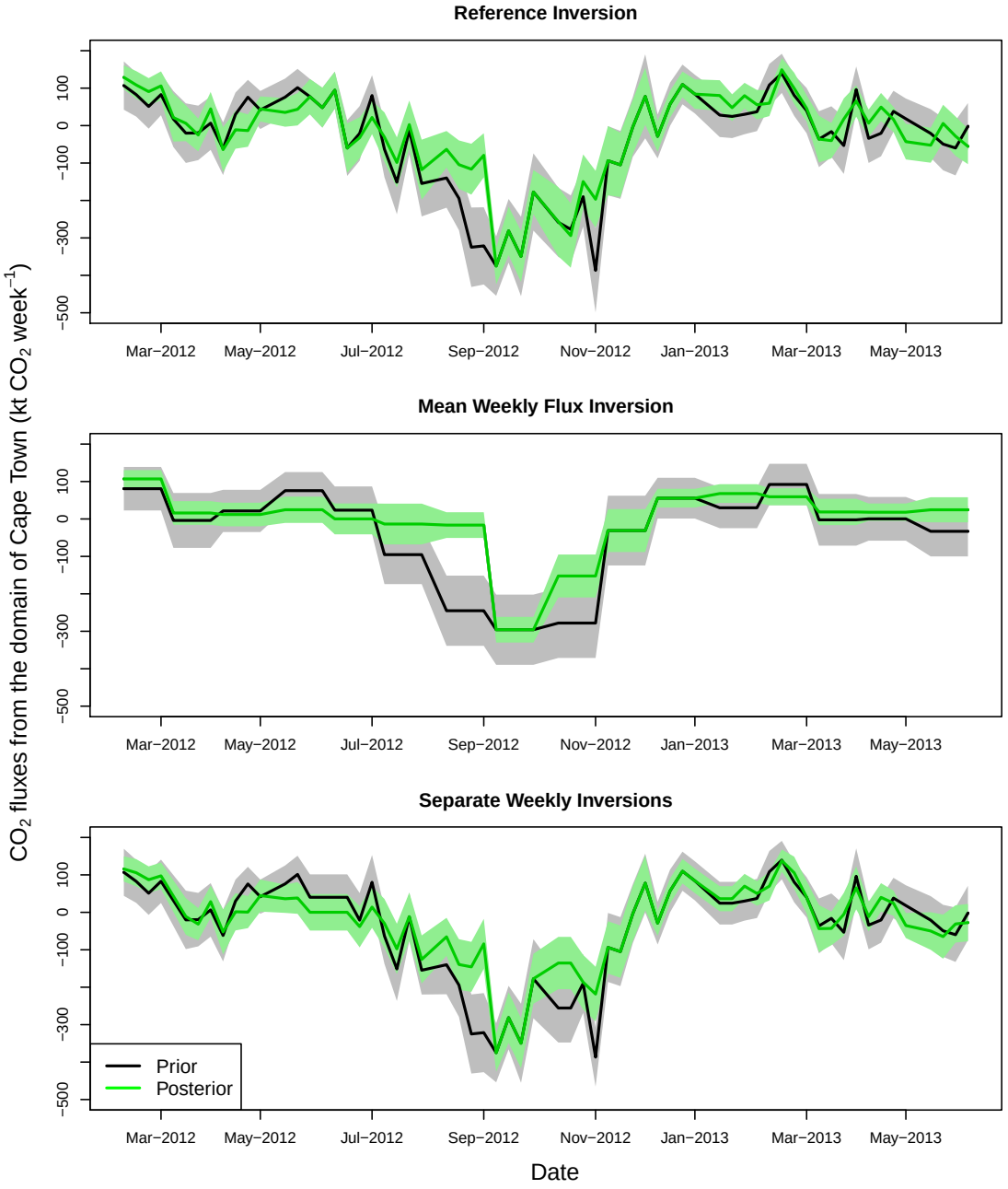


Figure C.41: Prior and posterior aggregated weekly fluxes over the inversion domain from March 2012 to June 2013 for the reference inversion, which was a monthly inversion solving for separate weekly fluxes (top), the inversion solving for the mean weekly fluxes (middle), and the separate weekly inversions (bottom).

## C.4 Monthly Aggregated Fluxes

Table C.1: Aggregated $CO_2$ flux estimates (kt $CO_2$) and their uncertainties expressed as standard deviations for each month over the four-week inversion period for the reference inversion, alternative prior product inversions, and the inversions removing spatial NEE correlation and temporal observation error correlation.

| | Ref | | | Carbon Assess | | | ODIAC | | |
|---|---|---|---|---|---|---|---|---|---|
| Month | Prior Flux (sd) | Posterior Flux (sd) | Uncertainty Reduction (%) | Prior Flux (sd) | Posterior Flux (sd) | Uncertainty Reduction (%) | Prior Flux (sd) | Posterior Flux (sd) | Uncertainty Reduction (%) |
| Mar-12 | 323 (61) | 434 (36) | 39.9 | 557 (6) | 499 (5) | 18.5 | 892 (59) | 847 (38) | 35.7 |
| Apr-12 | -16 (76) | 47 (51) | 32.5 | 431 (10) | 326 (9) | 13.6 | 604 (76) | 465 (53) | 29.2 |
| May-12 | 86 (58) | -44 (49) | 16.7 | 401 (9) | 289 (8) | 7 | 706 (59) | 388 (50) | 15.8 |
| Jun-12 | 302 (51) | 204 (47) | 8.7 | 433 (7) | 377 (7) | 5.3 | 992 (53) | 753 (48) | 8.8 |
| Jul-12 | 94 (65) | 24 (54) | 16.1 | 405 (8) | 340 (7) | 5.7 | 754 (66) | 560 (56) | 14.8 |
| Aug-12 | -381 (80) | -245 (71) | 11.9 | 317 (11) | 276 (11) | 5.4 | 315 (82) | 332 (72) | 11.6 |
| Sep-12 | -980 (96) | -363 (59) | 39 | 108 (13) | 37 (10) | 18 | -125 (97) | 20 (61) | 36.8 |
| Nov-12 | -1112 (96) | -897 (81) | 15.6 | 274 (8) | 212 (8) | 8.7 | -251 (96) | -283 (82) | 14.4 |
| Feb-13 | 119 (56) | 264 (36) | 36 | 436 (5) | 393 (4) | 16 | 1006 (57) | 886 (40) | 30.8 |
| Mar-13 | 369 (57) | 354 (35) | 38.2 | 556 (6) | 459 (5) | 19 | 941 (57) | 767 (38) | 33.9 |
| Apr-13 | -9 (72) | 7 (52) | 27.2 | 430 (10) | 307 (9) | 14.1 | 614 (71) | 408 (54) | 24.4 |
| May-13 | 1 (60) | 30 (39) | 35.3 | 400 (9) | 259 (8) | 14.5 | 625 (61) | 387 (41) | 32.7 |
| Jun-13 | -132 (69) | -131 (49) | 28.4 | 433 (7) | 272 (6) | 12.9 | 561 (70) | 257 (51) | 26.5 |
| | NEE Corr | | | Obs Corr | | | No Corr | | |
| Month | Prior Flux (sd) | Posterior Flux (sd) | Uncertainty Reduction (%) | Prior Flux (sd) | Posterior Flux (sd) | Uncertainty Reduction (%) | Prior Flux (sd) | Posterior Flux (sd) | Uncertainty Reduction (%) |
| Mar-12 | 323 (61) | 436 (36) | 39.9 | 323 (15) | 360 (14) | 10.6 | 323 (15) | 360 (14) | 10.7 |
| Apr-12 | -16 (76) | 40 (52) | 32.3 | -16 (19) | -17 (17) | 8.6 | -16 (19) | -18 (17) | 8.6 |
| May-12 | 86 (58) | -44 (49) | 16.6 | 86 (15) | 21 (14) | 5.1 | 86 (15) | 21 (14) | 5 |
| Jun-12 | 302 (51) | 204 (47) | 9 | 302 (13) | 260 (13) | 2.9 | 302 (13) | 260 (13) | 3 |
| Jul-12 | 94 (65) | 11 (55) | 15.9 | 94 (16) | 54 (16) | 4.6 | 94 (16) | 48 (16) | 4.6 |
| Aug-12 | -381 (80) | -238 (71) | 12 | -381 (20) | -352 (19) | 3.2 | -381 (20) | -352 (19) | 3.2 |
| Sep-12 | -980 (96) | -364 (59) | 39 | -980 (24) | -812 (21) | 11.1 | -980 (24) | -813 (21) | 11.1 |
| Nov-12 | -1112 (96) | -896 (81) | 15.6 | -1112 (24) | -1058 (23) | 5.1 | -1112 (24) | -1058 (23) | 5.1 |
| Feb-2013 | 119 (56) | 269 (36) | 35.9 | 119 (14) | 164 (13) | 9.5 | 119 (14) | 166 (13) | 9.6 |
| Mar-13 | 369 (57) | 357 (35) | 38 | 369 (14) | 353 (13) | 11.1 | 369 (14) | 353 (13) | 11.1 |
| Apr-13 | -9 (72) | 13 (52) | 27.1 | -9 (18) | -33 (16) | 7.8 | -9 (18) | -32 (16) | 7.8 |
| May-13 | 1 (60) | 29 (39) | 35.2 | 1 (15) | -25 (14) | 10.3 | 1 (15) | -27 (14) | 10.3 |
| Jun-13 | -132 (69) | -126 (49) | 28.5 | -132 (17) | -194 (16) | 8.7 | -132 (17) | -194 (16) | 8.8 |

[1]

[1]Prior and Posterior Flux refer to the total flux from the domain over the thirteen four-week periods. The sd of the fluxes refers to the uncertainty in the total flux estimate. The sd of the $\chi^2$ statistic refers to the standard deviation between the $\chi^2$ statistics of the thirteen four-week period $\chi^2$ Statistics. Ref = Reference Inversion; Carbon Assess = Carbon Assessment Inversion; ODIAC = ODIAC fossil fuel inversion; NEE Corr = Correlation for NEE fluxes only; Obs Corr = Correlation for observation errors only; No Corr = No correlation specified in prior covariance matrices; Double FF = Double fossil fuel uncertainties; Half FF = Half fossil fuel uncertainties; Double NEE = Double NEE uncertainties; Half NEE = Half NEE uncertainties; Domestic Homogenised = Domestic emission homogenised over the year; NEE Homogenised = NEE fluxes averaged over the domain; Simp Obs Error = Simple specification of observation error covariance matrix; Simp Obs with Large Night = Simple observation error covariance matrix with larger night-time error; Simp Obs No Corr = Simple observation error covariance matrix with no correlation; Mean Month = Inversion solving for mean weekly fluxes over the month; Week = Separate inversions for each week.

Table C.2: Aggregated $CO_2$ flux estimates (kt $CO_2$) and their uncertainties expressed as standard deviations for each month over the four-week inversion period for test cases considered different relative uncertainty in the fossil fuel and NEE fluxes, and inversion considered temporally homogenised prior domestic emissions and spatially homogenised prior NEE fluxes.

| | Double FF | | | Half FF | | | Double NEE | | |
|---|---|---|---|---|---|---|---|---|---|
| Month | Prior Flux (sd) | Posterior Flux (sd) | Uncertainty Reduction (%) | Prior Flux (sd) | Posterior Flux (sd) | Uncertainty Reduction (%) | Prior Flux (sd) | Posterior Flux (sd) | Uncertainty Reduction (%) |
| Mar-12 | 323 (61) | 460 (37) | 39.1 | 323 (61) | 408 (36) | 40.3 | 323 (121) | 402 (69) | 43.3 |
| Apr-12 | -16 (76) | 85 (52) | 32 | -16 (76) | 21 (51) | 32.7 | -16 (152) | 48 (97) | 36.6 |
| May-12 | 86 (59) | -31 (49) | 16.6 | 86 (58) | -48 (49) | 16.8 | 86 (117) | -62 (93) | 19.9 |
| Jun-12 | 302 (51) | 208 (47) | 8.7 | 302 (51) | 201 (47) | 8.7 | 302 (102) | 190 (92) | 10 |
| Jul-12 | 94 (65) | 40 (55) | 15.9 | 94 (65) | 15 (54) | 16.2 | 94 (130) | 37 (106) | 18.5 |
| Aug-12 | -381 (81) | -238 (71) | 11.8 | -381 (80) | -255 (71) | 12 | -381 (161) | -221 (139) | 13.5 |
| Sep-12 | -980 (96) | -362 (59) | 38.8 | -980 (96) | -363 (59) | 39.1 | -980 (192) | -331 (111) | 42.3 |
| Nov-12 | -1112 (97) | -890 (82) | 15.5 | -1112 (96) | -904 (81) | 15.6 | -1112 (193) | -893 (160) | 16.8 |
| Feb-13 | 119 (57) | 270 (37) | 35.5 | 119 (56) | 261 (36) | 36.1 | 119 (113) | 261 (69) | 38.8 |
| Mar-13 | 369 (57) | 371 (36) | 37.6 | 369 (57) | 341 (35) | 38.5 | 369 (114) | 338 (66) | 42.2 |
| Apr-13 | -9 (72) | 20 (52) | 26.9 | -9 (72) | 3 (52) | 27.3 | -9 (143) | 11 (100) | 30.2 |
| May-13 | 1 (61) | 37 (39) | 35.1 | 1 (60) | 32 (39) | 35.4 | 1 (121) | 36 (74) | 39.1 |
| Jun-13 | -132 (69) | -119 (50) | 28.3 | -132 (69) | -134 (49) | 28.5 | -132 (138) | -131 (95) | 31.4 |

| | Half NEE | | | Domestic Homogenised | | | NEE Homogenised | | |
|---|---|---|---|---|---|---|---|---|---|
| Month | Prior Flux (sd) | Posterior Flux (sd) | Uncertainty Reduction (%) | Prior Flux (sd) | Posterior Flux (sd) | Uncertainty Reduction (%) | Prior Flux (sd) | Posterior Flux (sd) | Uncertainty Reduction (%) |
| Mar-12 | 323 (30) | 447 (20) | 34.8 | 240 (61) | 379 (36) | 40 | 323 (29) | 196 (24) | 16.1 |
| Apr-12 | -16 (38) | 49 (28) | 26.8 | -99 (76) | 12 (51) | 32.6 | -15 (37) | -79 (30) | 17.8 |
| May-12 | 86 (29) | -18 (26) | 13 | 3 (58) | -79 (49) | 16.7 | 86 (28) | 12 (24) | 15 |
| Jun-12 | 302 (26) | 221 (24) | 6.9 | 219 (51) | 143 (47) | 8.7 | 303 (25) | 224 (23) | 6.8 |
| Jul-12 | 94 (33) | 34 (28) | 12.8 | 11 (65) | -24 (54) | 16.1 | 95 (31) | 7 (28) | 9.9 |
| Aug-12 | -381 (40) | -272 (36) | 9.9 | -464 (80) | -307 (71) | 11.9 | -380 (39) | -332 (37) | 6.8 |
| Sep-12 | -980 (48) | -423 (32) | 34 | -897 (96) | -344 (59) | 38.9 | -978 (49) | -632 (36) | 25.9 |
| Nov-12 | -1112 (48) | -914 (42) | 13.9 | -1029 (96) | -849 (81) | 15.6 | -1111 (52) | -1000 (46) | 11.4 |
| Feb-13 | 119 (28) | 269 (19) | 31.5 | 202 (56) | 309 (36) | 35.9 | 119 (29) | 75 (24) | 16.5 |
| Mar-13 | 369 (29) | 371 (19) | 32.8 | 286 (57) | 308 (35) | 38.2 | 368 (28) | 200 (23) | 19.1 |
| Apr-13 | -9 (36) | 7 (28) | 23 | -92 (72) | -25 (52) | 27.2 | -9 (34) | -68 (29) | 17 |
| May-13 | 1 (30) | 36 (21) | 30.1 | -81 (60) | 5 (39) | 35.4 | 2 (30) | -97 (24) | 19.3 |
| Jun-13 | -132 (35) | -144 (26) | 24.3 | -215 (69) | -152 (49) | 28.5 | -131 (34) | -214 (27) | 21.4 |

[2]

[2]Prior and Posterior Flux refer to the total flux from the domain over the thirteen four-week periods. The sd of the fluxes refers to the uncertainty in the total flux estimate. The sd of the $\chi^2$ statistic refers to the standard deviation between the $\chi^2$ statistics of the thirteen four-week period $\chi^2$ Statistics. Ref = Reference Inversion; Carbon Assess = Carbon Assessment Inversion; ODIAC = ODIAC fossil fuel inversion; NEE Corr = Correlation for NEE fluxes only; Obs Corr = Correlation for observation errors only; No Corr = No correlation specified in prior covariance matrices; Double FF = Double fossil fuel uncertainties; Half FF = Half fossil fuel uncertainties; Double NEE = Double NEE uncertainties; Half NEE = Half NEE uncertainties; Domestic Homogenised = Domestic emission homogenised over the year; NEE Homogenised = NEE fluxes averaged over the domain; Simp Obs Error = Simple specification of observation error covariance matrix; Simp Obs with Large Night = Simple observation error covariance matrix with larger night-time error; Simp Obs No Corr = Simple observation error covariance matrix with no correlation; Mean Month = Inversion solving for mean weekly fluxes over the month; Week = Separate inversions for each week.

Table C.3: Aggregated $CO_2$ flux estimates (kt $CO_2$) and their uncertainties expressed as standard deviations for each month over the four-week inversion period for the simplified observation error test cases, and the alternative control vector inversions.

| | Simp Obs Error | | | Simp Obs with Large Night | | | Simp Obs No Corr | | |
|---|---|---|---|---|---|---|---|---|---|
| Month | Prior Flux (sd) | Posterior Flux (sd) | Uncertainty Reduction (%) | Prior Flux (sd) | Posterior Flux (sd) | Uncertainty Reduction (%) | Prior Flux (sd) | Posterior Flux (sd) | Uncertainty Reduction (%) |
| Mar-12 | 323 (61) | 433 (36) | 40.4 | 323 (61) | 417 (38) | 38.1 | 323 (61) | 435 (36) | 40.4 |
| Apr-12 | -16 (76) | 62 (51) | 33.3 | -16 (76) | 6 (53) | 30.2 | -16 (76) | 55 (51) | 33.1 |
| May-12 | 86 (58) | -67 (48) | 17.3 | 86 (58) | -74 (49) | 15.8 | 86 (58) | -66 (48) | 17.2 |
| Jun-12 | 302 (51) | 202 (47) | 8.9 | 302 (51) | 199 (47) | 8.2 | 302 (51) | 197 (46) | 9.2 |
| Jul-12 | 94 (65) | 27 (54) | 16.6 | 94 (65) | -1 (55) | 15.1 | 94 (65) | 1 (54) | 16.4 |
| Aug-12 | -381 (80) | -240 (70) | 12.3 | -381 (80) | -242 (71) | 11.9 | -381 (80) | -229 (70) | 12.4 |
| Sep-12 | -980 (96) | -362 (58) | 39.5 | -980 (96) | -417 (60) | 37.1 | -980 (96) | -365 (58) | 39.5 |
| Nov-12 | -1112 (96) | -892 (81) | 15.8 | -1112 (96) | -923 (83) | 14.4 | -1112 (96) | -892 (81) | 15.8 |
| Feb-13 | 119 (56) | 263 (36) | 36.5 | 119 (56) | 259 (37) | 34.1 | 119 (56) | 268 (36) | 36.4 |
| Mar-13 | 369 (57) | 359 (35) | 38.8 | 369 (57) | 338 (36) | 36.5 | 369 (57) | 361 (35) | 38.6 |
| Apr-13 | -9 (72) | 12 (52) | 28 | -9 (72) | 7 (53) | 26.2 | -9 (72) | 17 (52) | 27.9 |
| May-13 | 1 (60) | 17 (39) | 36.1 | 1 (60) | 12 (40) | 34 | 1 (60) | 15 (39) | 36 |
| Jun-13 | -132 (69) | -139 (49) | 28.9 | -132 (69) | -159 (50) | 27.5 | -132 (69) | -135 (49) | 28.9 |
| | Mean Month | | | Week | | | | | |
| Mar-12 | 323 (30) | 428 (12) | 59.5 | 323 (59) | 406 (36) | 38.8 | | | |
| Apr-12 | -16 (37) | 64 (16) | 56.9 | -53 (76) | -26 (47) | 38 | | | |
| May-12 | 86 (29) | 47 (16) | 44.2 | 86 (58) | -5 (48) | 15.8 | | | |
| Jun-12 | 302 (25) | 98 (18) | 29.4 | 380 (51) | 151 (42) | 16.9 | | | |
| Jul-12 | 94 (32) | 1 (21) | 35 | 17 (70) | -100 (54) | 23.3 | | | |
| Aug-12 | -381 (40) | -54 (28) | 30.8 | -381 (80) | -265 (71) | 12.1 | | | |
| Sep-12 | -980 (48) | -66 (18) | 63.4 | -980 (96) | -435 (62) | 35.2 | | | |
| Nov-12 | -1112 (48) | -609 (29) | 38.5 | -956 (89) | -779 (74) | 16.8 | | | |
| Feb-13 | 119 (28) | 271 (13) | 54.1 | 116 (55) | 193 (35) | 37 | | | |
| Mar-13 | 369 (28) | 237 (12) | 58.8 | 369 (56) | 354 (37) | 33.7 | | | |
| Apr-13 | -9 (35) | 75 (18) | 49 | -9 (70) | -27 (53) | 24.4 | | | |
| May-13 | 1 (30) | 72 (12) | 60.1 | 1 (60) | 18 (40) | 32.2 | | | |
| Jun-13 | -132 (34) | 98 (17) | 50 | -132 (68) | -173 (53) | 23.2 | | | |

[3]Prior and Posterior Flux refer to the total flux from the domain over the thirteen four-week periods. The sd of the fluxes refers to the uncertainty in the total flux estimate. The sd of the $\chi^2$ statistic refers to the standard deviation between the $\chi^2$ statistics of the thirteen four-week period $\chi^2$ Statistics. Ref = Reference Inversion; Carbon Assess = Carbon Assessment Inversion; ODIAC = ODIAC fossil fuel inversion; NEE Corr = Correlation for NEE fluxes only; Obs Corr = Correlation for observation errors only; No Corr = No correlation specified in prior covariance matrices; Double FF = Double fossil fuel uncertainties; Half FF = Half fossil fuel uncertainties; Double NEE = Double NEE uncertainties; Half NEE = Half NEE uncertainties; Domestic Homogenised = Domestic emission homogenised over the year; NEE Homogenised = NEE fluxes averaged over the domain; Simp Obs Error = Simple specification of observation error covariance matrix; Simp Obs with Large Night = Simple observation error covariance matrix with larger night-time error; Simp Obs No Corr = Simple observation error covariance matrix with no correlation; Mean Month = Inversion solving for mean weekly fluxes over the month; Week = Separate inversions for each week.

## C.5 Spatial Distribution of Prior and Posterior Fluxes, and Uncertainty Reductions

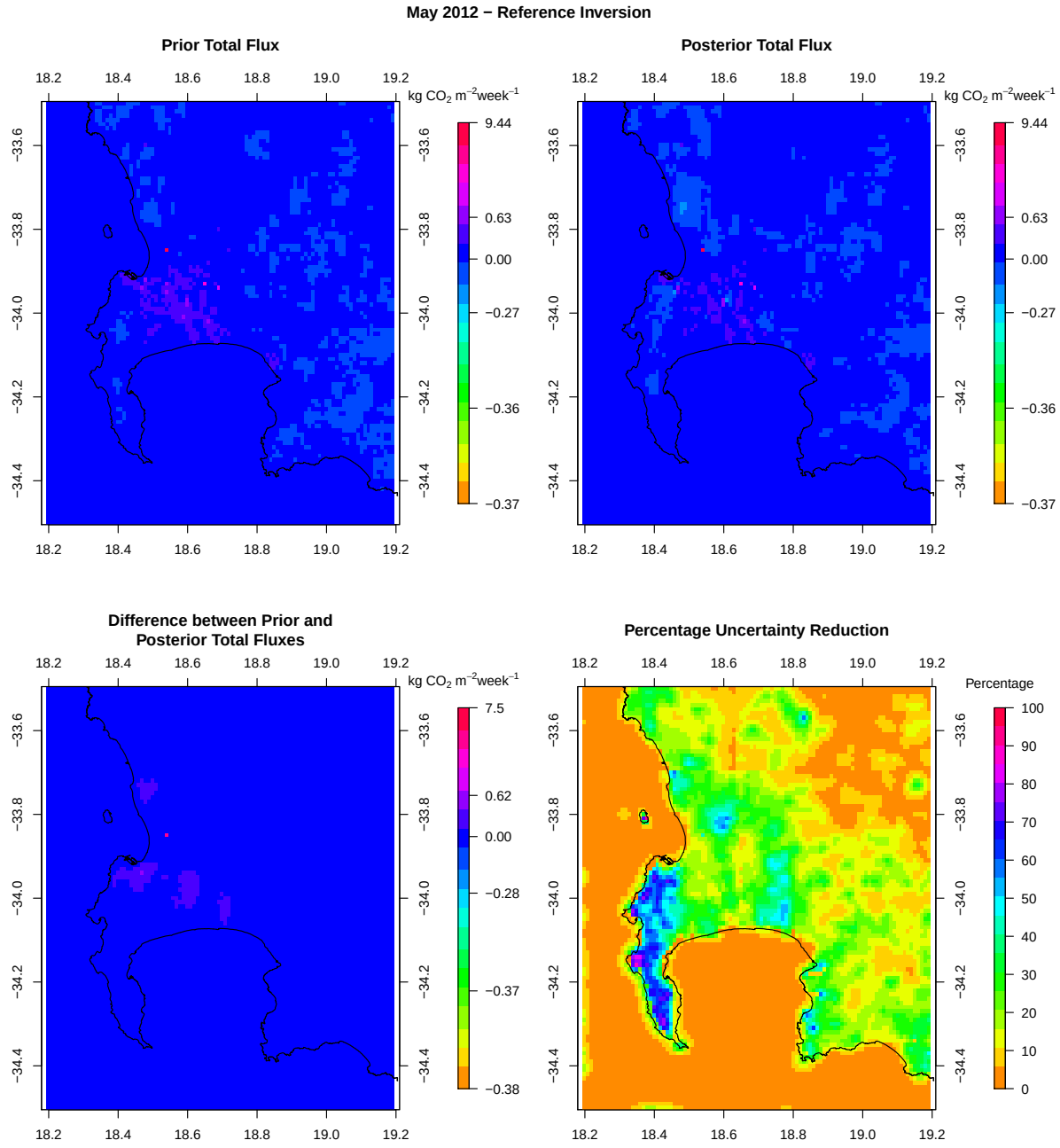


Figure C.42: Spatial distribution of the pixel-level prior and posterior $CO_2$ fluxes of the reference inversion, the difference between prior and posterior flux estimates, and the uncertainty reduction relative to the prior uncertainty for May 2012.

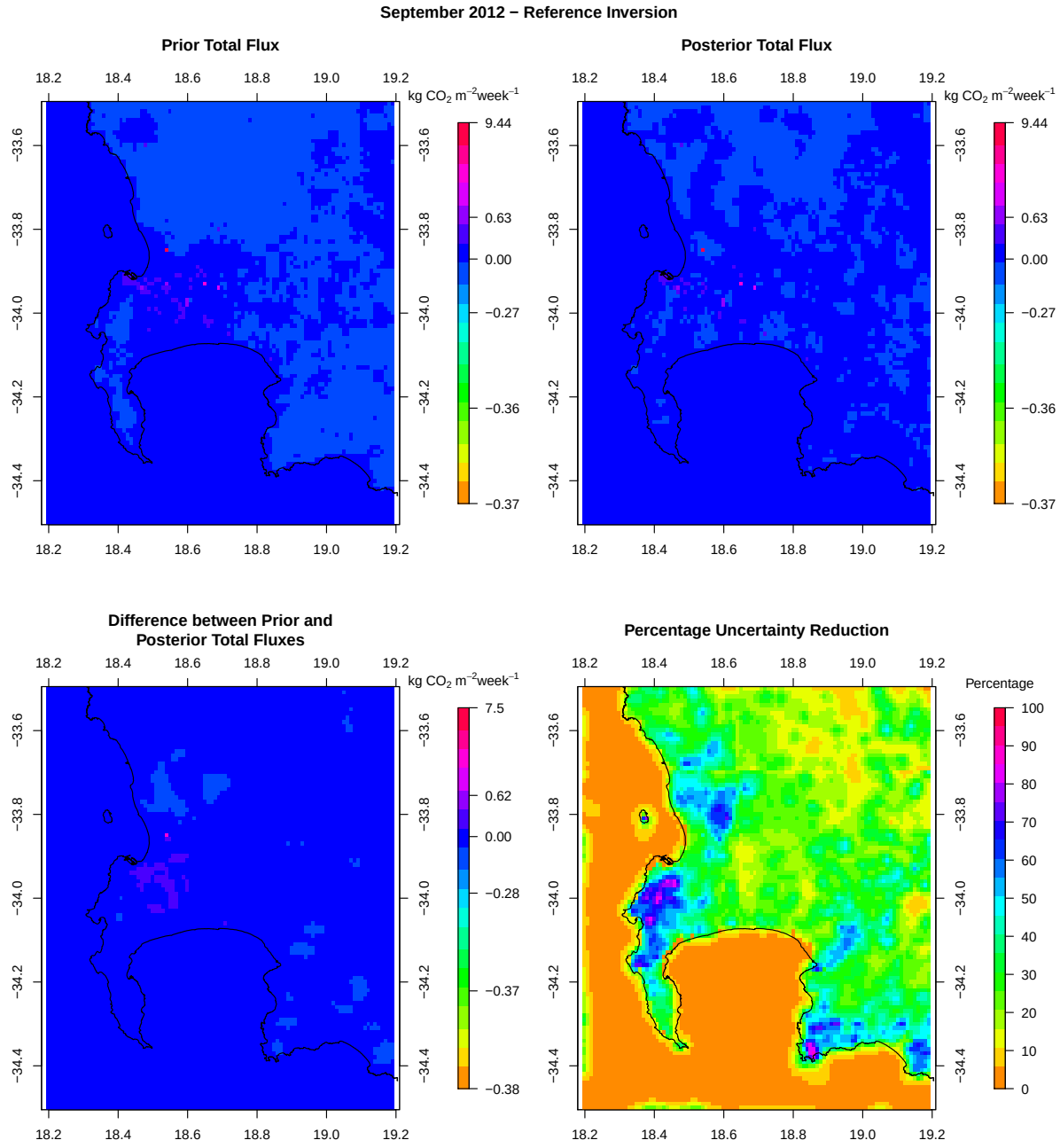


Figure C.43: Spatial distribution of the pixel-level prior and posterior $CO_2$ fluxes of the reference inversion, the difference between prior and posterior flux estimates, and the uncertainty reduction relative to the prior uncertainty for September 2012.

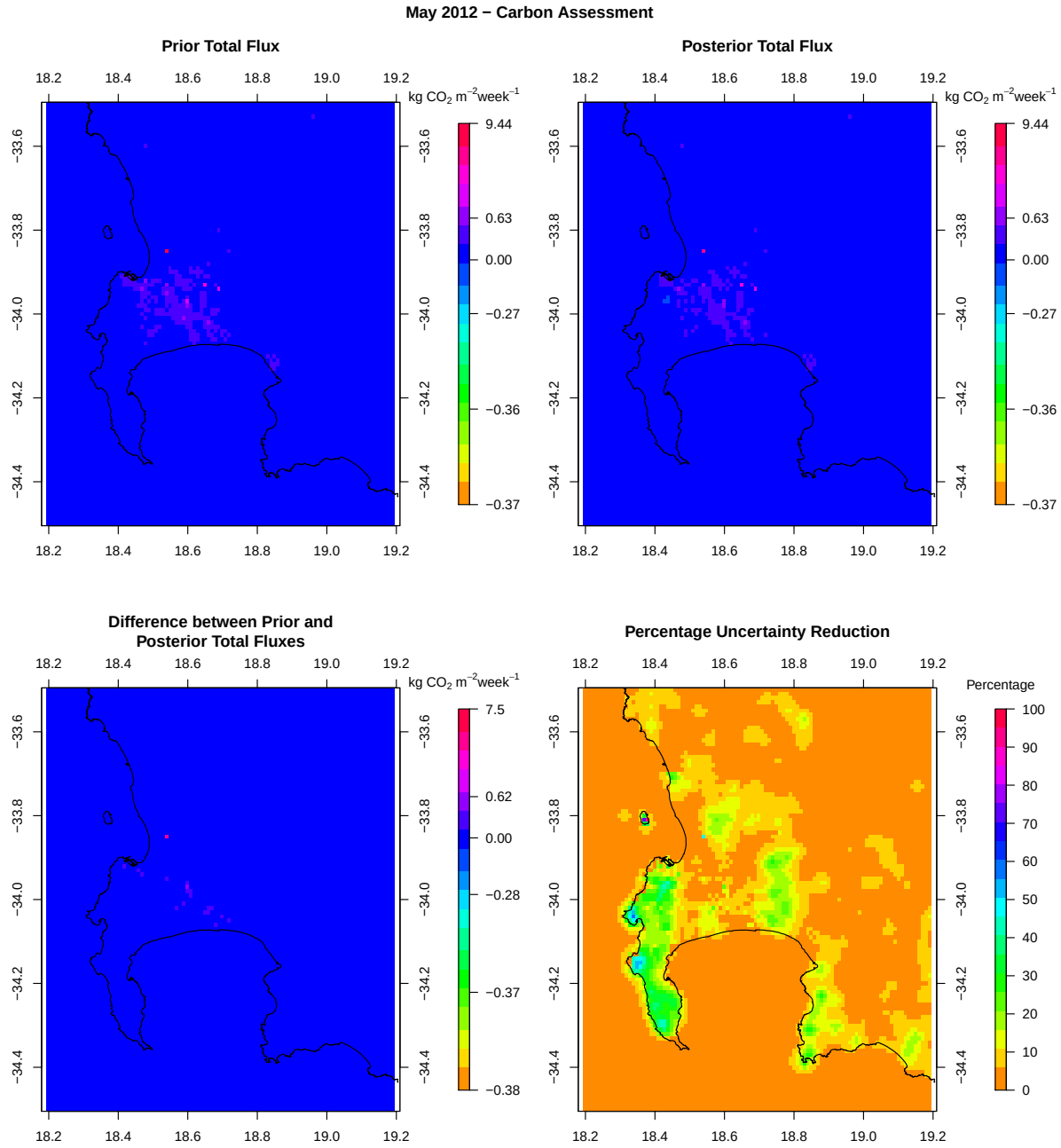


Figure C.44: Spatial distribution of the pixel-level prior and posterior $CO_2$ fluxes of the inversion using the carbon assessment product for the NEE prior flux estimates, the difference between prior and posterior flux estimates, and the uncertainty reduction relative to the prior uncertainty for May 2012.

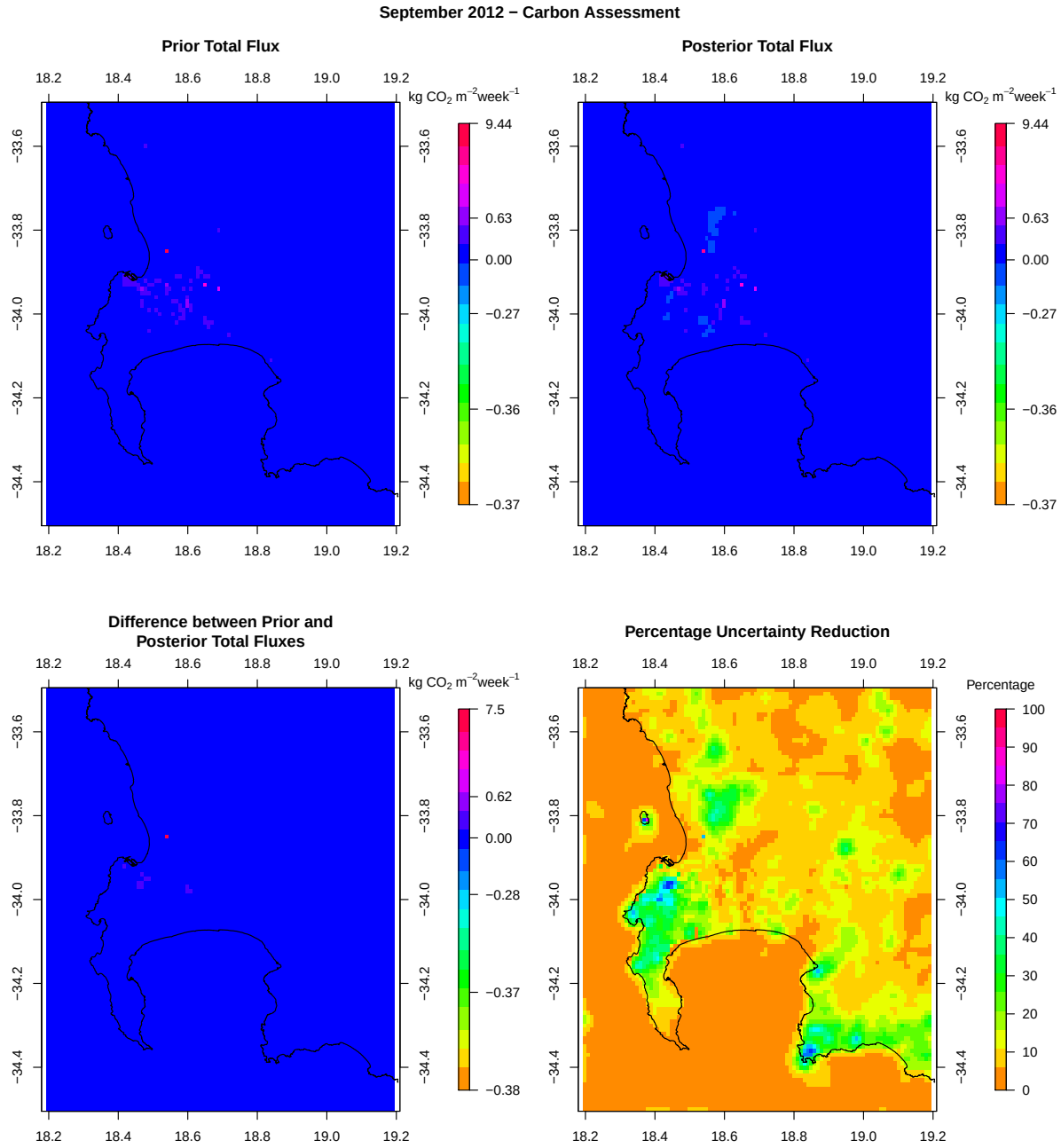


Figure C.45: Spatial distribution of the pixel-level prior and posterior $CO_2$ fluxes of the inversion using the carbon assessment product for the NEE prior flux estimates, the difference between prior and posterior flux estimates, and the uncertainty reduction relative to the prior uncertainty for September 2012.

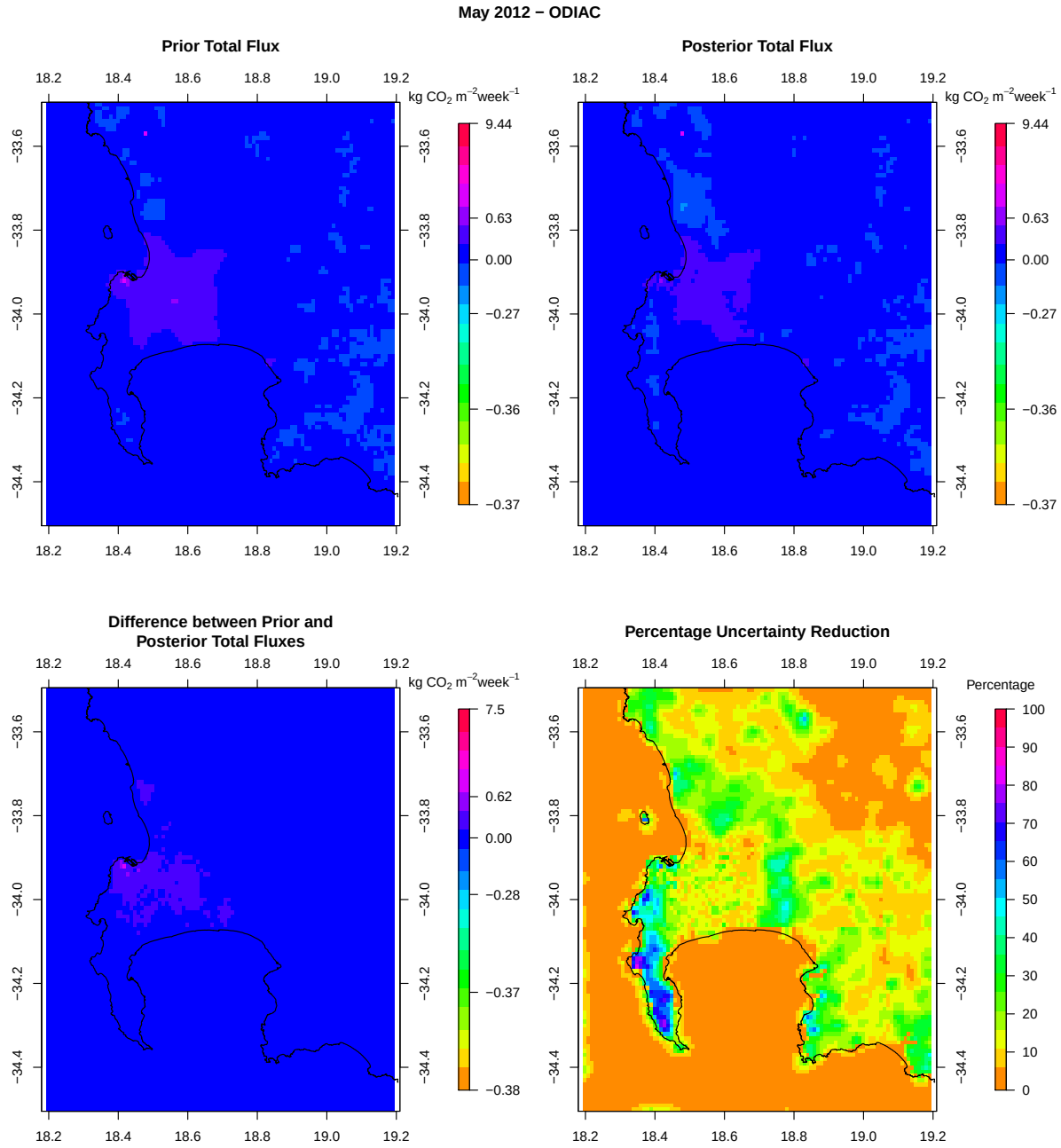


Figure C.46: Spatial distribution of the pixel-level prior and posterior $CO_2$ fluxes of the inversion using the ODIAC product for the fossil fuel flux prior estimates, the difference between prior and posterior flux estimates, and the uncertainty reduction relative to the prior uncertainty for May 2012.

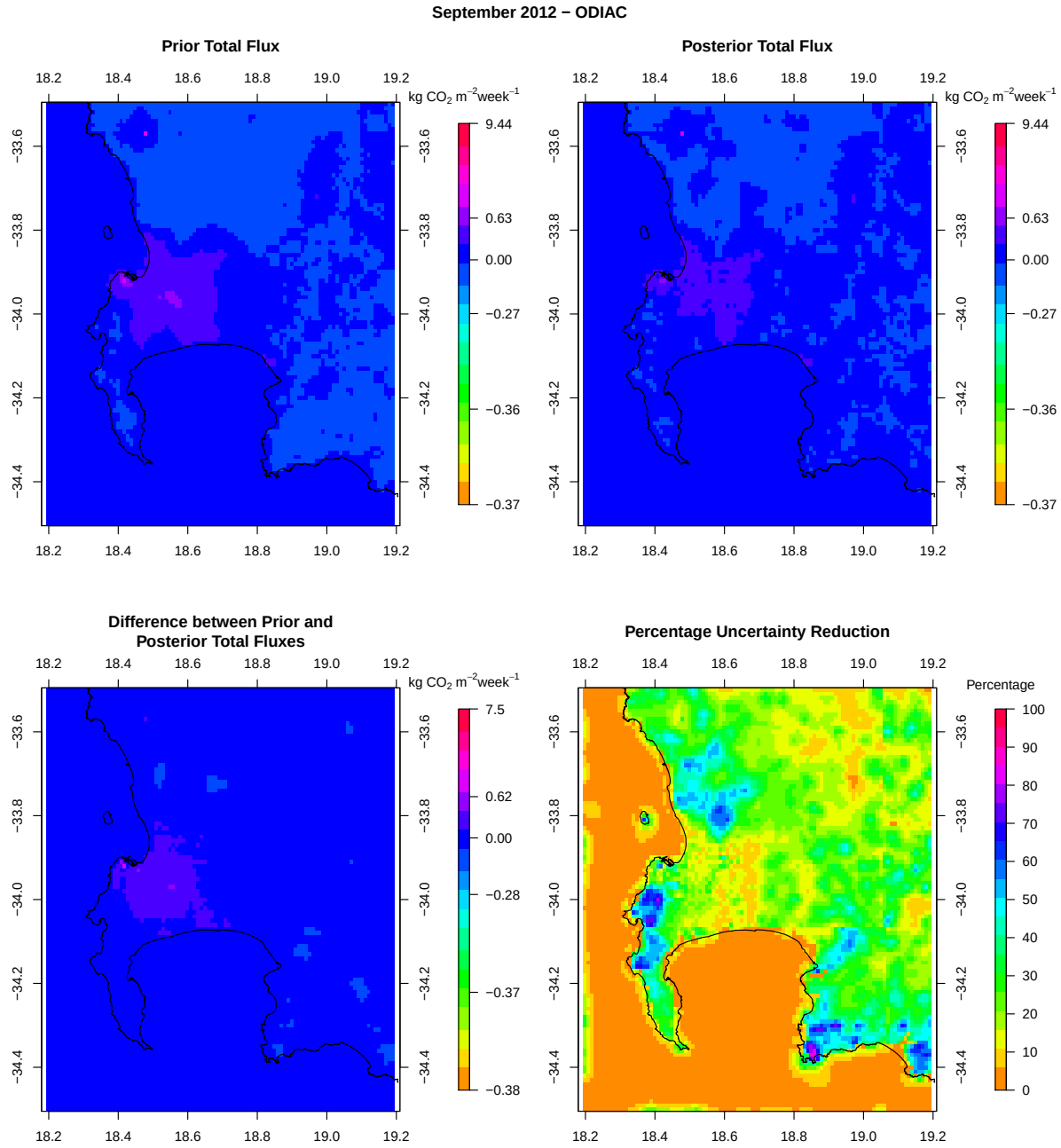


Figure C.47: Spatial distribution of the pixel-level prior and posterior $CO_2$ fluxes of the inversion using the ODIAC product for the fossil fuel flux prior estimates, the difference between prior and posterior flux estimates, and the uncertainty reduction relative to the prior uncertainty for September 2012.

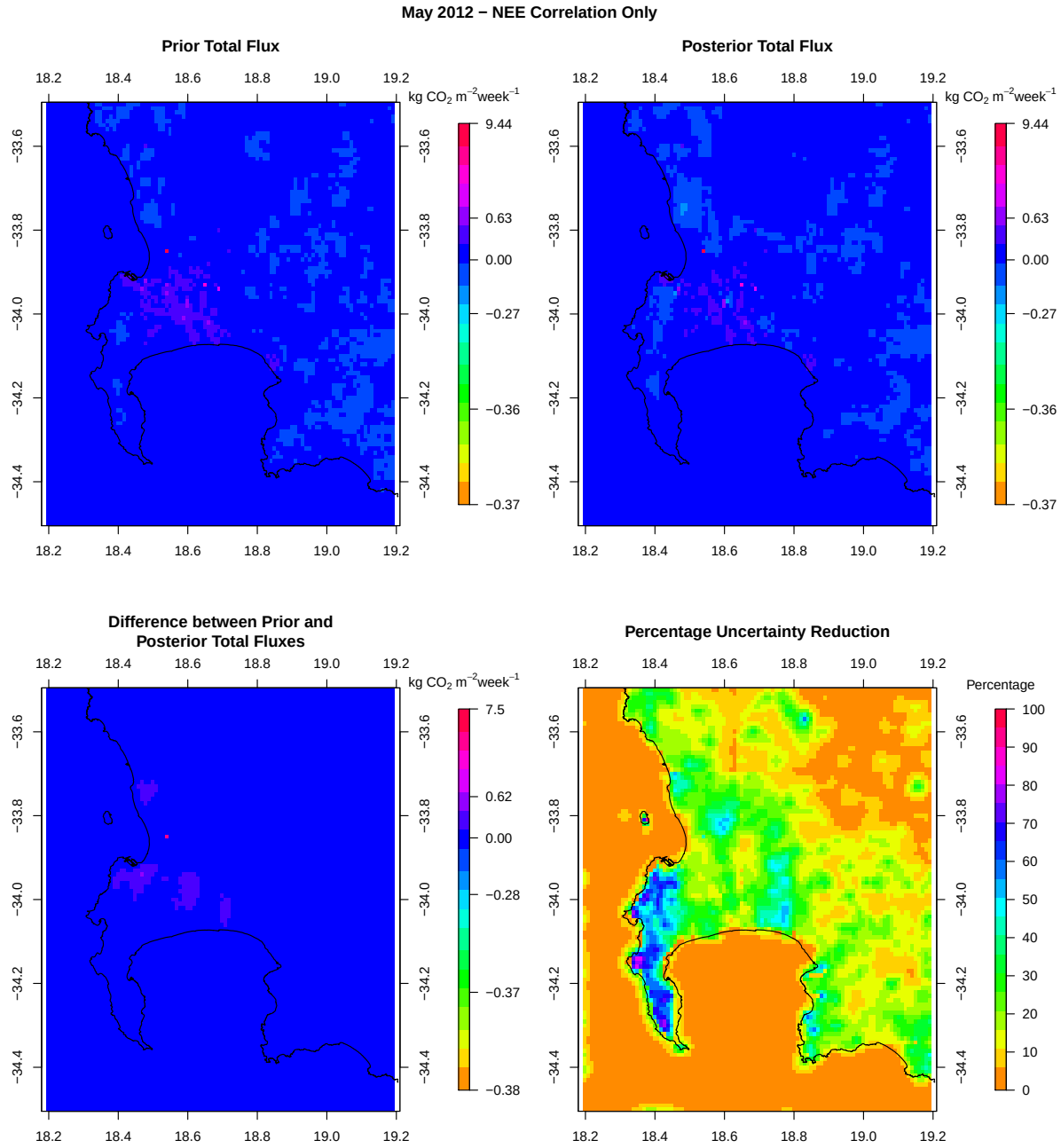


Figure C.48: Spatial distribution of the pixel-level prior and posterior $CO_2$ fluxes of the inversion accounting for only correlation between the NEE flux uncertainties, the difference between prior and posterior flux estimates, and the uncertainty reduction relative to the prior uncertainty for May 2012.

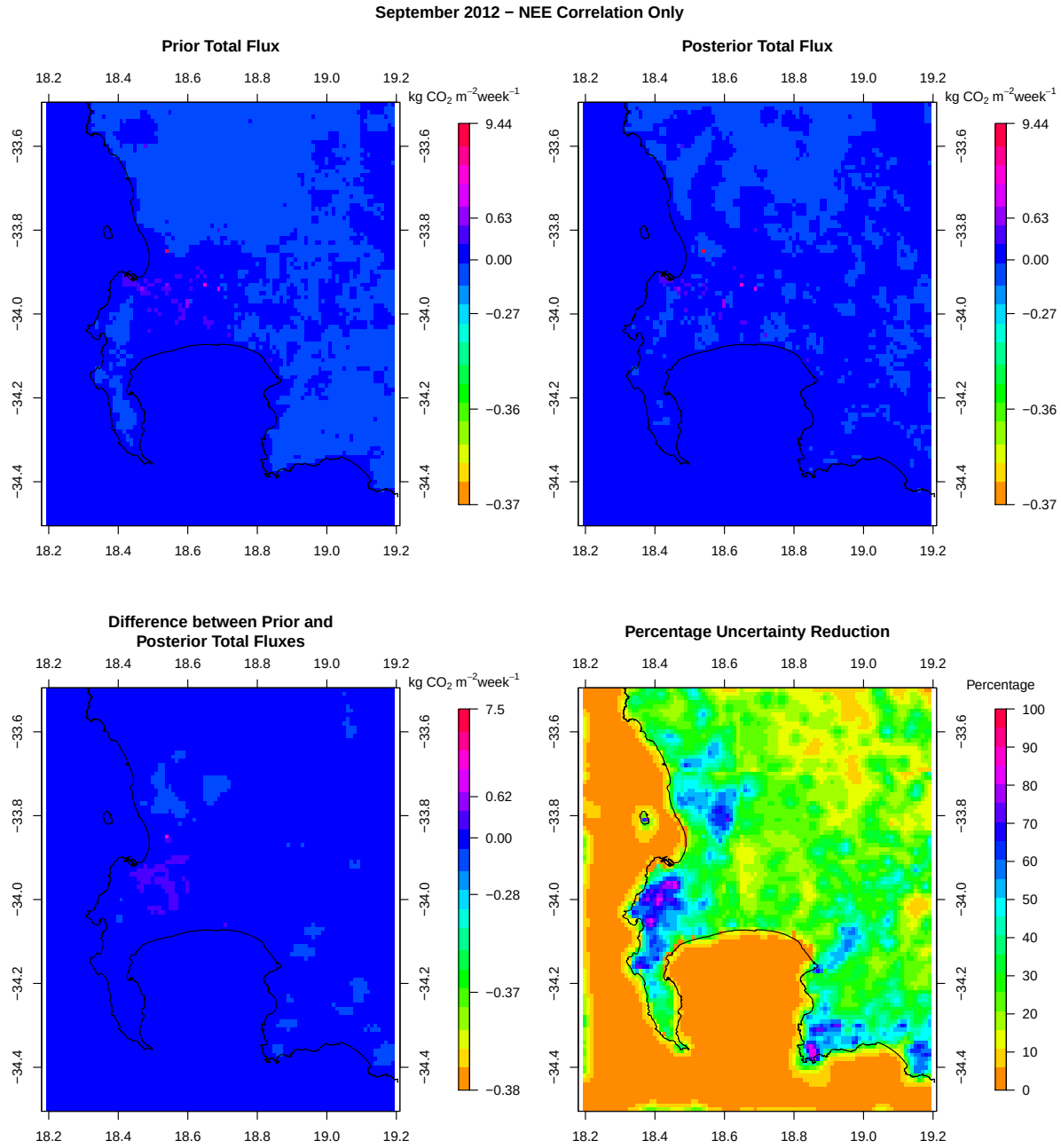


Figure C.49: Spatial distribution of the pixel-level prior and posterior $CO_2$ fluxes of the inversion accounting for only correlation between the NEE flux uncertainties, the difference between prior and posterior flux estimates, and the uncertainty reduction relative to the prior uncertainty for September 2012.

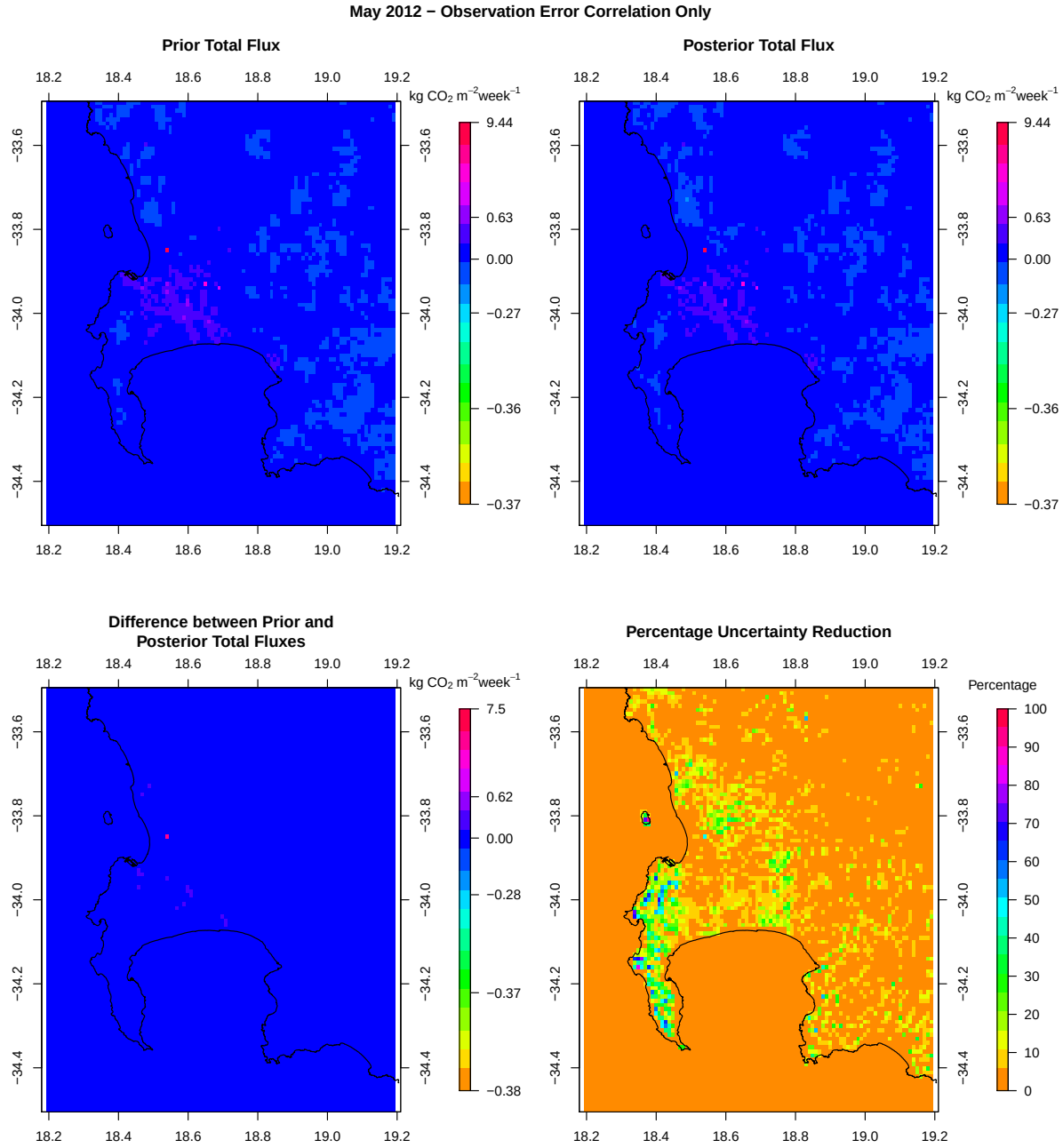


Figure C.50: Spatial distribution of the pixel-level prior and posterior $CO_2$ fluxes of the inversion accounting for only correlation between the observation errors with no correlation specified between the NEE flux uncertainties, the difference between prior and posterior flux estimates, and the uncertainty reduction relative to the prior uncertainty for May 2012.

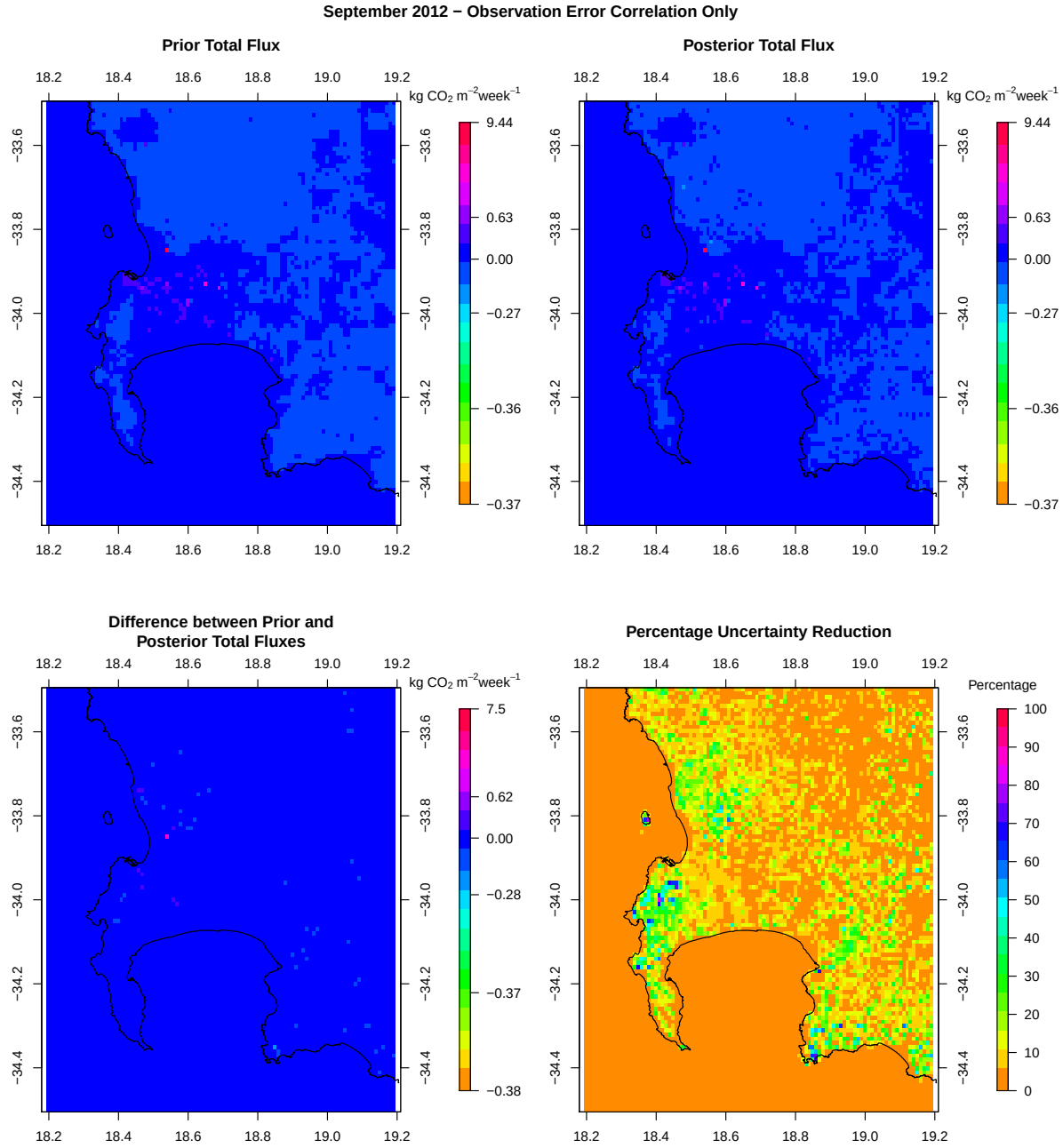


Figure C.51: Spatial distribution of the pixel-level prior and posterior $CO_2$ fluxes of the inversion accounting for only correlation between the observation errors with no correlation specified between the NEE flux uncertainties, the difference between prior and posterior flux estimates, and the uncertainty reduction relative to the prior uncertainty for September 2012.

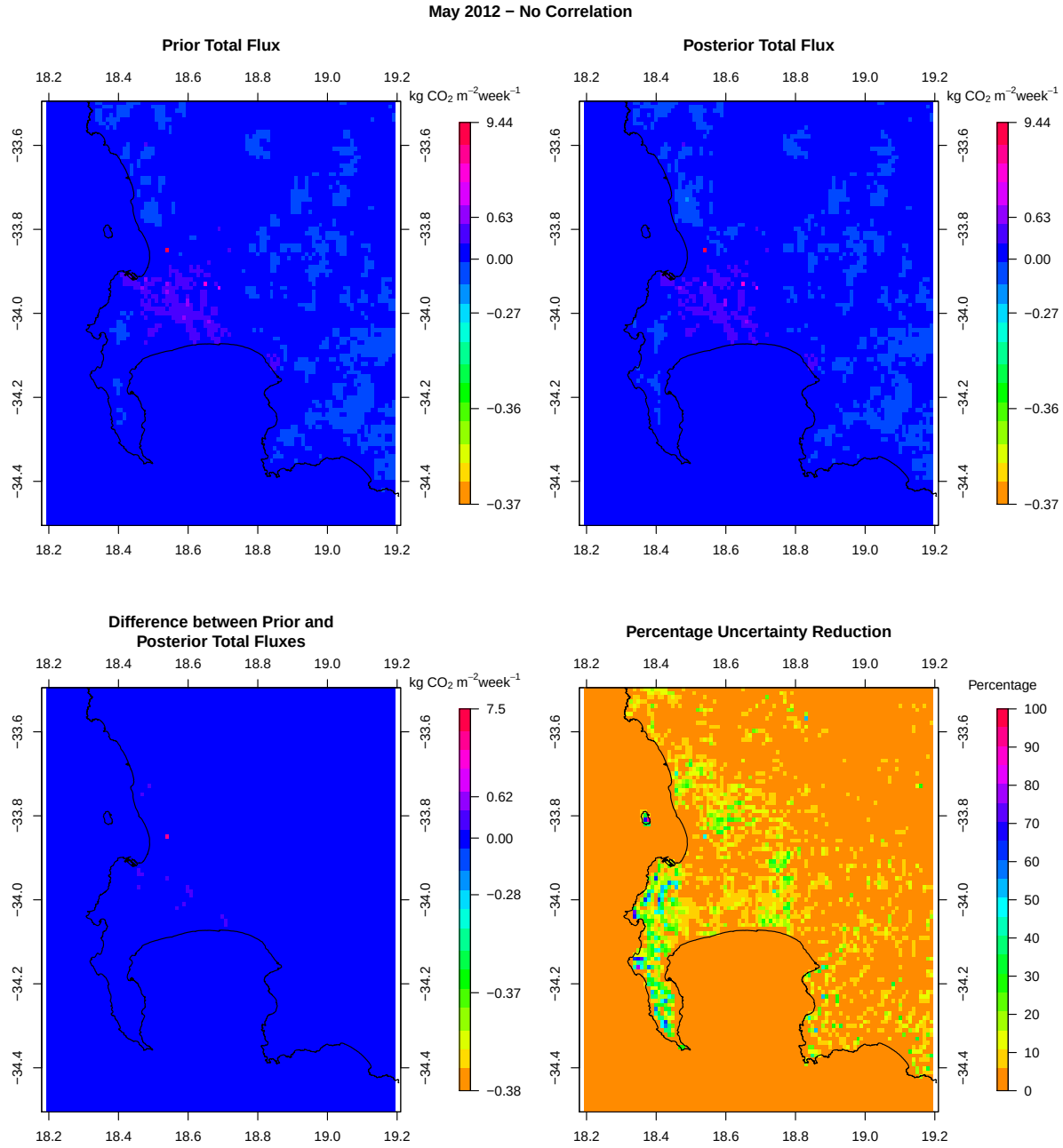


Figure C.52: Spatial distribution of the pixel-level prior and posterior $CO_2$ fluxes of the inversion specifying no correlation between the observation errors and no correlation between the NEE flux uncertainties, the difference between prior and posterior flux estimates, and the uncertainty reduction relative to the prior uncertainty for May 2012.

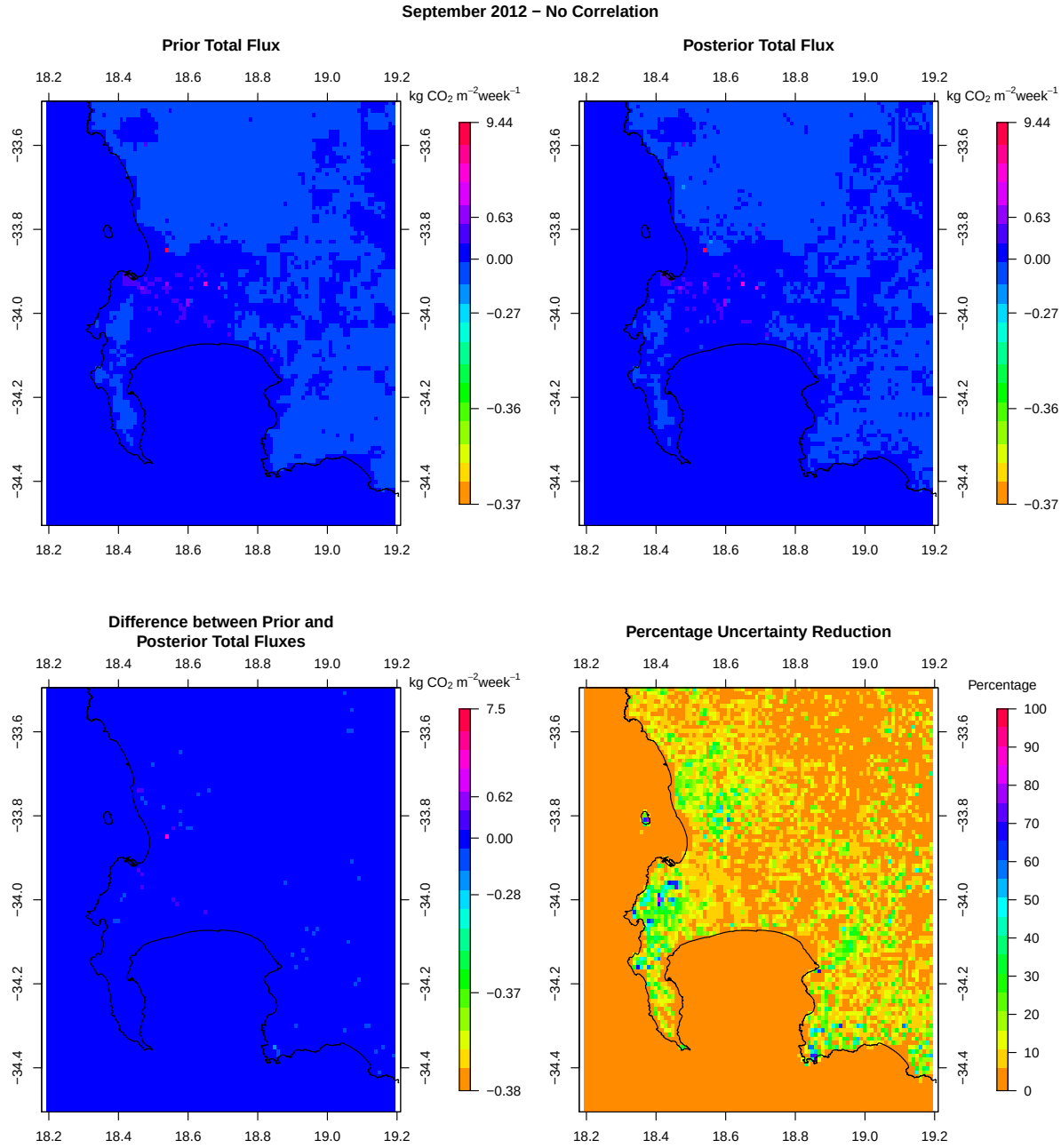


Figure C.53: Spatial distribution of the pixel-level prior and posterior $CO_2$ fluxes of the inversion specifying no correlation between the observation errors and no correlation between the NEE flux uncertainties, the difference between prior and posterior flux estimates, and the uncertainty reduction relative to the prior uncertainty for September 2012.

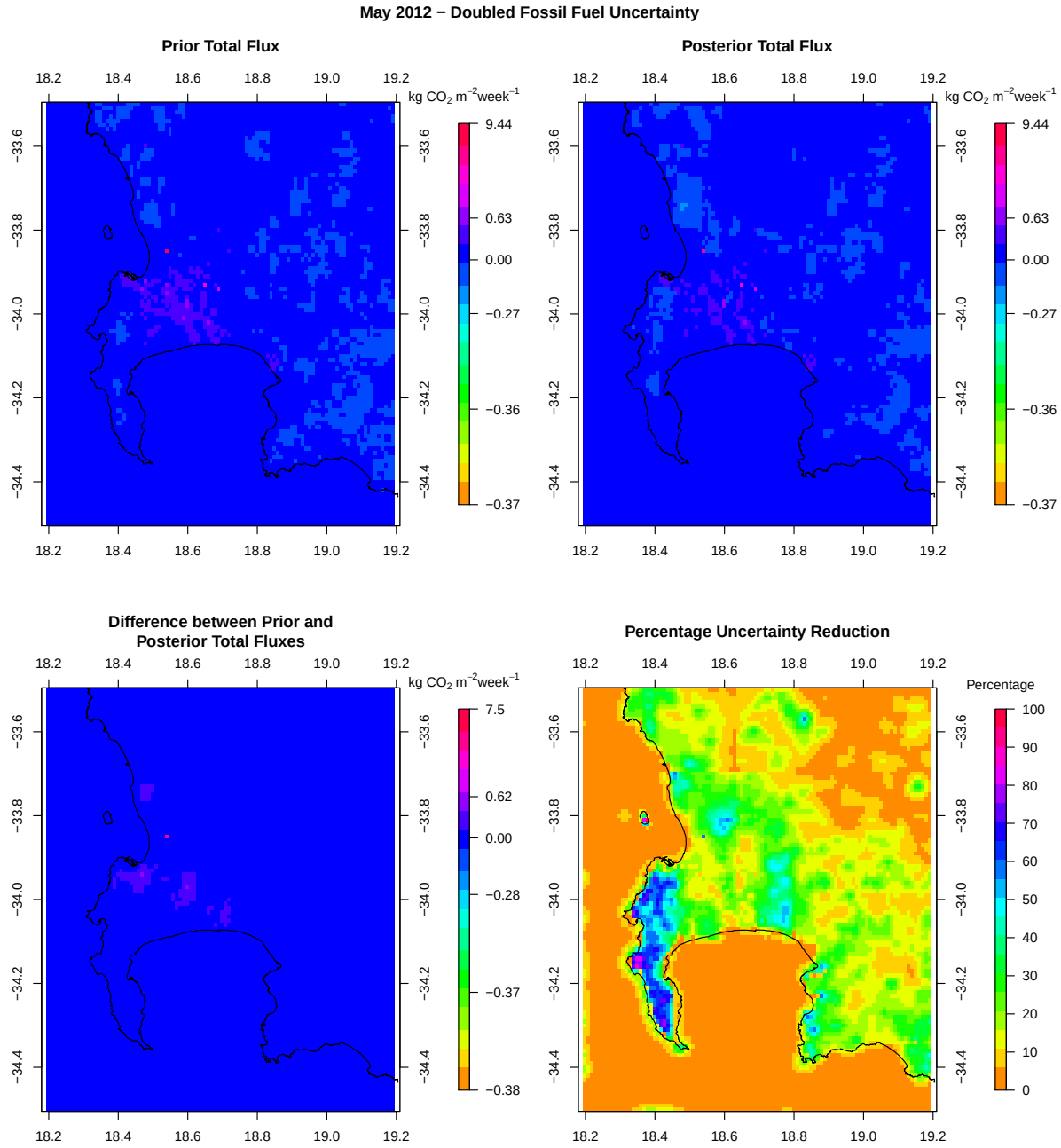


Figure C.54: Spatial distribution of the pixel-level prior and posterior $CO_2$ fluxes of the inversion with doubled fossil fuel flux uncertainties, the difference between prior and posterior flux estimates, and the uncertainty reduction relative to the prior uncertainty for May 2012.

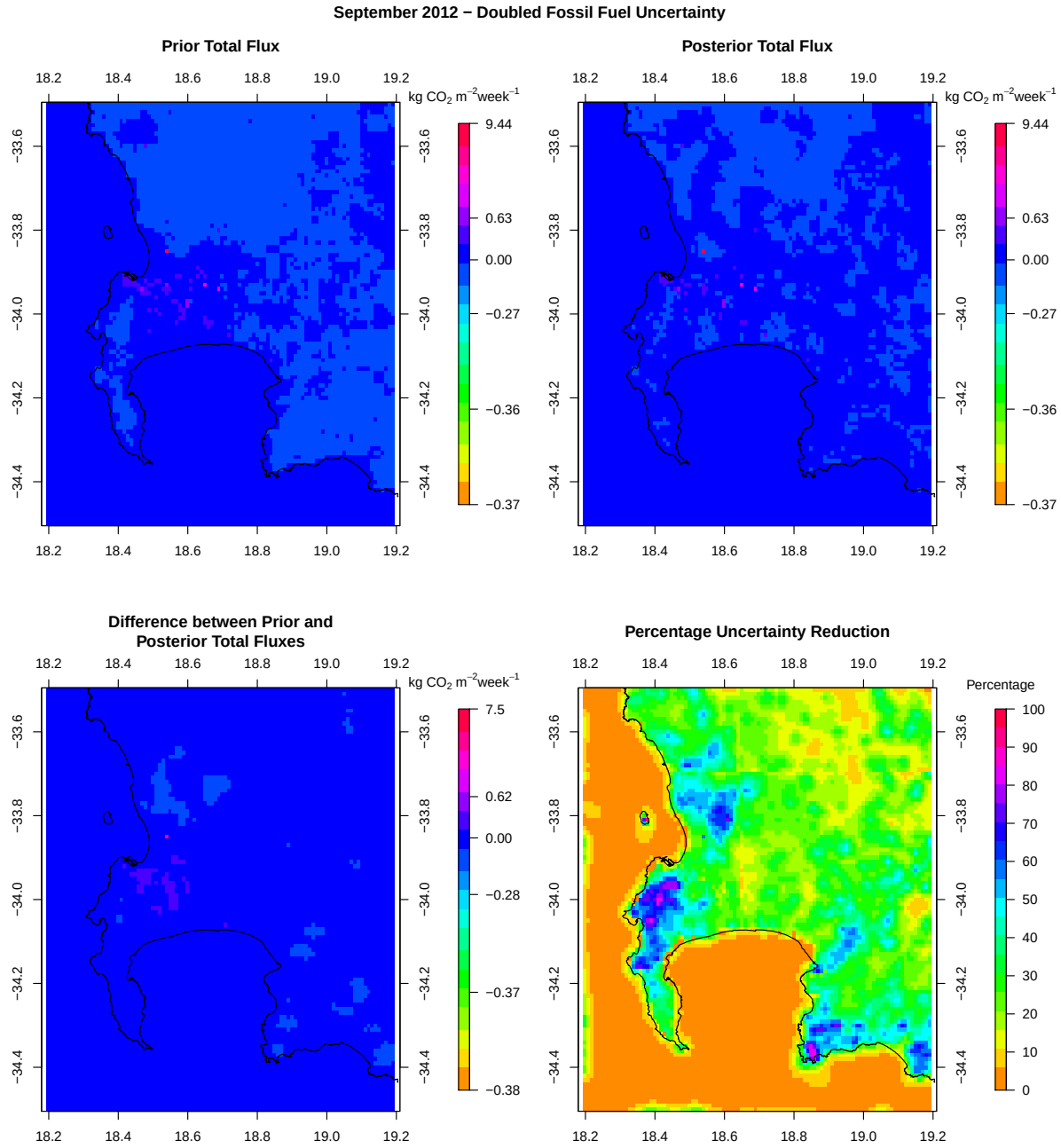


Figure C.55: Spatial distribution of the pixel-level prior and posterior $CO_2$ fluxes of the inversion with doubled fossil fuel flux uncertainties, the difference between prior and posterior flux estimates, and the uncertainty reduction relative to the prior uncertainty for September 2012.

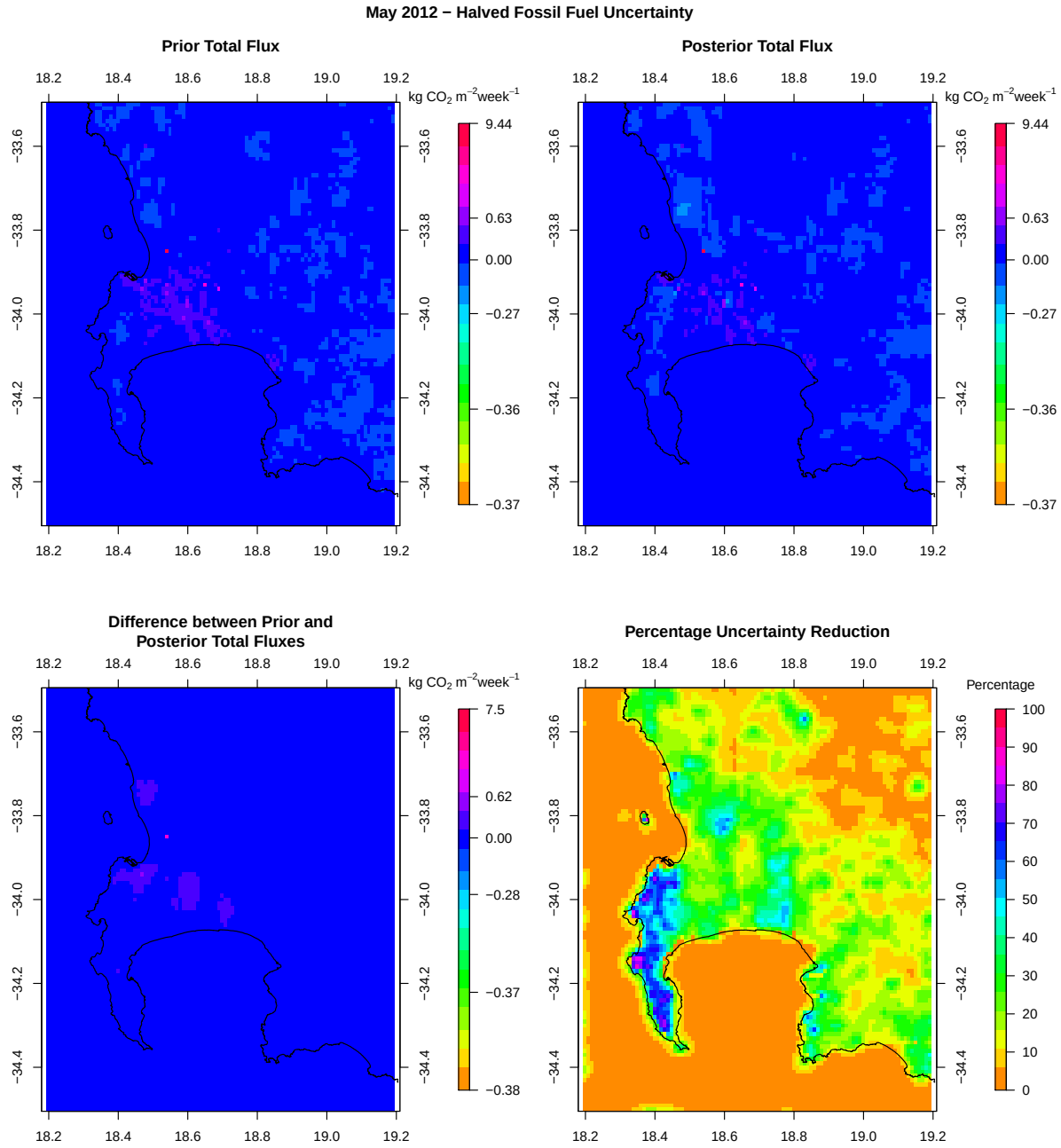


Figure C.56: Spatial distribution of the pixel-level prior and posterior $CO_2$ fluxes of the inversion with halved fossil fuel flux uncertainties, the difference between prior and posterior flux estimates, and the uncertainty reduction relative to the prior uncertainty for May 2012.

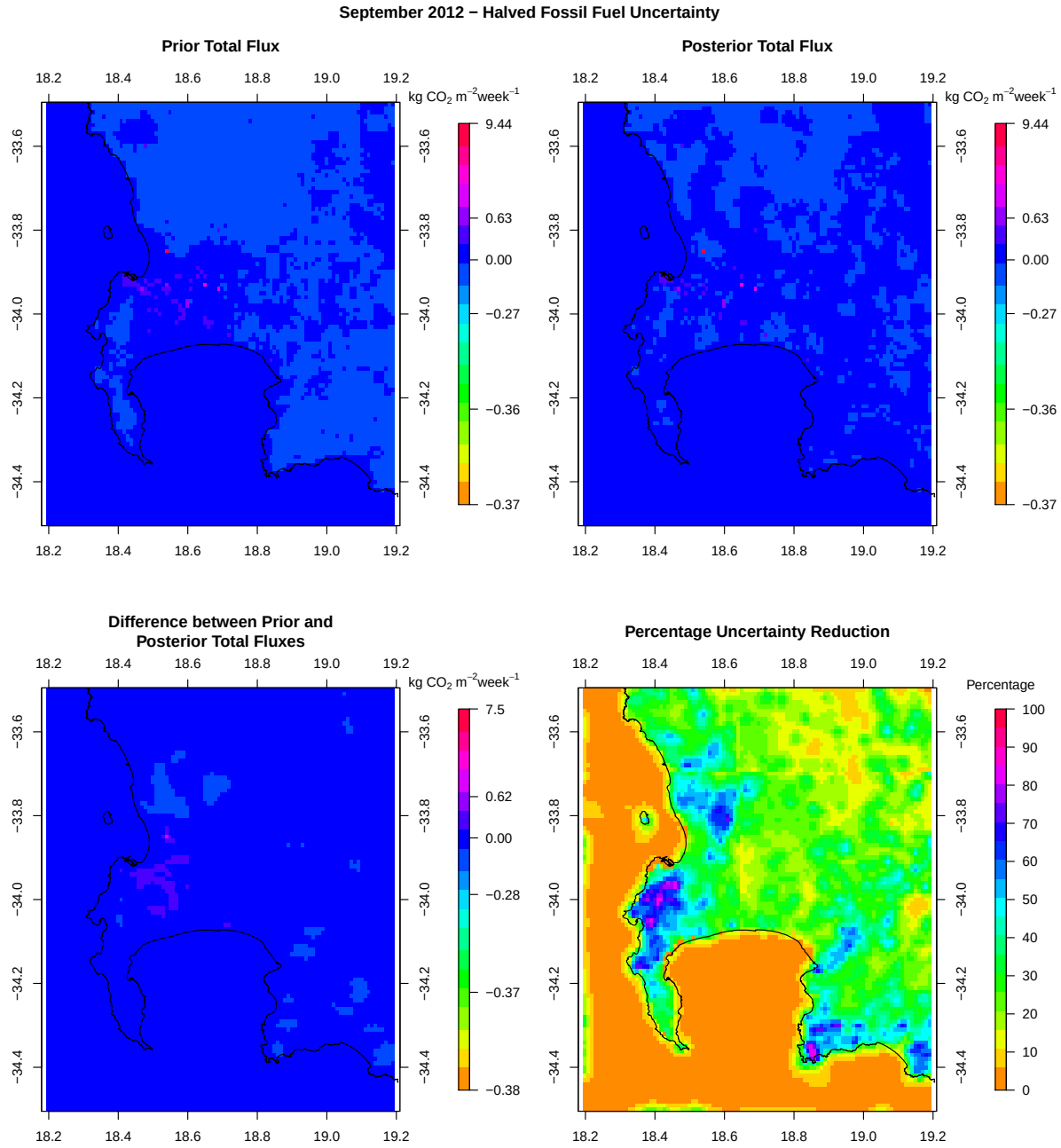


Figure C.57: Spatial distribution of the pixel-level prior and posterior $CO_2$ fluxes of the inversion with halved fossil fuel flux uncertainties, the difference between prior and posterior flux estimates, and the uncertainty reduction relative to the prior uncertainty for September 2012.

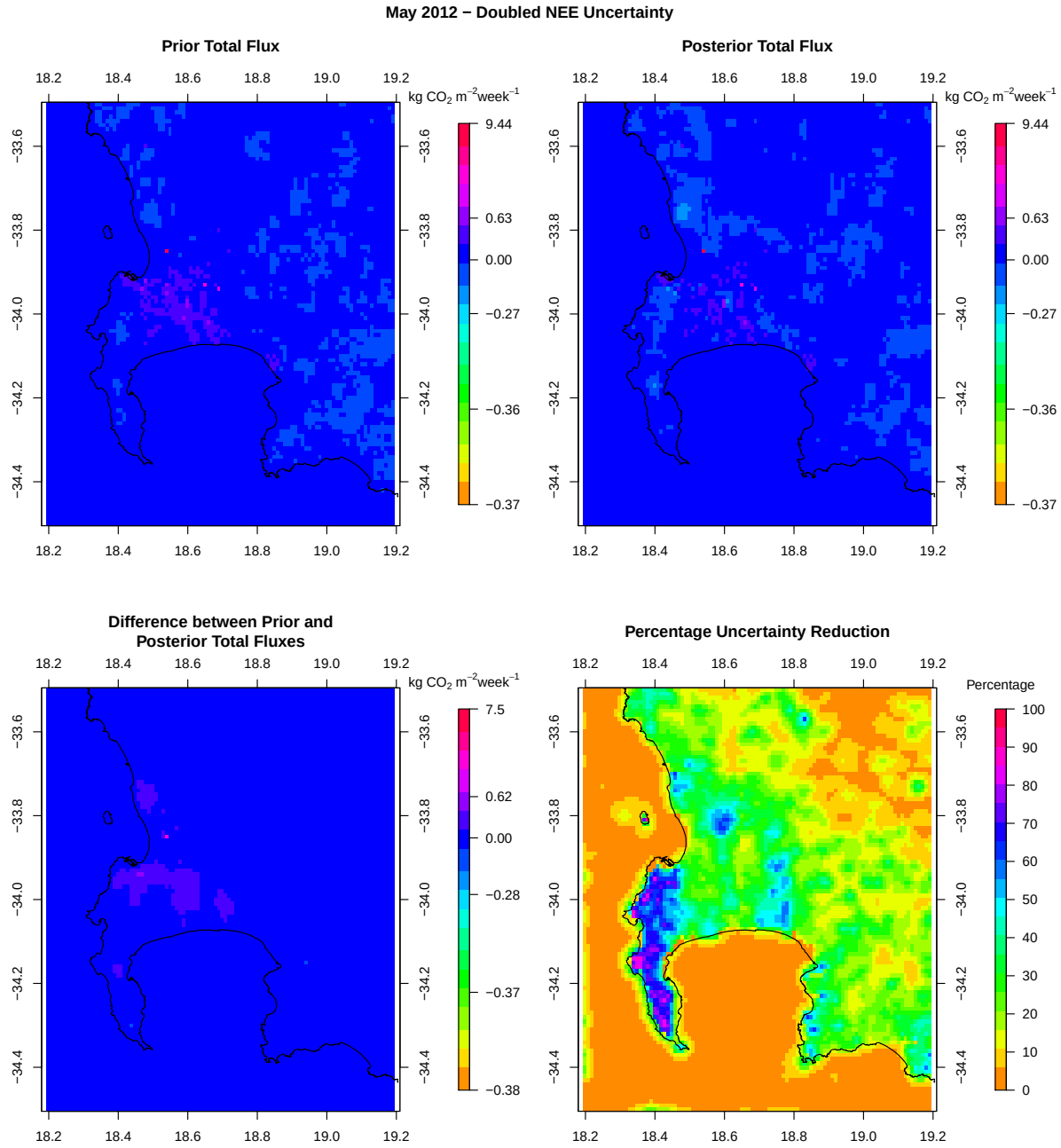


Figure C.58: Spatial distribution of the pixel-level prior and posterior $CO_2$ fluxes of the inversion with doubled NEE flux uncertainties, the difference between prior and posterior flux estimates, and the uncertainty reduction relative to the prior uncertainty for May 2012.

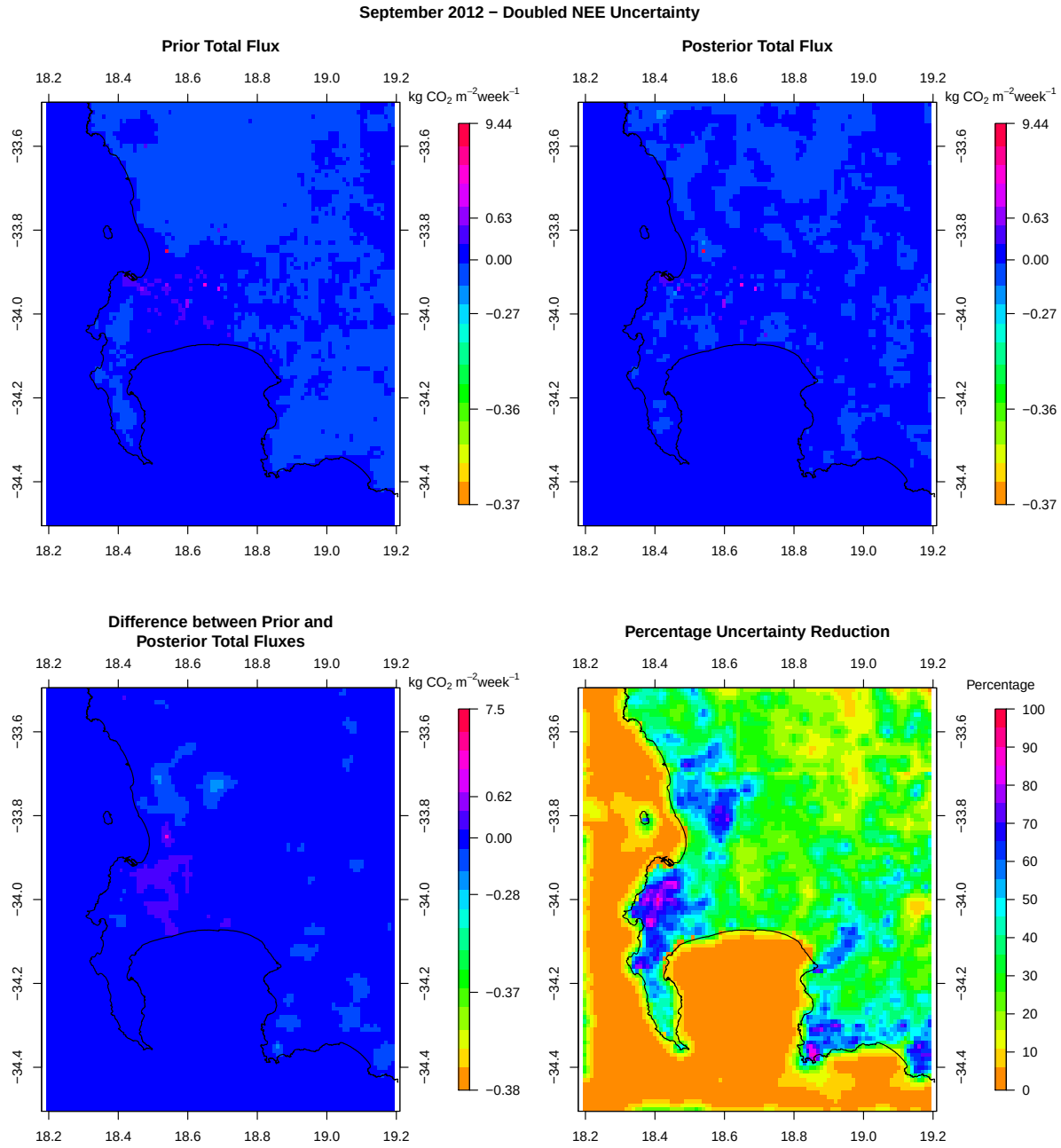


Figure C.59: Spatial distribution of the pixel-level prior and posterior $CO_2$ fluxes of the inversion with doubled NEE flux uncertainties, the difference between prior and posterior flux estimates, and the uncertainty reduction relative to the prior uncertainty for September 2012.

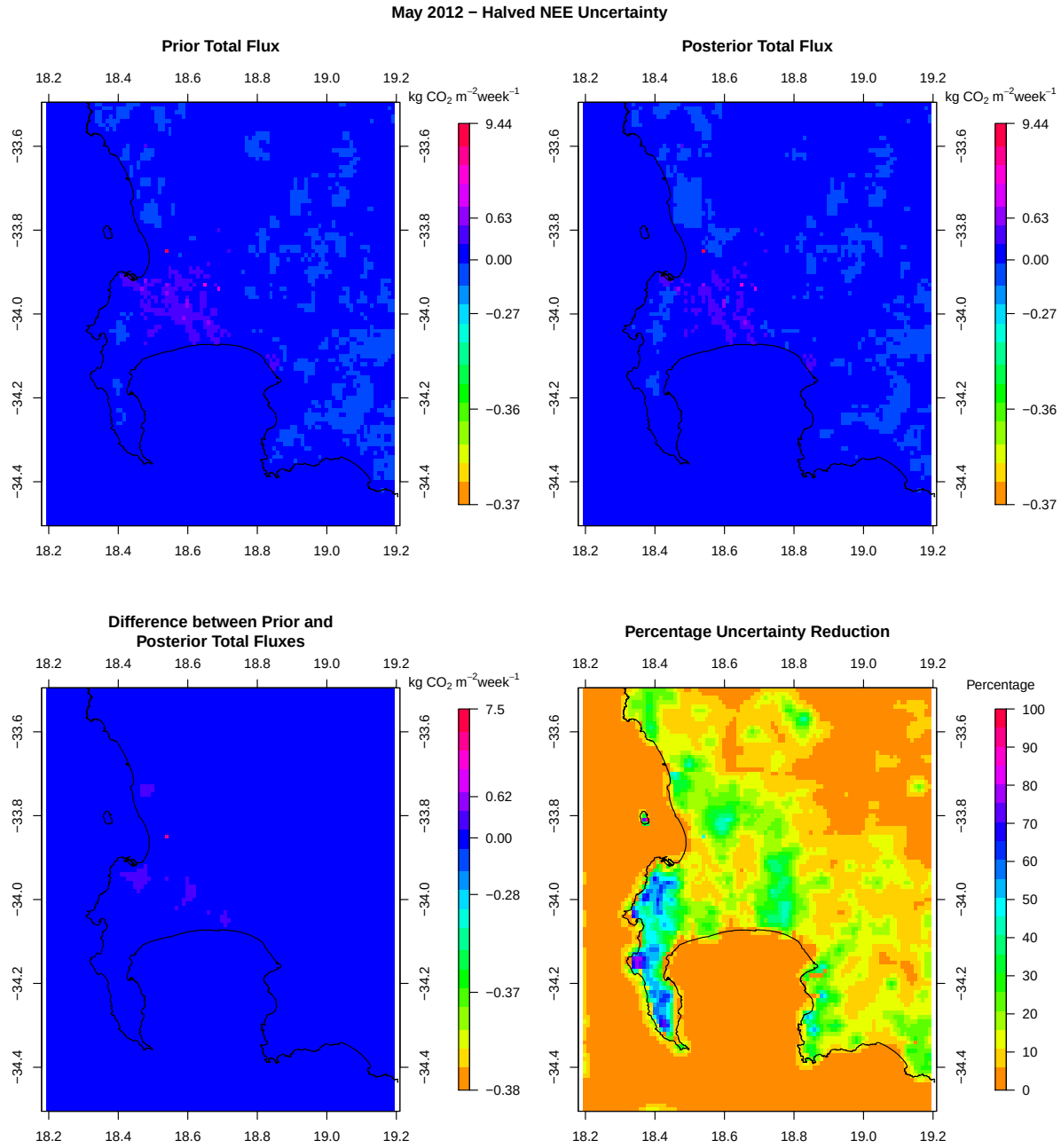


Figure C.60: Spatial distribution of the pixel-level prior and posterior $CO_2$ fluxes of the inversion with halved NEE flux uncertainties, the difference between prior and posterior flux estimates, and the uncertainty reduction relative to the prior uncertainty for May 2012.

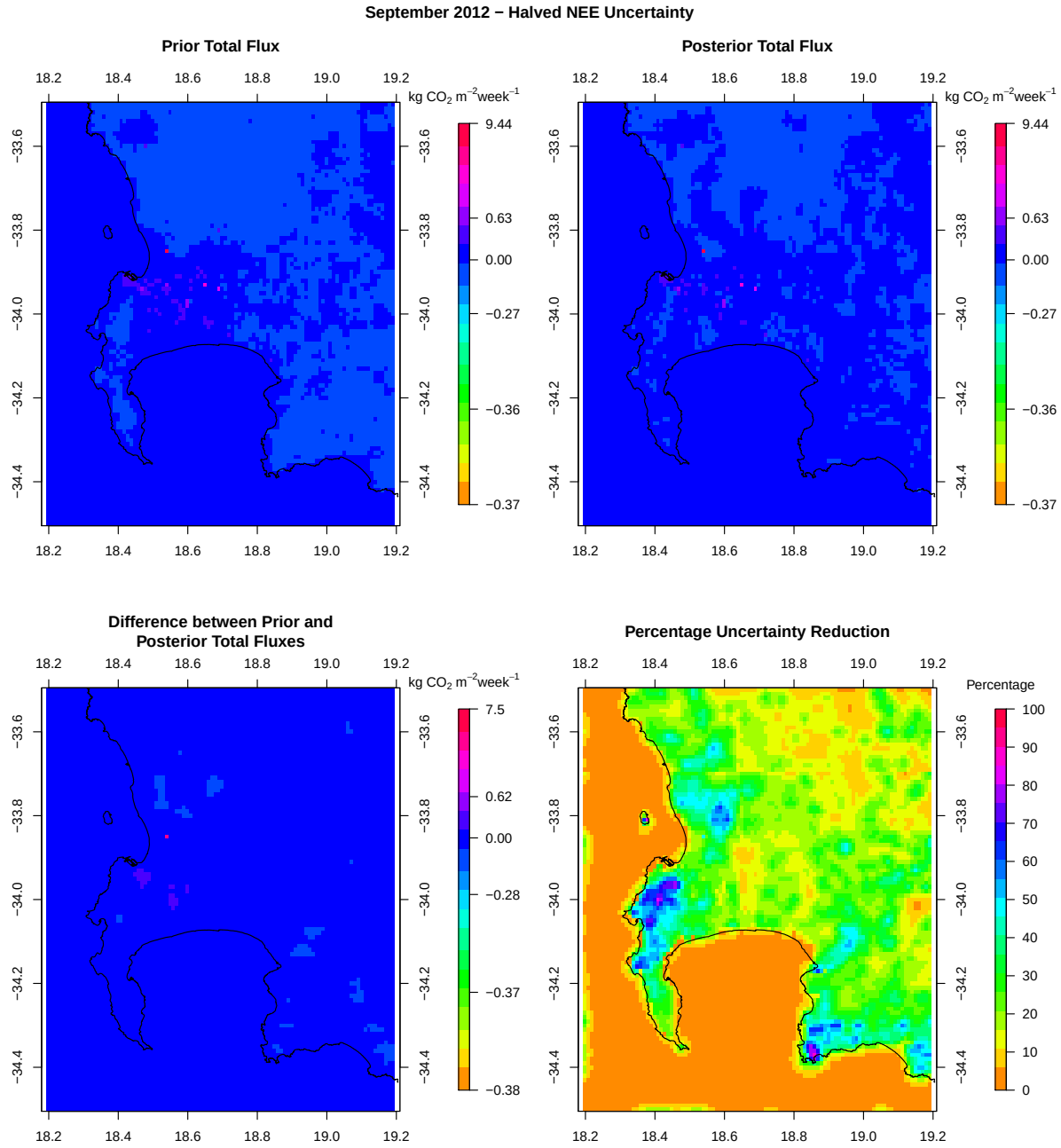


Figure C.61: Spatial distribution of the pixel-level prior and posterior $CO_2$ fluxes of the inversion with halved NEE flux uncertainties, the difference between prior and posterior flux estimates, and the uncertainty reduction relative to the prior uncertainty for September 2012.

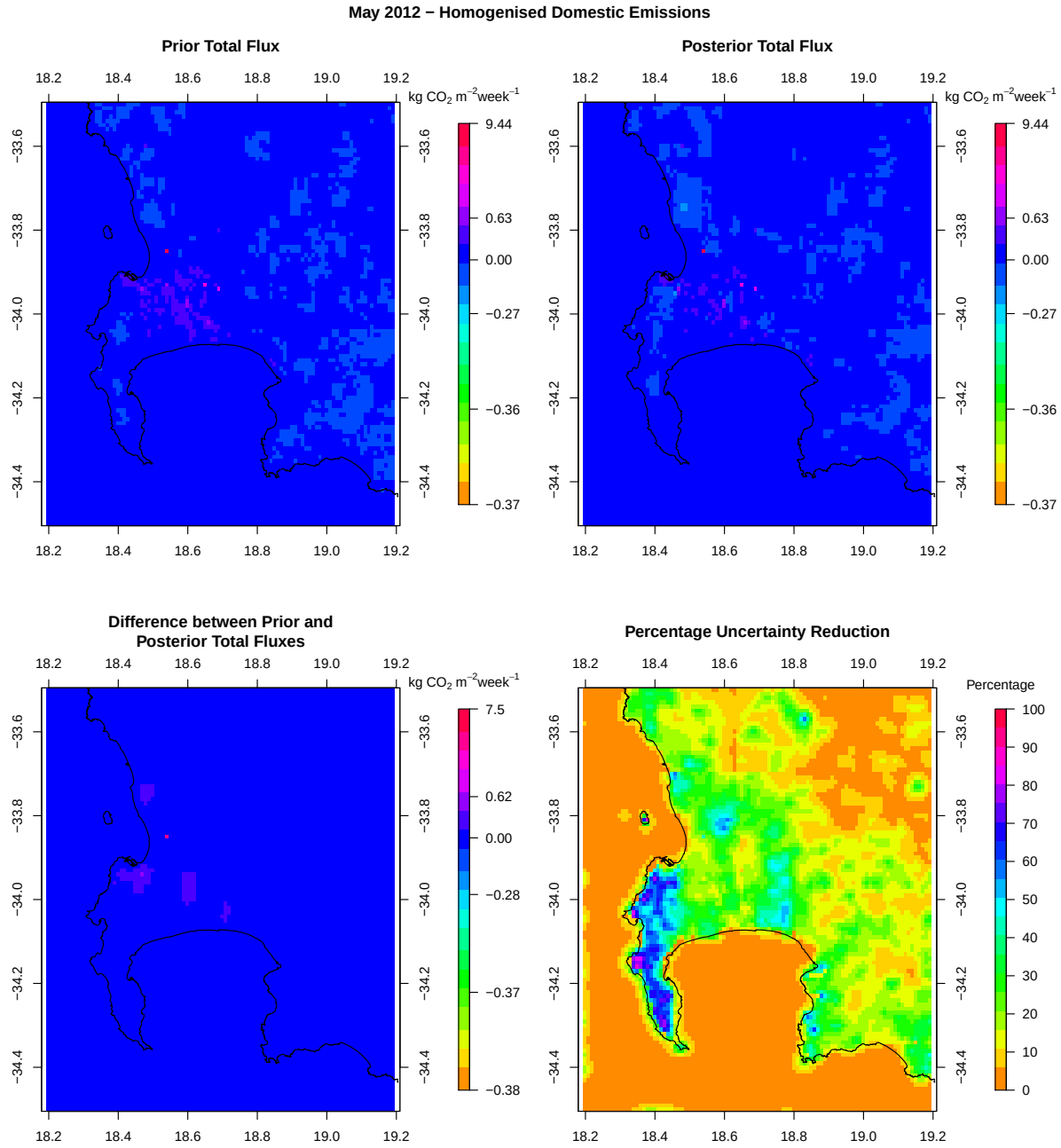


Figure C.62: Spatial distribution of the pixel-level prior and posterior $CO_2$ fluxes of the inversion with temporally homogenised domestic fossil fuel prior fluxes, the difference between prior and posterior flux estimates, and the uncertainty reduction relative to the prior uncertainty for May 2012.

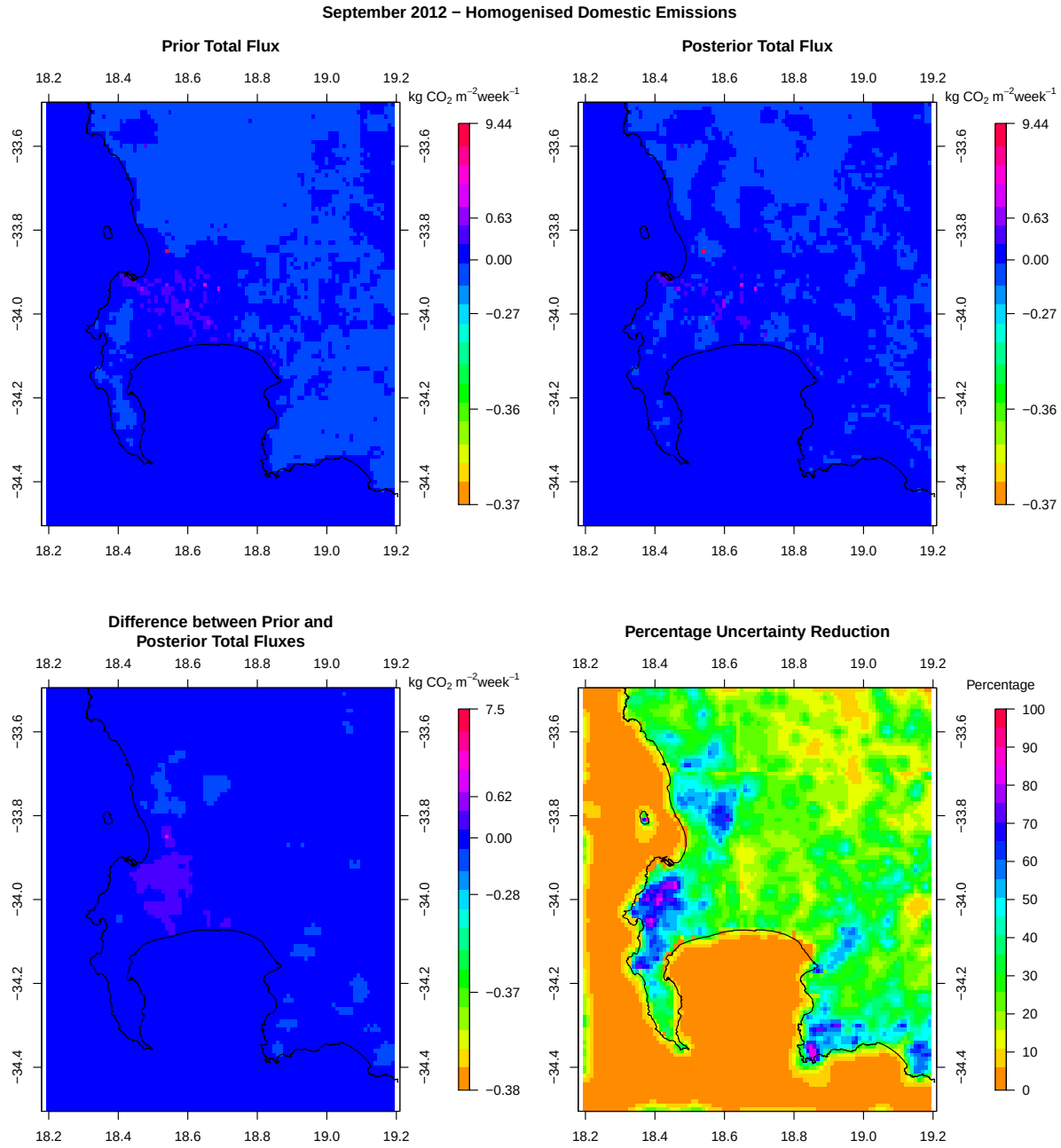


Figure C.63: Spatial distribution of the pixel-level prior and posterior $CO_2$ fluxes of the inversion with temporally homogenised domestic fossil fuel prior fluxes, the difference between prior and posterior flux estimates, and the uncertainty reduction relative to the prior uncertainty for September 2012.

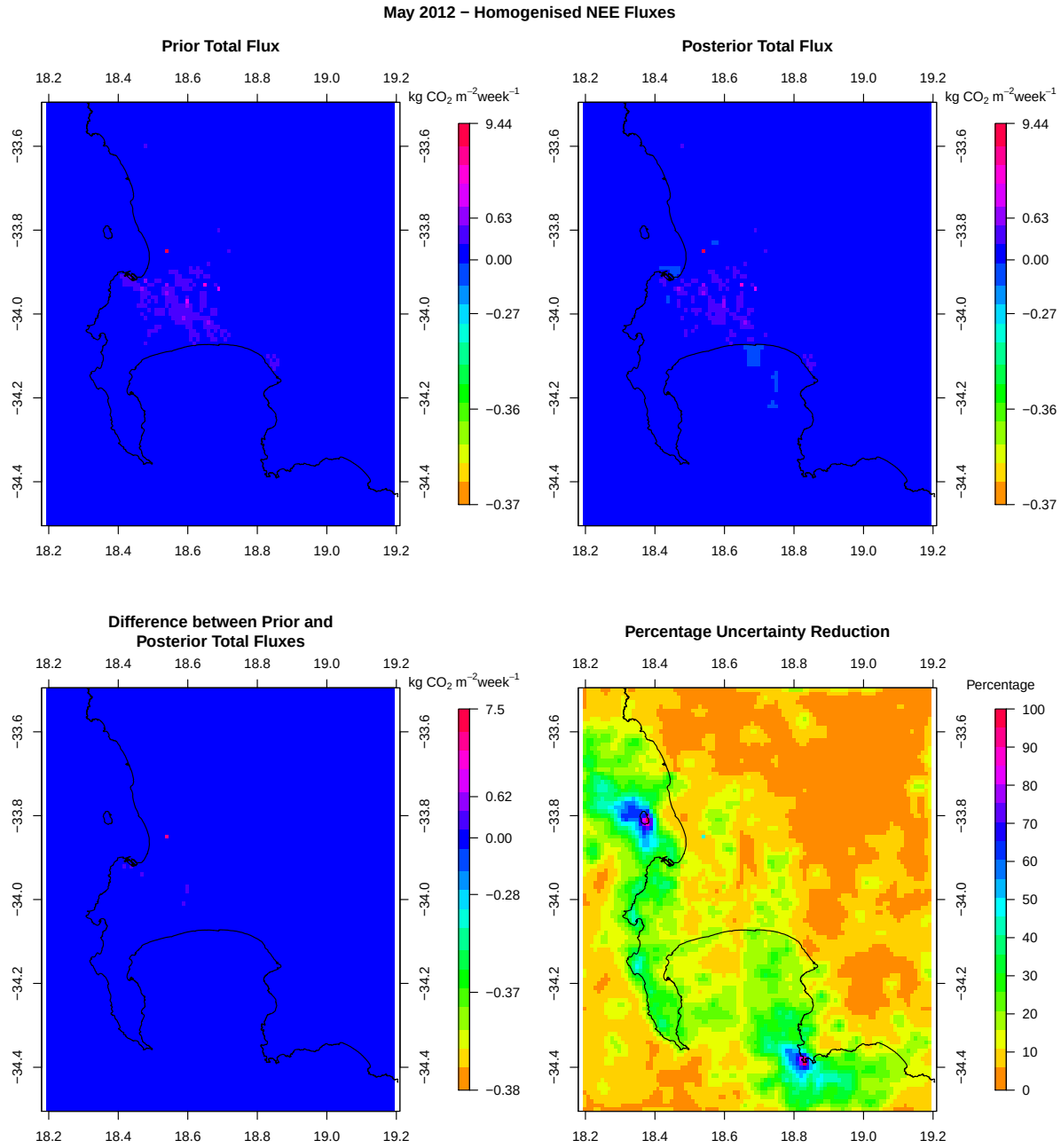


Figure C.64: Spatial distribution of the pixel-level prior and posterior $CO_2$ fluxes of the inversion with spatially homogenised NEE prior fluxes, the difference between prior and posterior flux estimates, and the uncertainty reduction relative to the prior uncertainty for May 2012.

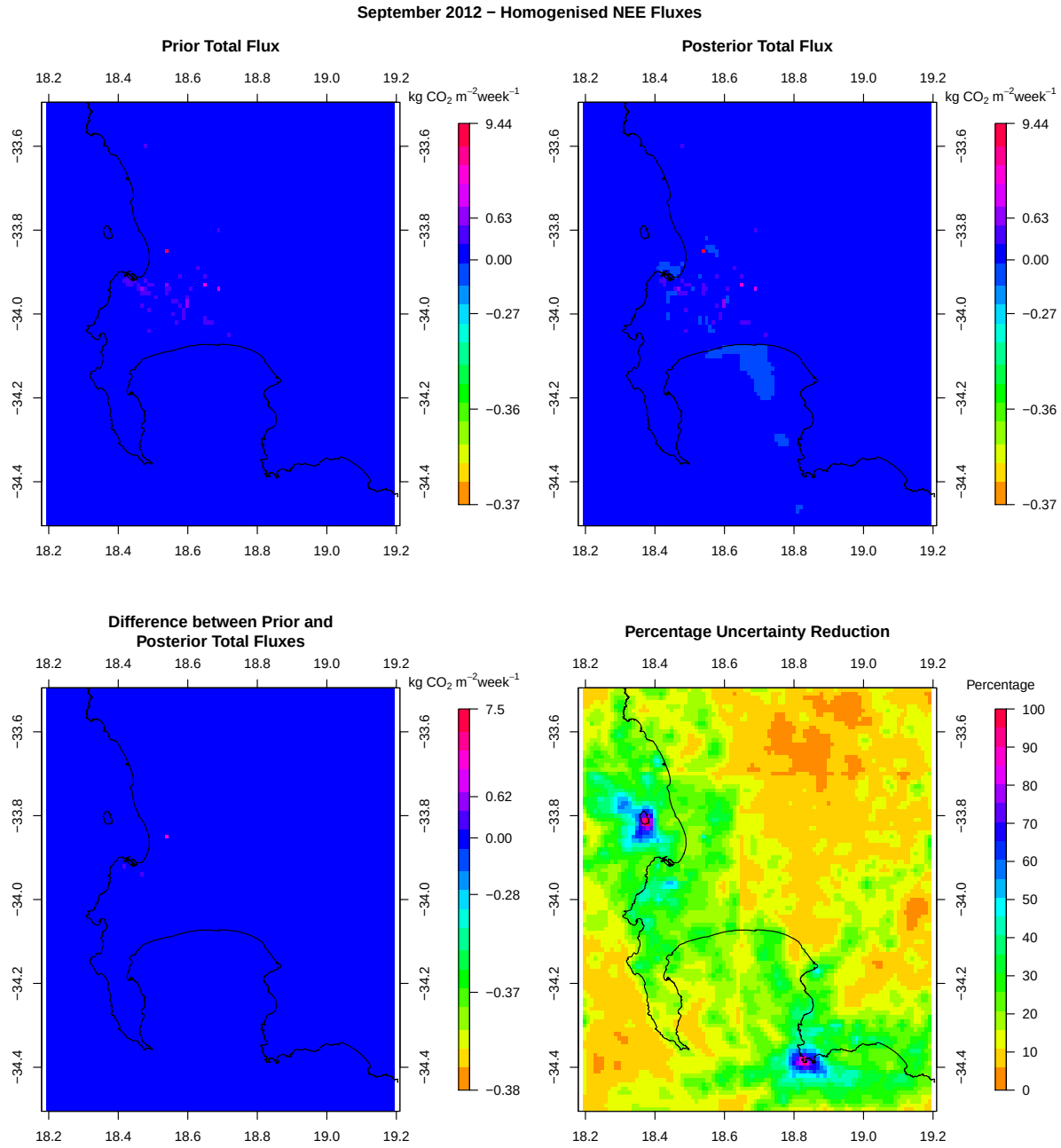


Figure C.65: Spatial distribution of the pixel-level prior and posterior $CO_2$ fluxes of the inversion with spatially homogenised NEE prior fluxes, the difference between prior and posterior flux estimates, and the uncertainty reduction relative to the prior uncertainty for September 2012.

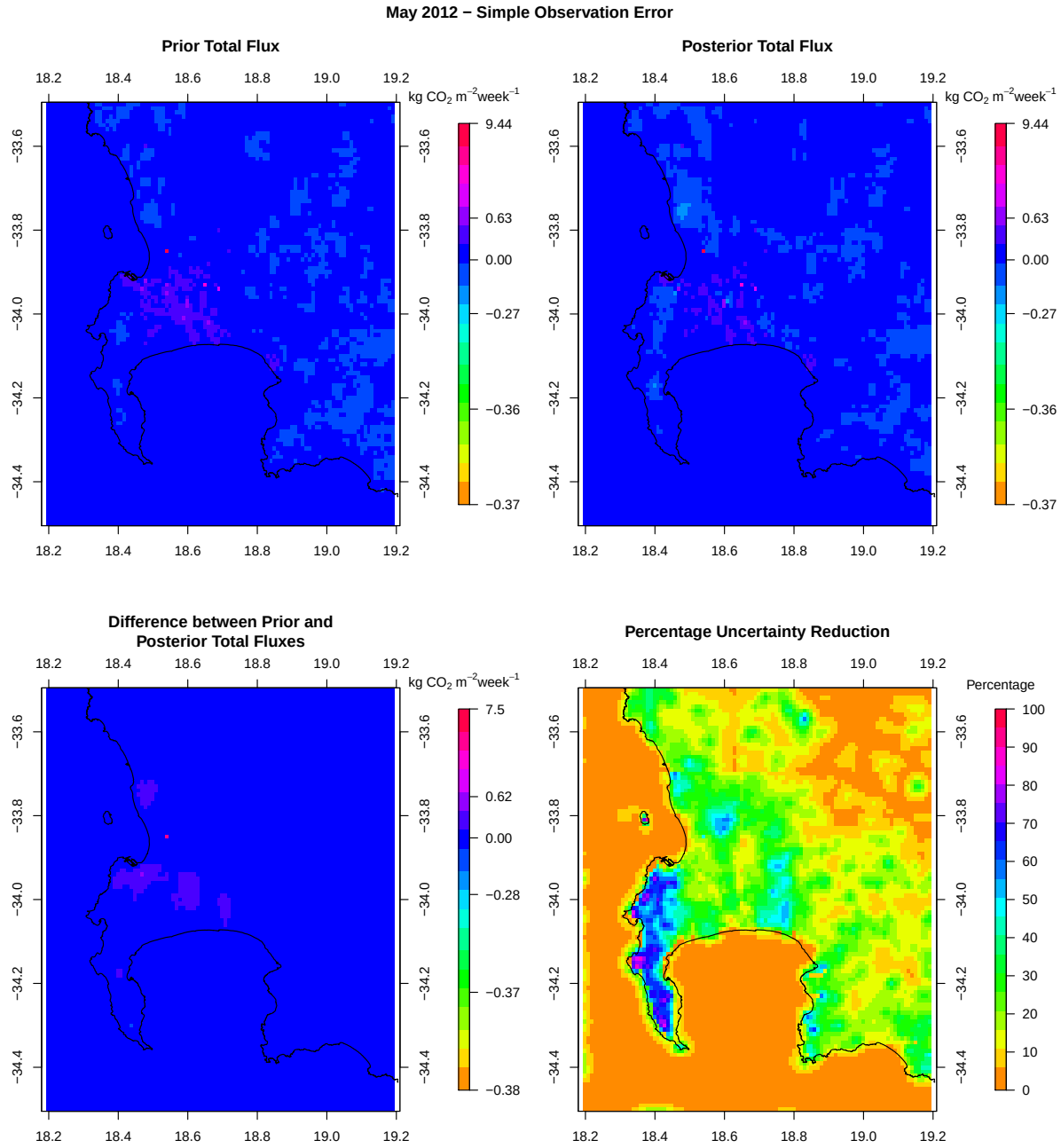


Figure C.66: Spatial distribution of the pixel-level prior and posterior $CO_2$ fluxes of the inversion specifying uncertainties of 2 ppm and 4 ppm for the day and night-time observation errors, the difference between prior and posterior flux estimates, and the uncertainty reduction relative to the prior uncertainty for May 2012.

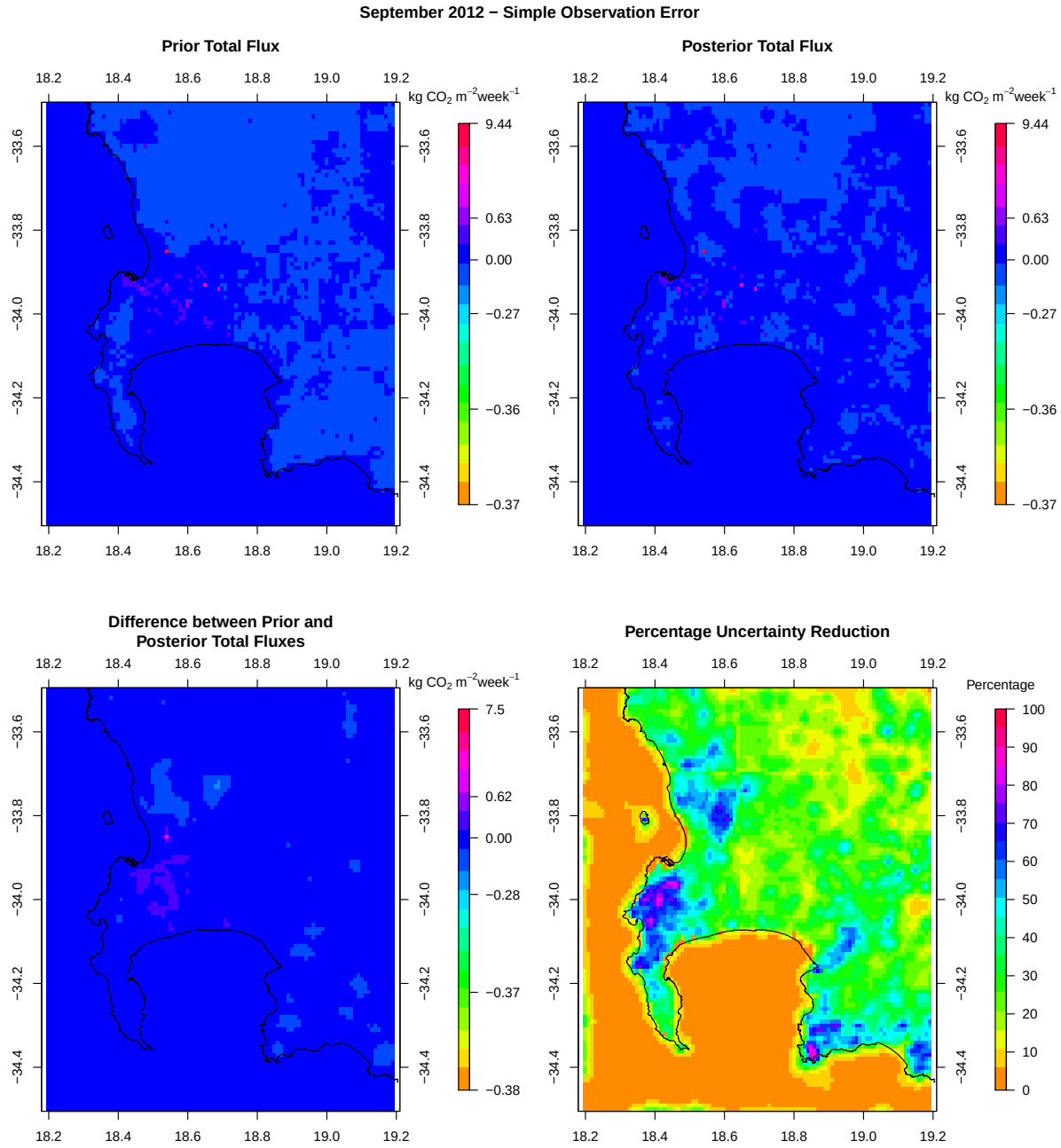


Figure C.67: Spatial distribution of the pixel-level prior and posterior $CO_2$ fluxes of the inversion specifying uncertainties of 2 ppm and 4 ppm for the day and night-time observation errors, the difference between prior and posterior flux estimates, and the uncertainty reduction relative to the prior uncertainty for September 2012.

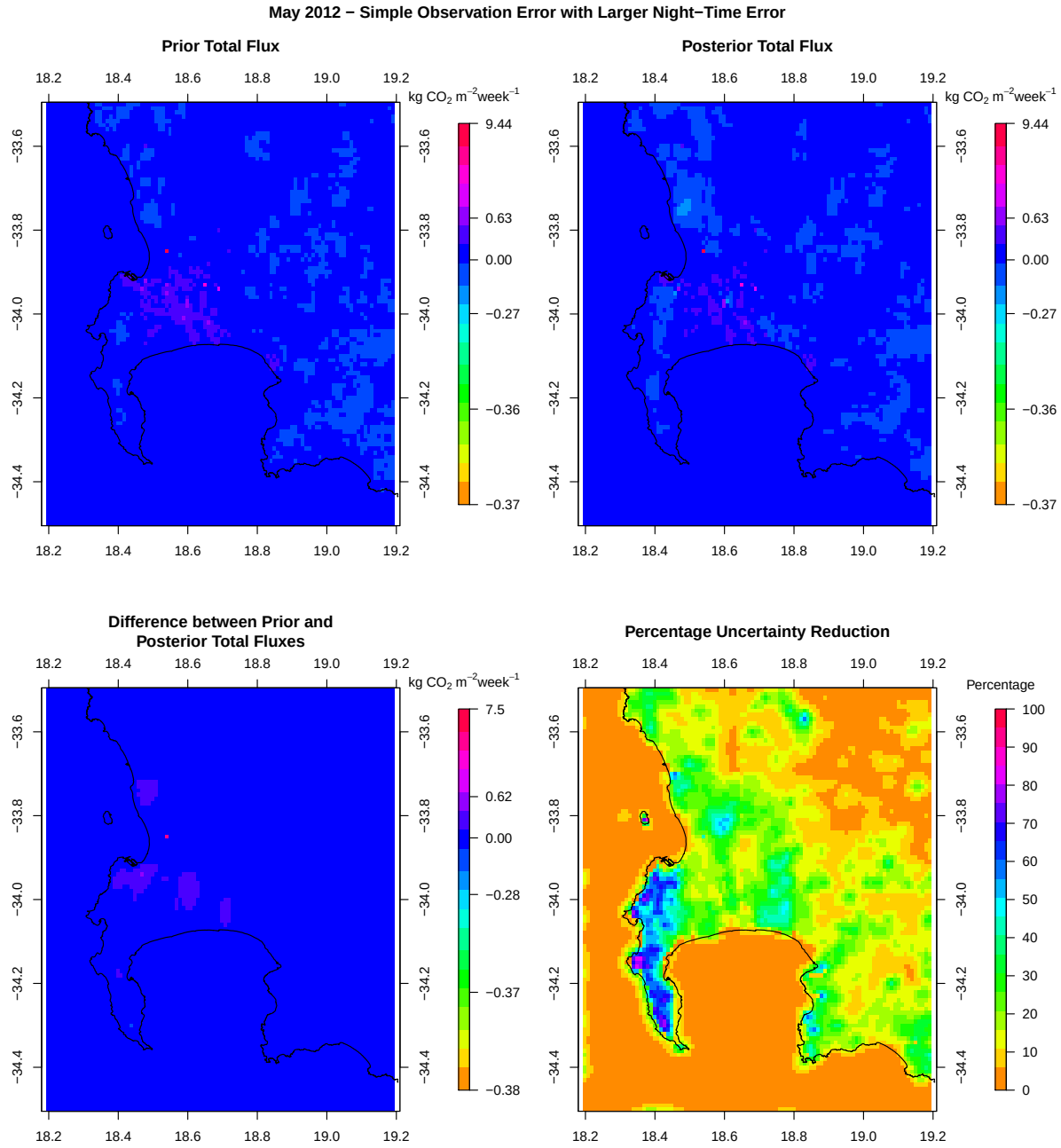


Figure C.68: Spatial distribution of the pixel-level prior and posterior $CO_2$ fluxes of the inversion specifying uncertainties of 2 ppm and 10 ppm for the day and night-time observation errors, the difference between prior and posterior flux estimates, and the uncertainty reduction relative to the prior uncertainty for May 2012.

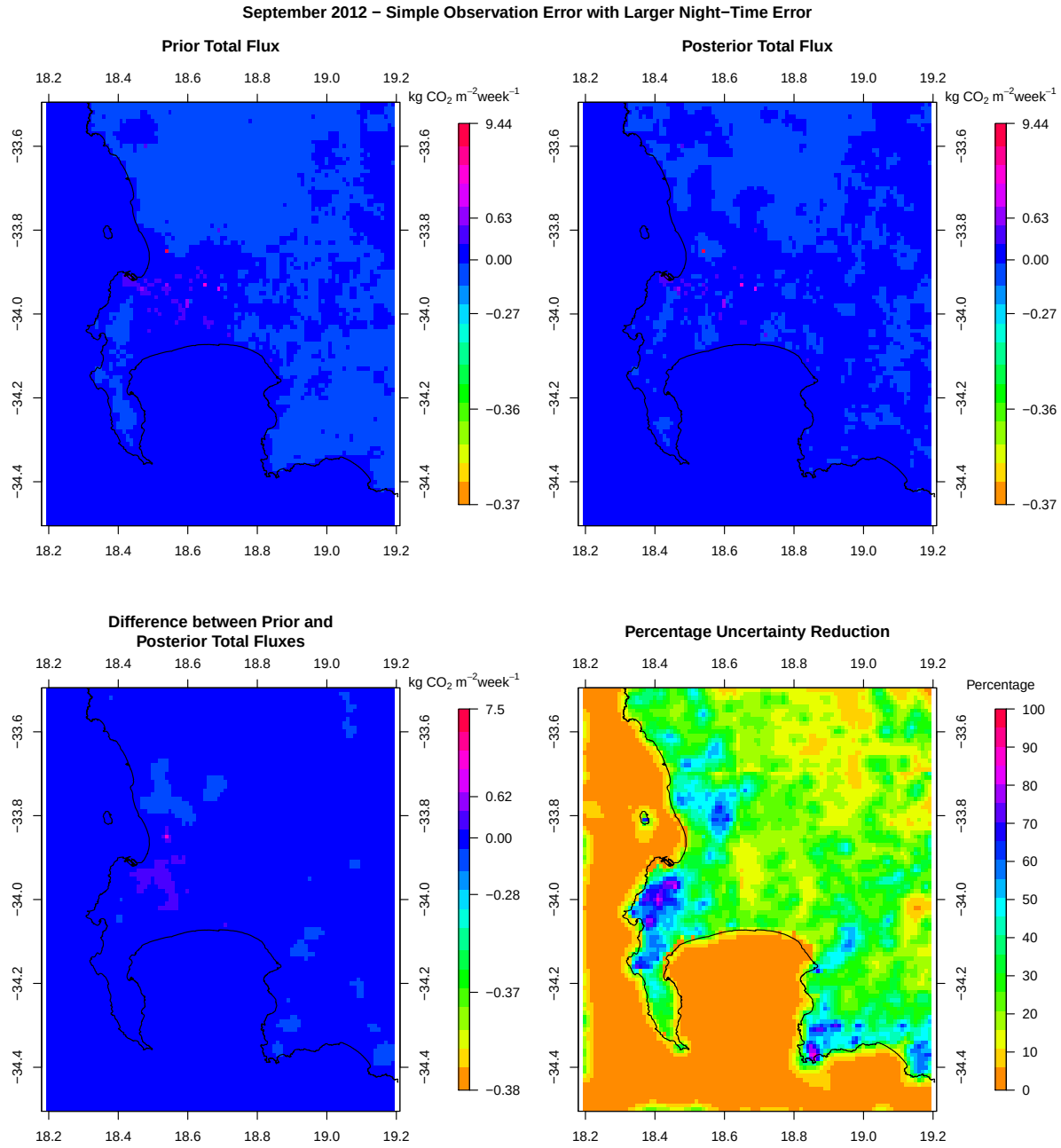


Figure C.69: Spatial distribution of the pixel-level prior and posterior $CO_2$ fluxes of the inversion specifying uncertainties of 2 ppm and 10 ppm for the day and night-time observation errors, the difference between prior and posterior flux estimates, and the uncertainty reduction relative to the prior uncertainty for September 2012.

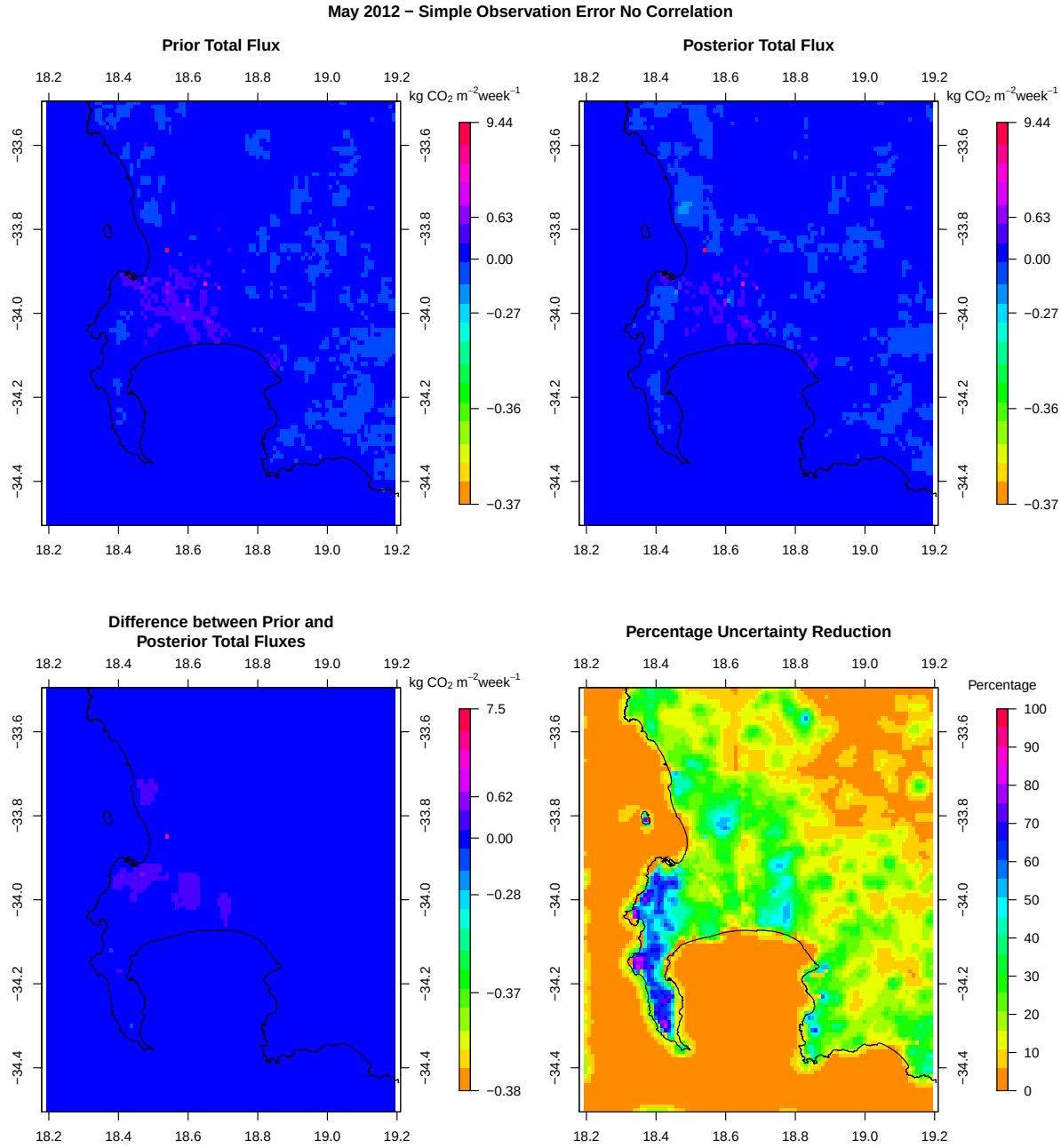


Figure C.70: Spatial distribution of the pixel-level prior and posterior $CO_2$ fluxes of the inversion specifying uncertainties of 2 ppm and 4 ppm for the day and night-time observation errors with no correlation, the difference between prior and posterior flux estimates, and the uncertainty reduction relative to the prior uncertainty for May 2012.

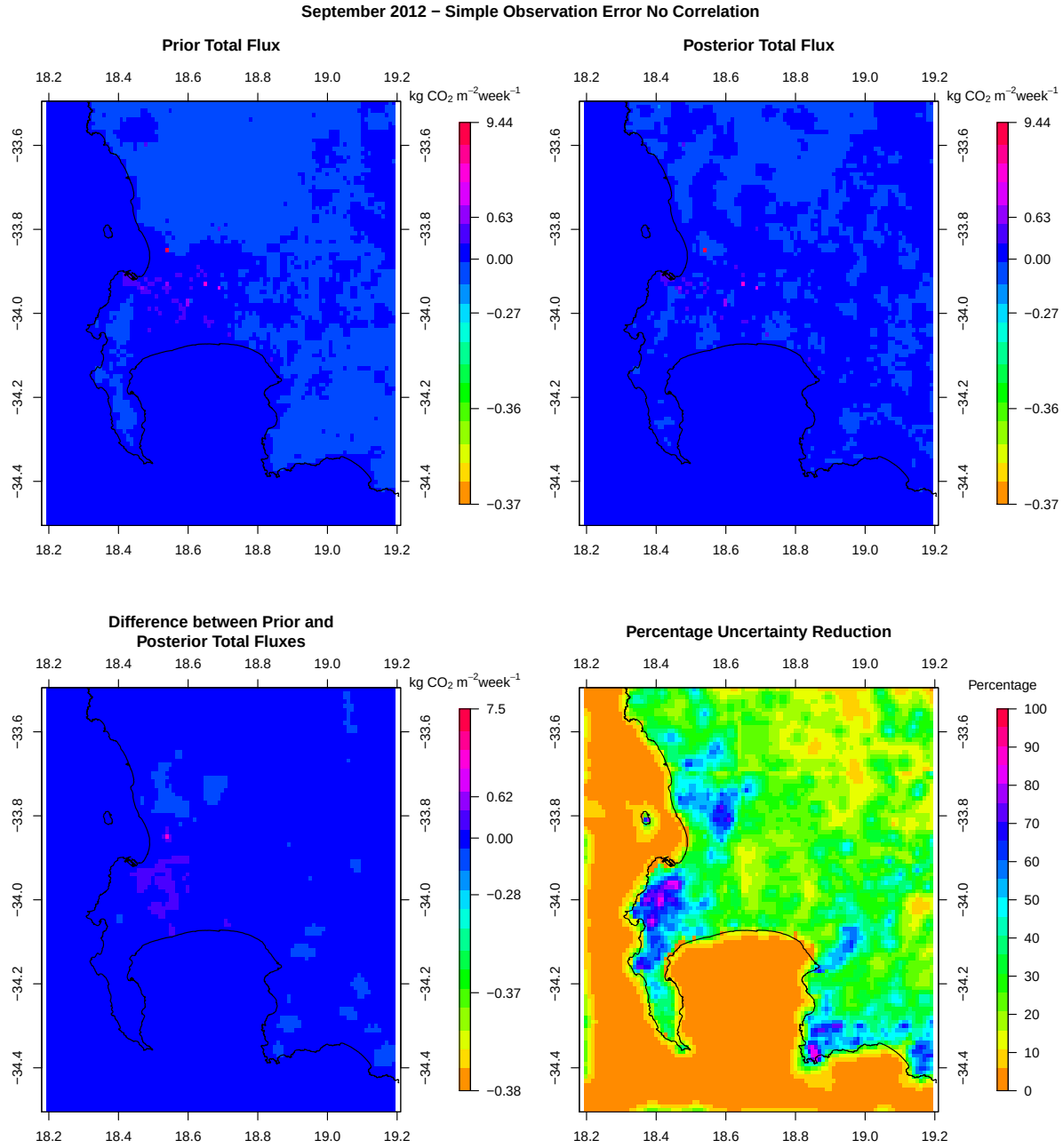


Figure C.71: Spatial distribution of the pixel-level prior and posterior $CO_2$ fluxes of the inversion specifying uncertainties of 2 ppm and 4 ppm for the day and night-time observation errors with no correlation, the difference between prior and posterior flux estimates, and the uncertainty reduction relative to the prior uncertainty for September 2012.

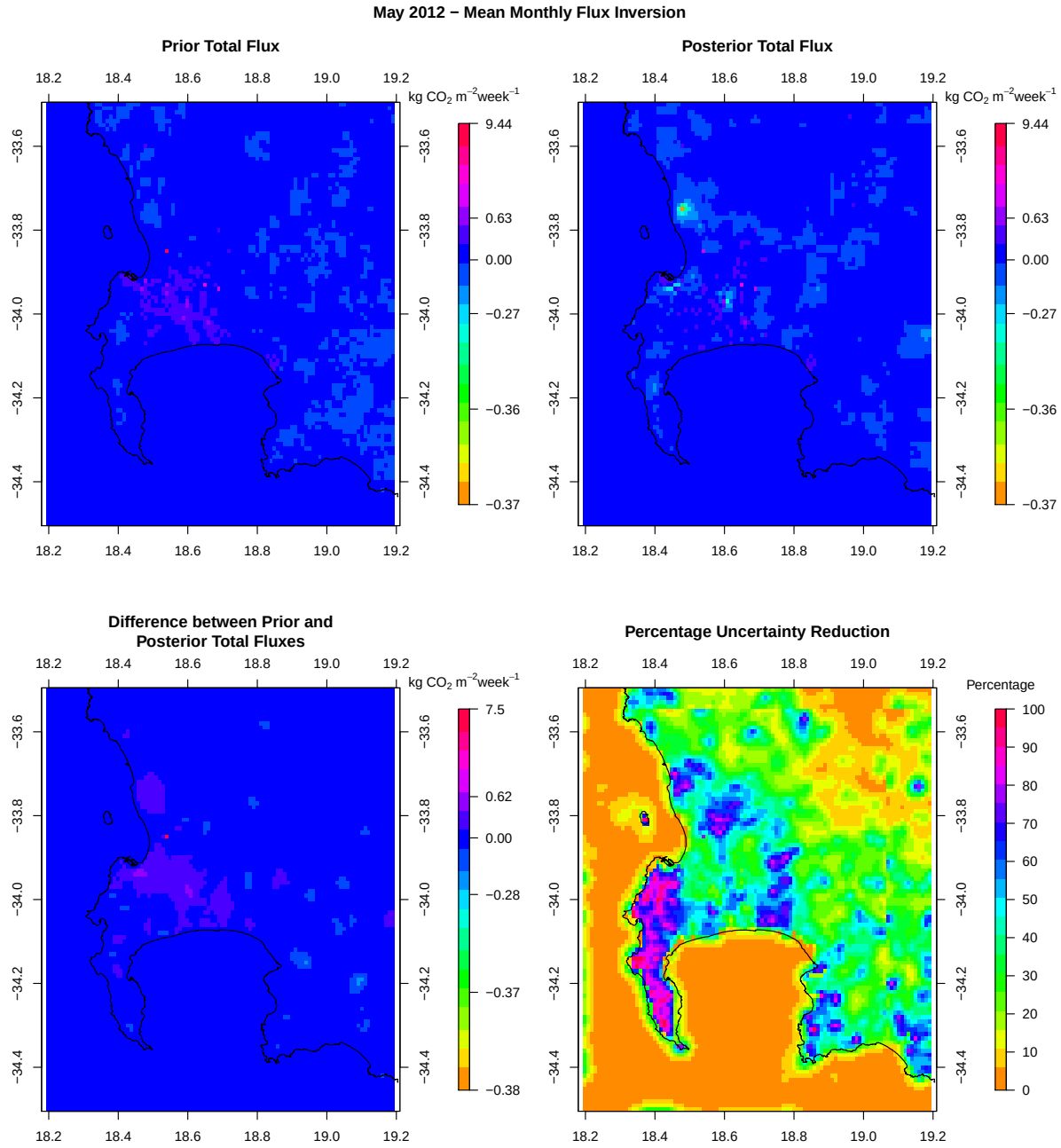


Figure C.72: Spatial distribution of the pixel-level prior and posterior $CO_2$ fluxes of the inversion solving for the mean weekly flux, the difference between prior and posterior flux estimates, and the uncertainty reduction relative to the prior uncertainty for May 2012.

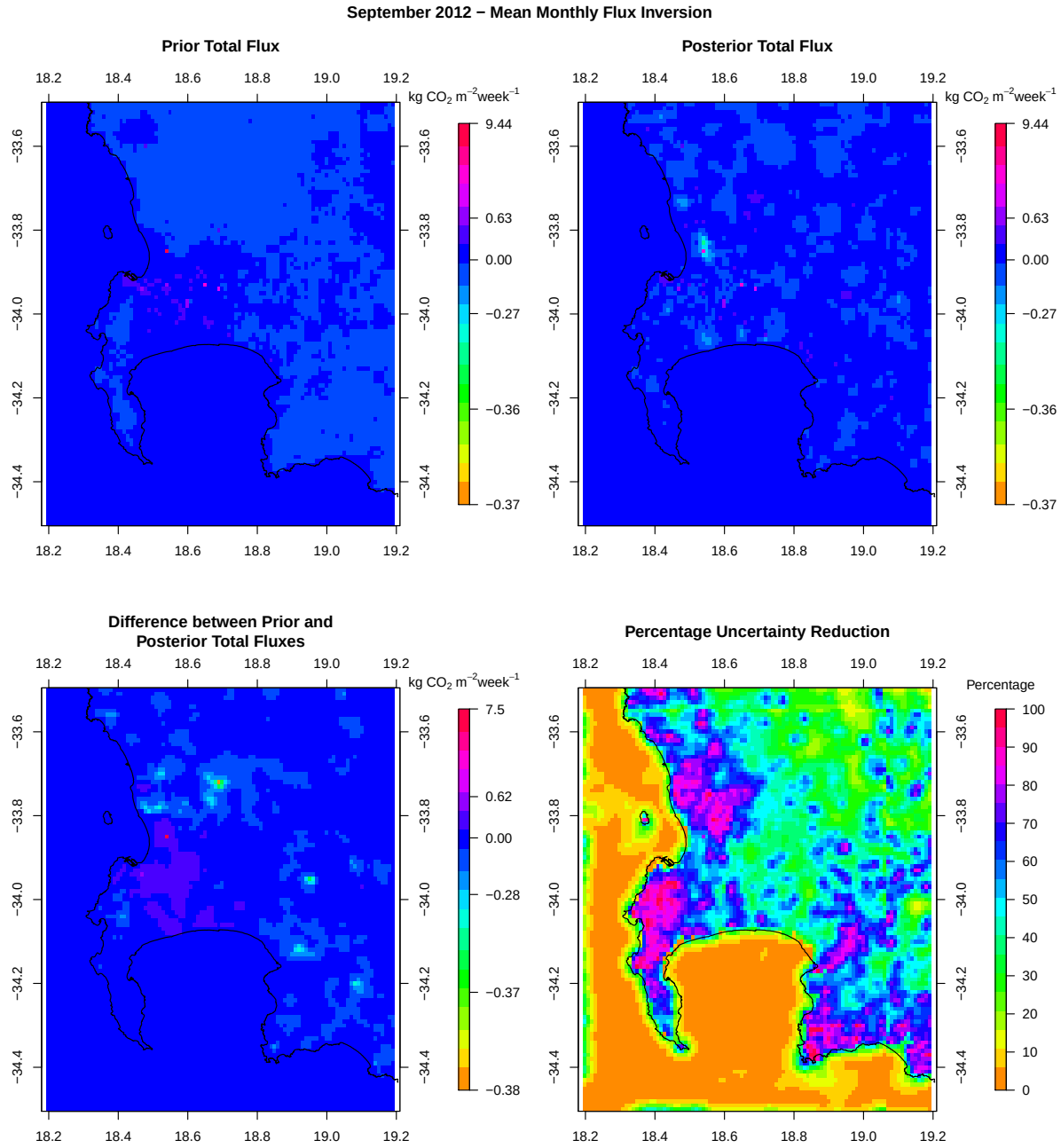


Figure C.73: Spatial distribution of the pixel-level prior and posterior $CO_2$ fluxes of the inversion solving for the mean weekly flux, the difference between prior and posterior flux estimates, and the uncertainty reduction relative to the prior uncertainty for September 2012.

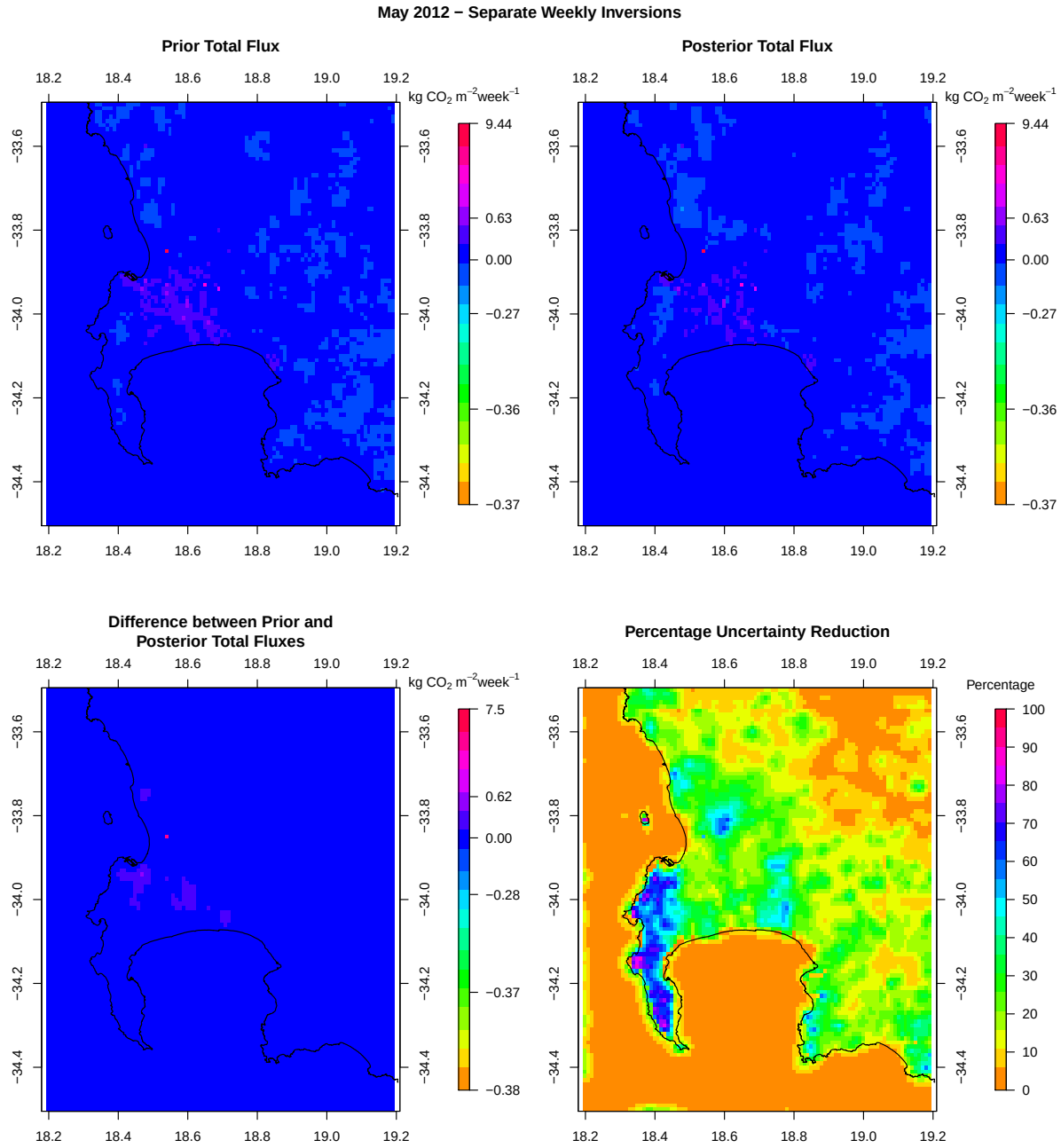


Figure C.74: Spatial distribution of the pixel-level prior and posterior $CO_2$ fluxes of the separate weekly inversions, the difference between prior and posterior flux estimates, and the uncertainty reduction relative to the prior uncertainty for May 2012.

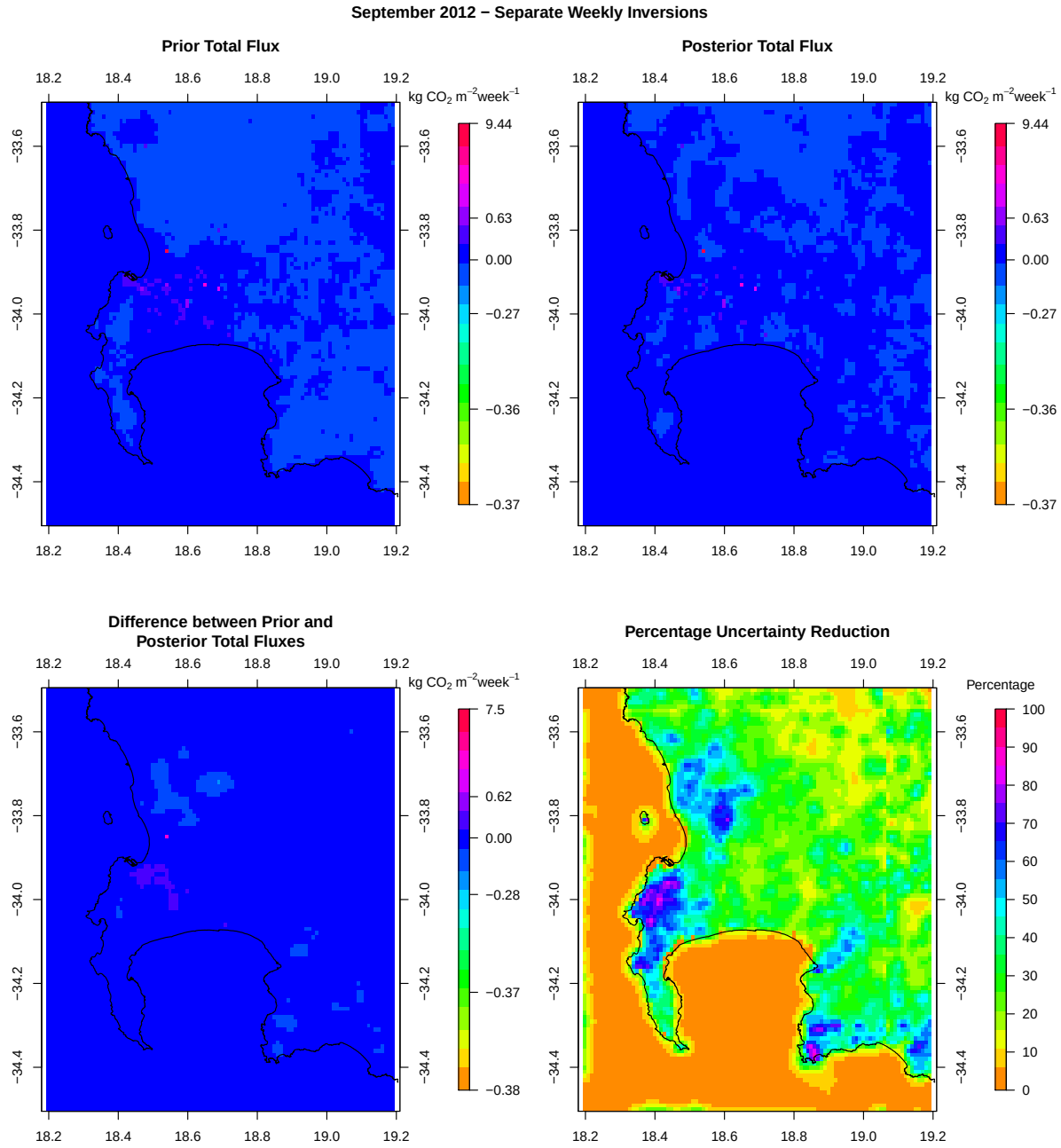


Figure C.75: Spatial distribution of the pixel-level prior and posterior $CO_2$ fluxes of the separate weekly inversions, the difference between prior and posterior flux estimates, and the uncertainty reduction relative to the prior uncertainty for September 2012.

## C.6 Toy Inversion

Here we consider a toy inversion problem introduced in Nickless et al. (2018). Let us consider an hourly measurement at a single site, with a fossil fuel flux daytime source, a fossil fuel flux night-time source, an NEE flux from the same location, and an NEE flux from a neighbouring pixel. We wish to solve for these four fluxes and the covariance matrix of the uncertainties in these fluxes. Selecting some of the most extreme values for the uncertainties and for the sensitivities for the current inversion framework we could get the following:

$$\mathbf{H} = \quad (0.0, 0.0126, 0.00902, 0.0032); \quad \mathbf{C}_{\boldsymbol{s}_0} = \quad \begin{pmatrix} 233 & 0 & 0 & 0 \\ 0 & 78 & 0 & 0 \\ 0 & 0 & 1578 & 1220 \\ 0 & 0 & 1220 & 1578 \end{pmatrix}; \quad \mathbf{C}_{\boldsymbol{c}} = 4$$

If we solve for the posterior uncertainty covariance matrix for a reference inversion we use:

$$\begin{aligned} \mathbf{C}_{\boldsymbol{s}} &= \left(\mathbf{H}^T \mathbf{C}_{\boldsymbol{c}}^{-1} \mathbf{H} + \mathbf{C}_{\boldsymbol{s}_0}^{-1}\right)^{-1} && \text{(C.1)} \\ &= \mathbf{C}_{\boldsymbol{s}_0} - \mathbf{C}_{\boldsymbol{s}_0} \mathbf{H}^T \left(\mathbf{H} \mathbf{C}_{\boldsymbol{s}_0} \mathbf{H}^T + \mathbf{C}_{\boldsymbol{c}}\right)^{-1} \mathbf{H} \mathbf{C}_{\boldsymbol{s}_0}. && \text{(C.2)} \end{aligned}$$

For this reference problem the solution is:

$$\mathbf{C}_{\boldsymbol{s}} = \quad \begin{pmatrix} 233 & 0 & 0 & 0 \\ 0 & 77.8 & -4.2 & -3.7 \\ 0 & -4.2 & 1500.2 & 1151.1 \\ 0 & -3.7 & 1151.1 & 1517.0 \end{pmatrix}$$

If we multiply the prior uncertainty covariance matrix by a constant, so that all the elements in the covariance matrix are multiplied by this factor, we can show that if there is no measurement error, i.e. $\mathbf{C}_{\boldsymbol{c}} = \mathbf{0}$, the posterior uncertainty covariance matrix can be obtained by multiplying the solution for the posterior uncertainty covariance matrix of the reference problem by this factor.

$$\begin{aligned} \mathbf{C}_{\boldsymbol{s}_{mod}} &= \left(\mathbf{H}^T \mathbf{C}_{\boldsymbol{c}}^{-1} \mathbf{H} + (a\mathbf{C}_{\boldsymbol{s}_0})^{-1}\right)^{-1} && \text{(C.3)} \\ &= a\mathbf{C}_{\boldsymbol{s}_0} - a\mathbf{C}_{\boldsymbol{s}_0} \mathbf{H}^T \left(\mathbf{H} a \mathbf{C}_{\boldsymbol{s}_0} \mathbf{H}^T + \mathbf{C}_{\boldsymbol{c}}\right)^{-1} \mathbf{H} a \mathbf{C}_{\boldsymbol{s}_0} && \text{(C.4)} \\ &= a(\mathbf{C}_{\boldsymbol{s}_0} - \mathbf{C}_{\boldsymbol{s}_0} \mathbf{H}^T \left(\mathbf{H} a \mathbf{C}_{\boldsymbol{s}_0} \mathbf{H}^T + \mathbf{C}_{\boldsymbol{c}}\right)^{-1} \mathbf{H} a \mathbf{C}_{\boldsymbol{s}_0}) && \text{(C.5)} \end{aligned}$$

Now make $\mathbf{C}_{\boldsymbol{c}} = \mathbf{0}$

$$\mathbf{C}_{\boldsymbol{s}_{mod}} = a(\mathbf{C}_{\boldsymbol{s}_0} - \mathbf{C}_{\boldsymbol{s}_0}\mathbf{H}^T\frac{1}{a}\left(\mathbf{H}\mathbf{C}_{\boldsymbol{s}_0}\mathbf{H}^T + \mathbf{C}_{\boldsymbol{c}}\right)^{-1}\mathbf{H}a\mathbf{C}_{\boldsymbol{s}_0}) \quad \text{(C.6)}$$

$$= a(\mathbf{C}_{\boldsymbol{s}_0} - \mathbf{C}_{\boldsymbol{s}_0}\mathbf{H}^T\left(\mathbf{H}\mathbf{C}_{\boldsymbol{s}_0}\mathbf{H}^T + \mathbf{C}_{\boldsymbol{c}}\right)^{-1}\mathbf{H}\mathbf{C}_{\boldsymbol{s}_0}) \quad \text{(C.7)}$$

$$= a\mathbf{C}_{\boldsymbol{s}} \quad \text{(C.8)}$$

We can demonstrate this in our toy example. If we make $\mathbf{C}_{\boldsymbol{c}} = 0$ the solution is

$$\mathbf{C}_{\boldsymbol{s}} = \begin{pmatrix} 233 & 0 & 0 & 0 \\ 0 & 73.8 & -78.4 & -69.4 \\ 0 & -78.4 & 131.1 & -60.8 \\ 0 & -69.4 & -60.8 & 444.4 \end{pmatrix}$$

and if we multiply $\mathbf{C}_{\boldsymbol{s}_0}$ by 2 then the solution is

$$\mathbf{C}_{\boldsymbol{s}_{mod}} = \begin{pmatrix} 466 & 0 & 0 & 0 \\ 0 & 147.5 & -156.8 & -138.8 \\ 0 & -156.8 & 262.1 & -121.4 \\ 0 & -138.8 & -121.4 & 888.8 \end{pmatrix}; \quad \mathbf{C}_{\boldsymbol{s}_{mod}} = 2\mathbf{C}_{\boldsymbol{s}}$$

For our original problem where $\mathbf{C}_{\boldsymbol{c}} = 4$, if we multiply $\mathbf{C}_{\boldsymbol{s}_0}$ by 2 the solution is

$$\mathbf{C}_{\boldsymbol{s}_{mod}} = \begin{pmatrix} 466 & 0 & 0 & 0 \\ 0 & 155.1 & -16.0 & -14.2 \\ 0 & -16.0 & 2860.6 & 2178.5 \\ 0 & -14.2 & 2178.5 & 2924.6 \end{pmatrix};$$

Compared to:

$$\mathbf{C}_{\boldsymbol{s}} = \begin{pmatrix} 233 & 0 & 0 & 0 \\ 0 & 77.8 & -4.2 & -3.7 \\ 0 & -4.2 & 1500.2 & 1151.1 \\ 0 & -3.7 & 1151.1 & 1517.0 \end{pmatrix}; 2\mathbf{C}_{\boldsymbol{s}} = \begin{pmatrix} 466 & 0 & 0 & 0 \\ 0 & 155.5 & -8.4 & -7.5 \\ 0 & -8.4 & 3000.4 & 2302.2 \\ 0 & -7.5 & 2302.2 & 3034.1 \end{pmatrix}$$

For those sources where sensitivities were zero, the uncertainty covariance $C_{s_{mod}}$ is equal to exactly $2 \times C_s$. Diagonal elements of $\mathbf{C}_{\boldsymbol{s}_{mod}}$ were approximately equal to the diagonal elements of $2\mathbf{C}_{\boldsymbol{s}}$, but non-zero off-diagonal elements were greater in size than non-zero off-diagonal elements $2\mathbf{C}_{\boldsymbol{s}}$.

# Bibliography

Nickless, A., Rayner, P. J., Engelbrecht, F., Brunke, E.-G., Erni, B., and Scholes, R. J.: Estimates of $CO_2$ fluxes over the city of Cape Town, South Africa, through Bayesian inverse modelling, Atmos. Chem. Phys., 18, 4765–4801, doi: 10.5194/acp-18-4765-2018, 2018.